Engineering topological states in arrays of magnetic molecules in interaction with a 2D superconductor

Danilo Longo

Sorbonne Université

École Doctorale 397 Physique et Chimie des Matériaux

Institut des NanoSciences de Paris

Engineering topological states in arrays of magnetic molecules in interaction with a 2D supercon ductor

par Danilo LONGO

Thèse de doctorat de Physique et Chimie des Matériaux

Dirigée par Nadine Witkowski et Tristan Cren

Presentée et soutenue publiquement le 13 mai 2019

Devant un jury composé de:

Sophie Guéron, DR CNRS, Laboratoire de Physisque des Solides, Rapportrice
Bertrand Kierren, Professeur, Institut Jean Lamour, Rapporteur
Clemens Winkelmann, Maître de Conférences, Institut Néel , Examinateur
Gwendal Feve, Professeur, Laboratoire Pierre Aigrain, Examinateur
Nicolas Lorente, Research Scientist, Centro de fisica de materiales, Examinateur
Christophe Brun, CR CNRS, Institut des NanoSciences de Paris, Invité
Tristan Cren, DR CNRS,Institut des NanoSciences de Paris, Co-Directeur de thése
Nadine Witkowski, Professeur, Institut des NanoSciences de Paris, Directrice de thèse

Table of contents

Abstract

Recent studies predicted that the interaction between a 2D superconductor and local magnetism could induce topological superconductivity accompanied by Majorana edge states. To address this challenge, we have studied a system based on the interaction between self-assemblies of molecular magnets, i.e. manganese phthalocyanines (MnPcs), and thin films of lead (1 and 3 monolayers) grown on Si(111) surfaces that show 2D superconductivity. Our Scanning Tunneling Microscopy (STM) experiments revealed that, adsorption of a tiny amount of MnPcs on a Pb monolayer is accompanied by a very small charge transfer inducing a macroscopic structural phase transition of the surface itself. Scanning Tunneling Spectroscopy (STS) experiments at 300mK on 3 monolayers thick islands of Pb/Si(111) showed the presence of non-trivial effects responsible for the spatial fluctuation of the coherence peaks amplitude on a length scale much smaller than the superconducting coherence length. Furthermore, contrary to what shown on bulk Pb substrates, STS experiments strongly suggest that isolated MnPcs are always found in a weak interaction regime with the 3 monolayers thick Pb islands. Our results together with the observation of an in-gap spectroscopic feature located at the edge of a self-assembled 2D domain of MnPcs pave the route to future studies for the engineering of superconducting topological phases.

Résumé

Des études récentes ont prédit que l'interaction entre un supraconducteur 2D et du magnétisme local pourrait induire une supraconductivité topologique accompagnée d'états de bord de type Majorana. Pour relever ce défi, nous avons étudié un système basé sur l'interaction entre des auto-assemblages d'aimants moléculaires, tels que les phtalocyanines de manganèse (MnPcs), sur des films minces de plomb (1 et 3 monocouches) épitaxiés sur des surfaces de Si(111) qui montrent une supraconductivité 2D. Nos expériences de Microscopie à effet tunnel (STM) ont révélé que l'adsorption d'une petite quantité de MnPcs sur la monocouche de Pb est accompagnée d'un très faible transfert de charge qui induit une transition de phase structurale macroscopique de la surface elle-même. Les expériences de Spectroscopie à effet tunnel (STS) à 300 mK sur des îlots tricouches de Pb/Si(111) ont montré la présence d'effets non triviaux responsables de la fluctuation spatiale de l'amplitude des pics de cohérence sur des longueurs bien inférieures à la longueur de cohérence supraconductrice. De plus, contrairement à ce qui a été montré sur des monocristaux de plomb, les expériences STS suggèrent que les MnPcs isolées sur des îlots tricouches de plomb se trouvent toujours dans un régime d'interaction faible avec le substrat. L'ensemble de nos résultats, ainsi que l'observation d'une signature spectroscopique localisée sur le bord d'un domaine auto-organisé de MnPcs ouvrent la voie à de futures études sur l'ingénierie des phases topologiques supraconductrices.

Remerciements

Tout d'abord je voudrais remercier tous les membres du jury qui ont accepté de consacrer une partie de leur temps à lire et juger mon travail de thèse.
Après cela, il est difficile de remercier en quelques lignes toutes les personnes qu'au cours des ces trois ans (ou même plus) m'ont accompagné dans cette merveilleuse aventure. En tout cas, il y a des gens que je tiens à remercier et desquelles je garderai un excellent souvenir.

Merci à Nadine Witkowski qui, après m'avoir amené au synchrotron (en Suède) seuelement deux semaines après mon arrivée en France, m'a fait confiance et m'a proposé un sujet de thèse très ambitieux que j'ai eu la possibilité de développer pendant ces anées. Je remercie également Tristan Cren, une personne toujours disponible pour discuter, qui m'a transmis l'amour pour une compréhension profonde de la réalité dans laquelle nous vivons. Un remerciement particulier à Christophe Brun qui m'a guidé et conseillé depuis le début de la thèse afin que même les plus petits aspects soient traités avec le plus grand soin et de la meilleure façon.

Comment ne pas remercier Hervé Cruguel (et son barbecue), Sébastien Royer (dit Sebatien roi), François Debontridder et Pascal David à qui j'ai eu le grand plaisir de donner beaucoup de "trucs a faire" pendant ces années et dont la contribution a été décisive pour l'avancement de ce travail. L'importance de leur soutien psychologique (très souvent autour d'un verre) à différentes occasions est remarquable.

Un merci général à toutes les personnes qui ont contribué à rendre l'expérience INSP très agréable. Je remercie en particulier Alberto Curcella, Léo Bossard-Giannesini, Clément Livache (avec son "melo di cotogno") et William Watkins avec qui j'ai partagé le bureau pendant les deux premières années et les événements extra-scientifiques qui ont tourné autour de cette salle. Je remerice aussi Corinne Poisson, Christophe Rafaillac et François Rey pour les nombreux cafés/verres pris ensemble. Je remercie également tous les autres membres des deux équipes avec qui j'ai eu le plaisir de partager mon expérience ainsi que tous les

doctorants de l'INSP. Je remercie aussi Greg Cabailh, Vincent Humblot et Emmanuel Lhullier parce que leurs conseils ont été éclairants à plusieurs reprises.

Un merci important va aux 3ML de plomb sur silicium, ces blagueurs qui ont eu le sadisme de se montrer au maximum de leur splendeur dans le tout premier échantillon et ensuite ... plus jamais !!! Merci!

Un grand merci va à tous les amis historiques sur lesquels je peux toujours compter:
Rita & Giuseppe (Rita) + Silvia, Gianchi (pour les amis Caligola), Federica & Simone + Filippo, Enrica, Ilaria & Massimiliano (merci à kuopio). Merci également à tous les amis que j'ai retrouvés au fil des ans loin de Lecce: Elisa & Ber, Alessandro & Ester, Alessandro Giachino, Francesca, Cippo, Anna, Daniela de Bari, Daniele & Clara, Stefania, Michelone, Ilaria, Junior, Omid, Valerio & Ginevra. Un merci spécial à Mattia, une personne sincère et humble chez qui j'ai trouvé une personne passionnée de la vie qui m'a apporté un soutien considérable au cours de ces années. Merci également aux amis de rouen, Andrea et Sorina, pour toutes les heures passées à jouer et pour toutes les expériences que nous avons vécues.

Un merci special c'est pour mes parents qui m'ont toujours encouragé dans les choix et m'ont soutenu chaque fois que j'en avais besoin. Merci à mes frères et soeurs mais sourtout à Noemi, Matteo, Martina et Antonio, étoiles polaires dans ma vie qui remplissent mon coeur de joie et positivité. Un grand merci à Marina et Rocco toujours présent dans les moments importants et prêt à me soutenir.

Une ligne seulement pour remercier "lozio" parce que sinon je ne pourrai plus jamais retourner en Italie. Un merci spécial à "zio Romeo" une des personnes les plus fortes que je connaisse, depuis toujours un modèle et un point de référence.

Le remerciement le plus important va à une personne spéciale qui a partagé avec moi chaque moment de cette expérience. Merci parce que tu m'as toujours soutenu avec douceur infinie et parce que tu as résisté à la rédaction! Merci parce que ta présence dans ma vie c'est enrichissant et me pousse à faire toujours de mon mieux. Merci Diletta.

Introduction

Research on superconductivity found renewed interest starting from the last decade, when theoretical works have announced the possibility to "fabricate" new topological phases in superconductive solid-state systems with peculiar electronic properties such as the presence of Majorana edge states. Direct experimental observation of these states would have huge technological impact because they are good candidates for engineering single qubits and their manipulation may be used to develop real quantum computational systems. Recent works have predicted that combination of superconductivity with spin-orbit coupling and Zeeman splitting can, under specific conditions, induce topological superconductivity with the emergence of Majorana edge states. These three ingredients, independently, have been the subject of intensive work in solid-state physics. However, their combination and the control of their relative strength appears extremely challenging from the experimental point of view for engineering such topological superconducting states.

In my thesis, I have studied a promising good candidate to address this challenge consisting in molecular magnets self-assembled on very thin films of lead grown on Si(111) surfaces. Recent investigation of very thin Pb films grown on Si(111) revealed the existence of 2D superconductivity down to a single atomic layer. Furthermore, proper growth conditions make it possible to obtain highly crystalline Pb films whose thickness can be tuned at the atomic level. More interestingly, the low dimensionality of Pb films induces an enhanced Rashba spin-orbit coupling. It is clear that using thin films of Pb provides us with two of the three ingredients needed to have a topological transition, i.e. superconductivity and built-in Rashba spin-orbit coupling. Local magnetism is introduced by depositing on top of the 2D substrate, organo-metallic molecular magnets, such as manganese phthalocyanines (MnPcs), that hold a magnetic ion in their center. The idea of using organic molecules instead of single magnetic atoms is prompted by the need to build large magnetic domains that can be easily obtained thanks to their self-assembly properties. Single atomic manipulation is a viable alternative but it can become time-consuming if very large domains are targeted. Furthermore, in case of strong interaction between molecules and substrate, the latter can naturally drive the formation of a wide variety of assemblies with different structures. A

last advantage of molecular magnets over single magnetic atoms is the possibility to tune their spin and thus their magnetic properties, e.g. by replacing central magnetic ion, while preserving all the other properties mentioned above.
Deposition of molecular magnets on top of a 2D superconductor induces the appearance of localized bound states within the superconducting gap known as Shiba states. Under right conditions, interaction between several Shiba states induced by a self-assembled array of molecular magnets may lead to their hybridization and realize new topological superconducting phases. The experimental signature of such phases is the emergence of chiral edge states surrounding the magnetic array, i.e. at the border between the topological region (the one covered by molecules) and the non-topological one (the rest of the sample). However, all these coupling conditions between molecules and substrate are not automatically fulfilled because many other effects may intervene when organic molecules adsorb on a substrate. Many of these effects depend on the relative strength of the molecule-molecule and molecule-substrate interactions. For this reason, in order to reach a deep understanding of the interplay between MnPcs and Pb thin films, a comprehensive study of the structure and self-assembly properties of MnPcs is a prerequisite to further investigate the emergence of topological superconductivity in a controlled manner.

This thesis is organized in 4 chapters as described below. The first and second chapter contain all the theoretical and experimental tools necessary to read the rest of the manuscript. Third and fourth chapter contain the experimental results obtained by means of Scanning Tunneling Microscopy and Spectroscopy on two different types of samples: MnPcs deposited on Pb monolayers grown on Si(111) (Chapter 3) and MnPcs deposited on 3 ML Pb films (or islands) grown on Si(111) (Chapter 4). It should be noted that each of these chapters has an introductory part which aims at providing the reader with an overview about the complexity of the system under investigation. The last chapter (Chapter 4) also contains the experimental results related to the magnetic coupling between either isolated or self-assembled MnPcs and 3 ML Pb films.

Chapter 1: The first chapter contains basic notions of superconductivity and Kondo effect needed to understand the following chapters. Furthermore, it introduces to the concepts of Shiba states arising from the interaction between magnetic impurities and conduction electrons of a superconductor. Particular attention is paid to the role of both magnetic (exchange interaction) and non-magnetic (diffusive interaction) terms in determining the properties of Shiba states. A bibliographic overview is also provided to show the state of the art on the subject. A the end of the chapter the necessary conditions to have a topological

superconductor is discussed together with the most important experimental evidences in this area.

Chapter 2: The operating principle of the experimental techniques used to probe structural and electronic properties of samples is given in this chapter, i.e. Low Energy Electron Diffraction (LEED), Scanning Tunneling Microscopy (STM) and Scanning Tunneling Spectroscopy (STS). As different experimental setups were used in this work, each of them isbriefly described. Furthermore, special attention is paid to a UHV suitcase that was purposely developed during this thesis to allow molecular evaporations in very clean conditions. In particular, all the technical difficulties related to its commissioning are presented. The last part of the chapter contains a very brief description of both the substrate on top of which our samples are grown, i.e. Si(111), and the organic molecules used to introduce magnetism in the system.

Chapter 3: This part presents the growth of self-assembled molecular magnets on top of a single atomic layer of Pb grown on top of Si(111). The idea is to use the particular structure of the $\sqrt{7} \times \sqrt{3}$-Pb phase, exhibiting groove domains, as a template surface for the self-assembly of linear chains of molecular magnets. However, molecular adsorption on top of the Pb monolayer results in unexpected effects.
The chapter starts with a bibliographic overview of the complex phase diagram characterizing the Pb monolayers which exhibit a number of surface reconstructions in a very tight range of coverages. The second part of the chapter presents the experimental preparation of the $\sqrt{7} \times \sqrt{3}$-Pb phase by means of Low Energy Electron Diffraction and Scanning Tunneling Microscopy, with particular attention on the difficulties in reaching a clean and defect-free surface. The main electronic properties of the $\sqrt{7} \times \sqrt{3}$-Pb phase are then listed. The central part of the chapter describes the unexpected and intriguing structural phase transition upon molecular adsorption. A novel self-assembling behavior of MnPcs on this surface is also evidenced.

Chapter 4: An alternative to the monolayer of Pb/Si(111) is given by 3 ML of Pb films in which 2D superconducting character is retained. The first part of the chapter gives a global overview about the important consequences of electron confinement (Quantum Well States) on both structural and electronic properties of Pb thin films. In the second part, I present the intriguing structural properties of an almost continuous 3 ML Pb film, a type of sample rarely observed. Contrary to what I observed in the case of a single atomic layer of lead, this sample presents self-organization of molecular magnets. The main electronic properties, i.e. Quantum Well States and superconductivity, probed by means of Scanning Tunneling

Spectroscopy (STS) at 300 mK, are discussed for a sample consisting of "disconnected" 3 ML Pb islands.
In particular, from the experimental results related to Quantum Well States, the intriguing interplay between confined electrons and structural relaxations in determining the moiré corrugation observed by STM on top of 3 ML Pb islands is discussed. Experimental results about the superconductivity of 3 ML Pb islands show the surprising role of moiré corrugation in modulating the superconducting coherence peaks on length scales much shorter than the superconducting coherence length. The presence of low-dimensional physics in 3 ML Pb islands is thus unveiled. The last part of the chapter is dedicated to the quest of topological superconductivity. The coupling between molecular magnets and superconductivity is investigated by means of Scanning Tunneling Spectroscopy at 300 mK. In particular, the issue of the interaction between an isolated molecular magnet and superconductivity related to the emergence of Shiba states is discussed. Finally, the experimental results dealing with the coupling of Shiba states within 2D molecular domains self-assembled on top of 3 ML Pb films and their possible implication in a topological transition are discussed.

Chapter 1

Interaction between magnetism and superconductivity: towards the topological superconductivity

1.1 A brief introduction to superconductivity

Superconductivity is an intriguing state of matter discovered in 1911 by Heike Kamerlingh Onnes [1]. The first experimental evidence of its existence was the sudden drop to zero of the resistivity of Hg below 4.2 K. By repeating the same experiment on different chemical elements it was ultimately shown that many materials exhibit this behavior. The second important property that characterizes the superconducting state is the perfect diamagnetism also known as Meissner-Ochsenfeld effect. In other words, a material in the superconducting state expels any external applied magnetic field. The first theory describing superconductivity is due to the brothers Fritz and Heinz London [2]. They developed a phenomenological theory able to explain the Meissner-Ochsenfeld effect by means of the introduction of a superconducting current density $\mathbf{j}_s(\mathbf{r})$ proportional to the potential vector $\mathbf{A}$:

$$\mathbf{j}_s(\mathbf{r}) = -\frac{n_s e^2}{m}\mathbf{A}(\mathbf{r}) \tag{1.1}$$

with n_s the superconducting electron density, e the elementary electric charge, m the electron mass and $\mathbf{A}(\mathbf{r})$ the potential vector satisfying the London Gauge ($\nabla \cdot \mathbf{A} = 0$). This relation can be used to calculate the characteristic length λ_L, known as penetration length, representing

the decay length of an external applied magnetic field within a superconductor:

$$\lambda_L = \frac{c}{e}\sqrt{\frac{m\varepsilon_0}{n_s}} \tag{1.2}$$

with c the speed of light in vacuum, e the elementary electron charge, m the electron mass, ε_0 the permittivity of free space and n_s the superconducting electron density. The phenomenological nature of this theory was not able to provide information about the microscopic mechanisms underlying superconducting behavior of materials.

The second important theory of superconductivity to be mentioned is due to Ginzburg and Landau [3]. It arises from a combination of the Schrodinger equation and the phase transition theory of Landau and it is still a macroscopic theory. The idea is to write the free energy associated to the superconducting state near the critical temperature (T_C) as a function of the temperature and the magnetic field. It is interesting to note that the free energy contains a complex order parameter $\Delta(\mathbf{r})$ which is zero in the normal state and different from zero in the superconducting state. The order parameter is a result of the phase transition theory itself and it is related to the superconducting density of electrons contributing to the superconducting state. Note that in the context of this theory $\Delta(\mathbf{r})$ also represents a macroscopic wavefunction of the coherent superconducting state. With the BCS theory, $\Delta(\mathbf{r})$ will be interpreted as the superconducting gap. By minimizing the free energy with respect to variations of both the order parameter and the magnetic field, Ginzburg and Landau were able to write their equations:

$$\frac{\hbar^2}{4m}(\frac{\nabla}{i} - \frac{2e}{\hbar}\mathbf{A}(\mathbf{r}))^2\Delta(\mathbf{r}) + \alpha_{GL}\Delta(\mathbf{r}) + \beta_{GL}|\Delta(\mathbf{r})|^2\Delta(\mathbf{r}) = 0 \tag{1.3}$$

$$\mathbf{j}_s(\mathbf{r}) = \frac{2e}{\hbar}\frac{\hbar^2}{4m}[\frac{1}{2}(\Delta^*(\mathbf{r})\nabla\Delta(\mathbf{r}) - \Delta(\mathbf{r})\nabla\Delta^*(\mathbf{r})) - \frac{2e}{\hbar}\mathbf{A}(\mathbf{r})|\Delta(\mathbf{r})|^2] \tag{1.4}$$

where $\hbar$ is the reduced Planck constant, m is the electron mass, e is the elementary electric charge, $\mathbf{A}$ is the potential vector, $\Delta(\mathbf{r})$ is the complex order parameter and $\mathbf{j}_s$ is the current density. Finally, α_{GL} and β_{GL} are parameters arising from the Ginzburg-Landau theory of phase transitions with $\beta_{GL} > 0$ and $\alpha_{GL}(T) = \alpha_0(T - T_C)$ ($\alpha_0 < 0$). The first equation describes the spatial evolution of the order parameter and the second the density current within the superconductor. This model makes it possible to deduce the coherence length ξ, another important characteristic length besides the penetration length:

$$\xi = \sqrt{\frac{\hbar^2}{2m|\alpha_{GL}|}} \tag{1.5}$$

with $\hbar$ the reduced Planck constant, m the electron mass and α_{GL} a parameter arising Ginzburg-Landau theory of phase transitions. This quantity is important when the system is perturbed from the equilibrium and gives the scale length over which the effect of the perturbation is exponentially attenuated. Furthermore, this model predicts the existence of two types of superconductors, i.e. type I and type II, having a different value of the parameter $\chi = \lambda/\xi$. In particular, for $\chi > 1/\sqrt{2}$ the superconductor is of type II and the superconducting state is completely destroyed above a critical magnetic field H_c. On the other hand, for $\chi < 1/\sqrt{2}$ the superconductor is of type I and it has two different critical magnetic fields (H_{c1} and H_{c2}). Above H_{c1} the system goes into the vortex state in which it is still superconductor but the magnetic field can penetrate within the bulk by means of the formation of supercurrent vortex. Above H_{c2} the superconducting state is definitely destroyed.

The last important theory of superconductivity to be discussed is the one developed by Bardeen, Cooper and Schrieffer and known as BCS theory [4]. It is the most important theory because it is the first to provide a microscopic explanation for the occurrence of superconductivity. The idea of the theory is that, at low temperature (below the critical temperature T_C), an attractive interaction (also extremely weak) destabilizes the conduction electrons near the Fermi surface and leads to the formation of the so-called Cooper pairs. In a Cooper pair teh two electrons have opposite spin and momenta. In this way the system can lower its total energy. Importantly, it was shown that the pairing superconducting potential is mediated by vibration of the crystalline structure through the electron-phonon interaction. The BCS hamiltonian describing a superconductor has the following form:

$$\hat{H}_{BCS} = \sum_{k,\alpha} \varepsilon_k \hat{c}^{\dagger}_{k,\alpha} \hat{c}_{k,\alpha} - V \sum_{k,k'} \hat{c}^{\dagger}_{k',\uparrow} \hat{c}^{\dagger}_{-k',\downarrow} \hat{c}_{-k,\downarrow} \hat{c}_{k,\uparrow} \tag{1.6}$$

where $\hat{c}^{\dagger}_{k,\alpha}$ ($\hat{c}_{k,\alpha}$) creates (destroys) an electron with momentum k, spin α and energy ε_k. The second term of this expression describes the destruction of a Cooper pair and the subsequent creation of another Cooper pair due to the attractive scattering potential V. Note that the total spin is conserved by the scattering potential V. The latter condition arises from the assumption of a local scattering potential of the form $V\delta(r)$ allowing only the s-wave ($l = 0$) scattering channel. Furthermore, the pairing potential V is supposed to be different from zero only for $-\omega_D < E_k < \omega_D$ (with ω_D the Debye energy). The wavefunction of the superconducting ground state was supposed to be a coherent state and it was written in the following way:

$$|\Psi_{BCS}\rangle = \prod_k (u_k + v_k \hat{c}^{\dagger}_{k,\uparrow} \hat{c}^{\dagger}_{-k,\downarrow}) |0\rangle \tag{1.7}$$

with a normalization condition for the coefficients u_k and v_k such as:

$$|u_k|^2 + |v_k|^2 = 1 \tag{1.8}$$

The BCS wavefunction can be intuitively seen as a superposition of empty and filled Cooper pair states. The coefficients u_k and v_k are related to the probability that a Cooper pair state $\hat{c}^{\dagger}_{k,\uparrow}\hat{c}^{\dagger}_{-k,\downarrow})|0\rangle$ is empty ($|u_k|^2$) or filled ($|v_k|^2$). The eigenvalues of the BCS hamiltonian E_k and the expressions for the coefficients u_k and v_k were found by means of a variational procedure minimizing the mean value of the ground state energy and which led to the following results:

$$u_k = \sqrt{\frac{1}{2}(1 + \frac{\xi_k}{E_k})} \tag{1.9}$$

$$v_k = \sqrt{\frac{1}{2}(1 - \frac{\xi_k}{E_k})} \tag{1.10}$$

$$E_k = \sqrt{\xi_k^2 + \Delta^2} \tag{1.11}$$

with $\xi_k = \varepsilon_k - \mu$ and $\varepsilon_k = \frac{\hbar^2 k^2}{2m}$. The minimization procedure also leads to the introduction of the following quantity representing the order parameter of the theory:

$$\Delta = V \sum_k u_k v_k \tag{1.12}$$

At this point, after diagonalization of the Hamiltonian, the BCS density of states can be deduced:

$$\rho(E) = \rho_0 \frac{|E|}{\sqrt{E^2 - \Delta^2}} \tag{1.13}$$

where ρ_0 is the density of states at the Fermi level in the normal state and Δ assumes the role of energy gap in the excitation spectrum of the superconductor and it can be ultimately interpreted as the energy required to break Cooper pairs. For this reason the density of states 1.13, also shown in Fig. 1.1, can be seen as a quasiparticle excitation density of states. In the context of the semiconductor model, describing the tunneling process in a superconductor, positive energy excitations correspond to the addition of single electrons within the system. Conversely, negative energy excitations correspond to the removal of single electrons or equivalently to the addition of holes within the system.

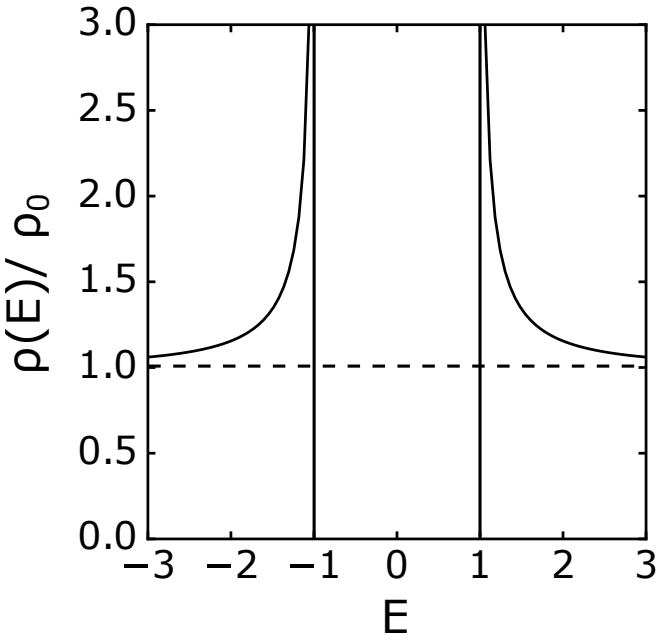

Fig. 1.1 BCS quasiparticle excitations density of states as a function of the energy and normalized to the value of ρ_0. The horizontal dashed line represents the density of states of the material in the normal state. Note that for $E >> \Delta$ the density of states of the normal state is recovered by the superconductor.

1.2 Kondo Effect

Generally, the electrical resistance of metals decreases with decreasing of the temperature. This is due to the fact that the motion of electrons through the crystal is less affected when the thermal vibrations of the atomic lattice are damped. However, at very low temperatures (typically below 10 K), the behavior of materials can be very different. For instance, Pb becomes superconducting and exhibits a sudden drop of the resistance (see green curve in Fig. 1.2). On the other hand, materials like gold remain in the normal conducting state and present a saturation value of resistance (see blue curve in Fig. 1.2). This residual resistance is strictly related to the concentration of defects within the crystal and it is ultimately due to scattering events between conduction electrons and static defects [5]. Accordingly, addition of impurities increases the value of the residual resistance. However, the behavior of the electrical resistance with temperature can be very different if the impurities of the system are magnetic. In this case, the resistance decreases with decreasing temperature, but below a certain temperature the resistance increases again (see red curve in Fig. 1.2). This effect is known as Kondo effect by the name of Jun Kondo who first provided the physical explanation in 1964 [6]. By means of a perturbative treatment of the problem, he was able to describe

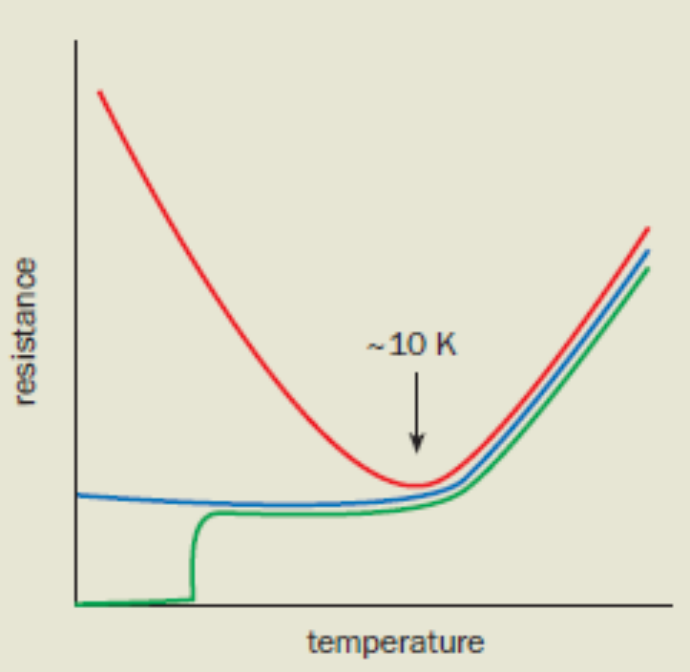

Fig. 1.2 Behavior of the electrical resistance for different materials. The resistance of materials like gold decreases with decreasing of temperature and saturates at a critical value depending on the concentration of static defects within the crystal (blue curve). Materials like Pb experience a superconducting transition and therefore below a critical temperature the electrical resistance suddenly drops to values close to zero (green curve). The resistance of materials containing magnetic impurities decreases with decreasing temperatures and start to increase again below the so-called Kondo temperature (red curve) [5].

the scattering of electrons by magnetic impurities and to ultimately write the following expression for the resistivity:

$$\rho(T) = \rho_{res} + aT^5 + bJ\ln(\frac{T}{c}) \tag{1.14}$$

where T is the temperature, J is the exchange coupling constant and a, b, c are constants. The first term is the residual resistivity (observed at low temperatures) associated to static defects and the second one is related to the phononic vibrations of the crystal dominating at high temperatures. The third term is the contribution of the Kondo model describing the resistivity at low temperature in presence of magnetic impurities. Note that this term dominates over the others at low temperatures. From previous expression it can be seen that, in order to have an increase of resistivity at low temperature, an antiferromagnetic coupling ($J < 0$) must be assumed between the conduction electrons within the metal and the spin of the impurity. It is interesting to note that the original model predicts real physical effects only down to a

temperature known as Kondo temperature (T_K). On the other hand, for temperatures below T_K it leads to an unphysical infinite increasing of the resistance.
The simplest model describing the Kondo physics that has enabled to overcome the problems of the original model below T_K is the Anderson model. The hypothesis behind this model is that, at temperatures below T_K, the number of degrees of freedom of the system is reduced preventing the occurrence of an infinite resistance [7]. The Kondo effect is ultimately explained by means of a antiferromagnetic exchange interaction between the conduction electrons of the metal and the spin of the impurity and, at temperatures below T_K, the latter is completely screened leading to the formation of a resonance at the Fermi level. The mechanism behind the formation of this resonance can be visualized by means of the

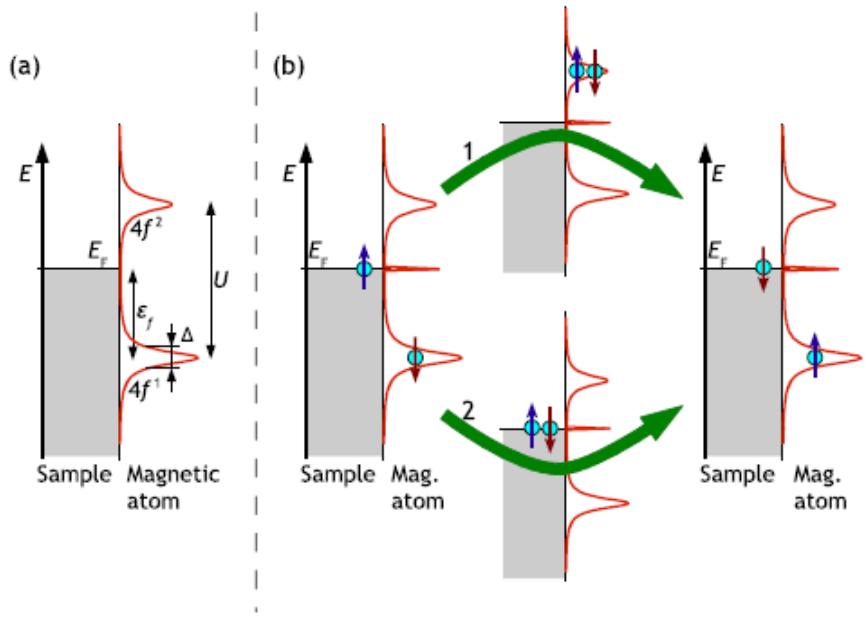

Fig. 1.3 (a) Electronic structure of a single impurity wit ha single magnetic orbital coupled to the continuum of the hosting metal (see text for further details). (b) Two possible paths through which the exchange interaction between the spin of the impurity and the conduction electrons of the metal can reverse the spin of the impurity itself. Note the appearance of the spin excitation state close to the Fermi level [7].

single impurity Anderson model. This model considers an impurity with a simple electronic structure consisting of just an orbital that can be unfilled, singly occupied or doubly occupied [7]. In the case of single occupation, this level has an energy ε_f below the Fermi level while, if the level is doubly occupied (electrons paired with opposite spins), its energy is located above the Fermi level due to the Coulomb repulsion U between the two electrons (see Fig. 1.3a). Furthermore, the hybridization between the impurity and the hosting material

induce a broadening of the impurity levels by an amount $\Delta = \rho_0 V$, where ρ_0 is the density of states at the Fermi level of the metal and V the hybridization matrix element (see Fig. 1.3a). In the initial state, the impurity is supposed to have a spin 1/2, meaning that its orbital is singly occupied. At this point the model supposes that the exchange interaction leads to spin-flip events of the impurity spin, i.e. the direction of the spin is changed from "up" to "down" and vice versa. A way to do this, is to fill the level with a second electron and then remove an electron (see the path number 1 of Fig. 1.3b). Another possibility is to empty the impurity level and refill it with another electron (see the path number 2 of Fig. 1.3b). In any case, these processes lead to the formation of a spin excitation state close to the Fermi level and the final state of the impurity can present an electron with reversed spin (see Fig. 1.3b). It is interesting to note that both paths described above are classically prohibited. In particular, the first requires an energy $|\varepsilon_0 + U|$ to doubly fill the impurity level while the second requires an energy $|\varepsilon_0|$ to remove an electron from the impurity level. In other words, in a classical picture it would be impossible to observe these processes without providing energy to the system. However, quantum mechanics allows both of them as very fast virtual processes [7]. It is also important to recall that Kondo effect is a many-body effect and therefore one has to imagine the occurrence of many spin reversing events as those described above due to the interaction between the magnetic impurity and the Fermi sea of the hosting metal. The ultimate result of this many-body process is the screening of the impurity spin accompanied by the appearance of the so-called Kondo resonance around the Fermi level. It is interesting to recall that all the transport properties of a material are always related to the electronic structure at the Fermi level. As a consequence, the appearance of the Kondo resonance can strongly affect the conducting properties of materials. Furthermore, the Kondo resonance is the signature of the emergence of a new ground state for the system consisting in a singlet non-magnetic state (because the spin of the impurity is screened). At T=0 K the Kondo resonance has a half-width at half-maximum Γ related to the Kondo temperature T_K by the following relation:

$$T_K = \frac{\Gamma}{k_B} \tag{1.15}$$

where k_B is the Boltzmann constant. Furthermore, Γ is related to the microscopic parameters of the system:

$$\Gamma = k_B T_K \sim \sqrt{2\Delta \frac{U}{\pi}} \exp[-\frac{\pi}{2\Delta}(|\frac{1}{\varepsilon_F}| + |\frac{1}{\varepsilon_F + U}|)^{-1}] \tag{1.16}$$

where Δ is the broadening of the impurity levels, U is the Coulomb repulsion and ε_F is the energy below the Fermi level of the impurity level. Note that the previous relation is valid only for $T = 0\ K$ and that, in general, the width 2Γ of the Kondo peak depends on the temperature, i.e. $2\Gamma = \sqrt{(\alpha K_B T)^2 + (2k_B T_K)^2}$. The Kondo temperature T_K is useful to

define the energy scale at which the Kondo effect takes place. In an intuitive way, at $k_B T_K$, the conduction electrons have Fermi velocities v_F low enough to experience the ferromagnetic exchange coupling with the spin of the impurity leading to the appearance of the Kondo resonance at the Fermi level.

1.2.1 Kondo effect and Scanning Tunneling Spectroscopy

It is interesting to mention that, usually, Scanning Tunneling Spectroscopy experiments might not detect a Kondo peak but rather a complex peak-dip feature. The explanation for this effect was given by Fano [8]. In particular, he proposed that, during the tunneling process, electrons can either directly tunnel into the empty states of the metal above the Fermi level (path 1 in Fig. 1.4a) or tunnel into the Kondo resonance (path 2 in Fig. 1.4a). The net tunneling current is the coherent superposition of these two paths that could lead to quantum interference processes. Therefore, density of states observed in Scanning Tunneling Spectroscopy experiments is given by the Fano equation [8]:

$$\rho(E) \propto \rho_0 + \frac{(q+\varepsilon)^2}{1+\varepsilon^2} \tag{1.17}$$

where $\varepsilon = \frac{E-E_K}{\Gamma}$ is the normalized energy (with E_K the actual energy position of the Kondo resonance and Γ its half-width at half-maximum), ρ_0 is the density of states at the Fermi level and q is the so-called form factor. As shown in Fig. 1.4b, the form factor q defines the actual shape of the Fano curve. In particular, for large (small) q the curve tends to a Lorentzian peak (dip). Furthermore, the form factor q can be expressed as follows:

$$q = \frac{t_2}{\pi \rho_0 V t_1} + \Lambda(\varepsilon) \tag{1.18}$$

where ρ_0 is the density of states at the Fermi level, V is the hybridization matrix element between the magnetic orbital of the impurity and the continuum of the hosting material, $\Lambda(\varepsilon)$ is a parameter taking into account the admixing of states from the continuum of the hosting material and t_1/t_2 are the tunneling matrix elements giving the probabilities for the tunneling electrons to take one of the two possible paths mentioned above. Equation 1.18 is important because it highlights the different microscopic aspects that could affect the appearance of the Kondo resonance experimentally measured by means of Scanning Tunneling Spectroscopy. For instance, if the tunneling channel through the Kondo resonance dominates, i.e. $t_2 >> t_1$, the form factor q is large and leads to a Fano peak. On the other hand, if the tunneling channel through the empty states of the metal dominates, i.e. $t_1 >> t_2$, the form factor q is small and leads to a Fano dip. Furthermore, in the case of magnetic molecules (not atoms) a Fano

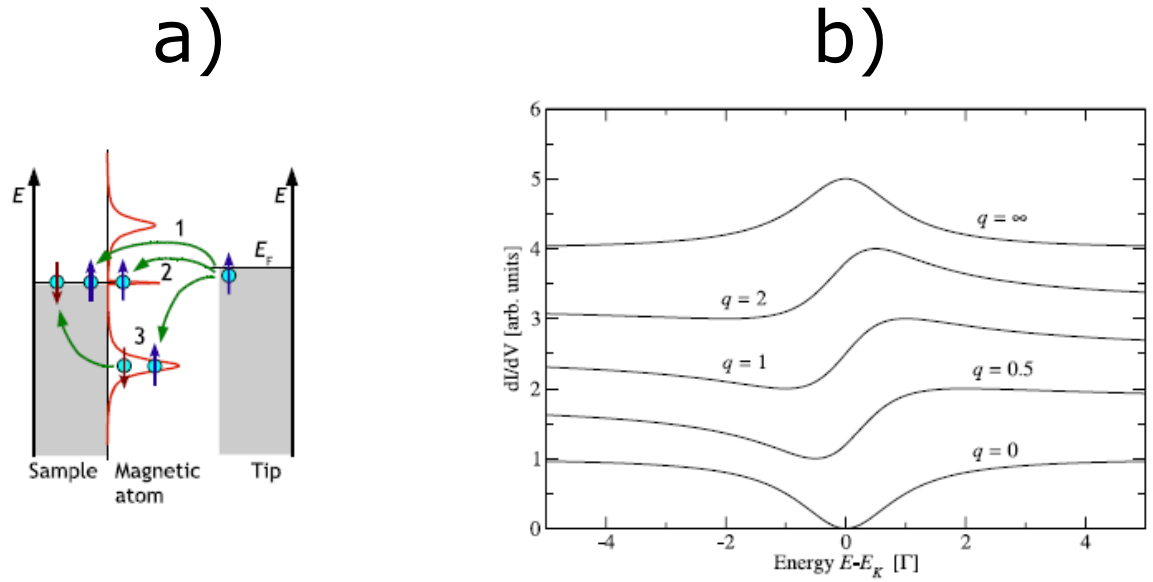

Fig. 1.4 (a) Possible paths through which electrons can tunnel during Scanning Tunneling Spectroscopy experiments. In the text we only consider direct tunneling into the empty states of the metal above the Fermi level (path 1) and the tunneling into the Kondo resonance (path 2) (b) Different curves traced starting from the Fano equation 1.17 for different values of the form factor q. Note that for small q the Kondo resonance appears as a dip feature while for large q appears as a peak [7].

peak is usually observed instead of a dip [7]. This is mainly due to the presence of molecular orbitals that decrease the probability for the electrons to directly tunnel into the empty states of the metallic surface, i.e. $t_2 >> t_1$. Experiments involving magnetic atoms/molecules deposited on metallic surfaces revealed correlation between the Kondo temperature T_K and either the coordination of the impurity with the substrate or the adsorption site [7]. Also changes in the density of states at the Fermi level ρ (for instance due to the adsorption of the impurity itself) can affect both the Kondo temperature and the shape of the Kondo resonance observed in tunneling spectra (see relation 1.18) [7, 9].

1.3 Magnetic impurities and superconductivity: Yu-Shiba-Rusinov states

The Abrikosov Gor'kov theory is the most used model used to describe the interaction between a random distribution of magnetic impurities, superconductivity and the effect of this interaction on both the density of states and the critical temperature of the system [10]. In general, the spin associated to a magnetic impurity adds an exchange component to the usual

non-magnetic scattering potential with Cooper pairs. This magnetic term turns the interaction into a pair-breaking interaction. As a consequence, the increasing of impurities concentration weakens the superconductivity with loss of local coherence and creation of impurity states within the superconducting gap. The magnetic-induced degradation of superconductivity is

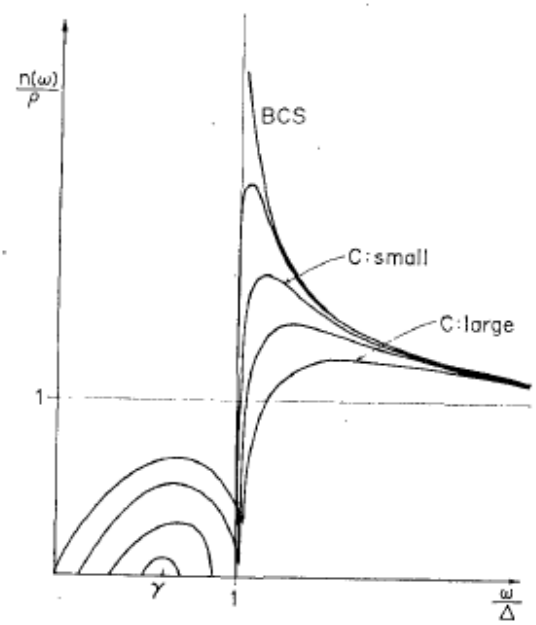

Fig. 1.5 Density of states of a superconductor interacting with a random distribution of magnetic impurities. By increasing the impurities concentration the coherence peaks amplitudes are reduced and the impurities band fill the superconducting gap [11].

represented in Fig. 1.5, where it can be easily seen that both the coherence peaks amplitudes and the superconducting gap are reduced with increasing of the impurities concentration. Ultimately, for impurities concentrations above a critical value the superconducting state is completely destroyed. In the following, we will focus on the limit of very low concentrations of magnetic impurities. In the particular case of a single magnetic impurity, e.g. either an atom or a molecule, on top of a superconductor, the scattering potential between the Cooper pairs of the substrate and the spin of the impurity can be written as the sum of a magnetic and a non-magnetic term:

$$\hat{H}_{int} = -\frac{JS}{2}(\hat{c}^{\dagger}_{0\uparrow}\hat{c}_{0\uparrow} - \hat{c}^{\dagger}_{0\downarrow}\hat{c}_{0\downarrow}) + K(\hat{c}^{\dagger}_{0\uparrow}\hat{c}_{0\uparrow} + \hat{c}^{\dagger}_{0\downarrow}\hat{c}_{0\downarrow}) \tag{1.19}$$

where $\hat{c}^{\dagger}_{0\sigma}$ ($\hat{c}_{0\sigma}$) is the creation (annihilation) operator of an electron with momentum k and spin $\sigma = \uparrow, \downarrow$, J is the exchange coupling constant, S the spin of the impurity and K

the non-magnetic coupling constant (associated to the diffusion potential of the impurity). It should be outlined that, with the index 0 of the creation (annihilation) operators, this expression supposes a local interaction occurring at the impurity site. In order to solve the whole problem of a magnetic impurity on a superconductor, the interaction term written above should be added to the BCS Hamiltonian. After that, eigenstates and eigenfunctions can be derived by means of a diagonalization procedure of the global Hamiltonian. The interaction between the Cooper pairs and the spin of the impurity results in the formation of a pair of excited bound states spatially centered on top of the impurity and with energy located inside the superconducting gap. These states are known in literature as Yu-Shiba-Rusinov states or more simply as Shiba states [11].

1.3.1 Energies of Shiba states

By means of a diagonalization procedure of the full Hamiltonian including the term related to superconductivity and the interaction term 1.19, the energies associated to a Shiba state $E_{Sh}^{\pm}$ can be written as a function of the magnetic (J) and non-magnetic (K) coupling:

$$E_{Sh}^{\pm} = \pm\Delta \frac{1-\alpha^2+\beta^2}{\sqrt{4\alpha^2+(1-\alpha^2+\beta^2)^2}} \tag{1.20}$$

where Δ is the superconducting gap and the two parameters $\alpha = \pi\rho_0 JS/2$ and $\beta = \pi\rho_0 K$ are related to J and K respectively (S is the spin of the impurity and ρ_0 is the density of states at the Fermi level in the normal state). The expression can be further simplified by introducing the scattering phase $\delta^{\pm}$:

$$\tan(\delta^{\pm}) = K\rho_0 \pm \frac{JS}{2}\rho_0 \quad \Rightarrow \quad E_{Sh}^{\pm} = \pm\Delta\cos(\delta^{+}-\delta^{-}) \tag{1.21}$$

From previous equations and from the upper part of Fig. 1.6, it can be seen that the interaction between a superconductor and a single magnetic impurity leads to the formation of a Shiba state, that is, a pair of excited states (corresponding to hole-like and electron-like states) within the superconducting gap and symmetrically located with respect to the Fermi level. The lower part of Fig. 1.6 shows a plot of the Shiba states energies as a function of the magnetic coupling parameter (see equation 1.20). Note that, in this plot, the non-magnetic contribution is neglected, i.e. $\beta = 0$. It is clear that the energy location of the Shiba states is related to the strength of the magnetic coupling. More interestingly, these energies do not depend on the sign of J, i.e. they do not depend on the ferromagnetic ($J > 0$) or antiferromagnetic ($J < 0$) nature of the magnetic coupling. Fig. 1.6 also shows that the energy position of

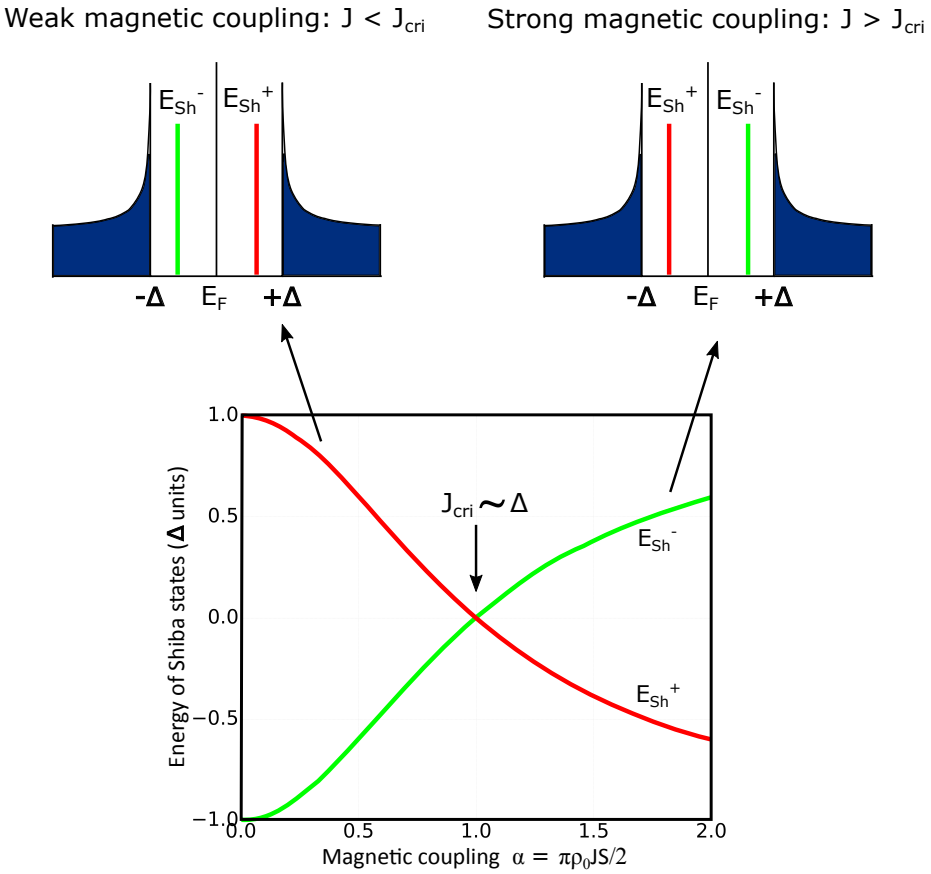

Fig. 1.6 Plot of the energy position of the peaks related to a Shiba state as a function of the magnetic term α and for $\beta = 0$ (starting from equation 1.21). Remember that α is in turn related to the magnetic coupling J ($\alpha = \pi\rho_0 JS/2$). The figure also shows that above a critical value J_{cri} the peaks reverse their position.

the positive/negative peak can be reversed if the strength of the exchange coupling J exceeds a critical value J_{cri}, but this aspect will be more discussed in section 1.3.2.

Yazdani et al. [12] were able to measure for the first time the Shiba states induced by Mn and Gd magnetic atoms deposited on top of a Nb(110) single crystal. Some time later, Ji et al. [13], thanks to the improved spatial and energetic resolution of tunneling spectroscopy, were able to visualize the wavefunction associated Shiba states. In particular, Fig. 1.7a shows a sketch of the system consisting of a 20 ML thick film of Pb grown on Si(111) on top of which either Mn or Cr atoms were deposited. Note that the experiments were carried out at 0.4 K and by means of a superconducting Nb tip. Fig. 1.7b shows the reference spectrum, which is proportional to the local density of states of the sample, taken away from magnetic impurities and showing the magnetically unaffected superconductivity of the Pb film. On the

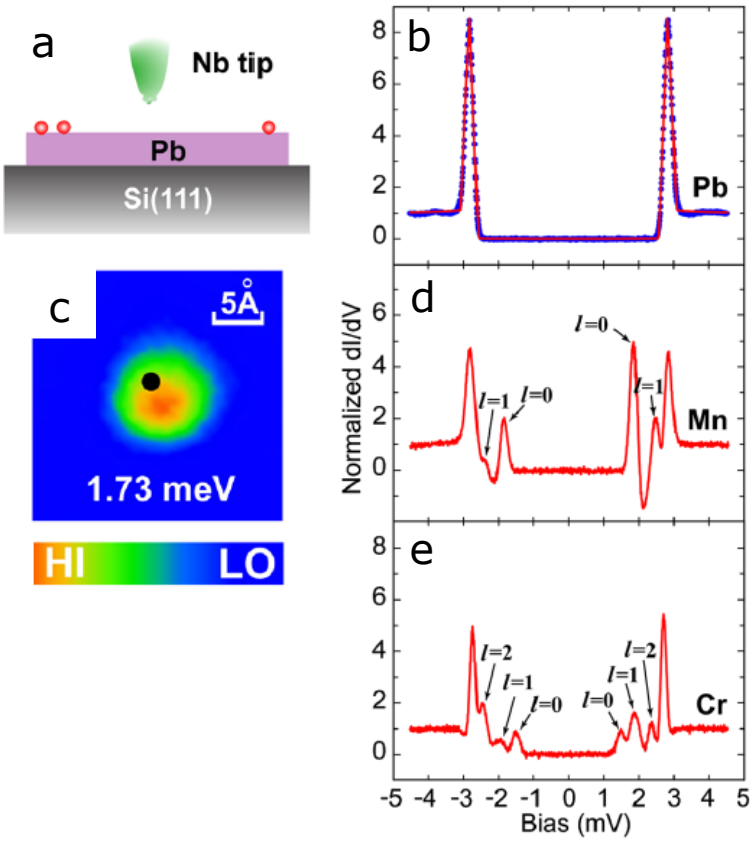

Fig. 1.7 (a) Sketch of the sample consisting of a 20 ML film of Pb grown on Si(111) on top of which either Mn or Cr atoms were deposited. (b) Reference spectrum showing the magnetically unaffected superconductivity of the Pb surface. (c) Spatial dependence of the local density of states on top of a Mn atom revealing the spectroscopic fingerprint related to the Shiba wavefunction. (d) and (e) Spectra acquired on top of a Mn and a Cr atom respectively revealing the presence of Shiba states within the superconducting gap. Different pairs of peaks are associated to the different scattering channels involving different angular momenta, i.e. $l = 0, 1, 2$ [13].

other hand, Fig. 1.7d and Fig. 1.7e display the tunneling spectra taken on top of the Mn and Cr atoms respectively. Comparison of these spectra with the reference shown in Fig. 1.7b reveals the appearance of Shiba states within the superconducting gap as a consequence of the magnetic interaction between adatoms and superconductivity. Fig. 1.7c shows the spatial dependence of the local density of states acquired on top of a Mn atom and reveals the experimental fingerprint of a Shiba state and its wavefunction. Interestingly, this figure shows that the Shiba states are centered on top of the magnetic impurity and their wavefunction rapidly decays on atomic distances. It is important to discuss the reason for which in Fig. 1.7d and Fig. 1.7e more than two peaks are detected within the superconducting gap, i.e. four on

top of Mn and six on top of Cr. This effect is related to the fact that the scattering processes between a magnetic impurity and a superconductor involve channels with different angular momenta, e.g. $l = 0, 1, 2$. Moca et al. [14, 15] have also shown that, in some cases, the internal orbital structure defining the spin of the magnetic impurity can manifest itself by means of Shiba multiplets within the superconducting gap. In the case of transition metals, for instance, the spin is determined by unpaired electrons within three d orbitals, which are usually degenerate in energy. When the magnetic impurity is deposited on top of a surface the environment symmetry can either partially or totally lift the degeneracy. At this point, each d orbital will couple to the substrate in a different way giving rise to different pairs of Shiba states depending on the strength of the coupling. The number of Shiba states actually observed is ultimately driven by the number of d orbitals still degenerate [15]. A very clear

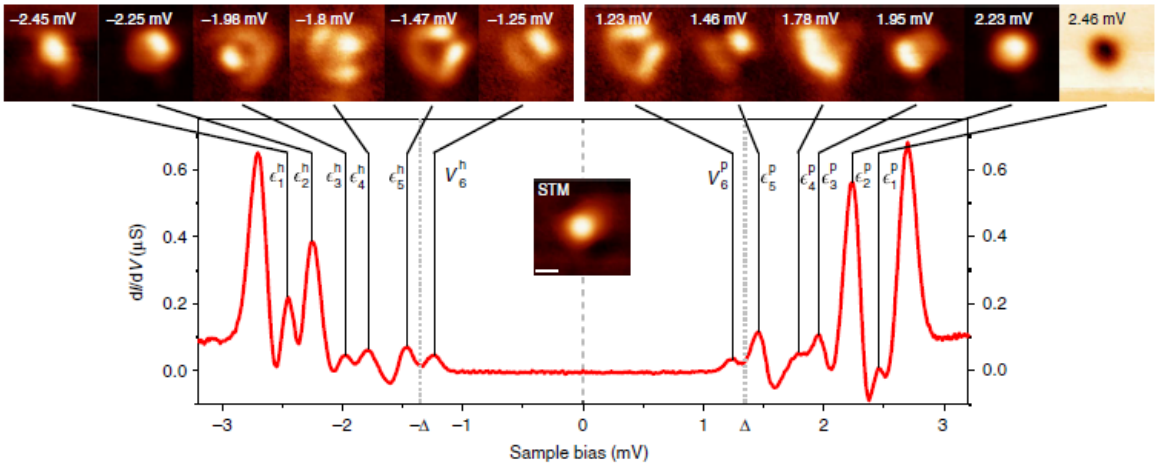

Fig. 1.8 The reduced symmetry of the environment around a magnetic impurity leads to the splitting of the impurity orbitals defining the spin itself. In the case of Cr atoms embedded below the Pb(111) surface, the splitting of all the five d orbitals leads to the appearance of five Shiba states, or equivalently of five pairs of peaks (bottom part of the figure). The upper part of figure shows that the wavefunction associated to each of these states has its own orbital character [16].

example of this effect was provided by Choi et al. [16, 15] by means of STM experiments and DFT calculations. The investigated system consists of Cr atoms deposited on top of a Pb(111) crystal. DFT calculations have shown that, in one of the adsorption configurations, Cr atoms are embedded below the Pb(111) surface. In this situation the local symmetry of the environment around the impurity is lowered leading to the splitting of all five d orbitals. This fact results in the occurrence of five separated scattering channels leading to the emergence of five Shiba states (or equivalently five pairs of peaks) at different energies (see the bottom part of Fig. 1.8). The most interesting thing is that the wavefunctions associated to each of

these states have their own aspect demonstrating that Shiba states really have e a specific orbital behavior with respect to the scattering events (see the upper part of Fig. 1.8).
At this point it should be outlined that the spin of the impurity can be treated in two different limits. The classical approximation assumes that the spin is large enough and that its value cannot be changed by the interaction with the Cooper pairs. On the other hand, the quantum approximation assumes that the spin of the impurity is small and therefore the internal degrees of freedom related to the spin itself may be changed by the exchange interaction with Cooper pairs. In particular, we will see that in the case antiferromagnetic coupling of the impurity the intervention of Kondo effect can screen the impurity spin.

1.3.2 Magnetic impurity with a classical spin

In this section we will see the effect of the magnetic interaction between an impurity with classical spin and a superconductor on both the Shiba states and the ground state of the system. To start, the non-magnetic contribution will be still neglected, i.e. we will consider $K = 0$ or equivalently $\beta = 0$ in the interaction Hamiltonian 1.19. When a classical magnetic impurity is coupled to a superconductor, the impurity spin cannot be screened by Kondo effect (if it is present) because its internal degrees of freedom cannot be changed. Fig. 1.6 shows that for weak magnetic coupling, i.e. $J \sim 0$, the Shiba states are close to the gap edges, i.e. $E_{Sh}^{\pm} \sim \pm\Delta$. In this case, since the magnetic impurity is only slightly coupled to the superconductor, the latter is not affected and it remains in the superconducting singlet state, i.e. total spin of the condensate is $S = 0$ (this case is depicted in Fig. 1.9a). The increasing of the magnetic coupling J leads the Shiba states to move within the superconducting gap towards the Fermi level (see Fig. 1.6). When J exceeds the critical value corresponding to the Cooper pair binding energy, i.e. $J_{cri} \sim \Delta$, the Shiba states cross the Fermi level and reverse the reciprocal energy position. At $J \sim \Delta$ a Cooper pair can be broken and one of the two electrons of the pair can be thought to be localized close on the impurity site and magnetically coupled with it. The presence of this unpaired electron with a preferential spin direction changes the total spin of the condensate by $\pm 1/2$. The sign of the spin variation is determined by the nature of the magnetic coupling between the unpaired electron and the magnetic impurity that can be ferromagnetic ($J > 0$) or antiferromagnetic ($J < 0$) (this case is depicted in Fig. 1.9b). It should be always kept in mind that the mechanism just described and the picture shown in Fig. 1.9b is only an oversimplified image of the actual physics behind that, instead, involves many-body events in which Cooper pairs are continuously broken and formed. Ultimately, the net result of the interaction between Cooper pairs and a classical magnetic impurity is to change the total spin of the condensate from a singlet state ($S = 0$) to a doublet state ($S = 1/2$) or vice versa as the strength of the magnetic coupling J

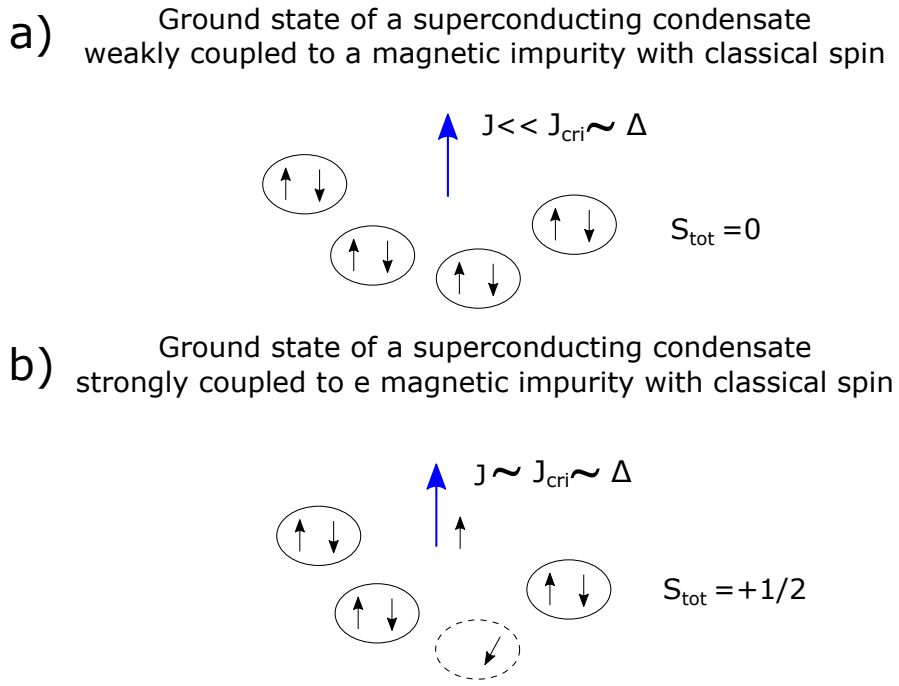

Fig. 1.9 (a) Ground state of the condensate in the case of a weakly coupled magnetic impurity with classical spin. Cooper pairs are only slightly affected by the presence of the impurity and therefore the total spin of the condensate remains $S = 0$. (b) Ground state of the condensate in the case of a strongly coupled magnetic impurity with classical spin. In this case, the strength of the exchange coupling is able to break a Cooper pair and localize one of the electrons at the impurity site. The unpaired electron will be magnetically coupled to the impurity spin depending on the nature of the exchange coupling, i.e. $J > 0$ or $J < 0$. Accordingly, the total spin of the condensate is changed by $\pm 1/2$. Adapted from [15].

is changed. The main message of this section is that the strength of the magnetic coupling J between an impurity with classical spin and a superconductor profoundly affects the energy position of the Shiba excitations and is responsible for the nature of the ground state of the condensate.

1.3.3 Magnetic impurity with quantum spin

In this section we will see how the magnetic interaction between an impurity with quantum spin and a superconductor affects Shiba states energy positions and nature of the ground state of the system. We can consider, for instance, the case of a spin 1/2 antiferromagnetically coupled to a superconductor. Under these conditions the quantum spin can be screened by means of Kondo effect. Direct consequence of this fact is the emergence of a competition between the Kondo ground state and the superconducting one. Similarly to what happens in the case of a classical spin, the transition from one to the other ground state depends on

the strength of the magnetic coupling J. In particular, if the magnetic coupling is weak, i.e. $k_B T_K << \Delta$, the Kondo screening cannot take place because the superconducting gap prevents the presence of electrons around the Fermi level, that is, those that are usually involved in the Kondo effect. In this case, the quantum impurity cannot be screened and the superconducting

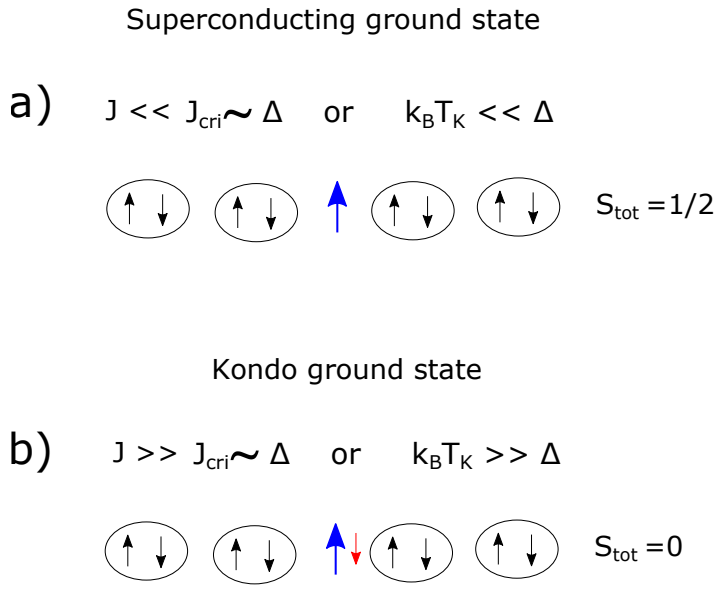

Fig. 1.10 (a) Ground state in the case of a quantum spin weakly coupled to a superconductor. Kondo effect cannot take place and therefore impurity spin cannot be screened. The total spin of the system is $S = 1/2$ and the superconducting ground state prevails over the Kondo ground state. (b) Ground state in the case of a quantum spin strongly coupled to a superconductor. Kondo effect screens the impurity spin and the total spin of the system is $S = 0$. In this case, the Kondo ground state prevails over the superconducting ground state. The red arrow represents a Kondo electron antiferromagnetically coupled to the impurity. Adapted from [15].

ground state prevails over the Kondo ground state (see Fig. 1.10a). Consequently, the system has a total spin S=1/2. Furthermore, the weak magnetic coupling implies that Shiba states are located close to the gap edges (see Fig. 1.6). On the other hand, if the magnetic coupling is strong, i.e. $k_B T_K >> \Delta$, the spin of the impurity is screened by means of Kondo effect and the Kondo ground state prevails over the superconducting one. As a consequence the total spin of the system will be S=0 (see Fig. 1.10b) and a Kondo resonance can be measured around the Fermi level. It is important here to stress the fact that, if the quantum impurity is strongly coupled to the superconductor, inversion of the peaks associated to the Shiba states is not observed. In other words, the behavior of Shiba states in the case of quantum impurity is different from what was shown in Fig. 1.6 in the case of a classical spin. This is because when the quantum spin start to be strongly coupled to the superconductor it is also

strongly screened through Kondo effect. In this condition, superconducting electrons are less affected by the presence of the impurity spin ad the exchange coupling J is renormalized by the intervention of Kondo effect, i.e. it is decreased. This fact implies that, at weak coupling, Shiba states are initially located to the gap edge. When increasing the coupling, the Shiba peaks start to move towards the center of the superconducting gap. Finally, when the coupling is strong enough to allow Kondo effect to screen the quantum spin, the reduction of the exchange coupling J (renormalized by Kondo effect) bring again the Shiba peaks close to the gap edge, i.e. Shiba states crossing does not occur.

1.3.4 Wavefunctions of the Shiba states

Recently, it was shown that the wavefunction associated to a Shiba state takes a different form depending on the dimensionality of the superconductor [17]. In particular, the asymptotic form ($r >> \lambda_F = 2\pi/k_F$) of the wavefunction $\Psi_{\pm}(r)$ for a 3D superconductor can be written as follows:

$$\Psi_{\pm}(r) = \frac{1}{\sqrt{N}} \frac{\sin(k_F r + \delta^{\pm})}{k_F r} \exp^{-\frac{\Delta \sin(\delta^{+} - \delta^{-}) r}{\xi}} \tag{1.22}$$

the index $\pm$ in $\Psi_{\pm}(r)$ refers to the part of the wavefunction associated to the peak at positive or negative energy of the Shiba state. r is the the distance from the center of the magnetic impurity, N is a normalization factor, k_F is the Fermi wavevector, λ_F is the Fermi wavelength, $\delta^{\pm}$ is the scattering phase introduced in equation 1.21 and ξ is the superconducting coherence length. On the other hand, in the case of a 2D superconductor, the wavefunction can be written in the following way:

$$\Psi_{\pm}(r) = \frac{1}{\sqrt{N\pi}} \frac{\sin(k_F r - \frac{\pi}{4} + \delta^{\pm})}{\sqrt{k_F r}} \exp^{-\frac{\Delta \sin(\delta^{+} - \delta^{-}) r}{\xi}} \tag{1.23}$$

Inspection, of previous expressions reveals the presence of different factors that modulate the decay of the wavefunction. The exponential decay is mainly governed by the coherence length ξ of the superconductor. Furthermore, the presence of scattering events at the scale of the Fermi wavelength λ_F leads to the appearance of an oscillating term. More interestingly, Ménard et al. [17] have shown that the interaction between a magnetic impurity and a 2D superconductor induces Shiba states extending far away from the impurity (up to $\sim$10 nm). Note that in Fig. 1.7 and Fig. 1.8 the Shiba states decay on atomic distances (few Å) and that, in both cases, the system involves a 3D superconductor. Ultimately, the difference between 1.22 and 1.23 resides in the spatial decay of the Shiba states away from the impurity, i.e. $\sim \frac{1}{r}$ in the 3D case and $\sim \frac{1}{\sqrt{r}}$ in the 2D case, and it is mainly due to the dimensionality of the superconductor. Fig. 1.11a shows the wavefunction related to a Shiba state induced by an

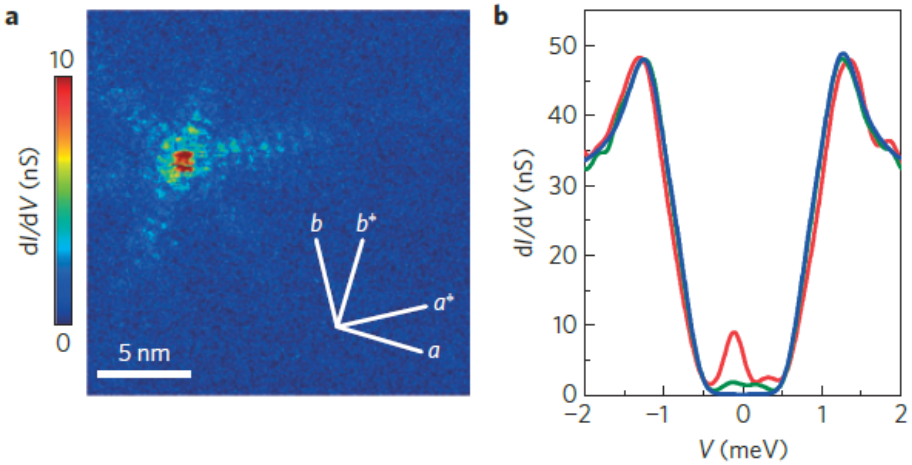

Fig. 1.11 (a) Experimental conductance map, representing the spatial variation of the density of states, taken at -0.13 mV and showing the star-shaped spectroscopic signature associated to the Shiba state wavefunction induced by a magnetic impurity embedded in a quasi-2D sample of $2H-NbSe_2$. (b) STS spectra acquired on the region shown in (a). The red spectrum was measured on top of the magnetic impurity, the green spectrum on the right branch of the star at $\sim$4 nm from the impurity site and the blue spectrum far away from the impurity where the superconductivity is not affected by its spin [17].

embedded magnetic impurity in a $2H-NbSe_2$ crystal. It is easy to see that the most intense part of the wavefunction is localized on top of the impurity site but then the star-shaped feature extends up to $\sim$10 nm away from the impurity itself. Fig. 1.11b shows the spectrum taken on top of the impurity revealing the Shiba state within the superconducting gap (red curve). The green curve shows the spectrum acquired on the right branch at $\sim$4 nm from the center of the impurity. Finally, the blue spectrum is acquired far away from the impurity and shows the unperturbed superconducting gap.

The lateral extent of Shiba states becomes important when magnetic coupling of different impurities on a superconductor is required. This is because the overlapping of Shiba states associated to different impurities can mediate their magnetic coupling [15]. For instance, the overlap of Shiba states associated to two impurities in a dimer may lead to an hybridization of the two states and consequent splitting in bonding and antibonding states if the two impurities are ferromagnetically coupled [13]. This process is similar to the formation of molecular orbitals starting from isolated atoms. Accordingly, the Shiba overlapping of a finite concentration of magnetic impurities may lead to the formation of the so-called Shiba bands [13]. Fig. 1.12a, b and c show the experimental results of Ji et al. [13] related to the magnetic coupling of Shiba states in Mn dimers deposited on top of a 20 ML film of Pb

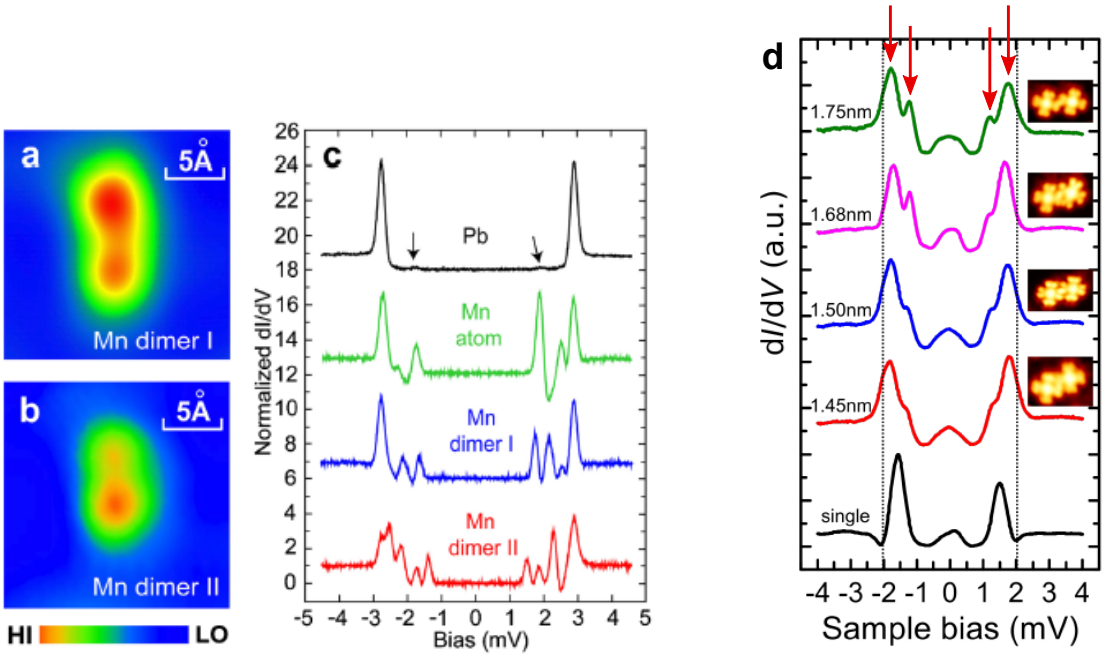

Fig. 1.12 (a) and (b): Topographic image of a Mn dimer with an interatomic distance of 6.1 Å (a) and 4.2 Å (b) [13]. (c): STS spectra taken on top of the Pb(111) surface away from impurities (black curve), on top of an isolated Mn atom (green curve), on top of a Mn belonging to dimer I (blue curve) and dimer II (red curve). Black arrows indicate the presence of impurity bands even on the bare Pb surface (away from impurities) [13]. (d): STS spectra taken on top of an isolated CoPc deposited on $2H-NbSe_2$ (black curve) and on top of a CoPc belonging to a dimer at different intermolecular distances (the remaining curves). Red arrows indicate splitted Shiba states [18].

grown on Si(111). In particular, by comparing the spectrum acquired on top of an isolated Mn atom (green curve in Fig. 1.12c) with that taken on top of the Mn belonging to the Dimer *II* (red curve in Fig. 1.12c), the splitting of the two initial Shiba states can be readily seen after coupling. As mentioned above this also indicates the presence of ferromagnetic interaction between the atoms. On the other hand, the spectrum taken on top of a Mn belonging to dimer I (blue curve in Fig. 1.12c), shows that only one of the two Shiba states splits in two peaks. This effect was ascribed to a non-ferromagnetic alignment between the spins of the impurities, probably due to the fact that the interatomic distance of dimer I is larger with respect to that of dimer II and the magnetic coupling between the two impurities is accordingly weaker. Another example of coupling between Shiba states in a dimer is provided by Kezilebieke et al. [18]. In particular, they have shown the splitting induced by the hybridization of Shiba states in dimers of magnetic organic molecules, i.e. CoPc, on top of a quasi-2d substrate of $2H-NbSe_2$ (see Fig. 1.12d). The black curve represents

the spectrum acquired on top of an isolated molecule. The two peaks of largest amplitude are associated to a Shiba state arising from the magnetic coupling between the molecule and the underlying superconductor. Note that two peaks close to zero energy are thermal peaks arising from the fact the a superconducting tip was used and experiments were carried out at rather high temperature. The other spectra are acquired on top of a molecule in a dimer at different intermolecular distances. It can be clearly seen that a splitting of the initial Shiba states occurs and it is more or less marked depending on the relative molecular configuration. This means that the coupling of different Shiba states also depends on the molecular configuration with respect to the substrate other than the intermolecular distance.

1.3.5 Effect of non-magnetic coupling of a classical spin

Until now the non-magnetic contribution to the scattering between a magnetic impurity and the Cooper pairs of a superconductor was neglected. The aim of this section is to qualitatively see how are affected the findings discussed in previous sections by the intervention of a non-magnetic interaction. In order to facilitate the reading of the text, the interaction Hamiltoninan 1.19 and the expression of the Shiba energies 1.21 in the classical limit are rewritten below:

$$\hat{H}_{int} = -\frac{JS}{2}(\hat{c}^{\dagger}_{0\uparrow}\hat{c}_{0\uparrow} - \hat{c}^{\dagger}_{0\downarrow}\hat{c}_{0\downarrow}) + K(\hat{c}^{\dagger}_{0\uparrow}\hat{c}_{0\uparrow} + \hat{c}^{\dagger}_{0\downarrow}\hat{c}_{0\downarrow}) \tag{1.24}$$

$$E^{\pm}_{Sh} = \pm\Delta\frac{1-\alpha^2+\beta^2}{\sqrt{4\alpha^2+(1-\alpha^2+\beta^2)^2}} \tag{1.25}$$

where $\hat{c}^{\dagger}_{0\sigma}$ ($\hat{c}_{0\sigma}$) is the creation (annihilation) operator of an electron with momentum k and spin $\sigma =\uparrow,\downarrow$, J is the exchange coupling constant, S the spin of the impurity, K the non-magnetic coupling constant (associated to the diffusion potential of the impurity), Δ is the superconducting gap and the two parameters $\alpha = \pi\rho_0 JS/2$ and $\beta = \pi\rho_0 K$ are related to J and K respectively (S is the spin of the impurity and ρ_0 is the density of states at the Fermi level in the normal state). Fig. 1.13 shows a plot of the Shiba energies $E^{\pm}_{Sh}$ as a function of the magnetic parameter α similar to that shown in Fig. 1.6. The different curves correspond to different values of the non-magnetic parameter β. It is clear that, even in presence of non-magnetic interaction, the Shiba states lie within the gap in symmetric positions with respect to the Fermi level. Furthermore, their energy position is strictly related to the strength of J but not to its sign ($J > 0$ represents ferromagnetic and $J < 0$ antiferromagnetic coupling). From this figure it is evident that the increase of the non-magnetic coupling β pushes the crossing point of the Shiba states towards higher values of J and the result does not depend

on the sign of β itself. In other words, the stronger the non-magnetic coupling β, the stronger the critical magnetic coupling J_{cri} needed to switch from weak to strong magnetic coupling between the impurity and the superconductor, i.e. to switch singlet to doublet ground state.

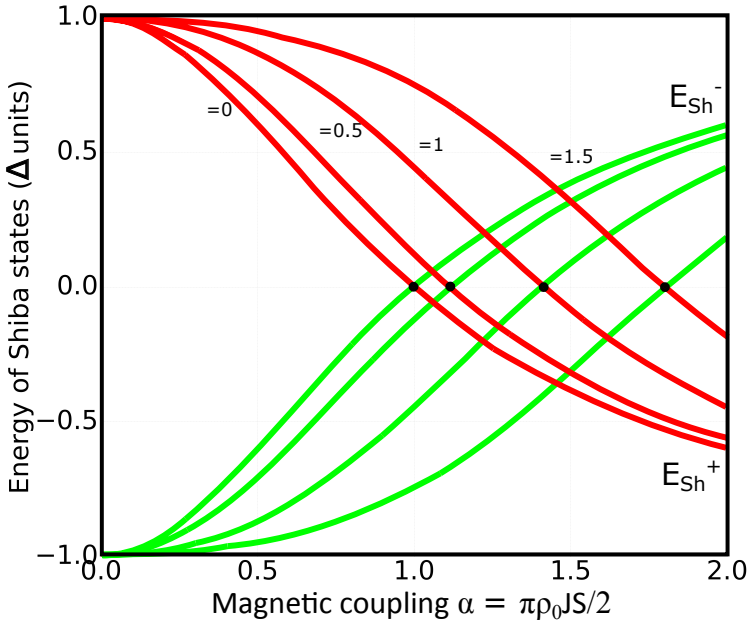

Fig. 1.13 Plot of the Shiba energies $E_{Sh}^{\pm}$ as a function of the magnetic parameter $\alpha = \pi\rho_0 JS/2$. Different curves correspond to different values of the non-magnetic parameter $\beta = \pi\rho_0 K$. The main effect of the non-magnetic interaction is the displacement of the crossing point of the Shiba states towards higher values of α, i.e. of J.

Until now we considered that, near the location of the magnetic impurity, the two peaks in the Local Density of States (LDOS) associated to a Shiba state, i.e. E_{Sh}^{+} and E_{Sh}^{-}, have the same amplitude (see Fig. 1.6). However, the presence of the non-magnetic interaction introduces an asymmetry in their relative amplitude. This fact can be easily understood by inspecting the following expression which represents the ratio of the wavefunction amplitudes associated to the peaks at positive (Ψ_+) and negative (Ψ_-) energy at the impurity site ($r = 0$)

$$\frac{\Psi_+(r=0)}{\Psi_-(r=0)} = \frac{\cos(\delta^+)}{\cos(\delta^-)} \tag{1.26}$$

where r is the distance from the center of the magnetic impurity, and $\delta^{\pm}$ is the scattering phase introduced in equation 1.21. It is important to remember that this relation only applies on top of the impurity and this is the reason for the notation $\Psi(\mathbf{r} = 0)$. Recalling that $\delta^{\pm}$ are defined by means of the relation $\tan(\delta^{\pm}) = K\rho_0 \pm \frac{JS}{2}\rho_0$, it is easy to see that, if there

is no magnetic coupling K, the ratio written above is one and the two peaks have the same amplitude. On the other hand, the addition of a finite K leads to a ratio different from one and thus to an asymmetry between the amplitudes of the two peaks. Fig. 1.14 shows a plot of the ratio 1.26 as a function of the magnetic coupling α and for different strengths of the non-magnetic β. It can be readily seen that once the nature of the magnetic coupling is established, e.g. either ferromagnetic ($J > 0$) or antiferromagnetic ($J < 0$), the direction of the asymmetry is fixed by the sign of the non-magnetic interaction β. For instance, if we suppose an impurity ferromagnetically coupled to a superconductor ($J > 0$), for positive β the positive peak associated to the Shiba state ($\Psi_+(0)$) will have a smaller amplitude with respect to that at negative energy ($\Psi_-(0)$) and vice versa. In the case of an antiferromagnetic coupling the opposite situation is found. Fig. 1.15 shows a sketch of the possible asymmetries

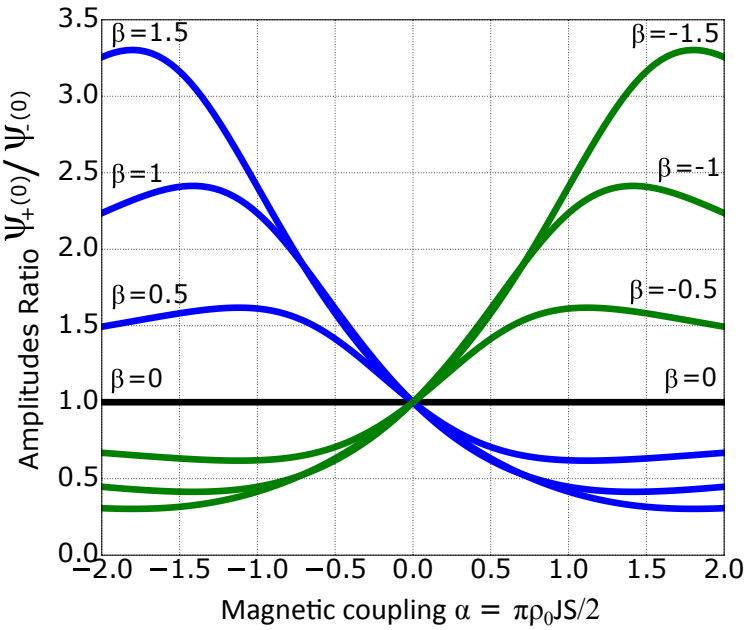

Fig. 1.14 Plot of equation 1.26, representing the ratio of the wavefunction amplitudes associated to the two peaks of a Shiba state, as a function of the magnetic coupling $\alpha = \pi\rho_0 JS/2$. Different curves correspond to different value of the non-magnetic term $\beta = \pi\rho_0 K$.

that may be encountered depending on the type of magnetic and non-magnetic coupling. Furthermore, this figure includes cases in which the strength of the magnetic coupling J is either smaller or larger than the critical value J_{cri} needed to switch from weak to strong coupling. Remember that when $J > J_{cri}$ the two peaks $\Psi_+(0)$ and $\Psi_-(0)$ reverse their energy position.

To conclude this section a qualitative interpretation of the non-magnetic interaction will be

given. To a first approximation it is largely due to the screened Coulomb potential of the impurity. The origin of the impurity charge is strictly related to both the type of impurity and the nature of the interaction between the impurity itself and the hosting material. For instance, in the case of magnetic molecules, e.g. MnPcs, deposited on top of a surface, the charge transfer could be one of the mechanisms leading to the charging of the molecule which is screened by the substrate and generate a non-magnetic potential. From equation 1.24 it is clear that if $K < 0$ the electrons gain energy in interacting with the impurity and vice versa. This means that $K < 0$ and $K > 0$ correspond to an attractive and a repulsive interaction respectively and that for $K < 0$ ($K > 0$) a positive (negative) charge is associated to the impurity. It is interesting to note that the asymmetry between the two peaks associated to Shiba states arises from a breaking of the particle-hole symmetry by the Coulomb potential. Furthermore, the asymmetry of the peaks could be affected by asymmetries in the normal state conductance of the superconductor [15].

1.3.6 Experimental studies about the competition between superconducting and Kondo ground state

In section 1.3.3 it was shown that the competition between superconducting and Kondo ground state depends on the strength of the interaction between a magnetic impurity and a superconductor. The actual existence of the phase transition from a ground state to the other was investigated by considering a hybrid system consisting of self-assembled MnPcs on top of a superconductive bulk monocrystal of Pb(111) [15, 19, 20]. In particular, it was observed that MnPcs on top of Pb(111) self-assemble in square lattices (Fig. 1.16a). More interestingly, each molecule within the assembly lies in a slightly different adsorption site and therefore exhibits a different strength of magnetic coupling with the substrate. As a consequence, the Shiba states measured on top of these molecules present a wide variation in energy. Fig. 1.16a shows a STM topographic image of a MnPcs island self-assembled on Pb(111). Fig. 1.16b shows the same region acquired in constant-height mode and tunneling bias voltage within the superconducting gap. The moiré-like pattern appearing in these conditions reflects the different interaction strength of molecules adsorbed on different sites of the Pb surface. The inspection of many molecules lying on different adsorption sites has allowed to Hatter et al. [19] to emphasize the existence of different magnetic coupling strengths between MnPcs and Pb(111). In particular, Fig. 1.17a shows a stack of STS spectra measured on top of 137 molecules and sorted in order to reveal the continuous variation of the Shiba states position within the superconducting gap and thus the different magnetic coupling with the substrate. Fig. 1.17b shows three representative spectra related to three different regimes of coupling.

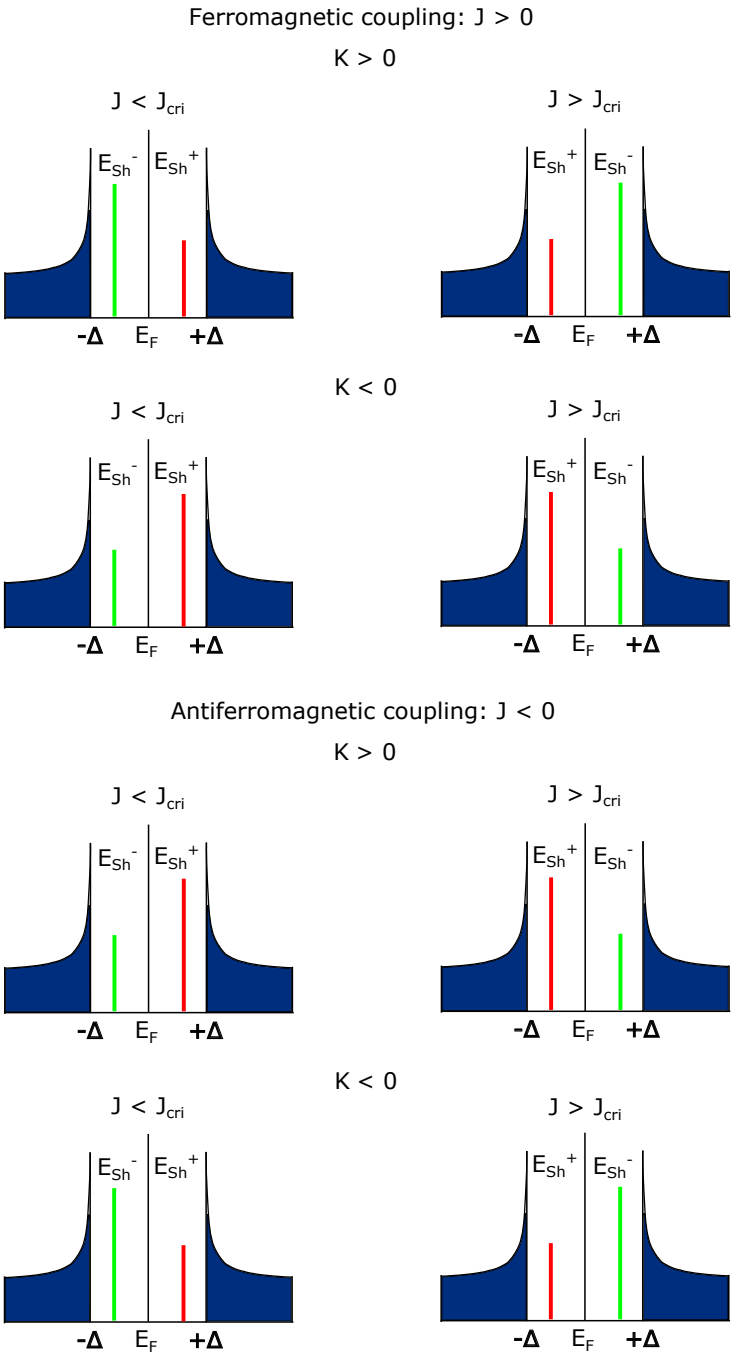

Fig. 1.15 Sketch of the possible amplitude asymmetries between the peaks of a Shiba state as well as their energy position depending on the type of magnetic (J) and non-magnetic (K) term. The two cases $J < J_{cri}$ and $J > J_{cri}$ are also taken into account.

In particular, spectrum I shows a regime in which the peaks at negative voltages are more intense than those at positive voltages. This condition was ascribed to a strong coupling J. By looking at the spectrum III, the opposite condition is observed and therefore it was interpreted

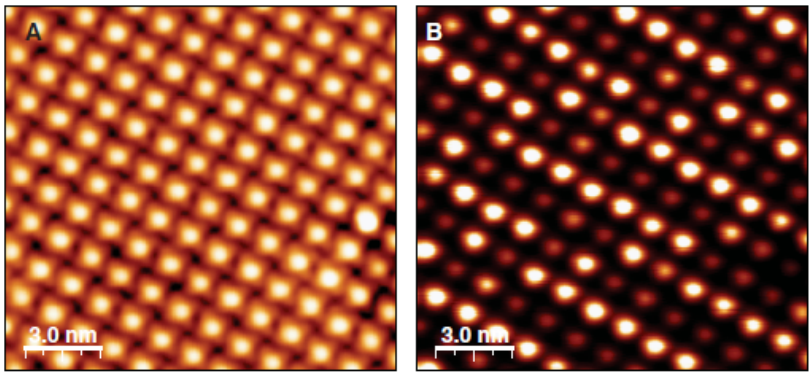

Fig. 1.16 (a) STM topographic image of a MnPcs island self-assembled on Pb(111) acquired in constant-current mode. (b) STM image of the same region shown in (1) but it is acquired in constant-height mode and tunneling bias voltage within the superconducting gap [20].

as a weak coupling J. Spectrum II represents an intermediary condition of magnetic coupling. Ultimately, from top to bottom, the spectra of Fig. 1.17a indicate a decreasing coupling strength J between MnPcs and Pb(111). In agreement with what has been said in section 1.3.3 about the competition between superconducting and Kondo ground state, spectrum I indicates the presence of a Kondo ground state, while spectrum III indicates the presence of a superconducting ground state. Spectrum II is a particular case close to the quantum phase transition [19, 21]. Note that the Shiba states in Fig. 1.17 are split in three different peaks.

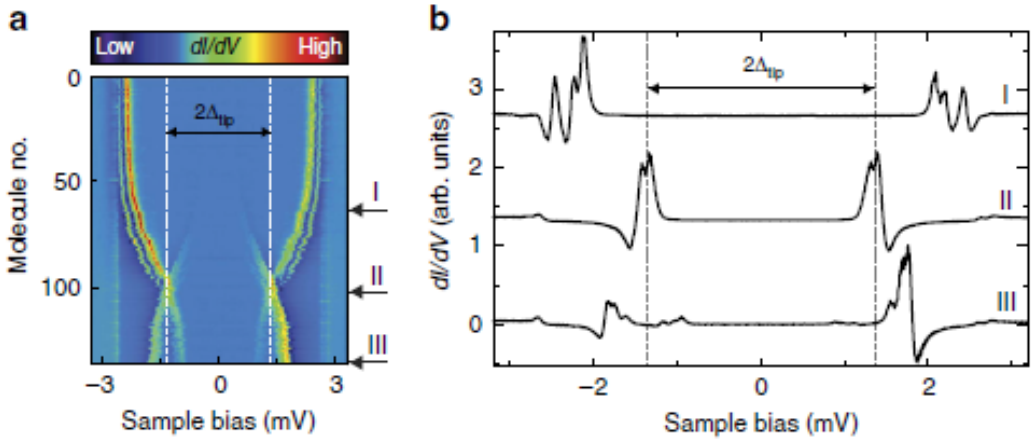

Fig. 1.17 (a) STS spectra taken on top of 137 MnPcs deposited on top of a Pb(111) crystal. The spectra are stacked and sorted to reveal a continuous variation of the Shiba positions within the superconducting gap and consequently to reveal the variation of magnetic coupling between molecules and substrate. (b) Representative spectra acquired on three MnPcs with Shiba states revealing three different coupling regimes [19].

This effect was attributed to the magnetic anisotropy of MnPcs [19]. Free MnPcs have a spin $S = 3/2$. However, once they adsorb on Pb(111), the total spin is decreased to $S = 1$ and it is given by the two partially filled orbitals d_{z2} and d_{xy}. The exchange interaction between molecules and surface is largely due to the spin of the d_{z2} orbital because the rest of the spin due to the d_{xy} orbital is delocalized on the molecular plane and it is not strongly coupled to the substrate. However, the splitting of Shiba states was interpreted as a result of the fact that these two orbitals are not completely independent but correlations between them can open additional exchange scattering channels leading to the Shiba splitting.
To conclude this section it should be emphasized that, in these studies, there is no determination of the non-magnetic potential and its possible changes while the molecules sit at various locations. Nevertheless, changes of K could also occur with different positions of the molecules, which would affect the asymmetry between the electron and hole part of the Shiba states. It would then strongly affect the analysis presented by the authors. Also the analysis presented here relies on the asymmetry amplitudes valid for a classical impurity but not valid for a quantum impurity.

1.4 Engineering of topological superconductivity

To understand what is topological superconductivity, one can think about the topological insulators. The latter are characterized by the presence of edge states lying within the insulating energy gap and topologically protected by specific symmetries of the system. In a similar way, also a superconductor may be, under certain conditions, in a topological phase characterized by the emergence of edge states known as Dirac edge states lying within the superconducting gap and topologically protected by specific symmetries of the system. Theoretical works have shown that the necessary condition to have a superconducting topological phase is that between zero and the Brillouin zone edge there must be an odd number of intersections between the Fermi level and the electronic bands. In particular, Sau et al. [22] have proposed a way to achieve this condition in a superconductor in order to obtain a topological superconductor. The basic idea is to introduce a Rashba spin-orbit coupling and a Zeeman splitting to the superconducting system. For simplicity, let's see what is the effect of these two ingredients when they are introduced within a 2D free-electronic system in the normal state:

$$H_0 = H_{free} + H_{Rashba} + H_{Zeeman} = \frac{\overrightarrow{p}^2}{2m} - \varepsilon_F + \alpha(\overrightarrow{\sigma} \times \overrightarrow{p}) \cdot \hat{z} + \mu_B B_z \sigma_z \tag{1.27}$$

with $\overrightarrow{p}$ the momentum, m is the electron mass, ϵ_F the Fermi energy, α the strength of the spin-orbit coupling, $\overrightarrow{\sigma}$ the Pauli matrices, $\hat{z}$ the unit vector perpendicular to the surface of the system, μ_B the Bohr magneton and B_z the strength of the magnetic field. Rashba spin-orbit coupling occurs in systems with strong spin-orbit coupling when the space-inversion symmetry is broken along one of the three directions, e.g. at the surface of the system. In our case, Rashba spin-orbit coupling occurs because we work at the surface of thin films of Pb. To start we suppose, in general terms, a 2D electron system with Rashba spin-orbit coupling and subject to an external magnetic field. Fig. 1.18a shows the band structure

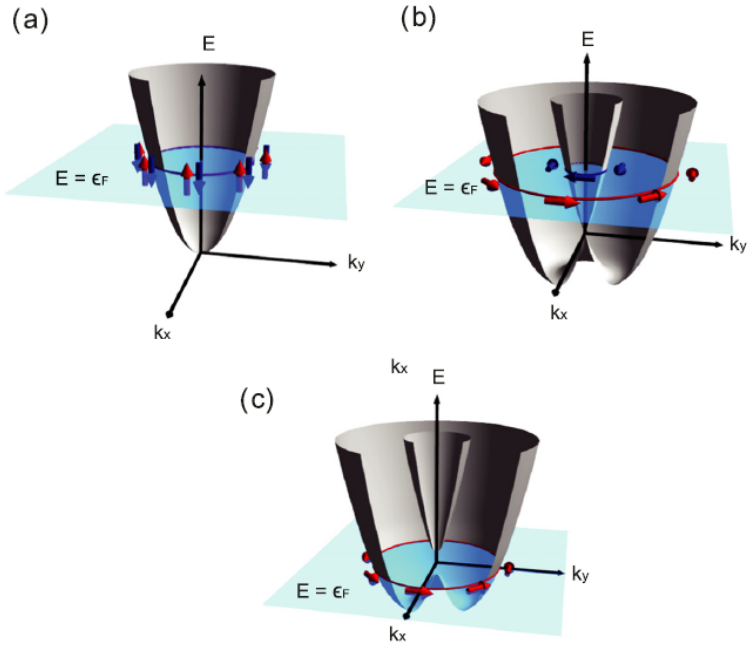

Fig. 1.18 Influence of Rashba spin-orbit coupling and Zeeman splitting on the electronic structure of 2D electron system. In any case, the cross section between the energy bands and the Fermi energy plane at ϵ_F identifies the Fermi surface which is indicated by a solid line. (a) Electronic structure of a simple 2D free electron system. (b) Spin-splitting induced by the Rashba spin-orbit coupling. (c) Gap opening induced by the combination of Rashba spin-orbit coupling and Zeeman splitting. In the latter case the Fermi level is adjusted to fall into the gap and induce a topological transition [23].

of the 2D free electron system. In this case, the two bands of spin up and spin down are degenerate and therefore there will always be an even number of intersections between the Fermi level and the bands themselves between zero and the Brillouin edge. As an odd number of crossings is required to have a topological phase, we can conclude that the system lies in a non-topological phase. Fig. 1.18b shows that the Rashba spin-orbit coupling induces a spin splitting of the two bands and leads to two chirally spin-polarized bands. Also in this case an

even number of crossings between the Fermi level and the electronic bands leaves the system in a non-topological phase. Finally, Fig. 1.18c shows that the additional application of an external magnetic field opens a gap $\mu_B B_z$ at $\overrightarrow{k} = 0$, i.e. where the two bands of Fig. 1.18b are degenerate. At this point, if we assume to have the control on the Fermi level we can adjust it within the gap as in Fig. 1.18c and induce a topological transition in the system. As the Fermi level crosses only one electronic band between zero and the Brillouin edge (odd number of crossings) we can conclude that the system is now in a superconducting topological phase. Sau et al. [22] have shown that if superconductivity is turned on in a 2D electron system with Rashba spin-orbit coupling and Zeeman effect as in Fig. 1.18c, the superconducting state will have topological properties equivalent to that of a chiral p-wave superconductor. On the other hand, it is important to note that topological superconductivity is not automatically achieved just by combining superconductivity, Rashba spin-orbit coupling and magnetism, but the additional condition must be fulfilled [22]:

$$C_0 = (\Delta^2 + \mu^2) - (\mu_B B_z)^2 < 0 \tag{1.28}$$

where Δ is the superconducting gap, μ is the chemical potential, μ_B is the Bohr magneton and B_z is the magnetic field. Therefore the necessary condition to have topological superconductivity is that $C_0 < 0$, otherwise the system remains in a non-topological phase. As already said in the introduction of this section, the main signature of topological superconductivity is the emergence edge states. If a one dimensional system is considered, end states are called Majorana end states while in other cases are they are generally called Dirac edge states. These exotic states emerge from many-body processes and represent zero-energy quasiparticle excitations. Direct experimental observation of these states would have huge technological impact because they are supposed to be used as single qubits and their manipulation may be used to develop real quantum computational systems.

As an illustration, Fig. 1.19 shows the complex interplay between the different quantities of relation 1.28 allowing the topological transition. In particular, in this figure, the superconducting gap is plotted as a function of the Zeeman splitting ($\mu_B B_z$). For different values of the Rashba spin-orbit coupling strength (α). First, in absence of Rashba spin-orbit coupling ($\alpha = 0$), the introduction of a magnetic field in a superconductor destroys the superconductive state above a critical value. This happens because at a certain point, the magnetic field spin-polarizes the system and breaks all the Cooper pairs (remember that Cooper pairs consist of electrons with opposite spins). It is clear then, that Rashba spin-orbit coupling allows the existence of superconductivity even in presence of a relatively strong magnetic field, i.e. for both $C_0 < 0$ and $C_0 > 0$ (C_0 was defined in equation 1.28). This is due to the

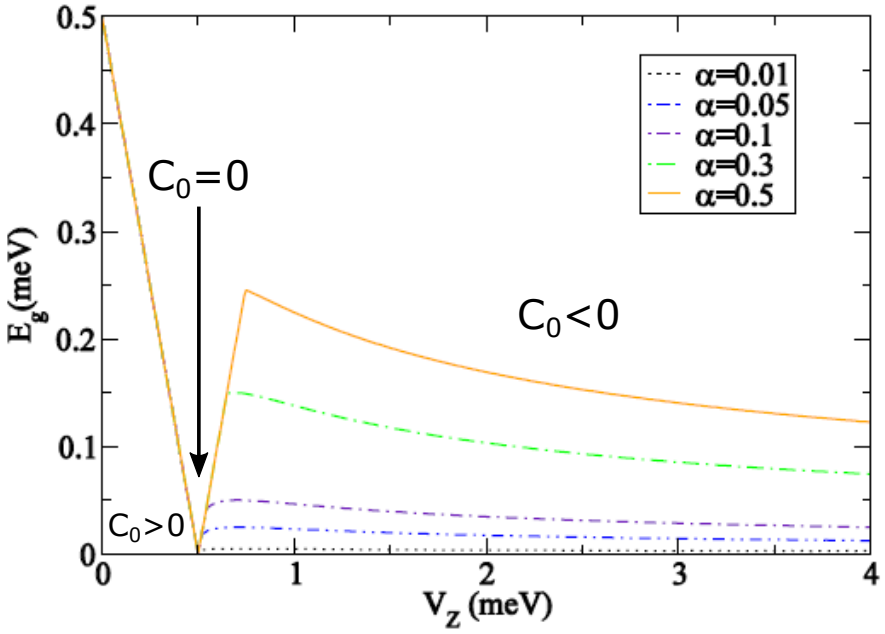

Fig. 1.19 Superconducting gap as a function of the Zeeman splitting $\mu_B B_z$. Different curves are traced for different values of the Rashba spin-orbit coupling strength (α). In the calculations $\Delta = 0.5$ and $\mu = 0$. Note that the gap closes when $\mu_B B_z = \sqrt{\Delta^2 + \mu^2}$, i.e. when $C_0 = 0$. For $C_0 > 0$ the superconductivity is non-topological, while for $C_0 < 0$ it becomes topological and supports Majorana edge states. Figure adapted from Ref. [22].

fact that the Rashba spin-orbit coupling introduces an in-plane component of the spin that helps the superconducting pairing. For $C_0 > 0$ the superconductivity shown in Fig. 1.19 is non-topological. On the other hand, the increasing of the Zeeman splitting above the critical value leads to the destruction of the non-topological pairing and the gap closure (see Fig. 1.19). By further increasing of Zeeman splitting ($C_0 < 0$), the Rashba spin-orbit coupling authorizes the re-opening of topological superconductivity inducing Majorana fermions at the edge of the system [22]. From this discussion it is clear that, in principle, a topological transition can be tuned by playing with the different electronic and magnetic effects, i.e. Zeeman splitting, Rashba spin-orbit coupling and Fermi level. In any case, the important result derived from Fig. 1.19 is that topological superconductivity is always separated by the non-topological one by means of a gapless point, i.e. when $C_0 = 0$ [22]. In other words, to switch from a non-topological superconductivity to a topological one, the closure of the gap is mandatory. This condition implicitly resides in the fact that two different topological phases have different electronic band structures that cannot be connected by continuous deformations and therefore, resulting in the breaking of the electronic configuration and the restoring of another one. In an equivalent way, the nature of the superconducting pairing in

the non-topological phase is different from that of the topological phase. It is very important to outline that the experimental signature to detect the presence of topological superconductivity is the detection of Majorana edge states.

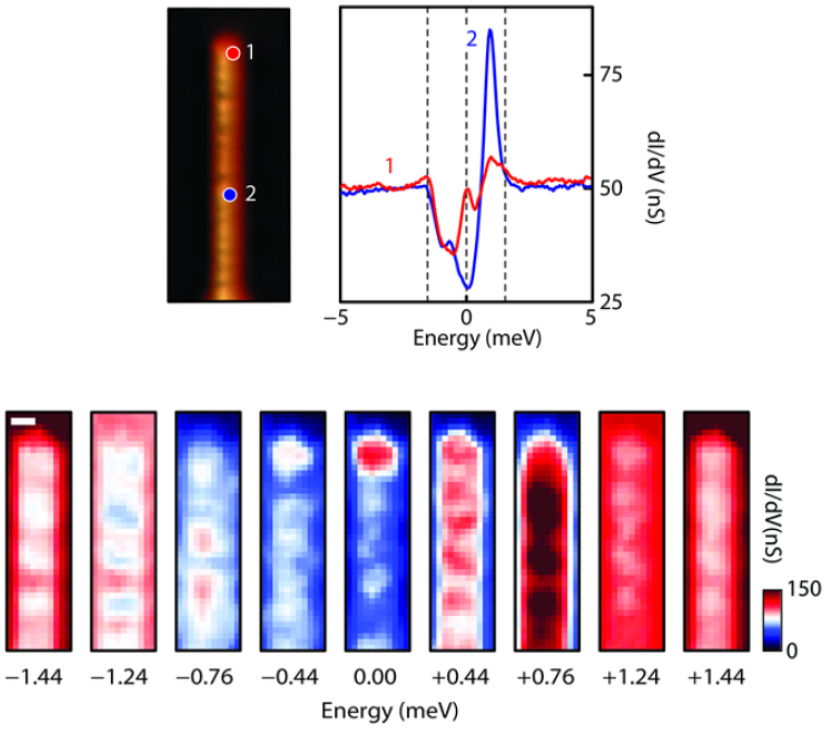

Fig. 1.20 (Top left) Topographic STM image showing the terminal part of a 1D chain of Fe atoms self-assembled on a Pb(110) surface. (Top right) STS spectra acquired at the end of the chain (1) and away from it (2), i.e. in the bulk of the chain itself. (Lower part) Spatial variation of the density of states at different energies acquired on the terminal part of a 1D chain of Fe atoms. The conductance map at zero energy shows a strong resonance at the end of the chain interpreted as a Dirac edge state. Figure adapted from [24].

From an experimental point of view, there are few works that have reported the observation of Majorana edge states and thus of topological superconductivity. The first is the work of Nadji-Perge et al. [24] in which 1D atomic chains of Fe were self-assembled on top of a Pb(110) surface. The anisotropy of the (110) surface acts as a template to form 1D magnetic structures with Fe. The upper right part of Fig. 1.20 shows the Scanning Tunneling Spectra (proportional to the local density of states) acquired on two point of the terminal part of a 1D atomic chain of Fe self-assembled on a Pb(110) surface (point 1 and 2 in figure). The red spectrum, corresponding to the end of the chain, shows the resonance centered at zero energy. The lower part of the same figure shows the spatial variation of the density of states

at different energies on the end of another atomic chain. The map at zero energy shows a strong resonance localized at the end of the chain. This edge features were interpreted as Majorana edge states signature of the presence of topological superconductivity. Note that in this case 1D chains would induce one-dimensional domains of topological superconductivity in correspondence of the chain itself. This is the reason for which Majorana edge states are expected at both ends of chain.

However, since different physical effects, e.g. trivial Shiba states, Kondo effect, etc.,

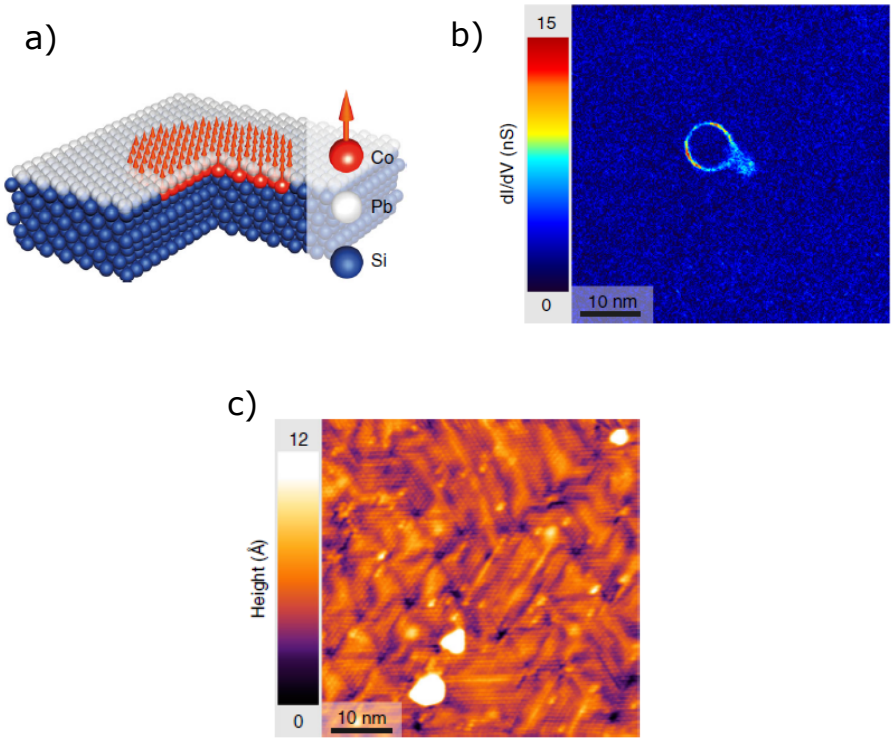

Fig. 1.21 (a) Sketch of the 2D magnetic islands of Co-Si grown on Si(111) and buried with a superconducting monolayer of Pb. (b) Spatial variation of the density of states measured at 1.32 meV revealing the Dirac edge states (the ring feature) at the edge of the 2D topological domain (disk within the ring). The rest of the sample (out of the ring) remains in a non-topological phase. (c) STM topographic image showing the surface reconstruction of the superconducting Pb monolayer covering the magnetic Co-Si islands grown on Si(111). This images was acquired on the same region shown in (b) [25].

may give rise to peaks at zero energy, it is still not clear if these zero energy peaks are effectively due to the emergence of topological superconductivity. This is the reason for which in this thesis we focused on the engineering of 2D topological superconductivity. In this case the Dirac edge states are expected to appear on the edge of the 2D topological domain. 2D topological superconductivity has been explored by Ménard et al. [25]. In that

study, 2D magnetic Co-Si islands were grown on Si(111) and subsequently buried below a superconducting Pb monolayer (see sketch of Fig. 1.21a). Fig. 1.21b shows the spatial variation of the density of states at 1.32 mV. The ring-like feature was interpreted as a 1D Dirac edge state linked to the edge of the topological region inside the ring itself. In this system, the 2D magnetic domain of Co-Si produces a Zeeman field strong enough to induce a topological transition in the above superconducting monolayer. Therefore, on top of the magnetic domain there exists a 2D domain with topological superconductivity, while the rest of the sample (out of the ring) remains in a non-topological phase. As already discussed above, Dirac edge states are localized at the edge of the topological domain. This figure is very interesting because it shows that inside and outside of the magnetic domain there is no spectroscopic difference between the two types of superconductivity. This clarifies the reason for which we consider the occurrence of Majorana edge states as the most important experimental signature of the presence of topological superconductivity. Fig. 1.21c shows an STM topographic image of the same region shown in Fig. 1.21b. The structure seen in this figure corresponds to the surface reconstruction of the Pb monolayer. This figure also reveals the main problem of this system, that is, the buried Co-Si magnetic islands are not accessible and therefore it is impossible to characterize their spin structure or just their structure.

In order to overcome this problem the idea of the present work is to use an hybrid system consisting of thin layers of Pb grown on Si(111) on top of which magnetic organic molecules, i.e. manganese phthalocyanines, are deposited. The use of thin layers of Pb allows us to have 2D superconductivity together with a strong Rashba spin-orbit coupling. The integration of magnetism by means of organic molecules makes it possible to easily probe the structure of both 1D and 2D self-assembled arrays of molecules because they can easily be images by STM. As already discussed in previous section the interaction between the molecular spin and the superconductivity will lead to the formation of Shiba states. The self-assembly of molecules may lead to the overlap of the corresponding Shiba states and thus to their hybridization. As a consequence Shiba bands may mediate a magnetic coupling leading to a magnetic order over the molecular domain, e.g. ferromagnetic. In the latter case, the average magnetic field arising from the magnetic domain may couple to the underlying superconductor and eventually drive a topological transition. However, as already mentioned above, all these coupling conditions are not automatically fulfilled because many other effects can intervene when molecules adsorb on top of a surface. For this reason, the main goal of this thesis is to investigate by means of surface characterization techniques, i.e. LEED, STM and STS, all the steps of the preparation of this hybrid system and try to understand how we can achieve the good conditions to have a topological transition.

Chapter 2

Experimental Methods

2.1 Surfaces, superstructures and Wood's Notation

When a metallic/semiconducting surface is created a huge number of atoms have to be removed by bond breaking. This implies both a very different surface electronic distribution with respect to that of the bulk and an increase of the total energy. A way to compensate this energy increase is given by a surface charge redistribution which is likely to drive a surface reconstruction, i.e. an ordered surface structure that may include one or few of the topmost layers. In this new structure has a different periodicity with respect to that of the bulk material and it is referred as superstructure. The most common notation to describe superstructures is the so-called Wood's Notation [26]. It considers the surface primitive vectors of the superstructure, e.g. $\mathbf{a}_s$ and $\mathbf{b}_s$, as multiple of those of the bulk-terminated unreconstructed surface, e.g. $\mathbf{a}$ and $\mathbf{b}$:

$$|\mathbf{a}_s| = m|\mathbf{a}| \qquad \text{and} \qquad |\mathbf{b}_s| = n|\mathbf{b}| \tag{2.1}$$

If the superstructure unit cell is rotated with respect to that of the unreconstructed surface the angle of rotation is explicitly indicated. The general form of a superstructure described by means of the Wood's Notation is

$$X(hkl) - m \times n - R\phi \tag{2.2}$$

with $X(hkl)$ the substrate unreconstructed surface, m and n the proportionality factors between the surface primitive vectors of the superstructure and those of the unreconstructed surface and ϕ the angle of rotation between the two. For instance, the surface reconstruction Si(111)-

7×7 means that the superstructure primitive vectors are seven times longer than those of the unreconstructed Si(111) surface.

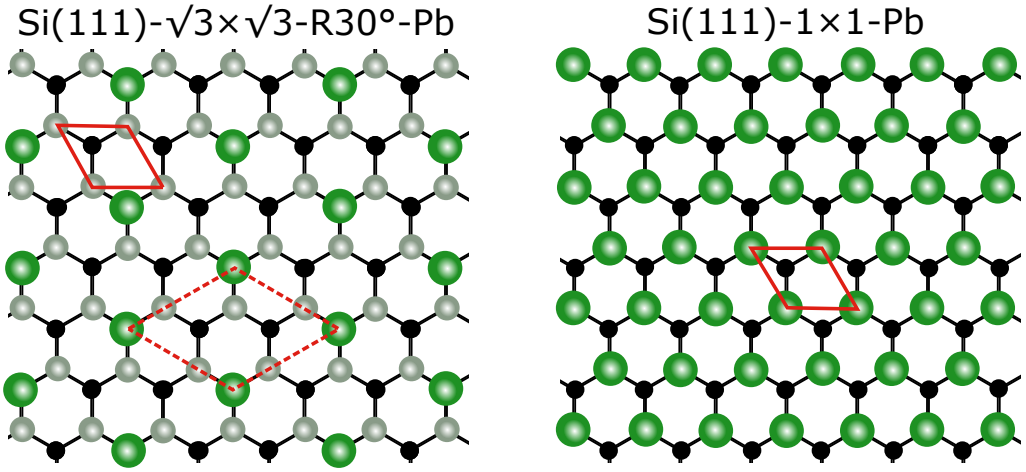

Fig. 2.1 Top-view of the (a) Si(111)-$\sqrt{3} \times \sqrt{3}$ -R30°-Pb and the (b) Si(111)-1×1-Pb superstructure. Small gray (black) balls represent Si atoms belonging to the (first) second atomic layer of the Si(111) substrate. Large green balls indicate the Pb atoms adsorbed in a (a) $\sqrt{3} \times \sqrt{3}$ lattice and a (b) 1×1 lattice. The $\sqrt{3} \times \sqrt{3}$ unit cell (dashed red line) is 30° rotated with respect to the 1×1 (solid red line).

When foreign species, as atoms or molecules, are adsorbed on metallic/semiconductive surfaces it is commonly observed that they self-assemble themselves to form superstructures whose periodicity may differ from that of the host substrate surface. In this case the Wood's Notation specify the adsorbate chemical symbol. For instance, the Si(111)-$\sqrt{3} \times \sqrt{3}$ -R30°-Pb superstructure shown in Fig. 2.1a means that Pb atoms (green circles) are adsorbed on the Si(111) surface and form a $\sqrt{3} \times \sqrt{3}$ superstructure 30° rotated with respect to the unreconstructed Si(111) surface (gray circles). In literature, commonly accepted variations of this notation can be found. For instance, when the context of the discussion is clear, the substrate and the angle of rotation could be removed. In the following, this latter notation will be adopted because the substrate will always be a Si(111) crystal. In this way the notation Si(111)-$\sqrt{3} \times \sqrt{3}$ -R30°-Pb reduces to $\sqrt{3} \times \sqrt{3}$ -Pb. Wood's Notation can be used only when superstructure and unreconstructed substrate surface have the same symmetry, otherwise the matrix notation must be used [26]. In the following, Wood's Notation will always be applicable.

A bulk-terminated unreconstructed surface has the surface lattice coinciding with one of those associated to the bulk atomic planes. In this case the superstructure is simply indicated

as 1×1. Also in the case were an adsorbate forms a lattice with a unit cell coinciding with that of the substrate unreconstructed surface the superstructure is indicated as 1×1. Fig. 2.1b shows the example of the Si(111)-1×1-Pb (or simply 1×1-Pb) superstructure.

2.2 Low Energy Electron Diffraction (LEED)

Davisson and Germer were among the first people to observe the electron diffraction process by exposing a nickel crystal to a monocromatic electronic beam [27]. In particular, they observed that the elastic scattering of electrons at the nickel surface produce an anisotropic angular distribution satisfying the optic diffraction grating formula or equivalently the Bragg condition

$$n\lambda = a \sin\theta \tag{2.3}$$

where n is an integer indicating the diffraction order, λ the wavelength of the electronic incident wave, a the lattice periodicity of the grid and θ the angle of incidence. Since diffraction processes are usually related to waves, this is one of the first experimental observations revealing the wavelike behavior of electrons and confirming the De Broglie's hypothesis. In this way, an electron with a certain momentum p can be also seen as a wave with wavelength $\lambda = h/p$ [28].

By using low energy electrons, typically 30-200 eV [26], the electron mean free path in solid matter is reduced to few atomic layers (see Fig. 2.2). This ensures that the electrons interact only with the first few layers of a sample, i.e. with its surface. At the same time, for these energies the De Broglie wavelength of electrons is comparable with interatomic distances within solid matter, i.e. $\lambda = \frac{h}{\sqrt{2mE}} \sim$ 1-2 Å [26]. As a result, for normal incidence, the diffraction grating formula 2.3 also applies to the elastic scattering of electrons with λ the De Broglie wavelength of electrons and a the atomic lattice periodicity of the sample surface. The atomic surface plays now the role of a grid and the relation 2.3 must be adapted to the 2D case.

Due to the fact that electrons are elastically scattered from different atomic planes, the Bragg condition also applies

$$\mathbf{k}_i^{\parallel} - \mathbf{k}_0^{\parallel} = \mathbf{G}_{lm} \qquad \text{with} \qquad |\mathbf{k}_i| = |\mathbf{k}_0| \tag{2.4}$$

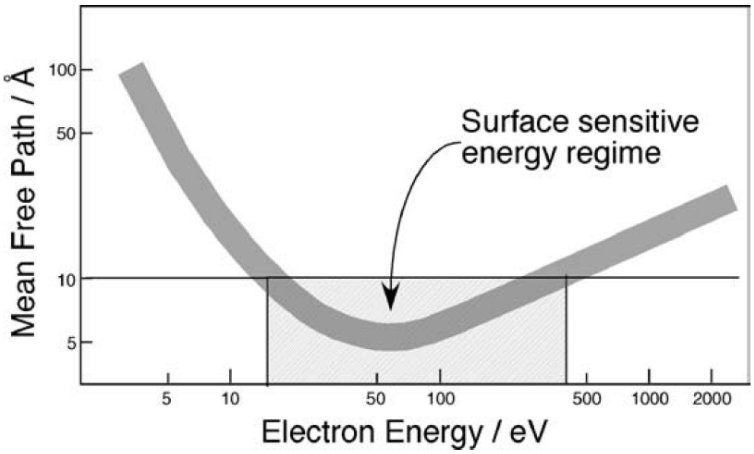

Fig. 2.2 Universal curve of the electron mean free path in solid matter [29].

where $\mathbf{k}_i^{\parallel}$ ($\mathbf{k}_0^{\parallel}$) is the incident (scattered) wave vector component parallel to the surface and $\mathbf{G}_{lm} = l\mathbf{a}^* + m\mathbf{b}^*$ is the 2D reciprocal lattice vector of the surface. Due to the elastic scattering condition the relations 2.4 establish the laws of conservation of momentum and energy respectively (the wave vector component normal to the surface is not conserved).

The main consequence of relations 2.3 and 2.4 is that a Low Energy Electron Diffraction (LEED) pattern, i.e. the spatial distribution of diffraction spots and their intensity, reflects the atomic structure of the probed surface. The first relation in 2.4 allows to label the diffracted beams by means of the reciprocal vector components $\mathbf{G}_{lm} = (l,m)$ (see Fig. 2.3). This implies that the spatial distribution of diffracted spots provides a map of the 2D reciprocal lattice making immediate the evaluation of the surface symmetry. On the other side, the diffraction spot intensity is related to the atomic distribution within the unit cell [26, 28]. It is clear, then, the reason for which Low Energy Electron Diffraction (LEED) is one of the most common diffraction techniques used to characterize the surface structure of crystalline samples under Ultra-High Vacuum (UHV).

The basic experimental set-up constituting the LEED system comprises an electron gun to produce a collimated beam of low energy electrons (30-200 eV) and a hemispherical fluorescent screen allowing to visualize the diffraction pattern of elastic electrons (see Fig. 2.4a) [26, 30]. The electron gun consists of a filament emitting electrons when it is heated with a Wehnelt and a system of electrostatic lenses (respectively W, A, B, C and D in Fig. 2.4a) that collimate, focus and define the energy of the electron beam. Between the electron gun/screen system and the sample a field-free space allows the electrons to go towards the

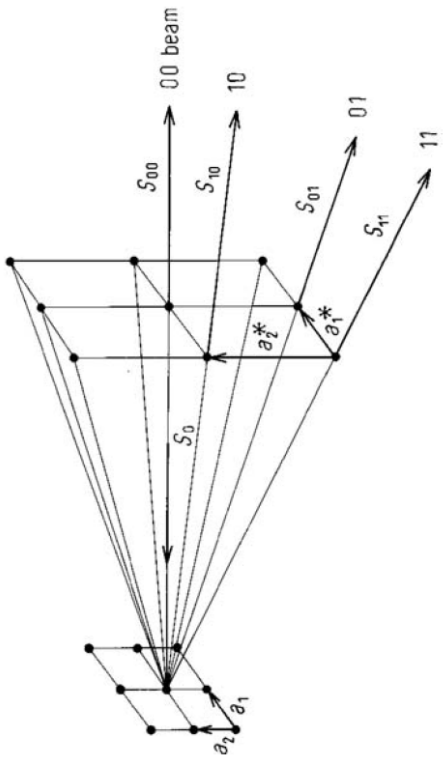

Fig. 2.3 Spatial distribution of the diffracted electron beams giving rise to a LEED pattern. In a normal incidence configuration incident electron beam (S_0) and specular beam (S_{00}) are superimposed [29].

sample surface and to be reflected on the screen. A positive high-voltage ($\sim$5 kV) is applied to the fluorescent screen in order to accelerate the diffracted electrons that can, in turn, excite the screen itself. In this way, the so-called LEED diffraction pattern can be displayed and examined. Fig. 2.4b shows two photos of the fluorescent screen with two LEED patterns arising from the same surface, i.e. a Si(111)-7×7 reconstructed surface, but measured at different electron energies. During the measurement of a LEED pattern the specular beam (S_{00} in Fig. 2.3) gives rise to the specular spot on the screen which is usually referred as $(0,0)$ spot and for normal incidence of electrons it is placed in the middle of the screen. All the other diffraction spots are distributed around the specular spot. From Fig. 2.4b it can be also seen that by increasing the electron energy the diffraction spots shrink towards the specular spot and more spots become visible. This is due to the fact that by changing the electron energy the De Broglie wavelength decreases, thereby reducing the angular distribution of the diffracted beams (see relation 2.3). During the scattering processes inelastic events may occur and their presence manifest itself by means of electrons scattered to random directions because they do not satisfy the Bragg condition 2.4. The net result of all the inelastic events

is a background illumination over the whole screen superimposed to the elastic diffraction spots. In order to reduce the inelastic intensity a negative voltage, called suppressor voltage, can be applied on an intermediary grid in front of the screen (see Fig. 2.4a).

From a point of view of the interpretation the 1×1 LEED pattern is the easiest because, as seen in Section 2.1, it is associated either to a bulk terminated unreconstructed surface or to the structure formed by a foreign adsorbate having a unit cell coinciding with that of the substrate unreconstructed surface. For instance, in Fig. 2.4b, the vertex of the hexagon represent the 1×1 pattern of the Si(111) unreconstructed bulk structure arising from few atomic layers below those involved in the surface reconstruction (the first three topmost layers [31]). In presence of superstructures differing from the 1×1, in addition to the 1×1 spots also called integer-order or main spots, new diffraction spots appear within the LEED patterns, the so-called fractional spots or superspots.

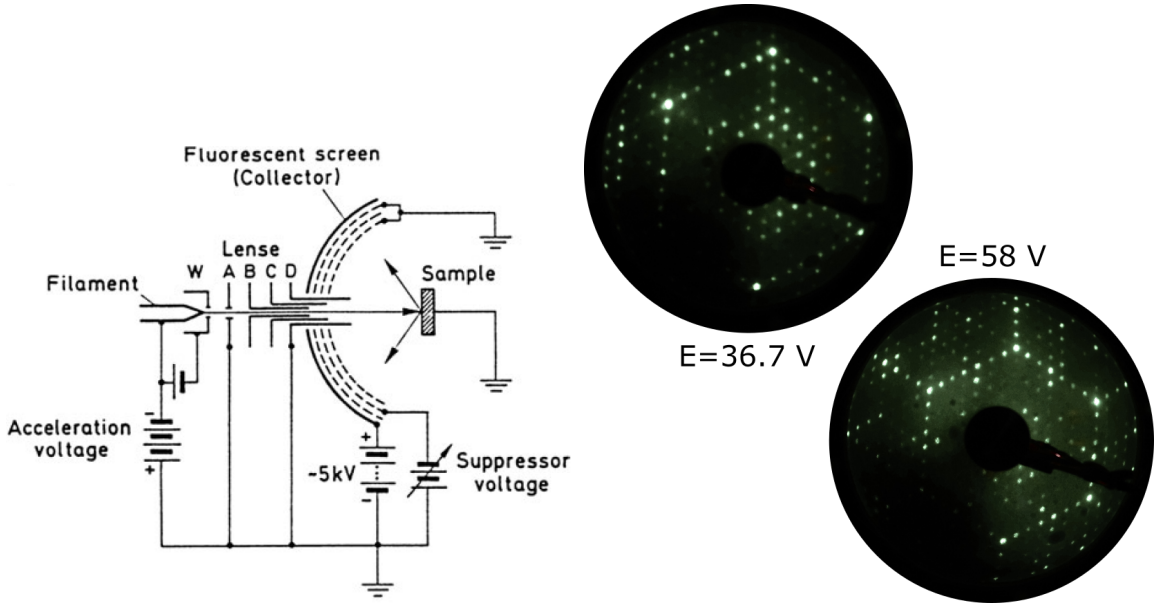

(a) (b)

Fig. 2.4 (a) Schematic of the experimental set-up to perform LEED measurements [30]. (b) LEED patterns arising from a freshly prepared Si(111)-7×7 reconstructed surface. Both the patterns were measured at room temperature and electron energy E=36.7 V and E=58 V.

As already discussed in Section 2.1, superstructures could be due to either surface reconstructions or foreign adsorbates. It should be kept in mind that the longer the superstructure period within the real space, the shorter its period within the reciprocal space and vice versa [26, 30]. Since the diffraction pattern seen on the screen is a direct view of the surface reciprocal lattice, whose spots can be labeled as the coordinates of the reciprocal lattice points given

by the reciprocal vector $\mathbf{G}_{lm} = (l,m)$, all the surface periodicities are immediately visible by simply inspecting the LEED pattern. Therefore, the longer the superstructure period within the real space, the more closely the superspots are spaced in a LEED pattern [26]. For instance, in Fig. 2.4b, besides the 1×1 pattern, the extra spots are due to the 7×7 reconstruction of the first three topmost layers [31]. Since the 7×7, in real space, implies a superstructure seven times larger than the 1×1, the resulting LEED pattern present extra spots with a spacing seven times smaller than that related to the 1×1 spots. It easy to see that the sides of the hexagon formed by the 1×1 are divided in seven parts by the extra spots.

To conclude about the operating principle of LEED, it is important to keep in mind that, in real experiments, the electron beam is not ideally monocromatic and collimated but small deviations in energy and direction are always present. This implies that electron waves have small phase variations. As a consequence, scattered waves coming from regions of the sample whose separation is larger than a characteristic length, called coherence length, cannot interfere in a coherent way to produce a diffraction pattern. In other words, the coherence length represents the size of the region that can be probed by the electrons. At a primary energy of $\sim$100 eV the coherence length typically is of the order of $\sim$100 Å [30]. The effects of the existence of a coherence length can be clearly seen in the case of coexistence of domains with different superstructures on the same surface. If the domains are bigger than the coherence length, the LEED pattern will exhibit the diffraction pattern corresponding to the probed superstructure. On the other hand, if the domains are smaller than the coherence length, the LEED pattern will be the superposition of the diffraction patterns arising from the different probed superstructures.

In the present work LEED was systematically used as a method to check the crystallographic quality of prepared surfaces. In particular, the LEED pattern from a clean and well-reconstructed surface consists of sharp spots and low background illumination. On the other hand, defects and contaminants broaden the spots and contribute to the background intensity. More importantly, LEED was a successful method to monitor the growth of different Pb structural phases on top of a Si(111) substrate (see Chapter 3). In particular, when a single Pb atomic layer grows on top of the silicon either a Pb coverage change of 0.01 ML or the temperature of the sample can modify its surface superstructure. Accurate inspection of the LEED pattern changes during the Pb growth has allowed me to finely control the preparation of each of these phases.

2.3 Scanning Tunneling Microscopy (STM)

2.3.1 General considerations

Scanning Tunneling Microscopy (STM) is an experimental method, developed by Binnig and Rohrer, to image surfaces at atomic resolution [32, 33]. It is part of the more general Scanning Probe Microscopy (SPM) whose basic principle is based on a small probe brought close enough to the surface to measure a particular property by means of a specific interaction, e.g. current, van der Waals or magnetic forces [28, 29, 34]. The aim of STM is to measure the tunneling electron current flowing between a sharp tip and the surface of the sample when they are close enough for the electrons to tunnel when a bias is applied (see Fig. 2.5). Since a current has to be measured, both the tip and the surface must be conductive. Typical materials used to fabricate tips are W or Pt/Ir. To a first approximation, the tunneling current depends exponentially on the tip-surface distance

$$I_T \propto \exp^{-2\kappa d}. \tag{2.5}$$

κ contains the details of the potential barrier between the surface and the tip (vacuum gap) and d is the tip-surface distance. Since $\kappa \sim 1$ Å^{-1}, if d changes by $\sim$1 Å, the tunneling current change by one order of magnitude [29]. Typical tip-surface distances are of the order of one nanometer (0.5-1.5 nm [28]) and applied voltages range between 2 mV and 2 V in absolute value [28]. In these conditions typical values for tunneling current (of the order of pA) lead to extreme vertical sensitivities within the sub-Å range [28, 29]. Moreover, the exponential dependence of the tunneling current on the tip-surface distance is responsible for the atomic resolution (lateral resolution) because with atomically sharp tips the tunneling process is really localized at the atomic apex of the tip itself. This means that if the tip is ideally prepared, all the tunneling current flows through one single atom at the tip apex. [28, 34].

When the tip is in tunneling regime, STM images are measured by scanning 2D regions of the surface in the form of an (x,y) matrix [28, 29, 34]. It is possible to do this thanks to the fact that the tip is fixed on a piezoelectric tube operated from an electronic controller also called feedback loop (see Fig. 2.5). Two dimensional regions are scanned by successive lines. During the scanning process the tunneling current is monitored and a feedback controller regulates the tip-surface distance acting by changing the extension of the piezoelectric tube in the z direction. STM images can be measured by means of two operating modes depicted in Fig. 2.5. In constant height mode (see Fig. 2.5a) the surface is scanned without regulating the tip-surface distance (feedback loop open) and therefore it cannot follow the surface

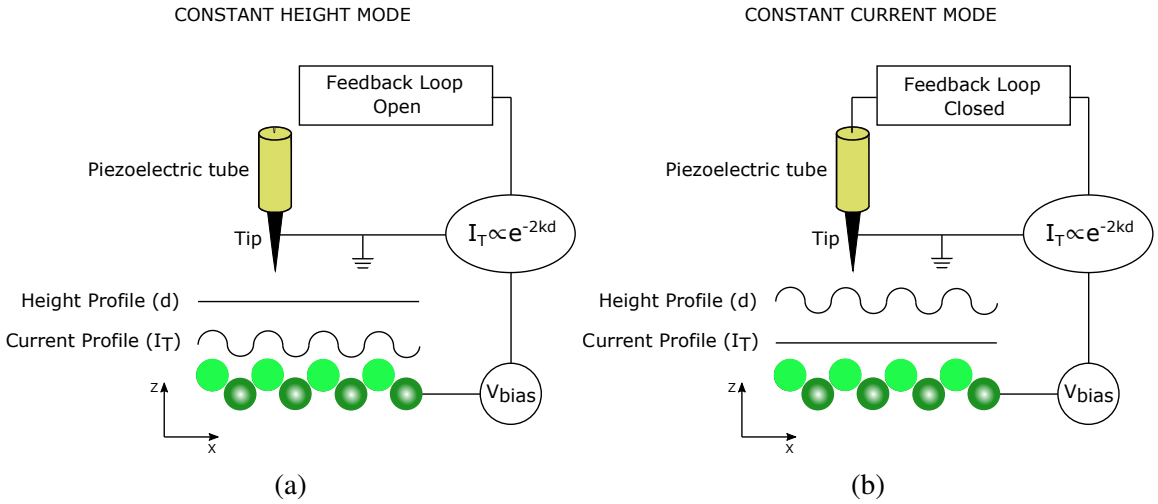

Fig. 2.5 Schematic sketch of the operating principle of a Scanning Tunneling Microscope (STM). (a) Constant height mode. (b) Constant current mode.

corrugation. The current variations $\Delta I_T(x,y)$, with respect to a defined setpoint, due to the surface corrugation are recorded when this method is used. In constant current mode (see Fig. 2.5b) the surface is scanned by keeping constant the local current value. Consequently, the tip can follow the surface profile by adjusting the distance to the surface. The variations $\Delta z(x,y)$ of the piezoelectric tube, with respect to a defined setpoint, are recorded. Depending on the operating mode, STM images are formed by plotting the variations $\Delta I_T(x,y)$ or $\Delta z(x,y)$ as a function of the (x,y) tip position. The intensities of $\Delta I_T(x,y)$ and $\Delta z(x,y)$ are represented by means of false color scales. Ultimately, an STM image is displayed in the form of a topview of the scanned 2D region where all the information is contained in the false color scale. In this thesis all topographic STM images were recorded in constant current mode.

2.3.2 Metal-Vacuum-Metal Tunneling Junction

Electron tunneling can take place between two metals when they are sufficiently close and a bias voltage is applied between them [28, 29, 34]. Fig. 2.6a shows that two metals, labeled as 1 and 2, close and not in electric contact keep their own Fermi levels. Φ_1 and Φ_2 represent their work function respectively, i.e. the energy required to extract an electron from the Fermi level to zero energy outside the crystal. In this situation, the vacuum gap between the two metals, whose width is indicate by d, generates a constant potential barrier for the electrons within them (indicated by a black solid line). Fig. 2.6b shows the electronic configuration of the two metals put in electric contact. The thermodynamic equilibrium condition requires the alignment of the Fermi levels and therefore no current flow in the system. This condition

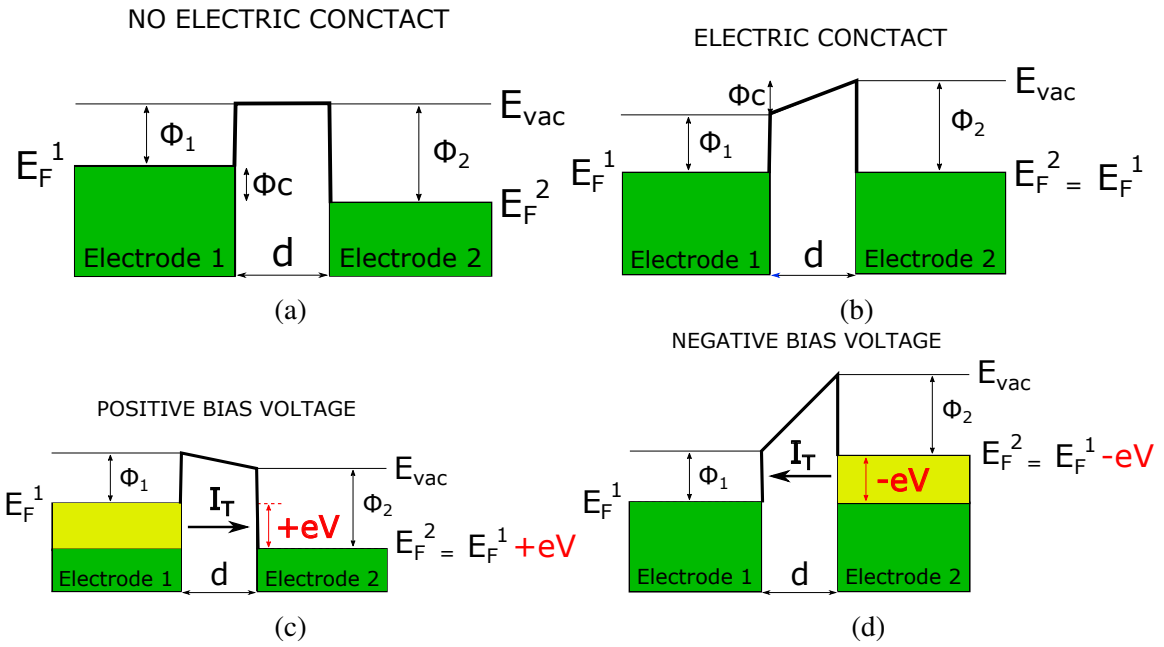

Fig. 2.6 Schematic sketch of the behavior of Fermi (E_F) and vacuum levels (E_{vac}) for two metallic electrodes separated by a distance d and forming a tunneling junction. (a) No electric contact. (b) In electric contact and thermodynamic equilibrium (without applied voltage). No current can flow through the junction. (c) [(d)] Positive [negative] applied voltage to electrode 1 makes available unfilled states in electrode 2 [1] within an interval $|eV|$ from the Fermi level. Electrons within the yellow stripe of electrode 1 [2] can tunnel through the junction. Φ_1 and Φ_2 represent the work function of the electrode 1 and 2 respectively. Φ_C represents the contact potential between the two electrodes.

is reached by means of the contact potential $\Phi_C = E_F^1 - E_F^2$ between the two materials that transforms the constant potential barrier in a trapezoidal potential barrier (indicated by a black solid line). At this point, a bias voltage V can be applied between the two metals the effect of which is to modify the relative alignment of the Fermi levels allowing the electrons to tunnel from the filled states of one electrode to the empty states of the other (see Fig. 2.6c and Fig. 2.6d). The direction of the tunneling current I_T depends on the relative potential. In particular, only the states within an interval eV from the Fermi level (yellow stripe in Fig. 2.6c and Fig. 2.6d) of the electrode 1, considered as reference, take part in the tunneling process. This is due to the fact that, in this context, the electrons elastically tunnel from one electrode to the other and therefore only horizontal transitions (without loss of energy) are considered. It should be pointed out that, in a classical picture no current could flow because of the potential barrier. However, since the two metals are close enough, the tunneling process is allowed by quantum mechanics. Ultimately, the tunneling current can be written

as follows [35]:

$$I_T \propto \int_0^{eV} \rho_1(r,E)\rho_2(r,eV-E)T(d,E,eV)dE \tag{2.6}$$

with

$$T(d,E,eV) = exp\left(-\frac{2d\sqrt{2m}}{\hbar}\sqrt{\frac{\Phi_1+\Phi_2}{2}+\frac{eV}{2}-E}\right). \tag{2.7}$$

In previous relations $\rho_1(r,E)$ and $\rho_2(r,eV-E)$ are the density of states of the electrodes 1 and 2, respectively, calculated in the position r where the tunneling process takes place. At this point it is clear that the two electrodes can be seen as the surface and the tip respectively. V represents the applied voltage measured with respect to the Fermi level of the surface (electrode 1) whose potential is taken as reference. E represents one generic energy level of those involved in the tunneling process, i.e. one of those within the interval eV from the Fermi level. $T(d,E,eV)$ is the tunneling transmission probability containing the information about the tip-surface distance d and the potential barrier between the two metals, i.e. its height relative to the electron energy involved in the tunneling process. $T(d,E,eV)$ contains the exponential dependence of the tunneling current written in relation 2.5.

Equation 2.6 shows that the tunneling current is always a convolution between the density of states of the tip and that of the surface sample regardless its flowing direction. The most important consequence is that STM images do not contain bare structural information about the surface only but incorporate information about the electronic structure of both the tip and the surface. For imaging in constant current mode and applied voltages around the Fermi level, i.e. $V \ll \Phi$, the transmission function $T(d,E,eV)$ can be considered just a constant [35]. Furthermore, the most commonly used materials to fabricate STM tips, e.g. W and Pt/Ir, are usually modeled as simple metals with constant density of states around the Fermi level. With these assumptions the tunneling current 2.6 mainly depends on the density of states of the surface ρ_1 integrated between E_F and $E_F + eV$. As a consequence, contrast changes within STM images can be related to the electronic structure of the sample in addition to other structural effects. Therefore, scanning at positive or negative voltage enables probing empty or filled states of the sample. This is because the direction of the tunneling current can be reversed by reversing the sign of the applied voltage, i.e. the electrons can start to tunnel from the filled states of the sample for positive voltages (see Fig. 2.6c) or they can reach its unfilled states for negative voltages (see Fig.2.6d). Fig. 2.7a and Fig. 2.7b show typical STM images of a freshly prepared Si(111)-7×7 surface taken at positive and negative voltage respectively (constant current mode). Green arrows indicate the same surface defect to emphasize that the two images were acquired by scanning over the same area of the sample. From these images it is clear that the surface is characterized by an hexagonal structural symmetry. On

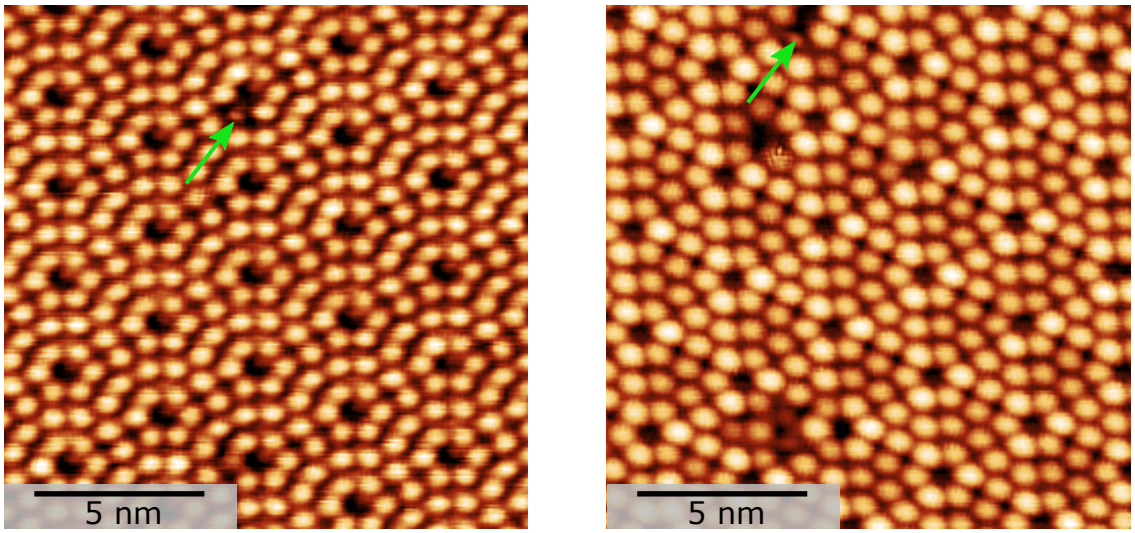

(a) (b)

Fig. 2.7 STM images of a Si(111)-7 × 7 surface measured at room temperature. (a) Image size: 15 × 15 nm^2, V_T: +2 V and I_T: 20 pA. (b) Image size: 15 × 15 nm^2, V_T: -2 V and I_T: 20 pA. Gren arrows indicate the same surface defect.

the other hand, the appearance of bright protrusions and the relative intensities completely change passing from positive to negative bias voltage. This is due to the different spatial modulation of the tunneling current as a result of the different spatial distribution of filled and unfilled states [35]. In other words, every surface has its own density of surface states and, by selecting a voltage, the tunneling current modulation gives their spatial distribution.

2.4 Scanning Tunneling Spectroscopy (STS)

As already said, it is not possible to separate the structural information from the electronic one within STM images. Anyway, it is possible to carry out this separation by means of Scanning Tunneling Spectroscopy (STS) measurements. This technique makes it possible to probe the electronic structure of surfaces around the Fermi level with spatial resolution [28, 29, 34, 35]. In a STS measurements the tip is firstly placed at a point of interest. Then, the feedback loop controlling the tip-surface distance is opened and subsequently the bias voltage is swept over a certain energy range. The resulting current curve $I_T(V)$ is finally recorded. Since the feedback loop is opened, the tip-surface distance remains constant during the voltage ramp, therefore from the expression of the tunneling current 2.6 it can be seen that current variations arise from both density of states and transmission function modulations. By differentiating the measured $I_T(V)$ curve a direct relation between the so-called differential

conductance $\frac{dI_T}{dV}$ and the density of states of the sample is obtained. This fact can be easily seen by differentiating the relation 2.6 [35]:

$$\frac{dI_T}{dV} = \rho_s(r,eV)\rho_t(r,0)T(d,eV,eV) + \int_0^{eV} \rho_s(r,E)\rho_t(r,eV-E)\frac{dT(d,E,eV)}{dV}dE \qquad (2.8)$$

The second term contains the voltage dependence of $T(d,E,eV)$. It can be shown that it is a smooth monotonic function of the applied voltage [35]. This implies that experimental $I_T(V)$ curves, besides the spectroscopic features of the sample, contain a smooth background if the voltage is ramped in a large range of values, i.e. $|V_{max}| \sim$1-2 V. On the other hand, if $I_T(V)$ curves are measured around the Fermi level, i.e. $|V| \ll \Phi$, this smooth contribution can be neglected. In any case, the first term is the most interesting because it directly relates the differential conductance curve $\frac{dI_T}{dV}(V)$ to the local density of states $\rho_s(r,eV)$ of the sample. It should be pointed out that, since the tip density of states $\rho_t(r,eV)$ is supposed to be uniform around the Fermi level, it is simply evaluated at the Fermi level itself, i.e. $eV = 0\ eV$.

To summarize, once the $I_T(V)$ curves are recorded at a certain point they must to be differentiated in order to extract the information about the electronic structure of the sample at that point. Then, the spatial resolution can be obtained by scanning 2D regions and by measuring $I_T(V)$ curves at each image pixel. The recorded curves are subsequently differentiated to obtain the $\frac{dI_T}{dV}(V)$ curves and reshaped to form differential conductance maps for each applied voltage. Contrast modulations in these maps reflect the spatial distribution of surface electronic states for a given energy, i.e. the spatial resolution of the surface electronic structure. Atomically resolved spectroscopy is one of the advantages of STS respect to the photoemission spectroscopy techniques that average over large portions of surface losing the local details.
We conclude this section by noting that, at absolute zero, the derivative of the current is directly proportional to the density of states (DOS). On the other hand, at finite temperatures the spectral features are broadened by a factor $\sim$3.5 k_BT. This is the reason for which we will perform experiments at temperatures as low as possible to avoid thermal broadening. In particular, our experimental setup allows us to work at 300 mK leading to a spectral resolution of 100 μeV ($\sim$3.5 k_BT).
It is also interesting to point out that the term $\rho_s(r,E)$ in equation 2.8 contains matrix elements that tend to privilege certain tunneling channels between the two electrodes. In particular these matrix elements induce a selectivity for k close to 0 that corresponds to slowly decreasing wave-functions in the vacuum.

2.4.1 Normal metal-Superconductor Tunneling

So far, the tunneling junction consisting of two metallic electrodes was discussed. To summarize, the tunneling current I_T curve is a nearly linear function of the applied voltage V on top of which the modulations due to the electronic structure of the sample Density of States (DOS) are superimposed. Therefore, the $\frac{dI_T}{dV}$ curve is nearly a constant (see the thin solid line in Fig. 2.8a and Fig. 2.8b respectively). If one of the electrodes becomes superconductive the general behavior of I_T changes.

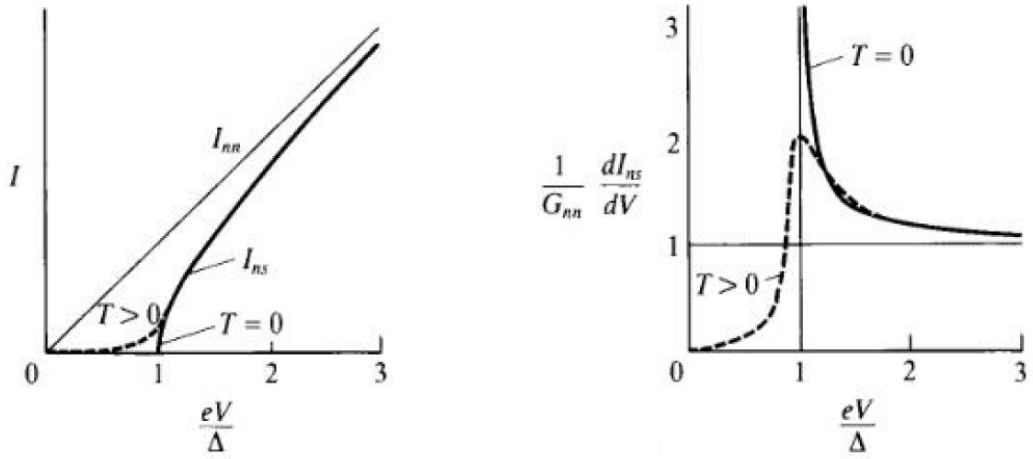

(a) (b)

Fig. 2.8 (a) Tunneling current I_T and (b) differential conductance $\frac{dI_T}{dV}$ as a function of the applied voltage eV. Thin solid lines refer to the curves (I_{nn} and $\frac{dI_{nn}}{dV}$) arising from a junction consisting of two normal metals. Thick and dashed lines represent the curves (I_{ns} and $\frac{dI_{ns}}{dV}$) arising from a junction formed by a normal metal and a superconductor at $T = 0\ K$ and $T \neq 0\ K$ respectively [36].

At T=0 K electrons cannot tunnel for voltages below $\frac{\Delta}{e}$ because the superconducting gap prevents the existence of available states around the Fermi level (see Fig. 2.9a) [36]. Starting from $|V| = \frac{\Delta}{e}$ a tunneling current starts to flow through the junction and excitations can be created within the superconductor. Yellow strip in Fig. 2.9a represents the fraction of electrons that participate to tunneling current. The behavior of I_T and $\frac{dI_T}{dV}$ is illustrated by the thick solid line in Fig. 2.8a and Fig. 2.8b respectively (it is the same regardless the sign of the applied voltage). At $T \neq 0\ K$ thermal excitations already present within the superconductor allow the tunneling process already for voltages below $\frac{\Delta}{e}$. This is illustrated in Fig. 2.9b, where the yellow regions represents the fraction of electrons that participate to tunneling for $eV < \Delta$. This also explains the tail of the dashed line in Fig. 2.8a. Ultimately, Fig. 2.8b shows that the differential conductance $\frac{dI_T}{dv}$, at low temperatures, better represents the BCS density

of states and conversely, at high temperatures, the curve is broadened in energy (remember that spectral features are broadened by a thermal factor $\sim$3.5 k_BT).

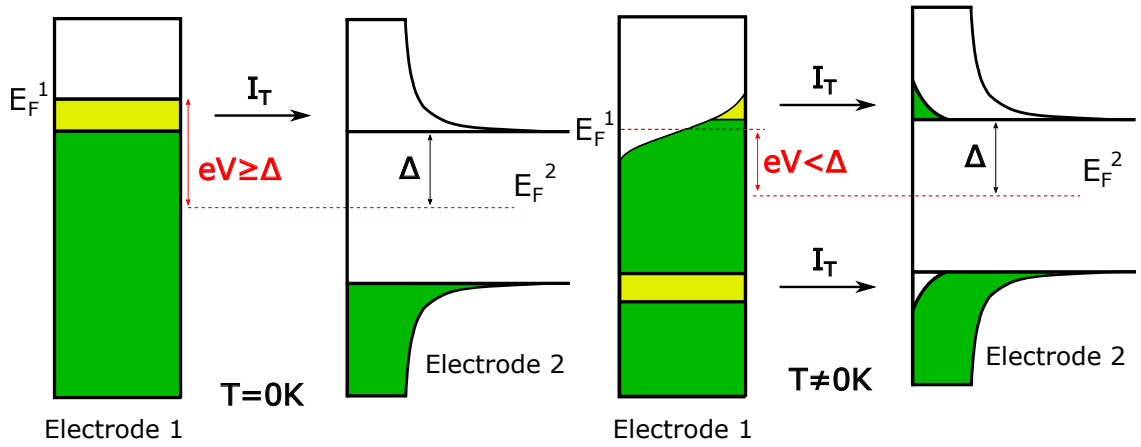

Fig. 2.9 Simple model of elastic tunneling through a junction consisting of a normal metal and a superconductor. Electron tunneling takes place from filled states of one electrode to empty states of the other. Density of states is plotted horizontally as a function of the electron energy. (a) Tunneling at $T = 0\ K$ and applied voltage $eV \geq \Delta$. (b) Tunneling at $T \neq 0\ K$ and applied voltage $eV < \Delta$. In this case the tunneling process involves thermally excited electrons and holes. Yellow regions represent the fraction of electrons that participate to tunneling.

2.4.2 Superconductor-Superconductor Tunneling

If both the electrodes of the tunneling junction are superconductive, at $T = 0$, the electrons cannot tunnel for voltages below $\frac{\Delta_1+\Delta_2}{e}$ (see Fig. 2.10a) [36]. Starting from $|V| = \frac{\Delta_1+\Delta_2}{e}$ the alignment between the filled BCS peak of one electrode and the unfilled one of the other allows the tunneling current to flow. This behavior can explain the jump in the tunneling current at $|v| = \frac{\Delta_1+\Delta_2}{e}$ of the thick solid line in Fig. 2.11. The same result is obtained regardless the sign of the applied voltage. At $T \neq 0\ K$, the thermal excitations already present within the superconductor allow the tunneling process, from the filled states of one electrode to the empty states of the other, already for voltages below $\frac{\Delta_1+\Delta_2}{e}$ [36]. In particular, the current increases up to $|V| = \frac{|\Delta_1-\Delta_2|}{e}$ when the nearly unfilled BCS peaks of the two electrodes align (see Fig. 2.10b). Above $|V| = \frac{|\Delta_1-\Delta_2|}{e}$ the density of thermal electrons contributing to the tunneling current is always the same but the empty density of states that can be probed is strongly decreased once the BCS peak has been overcome (see Fig. 2.10c). The net result is a peak of I_T centered on $\frac{|\Delta_1-\Delta_2|}{e}$ (see the dashed line in Fig. 2.11). Consequently, above

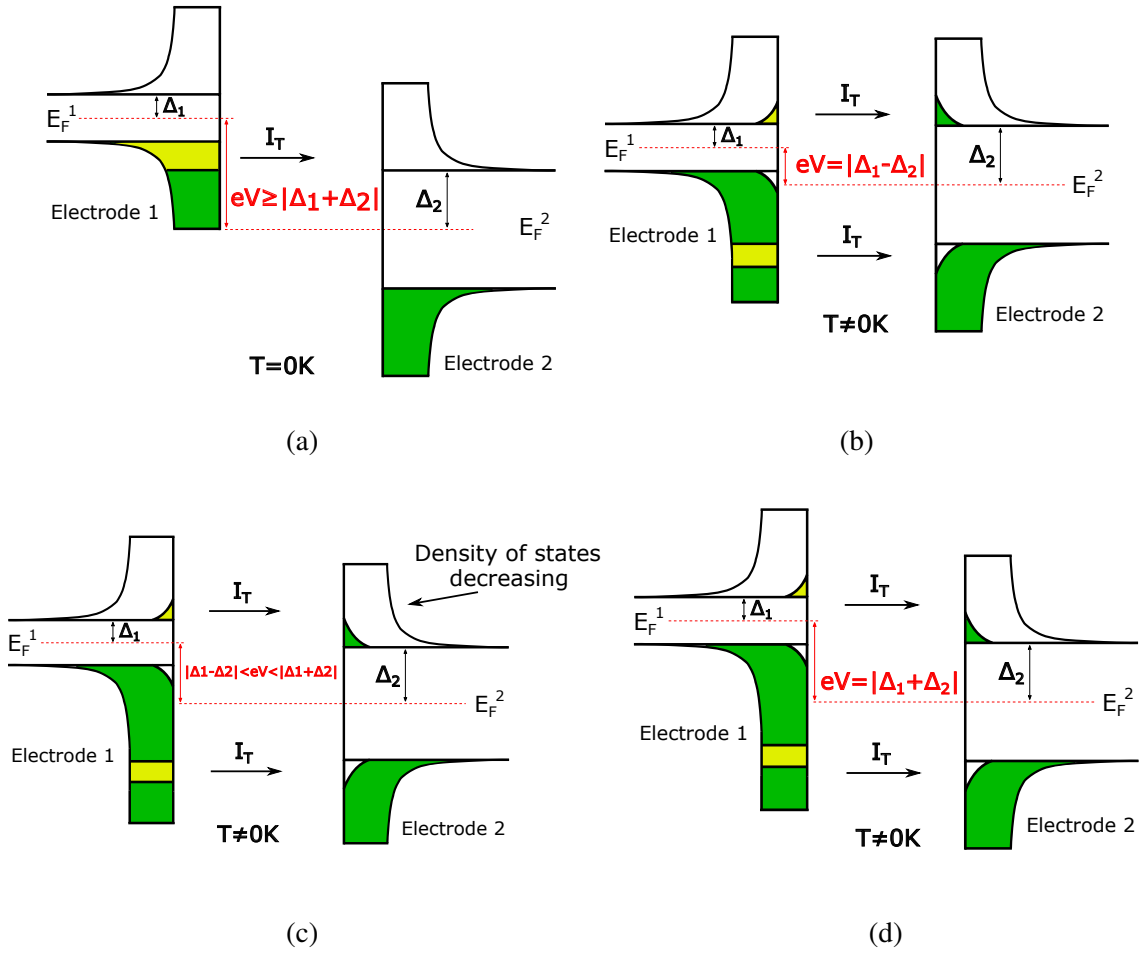

Fig. 2.10 Elastic tunneling through a superconductor-superconductor junction. Electron tunneling takes place from filled states of one electrode to empty states of the other. Density of states is plotted horizontally as a function of the electron energy. (a) Tunneling at $T = 0\ K$ and applied voltage $eV \geq \Delta_1 + \Delta_2$. (b) and (c) Tunneling at $T \neq 0\ K$ and applied voltage between $\Delta_1 - \Delta_2$ and $\Delta_1 + \Delta_2$. In this conditions the tunneling process involves thermally excited electrons and holes. (d) Tunneling at $T \neq 0\ K$ and applied voltage $eV = \Delta_1 + \Delta_2$. From this point, all the other electrons apart from the thermal ones start to contribute to the tunneling current. Yellow regions represent the fraction of electrons that participate to tunneling.

$|V| = \frac{|\Delta_1 - \Delta_2|}{e}$ the tunneling current decreases inducing a Negative Differential Resistance region between $\frac{|\Delta_1 - \Delta_2|}{e}$ and $\frac{|\Delta_1 + \Delta_2|}{e}$ (see Fig. 2.11) [36]. As shown in Fig. 2.11, starting from $V = \frac{|\Delta_1 + \Delta_2|}{e}$ the current steeply increases due to the alignment of the nearly filled BCS peak with the nearly unfilled one (see Fig. 2.10d). The two features at $V = \frac{|\Delta_1 - \Delta_2|}{e}$ and $V = \frac{|\Delta_1 + \Delta_2|}{e}$ of the tunneling current are experimentally useful to accurately determine the temperature dependence of both $\Delta_1(T)$ and $\Delta_2(T)$ [36]. In general, the energy resolution provided by the

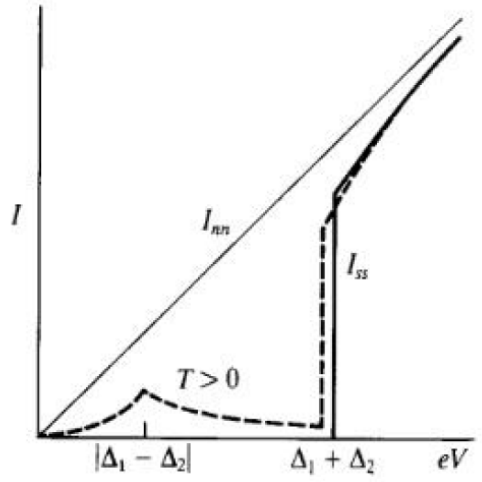

Fig. 2.11 Thin solid line represents the tunneling current I_T (I_{nn}) as a function of the applied voltage eV through a junction consisting of two normal metals. Thick and dashed lines represent I_T (I_{ss}) through a superconductor-superconductor junction at $T = 0\ K$ and $T = \neq 0\ K$ respectively. Two features at $|\Delta_1 - \Delta_2|$ and $|\Delta_1 + \Delta_2|$ are observed for $T \neq 0\ K$ [36].

superconductor-superconductor junction is improved. This is due to the existence of very sharp BCS peaks that somehow compensate the thermal broadening [36].

2.4.3 Topographic data analysis

All topographic STM images were treated with Gwyddion. The main methods used were the slope subtraction to correct the slope present in raw data and a noise filter based on the Fast Fourier Transform (FFT).

2.4.4 Spectroscopic data analysis

All spectroscopic data presented in this manuscript were processed with a Python program that I specifically developed. During STS experiments $I(V)$ curves are recorded. However, Fig. 2.12a shows that individual $I(V)$ curves are quite noisy (see black curve). The main sources of noise in this kind of experiments are mechanical and electromagnetic in nature. The first intervention to treat this kind of data is to apply a gaussian filter to the $I(V)$ signal. The principle of this filter is to convolute experimental data with a Gaussian function defined over an energy window whose width is adjusted in order to avoid physical information loss, i.e. it is usually smaller than the thermal broadening given by 3.5 k_BT. The red curve in Fig. 2.12a shows the result of this gaussian filtering process.
Fig. 2.12b shows the dI/dV curve obtained by the filtered signal of Fig. 2.12a. Remember

that dI/dV is directly related to the local density of states $\rho_s(r,eV)$ of the sample and thus to its local electronic properties (see section 2.4). By looking at Fig. 2.12b, it is clear that the gaussian filtering is not able to remove all the noise of the experimental signals. The strategy to overcome this problem is to select a 2D portion of the sample surface (for instance that shown in Fig. 2.13a), define a grid of points on it and for each point measure a $I(V)$ curve. After that, a Gaussian filter is applied to each $I(V)$ curve and dI/dV spectra are then calculated. At the end, an average over all the dI/dV curves taken at each point of the grid makes it possible to obtain clean spectra representing the local electronic properties of the whole region (see Fig. 2.13b). It is important to note that, during the measurement over the

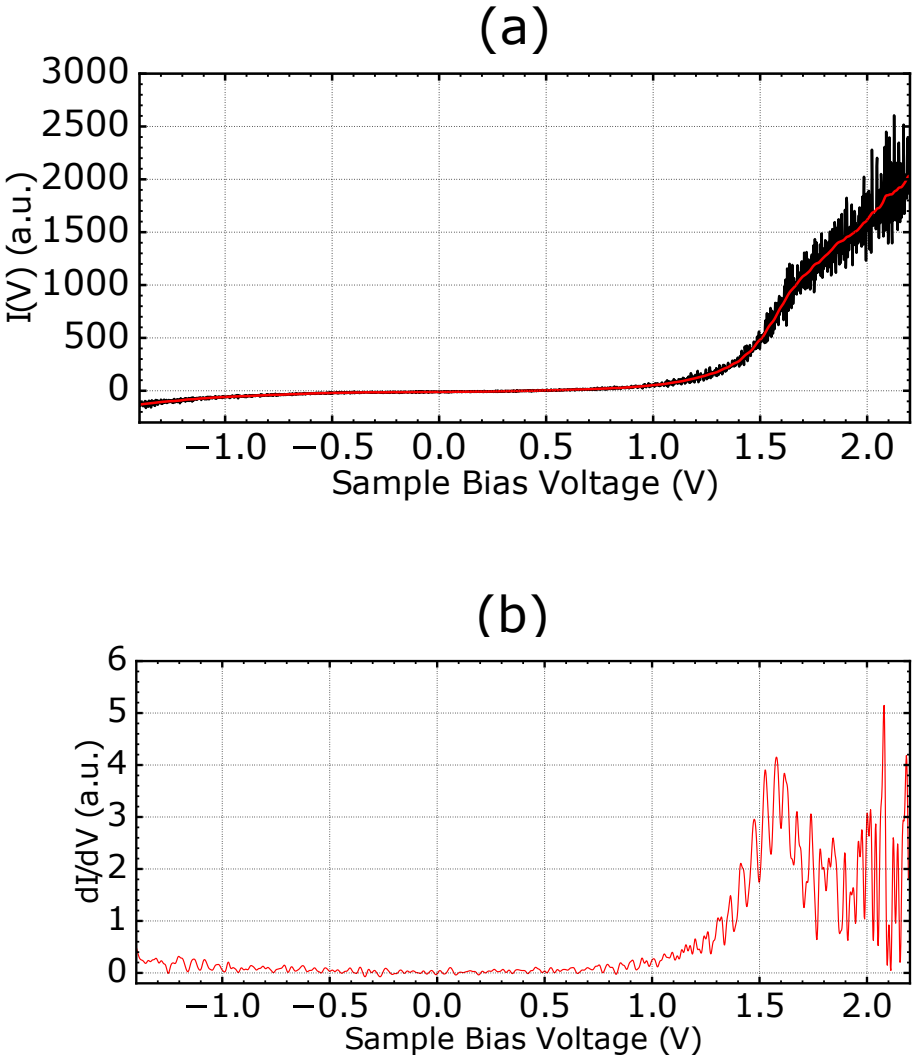

Fig. 2.12 (a) The black curve represents an individual raw STS spectrum while the red curve is the same spectrum filtered by means of a gaussian filter. (b) This curve represents the derivative of the filtered spectrum shown in figure (a). All the spectra contain 2000 points.

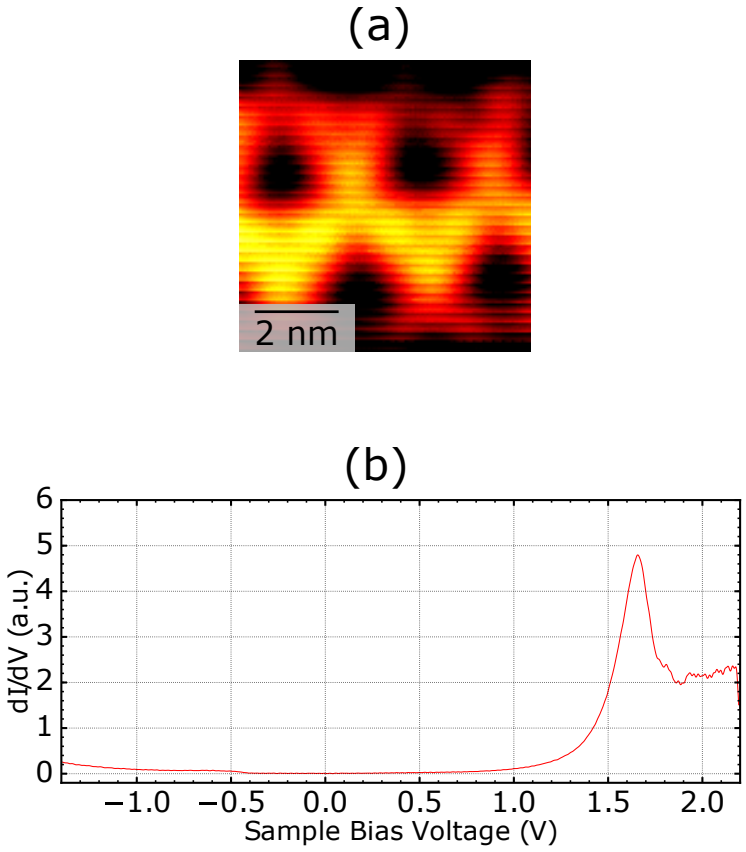

Fig. 2.13 (a) Topographic STM image simultaneously acquired during an STS experiment showing the investigated region of a 3 ML Pb island grown on Si(111). Image size: $6.9 \times 6.9\ nm^2$, V_T: $+1.7$ V and I_T: 50 pA. The image was taken over a 120×120 grid of pixels. (b) Mean dI/dV spectrum obtained by averaging all the spectra acquired on a 30×30 grid defined over the region shown in (a) after being filtered, derived and normalized.

grid, topography and spectroscopy are acquired with different setpoint conditions of voltage ($V_{set\,point}$) and current ($I_{set\,point}$) point by point. However, the same topographic/spectroscopic setpoint is applied to all the points of the grid. Another important thing to know about this topo-spectroscopy method is that topographic information is acquired with the feedback loop regulating the tip-surface distance closed while for spectroscopic data (I/V curves) it is opened to avoid regulation-induced artifacts.

In real experiments the spectroscopic setpoint is not necessarily the same at each point of the grid. For this reason, in order to put together and compare spectra taken on different points of the grid, all the spectra must be normalized. The normalization is carried out by considering regions of spectra with constant density of states, i.e. far from important spectroscopic features of the sample. For this purpose, the energy window over which $I(V)$ curves are acquired are always adjusted to guarantee the possibility of normalizing.

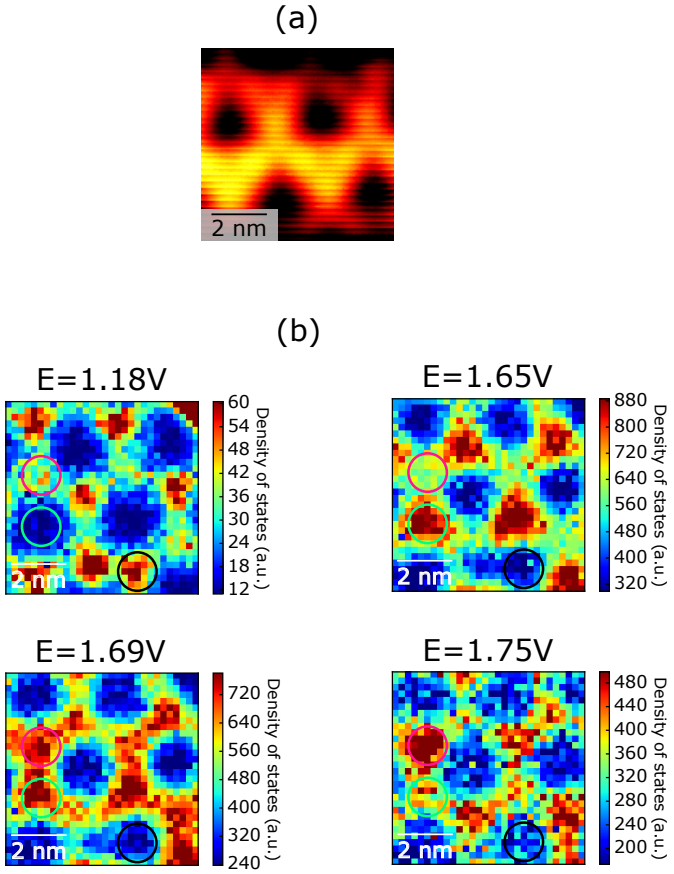

Fig. 2.14 (a) The same topographic STM image shown in Fig. 2.13a. (b) 2D differential conductance maps traced at different energies. These maps are represented by means of a false color scale in which blue indicates the lowest spectral intensities and red the highest ones. Spatial modulations of the contrast can be directly related to the to the spatial modulations of the sample LDOS.

The topo-spectroscopic method described above implicitly makes it possible to measure the local electronic properties of a sample with a certain spatial resolution given by the size of the scanning area and the number of points of the grid. The choice of a certain spatial resolution depends on the length scale over which the investigated physics occurs. In any case, it should be outlined that the duration of 300 mK experiments is limited by the ^3He condensation time, i.e. 35 hours. This time limits the time required to acquire an individual spectrum leading to the noisy spectra shown in Fig. 2.12 as well as the spatial resolution of the spectroscopic measurements, that is, the number of spectra per unit area. Therefore, in this kind of experiments a compromise between minimal noise expected for individual spectra and spatial resolution is necessary.

Once a topo-spectroscopic experiment ends the fact of having at each point of the grid an entire dI/dV spectrum makes it possible to extract position and energy dependent maps of

the differential conductance dI/dV itself and investigate the spatial evolution of the local electronic properties of the sample. Fig. 2.14b, for instance, shows maps at different energies obtained by dI/dV curves measured over the region depicted in Fig. 2.14a (which is the same shown in Fig. 2.13a). As will be done within this manuscript, another possibility is to average the spectra over different portions of the scanned region and show the corresponding dI/dV curves.

2.5 Ultra-High Vacuum (UHV) equipments

In different parts of the manuscript the extreme sensitivity of Pb/Si(111) thin films to contamination is discussed. In particular, the presence of foreign species, even in small amounts, during and/or after the preparation can affect different aspects of both their structure and their growth mode. In order to ensure favorable conditions for the growth of "proper" crystalline thin layers of Pb on top of the Si(111) substrate, all the experiments were performed under Ultra-High Vacuum (UHV) with base pressures better than 1×10^{-10} mbar and without ever exceeding 5×10^{-10} mbar at all stages of the sample preparation. In order to check the control over the large number of parameters involved in sample preparation, different aspects of the growth were characterized on different experimental systems, until all steps were fully mastered to perform STS experiments at 300 mK on the MnPc/Pb/Si(111) system. I present in the following the experimental equipment I used to achieve good preparation conditions.

2.5.1 Low Energy Electron Diffraction (LEED) setup

I first started experiments on this setup. It enabled the growth of a single atomic layer of Pb on a Si(111) substrate by means of Molecular Beam Epitaxy (MBE) and the structural characterization by means of LEED. As will be seen in Chapter 3, a large number of Pb surface reconstructions can be observed in the range between $\frac{1}{6}$-ML and 1.3 ML and by varying the sample temperature. In particular, the aim of these experiments was to optimize the parameters to prepare a particular reconstruction that can be found at 1.2 ML of Pb and below 270 K, the so-called $\sqrt{7} \times \sqrt{3}$ -Pb phase. As this setup allows to operate only at room temperature, in practice, only the room-temperature reconstruction of the 1.2 ML Pb monolayer was ultimately observed (details carefully discussed in Chapter 3).

These growth experiments were carried out in the UHV system shown in Fig. 2.15. It consists of three chambers connected by means of UHV gate valves and two load lock systems for the introduction of samples, i.e. silicon substrate in the present case. A system of transfer arms,

hooks and wobble sticks allows the sample to be displaced through the whole system. The base pressure, better than 1×10^{-10} mbar, can be achieved in each chamber after a bakeout procedure at 150° C and it is maintained over time through a pumping system including primary, turbomolecular, ionic and Titanium Sublimation pumps (TSP). The preparation

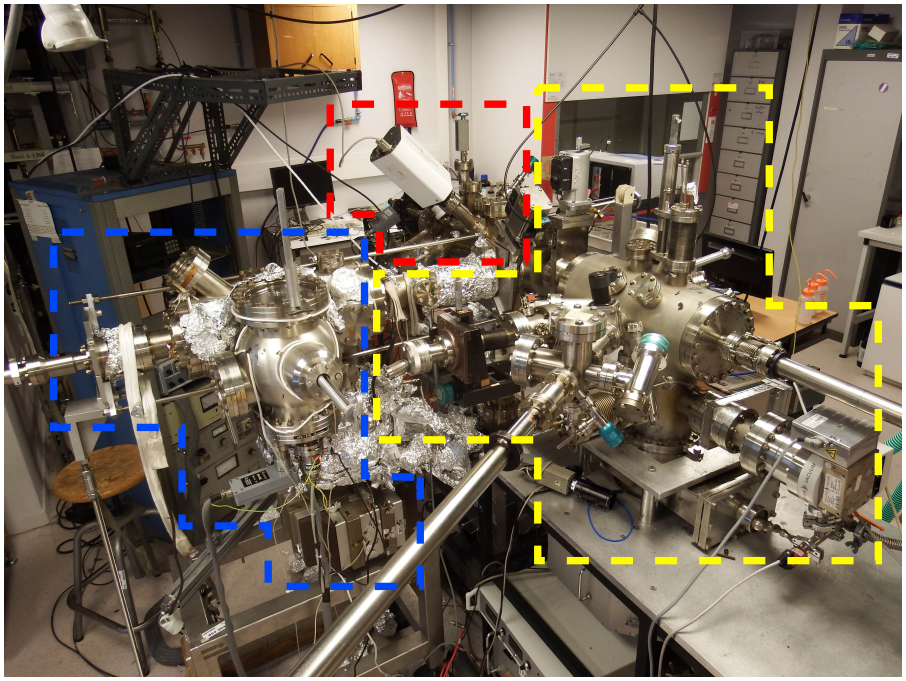

Fig. 2.15 Picture of the UHV experimental setup used for the room-temperature LEED characterization of the Pb monolayer growth on Si(111). Red dashed line: preparation chamber. Yellow dashed line: organic chamber. Blue dashed line: STM chamber.

chamber (see Fig. 2.15) is equipped with a Knudsen cell (Createc) for the evaporation of pure Pb (99.999%) on top of the Si(111). This kind of evaporators contain a crucible heated with a filament by Joule effect. As this heating method does not give rise to ionized Pb atoms during the evaporations, the atomic flux can be solely monitored and calibrated by means of a quartz balance. A water cooling system allows the crucible temperature to be stabilized and finely controlled. This chamber is also equipped with a 5 axes manipulator making it possible to heat samples either by resistive (up to ∼700° C) or by direct current heating (up to ∼1200° C). An ion gun together with the resistive heating allow samples to be prepared by means of sputtering and annealing cycles. Direct current heating was the method used in this work to prepare both the Si(111) and the Pb/Si(111) surfaces and their temperatures were read by means of an infrared pyrometer. Furthermore, the manipulator makes it possible to move the sample in front of the different preparation tools. The preparation chamber is also equipped with a LEED-Auger (Omicron) which provided a fast method to monitor the

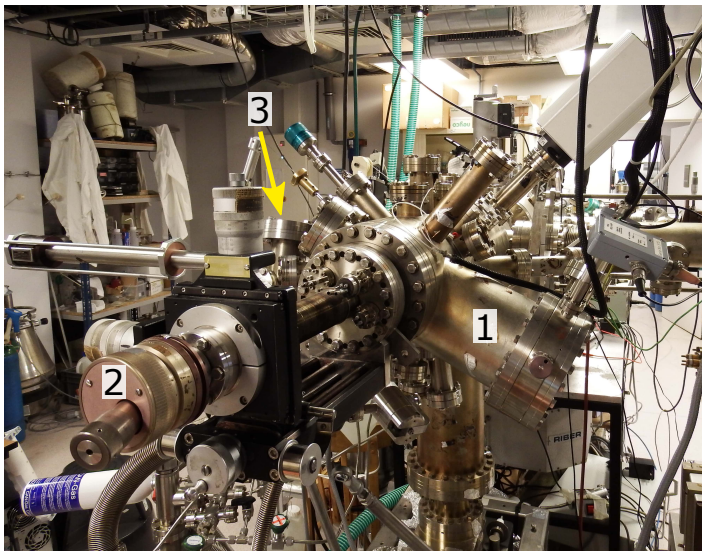

(a)

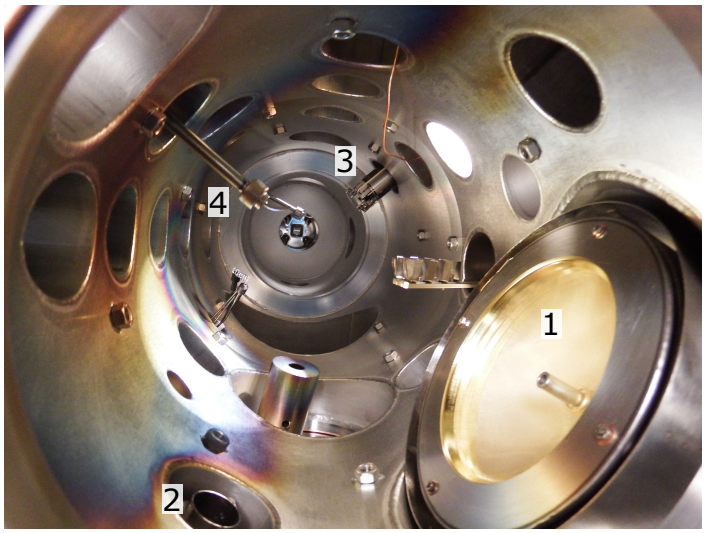

(b)

Fig. 2.16 (a) Picture of the preparation chamber: (1) LEED, (2) Manipulator, (3) Load lock system (b) Picture of the preparation chamber interior from the point of view of the manipulator: (1) LEED, (2) Ion gun, (3) Mass spectrometer, (4) Transfer hook.

structural evolution of the Pb/Si(111) surface as a function of the Pb coverage. Indeed, LEED was the main technique used in these experiments that allowed to adjust all the experimental parameters to prepare clean and well-reconstructed surfaces with very precise Pb coverages. Unfortunately, this chamber does not allow to work at low temperatures and therefore, as already mentioned at the beginning of this section, only room temperature phases of the Pb monolayer could be explored. For some experiments organic molecules can be too invasive or even act as contaminants. For this reason the second chamber (indicated by yellow dashed

line in Fig. 2.15), also called "organic chamber", is dedicated to the evaporation of organic molecules. This allows to separate "clean" preparations of inorganic samples from those involving organic molecules. This chamber is equipped with a 5 axis manipulator making possible to heat samples by direct current heating (up to $\sim$1200° C) or cool them down to nitrogen temperature ($\sim$120 K). Several flanges provide the possibility to install various evaporators at the same time and a quartz balance is used for the calibration of their flux. In practice, this chamber was not used for the evaporation of MnPcs in this work because, as will be discussed in the following section, a portable UHV suitcase was developed for this purpose. The third chamber (indicated by blue dashed line in Fig. 2.15) hosts a room temperature STM (Omicron) making possible the evaluation of the surface quality at the atomic scale. Unfortunately, the damping system was not able to properly decouple the STM from the frame of the system and mechanical vibrations have prevented me from measuring good images.

2.5.2 Development of a molecular UHV suitcase

Because Pb/Si(111) system is very sensitive to any contaminant, it is very important to separate the UHV environment in which Pb samples are prepared from that where instead magnetic impurities, molecules in our case, are involved. This is why a UHV suitcase dedicated to molecular evaporation was developed during the first year of my thesis (see Fig. 2.17). Its compactness has allowed the samples to be transferred from one experimental setup to another without breaking the UHV conditions. Furthermore, the possibility of carrying out molecular evaporation in this suitcase has allowed me to prepare molecular samples in different experimental setups and at similar conditions.

The chamber consists of a small sphere with numerous flanges for evaporation (see Fig. 2.17). A T-shaped UHV junction together with two valves constitute a pumping module through which the suitcase can be moved on different UHV systems without breaking the vacuum within the suitcase itself. During the experiments, samples can be transferred from the suitcase to another UHV system and vice versa thanks to a transfer arm. The base pressure, better than 1×10^{-10} mbar, can be reached after a bakeout at 150° C by pumping through the T-junction with an external pumping system consisting of a turbomolecular pump followed by a primary pump. The vacuum can be maintained over the time by means of an independent pumping system (SAES group) consisting of a small ionic pump combined with a Non-Evaporable Getter (NEG) pump. The operating principle of a NEG pump is based on the use of porous materials able to adsorb the gases present in the UHV environment. Typically, pumping speed and sorption capacity have low limits in this type of pumps and for this

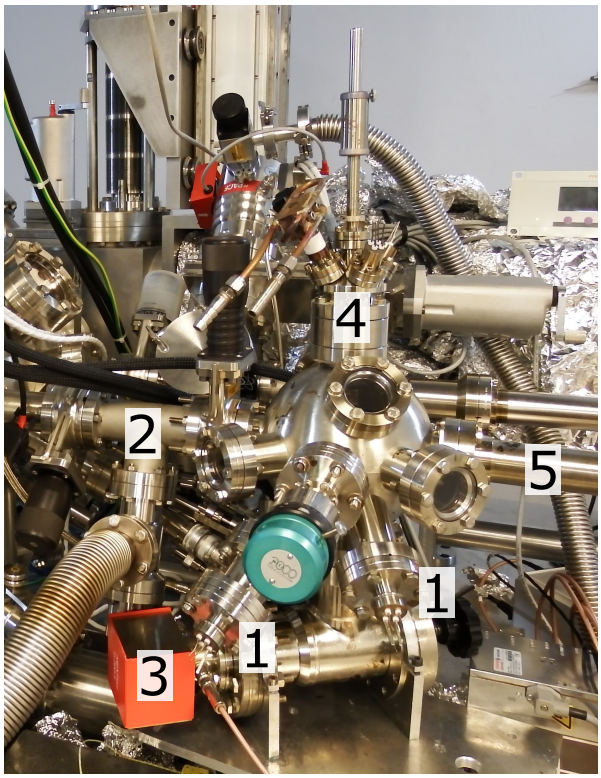

Fig. 2.17 Picture of the molecular UHV suitcase developed during this work: (1) Flanges allowing evaporators to be installed, (2) T-shaped UHV junction for pumping, (3) Ionic pump combined with the NEG pump, (4) Cryomanipulator, (5) Transfer Arm.

reason they are only used to improve and maintain the vacuum level at pressures better than 5×10^{-9} mbar. The low sorption capacity implies that, at some point, the NEG pump can no longer pump gases and it must be reactivated by heating it at high temperature. To prevent quick pumping capacity degradation, molecular evaporations were carried out at pressures lower than 1×10^{-8} mbar. The NEG activation procedure allows the adsorbed molecules to be released and the sorption capacity to be restored. Therefore, the procedure is accompanied by a pressure increasing in the surrounding environment up to $\sim 10^{-5}$ mbar. For this reason the activation is usually carried out during the bakeout of the whole system so that the released molecules are evacuated by the external pumping. The number of NEG activations is limited therefore a valve makes it possible to isolate the NEG pump and to bake only the suitcase thus avoiding unnecessary activations. Both the compactness and the lightweight (about 30 kilograms) of this combined pumping system make the suitcase easy to be transferred. Then, even if the ionic pump is not in use, the NEG continue to pump making it possible to preserve the vacuum during the transfer from one setup to another. Furthermore, this pumping system does not produce mechanical vibrations and this is very important if the

chamber is mounted on equipments sensitive to them like STM. The suitcase is also equipped with a small manipulator allowing the samples to be heated up to ∼200° C by means of resistive heating. It makes it also possible to cool samples down to nitrogen temperature (100 K) and consequently to carry out molecular evaporations with the substrate kept at low temperature. The cooling operating principle is based on a copper element within which liquid nitrogen can flow. A bath cryostat is connected on the copper element and the cooling power is transferred to the sample by means of a copper UHV feedthrough connecting the liquid nitrogen to a flexible copper braid fixed in proximity of the sample. The temperature reading of the sample is carried out by means of a thermocouple fixed in proximity of the sample.

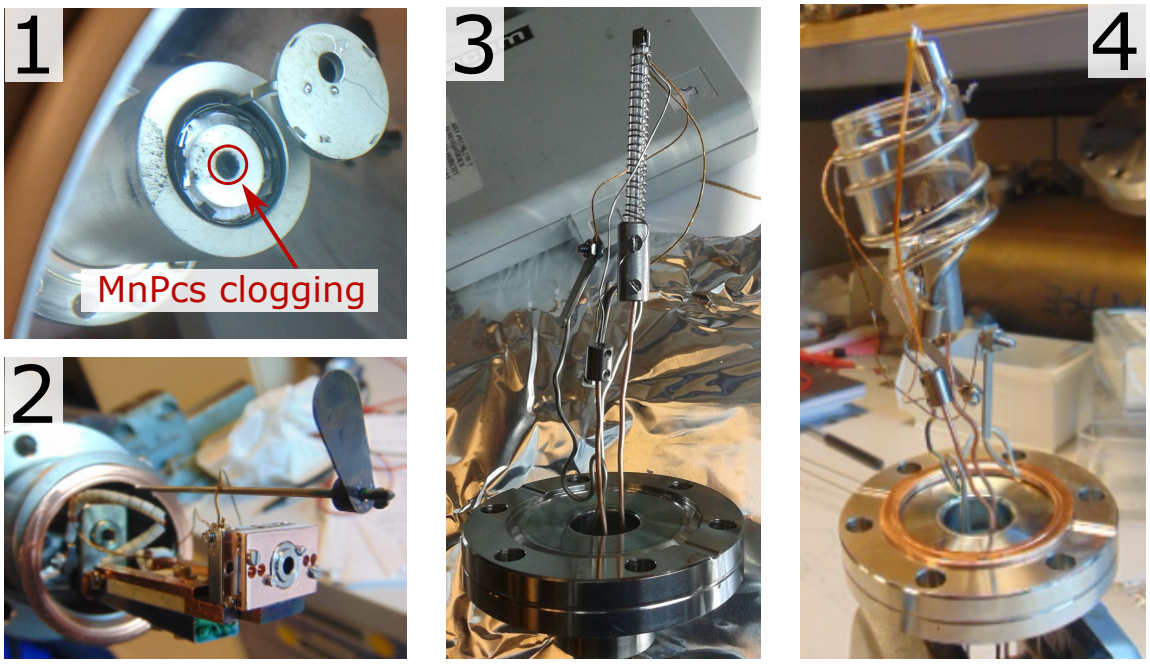

Fig. 2.18 Pictures of the different evaporators used for MnPcs: (1) Commercial Knudsen cell (Createc) clogged by MnPcs, (2) Commercial molecular evaporator (Ferrovac) clogged by MnPcs, (3) Homemade molecular evaporator with glass crucible and ∼2 mm in diameter clogged by MnPcs, (4) Homemade molecular evaporator with glass crucible and ∼24 mm in diameter (able to evaporate MnPcs).

The evaporation of MnPcs was a critical point in the commissioning of this system. Initially, a commercial Knudsen cell (Createc) with a Pyrolytic Graphite (PGR) crucible was used (see Fig. 2.18). During the first tests on the Environmental STM set-up, MnPcs were not observed at all on either the silicon or the Pb/Si(111) surface. This was due to the fact that already during the outgassing of both the evaporator and the MnPcs themselves, the

molecules grow on the evaporator aperture in the form of molecular crystals preventing the molecules themselves to go outside the evaporator and reach the sample. The first hypothesis about the cause of the problem was that the material with which the crucible was made is actually not adapted for the evaporation of organic molecules. For this reason, a commercial molecular evaporator (Ferrovac) with a tantalum crucible (6 mm in diameter) was used but also in this case the same behavior of MnPcs was observed, i.e. the crucible got clogged during the outgassing procedure (see Fig. 2.18).
At this point, I made an evaporator of my own to have a quick way to test different crucible solutions. In all cases, glass was used to fabricate the crucible because it is one of the most commonly used materials to evaporate organic molecules. The first option was a crucible with a diameter of $\sim$2 mm (see Fig. 2.18). The operating principle of the evaporator is simple. A tantalum wire is wrapped around the crucible and the two ends are connected to the copper electrodes of a UHV feedthrough by means of barrel connectors. In this way, when the evaporator is under UHV, a power supply can be connected from the outside to circulate a current within the circuit that will heat the crucible via Joule effect. Finally, a thermocouple junction is connected to the crucible aperture to measure the temperature. Unfortunately, also in this case the crucible got clogged during the outgassing procedure. It should be pointed out that this evaporation system with exactly the same crucible was suggested by Vincent Humblot (LRS laboratory) which routinely uses it to evaporate tartaric acid and other molecules without any problem. This means that the evaporation blockage observed with MnPcs is due to their intrinsic tendency to strongly interact between them leading to crystallization on the crucible walls. The solution to this problem was to increase the crucible diameter thus leaving room for the molecules to get out. MnPcs could be successfully evaporated from a crucible with a diameter of $\sim$24 mm (see Fig. 2.18). On the other hand, given the large size of the crucible, a thick wire with a diameter of 3-4 mm had to be used to sustain the crucible itself as well as to heat it. Since the resistance of a wire is inversely proportional to its section, an excessively high current was required to heat the crucible. Ultimately, a compromise between the diameter of the crucible and that of the heating wire should be found. At the end, the solution enabling the best practical conditions was a crucible with a diameter of $\sim$10 mm and a tantalum wire of $\sim$0.16 mm.

The heating method of this evaporator tends to heat the surrounding environment. This fact should be taken into account when MnPc evaporations are carried out onto a sample kept at low temperature (100 K) because it means that the sample might not necessarily be at the lowest temperature. At the end of Section 2.5.4 further details about how this effect could be taken into account are discussed.

2.5.3 Variable Temperature STM

After the LEED characterization of the Pb monolayer described in Section 2.5.1, a campaign of STM measurements (four weeks) was carried out at the "Environmental STM" set-up, an UHV system shared between different teams of INSP, LRS and LCPMR laboratories. The aim of these experiments was both to directly check the atomic structure of the surface and optimize the experimental parameters to prepare a Pb monolayer with $\sqrt{7} \times \sqrt{3}$ -Pb reconstruction. This setup is able to work at low temperature (down to 30 K) and therefore it is suitable to observe the $\sqrt{7} \times \sqrt{3}$ -Pb phase that, as already mentioned in Section 2.5.1, appears at temperatures below 270 K.

The experimental apparatus (shown in Fig. 2.19) consists of two chambers connected by means of a UHV gate valve, i.e. a preparation and a STM chamber. Samples are brought into the UHV environment by means of a load lock and a system of transfer arms and wobble sticks makes it possible to move them through the two chambers. The base pressure, better than 1×10^{-10} mbar, can be achieved in each chamber after a bakeout procedure at 150° C and is maintained over time through a pumping system including primary, turbomolecular, ionic and Titanium Sublimation pumps (TSP).

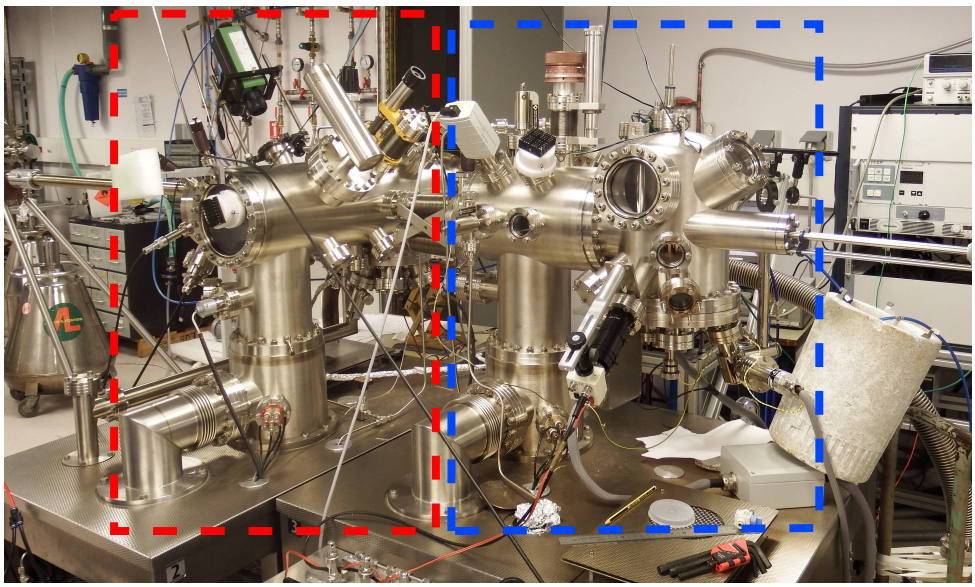

Fig. 2.19 Picture of the environmental STM set-up. Red dashed line: preparation chamber. Blue dashed line: variable-temperature STM chamber.

The Knudsen cell described in Section 2.5.1 was installed on the preparation chamber at the beginning of the experiments to evaporate pure Pb (99.999%) on top of the Si(111) substrate. The chamber is also equipped with a 4 axes manipulator making it possible to

heat samples either by resistive (up to 950° C) or by direct current (up to ∼1200° C). Also in this case, direct current heating was the method used to prepare both the Si(111) and the Pb/Si(111) surfaces and their temperature was measured by means of an infrared pyrometer. The chamber is also equipped with a LEED-Auger (Specs) and together with the fact that the manipulator permits to cool samples down to liquid nitrogen temperature (120 K) it was possible to carry out low-temperature LEED observations. In this way, it was possible to improve the experimental parameters to prepare a Pb monolayer with exactly 1.2 ML and a well-developed $\sqrt{7} \times \sqrt{3}$ -Pb reconstruction that, as already mentioned in Section 2.5.1, appears at temperatures below 270 K.

The STM chamber hosts a Variable Temperature Environmental STM (Omicron VT-STM) whose head is shown in Fig. 2.20a. This microscope can work in a range of temperatures going from ∼30 K up to ∼500 K and controlled conditions of pressure ranging from less than 1×10^{-10} mbar up to 10 mbar. The possibility of working in "environmental" conditions, i.e. high temperatures and high pressures of specific gases, makes this microscope a very versatile tool for the investigation of a large number of physico-chemical processes, e.g. growth of materials and catalysis. Furthermore, the fact that it is a somewhat "plug and play" instrument, i.e. the surface can be quickly checked even at low temperatures, makes it an efficient tool for time-consuming experiments like growth studies. Ultimately, the first campaign of experiments on this system allowed to finely adjust the parameters needed to prepare a single atomic layer of Pb on Si(111) with exactly 1.2 ML and a well-developed $\sqrt{7} \times \sqrt{3}$ -Pb reconstruction by means of direct check of its atomic structure.
Atomic resolution in STM experiments can be easily reached if during the scan either p_z or d_{z^2} orbitals are involved. This is one of the reasons for which d-band metals, e.g. Tungsten (W) or Platinum-Iridium (Pt-Ir), are the most commonly used materials to fabricate STM tips. Preparation of atomically sharp W tips requires an electrochemical etching procedure in a ∼2 molar solution of NaOH. After that, the tips are brought into UHV environment and outgassed at 200° C by means of the resistive heating block of the manipulator. The outgassing procedure is typically carried out overnight. At the end the tips are rapidly heated at high temperature by means of direct current heating until visible light is observed. The flashing of the tip is repeated four or five times in order to remove the native oxide layer from their surface. On the other hand, atomically sharp Pt-Ir tips can be obtained by simply cutting an end of the Pt-Ir wire with a pair of scissors. After that, Pt-Ir tips are brought into UHV conditions and outgassed at 200° C as already described above. Note that Pt-Ir tips do not need to be flashed at high temperature because they are quite inert to oxidation. An important feature that makes Pt-Ir tips more suitable for STS experiments than W tips is

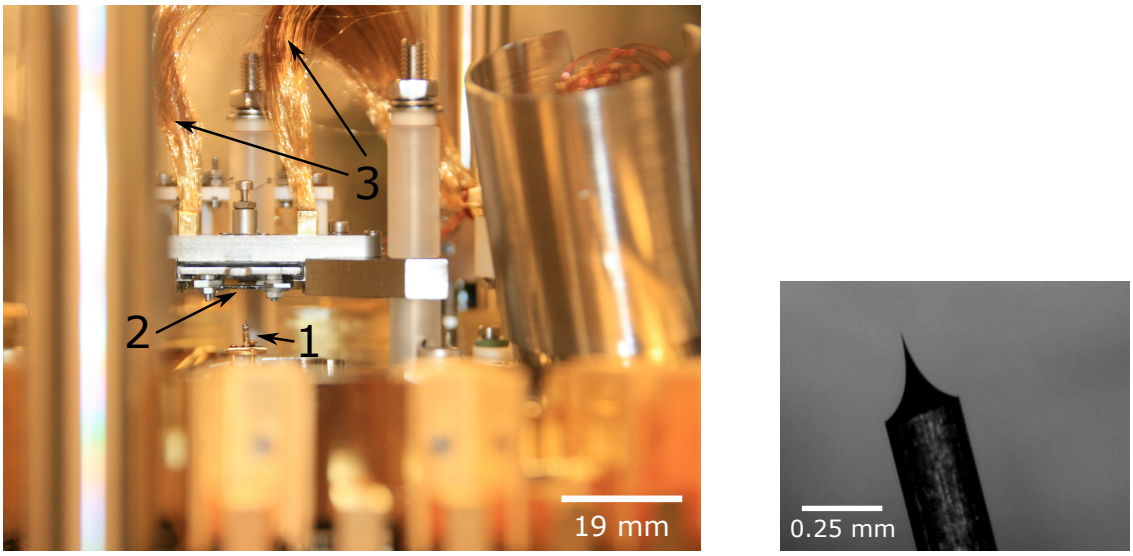

(a) (b)

Fig. 2.20 (a) Picture of the STM head: (1) Tip mounted on the tip-holder, (2) Si(111) sample mounted on the sample-holder, (3) Copper braid transferring the cooling power from the cold finger to the sample. (b) Picture of an electrochemically etched W tip taken with an optical microscope.

their flat density of states at the Fermi level. The result of STS measurements always is a convolution between the density of states of the sample and that of the tip. Accordingly, if the tip density of states is flat, it will be much easier to deconvolute the signal and extract the sample density of states. During the experiments on the "Environmental STM" only topographic images were acquired and therefore electrochemically etched W tips were used (like the one shown in Fig. 2.20b). On the other hand, all spectroscopic data reported in this manuscript were measured by means of Pt-Ir tips.

As already said in Section 2.3, the principle of STM is based on the control of the tip-surface distance within the sub-Å range. Consequently, both mechanical and electromagnetic oscillations coming from the external environment could affect the measurement and for this reason the microscope must be carefully isolated from them. The VT-STM used in these experiments is mechanically isolated by means of a damping system based on eddy currents. Basically, the microscope is mounted on a copper support suspended by springs. Furthermore, the copper support is immersed in a magnetic field generated by fixed permanent magnets. In these conditions oscillatory displacements of the conductor induce electrical currents according to the Faraday's law of induction which reduce the oscillations.

The liquid nitrogen cooling system was used in these experiments to directly observe the atomic structure of the $\sqrt{7} \times \sqrt{3}$ -Pb phase at $\sim$100 K. A nitrogen dewar must be connected on a flange close to the STM head in order to cool the microscope. By means of a pumping system the liquid nitrogen can circulate through an internal circuit. The cooling power is ultimately transferred to the sample by connecting the latter to the liquid nitrogen by means of a copper cold finger and a flexible copper braid fixed in proximity of the sample (see Fig. 2.20a).

The UHV suitcase was installed on the STM chamber in order to test the homemade evaporator described in Section 2.5.2. The biggest issue was the extremely high pressures during the molecular evaporations, i.e. $\sim 10^{-7}$ mbar. It should be kept in mind that, in normal conditions, if both evaporator and molecules are well-outgassed, for temperatures below that of evaporation the base pressure should be lower than $\sim 5 \times 10^{-10}$ mbar. On the other hand, if the evaporator is heated to the evaporation temperature, it should be possible to finely adjust the temperature to have very low molecular flux. This actually corresponds to pressures between 5×10^{-10} mbar and 5×10^{-9} mbar. It is clear then that the high pressures observed in our case were probably due to the fact that molecules were not well outgassed (probably MnPcs trap water molecules that are slowly released during the outgassing procedure).

Fig. 2.21a shows a typical STM image of the Pb monolayer grown on the Si(111) during the testing experiments. The image was acquired at room temperature (300 K). The holes on the surface and their structural consequences are discussed in detail in Chapter 3. The other images show subsequent evaporations of MnPcs on the same surface. Bright spots like those circled in Fig. 2.21b are individual MnPc molecules. A common feature of all the images is that molecules appear to be embedded inside the Pb surface, probably because molecules have a tendency to interact with the silicon substrate, i.e. at 300 K molecules are able to move the Pb atoms to gain access to the substrate. By observing the sequence of images it is clear that the increase of molecules is accompanied by the increase of embedded spots. In Fig. 2.21d embedded square lattices of MnPcs can be seen. Furthermore, each evaporation is accompanied by an increasingly pronounced corrugation of the Pb surface. By looking at Fig. 2.21d it can be seen that in some places embedded square lattices of molecules are clearly seen (green arrow) but in others they cannot be well discerned (white arrows). I interpreted the emergence of surface corrugation in different ways. First, it could be a real structural corrugation due to the compression of the Pb layer after embedding of MnPcs. Second, it could be related to electronic interference effects within the layer due to the increasing of surface defects. Third, it could be due to the fact that, where square lattices are not observed, the molecules are simply arranged in a disordered way and they are not

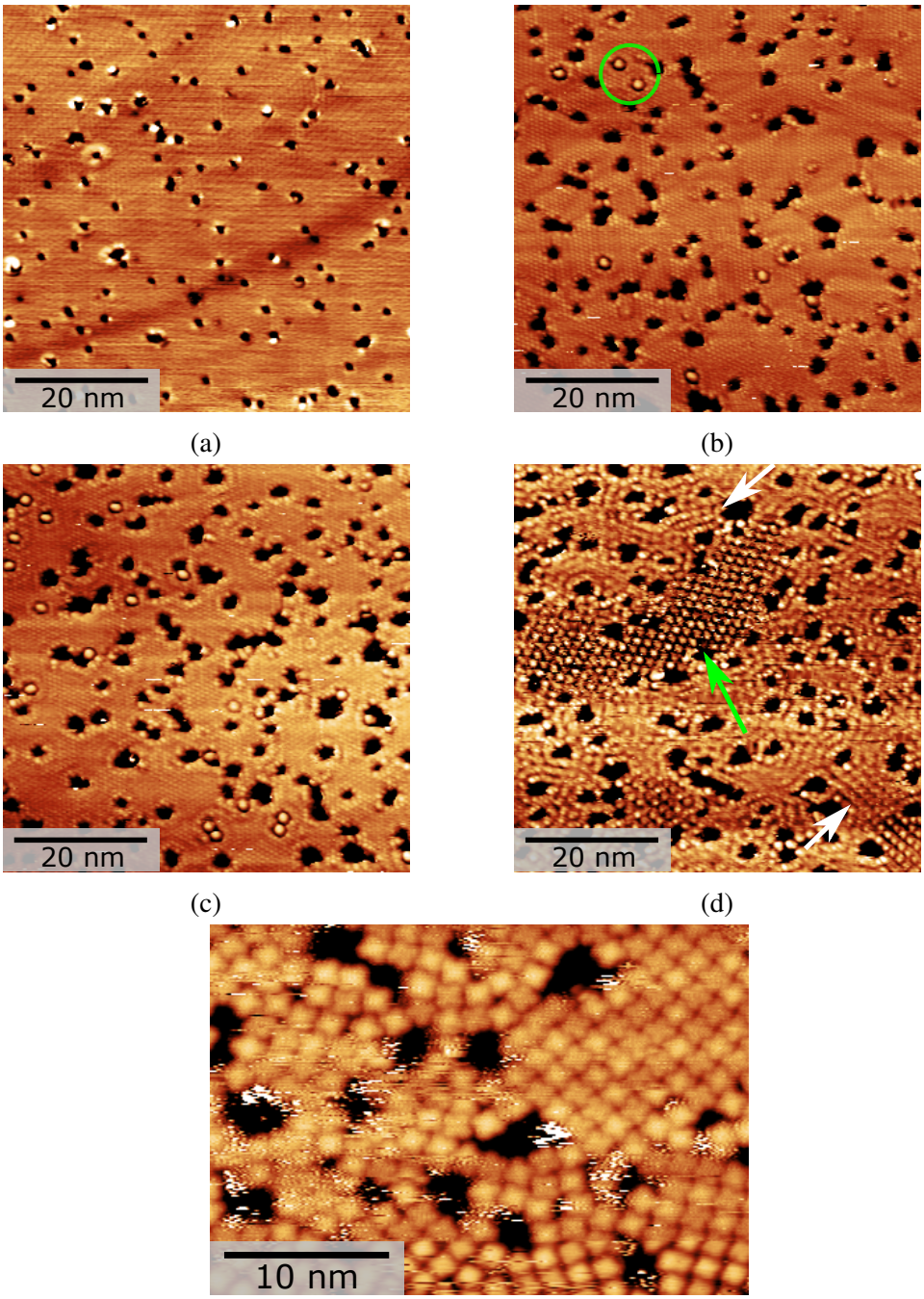

(a) (b) (c) (d) (e)

Fig. 2.21 (a): STM image of a clean Pb/Si(111) monolayer taken at room temperature (300 K). Image size: 60×60 nm^2, V_T: -2.3 V and I_T: 70 pA. (b), (c), and (d): STM images showing subsequent MnPcs evaporations on the same surface shown in (a). Image size: 60×60 nm^2, V_T: -2.3 V and I_T: 80 pA. (e): STM image showing the same images as (d) measured at low temperature (77 K). 32×22 nm^2, V_T: -2.5 V and I_T: 100 pA.

well resolved in STM images. Fig. 2.21e suggests that the latter hypothesis is the most likely because it represents the same sample shown in Fig. 2.21d but measured at low temperature (100 K). From Fig. 2.21e it is clear that the whole surface is covered by MnPcs and on the right side of the image square lattices are clearly seen. However, on the left side, molecules are arranged in a disordered (non-conventional) way to better accommodate the holes of the Pb surface.

In any case, the interpretation of these images could be even more complicated due the high pressure during the evaporation, i.e. it could be expected that other contaminants are evaporated together with the MnPcs. Indeed, by comparing these results with those shown later in Chapter 3, where the experiments were carried out in well-controlled and clean conditions, it can be seen that the behavior presented here is quite pathological. On one hand, there is a too large density of holes within the Pb overlayer. On the other hand, the presence of uncontrolled contaminants during MnPcs evaporation, probably affects the growth behavior of this system.

Careful analysis of the outgassing dynamics of the evaporator has allowed us to find a solution to the pressure problem. In particular, it was observed that after several days of continuous outgassing near the evaporation temperature, the evaporator pressure could reach the $\sim 10^{-9}$ mbar range. Starting from this point, if the evaporator comes into contact with atmospheric pressures, even if after the bakeout the base pressure of the system is of the order of 10^{-11} mbar (with the evaporator at room temperature), the evaporator must be again outgassed for several days as if it has never been outgassed before. This means that the molecules are able to trap a large amount of molecules present in the air (mainly water) which are released slowly during the outgassing. The solution to the problem was to drastically reduce the amount of MnPcs in the crucible to less than $\sim 1\ mm^3$. This has made it possible to outagass the evaporator in few hours, to reach ideal operating conditions with the possibility to prepare very clean samples which are discussed in the following chapters. In conclusion, it took me several months to learn how to work properly with MnPcs evaporators and reach the best experimental conditions and at the end I was able to evaporate very small fractions of molecules, i.e. one MnPc per nm^2 or even less, without the presence of other contaminants and in very good conditions of pressures ($\sim 1 \times 10^{-9}$ mbar).

2.5.4 Very-low temperature STM

Once the growth of the Pb monolayer was well characterized and the commissioning of the molecular UHV suitcase was completed, everything was ready for the experiments on the very-low temperature system.

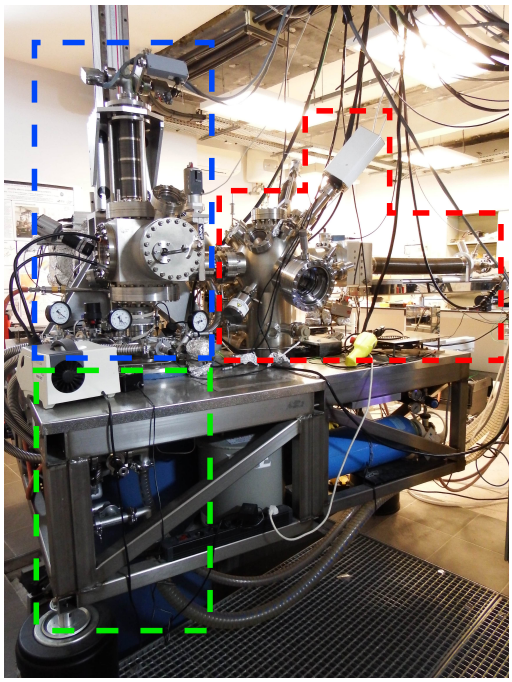

Fig. 2.22 Picture of the very-low temperature setup. Red dashed line: preparation chamber, Blue dashed line: STM chamber, Green dashed line: Cryostat.

Two types of experiments were performed on this system. First, topographic and spectroscopic measurements (STM/STS) on a Pb monolayer grown on Si(111) substrate without and with MnPcs molecules (Chapter 3). Second, growth of a few Pb layers (more than 1 ML) on Si(111) and topographic/spectroscopic measurements without and with MnPcs molecules (Chapter 4). Since the microscope is designed to work at low temperatures these growth experiments turned out to be very challenging, i.e. both the slow thermalization time of the microscope and the long transfer time of samples make these experiments very time consuming. Furthermore, the growth of thin layers of Pb is very sensitive to small amounts of foreign species, the presence of which is hard to control from one system to another. For this reason we were forced to carry out the experiments to characterize the growth of Pb thin layers within the same UHV setup housing the very-low temperature microscope. In particular, a lot of effort was spent to optimize the growth of trilayer Pb/Si(111) samples which took several months due to the presence of unknown contaminants.

The experimental system (see Fig. 2.22) consists of two chambers: a preparation and a STM chamber connected by means of a UHV gate valve. Samples are brought into the UHV environment by means of a load lock system and a system of transfer arms and wobble sticks makes it possible to move them through the whole system. A base pressure, better than 5×10^{-11} mbar, can be achieved in each chamber after a bakeout at 150° C for 3-4 days and it is maintained over the time through a pumping system including primary, turbomolecular, ionic and Titanium Sublimation pumps (TSP). The whole system is decoupled from mechanical vibrations by compressed air legs. Dedicated electronic filters isolate the system from high frequency noise.

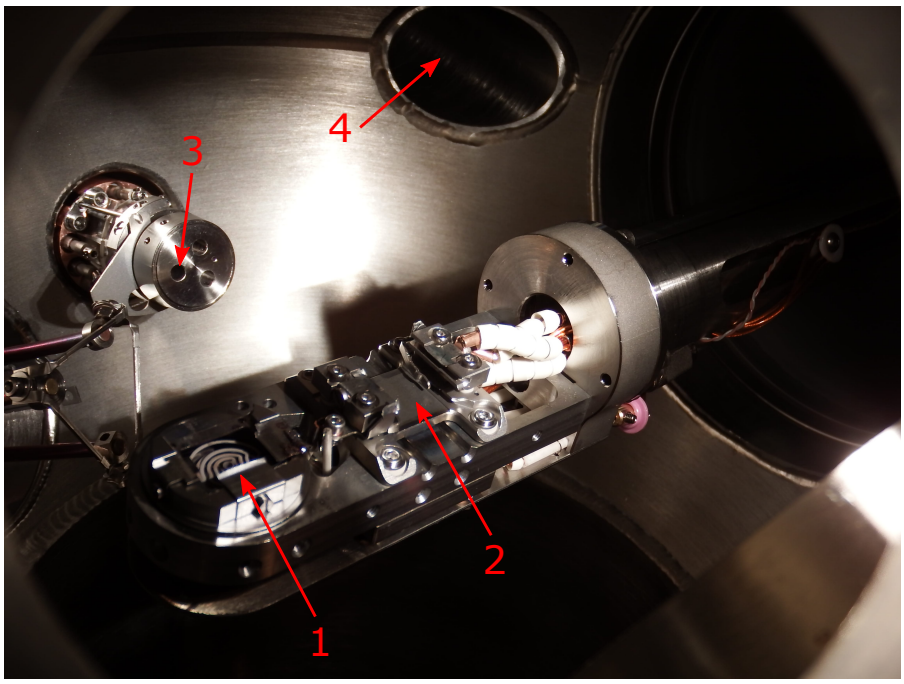

Fig. 2.23 Picture of the preparation chamber interior: (1) Resistive/electron beam heating module, (2) Direct current heating module, (3) Pb evaporator aperture, (4) Flange allowing the sample to be transferred between the preparation chamber and the molecular (MnPc) suitcase.

The preparation chamber is equipped with a 4 axes cryomanipulator which has two separated heating modules (see Fig. 2.23). One of them makes it possible to heat samples by either resistive (up to ∼900° C) or electron beam (up to ∼1200° C) heating and the other one by direct heating (up to ∼1200° C). Resistive heating was used to outgas silicon samples at 600° C as soon as they are inserted into the UHV environment. This heating method allows you to heat the entire sample holder and not just the sample. Sometimes, it was also used to prepare both Pb monolayer and 3 ML Pb islands on Si(111). However, most of the time, both Si(111) and Pb/Si(111) surfaces were prepared by direct current heating. The main

difference between direct current and resistive heating is that the latter method allows you to uniformly heat the surface of the sample, while the former exhibits a slight temperature gradient. In the case of Pb monolayer, this temperature gradient may lead to the coexistence of different structural phases on the same surface because a different amount of Pb desorbs from the surface depending on the local temperature (see Chapter 3 for details on the different structural phases and their preparation). On the other hand, in the case of 3 ML Pb islands on Si(111) there is no real difference between using one heating method or the other. The horizontal translation of the cryomanipulator allows the sample to be transfered between the preparation and the STM chamber by means of a motor. The fact that the manipulator can be cooled with liquid nitrogen ($\sim$100 K) makes it possible to carry out low-temperature growth experiments. For instance it was extensively used for the preparation of trilayer Pb/Si(111) samples (see Chapter 4). A triple electron beam evaporator (Omicron) is installed on the preparation chamber. It possesses three independent cells one of which contains pure Pb (99.999%) evaporated in the experiments of this work. The crucible is heated by electron bombardment and therefore a fraction of ionized Pb atoms is produced during the evaporation. In this way, the evaporation flux can be monitored and controlled at all times by measuring the current carried by these ionized atoms. The evaporation flux can also be commonly calibrated by means of a quartz balance. Both methods were used in the present work to optimize the flux of Pb atoms used to grow our samples. Let us mention that the presence of ionized Pb atoms can strongly affect both the structure and the growth mode of Pb thin films on Si(111). A water cooling system allows the evaporator temperature to be stabilized and finely controlled. The chamber is also equipped with a LEED-Auger (Omicron), an infrared pyrometer to measure the sample temperature, an ion gun, a mass spectrometer and a quartz balance for the flux calibration of evaporators.

The STM chamber hosts the homemade low temperature STM. The microscope is designed to work at $\sim$300 mK. The STM head contains a sapphire sample-holder able to move in the $X-Y$ plane (see Fig. 2.24). Both the $X-Y$ and the Z movement are controlled by piezoelettric tubes allowing for rough and fine motion. The $X-Y$ rough motion is used to explore the whole surface of a sample while the Z rough motion is used to approach the tip to the surface with the help of a camera ($\sim$20 μm). The Z fine movement is then used to put the tip in measurement position (tip-surface distances typically range from 0.5 to 1.5 nm [28]). The $X-Y$ fine movement is used during the acquisition of STM topographic images: the maximum area that can be scanned is around $6\times 6\ \mu m^2$ at room temperature and $2\times 2\ \mu m^2$ at 300 mK. The system is controlled by the Matrix electronic (Omicron) allowing for topographic and spectroscopic measurements. Once the STM tip is approached near to

the surface, the microscope head is transferred down to the cryostat by means of a transfer tube (1.8 m) moved by a motor (see Fig. 2.24). A series of heat exchangers mounted on the transfer tube help to maintain all the different parts of the system at low temperature.

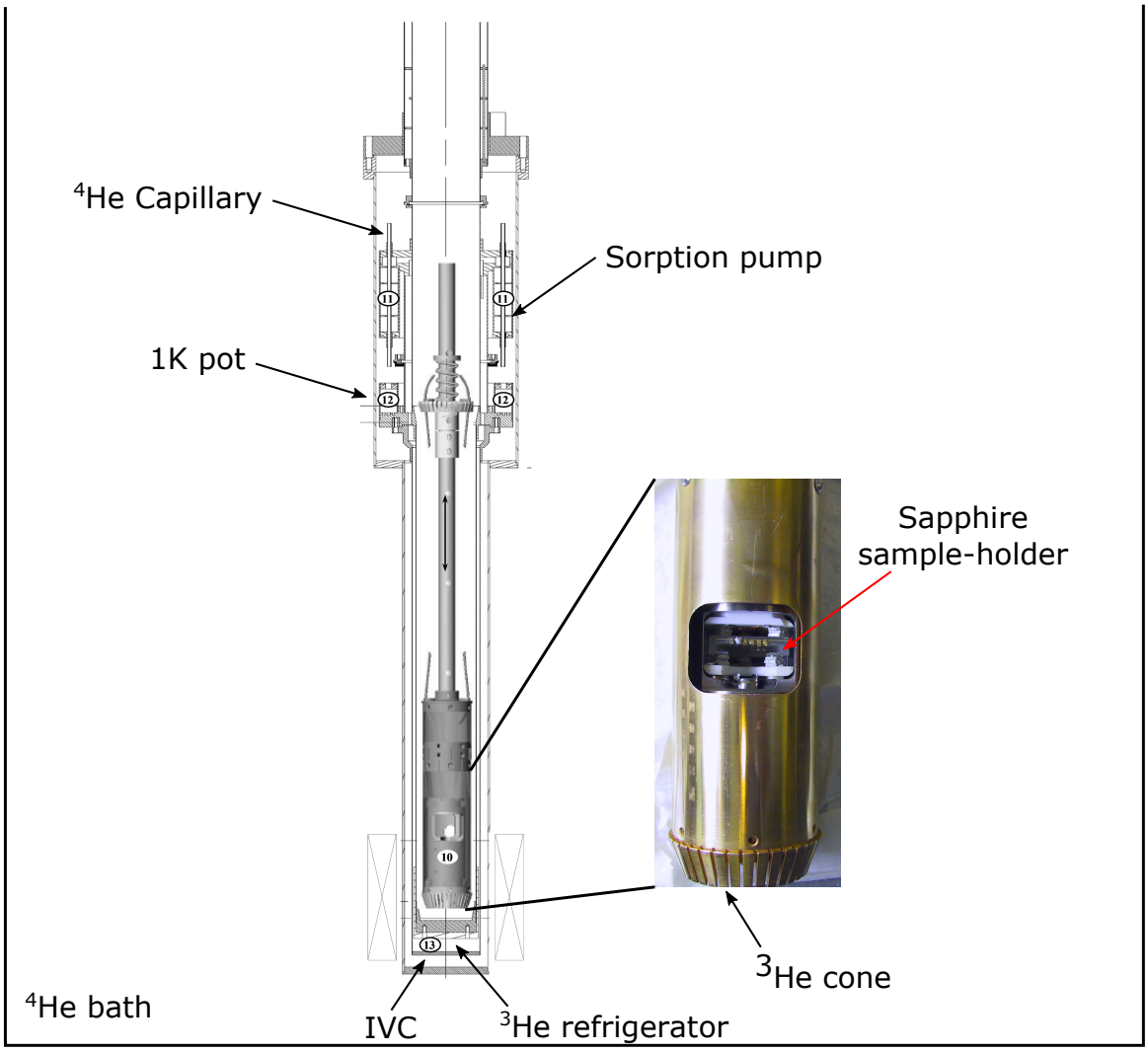

Fig. 2.24 Pictures of the cryostat and of the STM head.

The cryostat has a capacity of 60 liters and it can be filled either with liquid nitrogen or with liquid helium. When the cryostat is filled with liquid nitrogen and the microscope is thermalized at 77 K it can be operated at this temperature. If the microscope has to be cooled down to helium temperature a pre-cooling at nitrogen temperature is mandatory. After that, the liquid nitrogen must be removed from the cryostat by means of a gaseous flux of ^{4}He. The cryostat can then be refilled with liquid ^{4}He at 4.2 K. During this cooling procedure a ^{4}He exchange gas lies within the isolation volume (IVC) whose role is to put in thermal contact

the ^{4}He bath and the ^{3}He refrigerator (see Fig. 2.24). At the same time the microscope is in thermal contact with the ^{3}He refrigerator by means of the ^{3}He cone. Below 50 K the sorption pump start to pump the gaseous ^{3}He by adsorbing it on its walls. The ^{3}He pressure in the ^{3}He refrigerator can be adjusted by heating the sorption pump to ensure the presence of an exchange gas between the microscope and the IVC. In this way, the microscope can thermalize at $\sim$4.2 K. If lower temperatures are required, the first thing to do is to isolate the ^{4}He bath from the ^{3}He refrigerator by pumping the IVC, i.e. isolate the microscope from the ^{4}He bath. A capillary drains ^{4}He from the ^{4}He bath to the so-called "1 K Pot" and the external pumping of the latter makes it possible to cool it at $\sim$1.2 K.
We describe now the ^{3}He condensation process needed to reach 300 mK. The sorption pump can be heated above 40 K by means of a resistance so that the ^{3}He can desorb. The ^{3}He becomes liquid in contact with the 1 K-pot. The equilibrium temperature of the ^{3}He liquid-vapor is lowered first by lowering the temperature of the 1 K-pot (through a valve regulating the liquid flow). This occurs down to 1.4-1.5 K. Then, further cooling occurs through ^{3}He adsorption on the sorption pump lowering the pressure. The liquid ^{3}He drops into the ^{3}He refrigerator and reaches an equilibrium temperature of $\sim$300 mK. At this point, the liquid ^{3}He starts to slowly evaporate and it is pumped again by the sorption pump. However, as long as the ^{3}He refrigerator contains liquid ^{3}He the low temperature is maintained on the microscope. Normally, the liquid ^{3}He takes $\sim$36-42 hours to completely evaporate. Then the ^{3}He refrigerator heats up to $\sim$2 K because it is in poor thermal contact with the 1 K pot and it is isolated from the ^{4}He bath. The evaporation time of liquid ^{3}He represents therefore the experimental limitation of ultra-low temperature measurements.

The majority of topographic images of Chapter 3 were measured with electrochemically etched W tips whose preparation procedure was described in Section 2.5.3. Topographic and spectroscopic measurements of other chapters were performed with Pt-Ir tips directly cut from wires. Once introduced in the UHV environment they were outgassed at 200° C overnight by means of the resistive heating but they were not flashed at high temperatures.

The UHV suitcase was installed on the preparation chamber in order to carry out molecular evaporations. It should be pointed out that evaporations with the sample kept at nitrogen temperature were also performed. As already discussed in Section 2.5.2, during molecular evaporations the evaporator could heat the surrounding environment and therefore the sample might not necessarily be at the lowest temperature. Furthermore, certain preparations required the sample to be at low temperature for the entire duration of the experiment until finally transfered to the cooled microscope. However, during the transfer between the two cooled

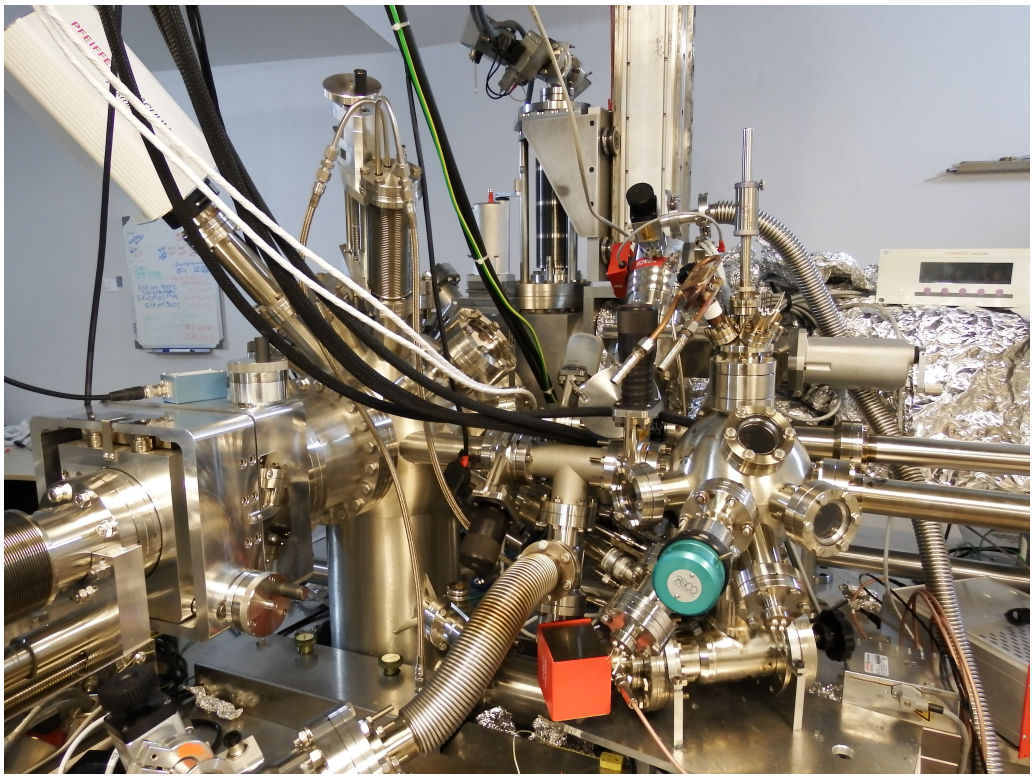

Fig. 2.25 Picture of the molecular suitcase installed on the ultra-low temperature setup.

manipulators of the preparation chamber and of the UHV suitcase the sample was no longer cooled. The dependence of the growth mode of Pb films on the substrate temperature (see Chapter 4) has made it possible to monitor the presence of unwanted heating effects during the preparation. Nevertheless, we verified that, when happening during the transfer of few minutes of a cold sample, uncontrolled heating does not significantly affect the preparation of sample. We guess that, in any case, the sample temperature always remains between 110 K and 250 K during unwanted heating linked to transfer.

2.6 Substrate preparation: Si(111)-7 × 7

In order to prepare clean and defect-free samples a proper preparation of the substrate is mandatory. In the present work the substrate used to grow thin layers of Pb is always a monocrystal of Si(111) (n-type, P-doped). A standard procedure was followed to prepare it. After being introduced in UHV environment both the sample is outgassed at ∼600° C overnight by means of resistive heating. This ensures that the pressure remains below 5×10^{-10} mbar during the whole further sample preparation procedure, Pb evaporation included. Subsequently, the sample is repeatedly flashed to ∼1150-1200° C for 5-30 sec by

means of direct current heating. This is done to remove the surface oxide. Finally, the Si(111)-7×7 surface reconstruction is prepared by means of a flash at 1100° C (10-30 sec) followed by an annealing at 950° C and slow temperature decreasing down to 550° C ($\sim$15 min). After that, the sample can be cooled down to room temperature (at least 20-30 min) and the clean Si(111)-7×7 surface is ready.

Chapter 3

MnPcs adsorption on a single atomic layer of Pb/Si(111)

3.1 Pb/Si(111) phase diagram

Single atomic layer of Pb grown on Si(111) has been widely investigated during the last 30 years because of its complex phase diagram consisting of many different surface reconstructions which depend on coverage, temperature and annealing history. A great experimental and theoretical effort has been made and is currently still ongoing to reveal all the physics that this peculiar system holds. In particular, characterization of the large number of different phases in a narrow range of coverage and determination of their atomic structure is one of the main problems. In the following, I will discuss in detail the phase diagram shown in Fig. 3.2 that I recompiled between 0.9 ML and 1.2 ML in order to include the most recent findings about the structural phases that can be found in this range [37, 38]. From now on it should be kept in mind that 1 ML = one Pb atom per surface Si atom and that the surface atomic density of the Si(111) is 7.84 $atoms/nm^2$.

It is important to point out that the phases described in the following discussion are annealed phases, i.e. they are obtained by depositing a certain amount of Pb on the Si(111)-7×7 reconstructed surface and then annealing the sample between $\sim$300° C and $\sim$400° C. The annealing process melts the Pb overlayer and removes the 7×7 reconstruction, leaving an unreconstructed Si(111) surface with 1×1 periodicity (see Fig. 3.1) [39]. During the annealing, part of the Pb desorbs from the surface and the remaining part diffuses to form ordered structures that reduce the interface energy. In other words, Pb atoms form different surface reconstructions depending on the coverage, time and temperature of annealing. Pb

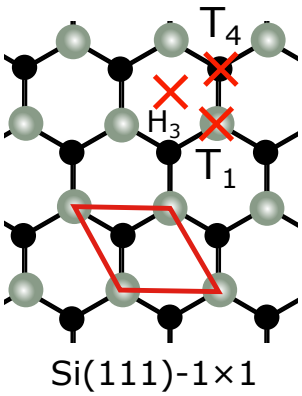

Fig. 3.1 Top-view of a bulk-terminated Si(111) surface. Gray and black balls represent silicon atoms belonging to the topmost and the second atomic layer respectively. Red crosses indicate the three high-symmetry adsorption sites labeled as T_1, H_3 and T_4 sites. Atoms adsorbed on T_1 sites sit directly on-top of Si atoms of the topmost atomic layer. H_3 and T_4 sites are also referred as "hollow sites" because they lie in the middle of the triangular hollows formed by the Si atoms in the first layer. Solid line indicates the 1×1 unit cell of the Si(111) surface.

adatoms have a large number of possible bonding sites on the Si(111) surface and therefore many surface reconstructions can be obtained. However, three high-symmetry bonding sites can be defined on this surface. Fig. 3.1 shows the top-view of a bulk-terminated Si(111) surface and red crosses indicate the three high-symmetry adsorption sites labeled as T_1, H_3 and T_4 sites. Pb atoms adsorbed on T_1 sites sit directly on-top of Si atoms of the topmost atomic layer. H_3 and T_4 sites are also referred as "hollow sites" because they lie in the middle of the triangular hollows formed by the Si atoms in the first layer. In particular, Pb atoms adsorbed on T_4 sites are above Si atoms belonging to the second layer and therefore they have four neighboring Si atoms (3 Si of the first layer and 1 Si of the second layer). On the other hand, Pb atoms adsorbed on H_3 sites have only three neighboring Si atoms (3 Si of the first layer).

As shown in Fig. 3.2, at room temperature, for Pb coverage between $\frac{1}{6}$-ML and $\frac{1}{3}$-ML we observe a "dilute" $\sqrt{3} \times \sqrt{3}$-Pb reconstruction labeled as γ-phase in Fig. 3.2. Generally speaking, this is an intermixed phase of Pb and Si atoms located, in a variable percentage, on the T_4 sites of the silicon substrate. A Pb coverage of $\frac{1}{6}$-ML corresponds to the so-called mosaic phase or γ phase (see Fig. 3.3a), a surface reconstruction with 0.5 Pb atoms per $\sqrt{3} \times \sqrt{3}$ unit cell, in which 50% of the atoms on T_4 sites are Pb and the remaining 50% are Si [37, 39, 40]. Fig. 3.3a shows also that the $\sqrt{3} \times \sqrt{3}$ unit cell is 30° rotated with respect to the 1×1 of the Si(111) surface. By increasing the Pb coverage the Si atoms are progressively replaced by Pb atoms and therefore the relative concentration is changed. At $\frac{1}{3}$-ML the

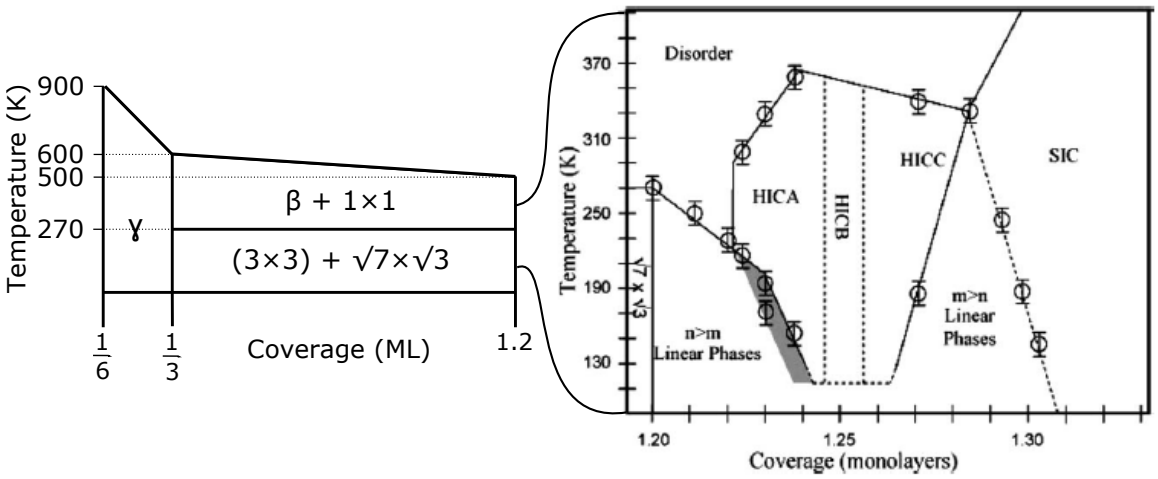

Fig. 3.2 Phase diagram of Pb/Si(111) monolayer

β phase is reached (see Fig. 3.3b), a surface reconstruction with 1 Pb atom per $\sqrt{3} \times \sqrt{3}$ unit cell in which 100% of the atoms adsorbed on T_4 sites are Pb [37, 39, 41]. The relative concentration of Pb and Si atoms achieved during the preparation of these phases, i.e. the actual coverage achieved between $\frac{1}{6}$-ML and $\frac{1}{3}$-ML, depends on the starting coverage of Pb, temperature and duration of annealing. In Fig. 3.3c and Fig. 3.3d typical LEED patterns arising from the mosaic phase and the β phase are respectively shown. They are very similar but the spots of the mosaic phase are globally brighter than those of the β phase [39, 42]. In Fig. 3.3e a STM image of the mosaic phase, taken at negative bias voltage, is shown. Pb and Si adatoms can be identified by means of the contrast difference: bright spots are associated to Pb adatoms while dark regions correspond to Si adatoms. This apparent height difference has been assigned to a different electronic structure between Pb and Si adatoms due to a charge transfer from a Si dangling bond to a Pb dangling bond [39, 40, 43]. Finally, in Fig. 3.3f a STM image, taken at negative bias voltage, is shown. In the right side of the figure there is a β phase region with a majority of bright spots corresponding to Pb adatoms sitting on T_4 sites. In general, it is difficult to have large patches of β phase and they are usually observed in coexistence with the 1×1-Pb phase (see left side of Fig. 3.3f). Furthermore, the regularity of β phase domains is often affected by the presence of substitutional Si adatoms remaining from the mosaic phase, i.e. dark spots within the β phase region in Fig. 3.3f [37, 44]. The coverage-induced phase transition between γ and β phase is completely reversible because it is experimentally observed that the β phase can be transformed into the mosaic phase by heating the sample to around 300° C [39]. This is interpreted as a sign of greater stability of the mosaic phase with respect to the β phase. Moreover, the density of Pb in the mosaic phase cannot be decreased below the 50% even if the sample is heated higher than 300° C. At

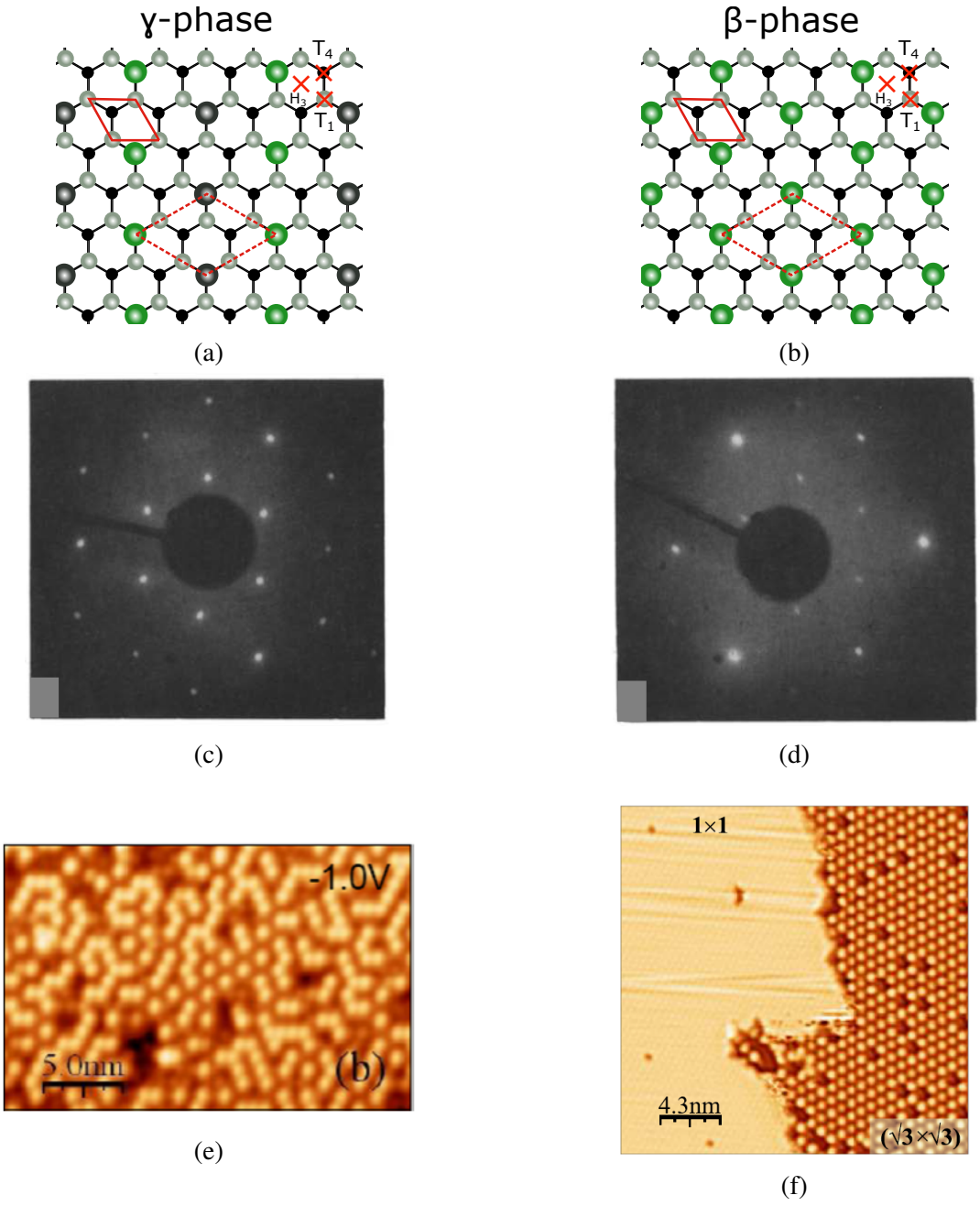

Fig. 3.3 (a)[(b)] Top-view of the γ [β] phase corresponding to $\frac{1}{6}$-ML [$\frac{1}{3}$-ML] of Pb. Small gray (small black) balls represent Si atoms belonging to the topmost (second) atomic layer. Large black (green) balls indicate Si (Pb) atoms adsorbed on T_4 sites. Red crosses indicate the three high-symmetry adsorption sites. Dashed (solid) lines indicate the $\sqrt{3} \times \sqrt{3}$ (1×1) unit cell. (c) and (d) Room temperature LEED pattern (E=80 eV) measured on γ and β phase respectively [39]. (e)[(f)] Room temperature STM image of the γ [β] phase measured on a sample with submonolayer Pb coverage [43]. Image size: 21×21 nm^2 [25×25 nm^2], V_T: -1.5 V [+1 V] and I_T: 100 pA [200 pA]. The image (f) also shows the coexistence of the β phase (right side) and the 1×1-Pb phase (left side).

around 600° C Pb starts to evaporate away from the surface and the $\sqrt{3} \times \sqrt{3}$-Pb regions start to disappear. In other words, it is not possible to obtain a $\sqrt{3} \times \sqrt{3}$-Si with 100% of Si atoms and this is due to the strong tensile surface stress that such a reconstruction would entail [39]. Consequently, all the system can do is to intermix Pb and Si atoms in a mosaic phase structure consisting in a pattern of alternating and disordered chains of Pb and Si atoms, thus increasing the distance between Si atoms and minimizing its total energy [39–41].

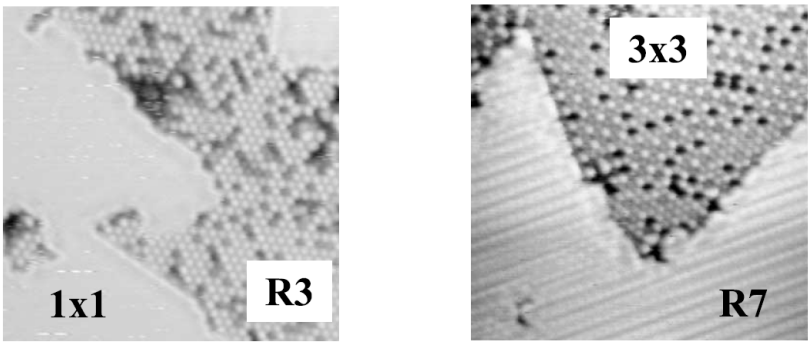

(a) (b)

Fig. 3.4 (a) and (b): STM images of Pb/Si(111) with a coverage below 1 ML. Image in (a) was measured at room temperature and coexisting regions of 1×1-Pb and $\frac{1}{3}$-ML $\sqrt{3} \times \sqrt{3}$-Pb (R3) phases are shown. Image size: 23×23 nm^2, V_T: +0.15 V and I_T: 100 pA. Image in (b) was measured at 57 K and coexisting regions of $\sqrt{7} \times \sqrt{3}$-Pb (R7) and 3×3-Pb phases are shown. Image size: 23×23 nm^2, V_T: -1 V and I_T: 200 pA [44].

As shown in Fig. 3.2, by increasing the coverage of Pb but still remaining below 1.2 ML, at room temperature, a coexistence between the 1×1-Pb and the $\frac{1}{3}$-ML $\sqrt{3} \times \sqrt{3}$-Pb (β) phases is observed, as shown in Fig. 3.3f and Fig. 3.4a. Several experimental studies, have reported a temperature-induced transformation of these phases for temperatures below ∼270 K [41, 44–46]. In particular, it was observed that, by cooling the sample below ∼270 K, 1×1-Pb regions transform into $\sqrt{7} \times \sqrt{3}$-Pb patches and β regions transform into 3×3-Pb structures. Moreover, it was shown also that this transition is fully reversible meaning that if the sample is heated up to room temperature the coexistence of β and 1×1-Pb phases is restored. Fig. 3.4a, shows an STM image taken at room temperature on the left side of which there is a 1×1-Pb region appearing as a quite flat surface with no special structure. Fig. 3.4b shows the same area of the sample measured at 57 K in which a new structure in place of the 1×1-Pb phase appears, i.e. the $\sqrt{7} \times \sqrt{3}$-Pb (labeled as R7 in figure), with the typical superstructure consisting in parallel straight rows of bright protrusions. The $\sqrt{7} \times \sqrt{3}$-Pb phase will be very important for us in the following of this chapter because its particular row structure could provide a good template surface for building one-dimensional self-assembled chains of MnPc molecules on top of it.

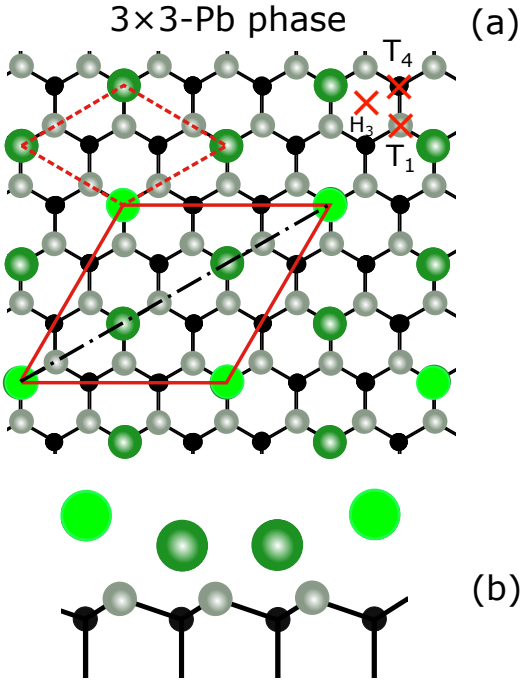

Fig. 3.5 (a): Top-view of the 3×3-Pb phase corresponding to $\frac{1}{3}$-ML of Pb. Solid (dashed) parallelograms indicate the 3×3 ($\sqrt{3} \times \sqrt{3}$) unit cell. (b): Side view of the atomic structure along the unit cell diagonal (black dotted-dashed line). Along this line, the atoms on the unit cell corners are higher than those inside leading to the one-up-two-down atom configuration responsible for the 3×3 periodicity of this phase. Small gray (black) balls represent Si atoms belonging to the topmost (second) atomic layer. Large green balls indicate Pb atoms adsorbed on T_4 sites. Red crosses indicate the three high-symmetry adsorption sites.

Conversely, when the temperature range is around 250-270 K, the $\sqrt{7} \times \sqrt{3}$-Pb superstructure disappears leaving just a 1×1-Pb structure. Similarly, on the right side of Fig. 3.4a, the β phase region transforms in the 3×3 structure in Fig. 3.4b. As can be seen, substitutional Si adatoms remaining from the mosaic phase or surface defects affect the regularity of the 3×3, i.e. black spot in 3×3 regions [37, 44].

As will immediately be clear, the mechanisms underlying these temperature-induced transitions are different for the 1×1-Pb and the β phase. In particular, the 1×1-Pb transformation can be seen as an order-disorder transition while the β phase transformation involves a redistribution of the valence charge resulting in a Charge Density Wave (CDW) that reduces the symmetry of the surface. The atomic model of the 3×3 reconstruction is shown in Fig. 3.5a. It consists, as for the β phase, of an hexagonal array of Pb atoms sitting on T_4 sites but here, the atomic lattice has a 3×3 periodicity. This periodicity is due to the one-up-two-down atom configuration shown in Fig. 3.5b. This figure shows the side view of the atomic structure along the 3×3 unit cell diagonal. It is clear that the atoms on the unit cell corners

are higher than those inside, i.e. one-up-two-down atom configuration. Recently, we have shown that Pb-substrate interaction, spin-orbit coupling and strong electronic correlations lead to stabilize a CDW having the one-up-two-down atom configuration that results in the 3×3 periodicity [47].

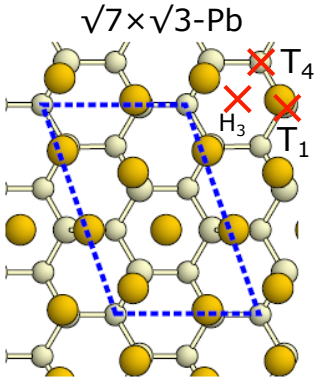

Fig. 3.6 Calculated atomic structure of the $\sqrt{7} \times \sqrt{3}$-Pb phase with the 1.2 ML model. Large yellow balls represent Pb atoms. Medium (Small) gray balls represent the topmost layer Si atoms (second-layer Si atoms). Dashed line represent the $\sqrt{7} \times \sqrt{3}$-Pb unit cell [48].

Fig. 3.6 shows the structural model of the $\sqrt{7} \times \sqrt{3}$-Pb phase. It was proposed by Kumpf on the basis of Surface X-Ray Diffraction (SXRD) measurements and it has been confirmed in several experimental and theoretical works [37, 46, 48–56]. According to this model, the $\sqrt{7} \times \sqrt{3}$-Pb is a quite flat and relatively close-packed hexagonal Pb layer. As shown in Fig. 3.6, in a single $\sqrt{7} \times \sqrt{3}$ unit cell there are 6 Pb atoms per 5 Si atoms, which means that this model has a coverage of $\frac{6}{5}$ ML = 1.2 ML. One of these Pb atoms is on a H_3 hollow site, four are almost T1 on-top sites and the remaining is in a bridge position above two Si atoms belonging to two different atomic planes. Moreover, the hollow site Pb atom has no bonds with the substrate while the others form a covalent-like bond with the underlying Si atoms, thus saturating all the dangling bonds. The unbound Pb is believed to be responsible for the small corrugation of this surface. Finally, all Pb-Pb bonds within the layer have a metallic character, in agreement with the 2D metallic behavior observed in other experimental and theoretical works [37, 46, 48–56]. There is another reason for which the $\sqrt{7} \times \sqrt{3}$-Pb is very interesting for the present work. Indeed this phase corresponds to the lower Pb coverage surface revealing 2D superconductivity [57].

Many studies have reported the reversible temperature-induced transition of the $\sqrt{7} \times \sqrt{3}$-Pb into a 1×1-Pb phase [38, 41, 44, 45, 49, 52, 58, 59]. Proposed models for the 1×1-Pb phase are based on experimental observations such as 1×1 diffraction patterns (Fig. 3.7b) or 1×1 structures in STM images (Fig. 3.7c). The simplest 1×1-Pb structure is displayed in Fig. 3.7a. It consists of one Pb atom per 1×1 unit cell sitting on a T_1 site, meaning that

this model has a coverage of 1 ML. This also means that when the $\sqrt{7}\times\sqrt{3}$-Pb becomes 1×1-Pb or vice versa, the system turns a structure with a coverage of 1.2 ML ($\sqrt{7}\times\sqrt{3}$-Pb phase) into one with coverage of 1 ML (1×1-Pb phase). This process is a bit tricky if we consider that through the phase transition the domains retain their shape, their size and no Pb is added/removed [38, 41].

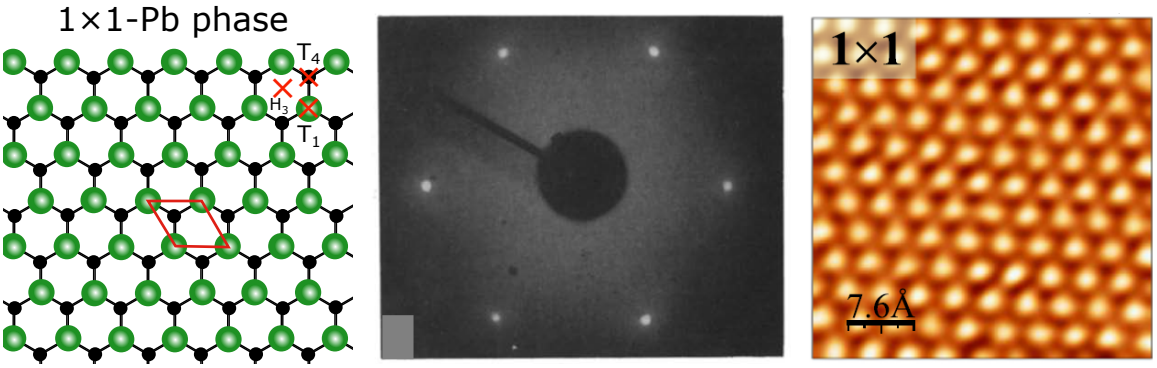

(a) (b) (c)

Fig. 3.7 (a) Top-view of the 1×1-Pb phase corresponding to Pb coverages below 1.2 ML. Small black balls represent Si atoms belonging to the second atomic layer. Large green balls indicate Pb atoms adsorbed on T_1 sites. Red crosses indicate the three high-symmetry adsorption sites. Solid line indicate the 1×1 unit cell. (b) LEED pattern of a 1×1-Pb reconstructed surface with a coverage of $\sim$0.9 ML. The pattern was measured at room temperature and E=80 eV [39] (c) STM image of Pb/Si(111) with a coverage below 1 ML measured at room temperature. Image size: 3.8×3.8 nm^2, V_T =+0.1 V and I_T =0.3 nA [43].

Jung et al. have conducted an interesting study, based on ab-initio molecular dynamics simulations, to clarify both the mechanism by which the temperature-induced structural change of the $\sqrt{7}\times\sqrt{3}$-Pb takes place and the structural model to be considered through the phase transition [51]. Starting from the $\sqrt{7}\times\sqrt{3}$-Pb model shown in Fig. 3.6 they describe the high-temperature 1×1-Pb structure as a disordered phase in which the net result of the Pb diffusion is the hopping process of a single Pb atom through the hollow sites (H_3 or T_4) of a '1×1'-Pb background lattice consisting of Pb atoms on T_1 sites (see Fig. 3.8). The origin of this behavior hides behind the time-scale. Above $\sim$270 K, in a short time-scale ($\sim$2 ps), the atomic diffusion involves two Pb atoms per unit cell and it actually breaks the $\sqrt{7}\times\sqrt{3}$ symmetry leading to a disordered phase. On the other hand, by averaging over larger time-scales, the net result of the diffusion per unit cell is to preserve the Pb occupation of T_1 sites, giving rise to a lattice with '1×1' periodicity, while a single Pb atom diffuses through the hollow sites (H_3 or T_4) of this lattice. Fig. 3.8 schematically shows the essence of this dynamic model. In particular, Fig. 3.8a shows a simplified sketch of the ordered $\sqrt{7}\times\sqrt{3}$-Pb structure for temperatures below $\sim$270 K. This sketch differs from the calculated one (see

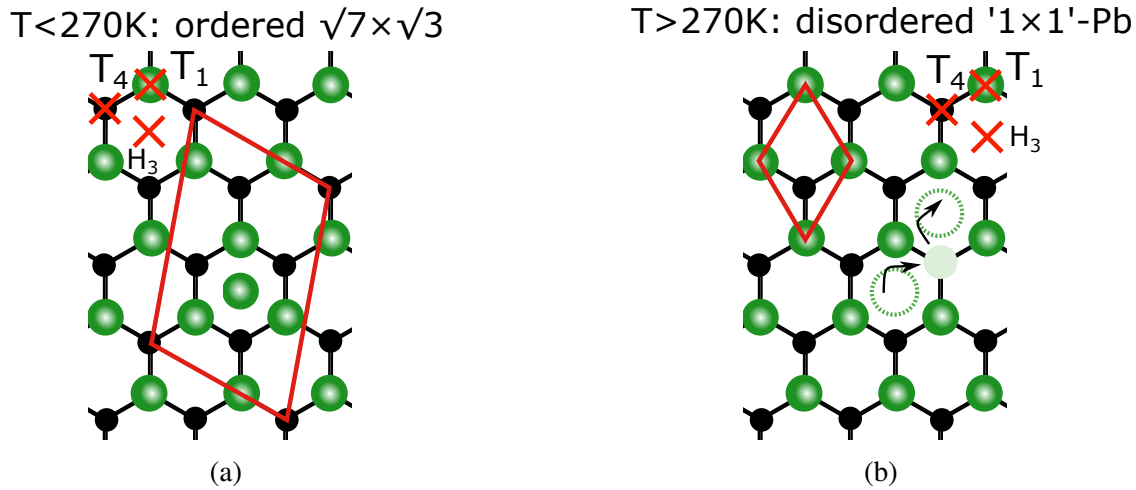

Fig. 3.8 Schematic sketch of the temperature-induced structural change between (a) $\sqrt{7}\times\sqrt{3}$-Pb and (b) disordered '1×1'-Pb structure. (a) For temperatures below ∼270 K the unit cell keeps the ordered $\sqrt{7}\times\sqrt{3}$-Pb structure with 5 Pb atoms on T_1 sites and the sixth Pb on a H_3 site. This model can be reviewed as a simple 1×1-Pb structure with an extra Pb atom on a H_3 site. (b) For temperatures sufficiently above ∼270 K the extra Pb atom starts to diffuse through the hollow sites of the 1×1-Pb lattice, e.g. it can jump firstly on a T_4 site (light green circle) and then again on a H_3 site (within the dotted green circle). The net result of this model is that at high temperatures the Pb occupation of T_1 sites is preserved, giving rise to a background lattice with periodicity '1×1' which is that experimentally observed. At the same time, the extra Pb atom diffuses through the hollow sites of this lattice. Small black balls represent Si atoms belonging to the second atomic layer. Large green balls indicate Pb atoms. Red crosses indicate the three high-symmetry adsorption sites. Solid lines indicate (a) the $\sqrt{7}\times\sqrt{3}$ unit cell and (b) the 1×1 unit cell.

Fig. 3.6) for the fact that, within the unit cell, five Pb atoms are exactly on T_1 sites, instead of having slightly off-center positions. Then, the sixth Pb is always on a H_3 site. In other words, the model can be seen as a simple 1×1-Pb structure (see Fig. 3.7a) with an extra Pb atom on a H_3 site. Then, Fig. 3.8b shows that for temperatures above ∼270 K, the extra Pb atom (on H_3 site) start to diffuse through the hollow sites (T_4 or H_3 sites) of the lattice 1×1-Pb lattice. The result of this model is that, at both low and high temperature, the Pb occupation of T_1 sites is preserved leading to a background lattice with '1×1' structure. In the context of the present model, this background lattice corresponds to that experimentally observed at temperatures higher than ∼270 K. It is interesting to note that the underlying Pb structure assumed by this dynamic model preserves a coverage of 1.2 ML through the phase transition from $\sqrt{7}\times\sqrt{3}$-Pb to 1×1-Pb and vice versa.

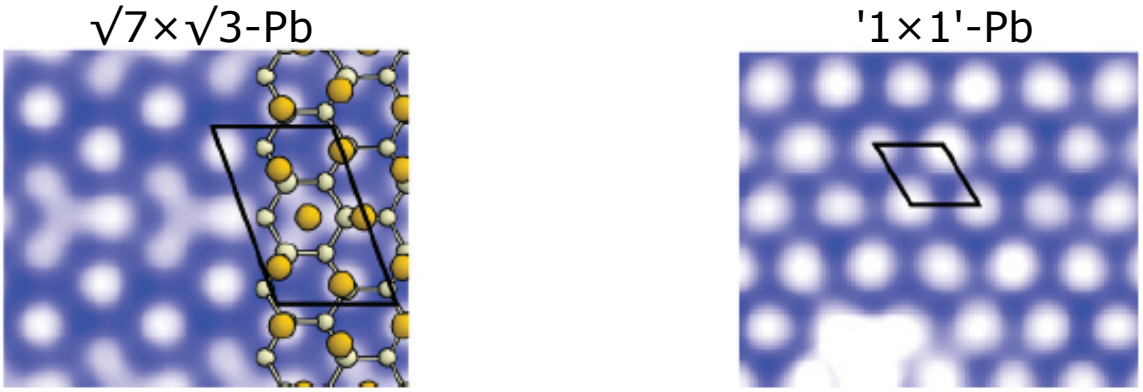

(a) (b)

Fig. 3.9 Simulated constant-current STM images. (a) Filled states image of the low temperature $\sqrt{7}\times\sqrt{3}$-Pb phase. On the right side the $\sqrt{7}\times\sqrt{3}$-Pb atomic model is superimposed and the unit cell is highlighted by black solid lines. (b) Filled states image of the high temperature '1×1'-Pb disordered phase. The 1×1 unit cell is highlighted by black solid lines. [51].

Simulated STM images shown in Fig. 3.9a and Fig. 3.9b, based on ab-initio molecular dynamics simulations, are able to reproduce the temperature-induced phase transition between $\sqrt{7}\times\sqrt{3}$ and the '1×1' phase. In particular, Fig. 3.9a displays an STM image for the ordered $\sqrt{7}\times\sqrt{3}$-Pb phase showing the extra Pb atoms adsorbed on H_3 sites that participate to the formation of Y-shape patterns. On the other hand, Fig. 3.9b shows a high temperature (400 K) STM image obtained by averaging the STM images of the atomic structure extracted every 1 ps from a Molecular Dynamics run of 15 ps. In this case, Pb atoms diffusing through the hollow sites ($H3$ and T_4) cannot be seen within the STM image and only a '1×1' pattern is observed corresponding to the Pb atoms on T_1 sites. These results support the idea that the '1×1' patterns observed in LEED or STM experiments are due to an average process over the atomic diffusion which is faster than the measuring process itself. Remarkably, Jung et al. [51] have also shown that the electronic properties of a Pb overlayer are weakly affected by the disordering process just described, i.e. covalent bonds between Pb atoms and substrate and the 2D metallic character of the layer are almost unaffected. This is in agreement with the work of Hsu et al. in which they calculated by DFT the surface energy and the band structure of two $\sqrt{7}\times\sqrt{3}$ models, i.e. one with a Pb atom placed on H_3 hollow site as proposed by Kumpf and the other with the Pb sitting on a T_4 hollow site. They found that the energy difference in placing the Pb atom in one or in the other hollow site is very small, i.e. $\sim$3 meV, and that the needed deformation to pass from one to the other is less than the typical Pb-Pb bond distance, i.e. 0.8 Å, resulting in a negligible deformation of the overall atomic structure and indistinguishable Pb surface band structure for the two configurations [54]. Finally, it is important to note that the idea of a'1×1' disordered phase was already

mentioned in previous works. For instance, Choi et al. have conducted an XPS study in which the analysis of the behavior of both Pb and Si core-levels through the transition from $\sqrt{7} \times \sqrt{3}$ to 1×1 agrees with a Pb overlayer based on a 1.2 ML model involving, at high temperatures, a hollow site diffusion of Pb atoms. [38, 45, 51, 52, 58].

In summary, when a Pb monolayer is prepared, different regimes of coverage give rise to different surface structures. For Pb coverage lower then 1.2 ML, coexistence of $\sqrt{7} \times \sqrt{3}$-Pb and dilute 3×3-Pb regions is observed. At a Pb coverage of 1.2 ML, 100 % of the surface is covered by a $\sqrt{7} \times \sqrt{3}$-Pb reconstruction. In ideal conditions, within the range of coverage between 1.2 ML and 1.3 ML, the system would tend to form a dense $\sqrt{3} \times \sqrt{3}$ structure on top of the Si(111). Due to the large lattice mismatch ($\sim$ 10%) between Si(111) and Pb(111) bulk lattice constants, i.e. 5.43 Å and 4.92 Å respectively, a commensurate $\sqrt{3} \times \sqrt{3}$-Pb would require a compression ($\sim$5%) of the Pb overlayer. However, this kind of structure has never been observed in real experiments, probably because it is not energetically allowed. In the rest of this section, it will be shown that a huge number of structural phases (known as Pb dense phases) can be obtained within the narrow range of coverage between 1.2 ML and 1.3 ML. In particular, the aim of the following discussion is to present as clearly as possible what is our current view about the dense phases of Pb on Si(111).

Ganz et al. [39] determined, by means of LEED experiments, the compression within the Pb layer at different Pb coverage (see Fig. 3.10). By varying the Pb coverage between $\sim$1 ML and $\sim$1.6 ML, they deduced that the compression continuously changes between 0% (see Fig. 3.10b) and 2.3% (see Fig. 3.10c) respectively. Furthermore, they have shown that the highest compression is reached at 1.3 ML of Pb, that is at the saturation coverage of the Pb monoalyer beyond which Pb islands start to grow. The discrepancy between measured compression of the Pb layer (2.3%) and the expect one for an uniform commensurate $\sqrt{3} \times \sqrt{3}$-Pb phase (5%) was ascribed to the presence of an incommensurate phase. This hypothesis was supported by the fact that diffraction spots related to the $\sqrt{3} \times \sqrt{3}$ symmetry (spots within the dashed green circles in Fig. 3.10) are not exactly at the $\sqrt{3} \times \sqrt{3}$ positions.
Careful inspection of LEED patterns reveals that the $\sqrt{3} \times \sqrt{3}$ spots have a trimer structure that shrinks by increasing the Pb coverage (compare Fig. 3.10b and Fig. 3.10c). In the following discussion, it will be shown that this shrinking is related to the existence of the dense phases between 1.2 ML and 1.3 ML each with its own structure.

The first thing to consider in order to understand the structure of the Pb dense phases is that all of them are based on a $\sqrt{3} \times \sqrt{3}$-Pb unit cell, 30° rotated with respect to the silicon

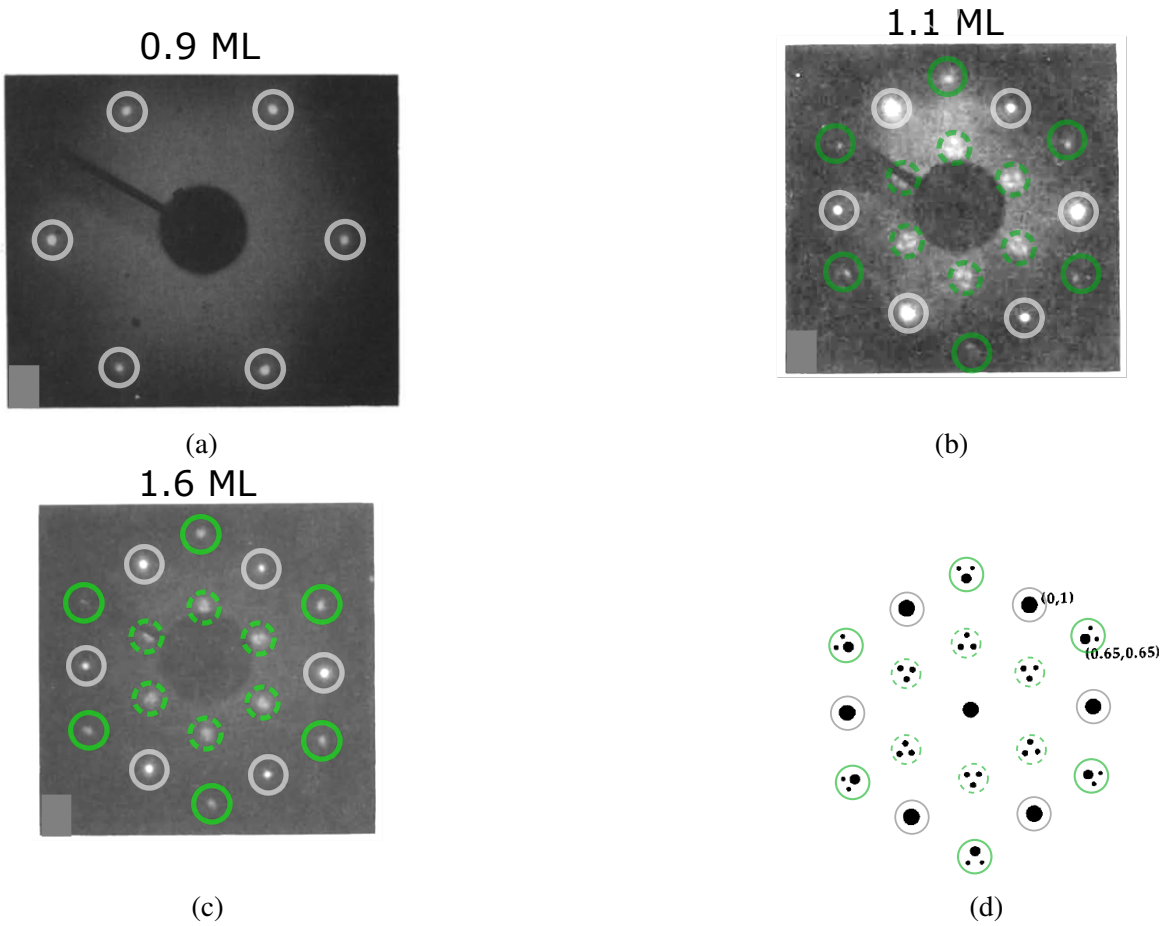

Fig. 3.10 LEED patterns measured at room temperature and E=80 eV on a Pb/Si(111) overlayer: (a) 1×1-Pb reconstructed surface with a coverage of $\sim$0.9 ML. (b) Rotated Incommensurate phase with a coverage of $\sim$1.1 ML. (c) Rotated Incommensurate phase with a coverage of $\sim$1.6 ML. (d) Rendering of the LEED pattern observed for the rotated incommensurate phase. Bright (large) spots within the solid grey circles represent the first-order bulk Si spots. Brighter (medium-size spots) within the solid green circles arise from the incommensurate overlayer. Weaker (small) spots arise from the internal structure of the overlayer [39].

substrate and with four Pb atoms per unit cell [37, 39, 45, 58–60]. Several DFT calculations revealed that the lowest energy structures of the dense $\sqrt{3} \times \sqrt{3}$-Pb are those shown in Fig. 3.11 [37, 61, 62]. Both structures have 4 Pb atoms per unit cell, meaning a coverage of $\frac{4}{3}$ ML = 1.33 ML, three of which sit on off-centered T_1 sites and the fourth is located either on a H_3 (see Fig. 3.11a) or on a T_4 site (see Fig. 3.11b). It was also shown that the two binding sites (H_3 and T_4) are almost degenerated in energy, i.e. they differ by less than few tens of meV, therefore the two models are almost degenerated too. Moreover, the two structures are separated by a small energy barrier of $\sim$0.59 eV which allows the coexistence

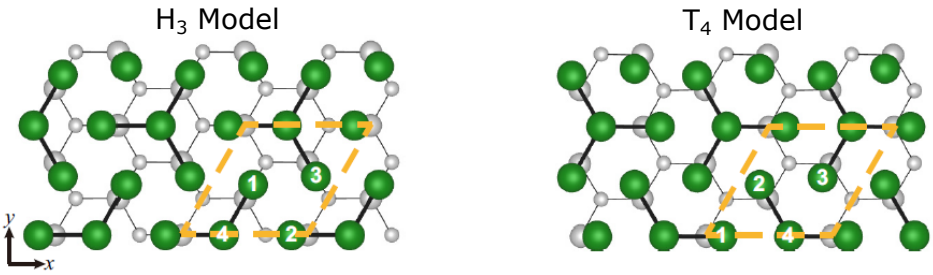

(a) (b)

Fig. 3.11 Calculated (a) H_3 and (b) T_4 structures of the Pb dense phases by means of 1.33ML models. Dashed lines indicate the $\sqrt{3}\times\sqrt{3}$ unit cell in which four Pb atoms are numbered. Three Pb atoms sit on off-center T_1 sites and the fourth is located either on a (a) H_3 either on a (b) T_4 site. Green balls represent the Pb atoms. Big gray balls represent the first-layer Si atoms while small gray balls the second-layer ones [61].

of both even at low temperatures. A recent study [61] has shown that including or not the spin-orbit coupling (SOC) in DFT calculations can influence the relative stability of these two structures. In particular, without SOC the T_4 structure is energetically more stable by 25 meV respect to the H_3 structure. On the contrary, with SOC the H_3 becomes more stable than the T_4 by 12 meV [61]. There is an apparent contradiction between these calculations and the previous discussion about the diffraction results because the latter considers the dense phases of Pb as incommensurate structures while the former assumes a commensurate model. The idea allowing to resolve this contradiction will be clear soon.

The starting point is the proposed model for the Hexagonal Incommensurate Phase type A (HICA) (see Fig. 3.12) [62]. HICA is a dense phase observed at room temperature and at around $\sim$1.25 ML. Within the hexagonal structure in Fig. 3.12 two types of triangular $\sqrt{3}\times\sqrt{3}$-Pb domains can be distinguished. Regions with yellow balls represent H_3 structures, while regions with green balls represent T_4 structures. The coexistence of H_3 and T_4 structures is in agreement with what has been said in the previous paragraph about the energy degenaracy of the models in Fig. 3.11. Due to symmetry and energetic reasons, different types of structures are always alternating and separated by domain walls with "almost" $\sqrt{7}\times\sqrt{3}$-Pb structure whose unit cell is displayed in Fig. 3.12 by a small white parallelogram. Domain walls do not have a standard $\sqrt{7}\times\sqrt{3}$-Pb structure because the domain wall unit cell contains atoms belonging to both the H_3 and the T_4 structure. On the other hand, in a standard $\sqrt{7}\times\sqrt{3}$-Pb phase, Pb atoms only sit on H_3 sites (see Fig. 3.6). The very important message here is that, contrary to what previous works assumed, the HICA phase is actually a commensurate structure with a large rhombic unit cell containing the two types of $\sqrt{3}\times\sqrt{3}$-Pb domains (H_3 and T_4) and a "almost" $\sqrt{7}\times\sqrt{3}$-Pb domain wall (see big white parallelogram in Fig. 3.12).

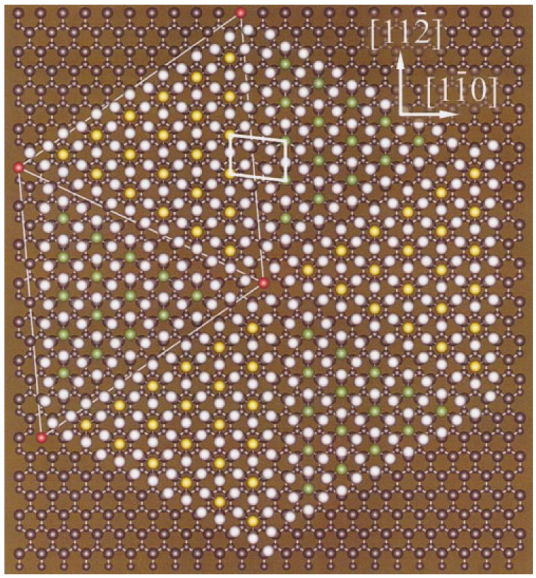

Fig. 3.12 Atomic structure of the HIC phase. Yellow (green) balls represent Pb atoms adsorbed on H_3 (T_4) sites. White balls represent Pb atoms on off-center T_1 sites. Large (small) black balls represent the first (second) layer Si atoms. Small white parallelogram indicates the "almost" $\sqrt{7} \times \sqrt{3}$-Pb unit cell of the domain walls between H_3 and T_4 domains. Big white parallelogram indicates the rhombic unit cell of the HIC phase. [62].

Furthermore, this big unit cell can be oriented along three equivalent directions giving to the surface an overall 3-fold symmetry [38, 62]. It is clear then, that the "Incommensurate" appearing within the name of this phase is retained only for historical reasons.

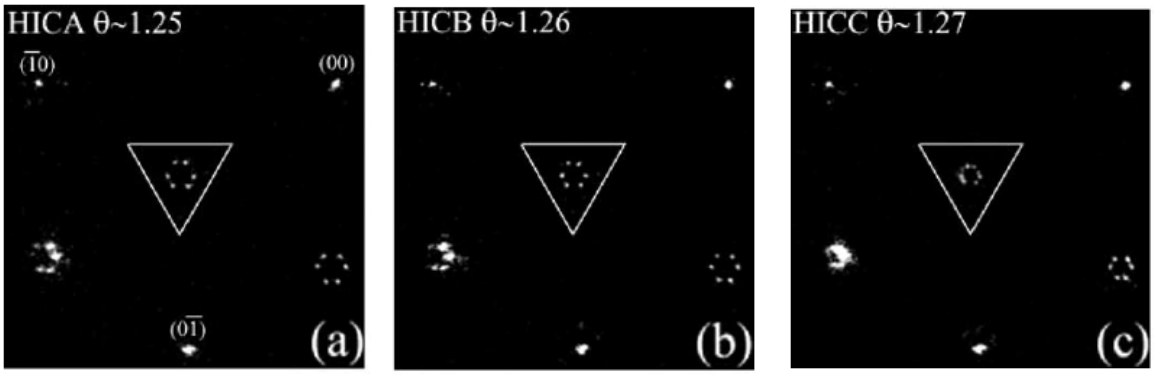

(a) (b) (c)

Fig. 3.13 SPA-LEED patterns measured at room temperature on a Pb/Si(111) overlayer: (a) HICA phase with a coverage of 1.25 ML, (b) HICB phase with a coverage of 1.26 ML, (c) HICC phase with a coverage of 1.27 ML. Hexagonal spots within the white triangle are related to the structure of these commensurate phases. The shrinking of the hexagon with the coverage indicates that the unit cell size increases [38].

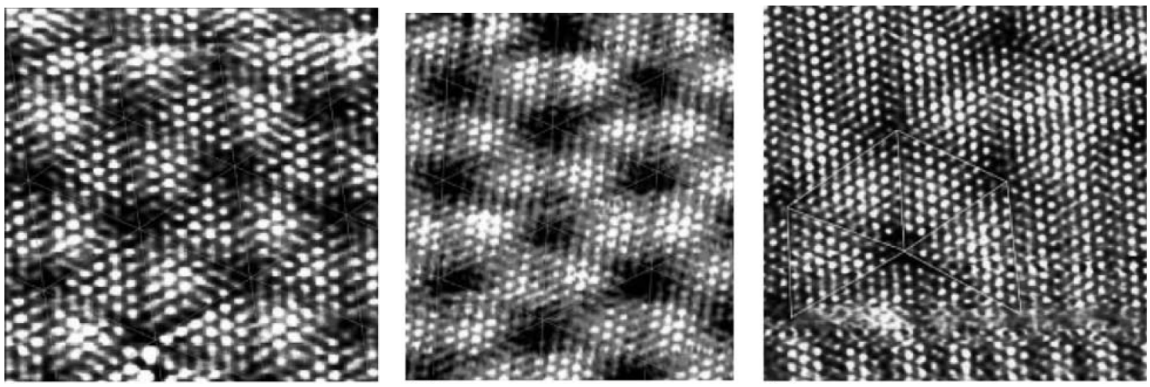

(a) (b) (c)

Fig. 3.14 STM images measured at room temperature on a Pb/Si(111) overlayer: (a) HICA (8.8×6.6 nm^2), (b) HICB (14.4×7.2 nm^2) and (c) HICC (12×12 nm^2). White protrusions represent the Pb atoms adsorbed either on H_3 or on T_4 sites from which the commensurate unit cell size (hexagon side) can be measured [38].

Starting from this result, the brilliant concept to understand all the Pb dense phases of Pb/Si(111) from 1.2 ML to 1.3 ML is that they can be built by combining dense $\sqrt{3}\times\sqrt{3}$-Pb regions separated by domain walls with "almost" $\sqrt{7}\times\sqrt{3}$-Pb structure. In this way a large commensurate unit cell can be always defined to describe the structure of these phases. As a result, we can claim that, unlike to what previously assumed, all the dense phases of Pb/Si(111) are actually commensurate with large unit cells. With this "simple" model, previous results have consistently been put together [38, 58, 60, 62]. The crucial misunderstanding in previous results resides in the LEED pattern interpretation. The fact that the spots within the dashed green circles in Fig. 3.10 are not exactly at the $\sqrt{3}\times\sqrt{3}$ positions was interpreted as the signature of an incommensurate structure. In fact, the important insight is that this type of LEED arises from a commensurate surface made up of commensurate domains separated by a regular arrangement of domain walls, e.g. the triangular $\sqrt{3}\times\sqrt{3}$-Pb domains in Fig. 3.12 are separated by hexagonally arranged domain wall. Fig. 3.13a shows the SPA-LEED pattern arising from the HICA structure in Fig. 3.12. The spots within the triangle are the same than those within the dashed green circles in Fig. 3.10. The difference here is that the three spots of Fig. 3.10 are additionally splitted because of a more regular ordering of the domain walls. It was proposed that this may depend on the sample preparation method [60]. The hexagonal configuration of the spots is due to the three-fold symmetry of the surface, i.e. alternating spots on the hexagon form two intertwined equilateral triangles arising from the three rotational domains. Thanks to this interpretation of diffraction patterns together with STM measurements, three different types of HIC were identified, i.e. HICA, HICB and HICC (see Fig.3.13). These phases differ in

coverage by ∼0.02 ML between 1.25 ML and 1.28 ML. From Fig.3.13 it is clear that by increasing the coverage, the hexagon shrinks exactly as shown in Fig. 3.10. In the current description of the surface as a commensurate structure with a large unit cell we know that this shrinking is an effect related to the increasing of the unit cell size with the coverage. STM images of the HIC phases are shown in Fig. 3.14. Bright protrusions represent Pb atoms adsorbed either on H_3 or on T_4 sites at the corners of the $\sqrt{3} \times \sqrt{3}$ unit cell from which the commensurate unit cell size of the surface can be measured. This size corresponds to the hexagon side length in Fig. 3.14 and it is simple to see that by increasing the coverage from ∼1.25 ML to ∼1.28 ML the commensurate unit cell gets bigger. Moreover, the unit cell changes its orientation and the atoms coherently adjust their structure [38, 62].

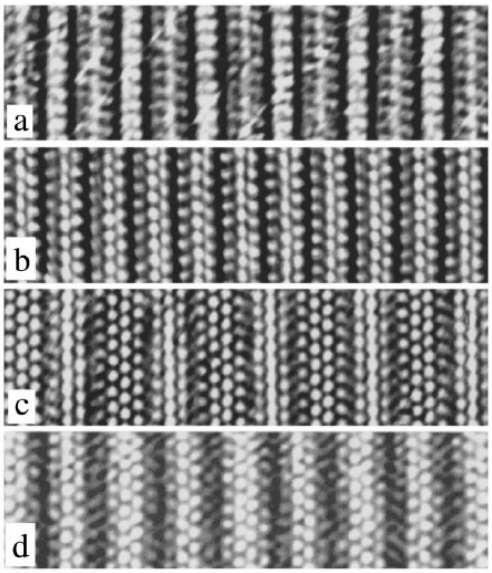

Fig. 3.15 STM images of linear phases between 1.25 ML and 1.3 ML: (a) (n=1 , m=1) at 1.263 ML. (b) (n=1 , m=2) at 1.27 ML. (c) (n=1 , m=3) at 1.28 ML. (d) (n=1 , m=3) at 1.285 ML. Dark rows represent the domain walls with "almost" $\sqrt{7} \times \sqrt{3}$-Pb structure and bright rows represent the $\sqrt{3} \times \sqrt{3}$-Pb domains [53].

By continuing to explore the phase diagram in Fig. 3.2 a new temperature-induced phase transition is observed from the HIC phases to the so-called "Devil's Staircase" (DS) or linear phases when the temperature is decreased. Here again, the atomic structure of these phases is based on a combination of $\sqrt{3} \times \sqrt{3}$-Pb and $\sqrt{7} \times \sqrt{3}$-Pb regions. In particular, the unit cells of these phases are built by combining an integer number n of $\sqrt{7} \times \sqrt{3}$ unit cells and an integer number m of $\sqrt{3} \times \sqrt{3}$ unit cells [38, 62, 53]. This is why they are commonly denoted as (n,m) phases. Some of these phases are shown in Fig. 3.15 and by looking at them is clear why they are called linear phases. Dark rows represent the domain walls with

"almost" $\sqrt{7}\times\sqrt{3}$-Pb structure and bright rows represent the $\sqrt{3}\times\sqrt{3}$-Pb domains. A regular $\sqrt{7}\times\sqrt{3}$-Pb, corresponding to (n = ∞ , m = 0), has a coverage of 1.2 ML, while the ideal $\sqrt{3}\times\sqrt{3}$-Pb, corresponding to (n = 0 , m = ∞) has a coverage of 1.33 ML. This means that a generic (n,m) linear phase has a coverage ranging between 1.2 ML and 1.33ML. Indeed, the two basic unit cells ($\sqrt{7}\times\sqrt{3}$ and $\sqrt{3}\times\sqrt{3}$) are able to arrange in a complex way giving rise to a huge number of different phases with variable periodicity in a narrow coverage range. Linear phases are still 3-fold degenerate with rotational domains along the three equivalent orientations. By means of STM and SPA-LEED measurements ∼18 different linear phases were identified by means of sequential deposition of few percent ML of Pb [53]. With this model the reversible coverage-induced phase transition between the $\sqrt{7}\times\sqrt{3}$-Pb and linear phases can be trivially explained by local atomic rearrangement. Less obvious is the explanation for the reversible temperature-induced phase transition between HIC and linear phases. A drastic and macroscopic atomic rearrangement results in a change of the domain walls configuration, from linear to hexagonal and vice versa. As can be seen from the phase diagram in Fig. 3.2, the critical temperature for this phase transition has a U-shape dependence on coverage which makes the linear phases more stable than the HIC phases even at room temperature for coverages above 1.29 ML. It is not clear which is the driving force behind all these transitions. It was proposed that [38, 53], dense phases of Pb are the result of long-range repulsive interactions arising from the compression due to the Pb coverage increasing. The rearrangement of the surface in domains separated by domain walls is a consequence of the natural tendency of the system to minimize the total energy [38, 53]. Furthermore, also the high Pb mobility ad the small energy difference between the Pb phases probably play an important role. Thus, the coverage/temperature-induced phase transitions consist in a rearrangement of the domain walls configuration, e.g. from linear to hexagonal, driven by the need of the system to minimize the total energy.

For the linear phases above 1.29 ML the temperature-induced transition goes toward a new phase that is the Striped Incommensurate Phase (SIC), without forming an HIC structure. Fig. 3.16 shows the SIC phase. Dark stripes represent the domain walls with almost $\sqrt{7}\times\sqrt{3}$-Pb structure, and brighter parts represent the $\sqrt{3}\times\sqrt{3}$-Pb domains. It has a saturation coverage of ∼1.3 ML and it is similar to the HIC but instead of having a hexagonal configuration of the domain walls, meandering paths are formed on the surface in order to accommodate the increasing coverage in $\sqrt{3}\times\sqrt{3}$-Pb structures [38, 58]. The SIC can be equally reached by adding a small amount of Pb on the HIC phases. The reverse process, i.e. passing from to SIC to HIC, is also possible by desorbing few Pb from the surface. The fact that the SIC does not undergo temperature-induced phase transitions by cooling it, may be due to the fact this is the most compressed phase and there exists only one domain wall

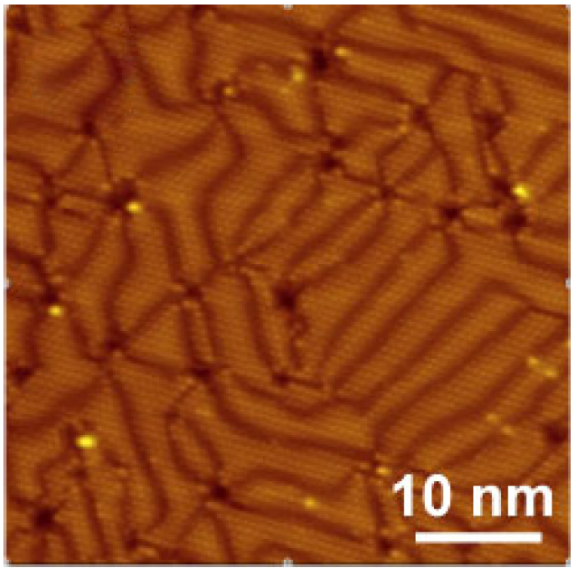

Fig. 3.16 STM image of the SIC phase of Pb/Si(111) measured at 78 K. Dark stripes represent the domain walls with almost $\sqrt{7} \times \sqrt{3}$-Pb structure, and brighter parts represent the $\sqrt{3} \times \sqrt{3}$-Pb domains [63].

configuration that minimizes the total energy of the system [45, 58]. Since the SIC is the densest phase, at this point, the coverage cannot be increased more than 1.3 ML and further deposition of Pb contributes to the growing of the subsequent layers of Pb. Note that the saturation coverage for a pure commensurate $\sqrt{3} \times \sqrt{3}$-Pb phase would be $\frac{4}{3}$=1.33 ML (see Fig. 3.11) but due to the fact that the real surface presents domain walls with a less dense structure, i.e. almost $\sqrt{7} \times \sqrt{3}$-Pb with coverage $\sim$1.2 ML, then the real saturation coverage is 1.3 ML.

It is interesting to point out that, as shown in Fig. 3.2, at sufficiently high temperature, all the dense phases transform reversibly into a simple 1×1 phase, i.e. all the complex surface superstructures suddenly disappear. Once again, Jung et al. argued that the model of order-disorder transition previously discussed for the $\sqrt{7} \times \sqrt{3}$-Pb phase (see Fig. 3.8) might be good also for the dense phases of Pb, i.e. HIC and SIC [51]. Actually, these phases are made up of $\sqrt{3} \times \sqrt{3}$-Pb regions separated by domain walls with "almost" $\sqrt{7} \times \sqrt{3}$-Pb structure. For the $\sqrt{7} \times \sqrt{3}$-Pb part the disordering model remains the same than that in Fig. 3.8. By looking to Fig. 3.11 it is clear that also the $\sqrt{3} \times \sqrt{3}$-Pb can be reviewed as a 1×1-Pb lattice with an extra Pb atom on a H_3/T_4 site. In this way it is easy to imagine that, for temperatures sufficiently above the transition temperature, the extra Pb atom has sufficient energy to overcome the activation energy barrier and start to diffuse through the hollow sites of the 1×1-Pb lattice. Therefore, also in this case the '1×1' patterns experimentally

observed are due to an average process over the atomic diffusion which is faster than the measuring process itself.

We conclude about the dense phases of Pb monolayer on Si(111). Starting from 1.2 ML, i.e. the 1×1-Pb (at room temperature) or $\sqrt{7} \times \sqrt{3}$-Pb (at low temperature) phase, we can move through the dense phases by adding little amount of Pb, i.e. by increasing the Pb coverage. Adding Pb on the sample has the effect of increasing the compression of Pb atoms within the layer and consequently increasing the long range repulsive interactions. The system response to such a process is to minimize its total energy by rearranging the surface in $\sqrt{3} \times \sqrt{3}$-Pb domains separated by domain walls with "almost" $\sqrt{7} \times \sqrt{3}$-Pb structure. As the the coverage is increased the system rearranges the domain walls configurations in order to adopt the most energetically stable for each coverage and this results in the different HIC (at room temperature) or linear phases (at low temperature) experimentally observed. The general trend of the system is to reduce the density of domain walls on the surface in order to form bigger and bigger $\sqrt{3} \times \sqrt{3}$-Pb domains. Ideally, the system would tend to form a pure commensurate $\sqrt{3} \times \sqrt{3}$-Pb at 1.33 ML that would require a compression of $\sim$5% within the layer. However, in real experiments this structure is never observed (probably because it is energetically forbidden) and a Striped Incommensurate Phase (SIC) phase if formed instead at a Pb coverage of 1.3 ML. The SIC is an incommensurate phase in which the domain walls meander irregularly in order to reduce their density and maximize the accommodation of Pb atoms in $\sqrt{3} \times \sqrt{3}$-Pb domains. The saturation coverage of the SIC is slightly smaller than that of an ideal commensurate $\sqrt{3} \times \sqrt{3}$-Pb because of the presence of "light domain walls" with an "almost" $\sqrt{7} \times \sqrt{3}$-Pb structure whose coverage is only $\sim$1.2 ML.

3.2 Experimental preparation of the $\sqrt{7} \times \sqrt{3}$-Pb phase

In this section I will describe the procedure through which I prepared the $\sqrt{7} \times \sqrt{3}$-Pb phase. As already mentioned it is an annealed phase meaning that it is obtained by depositing a certain amount of Pb on the Si(111)-7×7 reconstructed surface and then annealing the sample between $\sim$300° C and $\sim$400° C. The annealing process melts the Pb overlayer and removes the 7×7 reconstruction, leaving an unreconstructed Si(111) with 1×1 surface periodicity. From an experimental point of view it is important to note that, during the annealing, part of the Pb desorbs from the surface decreasing the actual amount of Pb remaining on the surface that will form the surface reconstruction. For this reason, the duration of Pb deposition is not directly related to the final Pb coverage on the surface and therefore the Pb flux that comes out of the evaporator does not require an extremely fine calibration. On the other

hand, due to the presence of many phases in a very narrow coverage range (∼0.1 ML), a precision of ∼0.01 ML is required to achieve a specific phase. This means that, for a given initially deposited Pb coverage, the growth of well controlled layers of Pb on Si(111) requires mastering of both the temperature and the time of annealing. These parameters were finely adjusted by checking the surface with either LEED or STM at the end of each annealing procedure.

The first five months of Ph.D I worked on the optimization of the above mentioned parameters to obtain the $\sqrt{7} \times \sqrt{3}$-Pb phase. As already seen in previous section, an uniform $\sqrt{7} \times \sqrt{3}$-Pb requires exactly 1.2 ML of Pb and temperatures below ∼250 K, i.e. it is a low temperature phase. On the other hand, the experimental equipment I've been working on in these months could not be operated below room temperature. This means that I could only gain access to the room temperature phases of the Pb monolayer. By looking at the phase diagram in Fig. 3.2, it is clear that the room temperature phase corresponding to 1.2 ML is the 1×1-Pb phase and therefore, the latter was the initial target phase.

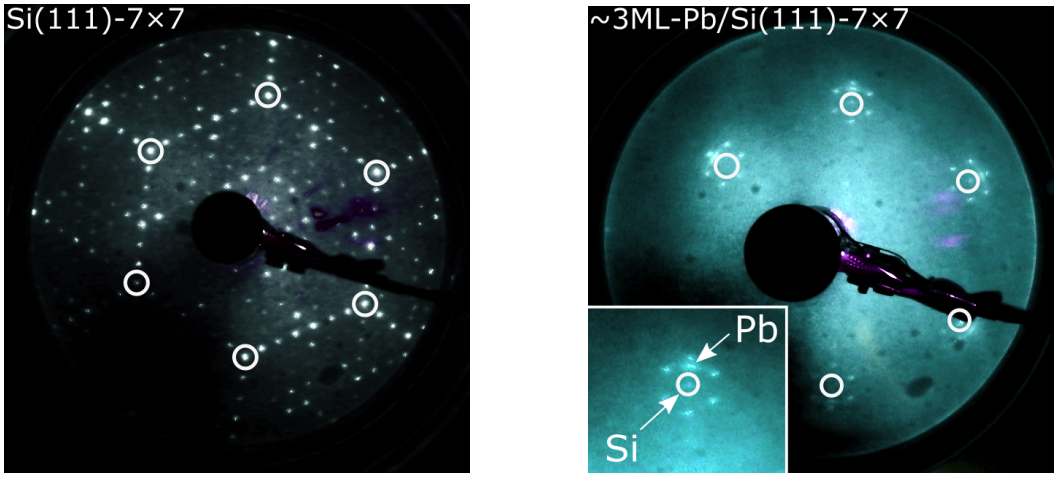

(a) (b)

Fig. 3.17 LEED patterns measured at room temperature and E=60 eV. (a) Freshly prepared Si(111)-7×7 reconstructed surface. (b) Pattern arising from a sample prepared by depositing at room temperature ∼3 ML (or maybe a bit more) of Pb on the Si(111)-7×7 surface. The inset of Fig. 3.17b shows the positions of both bulk Si and bulk Pb spots belonging to the the upper vertex of the hexagon in figure. Gray circles indicate the 1×1 spots arising from the bulk silicon substrate.

First of all, a Si(111)-7×7 reconstructed surface must be prepared by following the procedure already described in the experimental methods chapter. Fig. 3.17a shows typical LEED pattern of a freshly prepared Si(111)-7×7 surface. Gray circles indicate the 1×1 diffraction

spots arising from the bulk silicon substrate. The other spots are related to the 7×7 surface reconstruction. The UHV system where I performed the first calibrations experiments was not equipped with a quartz balance allowing me to calibrate the Pb flux that comes out of the evaporator. Therefore the only way that I could get to know the amount of Pb deposited on the silicon surface was to check the LEED pattern just after the evaporation and compare with literature [39, 52]. Fig. 3.17b shows the LEED pattern arising from a sample prepared by depositing at room temperature $\sim$3 ML (or maybe a bit more) of Pb on the Si(111)-7×7 surface. Gray circles still indicate the 1×1 diffraction spots arising from the bulk silicon substrate. Faint spots of the 7×7 reconstruction are still visible. Additional spots slightly moved away from the 1×1 silicon spots are associated to bulk Pb(111) crystals that form at these coverages [39]. Their position can be easily seen in the inset of Fig. 3.17b. The fact that both the Si and the Pb bulk spots are not rotated between them means that Pb crystals are aligned with Si substrate. The shift between the Si and Pb bulk spots reflects the mismatch existing between the bulk lattice constants, i.e. 5.43 Å for Si and 4.92 Å for Pb. Increased diffuse background intensity indicates a disordered growth of Pb on the substrate. The important thing here is to evaporate enough Pb to cover the whole surface with more than 1.3 ML, i.e. exceed the saturation coverage for a single monolayer. This assures us that there are no regions on the surface with a coverage lower than that expected, i.e. 1.2 ML, and that we can homogeneously reconstruct the surface by means of the annealing. Time and temperature of annealing were optimized by iterative cycles. Fig. 3.18a, Fig. 3.18b and Fig. 3.18c show three intermediate LEED patterns obtained after annealing the sample in Fig. 3.17b at $\sim$375° C for $\sim$30 sec, $\sim$8.3 min and $\sim$9.3 min respectively. From these figures is clear that the 7×7 spots have completely disappeared because annealing destroyed the reconstruction leaving a 1×1 unreconstructed surface (gray circles). Since these patterns are comparable with those shown in Fig. 3.10 and Fig. 3.13 they can be associated to HIC phases and therefore we can assign them a Pb coverage between $\sim$1.22 ML and $\sim$1.28 ML (see Fig. 3.2). The diffraction spots within the solid/dashed green circles are related to the overall $\sqrt{3} \times \sqrt{3}$ symmetry of the Pb overlayer that is 30° rotated respect the bulk Si spots. Triplet of spots within the dashed green circle, which are equivalent to those within the triangle in Fig. 3.13, spread with increasing the annealing time. This fact is coherent with the discussion done about the HIC phases in previous section. In particular, the spreading of the spots is related to the decreasing of the HIC unit cell size by decreasing the Pb coverage. This means that as we increase the annealing time, the greater the Pb desorption, i.e. decreasing of Pb coverage. Ultimately, in Fig. 3.18c we are very close to 1.2 ML and, indeed, annealing the sample at 375° C two minutes more causes the disappearance of the HIC diffraction spots and we obtain a perfect 1×1-Pb phase whose LEED pattern is shown in Fig. 3.19. This means

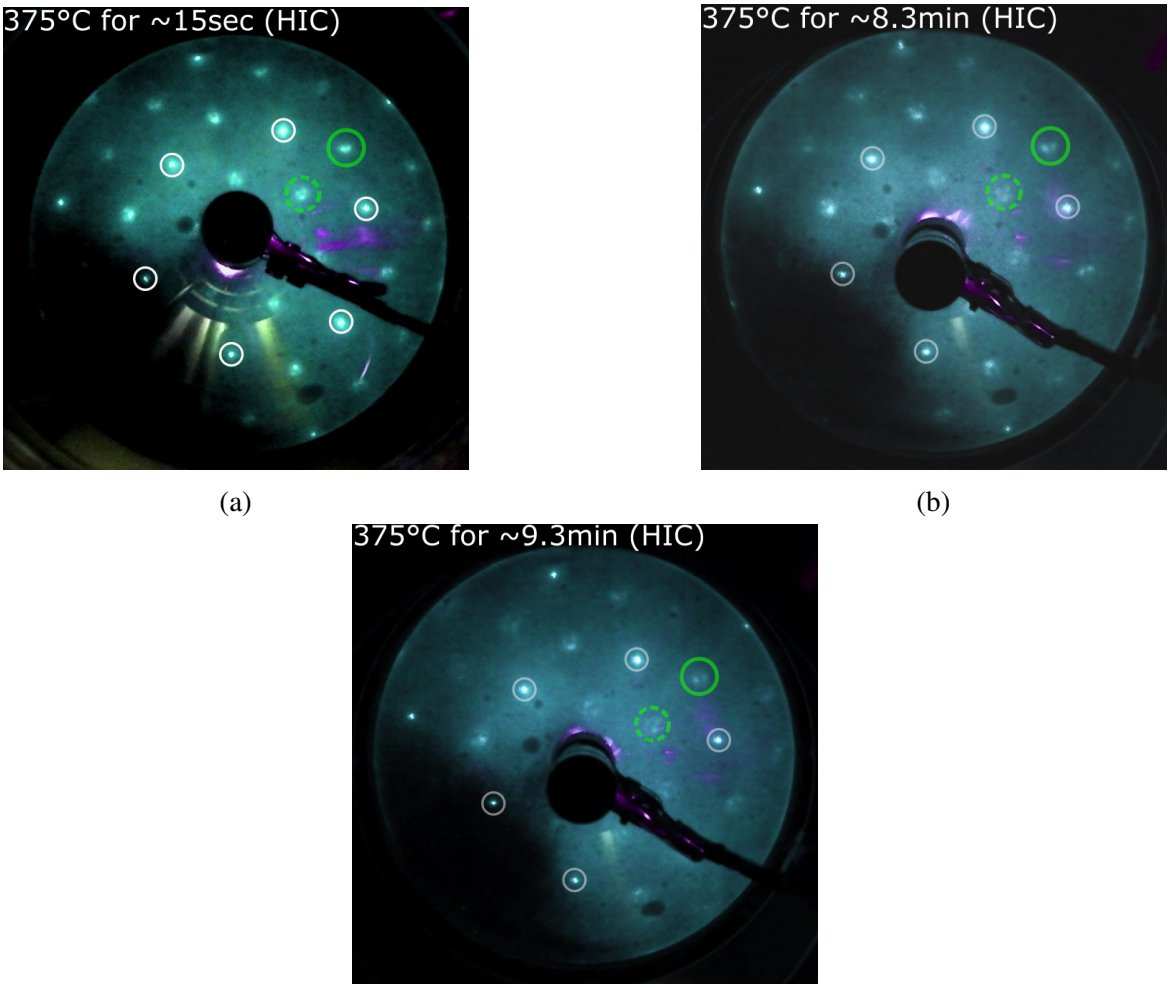

(a) (b)

(c)

Fig. 3.18 LEED patterns measured at room temperature and E=80 eV on a sample with ∼3 ML (or maybe a bit more) of Pb after being annealed at ∼375° C for (a) ∼30 sec, (b) ∼8.3 min and (c) ∼9.3 min. All the patterns correspond to HIC phases, i.e. Pb coverage between ∼1.22 ML and ∼1.28 ML. Gray circles indicate the 1×1 spots arising from the bulk silicon substrate. Spots within the solid/dashed green circles are related to the overall $\sqrt{3} \times \sqrt{3}$ symmetry of the Pb overlayer that is 30° rotated respect the bulk Si spots. Triplet of spots within the dashed green circle, spreading with increasing the annealing time, are related to both the size of the HIC unit cell and the Pb coverage.

that, at this point, we achieved ∼1.2 ML of Pb and that if we cool the sample below ∼270 K, then the surface will be covered by the $\sqrt{7} \times \sqrt{3}$-Pb. On the other hand, if we continue to anneal the sample, we'll start to go below 1.2 ML and we'll start to open dilute patches of β phase in coexistence with the 1×1-Pb. This would be revealed by the increasing intensity of the $\sqrt{3} \times \sqrt{3}$ spots in the LEED pattern. In order to show the sensitivity to the experimental parameters of the Pb/Si(111) system, Fig. 3.19b shows a sample that was annealed at slightly

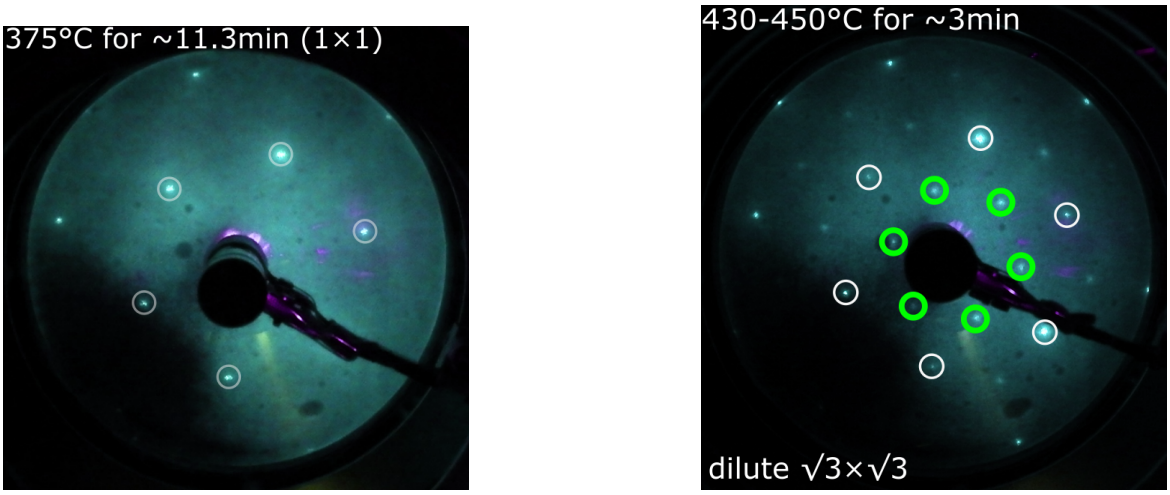

(a) (b)

Fig. 3.19 LEED patterns measured at room temperature and E=80 eV on a sample with ~3 ML (or maybe a bit more) of Pb after being annealed at (a) ~375° C [(b) between ~430° C and ~450° C] for (a) ~11.3 min [(b) ~3 min]. (a) This pattern corresponds to the 1×1-Pb phase with Pb coverage ~1.2 ML. (b) The relatively intense $\sqrt{3} \times \sqrt{3}$ spots (within green circles) reveal that we are below 1.2 ML, therefore dilute $\sqrt{3} \times \sqrt{3}$-Pb patches coexist with the 1×1-Pb. Gray circles indicate the 1×1 spots arising from the bulk silicon substrate.

higher temperatures, i.e. between 430° C and 450° C, respect to those used until now. Due to the relatively strong $\sqrt{3} \times \sqrt{3}$ spots, this pattern may correspond to a surface with well developed diluted $\sqrt{3} \times \sqrt{3}$-Pb patches (called β phase), meaning that we are well below 1.2 ML. Before this annealing the surface showed a LEED pattern similar to that shown in Fig. 3.18a. Therefore, changing the annealing temperature by only ~60° C completely changes the annealing time required to obtain the 1×1-Pb. In particular, annealing between 430° C and 450° C for ~3 min already brings us below 1.2 ML while, we can anneal for ~11 min at ~375° C and at the end we achieved ~1.2 ML. This reinforces once again that the experimental parameters, i.e. initial coverage, time and temperature of annealing, play an important role during the preparation of Pb monolayer phases. For this reason all the experimental parameters must be carefully optimized and then kept constant.

After the LEED characterization, in order to check the local atomic structure of the surface and also to refine the experimental parameters needed for a proper Pb monolayer preparation, I performed a campaign of STM measurements in the "Environmental STM". The aim of these experiments was to grow exactly 1.2 ML of Pb/Si(111), i.e. to grow a perfect 1×1-Pb phase at room temperature, and check that a homogeneous $\sqrt{7} \times \sqrt{3}$-Pb appears below 270 K. Also in this case, the experimental system was not equipped with a quartz balance therefore, before measuring the sample by STM, I used LEED to both monitor

the Pb monolayer preparation and adapt experimental parameters. Anyway, to make sure about the accuracy of the procedure, I validated each step of the preparation also with STM. Fig. 3.20a and Fig. 3.20b show typical atomically resolved STM images of a freshly

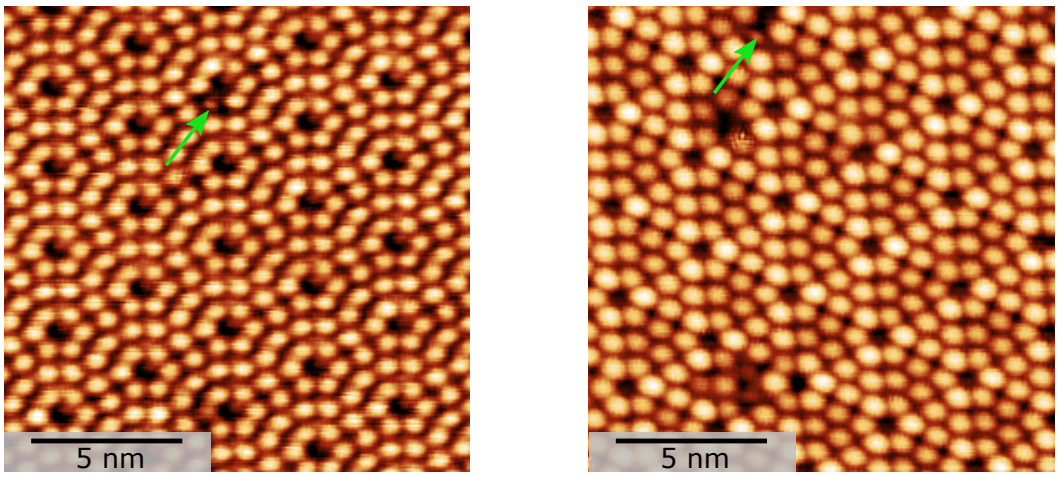

(a) (b)

Fig. 3.20 STM images of a freshly prepared Si(111)-7 $\times$ 7 surface measured at room temperature. (a) Image size= 15 $\times$ 15 nm^2, V_T: +2 V and I_T : 20 pA. (b) Image size= 15 $\times$ 15 nm^2, V_T: -2 V and I_T : 20 pA. Green arrows indicate the same surface defect.

prepared Si(111)-7 $\times$ 7 surface taken at positive and negative bias voltage respectively. Green arrows indicate the same surface defect to emphasize that the two images were acquired by scanning over the same region of the sample. Then, Pb was evaporated at room temperature on top of the silicon substrate for 30 minutes in order to have $\sim$3 ML (or maybe a little bit more). Subsequent annealing at $\sim$375° C for approximately 6 minutes led us to a Pb monolayer showing a 1 $\times$ 1 room temperature LEED pattern. Figure 3.21 shows a large scale STM image, taken a +2 V, of the surface resulting from this preparation procedure. At first glance, this image reveals two important features of the surface. First, the Pb layer is not homogeneous and hole-like defects are densely distributed over the surface. Second, smooth mostly structureless regions (indicated by white arrow) and wrinkled areas appearing as ordered arrays of bright protrusions with hexagonal symmetry (indicated by yellow arrow) can be found. It is interesting to note that wrinkled areas are localized around defects and the corrugation is more pronounced where the density of defects is higher. Large white area on the left of the image is a Pb island, one monolayer thick, grown on top of the Pb monolayer. These islands typically remain on the surface because during the annealing either not all the Pb desorbs or maybe part of Pb is trapped by surface defects.

Fig. 3.22a and Fig. 3.22b show the region evidenced by the white dashed rectangle in Fig. 3.21 scanned at +2 V and +0.5 V respectively. Green arrows indicate the same surface defect

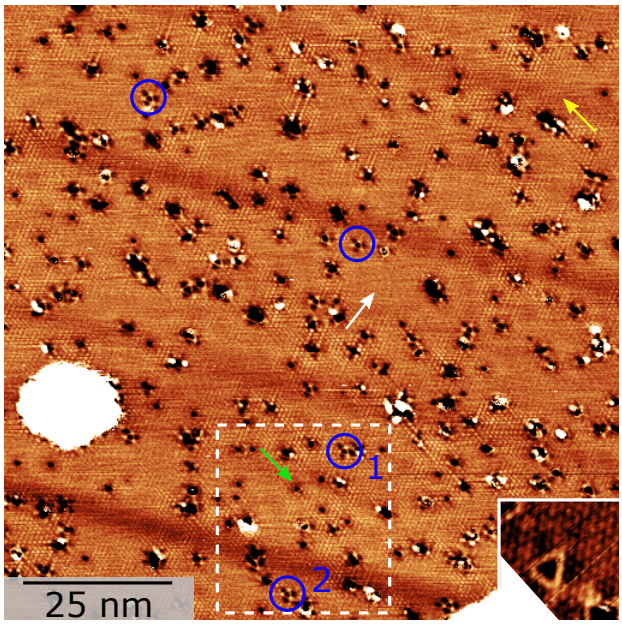

Fig. 3.21 Room temperature STM image of a Pb/Si(111) surface prepared by evaporating ∼3 ML of Pb and by subsequently annealing at ∼375° C for approximately 6 minutes. Image size= 100×100 nm^2, V_T: +2 V and I_T : 20 pA. White arrow indicates smoother regions of the surface. Yellow arrow indicates wrinkled regions with hexagonal symmetry that nucleate around defects. Blue circles indicate defects with hexagonal edge decoration. Green arrow indicates a surface defect that will be a reference point in the following figure. Inset represents the hole defect within the circle number 2 and it is imaged at +0.5 V.

which was indicated also in Fig. 3.21 (see green arrow). Fig. 3.22a, scanned with the same bias voltage than that of Fig. 3.21, confirms the presence of hexagonal structures around defects consisting of large bright protrusions. Surprisingly, as shown in Fig. 3.22b, the appearance of the surface evolves by changing the bias voltage and the large protrusions reveal an internal structure. In particular, this image shows that at +0.5 V smoother regions present small protrusions with an apparent hexagonal arrangement. On the other hand, wrinkled regions reveal that small protrusions are arranged in trimer structures. In a STM study Hwang et al. observed that the presence of defects within the 1×1-Pb phase can indeed induce the nucleation of small domains of trimers around defects themselves which are similar to those observed here [64]. Moreover, it was shown that for sufficiently large distances from defects a 1×1-Pb arrangement is restored. We interpreted this particular structure as an incommensurate phase stabilized by surface defects through deformation of the ideal 1×1-Pb atomic lattice, i.e. defects lead the Pb atoms to slightly move away from their ideal 1×1 positions. The bias-dependent appearance of these structures was also observed. In particular, trimers, observed at low voltages, transform into single large

protrusions arranged in a $\sqrt{3} \times \sqrt{3}$ lattice above +1 V. It is clear, then, that in our case the defects induce the nucleation of trimer domains across most of the surface. The domains do not completely relax in an ideal 1×1-Pb structure because of the high density of defects and therefore they are observed almost everywhere.

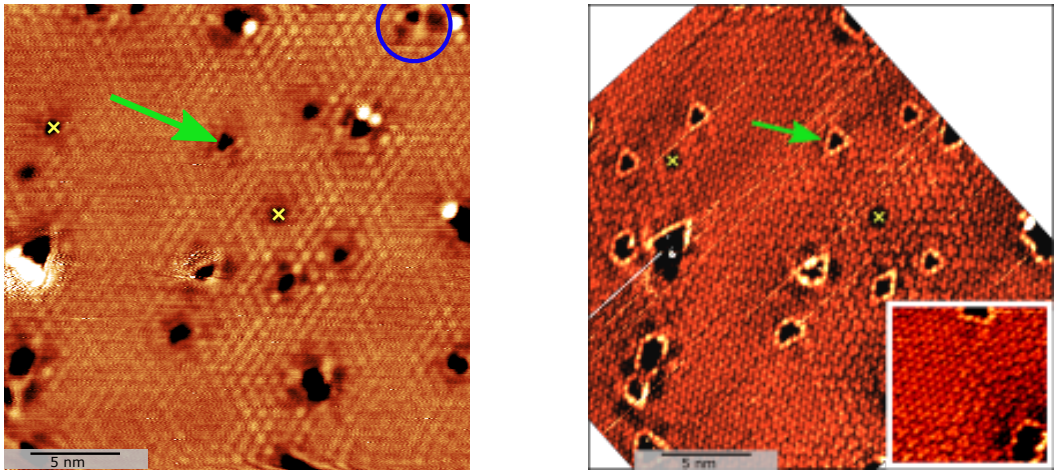

(a) (b)

Fig. 3.22 Room temperature STM images taken on the same region within the white dashed rectangle of Fig. 3.21. (a) Image size= 25×25 nm^2, V_T: +2 V and I_T : 20 pA. (b) Image size= 25×25 nm^2, V_T: +0.5 V and I_T : 20 pA. Yellow crosses indicate the same hole defect without edge decoration. Blue circle indicate the same defect within the circle number 1 of Fig. 3.21. Green arrow indicates the same surface defect which is also indicated in Fig. 3.21. The inset shows trimers of protrusions arranged in a $\sqrt{3} \times \sqrt{3}$ lattice. Image size= 8×8 nm^2, V_T: +0.5 V and I_T : 20 pA.

In line with this interpretation, in Fig. 3.22b, trimers can still be distinguished also in smoother regions. Since LEED measurements on this kind of sample always revealed clean 1×1-Pb patterns, it is not clear if our STM observations can be interpreted as the presence of a local incommensurate phase. On the other hand, Ganz et al. have proposed that if incommensurate regions are too small they may not contribute coherently to the LEED diffraction intensity and the resulting pattern may not show their presence [39]. In any case, the real atomic structure of this defect-induced phase is still under debate. Hwang et al. directly attribute trimers to the real atomic positions [37, 39, 59, 64]. On the other hand, Seehofer et al., based on the bias-dependent appearance of the surface structure, associate these observations to purely electronic effects [58]. From a more fundamental point of view, these two interpretations of the experimental results lead to two different atomic models. Several works have shown that the atomic model arising from Hwang interpretation [41, 59, 60, 64, 65], with a Pb coverage of 1 ML, is not energetically stable at low temperature

and it is not able to describe low temperature monolayer properties, i.e. the $\sqrt{7} \times \sqrt{3}$-Pb transition and related electronic properties [48–50, 54]. On the other side, there would be an atomic model that, at low temperature, should be compatible with the $\sqrt{7} \times \sqrt{3}$-Pb proposed by Kumpf, corresponding to 1.2 ML, that describes quite well the observed structural and electronic properties [37, 46, 48–56]. This complicated picture requires more experiments and calculations to clarify the all the details. An alternative interpretation could be given starting from the dynamical model of the room temperature 1×1-Pb phase discussed in previous section [51]. In this model, the net result of the Pb diffusion is the hopping of a single Pb atom through the hollow sites of an effective '1×1'-Pb lattice. The key aspect ensuring the 1×1 patterns experimentally observed by LEED and STM is that, even if all the Pb atoms randomly diffuse, the occupation of T_1 sites is preserved over the time. It is easy to imagine that if we include a defect within the atomic structure we reduce the atomic degrees of freedom around the defects, i.e. the Pb motion become anisotropic around defects. The net result would be to change the positional occupation of Pb atoms over the time that could result in a trimer structure around defects. In support of this, we observe that all the works proposing the trimer structure have been preformed on non-homogeneous surfaces, i.e. in presence of defects or source of surface stresses [41, 59, 60, 64, 65]. Interesting aspect of this interpretation would be the agreement between the coverage of the room temperature structure and that of the low temperature $\sqrt{7} \times \sqrt{3}$-Pb proposed by Kumpf, i.e. 1.2 ML. Also in this case, more calculations are mandatory to verify this picture. Interesting remarks can be done about the hole-like defects and their appearance with bias voltage. From Fig. 3.22a it is clear that at +2 V they mainly have either triangular (the smallest ones) or more irregular (the larger ones) shape. Moreover, some of these defects have decorated edges by an hexagonal arrangement of alternating bright and dark spots. In the following this decoration will be referred as hexagonal decoration. Four of these defects are indicated by blue circles in Fig. 3.21 and that within the circle number 1 is also shown in figure Fig. 3.22a. Surprisingly, at +0.5 V the appearance of defects also changes, i.e. shapes become very regular for both small and large defects, hexagonal edge decorations disappear and defects are simply decorated by small bright protrusions (see Fig. 3.22b). Inset of Fig. 3.21 shows the defect within the circle number 2 and imaged at +0.5 V. By looking a little closer to this inset it is evident that even if the edges are simply decorated a triangular configuration of large black spots can be still discerned. We think that this bias dependent appearance of defect edges could be related to the intrinsic electronic structure of defects themselves and therefore by imaging them with different voltages we are able to probe different electronic states.

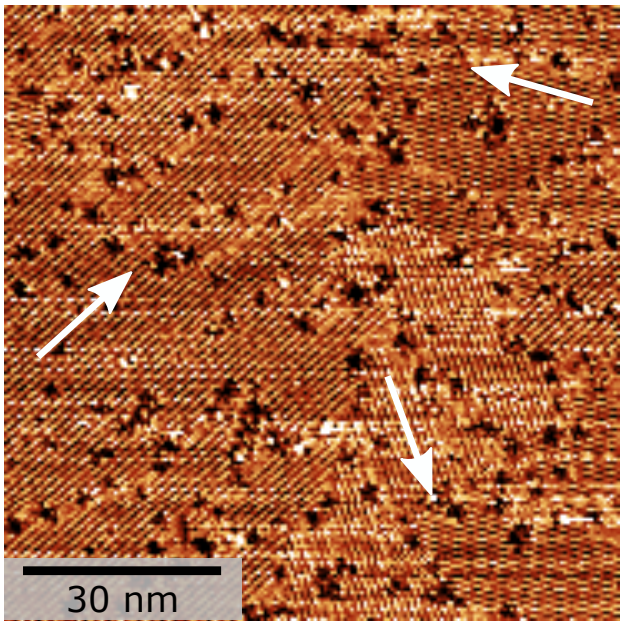

Fig. 3.23 STM image of the $\sqrt{7} \times \sqrt{3}$-Pb phase taken at 77 K. This sample is obtained by following the same procedure described in the text. (a) Image size= $90 \times 90\ nm^2$, V_T: +2 V and I_T : 20 pA. White arrows indicate the directions of the $\sqrt{7} \times \sqrt{3}$-Pb domains (120° rotated between them).

Ganz et al. observed similar defects with hexagonal edge decoration consisting in 6-spot patterns for similar voltages but all the spots were bright instead to be alternated between dark and bright and their origin was obscure [39]. Again, this difference of defect appearance could be related to the different nature of defects, i.e. different electronic structure. In line with this, by comparing defects indicated by yellow crosses in Fig. 3.22a and Fig. 3.22b they do not present edge decoration at all for any bias voltages. This is probably due to the fact that the nature of these defects is different from those decorated and therefore their electronic structure is different resulting in a different appearance when they are imaged by STM. Still, in Fig. 3.22a there are defects that do not present hexagonal edge decoration but then they have a simple decoration at +0.5 V. In order to verify if we prepared a Pb monolayer with the right coverage, i.e. 1.2 ML, we cooled the sample down to nitrogen temperature (77 K) and the result is shown in Fig. 3.23. Three rotational domains, 120° rotated from each other and whose directions are indicated by the white arrows in figure, coexist on the surface. As expected for the $\sqrt{7} \times \sqrt{3}$-Pb phase, these domains consist of parallel straight rows meaning that we effectively have 1.2 ML of Pb on top of the silicon substrate. On the other hand, the surface remains highly disordered because hole defects seen at room temperature are still there and they probably also limit the size of $\sqrt{7} \times \sqrt{3}$-Pb domains which are quite small, i.e. 10-40 nm wide against 100-120 nm of a homogeneous $\sqrt{7} \times \sqrt{3}$-Pb. In conclusion, we were

able to prepare a Pb monolayer with a coverage of ∼1.2 ML but, at room temperature, a high density of surface defects has stabilized a trimer structure that prevented us to have an ideal 1×1-Pb phase, even if LEED measurements gave us clean 1×1-Pb patterns. At 77 K trimer structures disappear and a $\sqrt{7} \times \sqrt{3}$-Pb phase could be stabilized over the whole surface. It is interesting to note that this behavior would be in agreement with a dynamical model of the trimer structure, i.e. at low temperature Pb motion is frozen also around the defects and the $\sqrt{7} \times \sqrt{3}$-Pb is restored everywhere on the surface. However, the high density of defects prevented us to have a crystalline and homogeneous $\sqrt{7} \times \sqrt{3}$-Pb phase. The origin of these defects is still unknown. The fact that the preparation of several samples led to similar features to those just discussed means that a contamination source was permanently present during the experiments. It is not clear if this contamination was already in the experimental setup, due to the fact that the "Environmental STM" is shared by several users that evaporate their own materials in the same sample preparation UHV chamber, or if it was embedded in the silicon substrate or even in the Pb evaporator. Anyway, it is important to remember that all the components within the UHV chambers have been backed and outgassed before the beginning of the experiments and during the sample preparation the pressure was better than 5×10^{-10} mbar.

At this point, beside the encountered contamination problems, the $\sqrt{7} \times \sqrt{3}$-Pb preparation has been validated in all of its stages with both LEED and STM. When the M3 STM microscope became available I transferred the procedure on this system. Primary goal of these experiments was to validate the growth of a homogeneous $\sqrt{7} \times \sqrt{3}$-Pb phase, i.e. to validate the growth of a 2D superconductor on top of the silicon substrate. Once this was achieved, MnPc molecules could be evaporated on top of this surface and, after checking both the actual amount of deposited molecules and their behavior on the surface, very low temperature (300 mK) STS measurements could be performed on this system in order to probe the effects induced by our magnetic molecules (MnPcs) on the $\sqrt{7} \times \sqrt{3}$-Pb superconductivity. In this case, the experimental setup was equipped with a quartz balance, therefore I could precisely calibrate the Pb flux coming out of the evaporator and consequently I could know the exact amount of Pb deposited on the silicon surface. I adapted the preparation parameters so that I could evaporate only a little bit more than 1.2 ML of Pb and then briefly anneal the sample. The parameters were optimized by looking at the surface with STM immediately after the preparation, allowing an immediate quality check of the prepared $\sqrt{7} \times \sqrt{3}$-Pb phase. From this point on, all the STM images were taken at liquid nitrogen temperature (77 K).
Fig. 3.24 shows a relatively large scale STM image, taken at +1 V, of the $\sqrt{7} \times \sqrt{3}$-Pb phase. This sample was obtained by firstly preparing the Si(111)-7×7 surface, as usual.

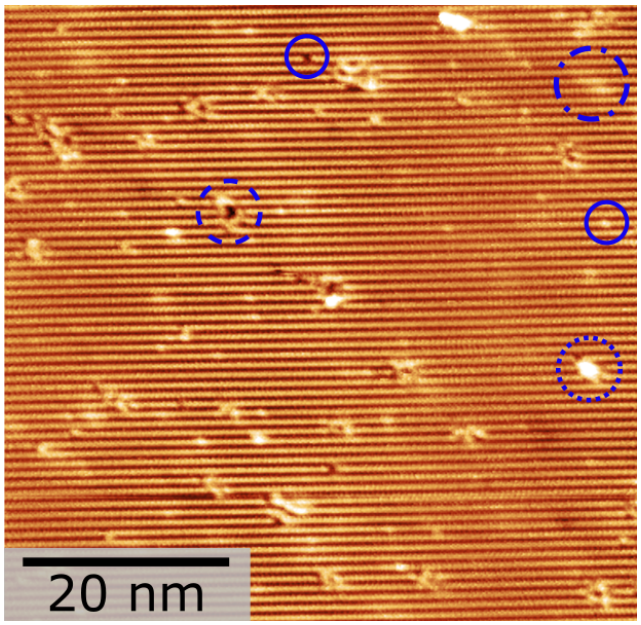

Fig. 3.24 STM image of a single $\sqrt{7} \times \sqrt{3}$-Pb domain taken at 77 K on a sample with 1.2 ML of Pb on Si(111). Dashed circle indicates holes defects with adatom edge decoration due to the nucleation of β phase regions. Solid circles identify vacancy and adatom defects.Dotted circle indicates either Pb or SiC clusters. Dashed-dotted circle highlights Si dopants. Image size= $60 \times 60\ nm^2$, V_T: +1 V and I_T : 20 pA.

Then, 1.65 ML of Pb were evaporated at room temperature on top of the silicon surface. Finally, a homogeneous $\sqrt{7} \times \sqrt{3}$-Pb was obtained by annealing the sample at $\sim$320° C for approximately 2 min 30 sec. This figure displays one of the three rotational domains with its typical row structure. It is immediately noticeable that the surface is very homogeneous and that hole defects similar to those observed on the Environmental STM are completely absent confirming that a source of contamination was present in previous experiments (compare with the STM image in Fig. 3.23). The mean size of single domains is found to be $\sim$100 nm that is significantly larger than we previously observed and it is of the order of the largest size that could be found on this surface. Occasionally, we observed small holes with adatom edge decoration, as the one within the dashed circle, but as they do not present a particular bias-dependent appearance we therefore associate them to the nucleation of β phase patches. This is probably due to the fact that the sample was heated longer than is necessary, i.e. we start to be slightly lower than 1.2 ML. On the other hand, very low density of these defects implies that we always could find large clean $\sqrt{7} \times \sqrt{3}$-Pb regions. Black and white dots, as those within solid circles, are Pb vacancies and adatom defects respectively. Larger white dots, as the one within the dotted circle, are nanometric-size clusters of either Pb or SiC. Moreover, faint large spatial modulations, as that within the dashed-dotted circle, are dopants

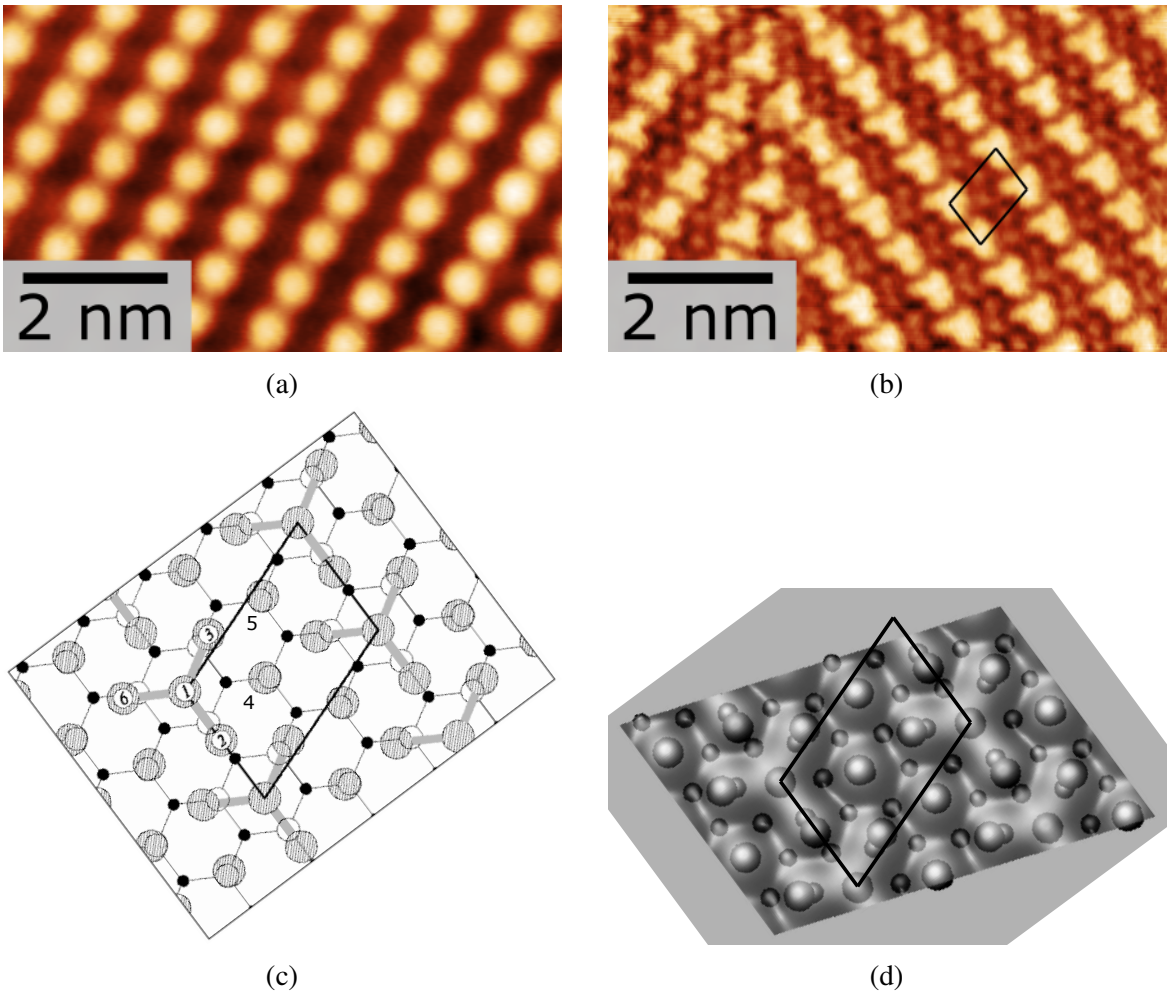

Fig. 3.25 (a) and (b): STM images of the $\sqrt{7} \times \sqrt{3}$-Pb phase taken at 77 K on a sample with 1.2 ML of Pb on Si(111). (a) Image size= 7.5×4.8 nm^2, V_T: +1.5 V and I_T : 30 pA. (b) Image size= 7.5×4.8 nm^2, V_T: +0.3 V and I_T : 20 pA. (c) Top view of the atomic model for the $\sqrt{7} \times \sqrt{3}$-Pb phase. Large gray balls represent Pb atoms and empty (black) balls indicate topmost (second layer) Si atoms [44]. (d) Top view of the calculated LDOS, integrated between E_F and E_F-0.5 eV, superimposed on the $\sqrt{7} \times \sqrt{3}$-Pb model. Large balls indicate Pb atoms and medium (small) balls represent topmost (second layer) Si atoms [49]. The $\sqrt{7} \times \sqrt{3}$-Pb unit cell is indicated by a black parallelogram.

located underneath the silicon substrate that can be imaged through the Pb layer because their electronic structure for some bias voltages makes a surface contribution.

Fig. 3.25a and Fig. 3.25b show STM images of the other two $\sqrt{7} \times \sqrt{3}$-Pb rotational domains taken at +1.5 V and +0.3 V respectively. The $\sqrt{7} \times \sqrt{3}$-Pb row structure is clearly visible in both images but there is a bias-dependent appearance of the surface. It was already observed

that for sufficiently high positive bias voltages only one large protrusion per $\sqrt{7} \times \sqrt{3}$-Pb unit cell is imaged (Fig. 3.25a). On the other hand, once the voltage is sufficiently decreased, each of these protrusions reveals a Y-like shape and between them new structures can be discerned too (Fig. 3.25b) [44, 49]. Several works have shown that this behavior of STM images can be coherently interpreted by considering the Kumpf model, shown in Fig. 3.25c, as the proper atomic structure of this phase [37, 44, 46, 49–51, 48, 52, 54] and here I will recall its main properties. The Pb layer exhibiting $\sqrt{7} \times \sqrt{3}$-Pb phase is quite flat and relatively close-packed. Pb atoms within the layer are bound together by metallic bonds conferring a 2D metallic behavior that manifests itself by the fact that we can scan this surface with very low bias voltages, i.e. below 20 mV. In a single $\sqrt{7} \times \sqrt{3}$-Pb unit cell, there are 6 Pb atoms per 5 Si atoms, resulting in a coverage of 1.2 ML. Five of these atoms (atoms 2, 3, 4, 5, 6 in Fig. 3.25c) are almost T1 on-top sites and they are covalently bound to the underneath silicon atoms saturating all the dangling bonds. Pb and Si orbitals are more or less hybridized if Pb atoms are more or less on top position with respect to the underneath silicon atoms. The remaining Pb atom (atom 1 in Fig. 3.25c) is on a H_3 hollow site, it has no bonds with the silicon substrate therefore its vertical position is not precisely defined and it is believed to be responsible for the small corrugation of this surface [37, 44, 46, 49–51, 48, 52, 54–56]. Brochard et al. have evaluated, by means of DFT calculations, the LDOS associated to the Kumpf model in order to relate the observed features in STM images with the atomic structure [49]. Fig. 3.25d shows the top view of the calculated LDOS, integrated over an energy range of occupied states, superimposed on the relaxed $\sqrt{7} \times \sqrt{3}$-Pb model. From this figure results that the occupied states are mainly localized on the triangular group of atoms 2, 3, 6 and to a lesser extent on the atom 1 in the middle of the triangle (compare Fig. 3.25c and Fig. 3.25d). This group of atoms clearly forms a Y-shaped LDOS responsible for the Y-shaped protrusion observed on STM images (compare Fig. 3.25d and Fig. 3.25b). Moreover, Fig. 3.25d shows that occupied states are also localized on atoms 4 and 5 which are responsible for the additional dimer structure observed between different Y-shaped protrusions (see Fig. 3.25b). This is not surprising because atoms 2, 3, 4, 5 and 6 are those interacting the most with the silicon substrate, i.e. they are indeed covalently bound, and therefore they contribute to the occupied density of states. Although Fig. 3.25b was taken at +0.3 V, i.e. probing the unoccupied states, and the LDOS in Fig. 3.25d was integrated over occupied states, it was shown that the Y-like protrusions are still visible for positive voltages but they become more diffuse and the relative brightness of protrusions depends on the particular bias voltage [37, 49]. Only single protrusions appear for sufficiently high positive voltages (see Fig. 3.25a). Indeed, it was also shown that the unoccupied states are mainly localized on atoms 1 and 2 that consequently contribute to the single protrusions in

Fig. 3.25a [37, 50]. Also in this case the result is not surprising because the atom 1 has no bonds with the silicon and among the five atoms covalently bound with the substrate the atom 2 is the least coupled due to the off-centered T_1 position, therefore these two atoms contribute to the unoccupied density of states.

3.3 Electronic properties of the $\sqrt{7}\times\sqrt{3}$-Pb phase

In this section I will summarize the main electronic properties of the $\sqrt{7}\times\sqrt{3}$-Pb phase. Jung et al.[48] have calculated by means of DFT calculations the band structure of this phase in order to compare it with that measured by Choi et al.[56] in their ARPES experiments.
In Fig. 3.26 calculated bands along the $\bar{K}_1-\bar{M}_1-\bar{\Gamma}$ direction are represented by circles, while the experimental ones are indicated by red lines. Looking near the Fermi level it is easy to see that within the diagram on the left all the calculated surface bands reproduce the behavior of the measured ones. Anyway, this is not the case for the two surface bands indicated by green arrows that are absent in calculations. In order to overcome this problem, the domain structure of the $\sqrt{7}\times\sqrt{3}$-Pb phase must be taken into account. Since ARPES is a macroscopic technique, we have to consider the presence of three rotational domains over the surface. Within the diagram on the right the band structure was calculated along the $\bar{K}_3-\bar{M}_3-\bar{\Gamma}$ direction which is 120° rotated respect to the previous one. It is clear that one of the two missing surface bands is recovered but the other is still missing (indicated by green arrow). The reason for this disagreement is still unknown. In any case, it was shown that considering the intrinsic domain structure of the $\sqrt{7}\times\sqrt{3}$-Pb phase allows both a proper interpretation of ARPES experiments and a better agreement between the experiments and calculations [48, 54–56]. Let us consider now the electronic orbitals contributions to the $\sqrt{7}\times\sqrt{3}$-Pb band structure in Fig. 3.26. Surface bands around the Fermi level reveal a Pb p_{xy} character, i.e. they involve Pb-Pb bonds within the Pb layer. Some of these bands cross the Fermi level and they form delocalized orbitals meaning that they are responsible for the density of states at the Fermi level and that the Pb layer has a metallic character. Moreover, these bands are located within the bulk band gap of the silicon substrate. In fact, in Fig. 3.26 Si valence band at Γ goes above E_F but it actually is an artifact because it should be about 0.2 eV below according to ARPES experiments. On the other hand, surface bands between -0.5 eV and -1 eV, having a small dispersion, mainly present Pb p_z and Si p_z character and therefore they involve bonds between Pb and Si atoms.
Fig. 3.26b represents the charge characters of the surface states S_1 and S_2 highlighted by arrows in Fig. 3.26a. The charge distribution of the S_1 surface state is spread over the Pb layer confirming that surface bands crossing the Fermi level effectively form delocalized

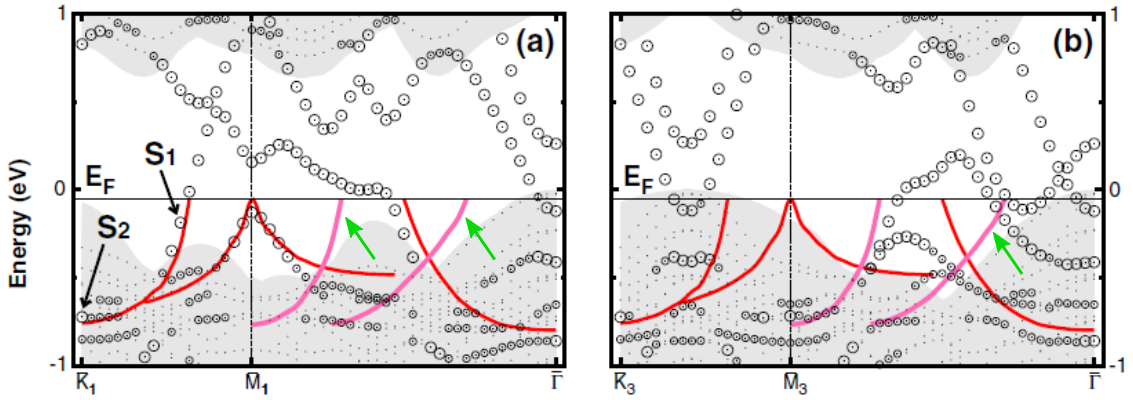

(a)

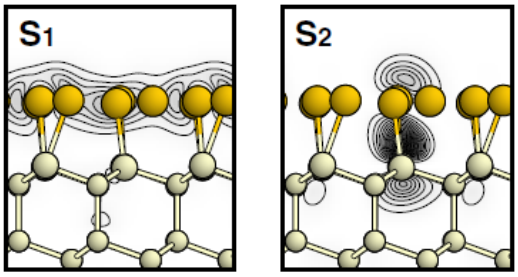

(b)

Fig. 3.26 (a) Band structure of the $\sqrt{7}\times\sqrt{3}$-Pb phase along (left) $\bar{K}_1-\bar{M}_1-\bar{\Gamma}$ and (right) $\bar{K}_3-\bar{M}_3-\bar{\Gamma}$. These two directions are 120° rotated between them. Gray regions indicate the projected bulk band structure. The Fermi level is defined relative to the valence band maximum at gamma. Small (large) circles represent surface states containing more than 55% (75%) of charge in the Pb and topmost Si layers. Red lines indicate ARPES bands measured in ref. [56] Green arrows indicate the experimental surface bands that are not reproduced by calculations. (b) Charge distribution of the two surface states, i.e. S_1 and S_2, indicated in (a) by black arrows [48].

sates and therefore Pb p_{xy} metallic orbitals are responsible for the transport properties of the Pb layer. On the other hand, the electronic charge of the S_2 surface state is localized between Pb and Si meaning that these atoms are involved in a covalent bond. This results also clarifies why the bands between -0.5 eV and -1 eV exhibit Pb p_z and Si p_z character. Fig. 3.27 shows the calculated projected density of states (PDOS) for the Pb and Si p orbitals of the $\sqrt{7}\times\sqrt{3}$-Pb/Si(111) (top) and of the $\sqrt{7}\times\sqrt{3}$-Pb isolated from the silicon substrate (bottom). It is easy to see that the substrate has no important effect on the Pb p_{xy} orbitals while it strongly modifies Pb p_z orbitals with the appearance of a peak at about -0.7 eV representing the covalent bond. This result shows that the metallic character of the $\sqrt{7}\times\sqrt{3}$-Pb, i.e. the

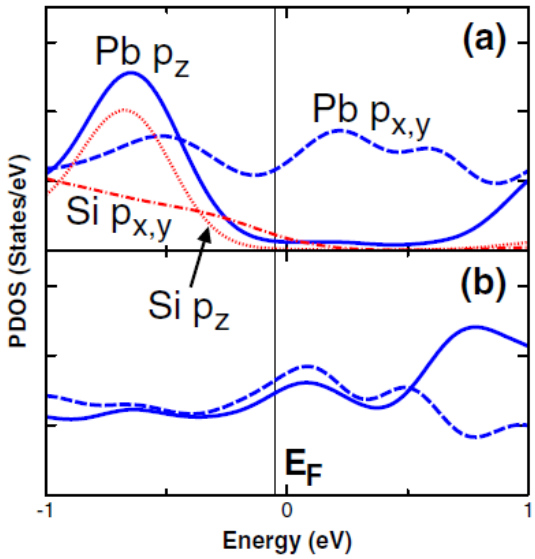

Fig. 3.27 Projected Density of States (PDOS) for the Pb and Si p orbitals for (top) $\sqrt{7} \times \sqrt{3}$-Pb/Si(111) and (bottom) $\sqrt{7} \times \sqrt{3}$-Pb isolated from the silicon substrate. Si PDOS was calculated for the topmost layer atoms.

density of states at the Fermi level, mainly arises from the Pb p_{xy} orbitals that are decoupled from the substrate. This fact has major consequences because although the strong covalent coupling between Pb and silicon substrate, all the physical and chemical properties depending the density of states at the Fermi level, e.g. transport or thermal properties, are effectively decoupled from the substrate and confined in the 2D Pb layer. In this sense, the $\sqrt{7} \times \sqrt{3}$-Pb phase can be see as a real 2D metallic system and in line with this it was shown that its electronic structure at the Fermi level exhibits 2D free-electron-like bands [54, 56].

3.4 MnPc adsorption and $\sqrt{7} \times \sqrt{3}$-Pb surface reconstruction

In this section, I will show that, MnPcs adsorption on top of a Pb monolayer exhibiting a $\sqrt{7} \times \sqrt{3}$-Pb phase induces an abrupt surface reconstruction towards the Striped Incommensurate phase. A possible explanation of the mechanism behind this restructuring process will proposed and it will be based on the combined effect of charge transfer from MnPcs to the Pb surface and local variation of the surface stress. Furthermore, I will show that, up to an MnPcs coverage of ∼4.6 molecules/100 nm^2, the strong interaction between MnPcs and Pb surface drives the formation of few stable molecular configurations, i.e. isolated MnPcs and trimers of MnPcs, reflecting the symmetry of the substrate.

3.4.1 MnPc-induced surface reconstruction

Fig. 3.28a displays the same surface already shown at the end of Section 3.2, where the experimental preparation of the $\sqrt{7} \times \sqrt{3}$-Pb was discussed, and it represents the surface before MnPc adsorption on the $\sqrt{7} \times \sqrt{3}$-Pb. I want just to recall that this surface was obtained by firstly preparing the Si(111)-7×7 substrate, then 1.65 ML of Pb were evaporated at room temperature and finally a homogeneous $\sqrt{7} \times \sqrt{3}$-Pb phase, with Pb coverage of 1.2 ML, was formed by annealing the sample at ∼320° C for approximately 2 min 30 sec. Fig. 3.28b shows that, after adsorption of ∼0.7 molecules/100 nm^2 of MnPcs between 77 K and 250 K, the $\sqrt{7} \times \sqrt{3}$-Pb undergoes an abrupt surface reconstruction. Note that STM images were acquired at 77 K. The typical row structure of the $\sqrt{7} \times \sqrt{3}$-Pb has disappeared and hole-defects with irregular shape and decorated edges cover uniformly the surface. What is really surprising is that, besides the hole-defects, this surface has a structure that resembles the SIC phase, corresponding to 1.3 ML, characterized by the typical striped structure due to alternation of $\sqrt{3} \times \sqrt{3}$-Pb domains (brighter regions) and "almost" $\sqrt{7} \times \sqrt{3}$-Pb domain walls (darker stripes). In agreement with this, bright domains in Fig. 3.28b actually reveal a $\sqrt{3} \times \sqrt{3}$-Pb structure with lattice parameter 0.67 ± 0.06 nm that is compatible with the expected one, i.e. 0.665 nm [58].
Fig. 3.28c shows the same STM image as the one displayed in Fig. 3.28b with adjusted contrast to make MnPc molecules visible. Typical four-lobe appearance [66–68] with a bright protrusion in the middle (Mn atom) suggests that MnPcs lie flat on the surface indicating a strong molecule/surface interaction. Isolated molecules (indicated by blue arrow) and trimers of MnPcs (indicated by yellow arrow) are the most frequently observed molecular configurations at ∼0.7 molecules/100 nm^2. Occasionally dimers of MnPcs are observed too

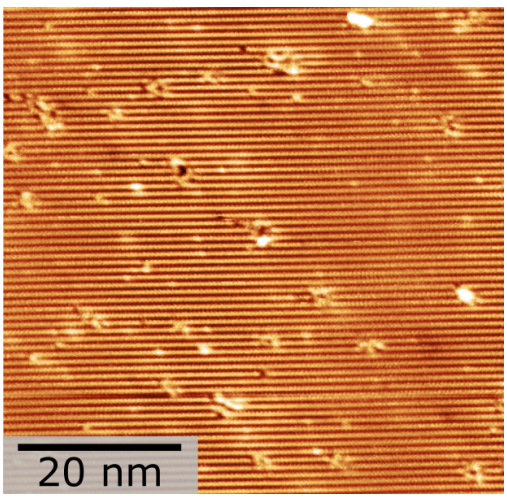

(a)

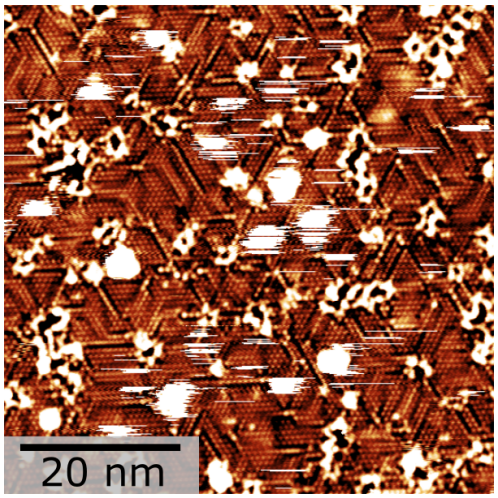

(b)

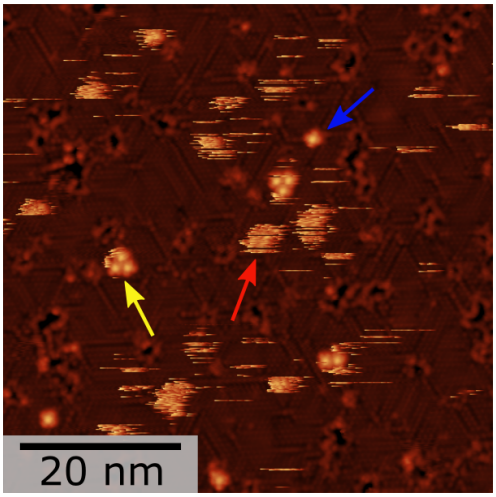

(c)

Fig. 3.28 (a) STM image of the $\sqrt{7} \times \sqrt{3}$-Pb phase with 1.2 ML of Pb on Si(111) before MnPcs adsorption. (b) STM image showing the surface reconstruction induced by adsorption of ∼0.7 molecules/100 nm^2 of MnPcs, between 70 K and 250 K, on the $\sqrt{7} \times \sqrt{3}$-Pb surface shown in (a). (c) The same STM image as displayed in (b) with adjusted contrast to make MnPc molecules visible. Blue arrow indicates an isolated MnPc. Yellow arrow indicates a trimer of MnPcs. Red arrow indicates a fuzzy diffusing molecular object. (a) Image size= 60×60 nm^2, V_T: +1 V and I_T : 20 pA. (b) and (c): Image size= 60×60 nm^2, V_T: +0.3 V and I_T : 20 pA. All the STM images were taken at 77 K.

(see Fig. 3.29b). Molecules tend to adsorb on defect-free regions.Within the STM images, taken at 77 K, fuzzy objects like that indicated by the red arrow in Fig. 3.28c were also observed. Their size is compatible with that of either isolated molecules or trimers. Fig. 3.29 may help better understanding their origin. In particular, Fig. 3.29a and Fig. 3.29b show the

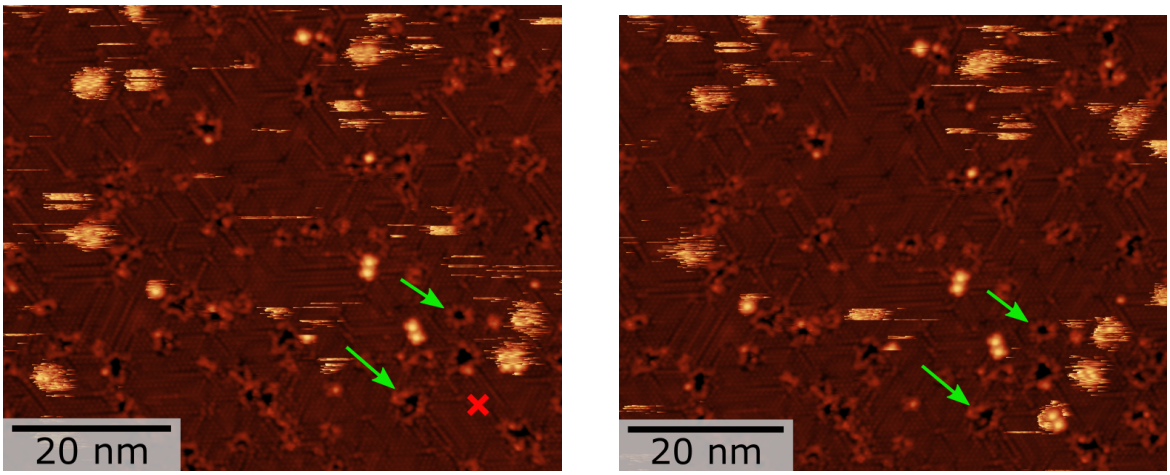

(a) (b)

Fig. 3.29 STM images of the same reconstructed surface showed in Fig. 3.28 with ∼0.7 molecules/100 nm^2 of MnPc deposited on top of the $\sqrt{7} \times \sqrt{3}$-Pb phase. The same region is imaged in (a) and (b) over two successive scans. Green arrows indicate the same hole defects within the two images. Red cross in (a) represents the region where a trimer of MnPcs appears in (b) due to the diffusion process possibly assisted by the STM tip. (a) and (b): Image size= 70×60 nm^2, V_T: +0.3 V and I_T : 20 pA. All the STM images were taken at 77 K.

same area of the sample imaged over two successive scans (green arrows show the same hole defects within the two figures). The red cross in the first scan (Fig. 3.29a) indicates the region where a trimer of MnPcs appears during the second scan (Fig. 3.29b). By comparing the positions of other fuzzy objects within the two figures it is easy to observe their movement. This means that, at 77 K, trimers of MnPcs are able to diffuse over the surface covering at least the size of the image itself, i.e. ∼70 nm. The same goes for isolated diffusing MnPcs. The reason for which they appear fuzzy is probably because of the interaction between the STM tip and mobile molecules during the scan. In Fig. 3.29 there are other fuzzy objects that remain in the same position over the two different scans. In this case, their appearance is probably due to the interaction between the STM tip and either vibrating or nearly-diffusing molecules. It is not excluded that the interaction itself between tip and molecules is able to activate the diffusion process at 77 K.

In summary, MnPcs adsorption (∼0.7 molecules/100 nm^2) on top of the $\sqrt{7} \times \sqrt{3}$-Pb phase induces a surface reconstruction towards a SIC-like phase. Part of the MnPcs is able to diffuse at 77 K under the effect of thermal energy whereas the rest are well anchored to the surface because they are either adsorbed on the hole defects edges or they are on a stable adsorption configuration allowing a strong molecule/surface interaction.

3.4.2 MnPcs self-assembly on the reconstructed surface

Another interesting aspect of MnPcs behavior on the Pb monolayer is their self-assembly. As already said, at ∼0.7 molecules/100 nm^2, the most frequently observed molecular configurations are isolated molecules, trimers and occasionally dimers. Several works have shown that the balance between molecule-molecule and molecule-substrate interaction is the most critical parameter affecting self-assembly of phthalocyanines on metallic surfaces [69, 70].

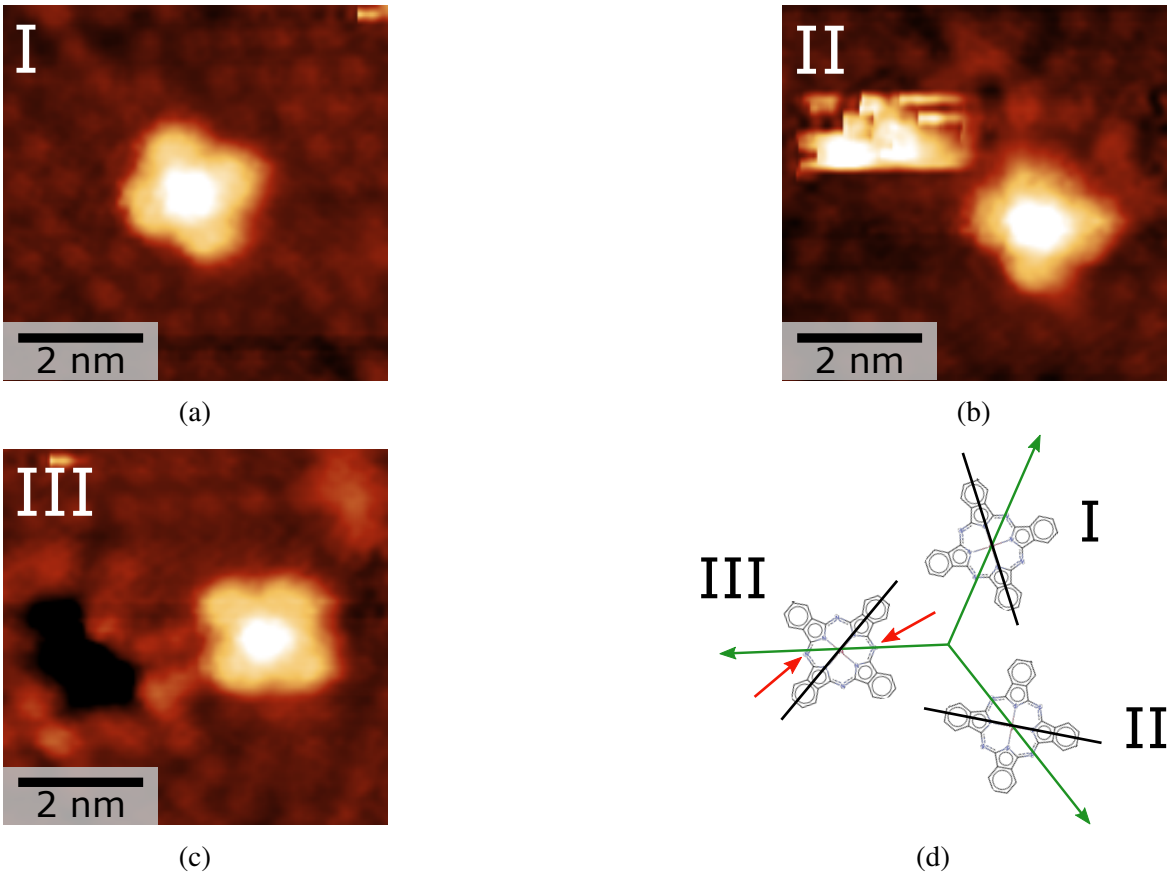

Fig. 3.30 (a), (b) and (c): STM images of the three possible adsorption configuration of isolated MnPcs on top of 1.2 ML of Pb/Si(111). Image size: 6×6 nm^2, V_T: +0.4 V and I_T : 80 pA. All the images were taken at 77 K. (d): Sketch adapted from experimental data showing the three possible orientations of isolated MnPcs respect to the Pb substrate directions represented by green arrows. Red arrows indicated the two nitrogen atoms of a MnPc through which a Pb direction passes. Black lines represent the main molecular axis of different isolated MnPcs that result to be 120° rotated each other as a consequence of the strong molecule-substrate interaction.

In particular, if the molecule-molecule interaction prevails over the molecule-substrate one, the fourfold symmetry of MnPcs drives their self-assembly in square lattices without strong relations with respect to the substrate even at very low coverage [71, 68, 70, 67, 69]. In our

case, it is clear that the molecule-substrate interaction is stronger than the molecule-molecule one because MnPcs prefer remaining isolated or at most self-organize in small clusters of two or three molecules.

To our knowledge, these trimer configurations, strongly reflecting the symmetry of the substrate, were not reported before [67, 68, 70–72]. For this reason, we will analyze the details of these structures. For the sake of completeness, the adsorption configuration of isolated molecules will be firstly discussed (see Fig. 3.30). A schematic sketch, drawn in Fig. 3.30d and based on experimental data, shows that isolated MnPcs assume only three orientations with respect to the directions of the substrate reflecting the threefold symmetry of the substrate. Due to the four-fold symmetry of MnPcs these three orientations are linked between them by 30° rotations. It is immediate to see that, for each configuration, one of the substrate directions (green arrows) is nearly aligned with two nitrogen atoms of the MnPc within the experimental error ($\sim$2°). These nitrogen atoms are indicated by red arrows in figure. More interestingly, main molecular axis (black axis within the sketch) of different isolated MnPcs result to be 120° rotated between them. Fig. 3.30c shows that this adsorption configuration is preserved also if MnPcs are located near hole defects. These observations reveal that the strong interaction between MnPcs and Pb monolayer pins the adsorption orientation of isolated MnPcs in only three configurations reflecting the threefold symmetry of the substrate.
Previous studies never reported this kind of MnPcs self-assembly on similar systems [67, 68, 70]. In particular, densely ordered square lattices of MnPcs were always observed on top of either bulk Pb(111) substrates or 2D islands of Pb(111) grown on Si(111) (thicker than 3 ML) [67, 68, 70]. On the other hand, on top of Au(111) substrates [70], dispersed adsorption of MnPcs was observed at low coverage [70]. Always in the case of Au(111), Liu et al. [72] have shown that fcc and hcp regions of Au(111) have different affinities to MnPcs, that is, MnPcs start to adsorb on top of fcc regions first and then on hcp. However, for higher coverage, close-packed square lattices of MnPcs are recovered on top of the Au(111) surface. Another interesting example is provided by Yoshizawa et al. [71], who reported self-assembled square lattices of MnPcs on top of the $\sqrt{7} \times \sqrt{3}$-In phase of a bi-layer of Indium grown on Si(111). This results is very interesting because, despite the considered substrate has properties very close to our, its response to MnPcs adsorption is very different. In particular, surface reconstruction of the Indium bi-layer was not reported, and MnPcs self-assemble in close-packed square lattices instead of remaining isolated or self-assembled in trimer structures. These considerations ultimately confirm that molecule-molecule and molecule-substrate interaction strongly depend on the particular considered molecule as well

as the substrate and that in our case the interaction between MnPcs and Pb monolayer is probably very strong.

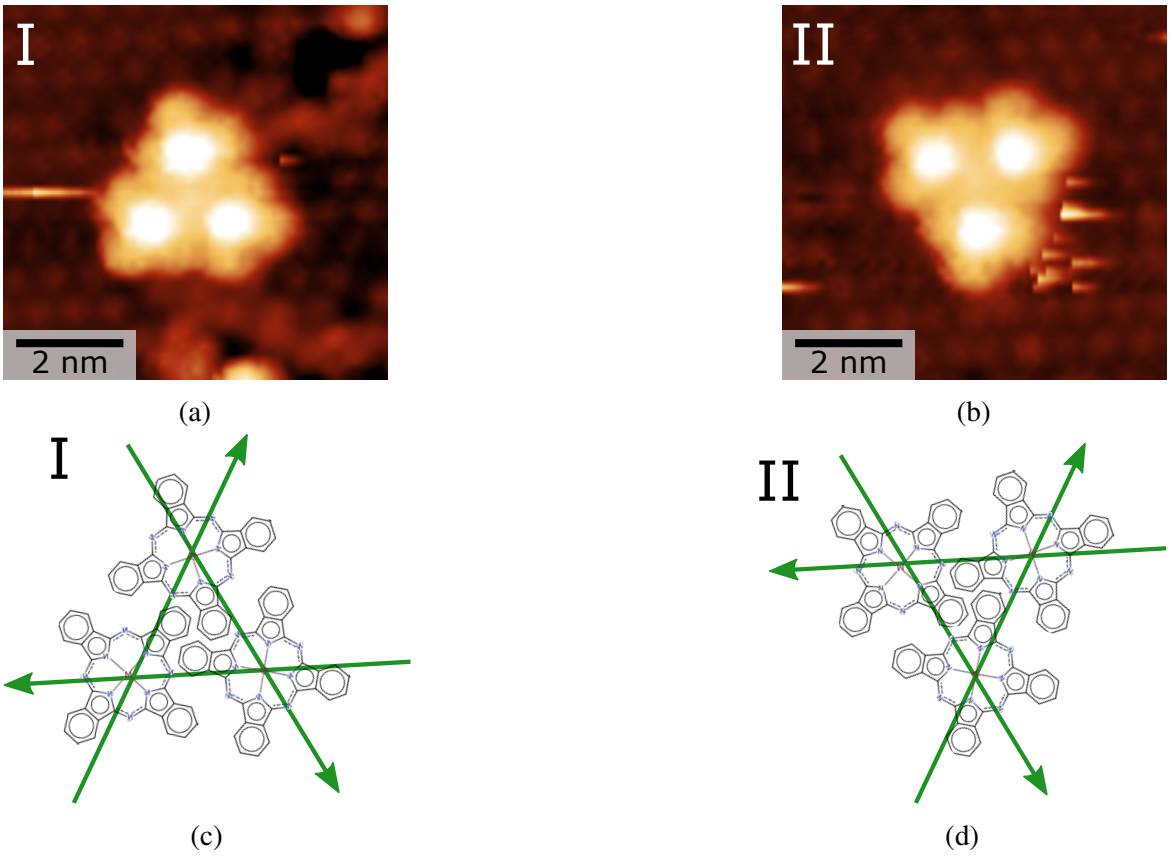

Fig. 3.31 (a) and (b): STM images of the two possible MnPc trimer configurations on top of 1.2 ML of Pb/Si(111), i.e. upwards trimer in (a) and downwards trimer in (b). Image size: 7×7 nm^2, V_T: +0.5 V and I_T : 50 pA. All the images were taken at 77 K. (c) and (d): Sketches drawn based on experimental data showing trimer orientation respect to the Pb substrate directions (represented by green arrows). Substrate directions pass through pairs of Mn atoms and three molecules have their N-N axis aligned with a substrate direction. The overall trimer orientation is linked to the substrate.

I will now describe self-assembled MnPcs trimer structures. The only two experimentally observed configurations are upwards and downwards trimers as those shown in Fig. 3.31a and Fig. 3.31b. Careful analysis of the molecular configuration in trimers reveals that MnPcs preserve exactly the same orientation with respect to the substrate as the one just discussed for isolated MnPcs (see Fig. 3.30d). Moreover, each trimer contains MnPcs having all three possible orientations observed in the case of isolated MnPcs. By looking at the sketches in Fig. 3.31c and Fig. 3.31d (drawn based on experimental data), it can be seen that, within the experimental error ($\sim2°$), each Pb direction (green arrows) approximately passes

through a pair of Mn atoms of different MnPcs. The Mn-Mn distances between pairs of Mn atoms belonging to the triangle vertices have similar values within the experimental error, i.e. 1.46 ± 0.06 nm for upwards trimers and 1.51 ± 0.06 nm for downwards trimers, and therefore they approximately form an equilateral triangle. These two values for upwards and down wards triangles are consistent with each other within the experimental error.
In summary, as a result of the strong molecule-substrate interaction, trimers of MnPcs reflect threefold symmetry of the substrate in terms of individual molecules orientations forming the trimer but also of the overall structure and orientation of the trimer itself. It should be emphasized that, even if MnPcs are achiral molecules, upwards and downwards trimers are chiral structures.

Discussion about trimer structures of MnPcs

Fig. 3.32 shows all the possible trimer configurations (drawn based on experimental data) with respect to the directions of the Pb substrate assembled starting from isolated molecules oriented as shown in Fig. 3.30d. Trimers within the same column are equivalent but with different chirality. Trimers belonging to different columns are linked each other by 30° rotations. Beyond 120° the sequence identically repeats due to the threefold symmetry of the structure itself. It should be also noted that, 30° rotations preserve the orientation with respect to the Pb substrate of each molecule within the trimer itself.
The most interesting aspect of Fig. 3.30d is that the different trimer configurations are not equivalent with regard to their orientation with respect to the substrate. In particular, the first/third configuration of chirality 1 and the second/fourth configuration of chirality 2 do not present Pb directions (green arrows) passing through Mn pairs as experimentally observed. The remaining configurations are in principle equivalent, however, only two of them are experimentally observed, i.e. those circled in red. These two configurations differ by 30° and have a different chirality. A possible explanation might be the existence of specific stable adsorption sites able to pin the orientation of the trimer structure with respect to the Pb substrate and thus the existence of preferential self-assembly of the system. In this way, the other configurations would be metastable and less populated (unpopulated in our case). This interpretation is reinforced by the results of previous theoretical calculations, based on first-principles simulations using the VASP code, showing that MnPcs adsorption on bulk substrates of Pb takes place with the Mn atom sitting on top sites of the Pb surface [9, 73]. Therefore, in our trimers, combined interaction of all three Mn atoms may lead to a preferential orientation with respect to the surface. It is not excluded that the interaction of these metastable configurations with the STM tip could drive the transition towards the most stable ones, i.e. those experimentally observed [74]. Furthermore, the process could

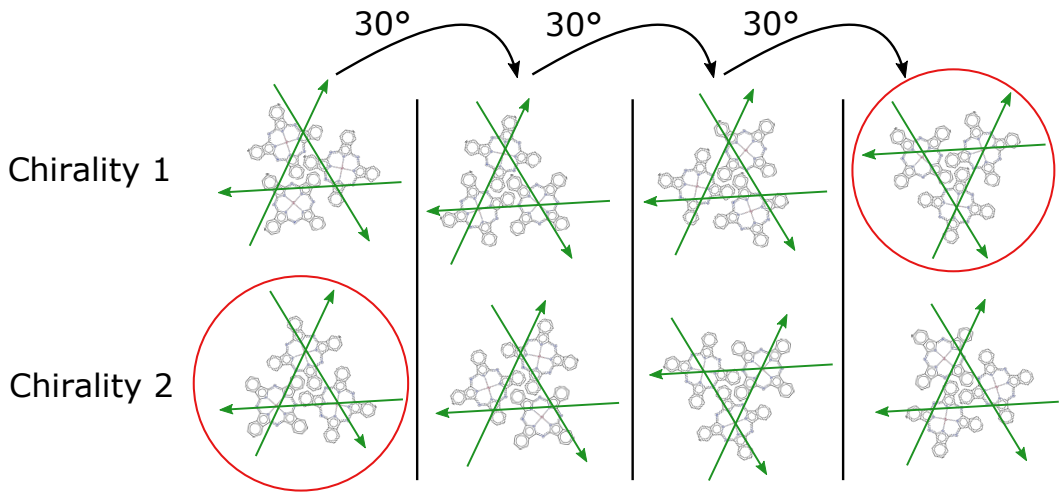

Fig. 3.32 Sketch of the possible trimer orientations with respect to the symmetry directions of the substrate (indicated by green arrows). Trimers in the same column are equivalent but with different chirality. Trimers belonging to different columns are linked to each other by 30° rotations. The two configurations circled in red correspond to those experimentally observed.

be facilitated by the temperature, because we already discussed that, at 77 K, molecular structures can easily diffuse over the surface.
In conclusion, analysis of molecular self-assembly on top of the MnPcs-induced SIC phase has revealed that the strong interaction between MnPcs and Pb surface drives the formation of few stable molecular configurations, i.e. isolated MnPcs and trimer of MnPcs, reflecting the symmetry of the substrate. In particular, trimers of MnPcs were not reported before on other substrates

MnPcs self-assembly at higher coverage

In this section, I will discuss self-assembly of MnPcs on top of the reconstructed Pb surface at higher coverage with respect to that considered until now, i.e. $\sim$0.7 molecules/100 nm^2. Fig. 3.33 illustrates the most representative molecular structures that are found when $\sim$4.6 molecules/100 nm^2 of MnPcs are deposited, between 77 K and 250 K, on top of a $\sqrt{7} \times \sqrt{3}$-Pb phase. In particular, Fig. 3.33a and Fig. 3.33b show that, when MnPc coverage is increased, single molecules try to bind on different sites of either upwards or downwards MnPc trimers always keeping one of the three possible orientations with respect to the Pb substrate. We also observed triangular or hexagonal shaped structures like those shown in Fig. 3.33c and Fig. 3.33d. They result from the binding of more than one MnPc on the same trimer (indicated by red crosses).

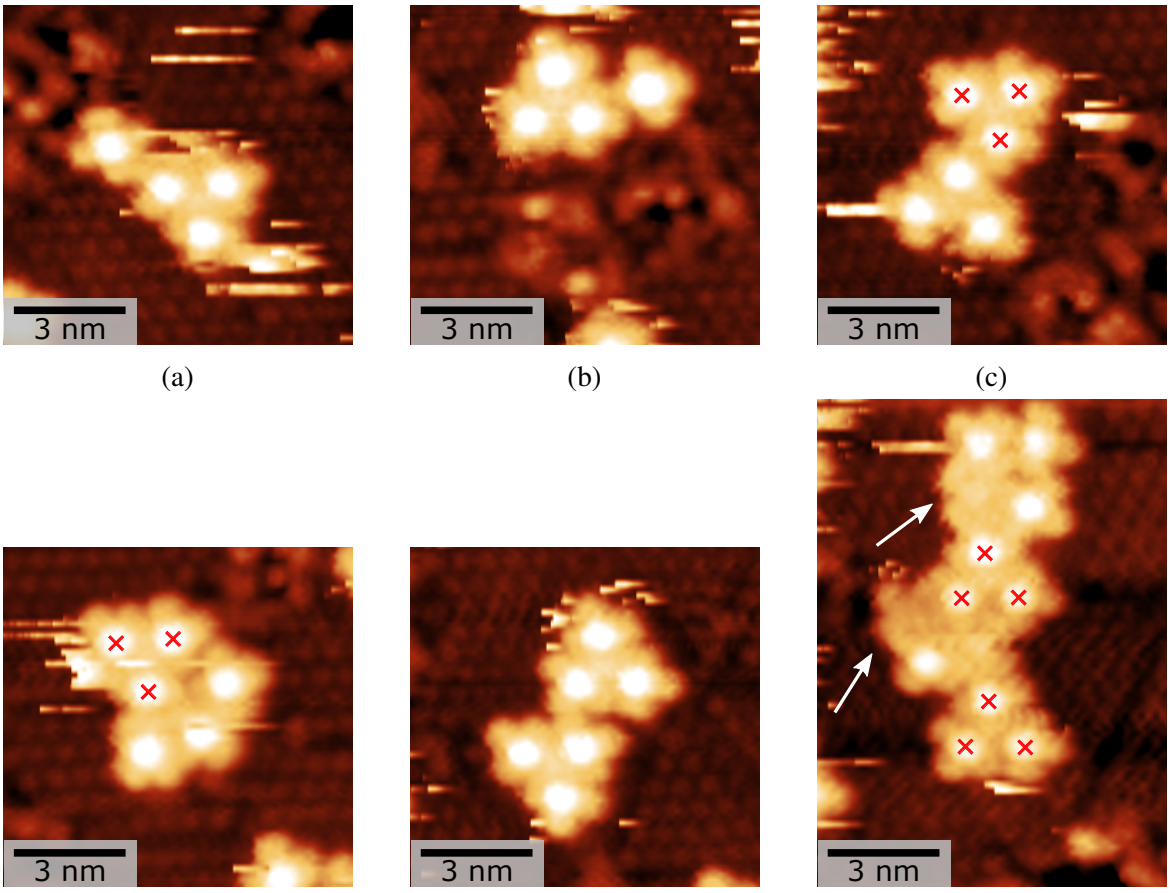

(a) (b) (c)

(d) (e) (f)

Fig. 3.33 Sequence of STM images showing the most representative molecular structures that may be found when ∼4.6 molecules/100 nm^2 of MnPcs are evaporated, between 77 K and 250 K, on top of a $\sqrt{7} \times \sqrt{3}$-Pb reconstructed surface. Red crosses indicate either upwards or downwards trimers of MnPcs similar to those displayed in previous figures. White arrows indicate metal-free phthalocyanines characterized by the absence of the Mn atom, i.e. the white protrusion in the middle of the molecule. (a),(c),(e): Image size: 9×9 nm^2, V_T: +0.4 V and I_T : 80 pA. (b),(d): Image size: 9×9 nm^2, V_T: +0.5 V and I_T : 50 pA. (f) Image size: 9×13 nm^2, V_T: +0.4 V and I_T : 80 pA. All the images were taken at 77 K.

Fig. 3.33c is very interesting because, the three MnPcs bound to the downwards trimer tend to form an upwards trimer. However, by comparing its structure with those previously discussed in Fig. 3.32, we can see that molecules are not in the right order to form one of the expected structures. We believe that this effect is always due to the existence of a strong molecule-substrate interaction prevailing on the molecule-molecule one. The balance between these two interactions generates anisotropic inter-molecular forces leading to complex and disordered structures.

Fig. 3.33e shows another example of trimers binding to each other on different sites to form larger assemblies. Finally, Fig. 3.33f represents one of the most complex molecular structures that has been observed on this kind of sample. They are characterized by an overall linear structure consisting of one or more trimers, e.g. the two highlighted by red crosses, joined together by means of other MnPcs. Rarely, within these large structures we find molecules in which the Mn central atom is not visible, i.e. molecules without the white protrusion in the middle of the structure (indicated by white arrows in Fig. 3.33f). They probably are residual metal-free phthalocyanines or the result of dissociation during the adsorption process. Because only a few percent of phthalocyanines present metal-free characteristic, the latter possibility can be exluded.

These results reveal that trimers are the most stable structures together with isolated molecules because they can easily reflect the threefold symmetry of the substrate although they are made of fourfold symmetric elements. On the other hand, by adding one or more MnPcs it becomes difficult to stack them to form a regular 2D molecular lattice still keeping the threefold symmetry. The same goes when several trimers bind to each other directly or by means of single MnPcs. In particular, when several molecules self-assemble, the system tends to form more or less linear structures depending on the relative molecular configuration.

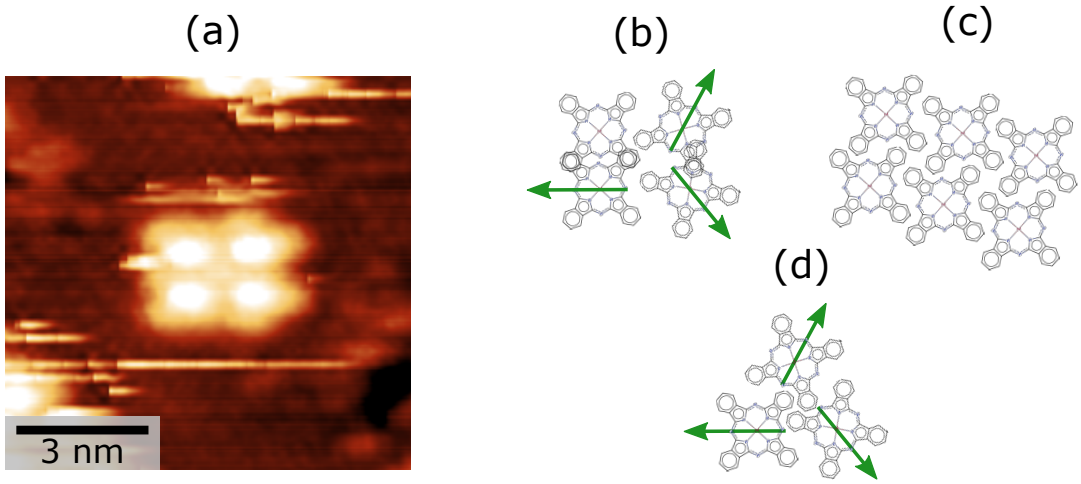

Fig. 3.34 (a) STM image showing an anomalous molecular structure that may be found when $\sim$4.6 molecules/100 nm^2 of MnPcs are evaporated, between 77 K and 250 K, on top of a $\sqrt{7} \times \sqrt{3}$-Pb reconstructed surface. Image size: 9×9 nm^2, V_T: +0.2 V and I_T : 50 pA. The image was taken at 77 K. (b) and (d) Sketch drawn based on experimental data showing the molecular structure with squared shape (b) and the trimer structure (d) formed by MnPcs on top of the Pb monolayer. (c) Sketch of the usual square self-assembly of MnPcs on other metallic substrates. Green arrows represent the symmetry directions of the Pb monolayer.

Another interesting example is provided by the STM image in Fig. 3.34a. This image was also taken on a sample with ∼4.6 molecules/100 nm^2 of MnPcs, and displays a molecular structure with square shape. Molecular configuration of this structure is schematically represented in Fig. 3.34b (based on experimental data). Fig. 3.34c shows a schematic sketch of MnPcs assembled in the square lattice usually observed on other metallic substrates [68, 67]. By comparing these figures it is easy to see that the structure in Fig. 3.34a is anomalous and differs from the usual square assembly of MnPcs. More interestingly, by comparing the orientation with respect to the substrate (green arrows) of each molecule within this structure (see Fig. 3.34b) with that of molecules within a trimer structure (shown in Fig. 3.34d), it easy to see that it is the same. This means that all the molecules within the square structure of Fig. 3.34b tends to retain always the same orientation with respect to the substrate. For this reason we believe that the square structure in Fig. 3.34a arises from the insertion of a fourth molecules within a trimer structure (the molecule in the upper left).

In conclusion, up to ∼4.6 molecules/100 nm^2 of MnPcs, the usual squared self-assembly of MnPcs is strongly frustrated upon adsorption on the Pb monolayer. Such behavior can be explained by a strong molecule-substrate interaction leading to a competition between the fourfold symmetry of MnPcs and the threefold symmetry of the substrate. This competition results in few stable structures, i.e. isolated molecules and trimers, reflecting the threefold symmetry of the substrate. When further MnPcs are added they self-assemble in non-trivial positions giving rise to complex structures incommensurate with the substrate symmetry. This is probably the reason why linear geometries are preferred, in order to minimize the total energy, when the number of involved molecules is increased.

3.4.3 Quantitative analysis of the surface reconstruction

In this section, I will go into the details of the surface reconstruction experienced by the $\sqrt{7}\times\sqrt{3}$-Pb phase upon MnPcs adsorption by showing the results of a quantitative analysis of STM images. In Section 3.1 we already discussed the $\sqrt{7}\times\sqrt{3}$-Pb phase that, with its 6 Pb atoms per 5 Si atoms in a $\sqrt{7}\times\sqrt{3}$-Pb unit cell, has a Pb coverage of 1.2 ML. Its surface atomic density ($n_{\sqrt{7}\times\sqrt{3}}$=9.40 $atoms/nm^2$) is close to that of the bulk Pb(111) surface and it results to be slightly expanded of about 0.1%. On the contrary, we know that if the densest phase of the Pb monolayer was a homogeneous $\sqrt{3}\times\sqrt{3}$-Pb, with 4 Pb atoms per 3 Si atoms in a $\sqrt{3}\times\sqrt{3}$-Pb unit cell, it would have a Pb coverage of 1.33 ML and a surface atomic density $n_{\sqrt{3}\times\sqrt{3}}$=10.44 $atoms/nm^2$. However, we also know that the system arranges the densest phase in a domain structure consisting of $\sqrt{3}\times\sqrt{3}$-Pb domains separated by meandering $\sqrt{7}\times\sqrt{3}$-Pb domain walls that lower the actual coverage to 1.3 ML, i.e. the

SIC phase, resulting in the surface atomic density n_{SIC}=10.19 $atoms/nm^2$. Since 1.3 ML represents the saturation coverage for the Pb monolayer, the SIC is the phase with the highest atomic density and also the most compressed with respect to the bulk Pb(111) surface (5%) [57]. From these basic considerations, MnPcs induce a compression of Pb atoms when adsorbed on the $\sqrt{7}\times\sqrt{3}$-Pb evidenced by a phase transition (towards the SIC phase) that normally takes place by adding further Pb to the layer (see Section 3.1). In particular, 1.2 ML of Pb atoms initially arranged in a $\sqrt{7}\times\sqrt{3}$-Pb phase must rearrange themselves in the denser and more compressed SIC phase (corresponding to 1.3 ML) upon MnPcs adsorption and without adding adding further Pb atoms. This also explains the reason for which the surface reconstruction is accompanied by the appearance of hole-defects.

In order to further confirm that the $\sqrt{7}\times\sqrt{3}$-Pb actually switches to an SIC structure, the estimated Pb atomic density upon MnPcs adsorption can be extracted from STM images. For that purpose, only STM images larger than at least 50×50 nm^2 were considered. The initially prepared surface, before MnPcs adsorption, was supposed to be a homogeneous $\sqrt{7}\times\sqrt{3}$-Pb phase with coverage 1.2 ML and atomic density $n_{\sqrt{7}\times\sqrt{3}}$=9.40 $atoms/nm^2$. From this assumption, it is possible to estimate the total number of atoms within the considered STM images. After MnPcs deposition, the difference between the total area of the considered STM image and the total area of the defective regions over the same STM image gives the area over which 1.2 ML of Pb atoms rearrange themselves and thus the variation of atomic density. The area covered by defective regions was estimated by considering hole-defects together with their edges. Furthermore, in this procedure it is implicitly assumed that the total number of Pb atoms on the surface remains unchanged.
Starting from the approximations above, several sources for uncertainties have to be considered to extract the density of Pb atoms from STM images. Considering that the initially prepared surface, before MnPcs deposition, is an homogeneous $\sqrt{7}\times\sqrt{3}$-Pb is a useful approximation but, in practice, it might not be the case because the surface preparation cannot be controlled down to single atoms and the actual coverage might not be exactly 1.2 ML. This fact implies two things. First, the assumption of 1.2 ML Pb coverage for the initial surface, before MnPcs deposition, represents either an overestimation or an underestimation of the actual number of atoms within the surface itself. Second, the atomic redistribution over the surface after MnPcs adsorption will be different depending on the presence of more or less dense regions because the latter can accommodate more Pb atoms and the former less. Another source of error in the procedure above is the inclusion of hole edges as part of the defects. This is also a useful approximation. However, the edges might even accommodate Pb atoms during the MnPcs-induced surface reconstruction and our estimation procedure

does not take into account their contribution. The absence of atomic resolution on the edges prevents from estimating their composition. Finally, the intrinsic error within the selection of defective surface must be taken into account. This was manually done by means of Gwyddion and its value strictly depends on how the regions are selected.
In conclusion, the estimated Pb atomic density of the reconstructed surface, after MnPcs deposition, is $n = \sim 10.46 \pm 0.29\ atoms/nm^2$. The error was established by repeating the estimation procedure several times on different images and by considering the half-dispersion of the obtained values. Interestingly, within the error, the estimated Pb atomic density is compatible with the expected value for the SIC phase, i.e. n_{SIC}=10.19 $atoms/nm^2$. Therefore, we can conclude that the $\sqrt{7} \times \sqrt{3}$-Pb actually transforms into the SIC phase upon MnPcs adsorption.

3.4.4 MnPcs adsorption directly on the SIC phase

In this section, I will present the results related to the adsorption of MnPcs directly on the Striped Incommensurate phase (SIC) and I will show that molecular self-assembly is exactly the same as that observed on the MnPc-induced SIC obtained by depositing MnPcs on the $\sqrt{7} \times \sqrt{3}$-Pb phase.
Fig. 3.35a shows an SIC phase prepared by depositing 4 ML of Pb on top of the Si(111)-7×7 reconstructed surface and subsequent annealing at 320° C for 1 min 10 sec. Then, $\sim$1.3 molecules/100 nm^2 of MnPcs were deposited at room temperature on top of the Pb monolayer. It is easy to see that SIC phase is not affected at all by the presence of MnPcs. This is probably due to the fact that the SIC is already the densest phase and therefore, even if a charge transfer from MnPcs to the surface takes place, the electronic charge donated to the Pb lattice cannot further increase the tensile stress and the surface cannot further contract. On the other hand, if a charge transfer between MnPcs and Pb monolayer takes place, the electron doping is likely to occur. Consequently, it cannot be excluded a change in both the electron density and the electronic properties of the Pb monolayer. For this reason, it would be interesting to perform spectroscopic experiments, e.g. ARPES, STS, to characterize the electronic properties of this type of sample. A recent study of Yoshizawa et al. [71], for instance, has shown by means of angle-resolved photoemission, X-ray magnetic circular dichroism and ab-initio calculations that the adsorption of phthalocyanines on top of a 2D superconductor, consisting of two atomic layers of indium grown on Si(111), can modify its superconducting critical temperature (T_C) in a controllable manner by replacing the magnetic atom in the middle of the molecular structure. The proposed mechanism is based on a competition between charge and spin effects. In particular, in the case of CuPcs, T_C modulations are ascribed to the hole-doping of the In substrate following the charge transfer between CuPcs

and substrate. This hole-doping process modulates the density of states at the Fermi level $\rho(E_F)$ of the superconductor and thus its critical temperature. Remember that, according to the BCS theory, T_C is related to $\rho(E_F)$. The role of the spin associated to the Cu atom can be neglected because ab-initio calculation show that the corresponding spin magnetic moment barely interacts with the indium substrate. On the other hand, in the case of MnPcs, the spin associated to the Mn atom strongly affects the conduction electrons of the substrate (prediction of ab-initio calculations). This magnetic effect dominates over the carrier doping process and leads to a suppression of the superconductivity with consequent modulation of T_C.

Fig. 3.35b shows the same STM image shown in Fig. 3.35a with adjusted contrast to make MnPcs visible. Four-lobe appearance suggests that the MnPcs lie flat on the surface. This image was taken at 300 mK and diffusing molecules were not observed meaning that the molecular diffusion is blocked at this temperature. Exactly as discussed in previous sections for the MnPcs-induced SIC, at low coverage, MnPcs are isolated or self-assemble in dimer/trimers reflecting the threefold symmetry of the substrate. A trimer is shown within the inset of Fig. 3.35b. Therefore, also in this case the molecule-substrate interaction prevails over the molecule-molecule interaction. Isolated molecules still adsorb with only three

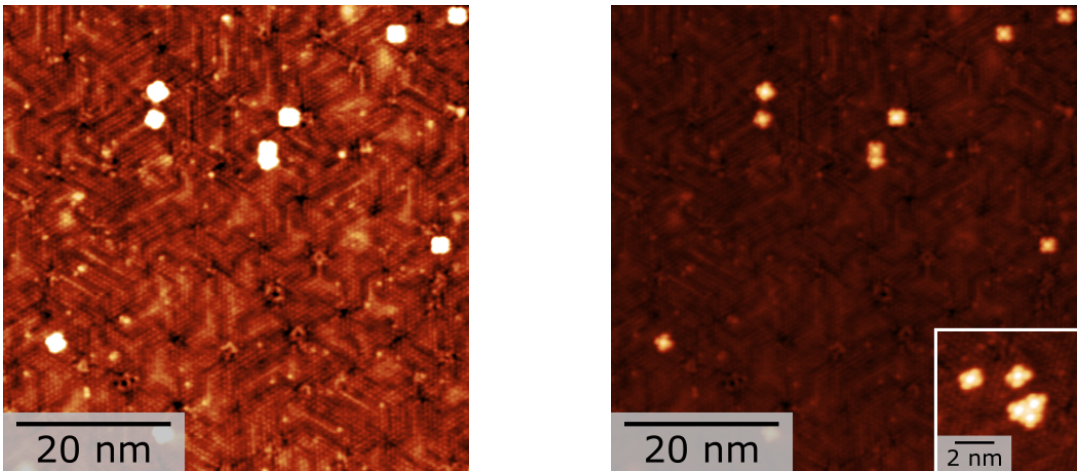

(a) (b)

Fig. 3.35 (a) STM image showing ∼1.3 molecules/100 nm^2 of MnPc deposited at room temperature on top of the SIC phase. (b) The same STM image shown in (a) with adjusted contrast to make MnPc molecules visible. Image size: 60×60 nm^2, V_T: -50 mV and I_T : 50 pA. Inset: STM image of the same surface showing the presence of MnPc trimers. Image size: 7×7 nm^2, V_T: -50 mV and I_T : 50 pA. All the images were acquired at 300 mK.

possible orientations with respect to the substrate (see Fig. 3.30d). These configurations are linked by a 30° molecular rotation. Similarly to what was shown in Section 3.4.2, only two

types of trimers are experimentally observed, i.e. those differing by 30° and with different chirality. With regard to what has been said in Section 3.4.2 about the absence of some trimer orientations, we recall that the most likely explanation is the existence of specific stable adsorption sites able to pin their orientation with respect to the substrate (see Section 3.4.2). In conclusion, we believe that the considerable similarity between the self-assembly of MnPcs on top of the SIC phase and on top of the MnPc-induced SIC discussed in previous sections implies that MnPcs do not see difference between the two structures confirming that the MnPc-induced SIC observed when MnPcs are deposited on top of the $\sqrt{7}\times\sqrt{3}$-Pb actually is a SIC phase. This result further confirms the quantitative analysis carried out in the previous section.

3.4.5 Coverage threshold of MnPcs for surface reconstruction

In this section I will show the results of the experiments carried out to determine what is the minimum amount of MnPcs needed to initiate the structural phase transition of the $\sqrt{7}\times\sqrt{3}$-Pb phase. To do this, we significantly reduced the coverage of MnPcs with respect to the $\sim$0.7 molecules/100 nm^2 considered in previous sections.
The fact that the MnPc-induced structural transition from the $\sqrt{7}\times\sqrt{3}$-Pb to the SIC phase can already take place between 77 K and 250 K means that, in this range of temperatures, the system already has enough energy to overcome a possible activation energy barrier related to the atomic redistribution between initial and final state. Accordingly, we could expect that MnPc deposition on the Pb monolayer kept at room temperature leads to equivalent results. For this reason, the samples discussed in this section were prepared by evaporating MnPcs on the Pb substrate kept at room temperature. In all cases STM images were acquired at 77 K. The STM image in Fig. 3.36a shows a Pb monolayer prepared in the $\sqrt{7}\times\sqrt{3}$-Pb phase, on which $\sim$0.019 molecules/100 nm^2 of MnPcs were deposited at room temperature. The most relevant aspect of this image is that the $\sqrt{7}\times\sqrt{3}$-Pb reconstruction remains globally unchanged. Furthermore, we were unable to image MnPcs on top of this sample, probably because they rest isolated and free to diffuse over the surface. For this reason, the molecular coverage was estimated by assuming proportionality of the deposited quantity with deposition time at constant flux. On the other hand, closer inspection of Fig. 3.36a reveals signs of surface modification with respect to the ideal $\sqrt{7}\times\sqrt{3}$-Pb. Even if the resolution of the image is a bit poor, we can clearly see the presence of double rows structures and more extended 2D structureless areas (indicated by black arrows). This is usually observed when the Pb coverage is slightly higher than 1.2 ML (few percent of ML), i.e. when we move through the phase diagram towards linear phases and small $\sqrt{3}\times\sqrt{3}$-Pb domains start to nucleate. In other words, Fig. 3.36a shows a Pb monolayer in which the atomic density is slightly higher

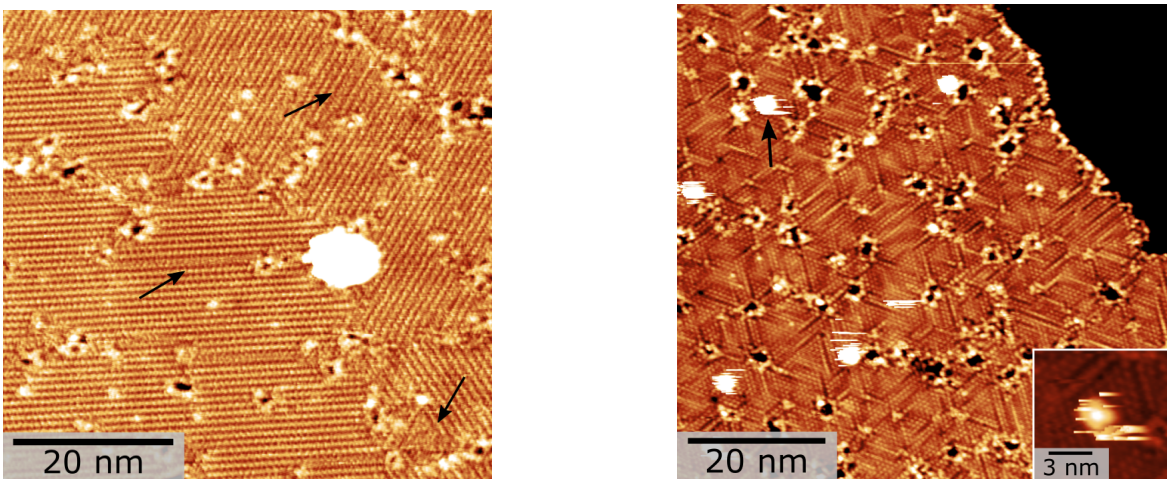

(a) (b)

Fig. 3.36 (a) [(b)]: STM image taken from a sample on which (a) ∼0.019 molecules/100 nm^2 [∼0.18 molecules/100 nm^2] of MnPc were evaporated, at room temperature, on top of a $\sqrt{7} \times \sqrt{3}$-Pb reconsstructed surface. (a) Black arrows indicate regions in which double rows structures and 2D structureless areas are present due to the fact in these regions the atomic density start to be slightly higher than that of a pure $\sqrt{7} \times \sqrt{3}$-Pb phase. Image size: 60×60 nm^2, V_T: +0.3 V and I_T : 20 pA. (b) Black arrow indicates a large white spot representing an isolated MnPc molecule. Image size: 70×70 nm^2, V_T: +0.1 V and I_T : 40 pA. Inset: STM image of the same surface with adjusted contrast to make the MnPc visible. Image size: 9×9 nm^2, V_T: +0.1 V and I_T : 40 pA. All the images were taken at 77 K.

than that of a pure $\sqrt{7} \times \sqrt{3}$-Pb phase.

So far, there are no obvious signs allowing to associate this atomic density variation to a molecular effect, because it could be simply due to a slightly different coverage of Pb within the initially prepared $\sqrt{7} \times \sqrt{3}$-Pb surface. Furthermore, the density of hole-defects is much smaller compared, for instance, to what previously shown in Fig. 3.28b or Fig. 3.29. The surface atomic density upon MnPcs adsorption, in this case, was estimated to be n=9.65 $\pm$ 0.29 $atoms/nm^2$. Within the uncertainty this value is compatible with that expected for an ideal $\sqrt{7} \times \sqrt{3}$-Pb, i.e. $n_{\sqrt{7} \times \sqrt{3}}$=9.40 $atoms/nm^2$.

From these considerations we can conclude that $\sqrt{7} \times \sqrt{3}$-Pb phase remains globally unchanged upon adsorption of ∼0.019 molecules/100 nm^2 of MnPcs at room temperature and MnPcs cannot be directly observed because of the low coverage.

Fig. 3.36b shows an STM image taken from a sample on which ∼0.18 molecules/100 nm^2 of MnPcs were evaporated, at room temperature, on top of the $\sqrt{7} \times \sqrt{3}$-Pb phase. It is clear that, in this case, the surface exhibits an abrupt surface reconstruction upon MnPc adsorption with similar features to the ones already shown in Fig. 3.28b, that is, a SIC-like structure together

with hole defects. White large spots in Fig. 3.36b (one of which is indicated by a black arrow) represent MnPcs that, in this case, can be imaged by STM. At this coverage MnPcs mainly remain isolated but occasionally trimer structures are observed. An isolated MnPc is shown within the inset of Fig. 3.36b. The surface atomic density, after MnPcs adsorption, is estimated to be n=10.32 $\pm$ 0.29 $atoms/nm^2$. Within the uncertainty, this value is compatible with the one expected for the SIC phase and thus with the fact that initial $\sqrt{7} \times \sqrt{3}$-Pb phase has been fully reconstructed in a SIC phase upon MnPcs adsorption. Furthermore, we confirm that the substrate temperature (room temperature or between 77 K and 250 K) during the MnPcs evaporation does not seem to play any relevant role in the reconstruction process.
In conclusion, the evaporation of $\sim$0.18 molecules/100 nm^2 of MnPcs at room temperature is already largely sufficient to completely reconstruct the initial $\sqrt{7} \times \sqrt{3}$-Pb phase in a SIC phase.

3.4.6 Proposed mechanism for the MnPcs-induced surface reconstruction

In this section, I will propose a possible explanation for the mechanism behind the MnPcs-induced surface reconstruction of the $\sqrt{7} \times \sqrt{3}$-Pb phase. All the discussion will be based on the comparison of our findings with those of other groups on similar systems.

Mass transport mediated by organic molecules

Matetskiy et al. [75] have investigated by LEED and STM experiments the adsorption of C_{60} molecules on top of both 1×1-Pb/Si(111) (at room temperature) and $\sqrt{7} \times \sqrt{3}$-Pb/Si(111) (between 30 K and 210 K). It was already reported in other studies that C_{60} molecules adsorbed on metallic bulk substrates tend to be partially embedded within the surface in order to increase their coordination. This is accompanied by expulsion of substrate atoms and consequent formation of metallic islands on the surface. Matetskiy et al. have observed that, at the early stages of the growth, C_{60} molecules preferentially adsorb on defective regions by forming embedded disordered islands. Contrary to what happens on bulk substrates, the expelled Pb atoms are reintegrated around the molecules by increasing the local atomic density. As a consequence, Pb phases denser than the initial 1×1-Pb/Si(111) or $\sqrt{7} \times \sqrt{3}$-Pb are observed around the molecules. In particular, by varying the molecular coverage between $\sim$1.17 molecules/100 nm^2 and $\sim$9.36 molecules/100 nm^2, they were able to observe variations of the local Pb coverage between $\sim$1.2 ML and $\sim$1.25 ML. In any case, the HIC phase (with Pb coverage of 1.25 ML) was the densest phase observed around the molecular islands. Once all defective regions are saturated by embedded disordered C_{60}

islands, further increasing of molecular coverage leads to the nucleation of crystalline C_{60} islands on top (not embedded) of clean Pb regions and further structural changes of the Pb substrate are not observed. If the initial Pb surface does not contain defective regions, Pb surface reconstruction is not observed upon C_{60} adsorption and only crystalline molecular islands on top (not embedded) of the surface are observed. The last observation implies that the presence of surface defects is mandatory to observe a surface reconstruction of the Pb monolayer.

Our findings reveal a different behavior of the Pb monolayer upon MnPcs adsorption. First, MnPcs are not known to be involved in mass transport processes upon adsorption on metallic substrates. Second, a preferential adsorption of MnPcs on defects of the Pb surface was not observed, but rather the opposite. Third, MnPcs are not observed to be embedded within the Pb surface. On the contrary, they were able to diffuse over the surface already at the early stages of growth. Fourth, a threshold coverage at which MnPcs self-assemble in crystalline islands was not observed up to $\sim$4.6 molecules/100 nm^2. Fifth, already at $\sim$0.18 molecules/100 nm^2 of MnPcs the $\sqrt{7} \times \sqrt{3}$-Pb phase (corresponding to 1.2 ML) was fully transformed into the SIC phase (corresponding to 1.3 ML) even very far from MnPcs and intermediate phases between the $\sqrt{7} \times \sqrt{3}$-Pb and the SIC were never observed (Fig. 3.36b).

From these considerations we believe that mass transport mechanism, mediated by MnPcs, driving the structural transformation of the Pb monolayer observed in out experiments could be excluded because it would involve a huge number of atoms per molecule.

Charge transfer and surface reconstruction

To understand the role of charge transfer in surface reconstruction, it is necessary to speak about another process that is strictly related: the adsorbate-induced surface stress modification. Surface stress is always present from the moment that the surface itself is created and it is the result of charge redistribution because of the absence of atoms above the surface [76]. The surface stress is called "tensile" when the surface tends to contract and it is called "compressive" when the surface tends to expand. Metallic surfaces usually have a tensile surface stress [76]. One of the possible charge redistribution paths in metallic surfaces is the accumulation of electronic charge between surface atoms. This results in a contraction of the bond lengths between surface atoms. Anyway, the surface atoms cannot fully contract because they are bound to the underlying crystal structure through chemical bonds. Therefore, a permanent tensile surface stress remains in clean metallic surfaces and it is one of the main

driving forces of surface reconstruction. When an electron donor molecule is adsorbed on top of a metallic surface the effect is to enhance the charge density between surface atoms and therefore enhance the tensile surface stress.

Sun et al. [77] have observed different surface reconstructions of the Au(111) surface depending on the adsorbed molecule, i.e. perylene and FePcs molecules. They have attributed the molecule-induced surface reconstruction process to the local modification of the surface stress due to the charge transfer. Usually, when molecules adsorb on metallic surfaces, a charge transfer between molecules and surface takes place and its strength depends on the strength of the molecule-surface coupling (but also on work function, etc.). As a consequence, the electrons belonging to the metallic surface reorganize themselves by changing the local charge distribution in proximity of the molecules. Since atomic structure and electronic configuration are intimately linked, the net result of this charge redistribution is a local surface stress (further details below) inducing local structural changes and in some cases local surface reconstruction. The propagation length of these structural changes are determined by the competition between the molecular-induced surface stress and the long-range elastic interactions within the metallic surface. Therefore, a stronger molecule-substrate coupling involves a stronger charge transfer which in turn is able to strongly perturb the original symmetry of the substrate and drive more radical surface reconstructions.

Different arguments can support the charge transfer as one of the key actors within the MnPc-induced surface reconstruction of the Pb monolayer observed in our experiments. Free MnPcs are characterized by an electronic configuration $(d_{xy})^1(d_\pi)^3(d_{z^2})^1$ with three unpaired electrons and a spin S=3/2 [78]. First-principles simulations predict that the preferential adsorption configuration of MnPcs on a bulk Pb substrate requires the Mn^{2+} ion sitting on top of a Pb atom [9, 73]. The d_{xy} orbital of the Mn^{2+} ion is weakly hybridized with the Pb substrate. Calculations also predict a strong chemical bonding between the dz^2 orbital of the Mn^{2+} ion and the p_z orbital of Pb. The last information is interesting because p_z orbital are responsible for both the coupling between Pb atoms and Si substrate and the stabilization of the $\sqrt{7} \times \sqrt{3}$-Pb phase by means of covalent bonds between Pb and Si atoms. More interestingly, calculations also predict a reduction of the molecular spin from S=3/2 to S=1 [9, 73]. This is probably due to a charge transfer occurring between MnPcs and Pb substrate. It should be pointed out that these calculations were performed by considering a bulk Pb substrate. Consequently, the results may not be directly applied to the 2D limit of the monolayer. Anyway, starting from the considerations of this section about the charge-induced tensile stress variations and the charge transfer between MnPcs and Pb we will assume that,

upon MnPc adsorption, the charge transfer takes place from MnPcs to the Pb surface and thus the latter becomes enriched of a supplementary amount of charge. This assumption is in line with the experimental observation that the $\sqrt{7}\times\sqrt{3}$-Pb phase transforms into a denser phase, i.e. the Striped Incommensurate phase. In any case, calculations addressing this issue are in progress at the time of writing of this manuscript.

Proposed mechanism

From the previous sections a mechanism for the MnPc-induced surface reconstruction of the $\sqrt{7}\times\sqrt{3}$-Pb can be finally proposed. When $\sim$0.18 molecules/100 nm^2 of MnPcs adsorb on the $\sqrt{7}\times\sqrt{3}$-Pb a charge transfer from MnPcs to the Pb surface takes place. The molecule-substrate interaction is mainly localized on the p_z orbitals of Pb, i.e. the orbitals responsible for the stability of the $\sqrt{7}\times\sqrt{3}$-Pb. For this reason MnPc adsorption is likely to result in a destabilization of the chemical bonds between Pb and Si. Simultaneously, the electronic charge donated by the molecules is required to remain within the Pb atomic layer because all the dangling bonds of the silicon substrate are saturated by the Pb atoms and there are no available bulk states within the semiconductive gap of the silicon. This means that the electronic charge accumulates within the Pb layer enhancing the tensile stress of the surface (see Section 3.4.6). At this stage, the weakening of chemical bonds between Pb and Si allows the Pb atoms to accommodate the tensile stress, i.e. the surface can contract and the surface reconstruction takes place. Other studies [56, 79] have shown that the surface electron density of the Pb monolayer is increased by passing from the $\sqrt{7}\times\sqrt{3}$-Pb phase to the SIC phase and the latter has a stronger metallic character compared with the former. In these works the transition was induced by increasing the Pb coverage which is directly related to the surface electron density. On the other hand, the formation of the SIC in our experiments is probably due to the fact that the $\sqrt{7}\times\sqrt{3}$-Pb is a fragile phase and by adding electrons the system can reach a more stable configuration, i.e. the SIC phase. In the end, this means that within the rich phase diagram of the Pb monolayer we identified a new parameter, in addition to temperature and coverage, causing structural phase transitions, i.e. the electron doping, whose intervention can completely change the relative stability of different phases.

The proposed scenario could be further refined by considering the effects related to the electron doping. In the work of Bondarenko et al. [80, 81] $\sim$0.1 ML of Na were deposited on top of an Au monoloayer in the Si(111)$\sqrt{3}\times\sqrt{3}$-Au phase. As a result of Na adsorption the transformation of a disordered and poorly conductive surface into a one with highly ordered-atomic structure and a spin-split metallic surface-state band was observed [81]. In particular, the original surface resembles the SIC phase of the Pb monolayer because it con-

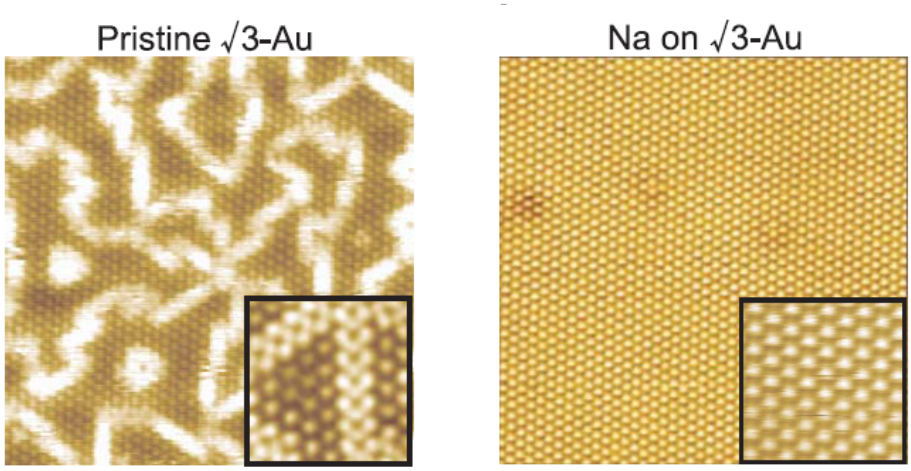

Fig. 3.37 STM images of the pristine Si(111)$\sqrt{3}\times\sqrt{3}$-Au phase (a) and the same surface after adsorption 0.15 ML of Na [81].

sists of $\sqrt{3}\times\sqrt{3}$ domains separated by meandering domain walls (see left part of Fig. 3.37). Na adsorption at 300° C transforms the initial disordered Au phase into a crystalline and defect-free $\sqrt{3}\times\sqrt{3}$ surface (see right part of Fig. 3.37). Low temperature STM images (110 K) reveal a random distribution of frozen Na clusters. On the other hand, room temperature images shows only a $\sqrt{3}\times\sqrt{3}$ phase because the Na clusters diffuse and they cannot be seen. By means of DFT calculations it was shown that the Na adsorption induces local structural distortion especially on the silicon substrate. Concerning the electronic properties, the reconstructed surface after Na adsorption reveals an improved surface conductivity given by electron filling of a metallic surface band and related development of a 2D electron gas. It was estimated that each Na atom donates $\sim$1.0 electron to the gold surface. Interestingly, 0.1 ML results to be an optimum coverage to improve electronic properties of the system because additional Na atoms degrade the structural order and conductivity.

Several similarities between this work and the MnPcs-induced surface reconstruction of the $\sqrt{7}\times\sqrt{3}$-Pb phase observed in our experiments can be found. First, strong structural changes upon adsorption of a small amount of a foreign species. Second, at low temperature the adsorbate diffusion can be blocked. Furthermore, the fact that Na is an electron donor species exactly as for MnPcs has to be considered. Therefore, it is not excluded that, in our case, besides the structural changes, the electron doping could play a role in tailoring the electronic properties of the Pb monolayer. For this reason, further measurements would be necessary to investigate if the electronic properties of the molecular-induced SIC phase coincide with

those of the standard SIC or additional differences could be induced by the MnPcs presence.

Another way to refine the mechanism proposed above could be to take into the fact that surface reconstruction takes place already between 77 K and 150 K and involves a region as large as the coherence length of LEED (not shown) and thus a huge number of Pb atoms. Several studies have shown that structural transformations involving an important mass transport within the Pb monolayer are due to fast and collective motion of Pb atoms [75, 82].

3.4.7 Conclusions

In summary, our experiments have revealed that MnPcs adsorption on top of the $\sqrt{7} \times \sqrt{3}$-Pb phase (corresponding to a Pb coverage of 1.2 ML) induces macroscopic structural phase transition of the Pb monolayer towards the SIC phase (corresponding to a Pb coverage of 1.3 ML).

In particular, our study show that the evaporation of a tiny amount of MnPcs, i.e. $\sim$0.18 molecules/100 nm^2, with substrate kept between 77 K and room temperature, is already largely sufficient to completely reconstruct the initial $\sqrt{7} \times \sqrt{3}$-Pb phase in a SIC phase. Such abrupt phase transition induced by diluted molecules has never been observed in the literature so far. Several group have already deposited MnPcs on both thick layers of Pb grown on Si(111) (starting from 11 ML) and bulk Pb substrates but similar reconstruction effects have never been observed until now [67, 68, 73]. Interestingly, it was also reported the adsorption of phthalocyanines on top of a In bi-layer but also in this case there was no trace of surface reconstruction [71]. Our quantitative estimation of the Pb atomic density variation through the MnPcs-induced structural transition agrees with the hypothesis that the $\sqrt{7} \times \sqrt{3}$-Pb phase actually transforms into the SIC phase upon MnPcs adsorption. This hypothesis is also supported by the similarity of MnPcs self-assembly on top of the pristine SIC phase of the Pb monolayer and on top of the MnPc-induced SIC.

We proposed a possible explanation of the mechanism behind the MnPcs-induced surface reconstruction of the Pb monolayer in which molecular adsorption may affect some of the chemical bonds between the Pb atoms and the silicon substrate responsible for the stability of the $\sqrt{7} \times \sqrt{3}$-Pb phase. At the same time, it has been proposed that MnPcs donate an electronic charge to the Pb surface increasing the tensile stress within the Pb film. The combinations of these two effects may be the driving force for the contraction of the Pb layer and thus of of the surface reconstruction.

Analysis of molecular self-assembly on top of the MnPcs-induced SIC phase has revealed that, at a MnPcs coverage of $\sim$0.7 molecules/100 nm^2, the strong molecule-substrate interaction leads to a competition between fourfold symmetry of MnPcs and threefold symmetry of the substrate. This competition results in a molecular self-assembly strongly different from that observed on bulk-like substrates. In particular, the square self-assembly of MnPcs usually observed on metallic samples is strongly frustrated and few stable molecular configurations are observed, i.e. isolated molecules and trimers, reflecting the threefold symmetry of the substrate. In particular, trimers of MnPcs observed in our experiments were not reported before on other substrates. This novel behavior is probably due to the strong interaction between MnPcs and Pb substrate. When further MnPcs are added (up to $\sim$4.6 molecules/100 nm^2), they tend to self-assemble in non-trivial positions giving rise to complex structures incommensurate with the substrate symmetry (linear geometries are preferred). DFT calculations calculations addressing this issue are in progress at the writing of this thesis. Furthermore, it would be interesting to carrying out other experiments, e.g. ARPES, STS measurements, in order to understand if the electronic properties of the MnPcs-induced SIC phase are modified with respect to the pristine SIC phase obtained without deposition of molecules. For instance, it would be interesting to investigate any MnPcs-induced spin-splitting effects similarly to what observed in the case of adsorption of Na on top of the Si(111)$\sqrt{3}\times\sqrt{3}$-Au phase [81].

Chapter 4

Thin films of Pb on Si(111)

4.1 Quantum well states and phase accumulation model

If one or more dimensions of a crystal become of the order of the electron's wavelength the electrons start to feel the quantum confinement effects. The simplest model to handle the electron confinement is the particle-in-a-box model. The most widespread case is that of an electron confined in a one-dimensional rectangular well with infinite walls. Fig. 4.1a shows the wavefunctions, also called Quantum Well States (QWS), with lowest energy resulting from the time-independent Schrödinger equation for a quantum well of width L. From the figure is clear that the wavefunctions of confined electrons are standing waves with nodes at the boundaries of the well and discrete wavelengths [83]

$$\lambda_n = \frac{2L}{n} \qquad n = 1,\ 2,\ ... \tag{4.1}$$

where L is the width of the well and n is the integer quantum number identifying the allowed wavefunctions with wavelengths λ_n. The De Broglie's relationship makes it possible to calculate the energy of the electron from its wavelength by means of the following relation

$$E_n = n^2 \frac{h^2}{8mL^2} \qquad n = 1,\ 2,\ ... \tag{4.2}$$

where h is the Plank's constant and m the electron mass. The n^2 dependence of energy levels indicates that they are more widely spaced as the energy increases. As can be seen from previous relations, the most important consequence of electron confinement is the quantization of the energy spectrum, i.e. the restriction of the allowed energies, or equivalently the wavevectors, that the electrons can assume.

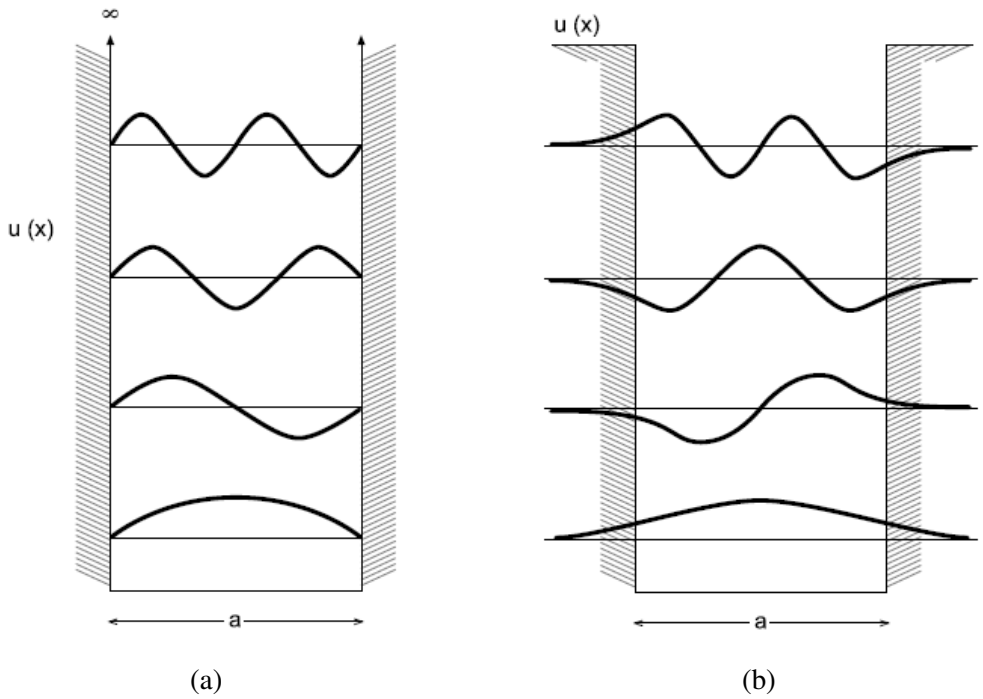

(a) (b)

Fig. 4.1 Lowest energy wavefunctions (QWS) associated to an electron confined in a one-dimensional rectangular well of width a and infinite (a) [finite (b)] walls [83].

In real systems the confining well has a finite depth meaning that the confining walls are finite rather than being infinite [83]. Fig. 4.1b shows the QWS with lowest energy of an electron confined in a finite quantum well. It is clear that the standing waves are quite similar to those obtained in the case of an infinite quantum well. However, since the well has a finite depth, the electron is not completely confined and its wavefunctions have exponential tails outside the well itself instead of having nodes at the boundaries (compare with Fig. 4.1a). The existence of the exponential tails is a consequence of both the finite height of the potential barrier and the quantum tunneling allowing the electron to leak out [83]. Exponential tails lead to the increase of the wavelength associated to the discrete bound states and consequent lowering of their energy respect to the infinite well case (from relations 4.1 and 4.2). However, this tail effect becomes negligible as the film thickness increases because the fraction of wavefunction out of the well becomes much smaller compared to that inside. In an equivalent manner, when the film thickness increases, the energy lowering of the discrete quantum well states is dominated by the well width L rather than the presence of exponential tails (see expression 4.2).

Fig. 4.2 shows an example of QWS experimentally observed by STM/STS on a Ag(111) surface [84]. This system is known to present a surface state with a 2D free electron character

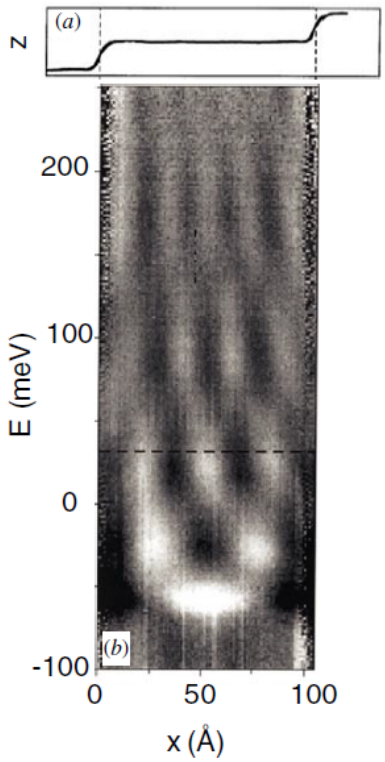

Fig. 4.2 Upper part: STM constant current line scan on a 104 Å wide Ag(111) terrace. The two atomic steps at the boundaries of the terrace are also visible. Lower part: Spatial variation of the density of states (STS differential conductance) as a function of the energy (bias voltage) measured along a line on the terrace between the two atomic steps [84].

within the plane parallel to the surface. The electrons are then laterally confined in a terrace between two parallel atomic steps acting as electronic mirrors (see the upper part of Fig. 4.2). The lower part of the figure shows the spatial variation of the density of states along a line as a function of the energy measured along a line between the two atomic steps. In other words, the spatial variations of the tunneling current detected by the STM tip along this line reflect the variations of the density of states related to the QWS. By varying the bias voltage, discrete QWS with different energies can be probed. It is interesting to note that the spatial variations for each QWS in Fig. 4.2 look very similar to those arising from the particle in a box model shown in Fig. 4.1b [83, 84].

In metallic thin films epitaxially grown on a semiconductor substrate the electrons are confined in the perpendicular direction to the surface of the film itself and the quantum well width is represented by its thickness [83]. Both the film/substrate interface and the film/vacuum interface play the role of confining barriers. In general, the confinement direction determines the direction along which the different electronic properties become quantized and the

standing waves develop (see Fig. 4.1 and Fig. 4.2). Consequently, in this case, the spatial variations of the charge density associated to the different discrete QWS standing waves lie inside the film and develop perpendicularly to its surface. For this reason they cannot be directly imaged by STM/STS as shown in the previous example.

In this work, we will focus on the particular case of metallic thin films of Pb epitaxially grown on a Si(111) substrate. At the film/vacuum interface the vacuum barrier acts as a confining barrier and it can effectively be described by the image potential [83]

$$V_{image} = -\frac{e^2}{4\pi\varepsilon_0 \cdot 4z} \tag{4.3}$$

with e the electronic charge, ε_0 the permittivity of free space and z the distance from the metallic surface. At the film/substrate interface, the semiconducting band gap of the silicon substrate acts as a confining barrier for the electrons within the film. This is because the electrons moving perpendicularly to the surface, i.e. along the confining direction, and having energies falling into the band gap cannot couple to the bulk states of the substrate and therefore cannot be scattered towards it. An exact addressing of the problem to calculate the QWS standing waves and related energies would require the knowledge of the microscopic details of the overall system making it extremely difficult to handle. Fortunately, the phase accumulation model, also known as Bohr-Sommerfeld quantization rule, solves the problem in a simple way by retaining the important information about the physics behind and by providing results accurate enough even for real systems [83]. The key idea of the model is that, regardless of the profoundly different nature of the confining barriers at the two interfaces, the net effect of their presence is to confine the electrons within the film by reflecting them back and forth between one interface and the other (see Fig. 4.3). The total phase difference accumulated during a round-trip of the electrons between the two interfaces is mainly due to two contributions, i.e. the propagation of the electrons through the film itself along the confining direction and the reflections at the confining barriers (see Fig. 4.3). The phase accumulation model states that if the total phase difference accumulated by the electrons during a round-trip is an integer multiple of 2π, then a QWS standing wave is produced within the metallic film [83]:

$$\Phi_{sub}(E) + \Phi_{vac}(E) + 2k_{\perp}(E)d = 2\pi n \tag{4.4}$$

where $k_{\perp}$ is the allowed electron wavevector along the confining direction, i.e. the perpendicular direction to the surface, d is the width of the quantum well roughly corresponding to the film thickness and n is an integer number. $2k_{\perp}d$ is the phase difference accumulated

during a round-trip of the electrons through the thickness of the film, i.e. along the confining direction. Φ_{sub} and Φ_{vac} are the phase shifts associated to the reflection of the electrons at the film/substrate and the film/vacuum interface respectively which account for the wavefunction tails out of the confining barriers. The strong simplification introduced by this model lies in the fact that the interaction between the electrons and both the vacuum and the substrate, i.e. the confining barriers, is described by means of the phase shifts Φ_{sub} and Φ_{vac} [83]. The different nature of the confining barriers is simply taken into account by considering different values for Φ_{sub} and Φ_{vac}. It is important to note that $\Phi_{sub}(E)$, $\Phi_{vac}(E)$ and $k_{\perp}(E)$ all depend on the energy of the electrons and therefore only a discrete set of energy values will fulfill the condition 4.4 leading to the quantization of both the energy and the QWS standing waves.

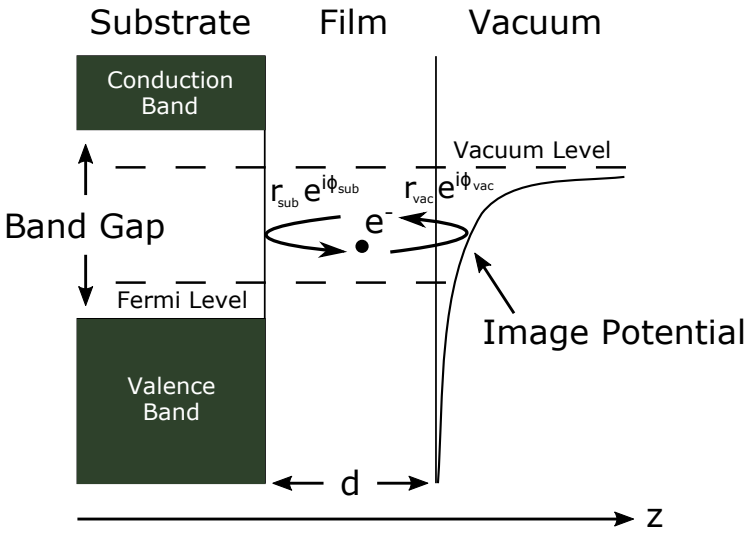

Fig. 4.3 Schematic picture of the phase accumulation model describing the confinement of electrons in metallic thin films epitaxially grown on a substrate. r_B and r_C are the reflection coefficients at the two interfaces. Φ_B and Φ_C are the phase shifts associated to the reflection of the electron at the two interfaces. Adapted from [83].

When dealing with metallic thin films their thickness is a discrete quantity given by an integer number N of atomic planes separated by an interlayer spacing a typically ranging between 0.2 and 0.3 nm. Consequently, the condition 4.4 can be rewritten by replacing d with Na [83]:

$$\Phi_{sub}(E) + \Phi_{vac}(E) + 2k_{\perp}(E) \cdot Na = 2\pi n \tag{4.5}$$

with N an integer number and a the atomic interlayer spacing. Furthermore, the width d of the well, representing the distance between the film/substrate interface and the film/vacuum interface, is measured by considering the location of barriers at one half of an atomic layer spacing above and below the film, i.e. the total width of the quantum well results to be approximately one atomic layer larger than the actual film thickness.

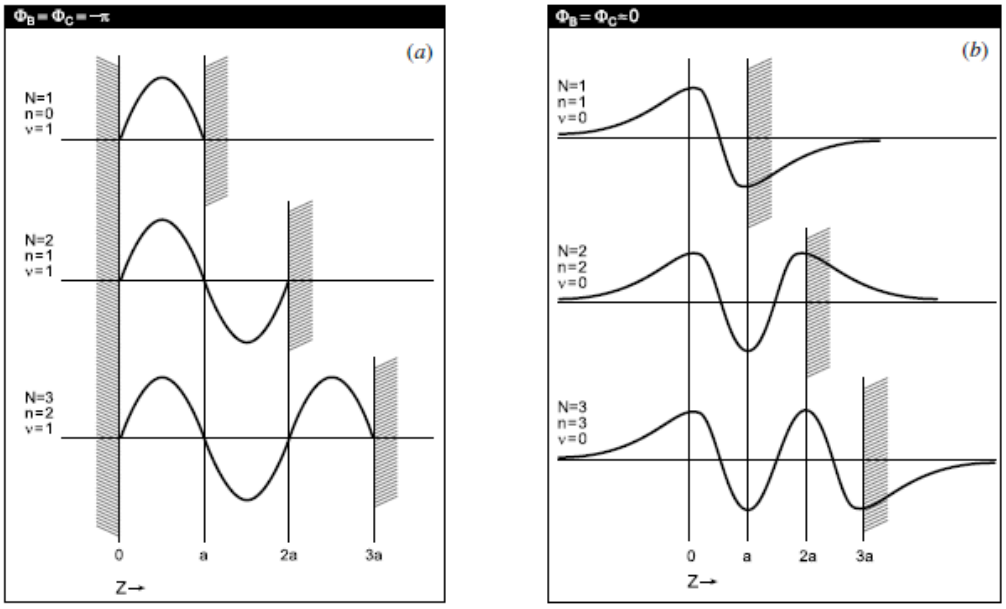

(a) (b)

Fig. 4.4 Wavefunctions of QWS associated to an electron confined in a one-dimensional rectangular well of width a, $2a$ and $3a$, i.e. 1, 2 and 3 atomic layers, calculated by means of the phase accumulation model. (a) $\Phi_{vac}(E) = \Phi_{sub}(E) = \pi$ to obtain the wavefunctions within an infinite quantum well. (b) $\Phi_{vac}(E) = \Phi_{sub}(E) = 0$. to obtain the wavefunctions with antinodes at the well boundaries, i.e. no phase shift [83].

It should be pointed out that the phase accumulation model equation 4.4 reproduces very well the QWS energy positions experimentally measured in metallic thin films [83]. Relations similar to those written for the particle in a box model, i.e. relations 4.1 and 4.2, can be derived from equation 4.4. However, a complete treatment of the problem must take into account the real band structure of the film to extract the proper quantization condition. Furthermore, by comparing Fig. 4.4 with Fig. 4.1 it is evident that the spatial distribution of the QWS standing waves obtained from the particle-in-a-box model and the phase accumulation model look very similar. It should be noted that Fig. 4.4 shows the QWS of electrons confined in thin film 1 ML, 2 ML and 3 ML thick. As already discussed, in the case of an infinite well, the electron wavefunction is fully confined inside the well with nodes at the boundaries. The same result is recovered in Fig. 4.4a by means of the phase accumulation model by assuming $\Phi_{vac}(E) = \Phi_{sub}(E) = \pi$ (see Fig. 4.4a), i.e. by assuming reflection phase shifts such that the incident and reflected waves cancel at the boundary. On the other hand, Fig. 4.4b shows that by assuming reflection phase shifts $\Phi_{vac}(E) = \Phi_{sub}(E) = 0$ leads to the wavefunctions with antinodes at the boundaries. From these results, it is clear that the choice of the reflection phase shifts is intimately linked to the spatial distribution of the QWS standing waves and

more specifically to their boundary conditions. Consequently, the standing waves calculated for a finite quantum well and shown in Fig. 4.1b can be recovered by means of the phase accumulation model as a general case in which the reflection phase shifts have intermediate values between zero and π [83].
It was already discussed that the non-zero values of the QWS standing waves to the well boundaries implies the existence of exponential tails out of the well. In the light of the relation between reflection phase shifts and boundary conditions of the wavefunctions, reduced spatial extensions of the exponential tails correspond to reflection phase shifts close to π, i.e. better localized electrons inside the well [83]. On the other hand, the spatial extension of the tails increases for reflection phase shifts that tend to zero, i.e. the electron localization is slightly lowered. In this sense the reflection phase shifts account for the wavefunction tails out of the quantum well. In an equivalent manner to what was shown for the particle in a box model, the presence of exponential tails increases the wavelength associated to the QWS standing waves and at the same time lower their energies relative to the case $\Phi_{vac}(E) = k_{\perp}(E) = \pi$ (corresponding to the infinite quantum well). Furthermore, as for the particle in a box model, the quantum number n corresponds to the number of wavefunction nodes within the well.

Before concluding this section, it should be pointed out that the phase accumulation model generates solutions that can lie out of the substrate band gap [83]. These solutions, called resonances, are allowed to be coupled with the bulk states of the substrate and therefore they cannot be properly considered confined states. However, it was shown that it is possible to experimentally observe these solutions and discern them from the bulk states because their wavefunction retain information about their nature and their amplitudes are enhanced at the surface.

4.2 Pb thin films and Quantum Size Effects (QSE)

As discussed in the previous section, electrons in metallic thin films grown on a semiconductive substrate are confined along the direction normal to the surface with formation of Quantum Well States (QWS). In this situation the electronic energies get separated in two-dimensional subbands written as follows [85, 83, 86–88]:

$$E = E_{\perp} + E_{\parallel} = \left(\frac{\hbar^2}{2m^*}\right)\left(\frac{n\pi}{Na}\right)^2 + \frac{(\hbar k_{\parallel})^2}{2m^*} \tag{4.6}$$

This equation explicitly shows that the electronic motion is quantized along the confining direction with the component $k_{\perp}$ fixed according to the selected QWS (subband) while it

remains free within the surface of the film with $k_{\parallel}$ ranging from 0 to $k_{\parallel max}$, with determined by the condition $E = E_{\perp} + E_{\parallel} = E_F$.

It is clear then that the electronic properties of metallic thin films can be very different from those of the not-confined bulk materials. In particular, in this section it will be shown that the thickness variation of Pb films grown on a Si(111) substrate by only one single atomic layer can strongly modulate the electronic density of states around the Fermi level and thus also the physical/chemical properties depending on it [85, 87, 88]. In general terms, the notion of Quantum Size Effects (QSE) refer to the fact that the physical/chemical properties of a confined system depend on its size. In other word, QSE allow both the occupation and the configuration of QWS to be tuned by varying the confinement of the system [89].

As widely discussed in the first section of Chapter 3, the first layer of Pb grown on a Si(111) substrate forms a great variety of surface reconstructions as the Pb coverage increases up to the saturation of the wetting layer at 1.3 ML (α phase reconstruction). The origin of this behavior was ultimately attributed to large lattice mismatch (10 %) between the Pb(111) and the Si(111) lattice constants. By further increasing the Pb coverage, flat islands of various sizes with steep edges and different heights start to grow [87, 88].

Fig. 4.5 shows a plot of the QWS energies (dots) as a function of the Pb film thickness, obtained by first-principles calculations in the paper of Wei et al. [88]. It can be easily seen that the branches of QWS, indicated by dotted lines and connecting similar QWS with the same quantum number k, move down in energy as the thickness increases. As a consequence, a new QWS (indicated by red dots in Fig. 4.5) crosses the Fermi level every $\sim$2.2 ML becoming a new filled QWS, i.e. the new Highest Occupied QWS (HOQWS). This periodic event leads to an oscillation of the HOQWS near the Fermi level with period $\sim$2.2 ML which is represented in Fig. 4.5 by green and red dots. From this figure it can be seen that, below 13 ML, odd thicknesses have the HOQWS close to the Fermi level (red dots) while for even thicknesses the HOQWS lies well below the Fermi level (green dots). Above 13 ML the situation is reversed and the origin of this effect will be discussed later. The above mentioned oscillation of QWS close to the Fermi level can be be qualitatively understood by means of the simple particle-in-a-box model. Indeed, by looking at the equation 4.2 it is clear that, for a fixed n, the energy of the QWS decreases as the well width L increases. The periodic QWS crossing of the Fermi level was also deduced by means of the phase accumulation model written in the following form [88]:

$$2k_{\perp}(E) \cdot Na + 2\Phi(E) = 2\pi n \tag{4.7}$$

with $\Phi_{sub}(E) = \Phi_{vac}(E) = \Phi(E)$ because the calculations are performed on freestanding Pb films, i.e. there is no substrate and the two confining interfaces are of the same type

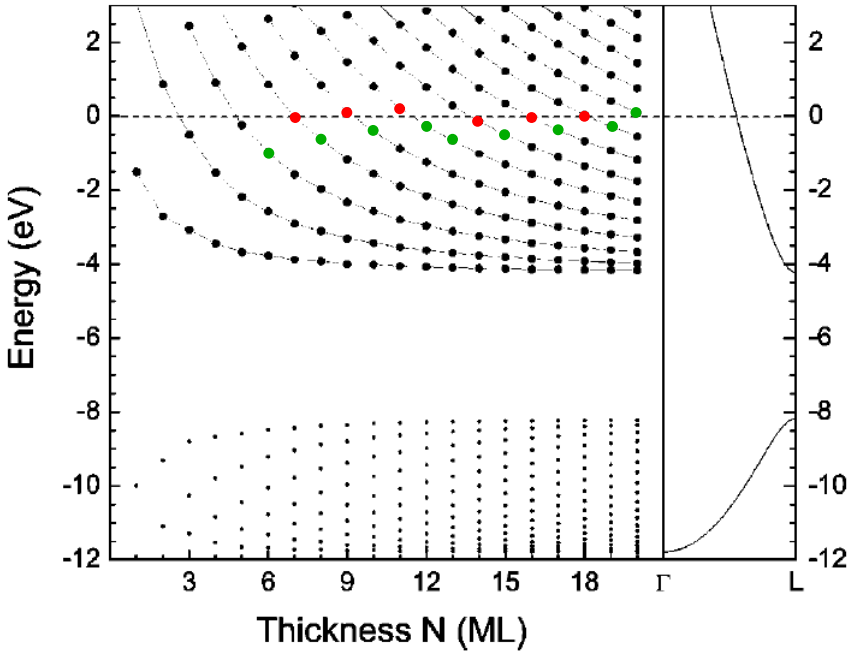

Fig. 4.5 Left panel: QWS energy positions at $\overline{\Gamma}$ as a function of the free-standing Pb(111) film thickness. The Fermi energy is located at energy equal to zero. Right panel: bulk energy dispersion along the [111] direction. Green and red dots highlight the thickness-induced oscillation of the HOQWS close to the Fermi level. In particular, green dots indicate the HOQWS well below to the Fermi level, while red dots represent the HOQWS close to the Fermi level. Adapted from [88].

film/vacuum. Then, the periodicity of the QWS Fermi level crossing can be expressed as follows:

$$\Delta N = \frac{\lambda}{2a} \sim 2.2\ ML \tag{4.8}$$

This value is in agreement with the calculations and it was obtained by considering that the interlayer spacing a for Pb films is equal to 0.286 nm [88] and that the electron wavelength at the Fermi level (λ_F) along the (111) crystallographic direction, i.e. the direction normal to the surface of the film (the confining direction), is $\sim$1.3 nm [88].

The previous result is important to understand the role played by QSE in both the growth and the properties of the Pb islands/films. For instance, Hupalo et al. [87] reported the low temperature (195 K) growth of Pb islands on Si(111) having stable thicknesses differing by two atomic layers. In particular, it was observed that, in a range of 2 ML to 9 ML, the preferred (stable) thicknesses are the odd ones, e.g. 3 ML, 5 ML, 7 ML, etc, while the unstable thicknesses are the even ones, e.g. 4 ML, 6 ML, etc. Note that these thicknesses are measured with respect to the wetting layer. This is clearly observed in Fig. 4.6a, where the just prepared sample exhibits a uniform distribution of even/odd thicknesses. On the

other hand, Fig. 4.6b shows that 40 min after the preparation the surface has evolved and mainly the stable o(dd) thicknesses can be found [87]. In other words, the stability of Pb islands displays an odd/even oscillation of period approximately equal to 2 ML with the odd thicknesses being the most stable. The most important result here is that the just mentioned stability oscillation can be understood as a QSE due to the periodic QWS Fermi level crossing as discussed above.

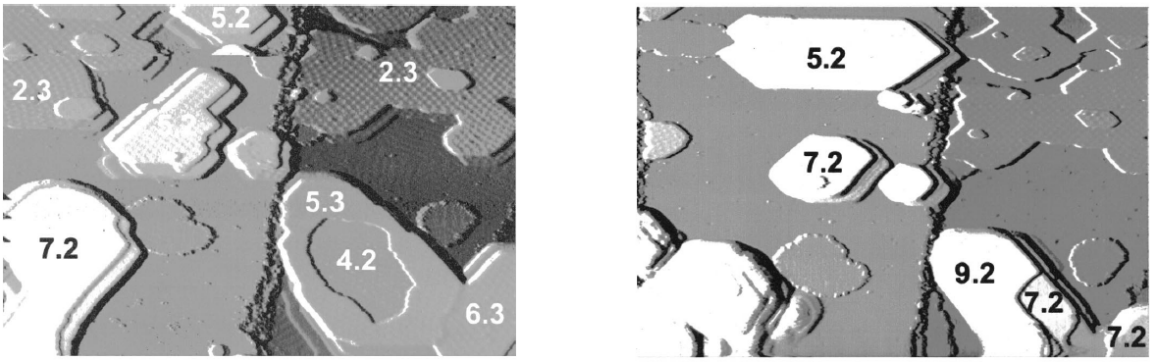

(a) (b)

Fig. 4.6 (a) STM image of a just prepared sample showing a uniform distribution of odd and even Pb island thicknesses grown on Si(111) with a Pb coverage of 3.3 ML (T=195 K). (b) STM image of the same area after 40 min showing the evolution of the surface towards the stable (odd) thicknesses. Image size: $100 \times 200\ nm^2$. The regions between islands is covered by the Pb wetting layer with α-phase reconstruction. The island thicknesses are measured respect to the wetting layer and their values is marked on top of them [87].

Fig. 4.7 shows the QWS around the Fermi level, probed by means of STS measurements, as a function of the Pb island thickness [87]. Note that the first QWS below the Fermi level is usually called Highest Occupied QWS (HOQWS), while the first QWS above the Fermi level is called Lowest Unoccupied QWS (LUQWS). Green (red) arrows indicate the QWS around the Fermi level of stable (unstable) thicknesses respectively. The important message of this paper is that the electronic structure of stable (odd) thicknesses is different from that of the unstable (even) ones and that the position of the HOQWS with respect to the Fermi level can be ultimately related to their stability [87, 90]. In particular, from Fig. 4.7, it can be seen that the HOQWS of stable (odd) thicknesses is located at lower energies with respect to that of the unstable (even) ones.

As discussed above, when the Pb island thickness increases by $\sim$2.2 ML, a new QWS moves below the Fermi level. Consequently, the HOQWS energy position oscillates relative to the Fermi level with a period of $\sim$2.2 ML by inducing oscillations of the total energy of the system with the same periodicity. We can try to understand the mechanism behind the energy oscillation that ultimately determines the stability of a given thickness. It should be kept in

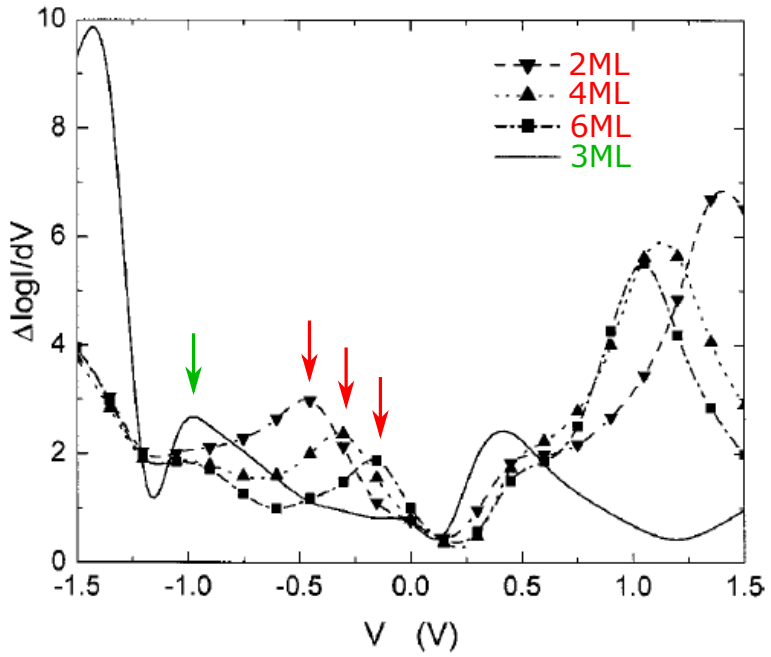

Fig. 4.7 ΔlnI/ΔlnV curves as a function of the bias voltage V for odd and even Pb island thicknesses. Green (red) arrows indicate the HOQWS well below (close to) the Fermi level of stable (unstable) thicknesses. In particular, for stable (odd) thicknesses the position of the HOQWS is at lower energy with respect to that of the unstable (even) ones. Adapted from [87].

mind that the energy position of the HOQWS affects the total energy of the system because it is the filled electronic level with the highest energy in the system. In particular, when a QWS crosses the Fermi level, it starts to be filled of electrons becoming the new HOQWS. The closeness of the latter to the Fermi level leads to an increase of the total energy of the system. As the thickness is increased by 1 ML, the number of electrons within the HOQWS increases but at the same time it continues to fall in energy, that is, the HOQWS moves away from the Fermi level towards lower energies leading to a decrease of the total energy of the system. If the thickness is further increased by 1 ML, a new QWS will cross the Fermi level and it will start to be filled of electrons leading to a new increase of the total energy. By repeating the same reasoning, the oscillation of the total energy of the system with the thickness is achieved (periodicity of $\sim$2.2 ML).

An equivalent way to describe the total energy oscillation induced by the oscillation of the HOQWS around the Fermi level is the following. The electrons within a QWS close to the Fermi level, i.e. Pb islands with even thicknesses, are closer to the vacuum level and their wavefunction leaks out of the film/vacuum interface more than that of electrons within QWS at lower energies, i.e. odd thicknesses. The leakage of the wavefunction corresponds to a

charge spilling. Whenever a charge spilling occurs, the system reacts by generating a dipole layer at the surface of the island to ensure the charge neutrality. Therefore, the dipole strength increases if the charge spilling increases. This is the reason for which a QWS close to the Fermi level is accompanied by a strong dipole. Ultimately, the oscillation of the HOQWS around the Fermi level (with period 2.2 ML) implies an oscillation of the dipole strength with the same periodicity (an even/odd oscillation of the dipole strength is achieved). Usually, the minimum total energy for the system is expected when the charge spilling is minimum, i.e. when the strength of the dipole is minimum and thus when the HOQWS is far from the Fermi level at low energies. These considerations allow us to conclude that the most stable thicknesses are those with the HOQWS at lower energies (see Fig. 4.7).
The main conclusion of this part is that the electronic structure of Pb islands can be related to their stability and the bilayer oscillation of the stability itself can be understood as a result of QSE. It is interesting to note that the same QSE mechanism of dipole oscillation is the basis of the work function, electron density and surface energy oscillations [87, 91, 92].

Another interesting work revealing the intricate role of QSE on the thickness-dependent stability of Pb islands on Si(111) is that of Zhang et al. [93, 94]. The aim of these papers was the investigation of both the growth mode and the stability of Pb films deposited at low temperature (145 K) on top of the Si(111)-7 $\times$ 7 surface. An extended range of coverages was investigated, i.e. up to 24 ML. Furthermore, the behavior of the films under annealing at room temperature has allowed to better understand what is the role of QSE during the growth and to what extent the different thicknesses are actually stable.

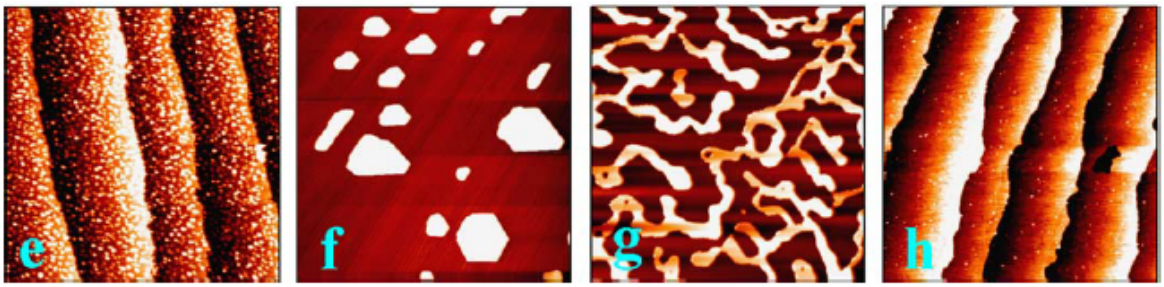

Fig. 4.8 Room temperature STM images of Pb films growth at low temperature (145 K). First panel: 1 ML, second panel: 3.5 ML, third panel: 6 ML and fourth panel: 10 ML. Image size: $2000 \times 2000\ nm^2$ [93].

Before analyzing the behavior of Pb films at room temperature let's resume the low temperature growth (180 K [95]) of Pb on Si(111)-7 $\times$ 7 [93, 94]. In the early stages of Pb deposition an amorphous wetting layer is formed and it is completed at $\sim$1.5 ML [95]. By increasing the coverage three dimensional islands, 5 ML thick, start to form above the wetting layer. A

2D growth mode follows up to 6 ML where a flat Pb film is completed [95]. In other words, up to 6 ML only lateral growth of islands takes place without increase of their thickness fixed at 5 ML. Above 6 ML a layer-by-layer growth mode follows. It should be outlined that 6 ML includes includes the wetting layer, i.e. it represents the total thickness from the Si(111) surface.

Fig. 4.8 shows room temperature STM images of annealed Pb films taken at different stages of the growth [93, 94]. The first panel displays the amorphous wetting layer surviving at room temperature. Remaining panels reveal a different evolution of the system. In particular, the second panel shows that, below 6 ML, three dimensional $\sim$10 ML thick Pb islands lie above the wetting layer. Furthermore, above 6 ML instead of having a layer-by-layer growth of uniform films, a network of 10 ML thick islands is observed (third panel) and a 2D growth mode follows up to $\sim$10 ML where a flat film is completed. The last panel shows that, above 10 ML, the films remain stable and uniform even at room temperature. The main result here is that, at low temperature, 5 ML represents a critical thickness below which Pb films are unstable. When the films are annealed at room temperature the critical thickness increases to 10 ML, i.e. below this thickness Pb films become unstable [93, 94].

In order to have more insight about the Pb films growth the so-called "electronic growth" model was addressed [93, 94, 96]. According to this model, the stability of thin films grown on semiconductor substrates critically depends on the different electronic contributions to the total energy of the system. More interestingly, this model makes it possible to explain how QSE can induce the presence of either "magic" or critical stable thicknesses. It considers three key ingredients: (1) electron confinement mediating an effective repulsive interaction within the film stabilizing the film itself; (2) charge spilling from the film to the substrate resulting in an attractive interaction that destabilizes the film; (3) interface-induced Friedel oscillations of electron density within the film able to both modulate the relative strength of previous competing interactions and tune the stabilities of the system as a function of the thickness [96].

Fig. 4.9 shows the total energy curves calculated by means of the "electronic growth" model for different metallic films on GaAs [96]. The red curve has a local minimum at $\sim$5 ML making the film stable at this thickness. Above 5 ML the curve is quite flat and thus all the thicknesses are stable, i.e. 5 ML represents a critical thickness. On the other hand, the green curve exhibits a strong minimum at 1 ML making film thicker than 1 ML unstable. In the context of this model this condition implies that it is not possible to grow flat and uniform film thicker than 1 ML but the system can always go into a rough phase with different thicknesses coexisting on the surface [96]. Blue and yellow curves represent a special case in which the Friedel oscillations contribution is particularly strong giving rise to

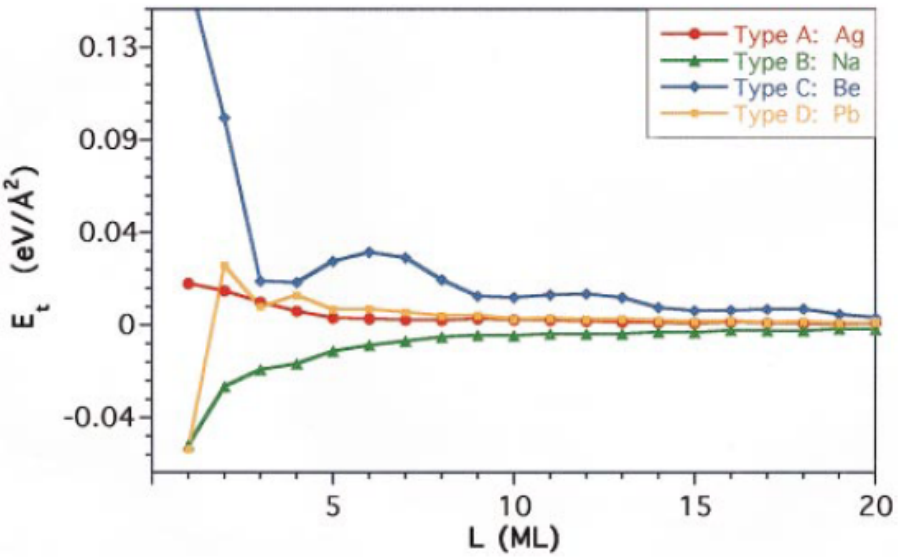

Fig. 4.9 Total energy curves calculated by means of the "electronic growth" model revealing different types of film stabilities for different metallic films on GaAs [96].

the oscillating behavior of the total energy with many local minimum. For the blue curve the local minimum at 3 ML indicates that the film is stable at this "magic" thickness, i.e. smaller and larger thicknesses are unstable. On the other hand, 9 ML represents a critical thickness because the oscillation is sufficiently damped to allow larger thicknesses to be stable. The most interesting case to us is the yellow curve because it represents the energy curve of Pb. It is characterized by a periodic oscillation with period of $\sim$2 ML (as previously discussed) damped by a factor $\propto \frac{1}{d^2}$ (with d the thickness of the film). These results show that the "electronic growth" model is very powerful because it captures the different electronic contributions to QSE. Moreover, it shows the important role of the latter in the thickness-dependent film stability for different cases [96]. It should be pointed out that in any case as the thickness increases the energy curve oscillations are completely damped and their value gradually approaches that of the bulk. This means that QSE and related oscillations can be better observed for very thin films when the electron confinement is strong [85, 88, 96, 91].

Coming back to the observations of Fig. 4.8, Zhang et al. make use of the "electronic growth" model to explain the evolution of Pb films from low to room temperature [93, 94]. The idea is that when Pb thin films are prepared at low temperature (145 K) the system lie in a local minimum of energy giving rise to a critical thickness of 6 ML. Thermal energy provided to the system by annealing at room temperature brings the system into an another local

minimum corresponding to a critical thickness of 10 ML [93, 94].

Above 10 ML the growth of Pb islands continues through an even/odd stability oscillation with a period of 2 ML similar to that previously discussed. In particular, it was observed that uniform flat films are obtained when the thickness is stable (see Fig. 4.10 (a)), while a non-uniform film with a mixture of adjacent stable thicknesses is observed when the sample is prepared with an unstable nominal coverage of Pb (see Fig. 4.10 (b)). Above 21 ML the Pb growth has a quasi layer-by-layer behavior and flat films are obtained for each thickness. To correlate the thickness stability information gained with STM to the electronic structure of Pb islands the HOQWS were measured by photoemission spectroscopy (PES) as a function of the island thickness [93, 94]. It is easy to see from Fig. 4.10 (c) that when the film is uniform, i.e. it has a stable thickness, one single sharp peak is observed, e.g. for 10 ML/12 ML/13 ML/15 ML/17 ML/19 ML, while when it is a mixture of adjacent stable thicknesses, e.g. for 11 ML/14 ML/16 ML/18 ML/20 ML, also the HOQWS is a mixture of the corresponding QWS, i.e. the peak is quite broad and not well developed. Therefore, the lineshape of QWS measured in photoemission gives information about the quality of the prepared films [97].
Also in this case the electronic structure of Pb islands can be related to their stability, i.e. thicknesses with larger separation of the HOQWS from the Fermi level are stable. Furthermore, the bilayer stability oscillation can be explained as a result of a QSE mechanisms similar to that previously described, i.e. a new QWS moves below the Fermi level as the Pb island thickness increases by $\sim$2.2 ML and the HOQWS energy position oscillates relative to the Fermi level with the same period [88, 93–95]. This oscillation of the density of states around the Fermi level implies an oscillation of the total energy and thus of the film stability. The switching from bi-layer growth below 20 ML to quasi layer-by-layer growth above 20 ML can be explained by means of the "electronic growth" model that predicts damped oscillations of the energy with period $\sim$2 ML (see Fig. 4.11) [93, 96, 94, 95]. In other words, for small thicknesses the energy difference between a stable and an unstable thickness is pronounced because of the strong oscillations of the energy itself, i.e. the system exhibits a bi-layer growth. For large thicknesses the energy difference is not appreciable because of the damped oscillations, i.e. there are no preferred thicknesses and a quasi layer-by-layer growth is allowed. This behavior can equivalently be seen as the result of the fact that QWS for small thicknesses are largely spaced in energy, therefore the energy variation between adjacent layers is pronounced. This effect is reduced at higher thicknesses where the QWS start to be close due to the electron confinement weakening. Fig. 4.11 shows calculated QSE-induced oscillations of the of Pb films surface energy as a function of the thickness, i.e. a measure of

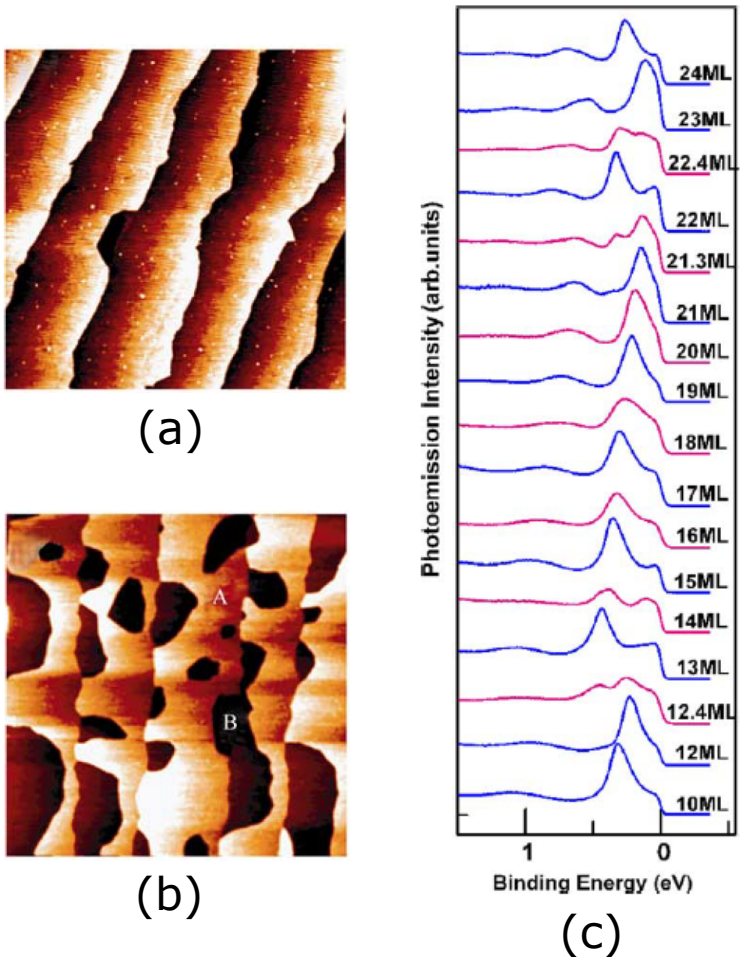

Fig. 4.10 Room temperature STM images of Pb films with nominal coverage of 13 ML (a) and 14 ML (b). (a) When the nominal coverage corresponds to a stable thickness uniform flat films are obtained. (b) When the nominal coverage corresponds to an unstable thickness rough films with a mixture of stable thicknesses are observed, e.g. in figure (b) the nominal coverage is 14 ML and a mixture of 13 ML and 15 ML is observed. Image size: $2000 \times 2000\ nm^2$ [94].

the relative stability of different film thicknesses. Both the damped character of the 2 ML oscillations as well as the film stability observed in experiments are well reproduced by these data [94].

Careful inspection of Fig. 4.11 reveals another interesting aspect. 13 ML, 22 ML and 31 ML correspond to turning point where the thickness stability is periodically transferred from even to odd thicknesses and vice versa [91, 94, 95]. The origin of this effect can be traced back to relation 4.8 and in particular to the mismatch between $\lambda_F/2$ and d leading to the stability period of $\sim$2.2 ML. In practice, ΔN must be an integer number because the film thickness can only change an integer number of atomic layers. Ultimately, the mismatch

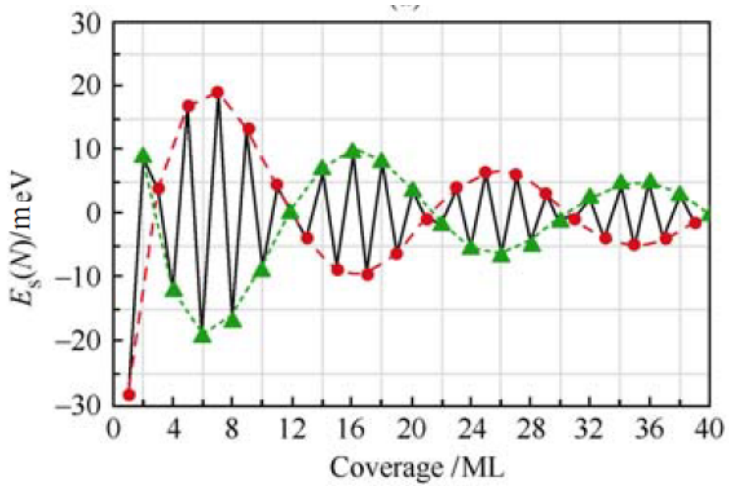

Fig. 4.11 Calculated surface energy of Pb films as a function of the thickness [94].

between the stability period 2.2 ML and the real thickness variation 2 ML gives rise to a beating effect with a ∼9 ML period which reverses the even/odd stability of thicknesses. This effect was experimentally observed in Fig. 4.10 by the occurrence of a HOQWS particularly far from the Fermi level at 13 ML and 22 ML indicating the odd/even switching [93, 94].

After the discussion about the role of QSE on both the growth mode and the stability of Pb films on Si(111), a brief overview about QSE on the other properties of this system will given. The work of Schulte et al. is one of the first to have shown that quantum confinement of electrons can have profound effect on other physical/chemical properties of the system [92].

4.2.1 QSE on charge density and the "apparent" step height of Pb thin films

Materzanini et al. [91] have investigated by means of ab initio calculations the QSE-induced oscillations on both the total energies and the electron densities of Pb films on Cu(111). Most of the calculations were performed on free-standing Pb slabs (with thicknesses ranging from 1 ML and 15 ML) and the effect of the substrate was separately taken into account by considering an in-plane compression within the slabs. The results about the total energy oscillations are in agreement with what was said so far [88, 93, 94, 96].
More interestingly, calculated oscillations of the electron densities coming out of the film/vacuum interface (due to the QWS standing waves) provide important information about the "apparent" height of Pb islands measured by STM. The term "apparent" refers to the fact that the actual thickness of an island is determined by two contributions: geometric

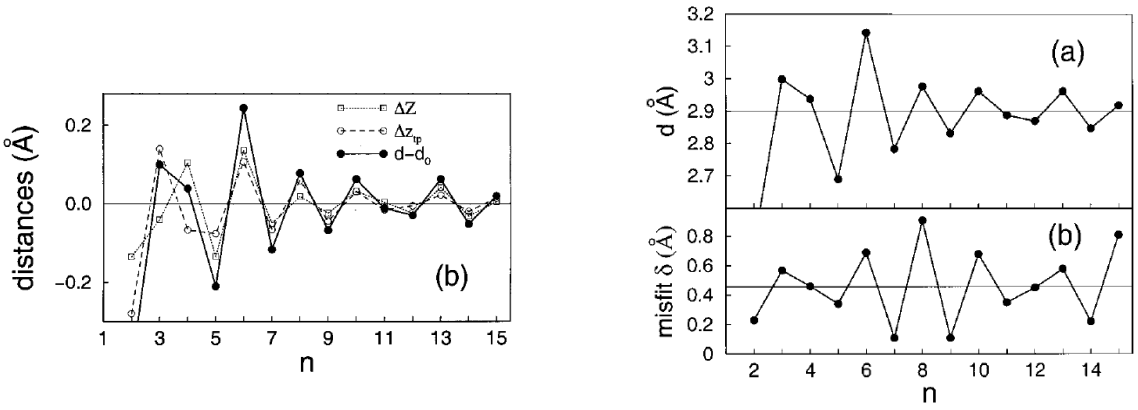

(a) (b)

Fig. 4.12 (a) Plot of the calculated quantities ΔZ, Δz and $\Delta Z + \Delta z = d - d_0$ as a function of the film thickness. Note how both the geometric (ΔZ) and electronic (Δz) effects contribute with similar magnitude to the total apparent height $d - d_0$. (b) Plot of the calculated apparent step height d and misfit function δ as a function of the thickness. Note that if δ is small also the apparent height d is small and vice versa [91].

and electronic. The geometric contribution is due to the interlayer relaxation that may take place during the growth of the film itself, while the electronic contribution is due to the exponential tails of the QWS standing waves extending out of the film/vacuum interface (see section 4.1). Fig. 4.12a shows a plot of the quantities ΔZ, Δz and $\Delta Z + \Delta z = d - d_0$ as a function of the film thickness. ΔZ (Δz) is the measure of the change in "apparent" height of a single atomic layer with respect to the expected value for the bulk Pb, i.e. 2.9 Å [91], due to geometric (electronic) effects. On the other hand, $\Delta Z + \Delta z = d - d_0$ represents the total "apparent" height. Positive or negative values of these quantities indicate expansion or contraction of the layer respectively. The main result of Fig. 4.12a is that, as for the other QSE-induced oscillations discussed so far, also the apparent height exhibits damped oscillations with a period of $\sim$2 ML. Surprisingly, geometric and electronic effects contribute with similar magnitude to the total "apparent" height meaning that neither of them can be neglected with respect to the other. These results are in agreement with the X-ray diffraction measurements performed by Czoschke et al. [98] that have revealed quasi bi-layer oscillations not only for the outermost layer but also within the structure of the film itself, i.e. oscillations in the atomic interlayer spacing. The origin of these oscillations can ultimately be ascribed to the charge density oscillations related to the QSE.

A better understanding of the electronic contribution to the apparent height can be obtained by considering that as the film thickness increases, every $\sim$2.2 ML, new QWS move below the Fermi level becoming the new HOQWS. The net result of the thickness increasing is the

energy oscillation of the HOQWS with respect to the Fermi level. Furthermore, the spatial extension of the exponential tails out of the film associated to the QWS standing waves depends on their energy (see Section 4.1). Consequently, the HOQWS oscillations induce oscillations of the electron density out of the film with the same period of ∼2.2 ML.
The relation between the geometric and the electronic contribution can be better understood by means of the so-called misfit function [91]:

$$\delta(N) = \left| N d_0 - m\frac{\lambda_F}{2} \right| \tag{4.9}$$

with N the number of atomic layers, d_0 their distance for the bulk Pb(111), i.e. 2.86 Å, and m an integer making δ a minimum. This function is a measure of the level of commensurability of the QWS standing waves within the quantum well width, i.e. within the thickness of the film. If δ is small the electrons are better confined within the film, i.e. the spatial extension of exponential tails out of the film/interface is reduced. On the other hand, if δ is large the exponential tails extend over larger distances out of the film. According to this interpretation, Fig. 4.12b shows that when δ is small also the apparent height d is small and vice versa. The oescillation of the interlayer distance d around the bulk value with a period of ∼2.2 ML is ultimately due to the HOQWS oscillation.
The problem of the "apparent" step height is important when Pb thin films are investigated by means of probes like STM or He atom scattering that are sensitive to the surface electron density and thus to their oscillations. Indeed, the STM/STS work of Su et al. [90] has revealed bilayer oscillations of Pb island "apparent" thicknesses around the theoretical expected values. In particular, it was observed that the "apparent" thickness of stable islands is contracted and that of unstable islands is expanded. The oscillating effect was attributed to QSE and both the electronic and the structural contributions were considered responsible for it.
Ultimately, the geometric and electronic contributions to the "apparent height" ΔZ and Δz are not independent but they are intimately linked between them. This happens because, when the film thickness is increased, new QWS move below the Fermi level and the film itself enriches of electrons leading to structural relaxation [91, 90, 98, 99]. Fig. 4.12a further highlights this correlation between electronic (Δz) and geometric (ΔZ) contribution. This phenomenon can be explained by thinking that the structural relaxation always acts to minimize misfit function 4.9 because the total energy of the system is minimized when the charge spilling is minimal, i.e. when confined electrons fit better into the quantum well [94, 87, 99]. As already said, each time new QWS move below the Fermi level the electron density outside the film oscillate as a function of the film thickness. Therefore, a larger structural relaxation is expected for a film with unstable thickness because confined electrons extend out of the

film and δ is large. On the other hand, a smaller structural relaxation is expected for a film with stable thickness because, in this case, the electrons are better confined within the film itself and δ is small [96, 91, 90]. In conclusion, the bilayer oscillation of the "apparent" height of a Pb film can be traced back to QSE and to the role of QWS in determining the stability of the film itself. The "apparent" height of a film is determined by both geometric and electronic contributions. Ultimately, stable thicknesses will exhibit smaller "apparent" heights and unstable thicknesses will exhibit larger "apparent" heights.

4.2.2 QSE on the work function of Pb thin films

QSE-induced oscillations of the charge density out of the Pb films discussed in previous section implicitly reflect oscillations in the work function of the system. Kim et al. [100] were able to reveal these oscillations by means of STM/STS measurements on Pb thin films grown on Si(111). The strategy was to experimentally measure the tunneling decay constant κ thanks to the fact that it is linked to the tunneling current I_T as follows:

$$I_T \propto \exp^{-2\kappa z} \qquad \Longrightarrow \qquad \kappa = -\frac{d\ln I}{2dz} \tag{4.10}$$

where z is the tip-to-sample distance. By approximating the tunneling barrier with a trapezoidal barrier (see Chapter 2) its effective height can be related to the tunneling decay constant κ:

$$\Phi_{eff} = \frac{(\hbar^2\kappa^2)}{2m} \sim \frac{(\Phi_s + \Phi_t - e|V_s|)}{2} \tag{4.11}$$

where Φ_t and Φ_s are the work functions of tip and sample respectively and V_s is the bias voltage between tip and sample. Previous equation provides a direct relation between the tunneling decay constant (experimentally measurable) and the work function of the sample. The importance of this study lies in the fact that it shows how the presence of QWS makes the approximation 4.11 inapplicable in most of the bias range. Furthermore, only when V_s approaches zero, the experimental measurements are able to reveal QSE-induced oscillations of the work function [100].

The reason for that lies within the definition of work function of a metal, that is, the energy difference between the Fermi level and the vacuum level. This definition intrinsically implies that, to measure the work function with STM/STS, bias voltages close to zero must be used. In this way, only the electrons around the Fermi level are involved in the tunneling process and variation of tunneling current can be connected to variations of κ and thus of the work function (see equation 4.10 and 4.11). The upper panel of Fig. 4.13 shows a plot of

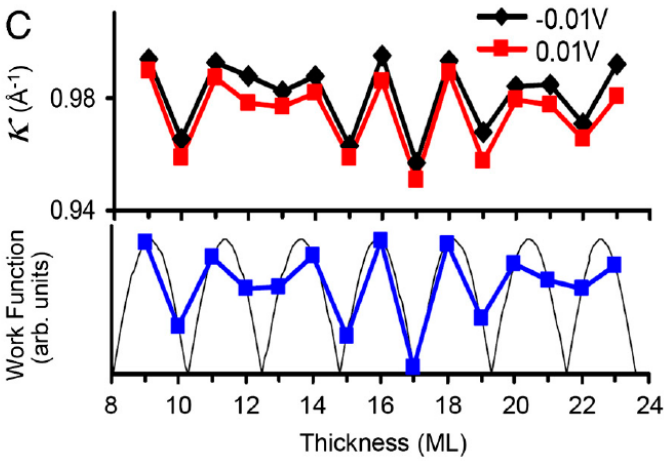

Fig. 4.13 Upper panel: Measured values of κ as a function of the thickness at + 0.01 V and - 0.01 V. Lower panel: Comparison between measured values of the work function and the simulated curve [100].

κ (extracted from STS measurements) as a function of the thickness. Bilayer oscillations, ascribed to QSE-induced oscillations of the work function, are observed for both positive and negative voltages (red and black points respectively). The lower panel of Fig. 4.13 shows the agreement between the experimental values of the work function extracted from κ (blue dots) and the simulated work function for a thickness that varies continuously (black line). The cusp points of the simulated curve correspond to the thicknesses where a QWS exactly crosses the Fermi level leading to a minimum of the work function [100]. This is because when the HOQWS is close to the Fermi level the effective barrier height separating the electrons from the vacuum is lower than that for the electrons within QWS at lower energies. QSE-induced work function oscillations can then be explained with the following argument. As the film thickness increases, new QWS move below the Fermi level. The discrete increasing of film thickness leads to the periodic oscillation of the HOQWS energy position (period of $\sim$2.2 ML) with respect to the Fermi level and thus also of the work function.

4.2.3 QSE on the electron-phonon coupling of Pb thin films

As already said in Section 4.2.1 the QSE can modulate the structure of thin films by means of either contraction or expansion of the interlayer spacing [99]. It is clear then, that QSE can induce modulations of the electron-phonon coupling by means of these structural changes. Zhang et al. [94, 101] have performed temperature-dependent photoemission experiments to measure the QWS of Pb thin films grown on Si(111) and extract the electron-phonon coupling

constant λ. In the temperature conditions of these kind of experiments, the peak width ΔE of the QWS is considered to be mainly due to the phonon broadening and it depends on the temperature T [94, 97, 101, 102]. In particular, for temperatures higher than one third of the Debye temperature, the width ΔE is mainly determined by the phonon broadening and it can be related to the temperature as follows

$$\Delta E \propto 2\pi\lambda k_B T \tag{4.12}$$

This equation predicts a linear increase of the QWS linewidth ΔE with the temperature, and the slope is determined by the electron-phonon coupling constant λ. Fig. 4.14a shows the experimental QWS peak widths, for 22 ML and 23 ML Pb films, measured as a function of the temperature confirming the linear behavior of ΔE. Careful inspection of the figure

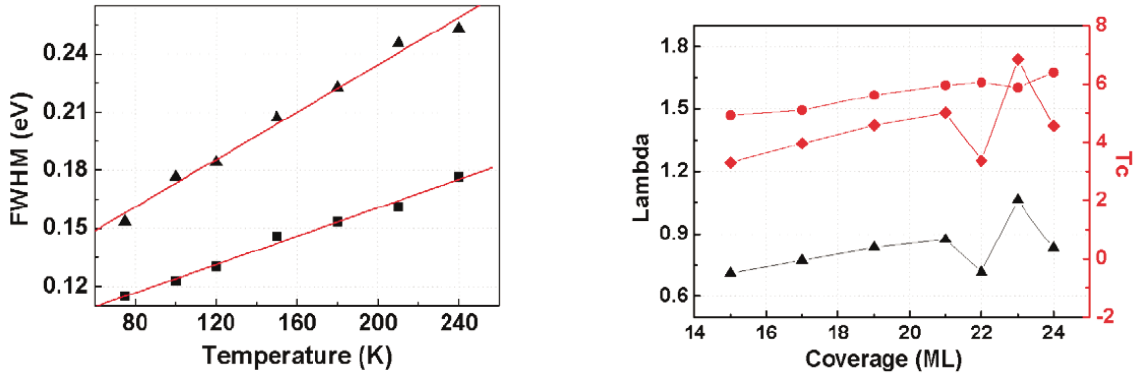

(a) (b)

Fig. 4.14 (a) Experimental QWS peak widths ΔE as a function of the temperature for 22 ML (square) and 23 ML (triangle) Pb films. (b) Upper part: Calculated (diamonds) and experimental (circles) values of T_c as a function of the Pb film thickness. Lower part: experimental values of λ (circles) as a function of the Pb film thickness. [101]

reveals a different slope for the two thicknesses that, by looking to equation 4.12, can be related to a change of the electron-phonon coupling constant when the thickness of the Pb film changes. The electron-phonon coupling constant can be derived from previous equation

$$\lambda = \frac{1}{2\pi k_B}\frac{d\Delta E}{dT} \tag{4.13}$$

The lower part of Fig. 4.14b shows the experimentally deduced values of λ (black experimental points) for different thicknesses. A monotonic behavior is observed up to 21 ML and starting from this value, λ oscillates with a period of $\sim$2 ML [94, 101]. Similar oscillations of λ were predicted for films with smaller thicknesses by Ligges et al. [102]. The origin of these

oscillations was ascribed to the oscillation of QWS close to the Fermi level. It is interesting to note that the curve of Fig. 4.14b tends to the bulk value of $\lambda \sim$1.1-1.7 [94, 102]. Ligges et al. [102] have proposed that the discrepancy between the value of λ measured on bulk Pb crystals and on thin films could be explained by considering in addition to confinement effects and related structural modifications also the effect of the silicon substrate on the QWS themselves. In particular, it was shown that, for Pb thin films, the QWS at Γ exhibit a p_z character. Furthermore, the main contribution to λ mainly arises from these p_z-like electrons. Interestingly, p_z orbitals are also those through which the Pb films interact with the substrate (at least the first Pb layer on top of the silicon). Ultimately, when the film thickness is decreased, the Pb/Si(111) interface effects cannot be neglected as in the case of a bulk sample. One of the possible interface-induced effects is the modification of the orbital character of QWS, i.e. p_z QWS acquire a partial p_x or p_y character. By recalling that λ is mainly due to p_z electrons, it is clear that such a substrate-induced modification could reduce the value of λ as experimentally observed. In conclusion, oscillations of λ are due to thickness-induced oscillations of the QWS close to the Fermi level. However, in this case the most important effect of QWS on λ is the monotonic modification of its strength as a function of the thickness, that is, in addition to the oscillations λ is reduced when the thickness is reduced. This is a direct effect of the Pb/Si(111) interface on QWS which in turn modify λ confirming the fact that the presence of the interface cannot be neglected when the thickness of the Pb film is reduced.

4.3 Pb/Si(111): Moiré corrugation

In the first part of this section, I will describe the origin of the moiré observed on top of Pb islands/films grown on Si(111). In the second part, I will focus on the role played by confined electrons (QWS) in determining the moiré corrugation observed in STM experiments. In the final part, I will show that, for very thin Pb layers grown on Si(111), structural effects at the Pb/Si(111) strongly contribute together with electronic effects in determining the moiré corrugation.

4.3.1 Structures at the Pb/Si(111) interface and moiré corrugation

When Pb islands, epitaxially grown on top of a Si(111) substrate, are observed by means of STM, different kind of superstructures are observed such as the one presented in Fig. 4.15 [103, 104]. To understand the origin of this phenomenon the first thing to know is that when Pb films are grown on Si(111) two different structures can be obtained at the Pb/Si interface:

one in which the 7×7 reconstruction is preserved and the other in which it is destroyed. If Pb is deposited directly on top of the Si(111)-7×7 surface, either at room or at low temperature, the 7×7 reconstruction is preserved during the growth [105]. This is the case illustrated in Fig. 4.15 (a). On the left an STM image of a Si(111)-7×7 reconstructed surface is shown while the image on the right is taken on a 14 ML Pb island grown on top of the Si(111)-7×7 surface itself. Different works agree about the fact that the periodic superstructure observed on top of the Pb island does not correspond to the top morphology of the island itself but it is the projected image of the buried Pb/Si(111)-7×7 interface [103, 104, 106]. Indeed, the superstructure consists of triangular domains (dark triangles) separated by domain walls (bright triangular edges) and both the periodicity and the axes of symmetry coincide with those of the Si(111)-7×7. Altfeder et al. [106] have proposed that the bright dots overlapped to the superstructure represent silicon clusters originating from some Si adatoms of the 7×7 reconstruction displaced by the Pb atoms during the growth. These defects are mainly located at the corner of the triangular domains [103].

An alternative method for growing Pb films/islands on Si(111) consists of a two-step

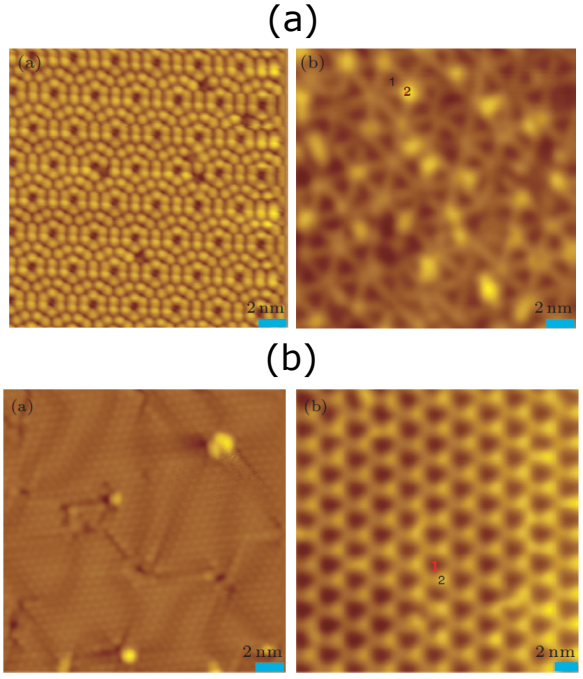

Fig. 4.15 (a): STM image of a Si(111)-7×7 reconstructed surface (left) and of a 14 ML Pb island directly grown on the Si(111)-7×7 (right). (b): STM image of the wetting layer with α phase reconstruction (1.3 ML) (left) and of a 14 ML Pb island grown on the Si(111)-α Pb surface (right) [103].

procedure [103, 104]. Note that this is the procedure used for the experiments described in the following of the manuscript (starting from section 4.4) because it allows the stabilization

of 3 ML Pb islands/films on Si(111). Firstly, a little more than 1 ML of Pb is deposited on the Si(111)-7 $\times$ 7 surface. Then, the sample is annealed at around 300° C. The annealing destroys the 7 $\times$ 7 reconstruction by leaving a bulk-terminated Si(111) surface. Furthermore, this step leads to a crystalline Pb wetting layer $\sim$1 ML thick exhibiting one of the surface reconstructions discussed in Chapter 3 depending on the Pb coverage left on the surface. In the second step Pb films/islands can be grown by depositing additional Pb at either room or low temperature. In particular, the growth of Pb islands/films starts only when the Pb wetting layer reaches the saturation coverage of 1.3 ML and thus the surface reconstruction we already called α phase [103, 107]. Fig. 4.15 (b) shows STM images of a sample prepared with this method. The left image displays the 1.3 ML α phase of the wetting layer while the right image shows the surface of a 14 ML Pb island grown on top of the α phase itself.

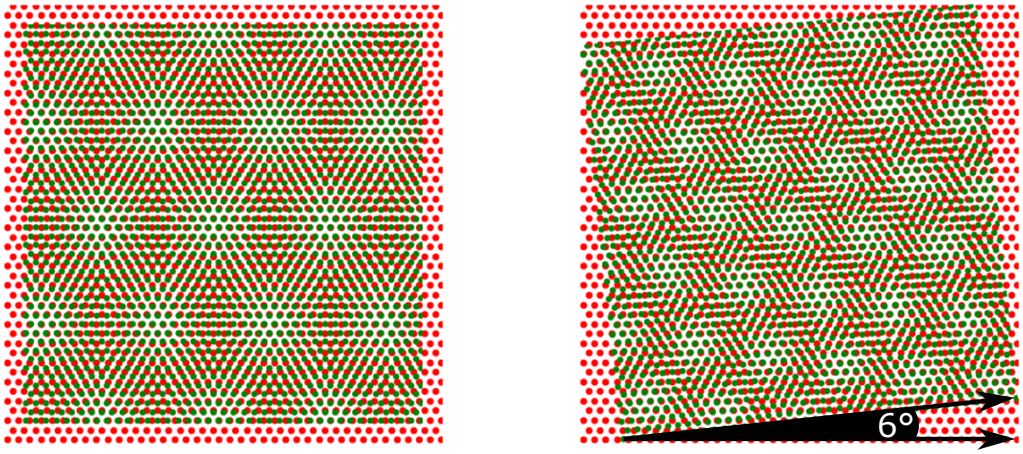

(a) (b)

Fig. 4.16 Schematic illustration of the moiré origin. (a): Two atomic lattices (green and red dots) with a lattice mismatch are superimposed with their close-packing directions aligned. As a consequence of the lattice mismatch a moiré superstructure (bright regions) appears and its orientation is aligned with those of the underlying lattices. (b): The same atomic lattices are now rotated by 6°. As a consequence both the period and the orientation of the moiré are changed.

Different studies [103, 104] agree on the fact that the hexagonal superstructure observed on top of Pb islands grown on Si(111) (see the right part of Fig. 4.15 (b)) is the projected image of the buried interface between Pb and Si(111). In particular, it was interpreted as a moiré effect at the Pb/Si(111) interface due to the overlapping of two atomic lattices with different lattice constants, i.e. the Pb(111): 0.350 nm and the Si(111): 0.384 nm [104]. Fig. 4.16 illustrates schematically the origin of a moiré pattern. In particular, Fig. 4.16a

shows two overlapped atomic lattices (green and red dots) with hexagonal symmetry and a lattice mismatch. The moiré superstructure can be easily identified by looking at the bright regions arranged in a hexagonal pattern. It is clear that the moiré retains the same hexagonal symmetry of the two underlying lattices and its axes of symmetry are accordingly aligned. Fig. 4.16b shows an interesting phenomenon taking place when one of the two lattices is rotated with respect to the other (6° in Fig. 4.16b). In this case, the moiré superstructure has a smaller periodicity with respect to the non-rotated case and presents a rotation. As will be shown later, a precise relation between period/orientation of the moiré as a function of the rotation angle between the two underlying lattices (6° in Fig. 4.16b) can be defined.

As already said, the origin of the moiré superstructure is the lattice mismatch between the Pb and Si. In order to minimize the strain, when Pb islands grow on top of the Si(111) surface, they actually grow with different orientations with respect to the substrate leading to different interfacial structures and therefore different moiré superstructures [104, 108]. Fig. 4.17a and Fig. 4.17b show a concrete case of Pb islands (11 ML) grown on Pb/Si(111)-α exhibiting moiré patterns with different periods and orientations due to the fact that they form different angles with respect to the silicon substrate.

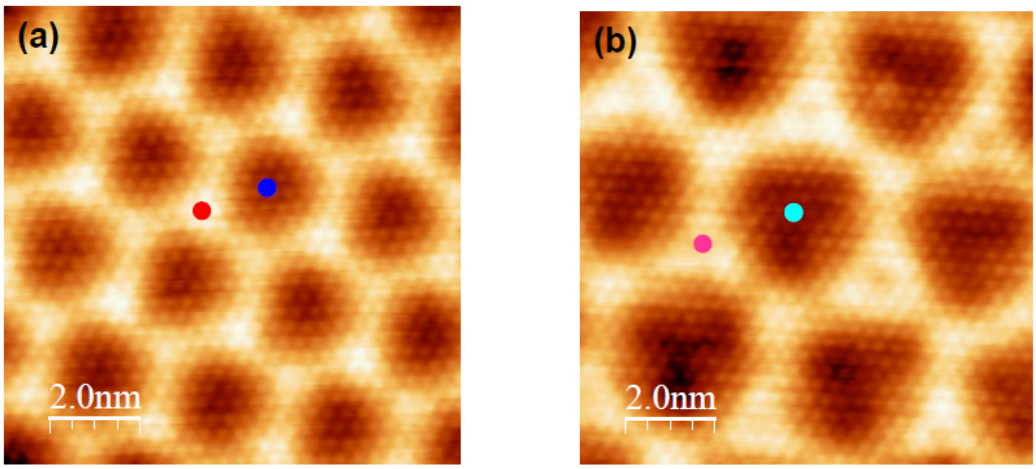

(a) (b)

Fig. 4.17 STM images taken on top of 11 ML Pb islands grown on top of the Pb/Si(111)-α surface. The large hexagonal structure represent the moiré pattern while the hexagonal lattice of small protrusions is the atomic resolution on the Pb surface. It is evident that the moiré on the left has a smaller period than that on the right and their orientation respect to the Pb lattice is different. This is due to the fact that the two islands form different angles respect to the silicon substrate [109].

The main conclusion of this section is the fact that the superstructures observed on top of Pb islands by means of STM are not related to the surface morphology of the island itself but they represent the projection of the buried Pb/Si(111) interface. Indeed, the change of the interface structure affects the appearance of the superstructure itself [106]. For instance, in Fig. 4.15 the Pb islands have the same thickness, i.e. 14 ML, and they are grown on the same Si(111) substrate. The two images actually differ only by the interfacial structure and this gives rise to a different superstructure. The same goes for Fig. 4.17 where the Pb islands have the same thickness, i.e. 11 ML, and the different structure at the Pb/Si(111) interface is given by the rotation of the islands themselves. This result is further confirmed by the fact that similar superstructures are not observed on top of bare Si(111) or Pb(111) [104].

4.3.2 STM subsurface imaging: Electronic origin of the moiré corrugation

The main conclusion of previous section is that when Pb islands grown on Si(111) are observed with STM, on certain conditions, a projected image of the buried Pb/Si(111) interface can be observed on top of the island itself and the process is non-destructive [103, 104, 106]. The aim of this section is to understand what is the origin of this phenomenon.

One of the mechanisms behind the STM subsurface imaging of the Pb/Si(111) interface can be certainly ascribed to electronic effects related to the presence of QWS in this system [104, 106, 110]. Altfeder et al. [106] have shown that a better image of the projected interface can be achieved when the bias voltage corresponds to the QWS energy. Fig. 4.18a shows the very interesting case of an STM image taken on top of a Pb island grown on the Si(111)-α surface [104]. Even if the island extends over several silicon terraces, the surface on top of the island is atomically flat and its thickness changes because of the underlying silicon steps. The peculiar structure of this case, schematically shown in the right part of Fig. 4.18a, further confirms that the STM image in figure Fig. 4.18a reveals the projection of the interface structure including the substrate steps. Careful inspection of the image reveals that the contrast of the moiré pattern changes with the island thickness, i.e. the terrace on the left presents bright protrusions on a dark background while the terrace on the middle exhibits dark holes on a bright background. For the terrace on the right the contrast is reversed again.

A similar effect of contrast switching can also be seen in Fig. 4.18b, though in this case it is a bias-induced contrast reversal. Both the STM images are taken on top of a Pb island directly grown on top of the Si(111)-7 $\times$ 7 surface [106]. At V_{bias}=-0.3 V the superstructure

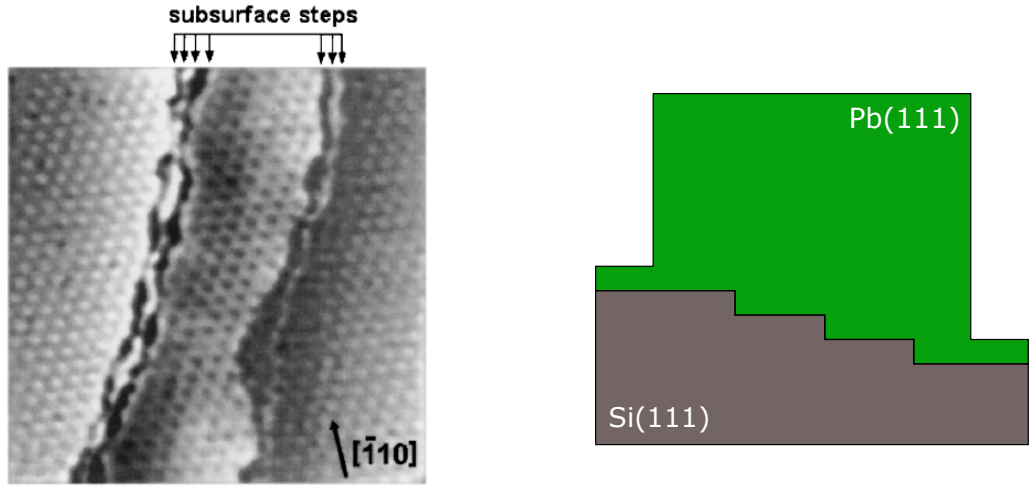

(a)

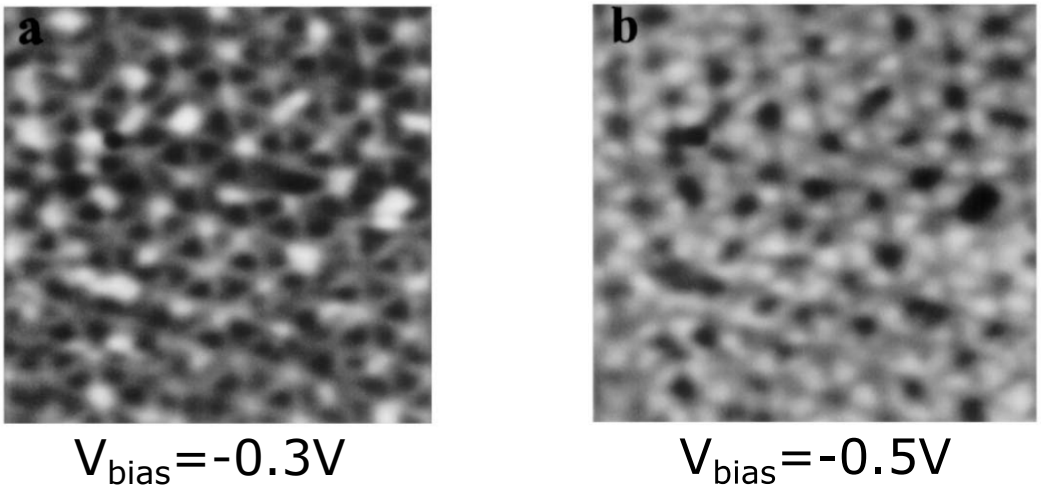

(b)

Fig. 4.18 (a) STM image of a Pb island grown on the Si(111)-α surface. It extends over several terraces and its appearance is schematically shown on the right part. The STM image reveals the projected image of the interface in which both the moiré and the substrate steps can be observed. A thickness-induced contrast reversal of the moiré can also be seen [104]. (b) STM images of a Pb island directly grown on top of Si(111)-7×7 surface. The image on the left is taken at -0.3 V and that on the right at -0.5 V. A bias-induced contrast reversal of the superstructure can be seen [106].

consists of dark triangular domains and bright domain walls/defects. On the other hand, at V_{bias}=-0.5 V the contrast of the superstructure is reversed with bright triangular domains and dark domain walls/defects. Also in this case the top of the islands is atomically flat. These findings confirm that all the superstructures observed with STM are not related to the surface

of the islands but rather on the buried interface.

Altfeder et al. [104, 106] have shown that the imaging of the buried Pb/Si(111) interface on top of Pb islands is made possible by the quantization of the electronic motion along the direction normal to the surface. Furthermore, the motion of electrons within Pb islands is highly anisotropic. In particular, STM and ARPES experiments have shown that the in-plane effective mass of electrons ($m_{\parallel}$) is much larger than the perpendicular one ($m_{\perp}$) [104, 106]. This means that QWS bands appear flat in the $k_{\parallel}$ direction and electrons essentially move perpendicularly to the surface of Pb islands [104, 106, 111]. This condition ensures the transmission of the buried interface image through many layers of Pb and with small lateral deviations. This is in line with the fact that buried structures can be imaged with high lateral resolution on top of islands with thicknesses up to $\sim$100 Å, i.e. $\sim$35 ML, without involving an important damping on the image itself [104, 106].

The mechanism through which confined electrons generate the projected image of the interface on top of Pb islands can be easily explained by means of the phase accumulation model already discussed in section 4.1 and rewritten below [103, 104, 106]

$$\Phi_{sub} + \Phi_{vac} + 2k_{\perp} \cdot Na = 2\pi n \tag{4.14}$$

According to the model, confined electrons are repeatedly reflected between the two interfaces, i.e. film/substrate and film/vacuum interface. As illustrated by equation 4.14, the interaction between electrons and the film/substrate interface is taken into account by means of the reflection phase shift Φ_{sub}. From what has been said in previous section, the structure of the Pb/Si(111) interface is locally non-homogeneous, for instance because of the mutual rotation of the Pb(111) and Si(111) atomic planes or vertical relaxation effects. As a consequence, Φ_{sub} is locally modulated becoming a function of the position on the interface, $\Phi_{sub}(x,y)$. This is the way with which confined electrons traveling throughout Pb islands retain local information about the Pb/Si(111) interface. From equation 4.14 the allowed values of $k_{\perp}$ can be written as follows:

$$k_{\perp} = \frac{\pi n}{Na} - \frac{\Phi_{sub}(x,y) + \Phi_{vac}}{2 \cdot Na} \tag{4.15}$$

It is obvious that the local modulations of $\Phi_{sub}(x,y)$ affect the values of $k_{\perp}$ forcing them to become functions of the lateral position $k_{\perp}(x,y)$. Therefore, energy positions of QWS and related wavefunctions calculated from equations 4.14 and 4.15 are accordingly forced to become functions of the lateral position (x,y). The ultimate effect of the spatial dependence

of $\Phi_{sub}(x,y)$ is the local spatial modulation of the exponential tails out of the surface (related to the QWS as discussed in section 4.1), and thus, of the Local Density of States (LDOS). The latter is the quantity actually probed by means of STM and its spatial modulations in turn give rise to tunneling current modulations revealing the image of the interface on top of Pb islands.

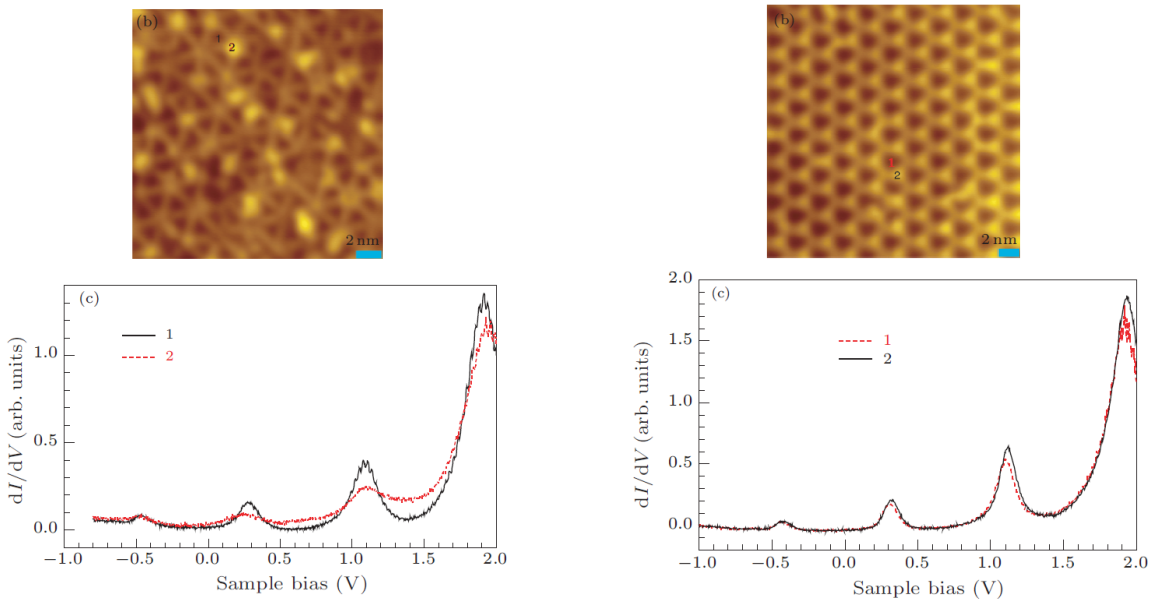

Fig. 4.19 (a) Upper part: STM image of a 14 ML Pb island directly grown on the Si(111)-7×7 surface (V_{bias}=1.5 V). Lower part: Differential conductance $\frac{dI}{dV}$ spectra measured on two different locations of the superstructure. (b) Upper part: STM image of a 14 ML Pb island grown on the Si(111)-α Pb surface (V_{bias}=1 V). Lower part: Differential conductance $\frac{dI}{dV}$ spectra measured on two different locations of the moiré [103].

This mechanism is illustrated in Fig. 4.19 for the two interfaces discussed above. The upper part of Fig. 4.19a shows a STM image taken on a 14 ML Pb island grown on top of the Si(111)-7×7 surface and exhibiting the superstructure associated to the Pb/Si interface [103]. The lower part of the figure contains the differential conductance (black and red curves) measured on two different locations of the superstructure (indicated on the topographic image), namely triangular dark domains (black curve) and bright domain walls or bright defects (red curve). Altfeder et al. [106] have shown that within the triangular domains the boundary conditions for having QWS are fulfilled and in fact the black spectrum displays well developed and sharp QWS. On the other hand, bright edges and defects give rise to strong scattering events that locally suppress the QWS formation. In line with this, the red

spectrum shows broad and not-well developed QWS. The spatial modulation of both the QWS properties and the LDOS is clear in this case and the origin of the superstructure image on top of the Pb island can be easily understood. Due to the large density of defects on this interface the electron confinement is disturbed and consequently the QWS are strongly spatially modulated. In line with this, it should be noted that the large width of QWS peaks observed in this case could be related to the enhanced electron-defect scattering [103]. It is interesting to outline that the subsurface imaging process provides a way to understand if defects live either at the Pb/Si(111) interface or on top of the Pb surface. As already said at the beginning of this section, the subsurface imaging of the Pb/Si(111) interface can take place only if the bias voltage corresponds to the QWS energy. As a consequence, for bias voltages different from the QWS energy, defects lying at the Pb/Si(111) interface cannot be observed. On the other hand, defects lying on top of the Pb surface will be always observable regardless of the bias voltage conditions because they are not buried under the Pb island but they directly affect the surface topography.

From these spectra the bias-induced contrast reversal shown in Fig. 4.18b can be also explained. The STM image in Fig. 4.19a is taken at V=1.5 V. By comparing the relative intensity of STS spectra at 1.5 V it is evident that the LDOS measured on top of defects or domain walls is higher than that on top of triangular domains. Consequently, the tunneling current measured on top of domain walls and defects is higher. This fact makes the contrast on top of domain walls and defects brighter than that on the triangular domains. By looking again to the STS spectra it is possible to find voltages where the relative intensity is reversed with respect to the situation just described, e.g. around 1.1 V. At these voltages, a contrast reversal of the superstructure image similar to that observed in Fig. 4.18b takes place.

The origin of the moiré superstructure shown in the upper part of Fig. 4.19b as well as the bias-induced contrast reversals can be explained with similar arguments. In this case the 14 ML Pb island is grown on top of the Si(111)-α surface. The lower part of the figure shows that QWS are sharp and well-developed in each point of the surface. This is due to the fact that the Si(111)-α interface is smoother than the Si(111)-7×7 one and with less defects therefore the electrons are better confined and the electron-defect scattering broadening is reduced [103, 106]. The spatial modulations of QWS properties are due to the interface effects discussed above.

Before concluding this section, the thickness-induced contrast reversal shown in Fig. 4.18a has to be explained. As already said many times in this chapter, as the thickness of a Pb

island changes, new QWS move below the Fermi level (every ∼2.2 ML). The net result is the oscillation of the HOQWS respect to the Fermi level when the thicknesses passes from odd to even and vice versa. As a consequence, the spatial extension of QWS exponential tails out of the surface and therefore also the LDOS oscillate with the thickness. This mechanism gives rise to a periodic contrast reversal of the projected interface image related to the oscillation of the tunneling current which is actually observed by means of STM [100, 104, 110].

4.3.3 Structural origin of moiré patterns

As already said in previous sections, moiré superstructure observed on top of Pb islands originates at the Pb/Si(111) interface because of the lattice mismatch between Si(111) and Pb(111). The electronic origin of moiré was discussed in previous section and it was interpreted as a result of the Pb/Si(111) interface STM imaging mediated by confined electrons (QWS) within the islands. On the other hand, Hupalo et al. [86] have investigated by means of LEED experiments the structural origin of moiré in the case of 3 ML Pb islands grown on Si(111). Interestingly, they have shown that the first layer of Pb at the Pb/Si(111) interface relaxes perpendicularly to the surface (see Fig. 4.20). The interfacial atoms, laying on different heights, induce a periodic geometrical corrugation whose wavelength is related to the moiré superstructure experimentally observed by LEED or STM. Even if the structural deformation is localized to the Pb/Si(111) interface, also the first few Pb layers above the interface are affected by the structural relaxation. This mechanism allows the geometric corrugation to propagate through several layers within the island thickness thus contributing to the moiré corrugation experimentally observed on top of the islands [112] (see Fig. 4.20).

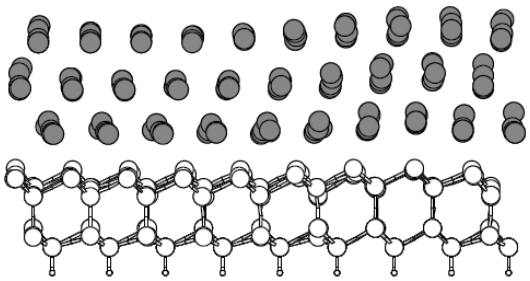

Fig. 4.20 Side view of a 3 ML Pb layer on Si(111) after relaxation [112].

Previous considerations allow us to conclude that, in general, moiré corrugation observed on top of Pb islands is a combination of geometric and electronic contributions. The geometric contribution is expected to exponentially decay with the thickness d of the islands because it is mainly due to vertical relaxation of Pb atoms at the Pb/Si(111) interface and therefore

it must remain localized at the interface itself [112, 109]. On the other hand, the electronic contribution (mediated by QWS) is expected to decay over larger thicknesses, i.e. $\frac{1}{d}$ or $\frac{1}{d^2}$ [112, 109]. Therefore, for thick islands (as those discussed in previous section), moiré pattern will mainly arise from electronic contribution of QWS, while for very thin Pb islands (as the trilayer Pb/Si(111) of our experiments), moiré pattern will have a strong geometric contribution. This is corroborated by the paper of Kim. et al [109] showing that 7 ML Pb islands exhibit a moiré pattern but the vertical corrugation of the island measured by STM is less then 2 pm. In other words, the tops of 7 ML Pb islands are atomically flat and the moiré pattern is mainly due to electronic contribution. Starting from this results we could say that 7 ML Pb islands can already be considered thick islands. However, it is not clear at what thickness the thin-to-thick transition takes place because, for instance, Chan et al. [112] have estimated that this transition occurs at 11 ML. On the other hand, Hupalo et al. [86] have shown that 3 ML Pb islands have a vertical corrugation of $\sim$48 pm. In this case, the moiré pattern has a strong geometric contribution. The fact that moiré corrugation on top of 3 ML Pb islands can be observed by means of LEED measurements suggests the strong structural contribution [86]. Remember that LEED is sensitive to atomic relaxations perpendicular to the surface and not to the electronic structure of the system.

In agreement with this, Hupalo et al. [86, 112] have also shown that, in STM topographic images, the contrast of a given moiré never changes when observed over a large range of positive/negative voltages. In other words, bright features in the corrugation remain bright and vice versa. Furthermore, calculations of Chan et al. [112] have shown that bright spots of a moiré pattern observed by STM correspond to Pb atoms of the first layer on top of T_1 sites of the silicon substrate. These atoms vertically relax and give rise to the bright features observed in STM images.

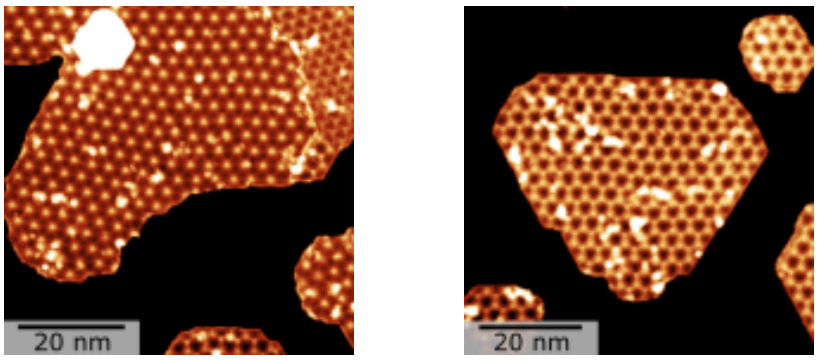

(a) (b)

Fig. 4.21 Topographic STM images of 3 ML Pb islands grown on Si(111) exhibiting a "protrusions" (a) and a "holes" moiré (b). (a): Image size: 65×65 nm^2, V_T: +50 mV and I_T : 50 pA. (b): Image size: 65×65 nm^2, V_T: +0.3 V and I_T : 50 pA.

The discussion above tells us that the origin of moiré corrugation in thin Pb films is not trivial to be explained. The last aspect that need to be considered to understand the structural origin of moiré corrugation on top of very thin Pb layers grown on Si(111) is the stacking sequence of Pb atomic planes within the layer itself. Fig. 4.21 shows two 3 ML Pb islands grown on Si(111) whose moiré corrugation surprisingly exhibits two different patterns. The moiré corrugation in Fig. 4.21a appears as a periodic distribution of "protrusions", while that in Fig. 4.21b appears as a distribution of "holes". Jian et al. [113] have proposed that 3 ML Pb islands always have an fcc stacking, but they can exhibit two different types of moiré patterns because of a different stacking sequence of the Pb atomic planes, i.e. ABC in the case of "protrusions" and ACB for the "holes" pattern [113, 112]. Different stacking sequences lead to different structures at the Pb/Si(111) interface. As a consequence, a different phase shift is introduced to the confined electrons (QWS) that are scattered by these two interfaces. Different phase shifts lead to different vertical charge oscillation patterns that were interpreted as responsible for the two moiré patterns observed by STM. This interpretation implies a strong electronic contribution to the moiré pattern due to the QWS. On the ther hand, Chan et al. [112] have also shown that STM images are sensitive to different stacking configurations trough a purely geometric effect. For both types of moiré corrugations, i.e. "protrusions" and "holes" moiré, the bright spots observed by STM were predicted to be due to Pb atoms located on T_1 sites of the Si(111) substrate. Different stacking configurations lead the first Pb layer on top of Si(111) to change its registry with respect to the Si(111) itself. As a consequence, when different stacking configurations are considered T_1 sites, on top of which Pb atoms reside, are not exactly equivalent for the two configurations. This mechanism was interpreted as responsible for the observation of "protrusions" and "holes" moiré corrugations.

It is interesting to note that other moiré patterns, like those shown in Fig. 4.22, can be observed on top of 3 ML Pb islands. Both moiré corrugations present periodicity of the superstructure much smaller than that of "holes"/"protrusions" moiré discussed so far (you can directly compare with small islands exhibiting "holes" moiré within the same figure). As already mentioned in previous section, this is a result of the rotation of Pb islands with respect to the silicon substrate [113, 86]. However, careful inspection of the bright protrusions of the moiré in Fig. 4.22b reveals a triangular fine structure that is not found in the moiré of Fig. 4.22a. This fact suggests that, also in this case, the origin of moiré corrugation cannot be simply interpreted by simple models, both structural and electronic effects must be considered together to correctly describe this system.

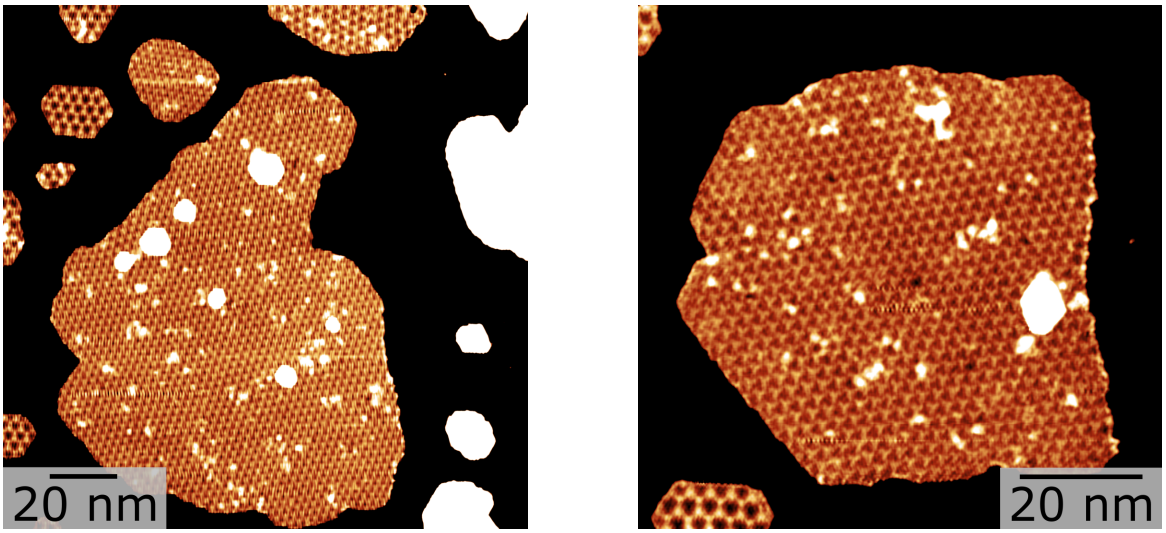

(a) (b)

Fig. 4.22 Topographic STM images of 3 ML Pb islands grown on Si(111) exhibiting small period moiré corrugations. (a): Image size: 155×155 nm^2, V_T: 1 V and I_T : 40 pA. (b): Image size: 85×85 nm^2, V_T: -1 V and I_T : 50 pA.

In conclusion, the origin of moiré corrugations on top of thin Pb films grown on Si(111) is not completely understood and this is probably due to the fact that both electronic and structural contributions participate to the formation of moiré patterns. Experimental results presented in the rest of the chapter were obtained by measuring 3 ML Pb islands/films grown on Si(111). Given the very thin thickness of this system, it will be important to take into account both structural and electronic contributions to the moiré corrugation observed in STM images. This is the reason for which in the first part we will focus on the structural aspects related to moiré and then we will also investigate the Quantum Well States.

4.4 MnPc on 3 ML Pb continuous films on Si(111)

The sample described in this section was prepared by following the two-step method described in section 4.3.1. The Si(111)-7×7 surface is firstly prepared by means of the procedure described in Chapter 2. Then, $\sim$1.65 ML of Pb were evaporated at room temperature on top of the silicon. Subsequent annealing at $\sim$320° C for 2 min 30 sec, by means of direct current heating, led us to a crystalline wetting layer with $\sqrt{7} \times \sqrt{3}$-Pb surface reconstruction and a nominal coverage of 1.2 ML. After that, 2 ML of Pb were deposited on top of the sample kept at $\sim$110 K for a total Pb coverage of $\sim$3 ML. This procedure leads to the growth of quasi-uniform 2 ML Pb films on top of the Pb/Si(111)-α surface (see Fig. 4.23). The

2 ML films start to grow only after the saturation of the Pb wetting layer, i.e. only after the conversion of the initial $\sqrt{7} \times \sqrt{3}$-Pb surface into the α phase corresponding to $\sim$1.3 ML (see section 4.3.1).

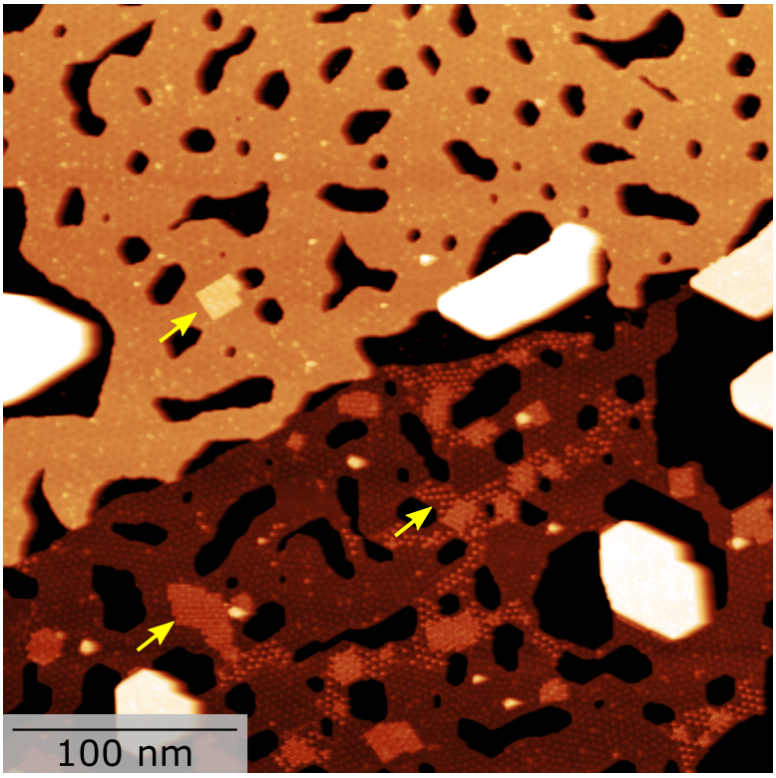

Fig. 4.23 STM image showing ML of MnPcs deposited on top of a quasi-uniform 3 ML Pb film grown on Si(111). Black areas are 2 ML deep holes in the film. White areas are 5 ML Pb islands. The two terraces exhibit two different moiré structures: the "holes" and the "protrusions" moiré. Yellow arrows indicate both assembled and dispersed MnPcs. Image size: $340 \times 340\ nm^2$, V_T: -1 V and I_T : 20 pA.

The growth of such very thin Pb films is made possible by the particular Pb/Si(111) interface structure prepared, i.e. the Pb/Si(111)-α phase, as well as the low temperature during the growth ($\sim$110 K) that play a crucial role in the thickness stabilization. Remember that different structures can be achieved at the Pb/Si(111) interface depending on whether Pb films are grown either directly on the Si(111)-7×7 or on a Pb crystalline wetting layer deposited on Si(111) (see section 4.3.1). At the end, $\sim 2.7 molecules/100\ nm^2$ of MnPcs were evaporated on top of the sample kept at $\sim$100 K. It should be outlined that the sample was kept at low temperature for the duration of the whole preparation until the transfer to the pre-cooled microscope. From now on, all the thicknesses will be measured with respect to

the Si(111) and therefore it will be called "3 ML Pb film".

Fig. 4.23 shows a representative STM image of the quasi-uniform 3 ML Pb film grown on the Si(111)-α surface. The image contains two terraces separated by an atomic step of the silicon substrate and represented by two different false colors within the figure. Both terraces show the presence of holes irregular in shape and 2 ML deeper (black areas). The presence of these holes is probably due to the fact that actual Pb coverage is slightly less than 3 ML and therefore the system cannot form a perfect uniform film. The widespread presence of 5 ML islands (white areas) is probably due to uncontrolled heating during the preparation of the sample which activated the diffusion of Pb atoms towards the next stable thickness. This fact also explains the presence of large emptied areas around every 5 ML island. More interestingly, Fig. 4.23 reveals the presence of two different types of terraces in terms of the Pb film structure. The upper terrace reveals a moiré structure consisting of a pattern of dark "holes" on a bright background. On the other hand, the lower terrace exhibits a moiré consisting of a pattern of bright "protrusions" on a dark background. Remember that the origin of the moiré on top of Pb islands grown on Si(111) was largely discussed in section 4.3.1.

Fig. 4.23 also reveals that MnPcs preferentially adsorb on top of "protrusions" terraces (some molecular domains are indicated by yellow arrows). The analysis of several STM images actually confirms that the majority of MnPcs adsorb on these terraces and only a few of them can be found on the "holes" moiré terraces. For instance, only a small domain can be found on the "holes" moiré terrace of Fig. 4.23. Selective adsorption of MnPcs and other phthalocyanines was already reported in literature. For instance, Liu et al. [66] have shown that adsorption of MnPcs on Au(111) is more stable on fcc regions than on hcp. In our case, selective adsorption of MnPcs on top of "protrusions" moiré terraces suggests that their atomic structure could be different than that of "holes" terraces. In agreement with this interpretation, in following sections I will show that the relative orientation with respect to the Si(111) substrate is different for "protrusions" and "holes" moiré terraces. Furthermore, additional structural differences between the two types of terraces cannot be excluded without further investigation. More interestingly, if we focus on the "protrusions" terrace (see Fig.4.24a), we can see that MnPcs self-assemble in different ways depending on the region. To understand this behavior it is important to highlight the this terrace in turn exhibits two types of moiré corrugations, i.e. the same already described in section 4.3.3 that we also called "holes" and "protrusions" moiré. In that section it was shown that these two moiré differ for the internal stacking of the Pb atomic planes. Therefore, also in this case,

different behavior of MnPcs can be understood by means of selective adsorption on top of regions having a different internal structure (in accordance with the observations of Liu et al. [66]). It is also important to note that, contrary to what we observed on top of the Pb monolayer, on top of 3 ML a square self-assembly of MnPcs is recovered on top of 3 ML Pb films, although it still remains very different from that observed on top of thicker films or bulk-like samples of Pb [68, 67, 73].

4.4.1 Structure of "protrusions" moiré Pb terraces + MnPcs

Fig.4.24a shows a representative STM image of the "protrusions" Pb terraces. The wide bright area on the left side of the image is a 5 ML island. As already mentioned in previous section, the 3 ML Pb film is not completely uniform and 2 ML deep holes are distributed over each terrace (dark regions). Interestingly, holes are not completely irregular in shape and some of them exhibit very faceted edges with hexagonal-like shapes. The rest of the surface is covered with the 3 ML Pb film exhibiting a "protrusions"-type moiré. MnPcs, appearing as either bright islands or bright spots on top of the 3 ML Pb film, are self-assembled in a different way according to the type of moiré on which they are adsorbed and will be discussed later.

Closer inspection of the "protrusions" moiré pattern reveals a very intriguing structure consisting of different moiré domains, each having its own period and orientation. In section 4.3.1, the origin of the moiré was interpreted as a result of the overlapping of two atomic planes with different lattice constants at the Pb/Si(111) interface, i.e. the Pb(111): 0.350 nm and the Si(111): 0.384 nm. Fig. 4.24b depicts a toy model to visualize the origin of the moiré pattern on the basis of the coincidence of certain atoms of two overlapped lattices. Note that the two lattices have an hexagonal symmetry and a lattice mismatch as in the case of Pb(111) and Si(111). Due to the symmetry of the problem, the resulting moiré pattern retains the same hexagonal symmetry. Furthermore, as the axes of symmetry of the two lattices are aligned, the moiré superstructure exhibits the same orientation. On the other hand, Fig. 4.24c shows the situation in which the two lattices are rotated by an angle of 6°. In this case the moiré pattern still keeps the hexagonal symmetry but the period is smaller and the orientation has changed in comparison with Fig. 4.24b.
The moiré problem in the case of 3 ML Pb films grown on Si(111) can be treated by means of a model that relates the moiré lattice parameter $L(\Theta)$ and its orientation $\Phi(\Theta)$ to the rotation angle Θ of the Pb(111) film with respect to the Si(111) substrate at the Pb/Si(111) interface (see Fig. 4.25 to understand the adopted notation) [114]. This model relies on geometric considerations about the commensurability of the Pb film on Si(111), i.e. the coincidence of

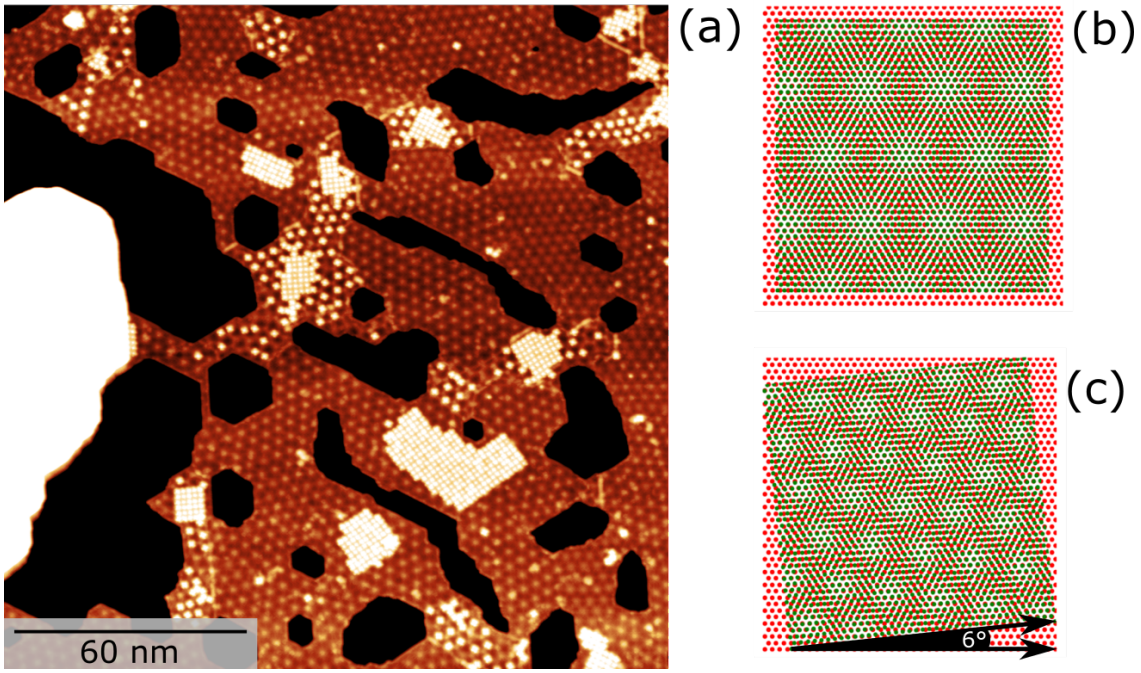

Fig. 4.24 (a) STM image of a terrace with a 3 ML Pb film exhibiting a "protrusions" moiré. The bright area on the left is a 5 ML Pb island and the dark regions are 2 ML deep holes within the film. Bright regions on top of the Pb film are self-assembled MnPcs. Image size: $170 \times 170\ nm^2$, V_T: +0.3 V and I_T : 40 pA. (b) and (c) Toy model illustrating the origin of the moiré (hexagonal bright regions) as a result of the overlapping of two mismatched lattices of dots (red and green) representing the Si(111) and the Pb(111) atoms.

certain atoms of the film and the substrate, when they are arbitrarily oriented to each other. According to this, a moiré pattern can be regarded as a beat of the two lattices and a spatial beating frequency can be attributed to the difference of the two reciprocal lattice vectors, i.e. $\mathbf{G}_{moiré} = \mathbf{k}_{Pb} - \mathbf{k}_{Si}$ [114]. Furthermore, different coincidence conditions, i.e. different spatial beating frequencies, may occur when different rotation angles Θ are considered [114]. Each of these frequencies leads to the formation of different moiré patterns. The analysis of all these spatial beating frequencies, e.g. first-order, second-order, etc., in terms of the rotation angle Θ ultimately allows the model to predict the moiré lattice parameter L and its orientation Φ as a function of Θ itself [114] (see Appendix 5 for demonstration).

$$L(\Theta) = \frac{a_{Si}}{\sqrt{1+x^2-2x\cos\Theta}} \tag{4.16}$$

$$\cos\Theta = \frac{1}{2x} + \frac{x}{2} - \frac{a_{Si}^2}{2xL(\Theta)^2} \tag{4.17}$$

$$\cos\alpha = \frac{1+\delta-\cos\Theta}{\sqrt{\delta^2+(2\delta+2)(1-\cos\Theta)}} \tag{4.18}$$

$$\Phi = \Theta + \alpha \tag{4.19}$$

where $x = \frac{a_{Si}}{a_{Pb}}$ and $\delta = \frac{a_{Si}}{a_{Pb}} - 1$ with a_{Si} and a_{Pb} the lattice constants of Si(111) and Pb(111) respectively. The equations written above, for instance, describe the so-called first-order moiré superstructures, that are found when the atomic lattices are slightly rotated between them. However, in the following section we will see that, if the two lattices are rotated by a large angle, the model can be extended by considering higher order spatial frequencies that give rise to higher order and more complex moiré superstructures. It is interesting to outline that this model relies only on geometric considerations and therefore by neglecting the actual interaction potentials between the overlapped lattices and thus real electronic structure and the physics of the system. However, I will soon show that this model is able to provide interesting information about the internal structural of the 3 ML Pb films grown on Si(111).

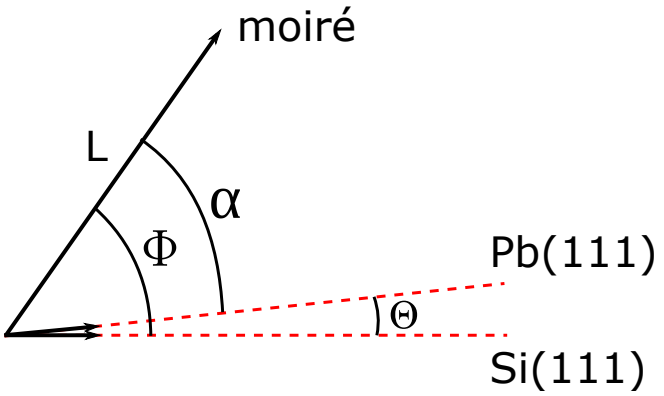

Fig. 4.25 Sketch of the quantities involved in the moiré model. L is the moiré superstructure lattice parameter and Φ (α) its orientation with respect to the Si(111) (Pb(111)). Θ is the rotation angle between the Pb(111) and the Si(111).

Fig. 4.25 schematically shows the quantities involved in previous equations. L represents the moiré lattice parameter and Θ the rotation angle between Pb(111) and Si(111). The latter is given from equation 4.17 which in turn can be directly derived from equation 4.16. Then, α is the orientation of the moiré with respect to the Pb(111) and it can be deduced from equation 4.18 by inserting the value of Θ obtained from 4.17. At the end, the orientation of the moiré Φ with respect to the Si(111) substrate can be simply calculated by the sum of Θ and α. From these relations, one sees that the rotation angle Θ between Si(111) and Pb(111) remains the independent variable which determines both the size and the orientation of the

moiré superstructure. The plots in Fig. 4.26 make explicit this point by showing the moiré

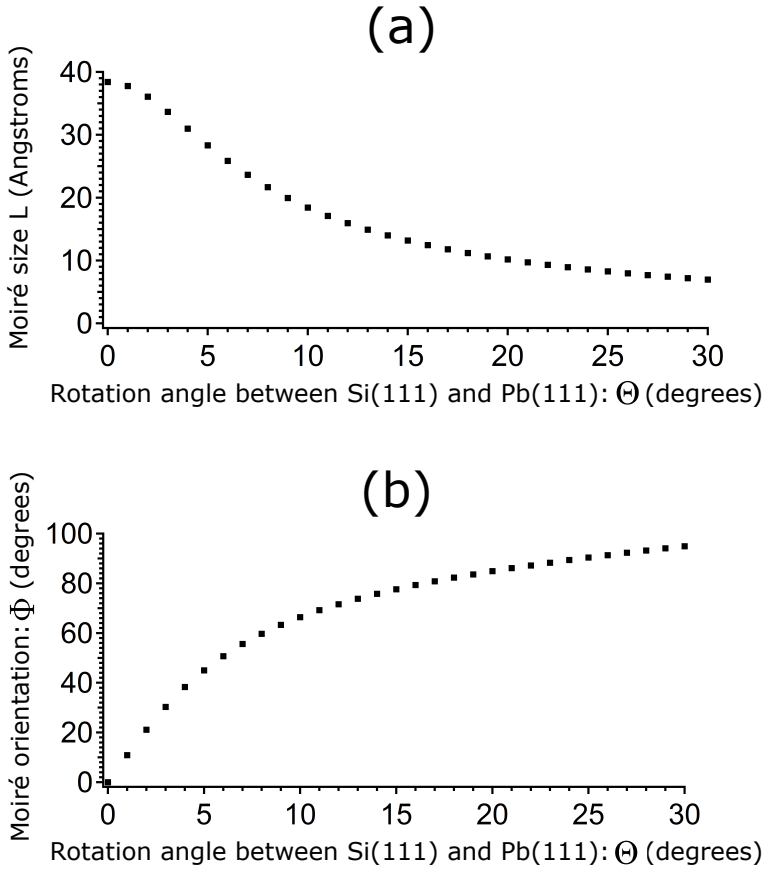

Fig. 4.26 Calculated period $L(\Theta)$ (a) and orientation $\Phi(\Theta)$ (b) of a moiré as a function of the rotation angle Θ between the two underlying lattices. Within the model, it was assumed that lattice constants of Pb(111) and Si(111) are close to bulk values (see text).

lattice parameter $L(\Theta)$ and its orientation $\Phi(\Theta)$ as a function of the rotation angle Θ. All the points were deduced from previous equations by assuming lattice constants close to bulk values, i.e. 0.350 nm for the Pb(111) 0.384 nm for the Si(111). Starting from these diagrams, it is easy to see that the rotation of the Pb(111) with respect to the Si(111) substrate by an angle Θ, induces both the shrinkage of the moiré lattice parameter L and the rotation Φ of the moiré with respect to the Si(111).

Before going any further, it should be outlined that the rotation of overlayers grown on substrates is a well known mechanism on other systems, e.g. graphene on Ir(111) [115], and it has largely been investigated [116]. However, several works have reported this effect also for Pb islands grown on Si(111). In particular, Yakes et al. [116] have focused on the first stages of Pb islands growth on Si(111)-α (similar to our conditions) and they found that

the orientation of islands with respect to the Si(111) substrate depends on the coverage. In particular, at low coverage, 3 ML islands are disconnected and aligned with the $[1\bar{1}0]$ axis of the substrate. With increasing the coverage above 1.5 ML, the islands start to coalesce and additional islands grow on top of them. In this case Pb islands have a preferred orientation of 5.6° with respect to the $[1\bar{1}0]$ direction of the substrate. These results were deduced from the analysis of both the length and the orientation of moiré patterns directly measured by means of SPA-LEED and STM. Furthermore, by modeling the moiré with equations similar to those described above, they were able to reproduce the diffraction experiments. From the results of their calculations one can conclude that, even though the system exhibits a preferential orientation for a specific coverage (for instance 5.6°), a dispersion of orientations around the preferred one can always be found. This is in global agreement with what we observe in Fig. 4.24, where different moiré domains, each with its own lattice parameter and orientation, are found, confirming that the 3 ML Pb film has different local orientations Θ with respect to the Si(111) substrate.

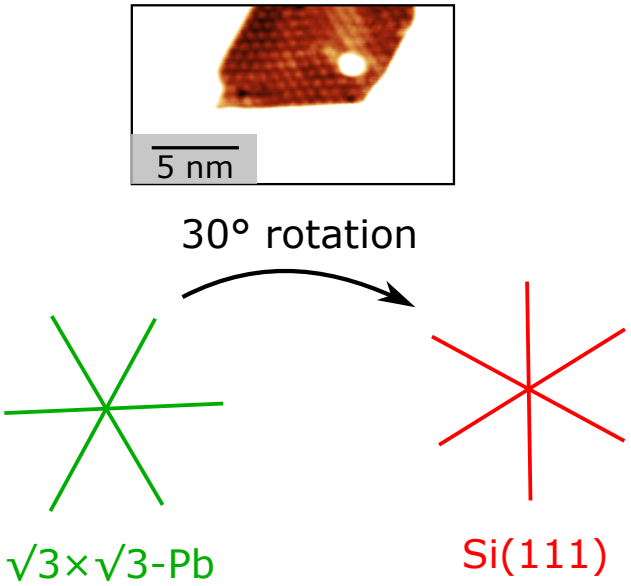

Fig. 4.27 Upper part: STM image showing the $\sqrt{3} \times \sqrt{3}$-Pb reconstruction that can be found at the bottom of the holes. Image size: $18 \times 10\ nm^2$, V_T: -1 V and I_T : 40 pA. Lower part: Green lines represent the symmetry directions of the $\sqrt{3} \times \sqrt{3}$-Pb structure deduced from the upper part of the figure. A rotation by an angle of 30° of these directions makes it possible to obtain the Si(111) directions (red lines).

In this section I will use the moiré model to determine the local orientation of the Pb film. This quantity is useful for instance to get information about the internal structure of the Pb film or to know if molecular assemblies have preferential orientations on the surface.

From Fig. 4.25 it is clear that the crucial information needed to apply the model is the direction of the Si(111) substrate against which all the other angles can be referred. To deduce this direction I used the STM image reported in Fig. 4.27 which displays one of the reconstructions that can be found at the bottom of the holes that break up the continuity of the 3 ML Pb film. This image was taken on the same region of the sample and under the same scanning conditions as Fig. 4.24, therefore it can be used to determine the Si(111) directions that are supposed to be fixed over the whole surface. The procedure is simplified by the fact that the atomic arrangement in Fig. 4.27 exhibits a $\sqrt{3} \times \sqrt{3}$-Pb reconstruction, i.e. (0.67±0.04) nm. It is well known that the $\sqrt{3} \times \sqrt{3}$-Pb structure is 30° rotated with respect to the Si(111) [58], therefore the directions of the latter can be easily deduced (see Fig. 4.27).

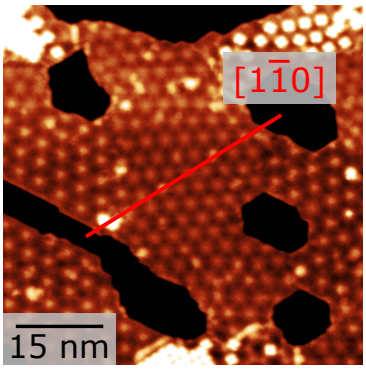

Moiré orientation (Φ)	Moiré size (L)
(33.1±3.1)°	(32.1±2.6)Å
(32.6±2.3)°	(31.2±3.2)Å
(35.7±4.5)°	(31.5±2.4)Å

(a)

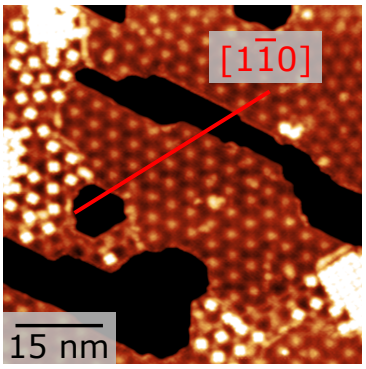

Moiré orientation (Φ)	Moiré size (L)
(-2.7±2.2)°	(36.1±2.2)Å
(0.4±2.8)°	(34.2±1.9)Å
(0.5±2.5)°	(36.1±2.4)Å

(b)

Fig. 4.28 (a): The upper part shows an STM image extracted from Fig. 4.24. In the middle of the image there is a moiré domain with small period and an orientation different from that of the [1$\bar{1}$0] direction of the Si(111). The table in the lower part contains the values of L and Φ deduced from the image above. Image size: 60×60 nm^2, V_T: +0.3 V and I_T : 40 pA. (b): The upper part shows an STM image extracted from Fig. 4.24. In the middle of the image there is a moiré domain with large period and almost aligned with the [1$\bar{1}$0] direction of the Si(111). The table in the lower part contains the values of L and Φ deduced from the image above. Image size: 60×60 nm^2, V_T: +0.3 V and I_T : 40 pA

As an example, I will describe for two representative cases the procedure that I followed to determine the local orientation of the Pb film starting from the experimentally observed moiré corrugations. The STM image on the left of Fig. 4.28a is extracted from the overview shown in Fig. 4.24. The moiré domain in the middle of the image exhibits one of the smallest periods of the whole terrace. Furthermore, the $[1\bar{1}0]$ direction of the Si(111) superimposed to the image reveals a different orientation of the moiré. Both the shrinkage and the rotation of the moiré are in agreement with the model discussed above and now we know that the origin of this effect lies in the local rotation of the 3 ML Pb film respect to the Si(111). The table in Fig. 4.28a displays the orientations Φ and the periods L of the moiré deduced from the STM image and measured with respect to the three equivalent directions of the Si(111). Ideally, all the values of Φ (L) should be approximately the same but, in practice, they are different. One of the reasons could lie in an small intrinsic distortion of the STM image itself. This fact actually has significant impact in the application of the moiré model. To understand this point, one only needs to consider that the values of L reported in the table vary from 31.2 Å to 32.1 Å. By looking at Fig. 4.26a it is easy to see that this variation of L corresponds to $\Theta \sim$3-4°. However, Fig. 4.26b reveals that this range of Θ leads to Φ between 30° and 40° which is in clear disagreement with the experimentally observed values (compare with values within the table of Fig. 4.28a). This behavior is basically due to the fact that the orientation of the moiré proceeds much faster than the turning of Pb, especially for small angles. The extreme sensitivity of the moiré orientation to the rotation of Pb makes this model unsuitable to determine Φ from Θ. However, if the association is done in the opposite direction, i.e. deduce Θ from Φ, the sensibility of the model is strongly reduced. In agreement with this, if we consider the values Φ reported within the table of Fig. 4.28a, i.e. $\Phi \sim$32.6-35.7°, the model of Fig. 4.26b allows us to deduce that Pb(111) and Si(111) are rotated by an angle Θ between 3° and 4°. Fig. 4.26a reveals that this range of Θ leads to values of L which are in agreement with the experimentally observed values (compare with values within the table of Fig. 4.28a). The STM image of Fig. 4.28b is also extracted from Fig. 4.24. The moiré in the middle of the image exhibits one of the largest periods and its orientation is almost parallel to the $[1\bar{1}0]$ direction. By using the measured values of Φ reported in the table of Fig. 4.28b and with arguments similar to the previous case, the model predicts an almost non-rotated Pb film with respect to the Si(111), i.e. $\Theta \sim$0°. One of the values Φ reported in the table is negative. However, within the error bar it remains consistent with the other two, i.e. an almost non-rotated moiré. The estimation of Θ from the moiré periods reported in the table leads to values between 2° and 3°. Similarly to what was assumed in ref. [116], we can say that Θ lower than 3° are consistent with both the Pb film and the moiré aligned with the Si(111). The reason for this assumption lies in the results of diffraction measurements

showing that even if the Pb film exhibits a preferential orientation with respect to the Si(111), a dispersion of orientations around the preferred one is always present. Therefore, even if the Pb film is essentially aligned with the Si(111), the existence of slightly rotated domains is not excluded. This effect can be automatically probed by diffraction measurements which are macroscopic, that is, sensitive to large areas of the sample including different moiré domains. The situation is different with STM measurements through which the local structure of a single moiré domain can be easily probed. Therefore, the most one can do in this case is to define a range of angles Θ consistent with a preferential orientation as we have just done.

4.4.2 Structure of "holes" Pb terraces + MnPcs

Fig. 4.29a shows a representative STM image for the "holes" Pb terraces. Before going any further, it is very important to bear in mind that this "holes" moiré corrugation is different from that discussed in section 4.3.3. The structure analyzed here is only observed in the case of continuous Pb films and it was reported only in one another work before [117]. This is the reason for which I tried to characterize it. The bright area in the middle is a MnPcs self-assembly that will be discussed later. The bright spot on the upper right part is a small $\sim$1 ML thick Pb cluster. Dark areas represent the 2 ML deep holes, some of which exhibit faceted edges and hexagonal-like shapes. The rest of the surface is covered by the 3 ML Pb film.

It is evident that the appearance of the "holes" moiré is very different from the "protrusions" one. The first important difference is that it is not divided in domains with different orientations and periods but it exhibits a quite uniform structure. The second difference is the presence of corrugations at two different length scales. As shown in Fig. 4.29a, the larger corrugation forms a hexagonal pattern rotated by an angle Φ of -8°$\pm$11° with respect to the Si(111) and a mean period L of (45.3$\pm$4.7) Å. The table in Fig. 4.29b shows the orientations of the moiré Φ with respect to the three equivalent directions of the Si(111) and the periods L deduced from the image of Fig. 4.29a. Φ, L and the directions of the Si(111) are defined in the same way as was done in Section 4.4.1. Even if this moiré does not form domains with different orientations and periods, the large error bars associated to its orientation reveals a certain degree of freedom in the rotation of the Pb film on top of the Si(111). Indeed, the slight rotation of the moiré can be readily seen from the image of Fig. 4.29a. The small scale corrugation forms a hexagonal pattern rotated by an angle of -29.7°$\pm$3.3° with respect to the Si(111) and a mean period of (6.5$\pm$0.6) Å. This hexagonal pattern has a $\sqrt{3} \times \sqrt{3}$ symmetry and it is 30° rotated with respect to the Si(111). Note that an ideal $\sqrt{3} \times \sqrt{3}$ lattice has a period of 6.65 Å. Fig. 4.29c shows the structure observed at the bottom of the hole in the upper right of Fig. 4.29a. Since the depth of the hole is consistent with 2 ML

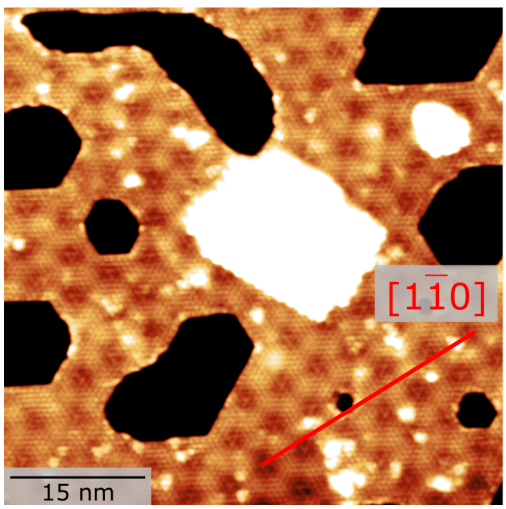

(a)

Moiré orientation (Φ)	Moiré size (L)
(-5.2±8.8)°	(46±4)Å
(-9.3±12.5)°	(45±4)Å
(-9.5±11.9)°	(45±6)Å

(b)

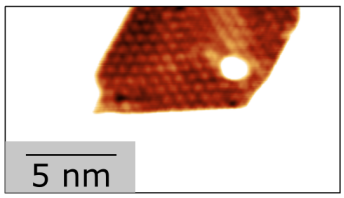

(c)

Fig. 4.29 (a) STM image of a terrace with a 3 ML Pb film exhibiting a "holes" moiré. The dark regions are 2 ML deep holes within the film while the bright regions in the middle and on the upper right are a self-assembly of MnPcs and a Pb cluster respectively. The [1$\bar{1}$0] direction of the Si(111) is superimposed as a reference for the moiré directions. Image size: $55 \times 55\ nm^2$, V_T: -1 V and I_T : 40 pA. (b) Orientations Φ and sizes L of the moiré measured from the STM image in (a) with respect to the three equivalent directions of the Si(111). (c) STM image of the $\sqrt{3} \times \sqrt{3}$-Pb structure at the bottom of the hole in the upper right of (a) Image size: $18 \times 10\ nm^2$, V_T: -1 V and I_T : 40 pA.

of Pb, this structure can be related to the reconstruction of the Si(111)-α surface, i.e. the reconstruction of the Pb monolayer. Indeed, we found that this corrugation exhibits an hexagonal structure with a period of (6.7±0.4) Å which is consistent with the $\sqrt{3} \times \sqrt{3}$-Pb structure of the Si(111)-α surface. As a consequence, this structure is rotated by an angle of 30° with respect to the Si(111). The latter outcome is interesting for two reasons. First, the faceted edges of the holes in Fig. 4.29a are aligned with the $\sqrt{3} \times \sqrt{3}$ structure of the Pb monolayer suggesting that also the 3 ML Pb film would be rotated by an angle of 30° with respect to the Si(111). Second, the small scale corrugation of the moiré with $\sqrt{3} \times \sqrt{3}$ symmetry makes an angle of 0.3°±3.3° with the $\sqrt{3} \times \sqrt{3}$ of the Pb monolayer meaning that they can be considered aligned.

The alignment between the $\sqrt{3} \times \sqrt{3}$ corrugation of the moiré and the $\sqrt{3} \times \sqrt{3}$ of the Pb monolayer could suggest that the former is related to the atomic structure of either the top of the 3 ML Pb film or of the Pb/Si(111) interface. However, the results of several papers suggest that this would not be the case [118, 119]. First, diffraction measurements on Pb islands grown on top of Si(111) have shown that both the internal structure and the Pb/Si(111) interface are close to the bulk Pb(111), i.e. they have a 1×1 structure and not a $\sqrt{3} \times \sqrt{3}$ [118]. Second, in a paper of Kobayashi [119] it was shown that STM is able to visualize

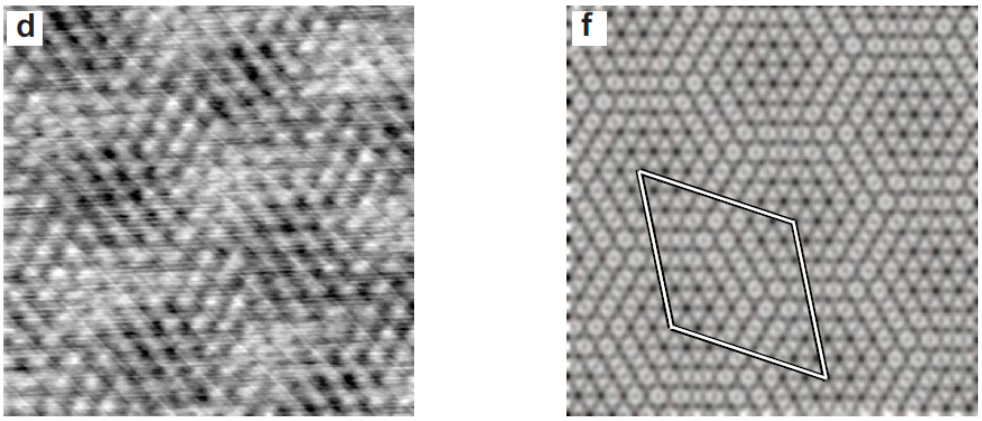

Fig. 4.30 Left: STM image of a graphene monolayer grown on Ir(111). Both the large and the small corrugations are interpreted as a moiré originating from the rotation of the graphene by an angle of 30°. Image size: $8 \times 8\ nm^2$, V_T: +0.2 V and I_T : 50 nA. Right: Simulated STM image ($8 \times 8\ nm^2$) reproducing all the moiré features of the STM image on the left [115].

moiré patterns or, more generally, nanoscale structures (like large defects) even if they are buried below many layers of matter. This result is due to the fact that tunneling electrons propagating through the material are scattered by the lattice-mismatched surface or defects. The electronic waves associated to electrons scattered by atomic-scale structures (like single atoms) decay much faster (on atomic scales) than those associated to electrons scattered by nanoscale structures (like moiré patterns or large defects) and they can propagate through many layers. This result explains why STM is quite insensitive to the atomic structure of inner layers while moiré patterns, that usually are nanoscale structures, can be imaged even if they are buried (think for instance to the moiré pattern shown in Fig. 4.17 arising from the Pb/Si(111) interface buried below 11 ML of Pb). These observations allow us to rule out the possibility that the small corrugation with $\sqrt{3} \times \sqrt{3}$ symmetry observed in our case is related to the atomic structure at the Pb/Si(111) interface.

The images of Fig. 4.30 are extracted from the paper of Loginova et al. [115] where different orientations of single layers of graphene grown on Ir(111) were characterized by means of LEEM, LEED and STM. In particular, these images will provide the strongest argument to rule out the fact that $\sqrt{3} \times \sqrt{3}$ corrugation is related to the actual atomic structure of the Pb film. On the left of Fig. 4.30, an STM image depicts the moiré pattern originating from both the lattice mismatch between graphene and Ir(111) and the rotation of the former with respect to the latter. This image is very similar to Fig. 4.29a and it also shows a hexagonal pattern with two different length scales. The small corrugation is rotated by an angle of 30° and the large one by an angle of 10° with respect to the Ir(111). By means of LEED

observations it was determined that in this configuration the graphene is globally rotated by an angle of 30° with respect to the Ir(111). Furthermore, they have observed that, inside the apparent depressions forming the large-scale corrugation, the small-scale exhibits a well-defined lattice of holes. On the other hand, outside of the long-range depressions, the small-scale corrugation forms bright regions of poorly ordered protrusions. Also in our case, closer inspection of the small corrugation observed on top of our 3 ML Pb film (see Fig. 4.29) reveals a non-uniform structure consisting of groups of either bright protrusions or dark holes separated by regions whose structure is not well defined. The right side of Fig. 4.30 shows a simulated STM image based on the graphene layer rotated by 30° on Ir(111) reproducing all the just described features. The most interesting thing of this work is the interpretation of both the corrugations as a moiré effect resulting from the 30° rotation of graphene on Ir(111).

In light of the above, we propose that also in our case both corrugations could be due to a moiré effect resulting from the 30° rotation of the Pb film on the Si(111). To support this idea we mention the work of Zeller et al. [114] where the moiré effect originating from hexagonally arranged adsorbate on hexagonal supports were studied in detail. As already mentioned in previous section this model relies only on geometric considerations about the coincidence of two hexagonal lattices arbitrarily oriented between them. In particular, from the analysis of the spatial beating frequencies originating from the coincidence of the two lattices, the model is able to predict the moiré lattice parameter L and its orientation Φ. The idea is that, each spatial beating frequency, e.g. first-order, second-order, etc., is due to a particular condition of coincidence between the two lattices and leads to the formation of a particular moiré pattern. The model applied in previous section describes a first-order moiré superstructure that is found when the atomic lattices are slightly rotated between them. The idea now is to extend the model by including the second order spatial beating frequency. The result is the emergence of moiré superstructures that can exhibit more complex appearance. In particular, it was shown that for Φ close to 30°, the moiré superstructure contains corrugations at two different length scales: a corrugation with periodicity larger than $\sim$20 Å and a fine structure with $\sqrt{3}\times\sqrt{3}$ periodicity. This condition is very similar to what we observe in Fig. 4.29. Similar moiré superstructure was also observed by Loginova et al. [115]. For this reason we applied the second order moiré model to the Pb film of Fig. 4.29. The equations describing a second-order moiré are written below [114]:

$$L(\Theta) = \frac{a_{Si}}{\sqrt{\left(\frac{3}{2}x\cos(\Theta) - \frac{\sqrt{3}}{2}x\sin(\Theta) - 1\right)^2 + \left(\frac{3}{2}x\sin(\Theta) + \frac{\sqrt{3}}{2}x\cos(\Theta) - \sqrt{3}\right)^2}} \tag{4.20}$$

$$\Phi(\Theta) = 60^\circ - \arccos\left(\frac{\frac{3}{2}x\cos(\Theta) - \frac{\sqrt{3}}{2}x\sin(\Theta) - 1}{\sqrt{\left(\frac{3}{2}x\cos(\Theta) - \frac{\sqrt{3}}{2}x\sin(\Theta) - 1\right)^2 + \left(\frac{3}{2}x\sin(\Theta) + \frac{\sqrt{3}}{2}x\cos(\Theta) - \sqrt{3}\right)^2}}\right) \tag{4.21}$$

Also in this case the expressions were adapted for the Pb/Si(111) system, therefore $x = \frac{a_{Si}}{a_{Pb}}$ with a_{Si} and a_{Pb} the lattice constants of Si(111) and Pb(111) respectively. All the quantities involved in these equations are defined exactly in the same way as was done in Fig. 4.25.

The plots of Fig. 4.31 compare the behavior of the size L (a) and the orientation Φ (b) of first order (green curves) and second order (red curves) moiré pattern as a function of the rotation angle Θ between the Pb film and the Si(111). In particular, green (red) curves were deduced from the first order (second order) moiré model described by equations 4.16 and 4.18 (4.20 and 4.21). It can be readily seen that first and second order moiré have opposite behavior. More importantly, for $\Theta \sim 30^\circ$, the first order model can never lead to a moiré pattern with L and Φ values similar to those observed on the "holes" terrace (see Fig. 4.29b). The difference between dotted and solid lines lies in the lattice constants values. In particular, dotted curves consider lattice constants close to the bulk values, i.e. a_{Si}=3.84 Å and a_{Pb}=3.5 Å, while solid lines are calculated by considering a compressed Pb film ($\sim$1%), i.e. a_{Si}=3.84 Å and a_{Pb}=3.46 Å. This level of compression is consistent with previous diffraction measurements carried out on 3 ML Pb islands grown on Si(111) [116]. From Fig. 4.31a it is evident that the greatest size L of the second order moiré obtained with a non-compressed Pb film is 40.5 Å for Θ=30°. However, it always remains below the experimentally observed values reported in Fig. 4.29b. The most intriguing result of Fig. 4.31a is that the introduction of a slight compression within the Pb layer allows the size L of the second order moiré to reach values consistent with those experimentally observed. Fig. 4.31b shows that the orientation Φ of the second order moiré is not strongly affected by the Pb compression. Furthermore, it can be easily seen that for Φ close to 30° the second order moiré orientation is dramatically affected by slight variations of Θ. Therefore, as already did in section 4.4.1, we estimate Θ from Φ. From Fig. 4.29b and Fig. 4.31b one can find that the mean orientation $\Phi \sim 8^\circ$ corresponds to $\Theta \sim 29^\circ$-30°. Then, from Fig. 4.31a this range of Θ corresponds to a second order moiré size L between 45.4 Å and 49.6 Å in agreement with the experimental values of Fig. 4.29b.
Finally, we can conclude that the intriguing structure observed in Fig. 4.29a, consisting of corrugations at two different length scales, is consistent with a second order moiré pattern born from the rotation of the 3 ML Pb film by an angle of 30° on the Si(111). Furthermore, by the results of the second order moiré model we can deduce that the Pb atoms within

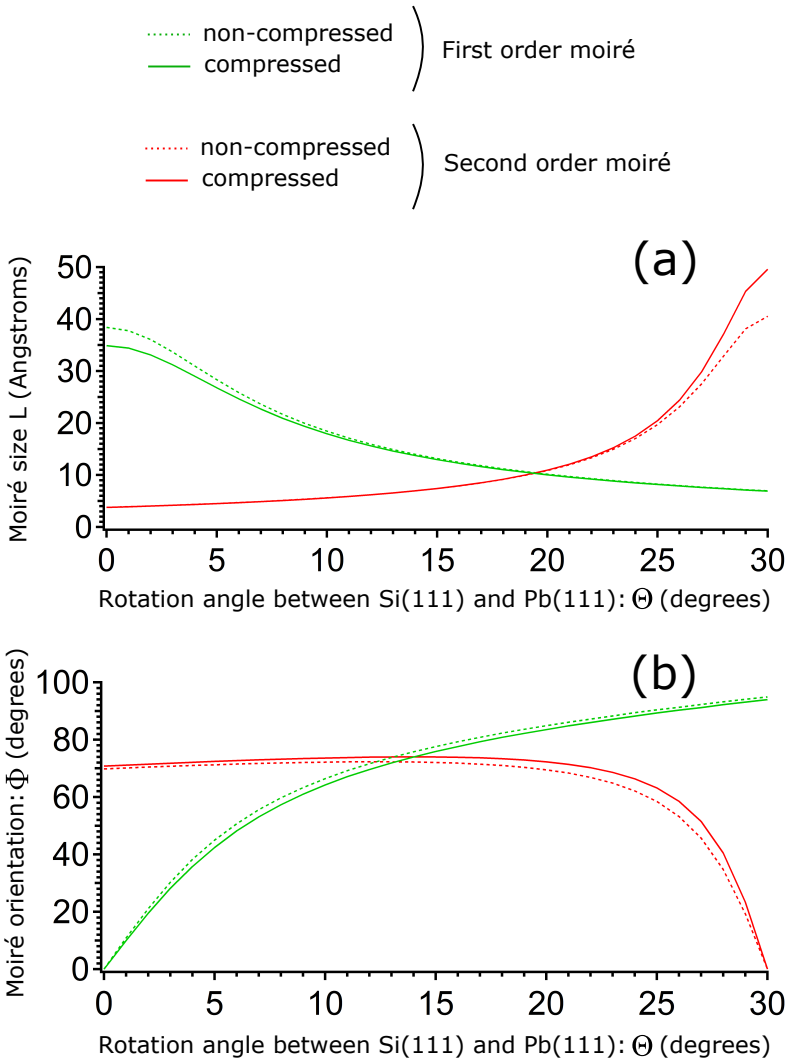

Fig. 4.31 Calculated period L (a) and orientation Φ (b) of first order (green curves) and second order (red curves) moiré as a function of the rotation angle Θ between the two underlying lattices. Within the model it was supposed that the lattice constant of the Pb(111) is close to the bulk value (dotted curves) and slightly compressed (solid curves).

the film are slightly compressed ($\sim$1%) with respect to the bulk Pb(111) positions. Due to the extreme sensitivity of the moiré orientation Φ to the rotation Θ of the Pb film we can also understand the reason for the large error bars on Φ (see Fig. 4.29b) and the orientation changes observed in Fig. 4.29a. Indeed, from Fig. 4.31b it can be clearly seen that tiny rotations of the Pb film (much smaller than 1°) induce strong rotations of the moiré (of the order of 10°).

4.4.3 Comparison between "protrusions" and "holes" terraces

I will conclude this section dedicated to the structure of the 3 ML Pb film grown on Si(111) by summarizing the results about the two types of terraces. At the beginning of this section it was shown in Fig. 4.23 that the deposition ∼2 ML of Pb on top of the Si(111)-α surface (at ∼110 K) leads to a quasi uniform ∼3 ML thick Pb film. Interestingly, the film presents two types of moiré patterns that lie on different silicon terraces and that we called "protrusions" and "holes" terraces. By comparing the experimental results with the predictions of a moiré model we deduced that the difference in the appearance of the two types of moiré reflects a more basic difference in the structural configuration of the Pb film. In particular, the "protrusions" moiré is a first order moiré involving only small rotations of the Pb film on the Si(111), i.e. less than 5°. Furthermore, the structure of the Pb film is assumed to be close to the bulk Pb(111), i.e. a_{Pb}=3.5 Å. On the other hand, the "holes" moiré is consistent with a second order moiré involving rotations of the Pb film of the order of 30°. In this case the model better describes the experimental results if the structure of the Pb film is slightly compressed with respect to that of the bulk Pb(111), i.e. a_{Pb}=3.46 Å. Of course, more refined models could be applied to extract more details about the atomic arrangement of this system.

To our knowledge there are no other papers reporting continuous 3 ML Pb films grown on Si(111) other than the work of Qin et al. [117]. In that paper the presence of terraces with different moiré corrugations was observed. However, the fine structure with $\sqrt{3} \times \sqrt{3}$ symmetry on the "holes" terraces was interpreted just as an atomic structure. Here, we propose that the mechanism giving rise the $\sqrt{3} \times \sqrt{3}$ pattern is a second order moiré with corrugations on two different length scales resulting from the rotation of the Pb film by an angle of 30° on the Si(111). It should be noted that the interpretation of Qin et al. of a $\sqrt{3} \times \sqrt{3}$ directly arising from atoms also implies a Pb film rotated by 30°. Even if it is known that the orientation of Pb islands can change (less than 6°) with coverage, a rotation angle of 30° was not reported elsewhere for this system [116]. The driving force of overlayer (monolayer or multilayer) rotations on substrates is believed to be the lattice mismatch between the two. A mismatched overlayer is naturally strained to achieve perfect coincidence with the substrate. However, the strain alone increases the energy strain and thus the total energy. The rotation of the overlayer is the response of the system to maximize the coincidence between atoms and minimize the strain. Another interesting information lies in the fact that most of the previous works remained in a "disconnected" regime, meaning that only disconnected Pb islands were investigated, whereas in my work I investigated both disconnected and continuous 3 ML films. I believe that the formation of strongly rotated 3 ML Pb films could be related to both the coverage and the continuity of the film itself.

Similar behavior was observed for Ag islands grown on H-terminated Si(111) and annealed to 480 K. In particular, it was reported that Ag islands exhibit different orientations depending on coverage, size and shape of the islands themselves. However, in that case, as the islands size increases they become better aligned with the substrate.

4.5 3 ML Pb islands on Si(111): Quantum Well States

4.5.1 Experiment and results

In this section we will start to investigate the electronic properties of 3 ML Pb islands grown on Si(111) with particular attention to the Quantum Well States (QWS). The sample was prepared by starting from the Si(111)-7×7 surface (see Chapter 2 for the preparation procedure). Then, $\sim$2.75 ML of Pb were evaporated at room temperature on top of the silicon substrate. Subsequent annealing at $\sim$320° C for 20 sec, by means of direct current heating, led us to a crystalline wetting layer with $\sqrt{7} \times \sqrt{3}$-Pb reconstruction and a nominal coverage of 1.2 ML. Finally, 2.1 ML of Pb were deposited on top of the sample kept at $\sim$220 K. This procedure results in the growth of 3 ML Pb islands on top of the Si(111). Note that islands start to grow only after the saturation of the Pb wetting layer, that is, only after that the initial $\sqrt{7} \times \sqrt{3}$-Pb surface is converted into the α phase corresponding to $\sim$1.3 ML (see section 4.3.1). As the 3 ML are unstable in temperature, the sample was kept at $\sim$220 K for the whole duration of the preparation until the transfer to the pre-cooled STM microscope. Fig. 4.32 shows a representative STM image of the investigated sample in which all the thicknesses are measured with respect to the Si(111) surface, therefore, the label 1 refers to the wetting layer (1 ML thick), the label 3 refers to 3 ML islands and so on. Remember that all topographic STM images are represented by using false colour scales in which each colour is linked to a different topographic height. According to this, in Fig. 4.32, the different colour (brown and red) used for the wetting layer (always labeled with 1) arises from a monoatomic step of the underlying silicon substrate.

From Fig. 4.32 it can be seen that a quite large part of the surface is covered by the wetting layer with a Si(111)-α phase (labeled with 1), while the rest of the surface is mainly occupied by disconnected 3 ML Pb islands. Single step islands (labeled with 4) on top of the 3 ML islands are frequently observed. Rarely, small 5 ML islands are found on the surface. Among the 3 ML islands, two types of moiré patterns already discussed in section 4.3.3, i.e. "protrusions" and "holes", largely discussed in section 4.4 can be recognized (labeled with 3a and 3b respectively). Furthermore, careful inspection of the 3 ML islands in Fig. 4.32 reveals the presence of shallow corrugations with small periods similar to those already discussed in

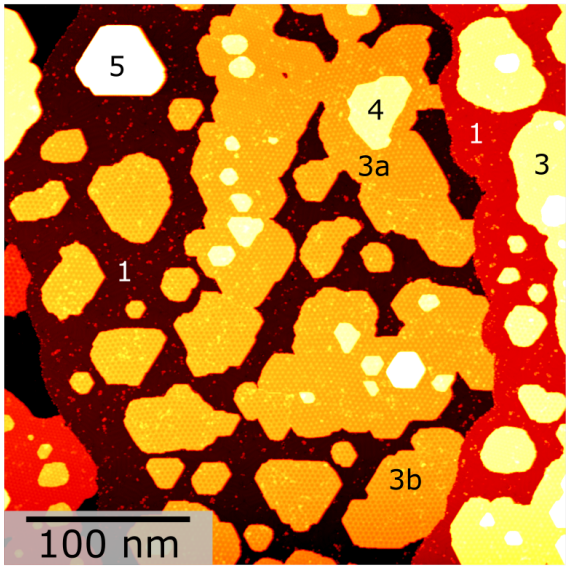

Fig. 4.32 Representative STM image of the sample used to investigate QWS. The numbers indicate the thickness of the different levels measured with respect to the Si(111). Image size: $340 \times 340\ nm^2$, V_T: +0.3 V and I_T : 50 pA. All the thicknesses are measured with respect to the Si(111) surface, therefore, the label 1 refers to the wetting layer (1 ML thick), the label 3 to the 3 ML islands and so on. Labels 3 a and 3 b refer to the "protrusions" and "holes" moiré corrugations respectively.

section 4.4 and resulting from the rotation of islands on Si(111). However, in the context of the QWS investigation presented here, we considered only the islands with the largest moiré periods, that is, the islands with either "protrusions" or "holes" moiré (labeled with 3a and 3b in Fig. 4.32). This is because they are supposed to be only slightly rotated with respect to the Si(111) substrate and therefore structural and electronic effects induced by rotations should be smaller. In this way, we could focus on the electronic differences of the two types of moiré and investigate the possible dependence on the atomic structure.

Before going any further, it should be noted that the appearance of both "protrusions" and "holes" moiré shown in Fig.4.34b and Fig.4.35b is different from that shown in Fig. 4.21a and Fig. 4.21b. Fig. 4.33 shows that this difference in the appearance is related to the bias voltage with which the STM images are acquired. In particular, Fig.4.34a and Fig.4.35a show that V_{bias}=1.7 V is close to the QWS energy and therefore STM images taken at this voltage will include the electronic contribution of the QWS itself (see Fig. 4.33). Lu et al. [120] have shown that this effect is intrinsic to the operating principle of STM. In particular, it

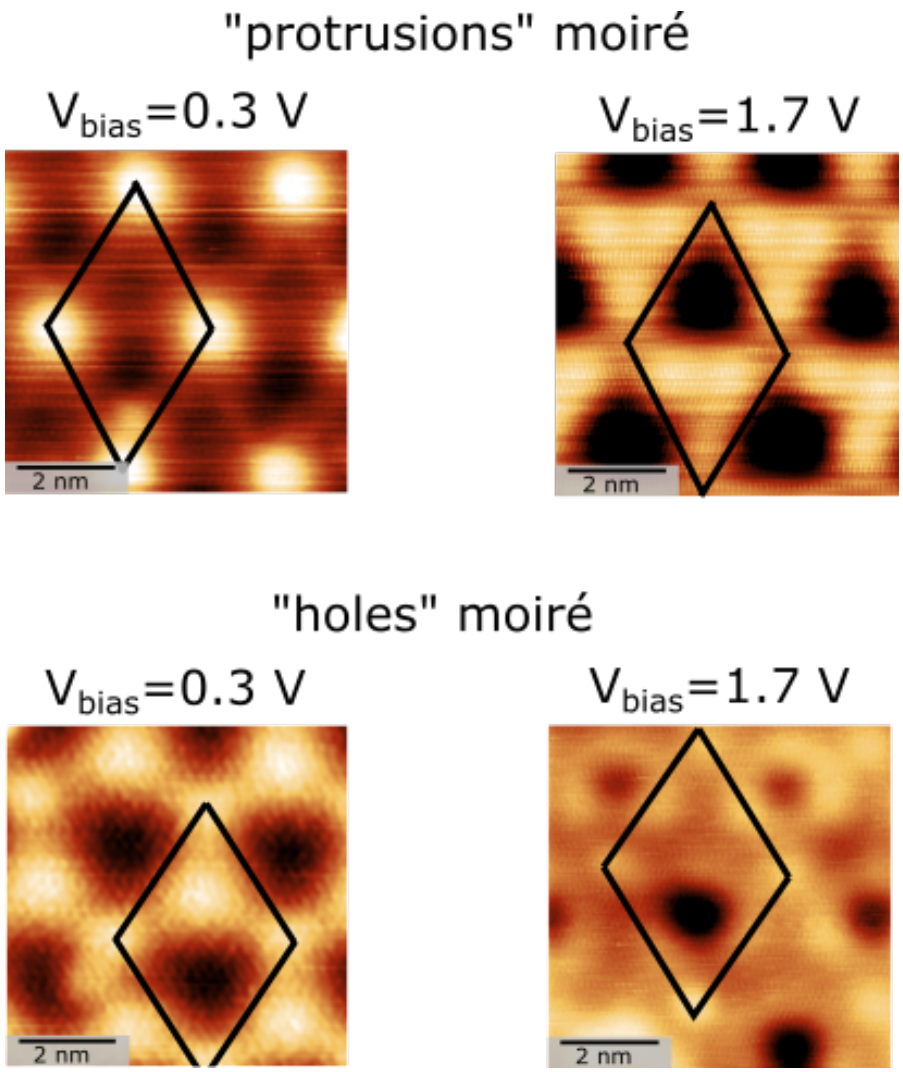

Fig. 4.33 Topographic STM images of 3 ML Pb islands exhibiting "protrusions" (top) and "holes" (bottom) moiré superstructures. (Top-left): Image size: $6.9 \times 6.9\ nm^2$, V_T: +0.3 V and I_T : 50 pA. (Top-right): Image size: $6.9 \times 6.9\ nm^2$, V_T: +1.7 V and I_T : 50 pA. (Bottom-left): Image size: $6.9 \times 6.9\ nm^2$, V_T: +0.3 V and I_T : 100 pA. (Bottom-right): Image size: $6.9 \times 6.9\ nm^2$, V_T: +1.7 V and I_T : 50 pA.

should be taken into account that, when STM images are acquired, the Integrated Density of States (IDOS) is the quantity actually measured. For a given bias voltage V, the electronic states contributing to the tunneling current are those between the E_F and $E_F + eV$. If the bias voltage reaches the QWS position, the latter will contribute to the STM image proportionally to its intensity. In particular, if the electronic contribution is strong enough, it will overcome that of the real surface topography and the resulting STM image will be very far from the real appearance of the surface. In this sense, STM images are always a convolution of the real surface topography and its electronic structure. It is also for the same reason that STM

images taken at very low voltages are considered to show the real topography of a surface, because in this case the electronic contribution to the IDOS can be usually neglected. In agreement with this fact, we can consider that the images of Fig. 4.33, acquired at low voltages (V_{bias}=0.3 V), show something which is very close to the real structure of the surface. This is also corroborated by the spectra in Fig.4.34a and Fig.4.35a which reveal that close to 0.3 mV the density of states is low enough to neglect the electronic contribution in STM images.

All the spectra presented in Fig. 4.34 and Fig. 4.35 were obtained by STS measurements performed on Pb islands with "protrusions" and "holes" moiré respectively. In particular, Fig. 4.34a shows local dI/dV spectra measured on the three positions indicated by the circles on the topographic image of Fig. 4.34b. A one-to-one correspondence between the colours of the spectra and those of the circles exists. During the experiments, I/V curves were measured at each point of the region depicted in Fig. 4.34b on a 30×30 grid of pixels. The topographic image was simultaneously acquired with a 120×120 grid of pixels. The spectra were then filtered, derived and normalized to obtain dI/dV curves at each point of the region. Finally, each dI/dV spectrum of Fig. 4.34a was obtained by averaging over all the spectra within the respective circle indicated in Fig. 4.34b. The spectra shown in Fig. 4.34a are measured at positive bias voltages, therefore they are proportional to the empty density of states of the Pb island with "protrusions" corrugation. The peak at around 1.63 V is the Lowest Unoccupied QWS of the island. Careful inspection of the circles in Fig. 4.34b reveals that they are located on the three non-equivalent positions of the moiré unit cell drawn in the image itself and that the QWS is spatially modulated by the moiré pattern in terms of its energy position and intensity. To further highlight the correlation between the QWS spatial modulation and the moiré, 2D conductance maps at different energies are plotted from Fig.4.34c to Fig. 4.34f. All the conductance maps are represented by means of a false color scale in which blue indicates the lowest spectral intensities and red the highest ones. By comparing the conductance maps, it can be easily seen that each of them shows a different spatial contrast but in all cases its period matches that of the moiré (compare with the corresponding topography in Fig.4.34b). Interestingly, the contrast of a conductance map at a given energy can be directly related to the spatial intensity modulations of the QWS at that energy. For instance, if we consider the map taken at $E = 1.65\ V$ (see Fig. 4.34d), we can see that red regions, like that within the green circle, correspond to the green spectrum of Fig. 4.34a which, at $E = 1.65\ V$, has the highest intensity compared with the others. On the other hand, blue regions, like that within the black circle, correspond to the black spectrum of Fig. 4.34a which, at $E = 1.65\ V$, has the lowest intensity compared to the others. Therefore, as already

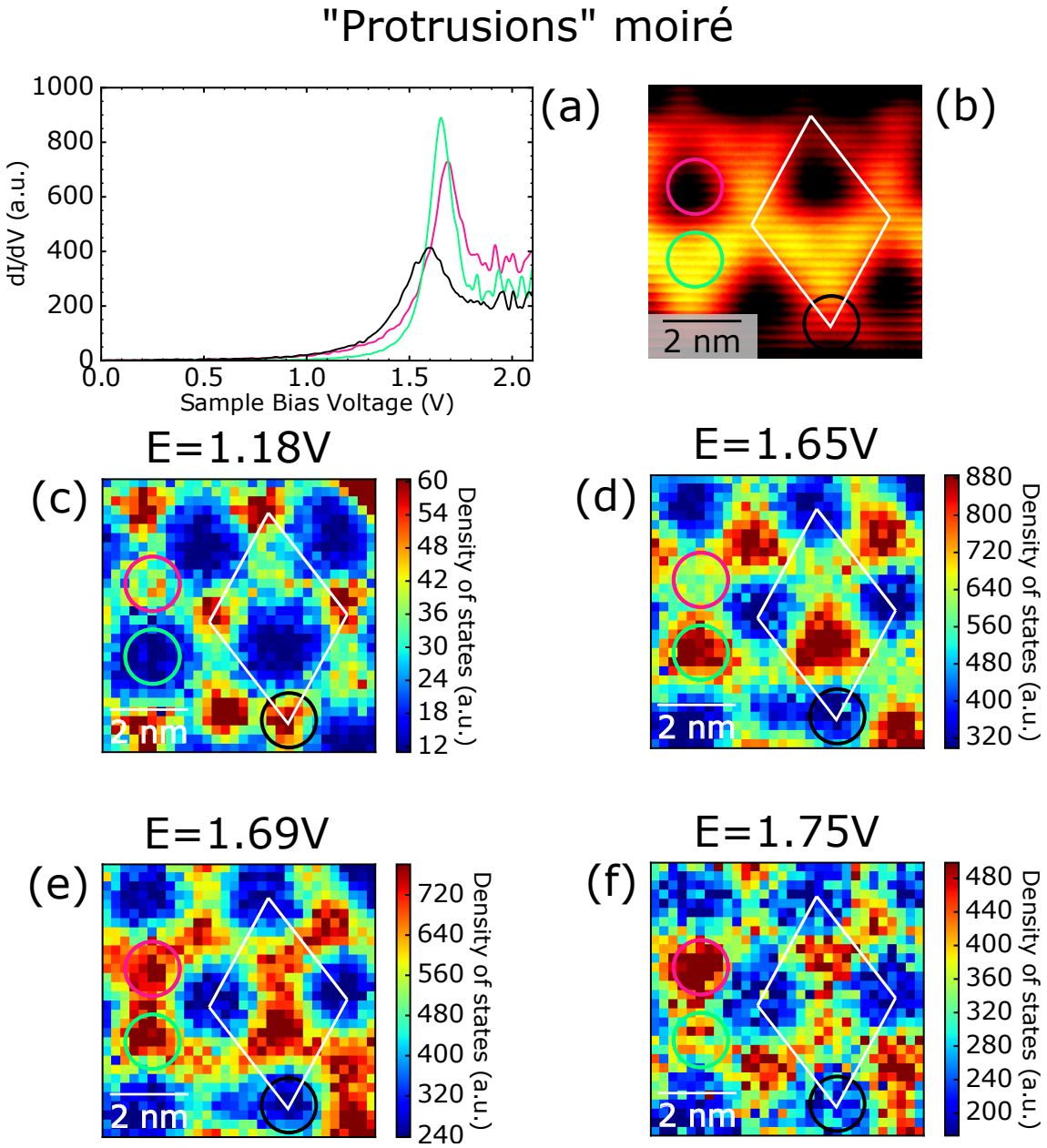

Fig. 4.34 (a): Local STS spectra acquired on top of a 3 ML Pb island with "protrusions" moiré. (b): Topographic STM image simultaneously taken during the STS experiments and representing the investigated region of the island. Image size: $6.9 \times 6.9\ nm^2$, V_T: +1.7 V and I_T : 50 pA. Colours of the circles correspond to those of the spectra in (a) and each spectrum was traced by averaging over all the spectra within the corresponding circle. (c)-(f): 2D conductance maps at different energies over the scanned region shown in (b). The moiré unit cell is indicated by a white parallelogram.

announced, the contrast of a conductance map at a given energy can be directly related to the combined spatial modulations of energy and intensity of the QWS. Another interesting aspect

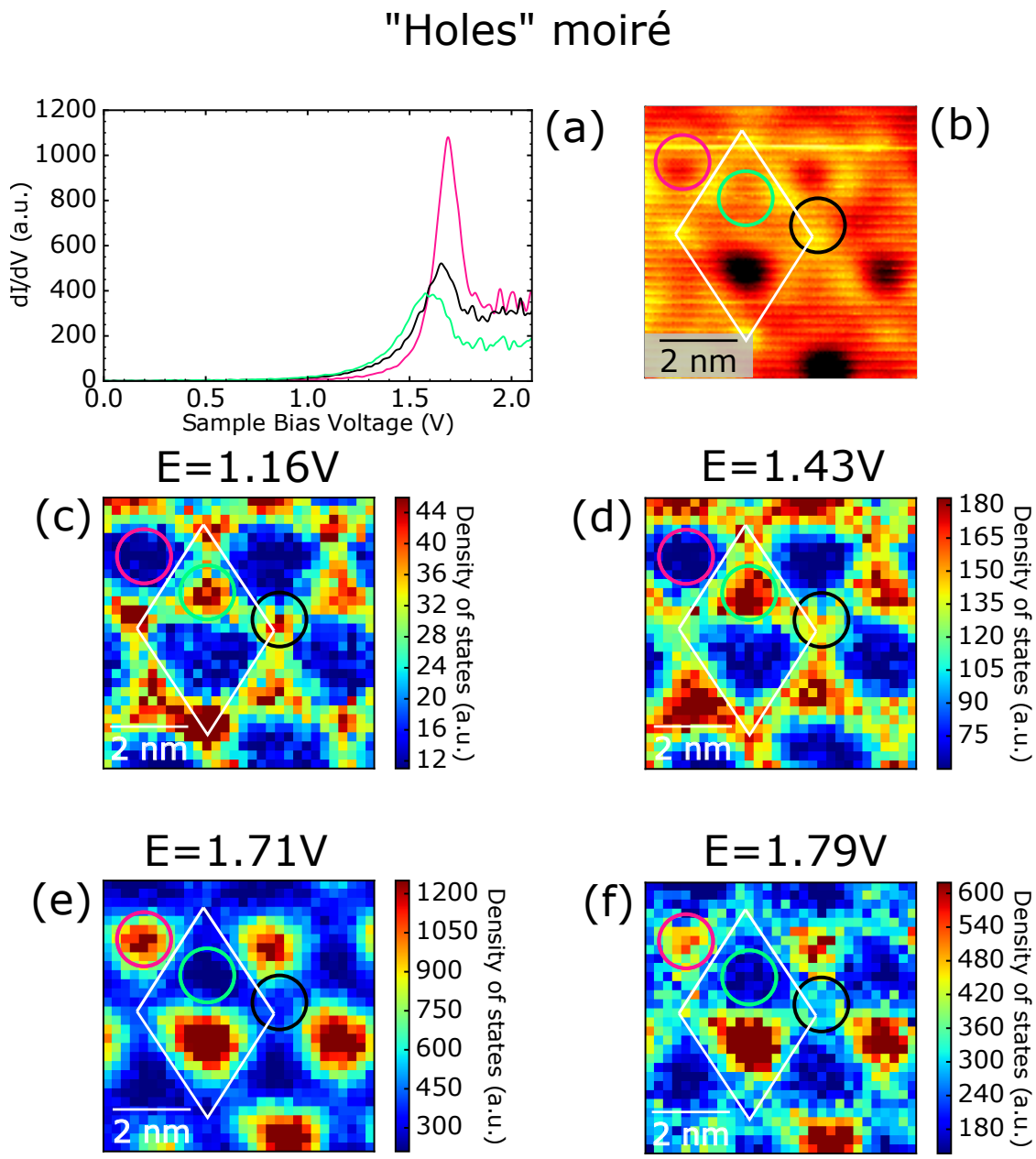

Fig. 4.35 (a): Local STS spectra acquired on top of a 3 ML Pb island with "holes" moiré. (b): Topographic STM image simultaneously taken during the STS experiments and representing the investigated region of the island. Image size: $6.9 \times 6.9\ nm^2$, V_T: +1.7 V and I_T : 50 pA. Colours of the circles correspond to those of the spectra in (a) and each spectrum was traced by averaging over all the spectra within the corresponding circle (c)-(f): 2D conductance maps at different energies over the scanned region shown in (b). The moiré unit cell is indicated by a white parallelogram.

about the spectral contrast should be highlighted. By comparing the conductance maps of Fig. 4.34c and Fig. 4.34d, it is clear that a contrast reversal takes place, that is, regions with

high spectral intensity turn into low ones and vice versa. With the same arguments used before, it can be shown that this effect is related to the spatial modulations of both intensity and energy of the QWS.
Fig. 4.35 shows STS spectra, topography and conductance maps measured on top of a 3 ML Pb island with "holes" moiré corrugation. Also in this case, I/V curves were measured at each point of the region depicted in Fig. 4.35b on a 30×30 grid of pixels and the topographic image was simultaneously acquired with a 120×120 grid of pixels. A spatial modulation of both intensity and energy of the QWS is observed also in this case and considerations similar to those made for the "protrusions" moiré apply to the contrast of the 2D conductance maps.

4.5.2 Discussion

A possible interpretation of the moiré-induced intensity spatial modulation of QWS observed in our experiments was already given by Lu et al. [120] in the case of 3 ML Pb islands grown on Si(111). They have suggested that it could reflect the spatial modulation of the density of states due to the structural relaxation of the island which is responsible for the emergence of the moiré itself. On the other hand, Altfeder et al. [104] provided a possible explanation for the moiré-induced spatial modulation of the QWS energies. They have proposed that the relaxation effects at the Pb/Si(111) interface could lead to spatially dependent reflection phase for the confined electrons within the Pb islands. The correlation between reflection phase and energy of QWS can be seen by the quantization condition discussed at the start of this chapter. These considerations imply that a spatial modulation of the reflection phase directly implies a spatial modulation of the QWS energy.
Our results are in agreement with these interpretations because previous theoretical studies have confirmed the presence of relaxation at the Pb/Si(111) interface [112, 121]. More interestingly, by comparing the conductance maps of Fig. 4.34 and Fig. 4.35 acquired at similar energies for "protrusions" and "holes" moiré superstructures, it is clear that the QWS are modulated in a different way in the two islands, that is, different patterns can be seen for similar energies. This fact probably reflects the different internal structure of the islands. In section 4.3.3, the origin of the different appearance of "protrusions" and "holes" moiré due to a different fcc stacking sequence was discussed. We recall here the most important results about this point.
Jian et al. [113] have investigated the origin of the two types of moiré on 3 ML Pb islands grown on Si(111). In this case, moiré corrugation observed on top of islands was attributed to the spatially modulated reflection phase at the Pb/Si(111) interface leading to the modulation of the QWS energy. Accordingly, the existence of two different moiré corrugations, i.e. "protrusions" and "holes", was ascribed to a different stacking of the Pb atomic plane giving

rise to two different Pb/Si(111) interfaces and consequently to two different reflection phases. On the other hand, Chan et al. [112] have interpreted the existence of the two types of moiré as due to a purely geometric effect resulting from the different stacking sequence. In particular, they have observed that the Pb/Si(111) relaxes giving rise to a strong corrugation on top of 3 ML Pb islands. Furthermore, they have shown that bright features observed on STM images of the two types of moiré always correspond to Pb atoms of the first layer on top of $T1$ sites of the Si(111) substrate. The difference in contrast between "protrusions" and "holes" moiré ultimately arises from the change in the registry of the Pb atoms with respect to the silicon substrate when the stacking sequence is changed.

It is clear that the origin of the moiré corrugation on top of very thin Pb layers is not completely understood. However, our results show that a strong correlation between electronic and structural contributions exists. It is also interesting to mention the study of Hupalo et al. [121] of STS measurements on top of 3 ML Pb islands grown on Si(111). The main difference between that study and our experiments is that, contrary to what we observed, they do not detect contrast reversal within STS images at different energies. Their conclusion was that, at any energy, bright features in STS maps always remain bright and dark features always remain dark. In our case, however, a contrast reversal (for instance between Fig. 4.34c and Fig. 4.34d or between Fig. 4.35d and Fig. 4.35e) can be easily seen. This difference is probably due to the fact that Hupalo et al. [121] do not have access to the fine structure of the QWS because a small set of energies was probed around the QWS. On the other hand, in our experiments the spectra were taken by measuring the whole spectrum between 0 V and 2.1 V. This method has enabled us to probe the details of the QWS structure with an energy resolution of 1.8 mV and to detect the presence of contrast reversal at different energies around the QWS. Furthermore, Hupalo et al. have calculated the images shown in Fig. 4.36. These images represent STS maps of 3 ML Pb islands at +1 V and 2 V for unrelaxed (on the left) and relaxed (on the right) structures. These images are the calculated counterpart of the experimental conductance maps shown in Fig. 4.34 and Fig. 4.35. Calculated images were used in the paper to conclude that Pb islands have a relaxed structure because they do not exhibit a contrast reversal similarly to what they observed in experiments. However, even if the quality of the image at 1 V for the relaxed island is not good, careful inspection reveals a change of contrast with respect to the image at 2 V (always for the relaxed structure). More interestingly, the pattern of the image at 1 V (relaxed structure) is very similar to our maps taken at similar energies in Fig. 4.34c or Fig. 4.35c and the contrast reversal between 1 V and 2 V goes in the same direction than our findings.

The important result is that, in agreement with above mentioned calculations, the inclusion of structural relaxation within Pb islands seems to better describe the spatial modulations of the QWS energies as well as the contrast reversal observed in experiments. All these considerations suggest that the origin of the moiré is probably due to a complex interplay between structural and electronic effects that cannot be considered separately.

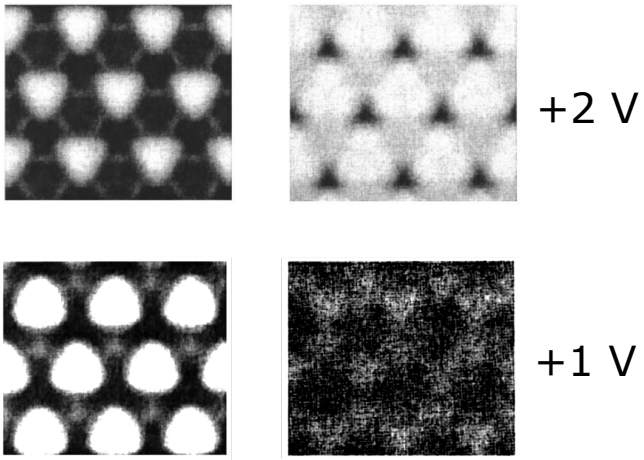

Fig. 4.36 Calculated STS images for 3 ML Pb islands on Si(111) as a function of the voltage. The results are reported for both unrelaxed (left) and relaxed (right) islands. The system is modelled by supposing a Pb/Si(111) interface with an α-phase reconstruction [121]. In our experiments, the Pb wetting layer exhibits an α-phase reconstruction.

In conclusion, the experimental observation of QWS on Pb islands exhibiting "protrusions" and "holes" moiré make it possible to directly associate the observed spatial modulation of the density of states to the modulation of QWS energy and intensity. Furthermore, by comparing our experimental STS maps with the calculated ones, we were able to confirm the strong correlation between confined electrons and internal structure of 3 ML Pb islands in determining the moiré pattern of the islands. In particular, the spatial modulation of the QWS energy could be related to the Pb/Si(111) interface modification. This correlation is corroborated by the different QWS spatial modulation observed on top of islands having different structures at the Pb/Si(111) interface, i.e. islands exhibiting "protrusions" and "holes" moiré superstructures. We can therefore conclude that moiré patterns observed on top of 3 ML Pb islands are the results of a complex interplay between electronic and structural effects. For this reason, a refined theoretical model including all the physics, e.g. substrate, stacking sequence, relaxation, spin-orbit coupling, etc., is highly desirable to have more insight into the intricate relation between electronics and structure in this system.

4.6 3 ML Pb islands on Si(111): Superconductivity

4.6.1 Superconductivity vs structure and rotation

In this section we will continue to investigate the electronic properties of 3 ML Pb islands grown on Si(111) by measuring their superconductivity. In particular, here we will focus on the role of both internal structure of Pb islands and their rotation with respect to the Si(111) substrate in determining superconducting properties. Scanning Tunneling spectroscopy (STS) experiments were carried out at 300 mK on the same sample already described at the start of section 4.5. The higher part of Fig. 4.37 shows topographic images of 3 ML Pb islands, exhibiting "protrusions" and "holes" moiré respectively. As already discussed in Section 4.3.3 and 4.5, different appearance of moiré corrugation is ascribed to the different stacking sequence of the Pb atomic planes within the island itself. The lower part of the

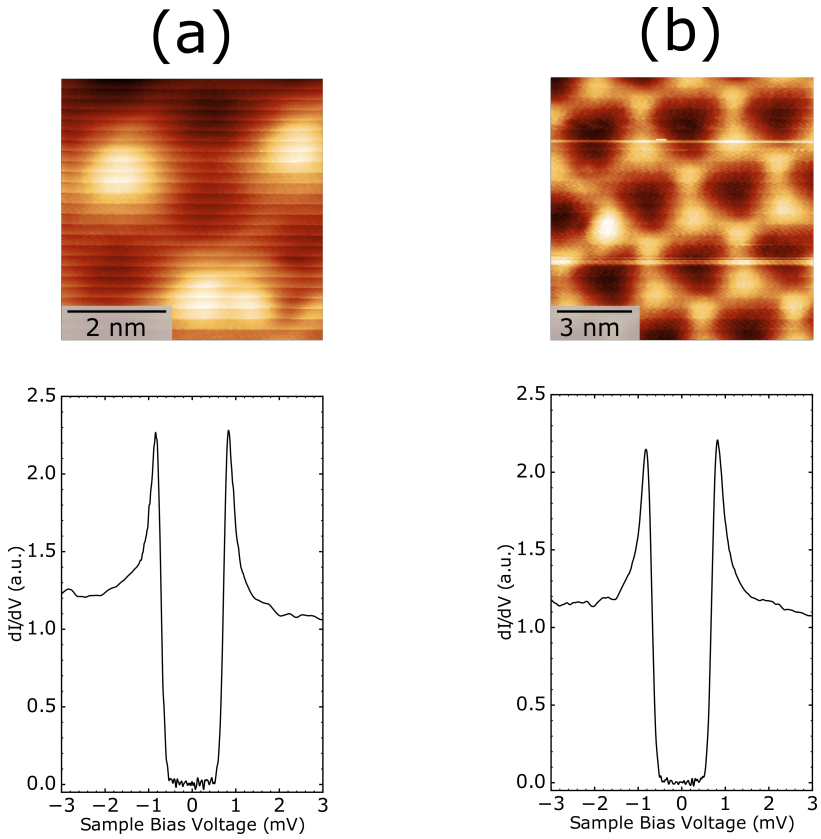

Fig. 4.37 Upper part of (a) and (b): STM images showing 3 ML Pb islands grown on Si(111) with "protrusions" and "holes" moiré respectively. (a) Image size: $5.3 \times 5.4\ nm^2$, V_T: +50 mV and I_T: 40 pA. (b) Image size: $10.4 \times 10.4\ nm^2$, V_T: +50 mV and I_T: 40 pA. Lower part of (a) and (b): STS spectra averaged over the respective topographic region shown in the upper part ($V_{set\,point} = 8\ mV, I_{set\,point} = 200\ pA$).

same figure shows representative dI/dV spectra measured over the respective topographic region shown above. During the experiments, I/V curves were measured at each point of the corresponding region on a 25×25 grid of pixels. The topographic image was simultaneously acquired with a 250×250 grid for the "protrusions" moiré and a 200×200 for the "holes" moiré. The spectra were then filtered, derived, and normalized to obtain dI/dV curves at each point of the region. Finally, the spectra in Fig. 4.37a and Fig. 4.37b were obtained by averaging over all the spectra. Unless otherwise specified, the experiments were carried out with Pt-Ir tips in the normal state.

Similarity of the spectra shown in Fig. 4.37 suggests that structural differences between Pb islands exhibiting different moiré corrugations have no role in determining their superconductive properties. Direct measurement of the peak-to-peak distance gives us the superconducting gap of the two islands, that is, $\Delta = (0.85 \pm 0.01)$ mV for the "protrusions" island and $\Delta = (0.86 \pm 0.02)$ mV for the "holes" one.
These values are close to those estimated by Qin et al. [117]. In that paper, tunneling spectra were measured as a function of the temperature. Then, based on the BCS model, the dependence of the gap Δ as a function of the temperature was fitted and the superconducting critical temperature of the 3 ML Pb film was estimated to be $T_C = \sim 4.9\ K$. From this procedure, the superconducting gap at $\sim$0 K results to be $\sim$0.8 mV which is close to our findings. In that study, the closeness of the Pb film critical temperature to the temperature limit of the experimental setup ($\sim$3.4 K), prevented them from obtaining sensitive data.
It is interesting to mention that the experiments of that paper were performed on a continuous 3 ML Pb film similar to that described in section 4.4.1. As already discussed in that section, when the 3 ML Pb film becomes continuous, different terraces of the sample exhibit two different structures. One is characterized by a Pb film slightly rotated with respect to the Si(111) (less than 6°) with Pb atoms close to the bulk Pb(111) positions. For the other terrace, we have proposed that the film is 30° rotated on the Si(111) and the Pb atoms are slightly compressed with respect to the bulk Pb(111) positions. Qin et al. [117], in their study have shown that 30° rotated terraces have a lower critical temperature with respect to the slightly rotated ones, i.e. T_C $\sim$3.65 K [117]. The difference of critical temperature further confirms that the two terraces of continuous Pb films are profoundly different also from an electronic point of view. The value of Δ that we used above to compare our results is that related to the slightly rotated terrace. This is justified by the fact that spectra of Fig. 4.37 were taken on a sample with disconnected 3 ML Pb islands (see the start of section 4.5 for topographic details about the sample) whose structure is found to be very close to the slightly rotated terraces of continuous Pb films (see Section4.4). Furthermore, we never observed 30° rotated

islands on disconnected samples.

From these considerations we can conclude that disconnected Pb islands and slightly rotated terraces of continuous Pb films exhibit very close superconducting properties confirming that they have similar structural and electronic properties.

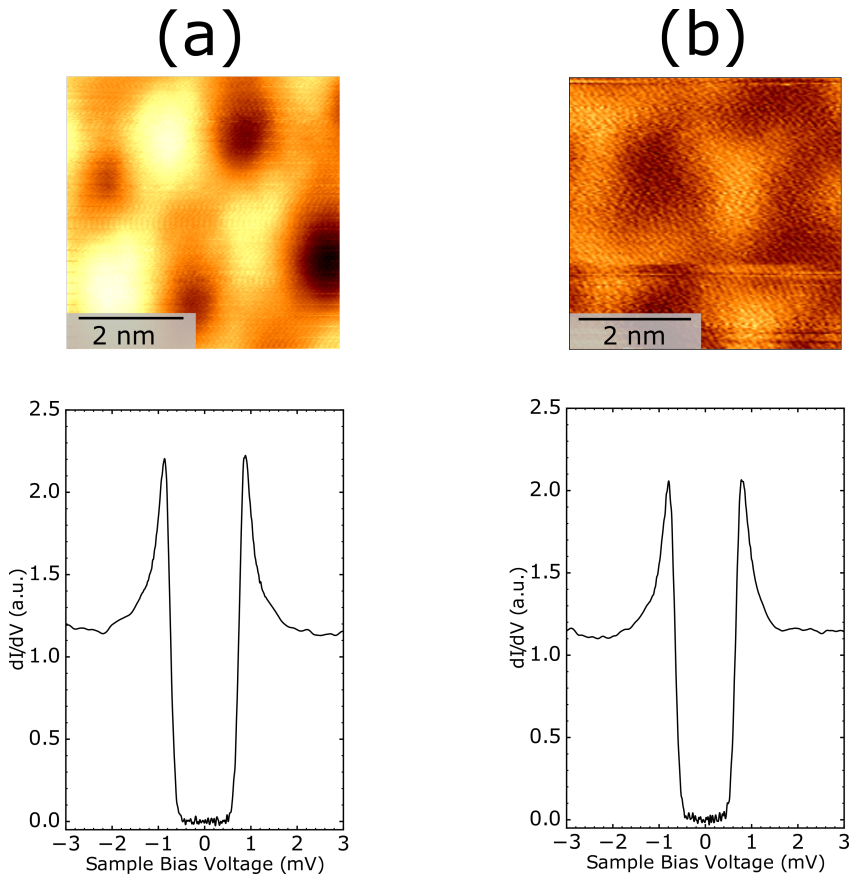

Fig. 4.38 Upper part of (a) and (b): STM images showing 3 ML Pb islands grown on Si(111) with small period moiré corrugations. (a) Image size: $5.2 \times 5.2\ nm^2$, V_T: +50 mV and I_T: 40 pA. (b) Image size: $4.8 \times 4.8\ nm^2$, V_T: +50 mV and I_T: 50 pA. Lower part of (a) and (b): STS spectra averaged over the respective topographic region shown in the upper part ($V_{set\,point}$=8 mV, $I_{set\,point}$=200 pA).

Pb islands discussed so far correspond to islands aligned with the silicon substrate. In order to see if rotations with respect to the Si(111) induce changes in their electronic properties, we also considered islands exhibiting moiré corrugations with smaller period than those shown before. The higher part of Fig. 4.38 shows two representative STM images of this kind of islands. Remember that all the details about the relation between moiré period and orientation of Pb islands with respect to the Si(111) were discussed in section 4.4.1. On the other hand, structural and electronic effects behind the appearance of moiré patterns on

top of Pb islands was discussed in section 4.3.3. The lower part of Fig. 4.38 shows dI/dV spectra measured over the respective topographic region shown above. Also in this case, during the experiments, I/V curves were measured at each point of the corresponding region on a 25×25 grid for the moiré in Fig. 4.38a and a 26×26 grid for the moiré in Fig. 4.38b. Topographic image was simultaneously acquired with a 250×250 grid for the moiré in Fig. 4.38a and a 180×180 grid for the moiré in Fig. 4.38b. The spectra were then filtered, derived, and normalized to obtain dI/dV curves at each point of the region. Finally, the spectra in Fig. 4.38a and Fig. 4.38b were obtained by averaging over all the spectra.
Also in this case, the similarity of the spectra shown in Fig. 4.38 suggests that structural differences between the two Pb islands have no role in determining their superconducting properties. The superconducting gap derived from the peak-to-peak distance results to be $\Delta = (0.88 \pm 0.01)$ mV for the spectrum of Fig. 4.38a and $\Delta = (0.84 \pm 0.02)$ mV for the spectrum of Fig. 4.38b. Interestingly, these values are consistent with those found for non-rotated islands.

From these results, we can conclude that, at least to a first approximation, the structural differences existing among 3 ML Pb islands, due to different stacking sequence and small rotations (less than 6°) with respect to the Si(111), do not affect their superconducting gap.

4.6.2 Superconductivity vs moiré corrugation

In previous section we studied the superconductivity of Pb islands having different internal structures, in terms of stacking sequence of the atomic planes, and rotations with respect to the silicon substrate. We concluded that all these structural changes do not affect the superconducting gap of the islands. On the oter hand, in this section, we will show that moiré corrugation can induce fluctuations of the superconducting coherence peaks.
Fig. 4.39a shows a topographic image of a 3 ML Pb island with a small period moiré. During the STS experiment, I/V curves were measured at each point of the same region on a 55×55 grid of pixels. A Pt-Ir tip in the normal state was used. The topographic image was simultaneously acquired with a 550×550 grid of pixels. The spectra were then filtered, derived, and normalized to obtain dI/dV curves at each point of the region. Two representative local dI/dV spectra are shown in Fig. 4.39b. These curves were obtained by averaging over all the spectra within the circle of the corresponding color traced in Fig. 4.39a. Inspection of the two spectra reveals a modulation of the coherence peak amplitudes. In particular, the coherence peak at negative energy has an amplitude of 2.49 a.u. for the black spectrum and of 2.28 a.u. for the pink one. This means that the peak height modulation actually is very small, i.e. less than 10 %.

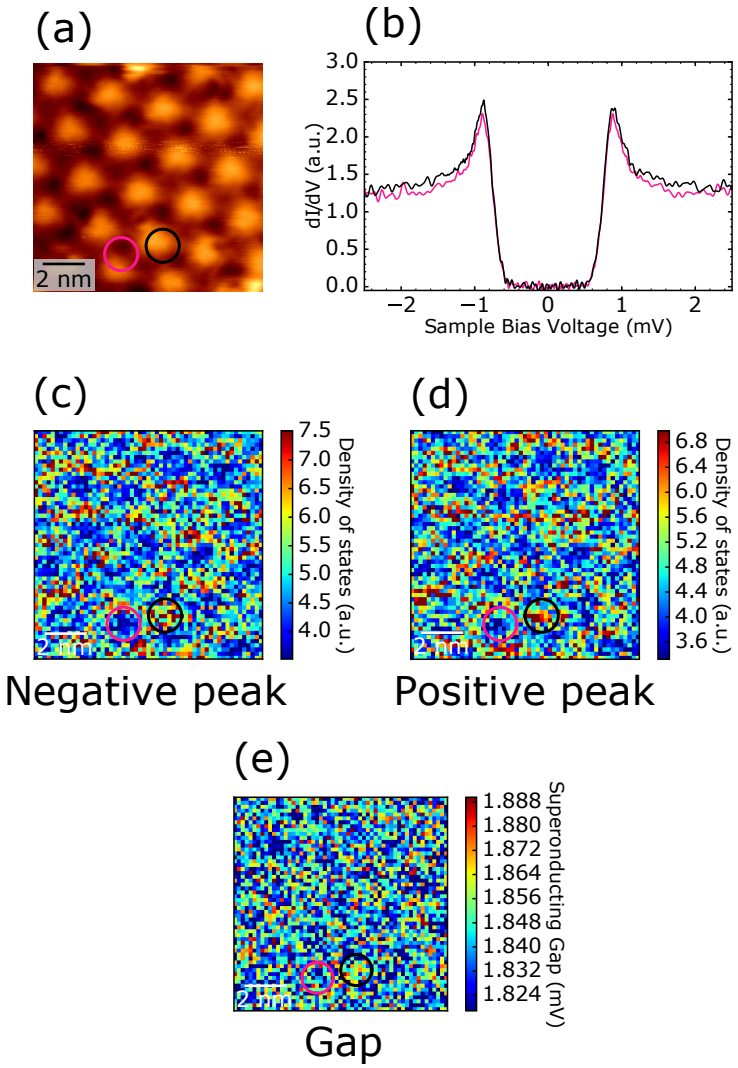

Fig. 4.39 (a): STM image showing a 3 ML Pb island grown on Si(111) with a small period moiré. (a) Image size: $10.8 \times 10.9\ nm^2$, V_T: +50 mV and I_T: 30 pA. (b): Two STS local spectra averaged over the spectra within the circles of the corresponding color depicted in (a) ($V_{set\,point}$=8 mV, $I_{set\,point}$=200 pA). The coherence peak at negative energy has an amplitude of 2.49 a.u. for the black spectrum and of 2.28 a.u. for the pink one. This means that the peak height modulation is very small, i.e. less than 10 %. (c) and (d): 2D conductance maps at the energies of the coherence peaks revealing the spatial modulations of the peaks amplitudes related to the moiré of the island. (e): 2D map representing the spatial distribution of the energy distance between the two coherence peaks (2Δ) over the scanned region.

In order to see if this modulation is related to the surface structure, 2D conductance maps at the energies of the coherence peaks are shown in Fig. 4.39c and Fig. 4.39d. Interestingly, these maps reveal that the peak amplitudes are spatially modulated with the same wavelength of the moiré observed in topography. This result is very interesting because, usually, co-

herence peak amplitudes are not expected to be affected on length scales smaller than the superconducting coherence length. In the case of 3 ML Pb islands, the superconducting coherence length is around 30 nm. This means that the modulations shown in Fig. 4.39 occur at length scales much smaller than the coherence length of the system.
Brun et al. [122] have measured a similar effect on the Pb monolayer grown on Si(111) and exhibiting the Striped Incommensurate phase. In that case, peak amplitudes modulations cannot be directly related to structural defects visible in topography. However, also in that case, the fluctuations occur on length scales below 10 nm which are much smaller than the Pb monolayer coherence length ($\sim$50 nm). Spatial fluctuations of the coherence peaks are not fully understood yet but are believed to be linked to short-range fluctuations of the electron-phonon coupling constant, going beyond theory of disorder on diffusive systems which typically average over short wavelength variations.
Starting from this interpretation, we believe that the spatial modulations of the coherence peaks shown in Fig. 4.39 have the same origin. The interesting aspect in our case is that we can relate spectroscopic modulations with a feature directly observable in topography, i.e. moiré corrugation. The origin of this behavior probably lies in the fact that moiré corrugation acts as a periodic potential of disorder. Another interesting aspect of our results is about the strength of the peak modulation. In the paper of Brun et al. [122] the fluctuations are very strong, that is, of the order of $\sim$20%, whereas in our case the effect is much weaker, i.e. less than $\sim$10%. This is in agreement with the fact that similar modulation effects were only observed in pure 2D systems, e.g. a Pb monolayer. The fact that we can detect this effect in 3 ML Pb islands suggests that the system is not purely 2D but still remains in a quasi-2D regime.
For the sake of completeness, Fig. 4.39e shows a 2D map representing the spatial distribution of the peak-to-peak distance over the same topographic region. This image indicates that the spatial distribution of the superconducting gap is roughly uniform thus confirming the results of previous section.

In conclusion, by investigating the superconductivity of 3 ML Pb islands grown on Si(111), we found that the moiré corrugation affects the coherence peaks on a scale length much smaller than the coherence length of the system. We interpret this effect by assuming that the moiré corrugation acts a periodic potential of disorder. Interestingly, the correlation between moiré pattern and spatial fluctuation of the coherence peaks reveals the presence of low-dimensional physics in 3 ML Pb islands previously found only in pure 2D systems.

4.6.3 Multi-gap superconductivity in 3 ML Pb islands

In this section, I will present the results of STS experiments performed on 3 ML Pb islands with a Pb-coated superconducting tip. The improved energy resolution provided by the superconducting tip has enabled us to have access to the fine details of 3 ML Pb islands electronic properties. The most important result will be the detection of a superconductivity with multi-band character that was not observed before in this system.

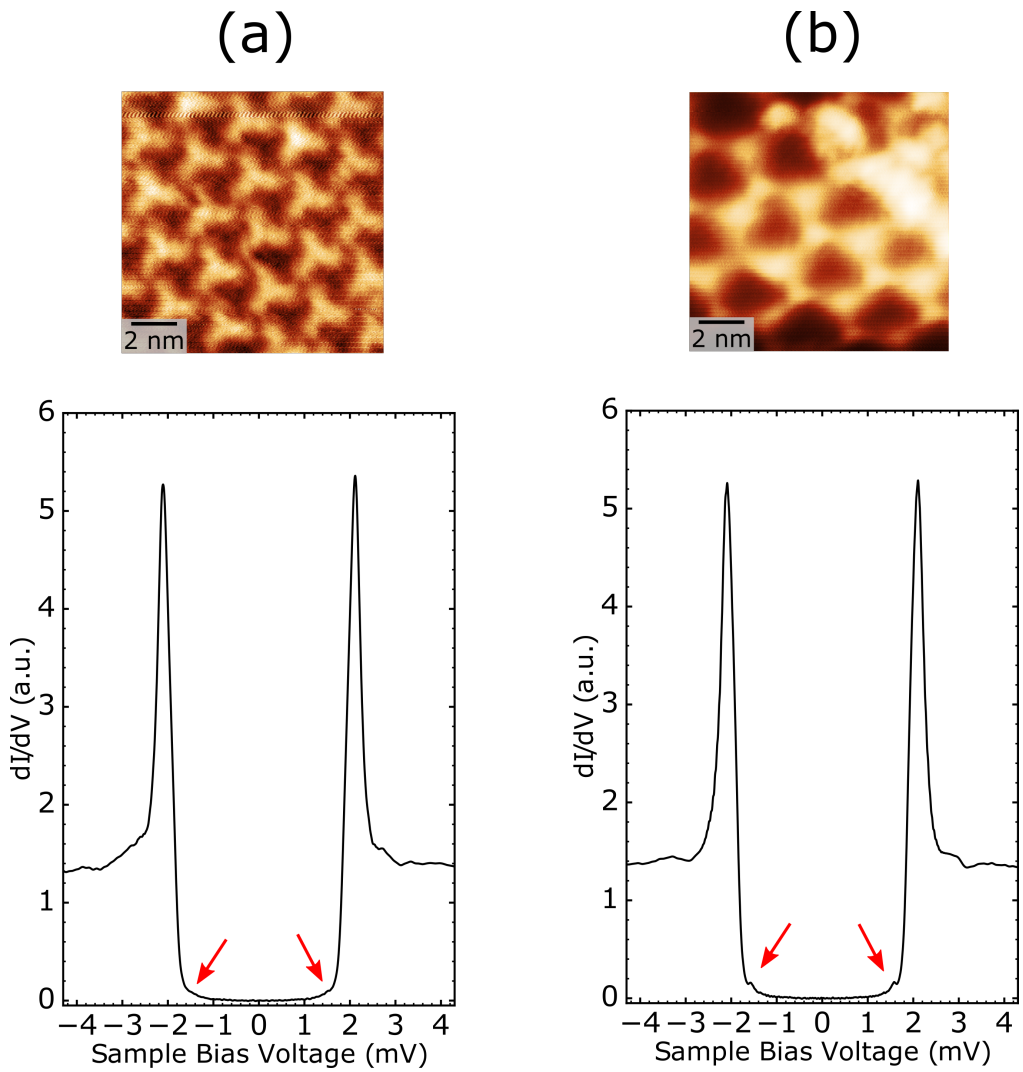

Fig. 4.40 Upper part of (a) and (b): STM images showing 3 ML Pb islands grown on Si(111) with small period and "holes" moiré corrugation respectively. (a) Image size: $11.2 \times 11.2\ nm^2$, V_T: +10 mV and I_T: 50 pA. (b) Image size: $11.1 \times 11.1\ nm^2$, V_T: +10 mV and I_T: 50 pA. Lower part of (a) and (b): STS spectra averaged over the respective topographic region shown in the upper part ($V_{set\,point}$=8 mV, $I_{set\,point}$=200 pA). Red arrows indicate two small peaks related to the multi-band character of Pb islands.

Fig. 4.40 shows topographic images of 3 ML Pb islands with small period (a) and "holes" moiré corrugation (b). The lower part of the same figure shows dI/dV spectra measured in Superconductor-Insulator-Superconductor (SIS) tunnel configuration (see Chapter 2) over the respective topographic region shown above. During the experiments, I/V curves were measured at each point of the corresponding region on a 50×50 grid for the moiré in Fig. 4.40a and a 67×67 grid for the moiré in Fig. 4.40b. The topographic image was simultaneously acquired with a 400×400 grid for the moiré in Fig. 4.40a and a 400×400 grid for the moiré in Fig. 4.40b. The spectra were then filtered, derived, and normalized to obtain dI/dV curves at each point of the region. Finally, the spectra in Fig. 4.40a and Fig. 4.40b were obtained by averaging over all the spectra.
As already seen in Chapter 2, spectra acquired in SIS configuration show two sharp peaks located at $|\Delta_{tip} + \Delta_{sample}|$, where Δ_{tip} and Δ_{sample} are the superconducting gap of tip and sample respectively. For the spectra of Fig. 4.40 we found $|\Delta_{tip} + \Delta_{sample}| = 2.12$ mV. Then, by comparing spectra acquired with both normal and superconducting tip on 5 ML reference Pb islands we estimated the tip energy gap, i.e. $\Delta_{tip} \sim 1.37$ mV, which is consistent with the value of bulk Pb usually ranging between 1.3 mV and 1.4 mV. From these considerations, we can deduce $\Delta_{sample} \sim 0.75$ mV for both the islands. It should be outlined that this value is slightly different from those observed in previous sections with a tip in the normal state. This is probably due to the fact that the energy gap of the tip can be slightly different from one experiment to another. We can therefore consider that the value of the gap Δ_{sample} obtained with the superconductive tip is consistent with those previously obtained with the normal tip.

Comparison of the spectra in Fig. 4.40 shows that they are not exactly the same. In particular, the spectrum in Fig. 4.40b has two small peaks at ± 1.54 mV highlighted by red arrows. The presence of these peaks is probably related to the fact that our 3 ML Pb island is a multi-band superconductor. We have seen that, due to Quantum Size Effects, 3 ML islands are expected to have only 2 sub-bands crossing the Fermi level (associated to the QWS). The participation of these sub-bands to superconductivity leads to the occurrence of two superconducting gaps. Ruby et al. [123] were able to detect, already in the case of bulk Pb, two superconducting gaps separated by 150 μeV. In our case the two gaps are separated by 0.58 meV. Furthermore, they have shown that the amplitude of these gaps depend on the surface orientation of the Pb monocrystal as well as on the selective tunneling through different Fermi surfaces. These arguments could be used to explain why the two islands of Fig. 4.40a and Fig. 4.40b show similar large gap feature but different small gap. Note that red arrows in Fig. 4.40a indicate a slight modulation that could be related to the presence of a small gap.
In conclusion, our STS experiments on 3 ML Pb islands with a superconducting tip reveal

the presence of superconductivity with multi-band character that was not done before on this system.

4.6.4 Multi-gap superconductivity in 5 ML Pb islands

Superconductivity with multi-band character in 3 ML Pb islands was discussed in previous section. Here, we will show that also in the case of 5 ML Pb islands we were able to detect a similar effect. STS experiments were carried out on top of 5 ML Pb islands grown on the sample already discussed in section 4.5. As for the 3 ML islands, the spectra were acquired at 300 mK. We will start to present the data acquired with a Pt-Ir tip in the normal state.

Fig. 4.41 shows topographic images of 5 ML Pb islands exhibiting a small period (a) and a

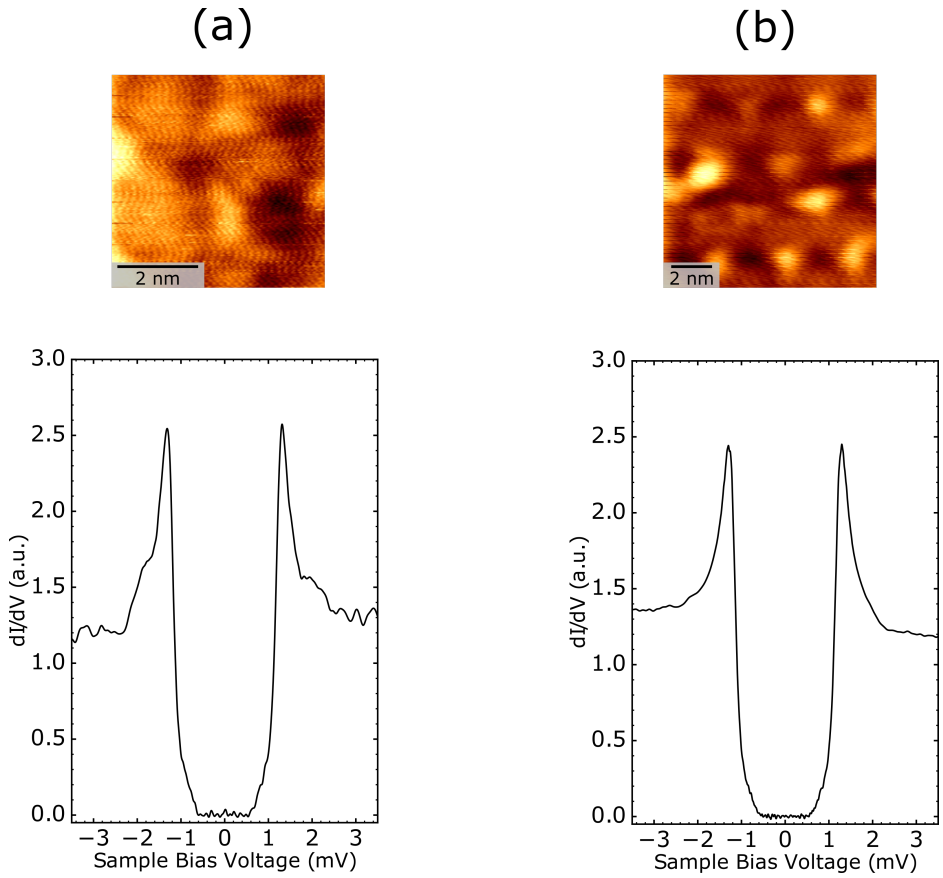

Fig. 4.41 Upper part of (a) and (b): STM images showing a 5 ML Pb island grown on Si(111) with small period (a) and a "protrusions" (c) moiré corrugation. (a) Image size: $5.3 \times 5.2\ nm^2$, V_T: +50 mV and I_T: 40 pA. (b) Image size: $10.4 \times 10.4\ nm^2$, V_T: +50 mV and I_T: 40 pA. Bottom part of (a) and (b): STS spectra averaged over the respective topographic region shown in the upper part ($V_{set\,point}$=8 mV, $I_{set\,point}$=200 pA).

"protrusions" moiré respectively (b). The lower part of the same figure shows dI/dV spectra

measured over the respective topographic region shown above. During the experiments, I/V curves were measured at each point of the corresponding region on a 10×10 grid for the moiré in Fig. 4.40a and a 50×50 grid for the moiré in Fig. 4.40b. The topographic image was simultaneously acquired with a 200×200 grid for the moiré in Fig. 4.40a and a 500×500 grid for the moiré in Fig. 4.40b. The spectra were then filtered, derived, and normalized to obtain dI/dV curves at each point of the region. Finally, the spectra in Fig. 4.41a and Fig. 4.41b were obtained by averaging over all the spectra.

The energy gap derived from the peak-to peak distance is $\Delta = (1.33 \pm 0.02)$ mV for the small period moiré and $\Delta = (1.3 \pm 0.01)$ mV for the "protrusions" moiré. Similarly to what observed in the case of 3 ML Pb islands, the energy gap is almost the same for the two types of moiré indicating that it is not affected by the underlying structural differences between the two islands.

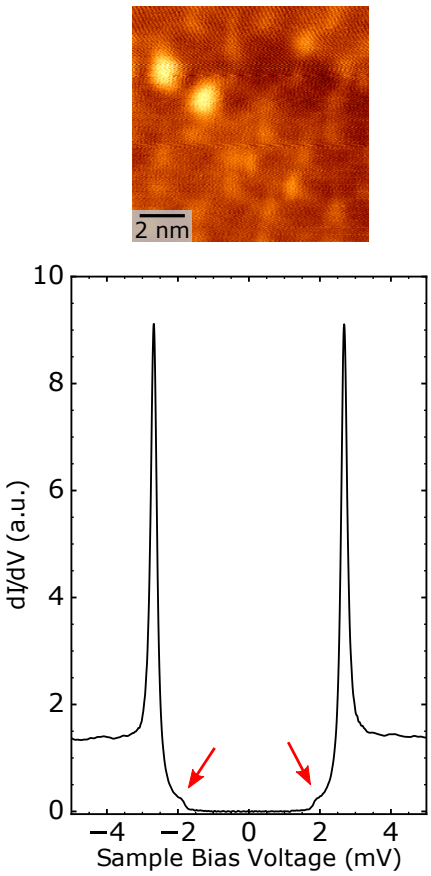

Fig. 4.42 Upper part: STM image showing a 5 ML Pb island grown on Si(111). Image size: $10.4 \times 10.4\ nm^2$, V_T: +0.20 mV and I_T: 50 pA. Lower part: STS spectra averaged over the respective topographic region shown in the upper part ($V_{set\,point}$=8 mV, $I_{set\,point}$=200 pA). Red arrows indicate the features related to the multi-band character of the Pb island.

More interestingly, Fig. 4.42 shows a dI/dV spectrum measured in Superconductor-Insulator-Superconductor (SIS) tunnel configuration on top of a 5 ML Pb island. During the experiments, I/V curves were measured at each point of the corresponding region on a 33×33 grid and the topographic image was simultaneously acquired with a 330×330 grid of pixels. The spectrum in Fig. 4.42 was obtained by averaging over all the spectra.
As already observed for 3 ML Pb islands, also 5 ML islands exhibit a multi-gap character and red arrows indicate the corresponding spectral feature. Always due to Quantum Size Effects, 5 ML Pb islands are expected to have only 3 sub-bands crossing the Fermi level that can participate to superconductivity and lead to the emergence of three gaps. The experimental signature of multi-gap superconductivity can be seen in Fig. 4.42 where small features (indicated by red arrows) besides those related to the large gap are observed.
In conclusion, our STS experiments on 5 ML Pb islands with a normal tip reveal a superconducting gap that is independent of the internal structure of the Pb islands themselves and their rotation with respect to the Si(111) substrate. Furthermore, STS experiments with a superconducting tip have shown the presence of superconductivity with multi-band character. Also in this case, similar measurements were not done before on this system.

4.7 Shiba states of isolated MnPcs on 3 ML Pb islands

4.7.1 Experiment and results

In this section, I will focus on the interaction between the magnetism of single MnPcs and the superconductivity of 3 ML Pb islands. The Pb/Si(111) sample is the same already described in section 4.5, consisting of 3 ML Pb islands grown on Si(111) on top of which $\sim$0.13 $molecules/100\ nm^2$ of MnPcs were deposited at low temperature ($\sim$100 K). STS experiments were carried at 300 mK by means of a Pt-Ir tip in the normal state.
The results shown in Fig. 4.43 represent the whole set of data acquired during these experiments. Fig. 4.43a shows an STM image taken just before the STS experiment depicting a single MnPc on top of a 3 ML Pb island exhibiting a "holes" moiré. MnPc has the typical appearance with a bright protrusion in the middle, representing the Mn atom, and four lobes corresponding to the ligands of the molecule [70]. Fig. 4.43b shows a topographic STM image simultaneously acquired during the STS experiment over the same region shown in Fig. 4.43a. Careful inspection of this image reveals that MnPc molecule moved several times during the STS experiment, by changing both adsorption site and orientation. We ascribe this effect to the voltage ramp during the acquisition of I/V spectra. This is probably due to the variable electric field generated by the tip leading to the excitation of some molecu-

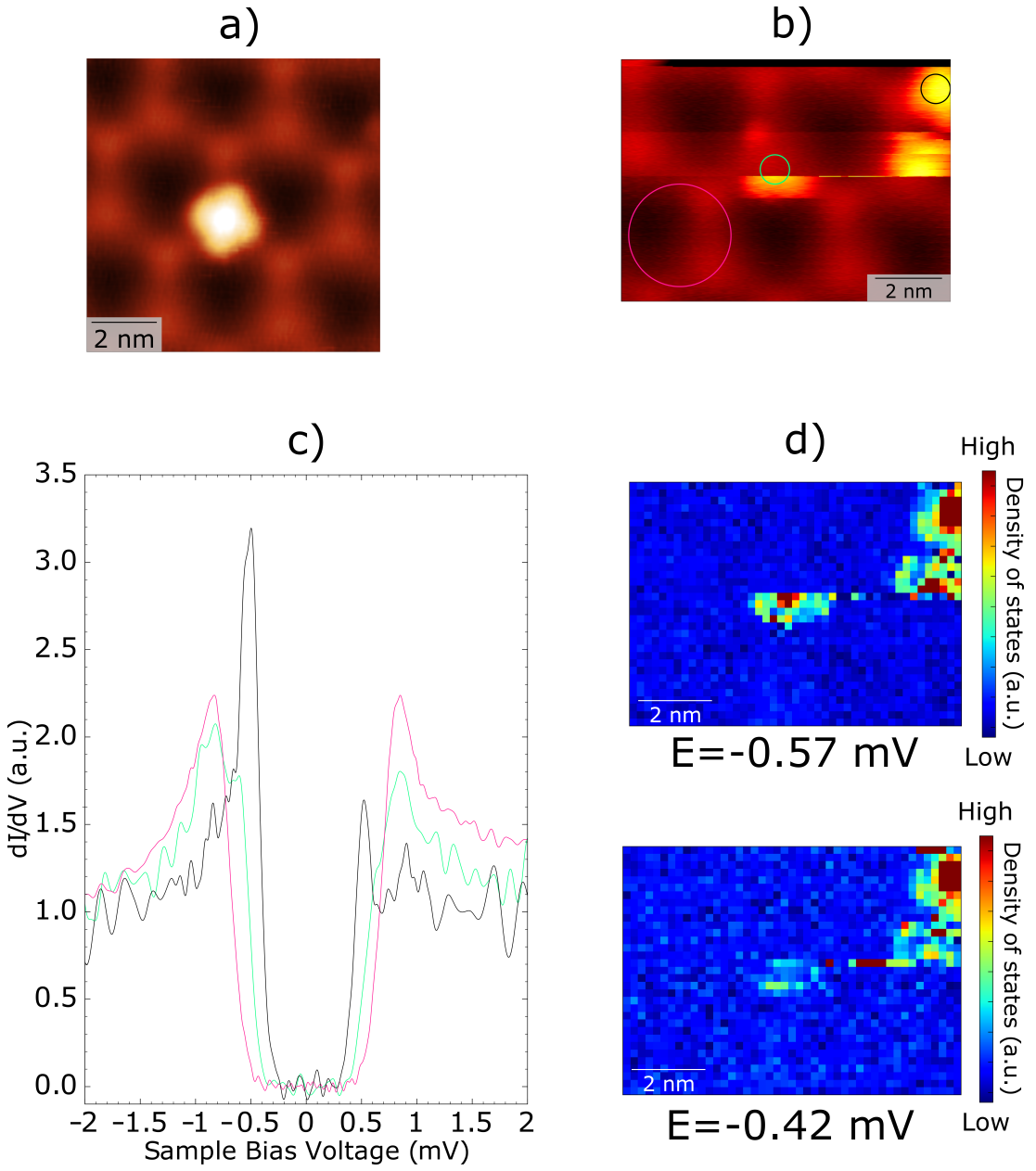

Fig. 4.43 Magnetic interaction between isolated MnPc and a 3 ML Pb island exhibiting "holes" moiré corrugation. (a): Topographic STM image taken before the STS experiment. Image size: $9 \times 9\ nm^2$, V_T: +0.25 V and I_T : 100 pA. (b): Topographic STM image taken during the STS experiment (Image size: $9 \times 6.5\ nm^2$). (c) Local dI/dV STS spectra measured within the region identified by the circles of the corresponding colour. (d): 2D dI/dV conductance maps acquired at -0.57 mV and -0.42 mV over the region shown in (b).

lar vibrational modes and thus to sudden configuration changes. The same behavior was observed for MnPcs on top of 3 ML Pb islands with different types of moiré corrugations. Regardless of this problem, we were able to gain some interesting information about the

interaction between molecular spin and superconductivity.
Fig. 4.43c shows local dI/dV STS spectra obtained by averaging all the spectra within the corresponding circle drawn in (b). Note that a one-to-one correspondence between the colours of the spectra and those of the circles exists.
Pink spectrum was acquired away from the molecule and therefore it represents the spectrum of the superconducting 3 ML Pb island unaffected by the presence of the spin associated to the MnPc. Green and black spectra were acquired on top of the MnPc in the two different adsorption configurations. Comparison of these curves shows that the spectral signature on top of MnPc is different from that of the bare Pb superconductivity. In particular, coherence peaks have asymmetric amplitudes and the superconducting gap width is apparently reduced. In Chapter 1, it was shown that the local interaction between magnetism of atoms/molecules and superconductivity leads to the emergence of Shiba states within the superconducting gap. Shiba states consist of pairs of peaks symmetrically located with respect to the Fermi level. Interestingly, it was also shown that, due to the non-magnetic scattering channel between impurity and conduction electrons of the superconductor, the two peaks associated to a Shiba state exhibit asymmetric amplitudes. From these considerations, we ascribe the above mentioned spectroscopic signature on top of the MnPc to the presence of Shiba states close to the gap edge induced by the magnetic coupling between molecular spin and superconductivity. Comparison of the spectra taken on top of the MnPc lying in two different configurations reveals that the energy of Shiba states is different in the two cases. As discussed in Chapter 1, the energy of Shiba states is related to the strength of the magnetic coupling. In accordance with this, the spectra in Fig. 4.43c tell us that the strength of the magnetic coupling between MnPcs and 3 ML Pb islands depends on the adsorption configuration of the MnPcs themselves. Similar results have already been reported in the case of MnPcs deposited on bulk crystals of Pb [15, 19, 21].
Fig. 4.43d shows two differential conductance maps acquired at -0.57 mV -0.42 mV over the same region shown in Fig. 4.43b. These maps corroborate the presence of two distinct Shiba states associated to the two adsorption configurations of the molecule. In particular, at -0.57 mV Shiba states related to the initial position of the MnPc (in the middle of the image) are well developed. On the other hand, at -0.42 mV, i.e. the energy of the Shiba state induced by the molecule in the upper right, almost no signal can be detected in the initial adsorption configuration.

4.7.2 Discussion

The first thing to point out about the experimental results of Fig. 4.43d, is that the spatial extension of Shiba states induced by MnPcs on top of 3 ML Pb islands grown on Si(111) is

limited to the region occupied by the molecules themselves. This observation is different from the study of Ménard et al. [17], where a magnetic impurity embedded in a quasi-2D $2H-NbSe_2$ crystal induces long-range Shiba states extending up to $\sim$10 nm away from the impurity. The main argument to explain that behavior was about the dimensionality of the superconducting system that, decreased to 2D, leads to a slower spatial decay of the wavefunction associated to the Shiba states with respect to the 3D case. Accordingly, a possible interpretation of our results could be the following. Even if 3 ML Pb islands can be considered a quasi-2D electron system, they already start to be in a 3D limit and therefore Shiba states induced by magnetic impurities are localized around the magnetic atom and extend to the molecule's ligands. This behavior is different from the one found in MnPc deposited on bulk Pb(111) [73] where Shiba states are located only on the magnetic atom but does not extend to the ligands.

Another interesting new aspect of our results is the strength of the coupling between MnPcs and 2D superconductivity of 3 ML Pb islands. In section 1.3.5, the effect of both magnetic and non-magnetic part of the interaction between isolated magnetic impurities and conduction electrons of a superconductor was discussed. In particular, it was shown that the energy of Shiba states is closely related to the strength of the magnetic coupling J. On the other hand, the asymmetry of the peaks related to Shiba states is determined by the non-magnetic interaction. Our measurements on top of many isolated MnPcs on 3 ML Pb islands, always revealed Shiba states close to gap edge with an asymmetry of the peaks always in the same direction, i.e. amplitude of the peak at negative energy larger than that of the peak at positive energy, (see Fig. 4.43c). This observation is clearly different from what previously observed in the case of MnPcs deposited on bulk Pb(111) substrates or on thicker islands of Pb grown on Si(111). In these cases, in fact, Shiba states are observed at different energies, even in the middle the superconducting gap, and with different asymmetries of the peaks associated to the Shiba states. The latter observation indicates that, in the case of bulk substrates, the coupling of MnPcs exhibit a wide range of strengths (see Fig. 1.15). On the other hand, in our case the observation of Shiba peaks always with the same asymmetry suggests that MnPcs on top of 3 ML Pb islands are always coupled in a comparable regime regarding J and K. The question that remains to be understood is whether they actually are strongly or weakly coupled.
By looking at Fig. 1.15, it is evident that the strength of the coupling cannot be determined just by the asymmetry of the Shiba states. However, starting from the results of Fig. 4.43c together with simple considerations I tried to estimate what could be the actual strength of the coupling. We know that the spin of MnPcs is due to the Mn atom in the middle of

the molecular structure. Then, we also know that adsorption of MnPcs on top of a bulk Pb surface reduces the molecular spin from $S = 3/2$ to $S = 1$ [19]. At this point, the remaining spin is due to the partially filled d_{z^2} and d_{xy} orbitals. On the other hand, the exchange interaction between MnPcs and Pb surface is mediated by the spin of the d_z orbital because the d_{xy} orbital is delocalized on the molecular plane, i.e. over the ligands, and it is weakly coupled to the surface. Interestingly, previous works have reported the occurrence of Kondo effect when MnPcs are deposited on top of bulk Pb(111) or thin Pb films grown in Si(111) [19, 21, 73]. As the Kondo effect requires an antiferromagnetic coupling ($J < 0$) between magnetic impurity and metallic substrate, we can suppose that also in our case MnPcs are antiferromagnetically coupled ($J < 0$) with 3 ML Pb islands.
By remembering the discussion of section 1.3.5, we know that the asymmetry of Shiba peaks is given by the sign of K that is related to the non-magnetic diffusion of conduction electrons of the substrate through the electrostatic potential of the impurity. As already discussed in section 3.4.6, the above mentioned reduction of the molecular spin upon adsorption of MnPcs on Pb surfaces can be ascribed to a charge transfer from the molecule to the substrate that leaves an unbalanced positive electronic charge localized on top of the molecule. As we do not know how the electronic charge distributes to the molecule after charge transfer, we will suppose that the positive charge is uniformly distributed. This assumption implies that the β parameter discussed in section 1.3.5 is negative.
From previous considerations, we can finally assume that, when MnPcs are adsorbed on top of 3 ML Pb islands, both the exchange coupling J and the non-magnetic potential K associated to the molecules are negative ($J < 0$ and $K < 0$). By looking to Fig. 1.15, it is easy to verify that this conditions corresponds to a magnetic impurity with a weak magnetic coupling inducing Shiba peaks close to the gap edge with the amplitude of the peak at negative energy larger than that of the peaks at positive energy. Interestingly, this condition agrees with our experimental observations.

In conclusion, STS measurements on 3 ML Pb islands grown on Si(111) revealed that, contrary to what observed on other quasi-2D or bulk systems, Shiba states induced by isolated MnPcs are localized on the whole molecule with a larger amplitude on the magnetic atom of the molecule. Furthermore, Shiba states are always found close to the gap edge and with the same asymmetry, i.e. amplitude of the peak at negative energy larger than that of the peak at positive energy, indicating that coupling strength between MnPcs and substrate falls always in the same regime. Starting from our experimental results together with simple considerations about the system, we proposed that MnPcs are antiferromagnetically coupled to the substrate and that a positive charge is uniformly distributed over the molecule as a

result of a charge transfer between MnPcs and Pb surface. This condition has allowed us to deduce, in agreement with experimental observations, that MnPcs on top of 3 ML Pb islands are always weakly coupled. A similar result was not reported before in similar systems and for this reason further investigation is needed. In particular, it should be outlined that we deduced the strength of the coupling by imposing a number of assumption. For this reason, theoretical calculations, taking into account the physics involved in our system, are necessary to confirm the proposed scenario.

4.8 Coupling of Shiba states within 2D islands of MnPcs

4.8.1 Experiment and results

In this section, I will focus on the coupling of different Shiba states induced by 2D self-assembled islands of MnPcs on top of a 3 ML Pb film grown on Si(111). The Pb/Si(111) is the same already described in section 4.4, consisting of a quasi-uniform Pb film on top of which $\sim$2.7 $molecules/100\ nm^2$ of MnPcs were deposited at low temperature (110 K). In particular, here we will focus on terraces on top of which the majority of MnPcs was adsorbed, i.e. terraces exhibiting "protrusions" moiré corrugation (see Fig. 4.44). STS experiments were carried out at 300 mK by means of a Pt-Ir tip in the normal state.

The most important results of these experiments are shown in Fig. 4.45. In particular, Fig. 4.45a shows a STM image taken just before the STS experiment depicting a self-assembled 2D island of MnPcs. Fig. 4.45b shows a differential conductance map acquired at -0.11 mV, i.e. inside the superconducting gap, over the same region shown in Fig. 4.45a. Away from the molecular island, the low density of states (blue color) indicates the presence of the superconducting gap associated to the Pb film filled with quasiparticle states. In the same way, inside the molecular domain, quite uniform regions with low density of states can be found, without the appearance of isolated Shiba states to any energy. The most interesting aspect of this image is the presence of a spectroscopic signature with increased intensity surrounding the molecular domain and defining its edge. It is remarkable how this "edge" feature does not disperse within the molecular islands but it remains confined to its edge and it extends far away from the molecules themselves.

Fig. 4.45c shows local dI/dV spectra obtained by averaging all the spectra within the region defined by the corresponding cross. Note that a one-to-one correspondence between the colours of the spectra and those of the crosses exists. Analysis of the behavior of these spectra confirms the scenario described above. In particular, green spectrum was acquired away from the molecular island and therefore it represents a reference spectrum. The black curve taken

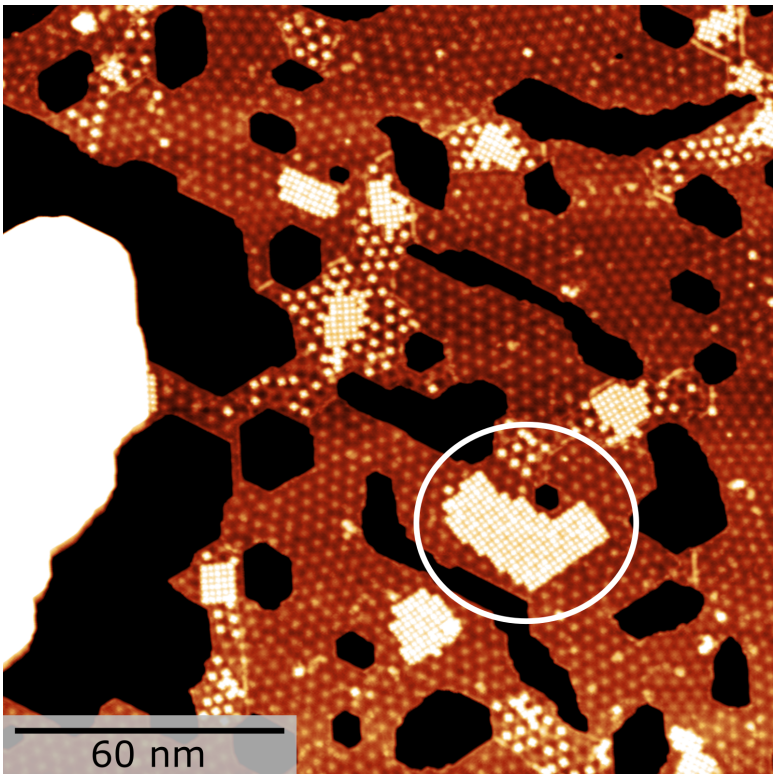

Fig. 4.44 STM image of a terrace with a 3 ML Pb film exhibiting a "protrusions" moiré. Bright regions on top of the Pb film are self-assembled islands of MnPcs. Image size: $170 \times 170\ nm^2$, V_T: 0.3 V and I_T: 40 pA. White circle indicates the MnPcs island measured by means of STS experiments.

inside the molecular domain closely resembles the reference spectrum. More interestingly, the blue spectrum shows that, in correspondence of the "edge" feature extending out of the molecular domain (see the position of the blue cross in Fig. 4.45a), the superconducting gap is suppressed more than that of the black curve (measured in correspondence of the molecules).

In conclusion, the experimental results show that over the considered region, including a self-assembled 2D island of MnPcs, a superconducting gap filled with quasiparticle states is observed everywhere, i.e. inside and away from the molecular island, and a spectroscopic feature linked to the edge of the molecular domain presents a suppressed gap. Therefore, the superconductivity outside and inside the molecular domain are separated by the "edge" feature. Fig. 4.46 several 2D differential conductance maps measured at different energies revealing what is the effect of MnPcs on the superconductivity of the Pb film. From this figure it is clear that the "edge" feature has its own energy dispersion different from the other parts of the sample and it always remains linked to edge of the molecular domain.

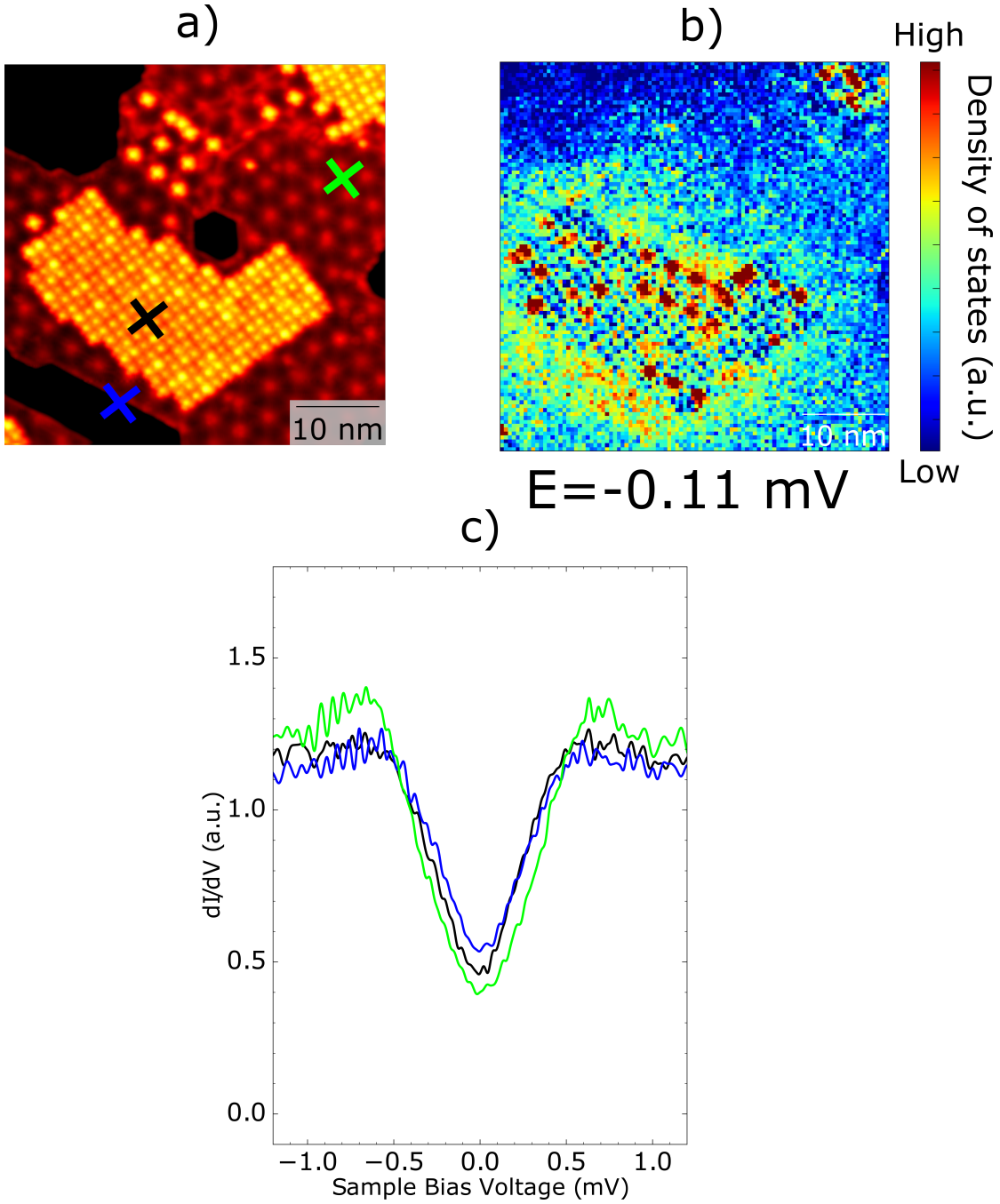

Fig. 4.45 Magnetic interaction between a 2D self-assembled island of MnPcs and a 3 ML Pb film exhibiting a "protrusions" moiré. (a): Topographic STM image taken before the STS experiment. Image size: $45.7 \times 45.7\ nm^2$, V_T: -0.05 V and I_T : 20 pA. (b): 2D dI/dV conductance map acquired at -0.11 mV over the region shown in (a). (c): Local dI/dV STS spectra measured on the points identified by the cross in (a) of the corresponding colour. The experiments were carried out at 300 mK.

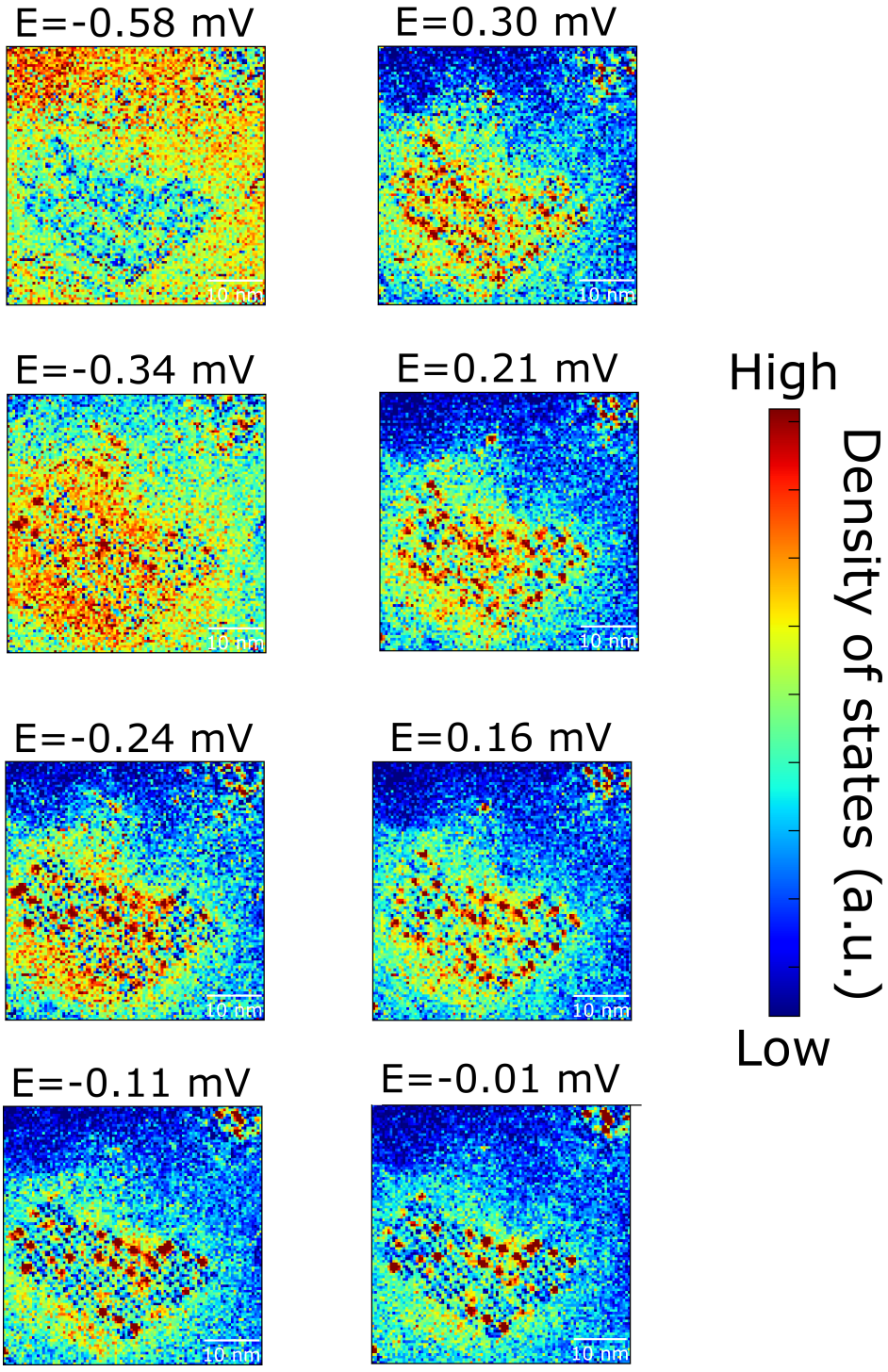

Fig. 4.46 Magnetic interaction between a 2D self-assembled island of MnPcs and a 3 ML Pb film exhibiting a "protrusions" moiré. 2D dI/dV conductance maps acquired at different energies and at 300 mK.

4.8.2 Discussion

The interpretation of our findings is to consider that the magnetic domain of MnPcs drives the 3 ML Pb film into a topological superconducting phase whose spectroscopic signature is the "edge" feature shown in previous section. In this scenario, the "edge" features would represent the edge states surrounding the topological domain. In particular, if that were the case, the area shown in Fig. 4.45 would be divided in two different regions, that is, the topological (below the molecular island) and the non-topological region (the rest of the sample). In agreement with previous studies [25], the two regions would be separated by the "edge" feature.

However, due to different aspects, the interpretation of our results is more complicated. For instance, inspection of spectra in Fig. 4.45 shows that the superconductivity is suppressed, with reduced coherence peaks and strong gap filling, even far from the molecules. We interpret this observation as due to the high concentration of magnetic molecules on the sample that affect the superconductivity of the system (see Fig. 4.44).
Our interpretation of a topological transition induced by the molecular island is based on the fact that the majority of the Shiba states related to different MnPcs couple between them to form Shiba bands. A recent work showed that the coupling of different Shiba states could drive a topological transition [124]. The necessary condition to couple different Shiba states is that they lie at the same energy. From these considerations and from Fig. 4.46, we can deduce that the regions inside the molecular domain having a uniform density of states without the appearance of isolated Shiba states (appearing as red spots at different energies) at any energy represent regions in which Shiba states are coupled to each other and form Shiba bands.
Previous studies have shown that the energy of Shiba states induced by MnPcs strongly depends on the adsorption configuration. Also our experiments on isolated MnPcs on 3 ML Pb islands have revealed a more homogeneous behavior suggesting a majority of weak coupling cases (see previous section). Furthermore, it was shown that MnPcs islands self-assembled on top of bulk crystals of Pb(111) usually exhibit an incommensurate structure with respect to the substrate [73, 19, 21]. Accordingly, different molecules induce individual Shiba states at different energies depending on the adsorption site that will be not able to couple between them and give rise to Shiba bands. This fact is also responsible for the appearance of a moiré-like superstructure in topographic images [73].
In our experiments, some regions of the molecular domain do not reveal the presence of isolated Shiba states. We interpret this fact by considering that the molecules are probably in a commensurate configuration with respect to the substrate and therefore the induced Shiba

states lie at the same energy and can couple between them to originate Shiba bands. This mechanism ultimately drive the topological transition.
The emergence of isolated Shiba states at well-defined energies indicates the presence of molecules that are not coupled with the others to form a Shiba band. The most interesting aspect is that the molecules giving rise to isolated Shiba states can be readily identified from the topographic STM image because they have a brighter appearance with respect to the other molecules (compare Fig. 4.45b and Fig. 4.45a).
The appearance change of phthalocyanines adsorbed on metallic surfaces can be due to different effects. Previous studies have shown that the brighter/darker appearance can be due to a different adsorption site [73]. In particular, different adsorption sites provide different chemical environment to the molecule. Accordingly, the coupling strength and thus the local density of states around the molecule can be modulated by the adsorption on different sites [125]. These local changes can be easily detected with STM which is directly sensitive to the local density of states.
From these considerations, the presence of molecules not coupled with the others and giving rise to isolated Shiba states could be interpreted in the following way. We believe that, on 3 ML Pb films, molecules tend to be in a commensurate configuration with respect to the substrate. The driving force could be due to the geometric corrugation of the moiré pattern. However, if a small lattice mismatch between molecular lattice and substrate exists, the former cannot accommodate a commensurate structure over long distances and therefore the structure must relax with molecules that are not in phase with the others. In this way, out of phase molecules will have different adsorption sites with respect to the others with consequent change in their appearance and emergence of isolated Shiba states.

In conclusion, starting from the results of STS measurements on 3 ML Pb films grown on Si(111) we believe that, contrary to what is observed on bulk Pb(111) substrates, MnPcs are probably able to form 2D self-assembled lattices commensurate with respect to the substrate. The interaction of these commensurate magnetic structures give rise to Shiba states at similar energies that can couple each other by leading to the formation of Shiba bands. This mechanism is responsible for the topological transition in correspondence of the magnetic domain and the spectroscopic signature is given by the emergence of the "edge" feature surrounding the magnetic domain of MnPcs.
It is important to outline that further investigation is needed to confirm this novel result. In particular, further experiments must be carried out to reproduce conditions similar to those described in this section, possibly with larger molecular domains. On the other hand, theoretical calculation are mandatory to explore the physical details behind this system and

to know if the conditions of our experiment, a topological transition can be actually induced. From our preliminary results, it seems that we are in a weak coupling regime with both J and K being negative. Theoretical calculations predict topological phases for ordered weakly Shiba states assuming J>0 and K=0 [126].

Conclusion

In this thesis I reported on both structural and electronic effects of the interaction between molecular magnets, i.e. MnPcs, and 2D superconducting systems, i.e. single atomic layer of Pb/S(111) and 3 ML Pb/Si(111) films, in order to engineer topological superconductivity.

In the case of the Pb monolayer the aim was to use the peculiar surface structure of the $\sqrt{7} \times \sqrt{3}$-Pb phase, exhibiting groove domains, as a template surface in order to obtain self-assembled linear molecular chains eventually magnetically ordered and coupled to the superconducting substrate. However, the experiments revealed unexpected and intriguing side effects of the molecular adsorption. In particular, the deposition of a tiny amount of MnPcs, i.e. $\sim$0.18 $molecules/100\ nm^2$, on top of the Pb monolayer is already enough to induce a macroscopic structural phase transition. Such abrupt phase transition induced by dilute molecules has never been observed in the literature so far. I proposed a possible mechanism behind this effect in which molecular adsorption may affect some of the chemical bonds between the Pb atoms and the silicon substrate responsible for the stability of the $\sqrt{7} \times \sqrt{3}$-Pb phase. Simultaneously, it has been proposed that MnPcs donate an electronic charge to the Pb surface increasing the tensile stress within the Pb film. The combination of bond weakening and increase of the tensile stress may be the driving force for the contraction of the Pb layer and thus of the surface reconstruction. Furthermore, I observed that the molecular self-assembly on top of the Pb monolayer is strongly different from that observed on films with higher thicknesses. In particular, the square self-assembly of molecular magnets usually observed on metallic surfaces is strongly frustrated, and molecules remain isolated or at most they form trimer structures reflecting the threefold symmetry of the substrate. This novel behavior is probably due to the strong molecule-substrate interaction prevailing on the molecule-molecule one. DFT calculations addressing this issue are in progress at the time of writing of this thesis.

To avoid this behavior, a quasi-2D system was alternatively studied consisting of 3 ML of Pb grown on Si(111). Being a metastable system its growth is particularly challenging to

control. Careful analysis of the moiré corrugations observed in STM images has allowed me to determine the presence of two very different structures coexisting on the same sample. I proposed that at lower Pb coverage, i.e. in presence of disconnected Pb islands, only one type of structure is present consisting of Pb islands largely aligned with the silicon substrate or at most slightly rotated (less than $\sim 5°$). In this structure, Pb atoms are close to the bulk Pb(111) positions with a lattice parameter of $a_{Pb} = 3.5$ Å. On the other hand, at higher coverage, i.e. in presence of a continuous film, the system splits into two phases occupying different terraces. The first type of terrace has a structure similar to that observed for disconnected islands. More interestingly, the second type of terrace reveals a new structure consisting of Pb films greatly rotated with respect to the silicon substrate, i.e. by 30°. Furthermore, I proposed that Pb atoms inside this novel structure would be slightly compressed with respect to the bulk Pb(111) with a lattice parameter of $a_{Pb} \sim 3.46$ Å. Contrary to the Pb monolayer case, on the quasi-2D system of 3 ML Pb films a square self-assembly of molecular magnets is recovered.

In order to investigate the effect of molecular adsorption on the electronic properties of the Pb substrate I carried out experiments on bare 3 ML Pb islands. The vertical confinement existing in 3 ML Pb films/islands lead to the existence of Quantum Well States (QWS). The experiments on (QWS) revealed that, as already reported, the density of states of electrons confined within the Pb islands and the energy of Quantum Well States are modulated by the moiré corrugation observed in usual topographic STM images. Experimental observation of QWS on 3 ML Pb islands exhibiting different moiré corrugations and comparison with previous calculations have allowed me to corroborate the strong correlation between spatial modulations of QWS energies and internal structure of the islands themselves, in particular the Pb/Si(111) interface structure would play a crucial role. Ultimately, the moiré corrugation of 3 ML Pb islands observed in STM image could be considered as the result of a complex interplay between electronic and structural relaxation effects. For this reason, a refined theoretical model including all the physics, e.g. substrate, stacking sequence, relaxation, spin-orbit coupling, is highly desirable to have more insight into the intriguing properties of this system.

The experiments in the superconducting state carried out at 300 mK have revealed that, in general, the superconducting gap is not dramatically affected by structural differences, e.g. stacking sequence and rotations with respect to the silicon substrate (less than $\sim 5°$), existing between 3 ML Pb islands having different moiré corrugations. Interestingly, I was able to detect small spatial fluctuations of the coherence peaks amplitudes correlated with the

moiré corrugation. Based on previous observations of a similar behavior of the coherence peaks on the Pb monolayer, I proposed that this effect is correlated to the periodic structural deformations underlying the moiré patterns. In other words, moiré patterns act as a periodic potential of disorder affecting the electron-phonon coupling in a periodic way and thus the coherence of the superconducting state at length scales much shorter than the superconducting coherence length. This intriguing result reveals the presence of low-dimensional physics in 3 ML Pb islands previously reported only in the case of pure 2D systems. Furthermore, Scanning Tunneling Spectroscopy experiments have allowed to detect for the first time the presence of superconductivity with multi-band character in 3 ML and 5 ML Pb islands.

Last but not least I investigated the magnetic interaction between MnPcs and the superconductivity of 3 ML Pb islands grown on Si(111). It was very difficult carrying out STS experiments due to the measurement itself inducing vibrational excitations and leading to the displacement of the molecules. Nevertheless, I was able to extract reliable information in the case of isolated molecules. Experimental data show that the strength of the coupling crucially depends on the adsorption site as already reported for the same molecules deposited on bulk-like Pb substrates. Interestingly and contrary to what observed on bulk-like Pb substrates, Shiba states induced by isolated MnPcs are always found close to the gap edge and with the same asymmetry of related peaks. Based on simple assumptions on the system, I interpreted experimental results by considering that MnPcs are always weakly coupled to the superconducting Pb islands suggesting negative J and K parameters. In the case of self-organized 2D domains of MnPcs on 3 ML Pb films, despite the filling of the superconducting gap due to the massive presence of molecules on the surface, interesting intra-gap spectroscopic signature located at the edge of a molecular domain was observed that could be related to non-trivial superconducting effects.

In conclusion, the main goal of this thesis was to investigate the nature of the interaction of MnPcs deposited on very thin films of Pb and try to understand the conditions leading to a favourable coupling for inducing a topological transition. All the original results listed above, show that interaction between molecules and substrate are very complex and involve non-trivial facets. The interesting observation of in-gap spectroscopic feature at the edge of a self-assembled 2D island of molecular magnets pave the route to future engineering studies with the present system. Now that spectroscopic data on isolated molecular magnets (MnPcs) on 3 ML Pb islands were obtained, ab-initio modeling of the exchange interaction, including spin-orbit coupling, would be highly desirable. This would help to provide reasonable parameters enabling the modeling of the proper coupling of Shiba states in 2D arrays on

3 ML Pb islands. Since topological phases can be formed in these conditions, it would clarify the experimental range of parameters under which these could be observed.

Chapter 5

Relations between the moiré parameters $L(\Theta)$, $\Phi(\Theta)$, $\alpha(\Theta)$ and the rotation angle Θ of Pb(111) with respect to the Si(111)

In this appendix I will provide a demonstration of equations 4.16, 4.17 and 4.18 that relate the main parameters of a moiré pattern, i.e. $L(\Theta)$, $\Phi(\Theta)$, $\alpha(\Theta)$ respectively, to the rotation angle Θ of Pb (111) with respect to the Si(111) substrate. To do this I will show that the

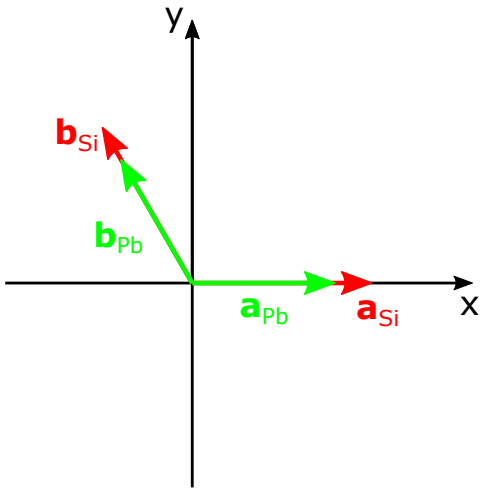

Fig. 5.1 Sketch of the lattice vectors associated with the superimposed hexagonal lattices of Si(111) (red vectors) and Pb(111) (green vectors). Note that in this case the two lattice are aligned to each other.

relative configuration of the lattice vectors associated with the two superimposed hexagonal lattices of Pb(111) and Si(111) at the Pb/Si(111) interface determine the properties of the

lattice vectors associated with the moiré pattern. I will start to consider the case in which the Pb(111) lattice is aligned with respect to the Si(111) one (see Fig. 5.1).
We can then write the expressions of the lattice vectors:

$$\begin{cases} \mathbf{a}_{Si} = a_{Si}(1,0) \\ \mathbf{b}_{Si} = a_{Si}(-\frac{1}{2}, \frac{\sqrt{3}}{2}) \end{cases} \qquad \begin{cases} \mathbf{a}_{Pb} = a_{Pb}(1,0) \\ \mathbf{b}_{Pb} = a_{Pb}(-\frac{1}{2}, \frac{\sqrt{3}}{2}) \end{cases} \tag{5.1}$$

where a_{Si}=0.384 nm and a_{Pb}=0.350 nm are the bulk lattice constants of Si(111) and Pb(111) respectively. Starting from these expressions we can calculate the corresponding vectors within the reciprocal space:

$$\begin{cases} \mathbf{a}^*_{Si} = \frac{2\pi}{a_{Si}}(1, \frac{1}{\sqrt{3}}) \\ \mathbf{b}^*_{Si} = \frac{2\pi}{a_{Si}}(0, \frac{2}{\sqrt{3}}) \end{cases} \qquad \begin{cases} \mathbf{a}^*_{Pb} = \frac{2\pi}{a_{Pb}}(1, \frac{1}{\sqrt{3}}) \\ \mathbf{b}^*_{Pb} = \frac{2\pi}{a_{Pb}}(0, \frac{2}{\sqrt{3}}) \end{cases} \tag{5.2}$$

If we rewrite the lattice constant a_{Si} of the Si(111) as a function of that of the Pb(111) through the lattice mismatch δ between the two, i.e. a_{Si}=$(1+\delta)a_{Pb}$, we obtain the following expressions:

$$\begin{cases} \mathbf{a}^*_{Si} = \frac{2\pi}{a_{Si}}(1, \frac{1}{\sqrt{3}}) = \frac{2\pi}{a_{Pb}(1+\delta)}(1, \frac{1}{\sqrt{3}}) \\ \mathbf{b}^*_{Si} = \frac{2\pi}{a_{Si}}(0, \frac{2}{\sqrt{3}}) = \frac{4\pi}{\sqrt{3}a_{Pb}(1+\delta)}(0,1) \end{cases} \qquad \begin{cases} \mathbf{a}^*_{Pb} = \frac{2\pi}{a_{Pb}}(1, \frac{1}{\sqrt{3}}) = \frac{2\pi}{a_{Pb}}(1, \frac{1}{\sqrt{3}}) \\ \mathbf{b}^*_{Pb} = \frac{2\pi}{a_{Pb}}(0, \frac{2}{\sqrt{3}}) = \frac{4\pi}{\sqrt{3}a_{Pb}}(0,1) \end{cases} \tag{5.3}$$

By considering that, in the reciprocal space, a moiré pattern can be defined as the difference between the lattice vectors of Si(111) and those of Pb(111) [114], i.e. $\mathbf{g}^*_{moiré} = \mathbf{g}^*_{Pb} - \mathbf{g}^*_{Si}$, we can deduce the two lattice vectors of the moiré:

$$\begin{cases} \mathbf{a}^*_{moiré} = \mathbf{a}^*_{Pb} - \mathbf{a}^*_{Si} = \frac{2\pi}{a_{Pb}}(\frac{\delta}{1+\delta}, \frac{\delta}{\sqrt{3}(1+\delta)}) \\ \mathbf{b}^*_{moiré} = \mathbf{b}^*_{Pb} - \mathbf{b}^*_{Si} = \frac{4\pi}{\sqrt{3}a_{Pb}}(0, \frac{\delta}{1+\delta}) \end{cases} \tag{5.4}$$

At this point we can easily calculate the lattice vectors of the moiré pattern within the direct space:

$$\begin{cases} \mathbf{a}_{moiré} = (\frac{a_{Pb}(1+\delta)}{\delta}, 0) \\ \mathbf{b}_{moiré} = \frac{a_{Pb}(1+\delta)}{\delta}(-\frac{1}{2}, \frac{\sqrt{3}}{2}) \end{cases} \tag{5.5}$$

From previous expressions it easy to see that $|\mathbf{a}_{moiré}|$ and $|\mathbf{b}_{moiré}|$, representing the moiré lattice parameter L observed in STM images, assume the same value and that they are aligned with the lattice vectors of Si(111) and Pb(111) (compare reations 5.1 and 5.5):

$$L = |\mathbf{a}_{moiré}| = \frac{a_{Pb(1+\delta)}}{\delta} = \frac{a_{Si}}{\delta} = |\mathbf{b}_{moiré}| \tag{5.6}$$

This result shows that the moiré pattern originating from the overlapping of two hexagonal lattices keeps the hexagonal symmetry. Furthermore, now we know that if the Pb(111) overlayer is aligned with the Si(111) substrate the resulting moiré is also aligned with the two underlying lattices.

In order to generalize previous results, I will now consider the case in which the Pb(111) is rotated by an angle Θ with respect to the Si(111) (see Fig. 5.2). As I have just shown,

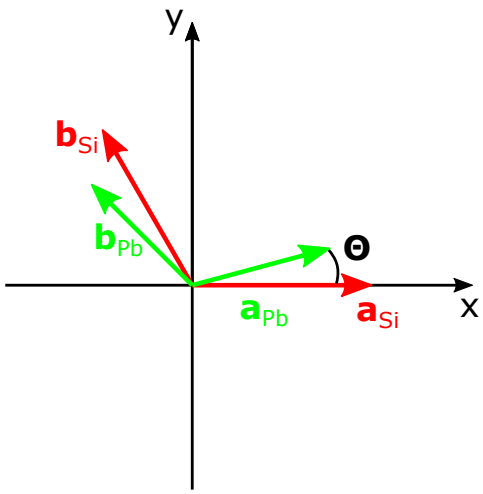

Fig. 5.2 Sketch of the lattice vectors giving rise to the superimposed hexagonal lattices of Si(111) (red vectors) and Pb(111) (green vectors) rotated by an angle of Θ.

calculations on **a** and **b** vectors lead to the same conclusions, therefore in the following I will develop the procedure only for **b** vectors. In particular, we can adapt expressions 5.1 by considering the rotation angle Θ between Si(111) and Pb(111):

$$\begin{cases} \mathbf{b}^*_{Si} = \frac{4\pi}{\sqrt{3}a_{Pb}(1+\delta)}(0,1) \\ \mathbf{b}^*_{Pb} = \frac{4\pi}{\sqrt{3}a_{Pb}}(-\sin\Theta, \cos\Theta) \end{cases} \tag{5.7}$$

With calculations similar to those shown above, we can deduce the expression of the moiré lattice vector in the reciprocal space:

$$\mathbf{b}^*_{moiré} = \mathbf{b}^*_{Pb} - \mathbf{b}^*_{Si} = \frac{4\pi}{\sqrt{3}a_{Pb}}(-\sin\Theta, \cos\Theta - \frac{1}{1+\delta}) \tag{5.8}$$

By comparing equations 5.4 and 5.5, it is easy to see that the length of the moiré lattice vector in the direct space ($|\mathbf{b}_{moiré}|$) is related to that in the reciprocal space ($|\mathbf{b}^*_{moiré}|$) by a factor $\frac{4\pi}{\sqrt{3}}$, i.e. $|\mathbf{b}_{moiré}| = \frac{4\pi}{\sqrt{3}|\mathbf{b}^*_{moiré}|}$. From this relation we can directly deduce the moiré lattice parameter $L(\Theta)$ as a function of the rotation angle Θ:

$$L(\Theta) = |\mathbf{b}_{moiré}| = \frac{4\pi}{\sqrt{3}|\mathbf{b}^*_{moiré}|} = \frac{a_{Pb}(1+\delta)}{\sqrt{\delta^2 + 2(1+\delta)(1-\cos\Theta)}} \tag{5.9}$$

If we consider that $\delta = \frac{a_{Si}}{a_{Pb}} - 1$ and we define that $x = \frac{a_{Si}}{a_{Pb}}$, equation 4.16 is verified. In other words, the moiré lattice parameter $L(\Theta) = |\mathbf{b}_{moiré}|$ as a function of Θ can be expressed in the following way:

$$L(\Theta) = \frac{a_{Si}}{\sqrt{1 + x^2 - 2x\cos\Theta}} \tag{5.10}$$

From this result equation 4.17 can be directly shown by deriving $\cos\Theta$:

$$\cos\Theta = \frac{1}{2x} + \frac{x}{2} - \frac{a^2_{Si}}{2xL(\Theta)^2} \tag{5.11}$$

Also for equation 4.18 one can just consider the scalar product $\mathbf{b}^*_{moiré} \cdot \mathbf{b}^*_{Pb} = |b^*_{moiré}||b^*_{Pb}|\cos\alpha$ in the reciprocal space and calculate the following quantity:

$$\cos\alpha = \frac{\mathbf{b}^*_{moiré} \cdot \mathbf{b}^*_{Pb}}{|b^*_{moiré}||b^*_{Pb}|} = \frac{1 + \delta - \cos\Theta}{\sqrt{\delta^2 + (2\delta+2)(1-\cos\Theta)}} \tag{5.12}$$

As the angle between the two lattice vectors associated to Si(111) and Pb(111) in the reciprocal space is the same also in the direct space, we can conclude that the α angle deduced by previous equation also represents the angle between moiré and Pb(111) in the direct space.

References

[1] H.K. Onnes. The resistance of pure mercury at helium temperatures. *temperatures. Commun. Phys. Lab. Univ. Leiden*, 12, 1911.

[2] H. London F. London. The electromagnetic equations of the supraconductor. *Proceedings of the Royal Society of London A,*, 149:71–88, 1935.

[3] L. D. Landau V. L. Ginzburg. Contribution to the theory of superconductivity. *Zh. Eksp. Teor. Fiz.*, 20, 1950.

[4] J. Bardeen, L. N. Cooper, and J. R. Schrieffer. Theory of Superconductivity. *Physical Review*, 108(5):1175–1204, December 1957.

[5] Leo Kouwenhoven and Leonid Glazman. Revival of the Kondo effect. *Physics World*, 14(1):33–38, January 2001.

[6] J. Kondo. Resistance Minimum in Dilute Magnetic Alloys. *Progress of Theoretical Physics*, 32(1):37–49, July 1964.

[7] Markus Ternes, Andreas J Heinrich, and Wolf-Dieter Schneider. Spectroscopic manifestations of the Kondo effect on single adatoms. *Journal of Physics: Condensed Matter*, 21(5):053001, February 2009.

[8] U. Fano. Effects of Configuration Interaction on Intensities and Phase Shifts. *Physical Review*, 124(6):1866–1878, December 1961.

[9] Ying-Shuang Fu, Shuai-Hua Ji, Xi Chen, Xu-Cun Ma, Rui Wu, Chen-Chen Wang, Wen-Hui Duan, Xiao-Hui Qiu, Bo Sun, Ping Zhang, Jin-Feng Jia, and Qi-Kun Xue. Manipulating the Kondo Resonance through Quantum Size Effects. *Physical Review Letters*, 99:256601, 2007.

[10] L. P. Gor'kov A. A. Abrikosov. Contribution to the theory of superconducting alloys with paramagnetic impurities. *Soviet Physics JETP*, 12, 1961.

[11] Hiroyuki Shiba. Classical Spins in Superconductors. *Progress of Theoretical Physics*, 40(3):435–451, September 1968.

[12] A. Yazdani. Probing the Local Effects of Magnetic Impurities on Superconductivity. *Science*, 275(5307):1767–1770, March 1997.

[13] Shuai-Hua Ji, Tong Zhang, Ying-Shuang Fu, Xi Chen, Xu-Cun Ma, Jia Li, Wen-Hui Duan, Jin-Feng Jia, and Qi-Kun Xue. High-Resolution Scanning Tunneling Spectroscopy of Magnetic Impurity Induced Bound States in the Superconducting Gap of Pb Thin Films. *Physical Review Letters*, 100(22), June 2008.

[14] Cătălin Paşcu Moca, Eugene Demler, Boldizsár Jankó, and Gergely Zaránd. Spin-resolved spectra of Shiba multiplets from Mn impurities in MgB 2. *Physical Review B*, 77(17), May 2008.

[15] Benjamin W. Heinrich, Jose I. Pascual, and Katharina J. Franke. Single magnetic adsorbates on s -wave superconductors. *Progress in Surface Science*, 93(1):1–19, February 2018.

[16] Deung-Jang Choi, Carmen Rubio-Verdú, Joeri de Bruijckere, Miguel M. Ugeda, Nicolás Lorente, and Jose Ignacio Pascual. Mapping the orbital structure of impurity bound states in a superconductor. *Nature Communications*, 8:15175, May 2017.

[17] Gerbold C. Ménard, Sébastien Guissart, Christophe Brun, Stéphane Pons, Vasily S. Stolyarov, François Debontridder, Matthieu V. Leclerc, Etienne Janod, Laurent Cario, Dimitri Roditchev, Pascal Simon, and Tristan Cren. Coherent long-range magnetic bound states in a superconductor. *Nature Physics*, 11(12):1013–1016, December 2015.

[18] Shawulienu Kezilebieke, Marc Dvorak, Teemu Ojanen, and Peter Liljeroth. Coupled Yu–Shiba–Rusinov States in Molecular Dimers on NbSe $_2$. *Nano Letters*, 18(4):2311–2315, April 2018.

[19] Nino Hatter, Benjamin W. Heinrich, Michael Ruby, Jose I. Pascual, and Katharina J. Franke. Magnetic anisotropy in Shiba bound states across a quantum phase transition. *Nature Communications*, 6(1), December 2015.

[20] K. J. Franke, G. Schulze, and J. I. Pascual. Competition of Superconducting Phenomena and Kondo Screening at the Nanoscale. *Science*, 332(6032):940–944, May 2011.

[21] Nino Hatter, Benjamin W. Heinrich, Daniela Rolf, and Katharina J. Franke. Scaling of Yu-Shiba-Rusinov energies in the weak-coupling Kondo regime. *Nature Communications*, 8(1), December 2017.

[22] Jay D. Sau, Sumanta Tewari, Roman M. Lutchyn, Tudor D. Stanescu, and S. Das Sarma. Non-Abelian quantum order in spin-orbit-coupled semiconductors: Search for topological Majorana particles in solid-state systems. *Physical Review B*, 82(21), December 2010.

[23] Takashi Uchihashi. Engineering topological superconductors using surface atomic-layer/molecule hybrid materials. *Nanotechnology*, 26(34):344004, August 2015.

[24] S. Nadj-Perge, I. K. Drozdov, J. Li, H. Chen, S. Jeon, J. Seo, A. H. MacDonald, B. A. Bernevig, and A. Yazdani. Observation of Majorana fermions in ferromagnetic atomic chains on a superconductor. *Science*, 346(6209):602–607, October 2014.

[25] Gerbold C. Ménard, Sébastien Guissart, Christophe Brun, Raphaël T. Leriche, Mircea Trif, François Debontridder, Dominique Demaille, Dimitri Roditchev, Pascal Simon, and Tristan Cren. Two-dimensional topological superconductivity in Pb/Co/Si(111). *Nature Communications*, 8(1), December 2017.

[26] K Oura, V.G. Lifshits, A.A. Saranin, A.V. Zotov, and M. Katayama. Surface Science - An Introduction. *Springer*, 2003.

[27] C. Davisson and L. H. Germer. Diffraction of Electrons by a Crystal of Nickel. *Physical Review*, 30:705, 1927.

[28] D. John O'Connor, Brett A Sexton, and Roger St. C Smart. *Surface Analysis Methods in Materials Science*. Springer Berlin Heidelberg, 1992.

[29] Kurt W. Kolasinski. Surface Science: Foundations of Catalysis and Nanoscience - Second Edition. *John Wiley and Sons Ltd*, 2008.

[30] H. Lüth. Solid Surfaces, Interfaces and Thin Films - Fifth Edition. *Springer*, 2010.

[31] Kunio Takayanagi, Yasumasa Tanishiro, Shigeki Takahashi, and Masaetsu Takahashi. Structure Analysis of Si(111)-7 x 7 reconstructed surface by transmission electron diffraction. *Surface Science*, 164:367–392, 1985.

[32] G. Binnig, H. Rohrer, Ch. Gerber, and E. Weibel. 7×7 Reconstruction on Si(111) Resolved in Real Space. *Physical Review Letters*, 50:120, 1983.

[33] Gerd Binnig and Heinrich Rohrer. Scanning tunneling microscopy—from birth to adolescence. *Reviews of Modern Physics*, 59:615, 1987.

[34] Vij D.R. Handbook of Applied Solid State Spectroscopy. *Springer US*, 2006.

[35] Bonnel Dawn A. Scanning Probe Microscopy and Spectroscopy - Theory, Techniques and Applications - Second Edition. *Wiley-VCH*, 2000.

[36] Tinkham Michael. Introdution to Superconductivity - Second Edition. *Dover Publications*, 2004.

[37] Tzu-Liang Chan, C. Z. Wang, M. Hupalo, M. C. Tringides, Zhong-Yi Lu, and K. M. Ho. First-principles studies of structures and stabilities of Pb/Si(111). *Physical Review B*, 68:045410, 2003.

[38] S. Stepanovsky, M. Yakes, V. Yeh, M. Hupalo, and M.C. Tringides. The dense α-$\sqrt{3} \times \sqrt{3}$Pb/Si(111) phase: A comprehensive STM and SPA-LEED study of ordering, phase transitions and interactions. *Surface Science*, 600:1417–1430, 2006.

[39] Eric Ganz, Ing-Shouh Hwang, Fulin Xiong, Silva K Theiss, and Jene Golovchenko. Growth and morphology of Pb on Si(111). *Surface Science*, 257:259–273, 1991.

[40] J.M. Gómez-Rodriguez, J.-Y. Veuillen, and R.C. Cinti. Scanning tunneling microscopy study of the Si(111)-($\sqrt{3} \times \sqrt{3}$)-Pb mosaic phase. *Surface Science*, 377-379:45–49, 1997.

[41] J. Slezák, P. Mutombo, and V. Cháb. STM study of a Pb/Si(111) interface at room and low temperatures. *Physical Review B*, 60:13328, 1999.

[42] Eric Ganz, Fulin Xiong, Ing-Shouh Hwang, and Jene Golovchenko. Submonolayer phases of Pb on Si(111). *Physical Review B*, 43:7316, 1991.

[43] N Nicoara, J Méndez, and J M Gómez-Rodríguez. Growth of ordered molecular layers of PTCDA on Pb/Si(111) surfaces: a scanning tunneling microscopy study. *Nanotechnology*, 27:365706, 2016.

[44] O Custance, J.M. Gómez-Rodriguez, A.M. Baró, L. Juré, P. Mallet, and J.-Y. Veuillen. Low temperature phases of Pb/Si(1 1 1). *Surface Science*, 482-485:1399–1405, 2001.

[45] Kotaro Horikoshi, Xiao Tong, Tadaaki Nagao, and Shuji Hasegawa. Structural phase transitions of Pb-adsorbed Si(111) surfaces at low temperatures. *Physical Review B*, 60:13287, 1999.

[46] Christian Kumpf, Oliver Bunk, Jan H. Zeysing, Martin M. Nielsen, Mourits Nielsen, Robert L. Johnson, and Robert Feidenhans'l. Structural study of the commensurate–incommensurate low-temperature phase transition of Pb on Si(111). *Surface Science*, 448:L213–L219, 2000.

[47] C. Tresca, C. Brun, T. Bilgeri, G. Menard, V. Cherkez, R. Federicci, D. Longo, F. Debontridder, M. D'angelo, D. Roditchev, G. Profeta, M. Calandra, and T. Cren. Chiral Spin Texture in the Charge-Density-Wave Phase of the Correlated Metallic Pb / Si (111) Monolayer. *Physical Review Letters*, 120:196402, 2018.

[48] Sung Chul Jung and Myung Ho Kang. Triple-domain effects on the electronic structure of Pb/Si(111)-($\sqrt{7} \times \sqrt{3}$): Density-functional calculations. *Surface Science*, 605:551–554, 2011.

[49] S. Brochard, Emilio Artacho, O. Custance, I. Brihuega, A. M. Baró, J. M. Soler, and J. M. Gómez-Rodríguez. *Ab initio* calculations and scanning tunneling microscopy experiments of the Si (111) - ($\sqrt{7} \times \sqrt{3}$) - Pb surface. *Physical Review B*, 66:205403, 2002.

[50] P. Cudazzo, G. Profeta, and A. Continenza. Low temperature phases of Pb/Si(111) and related surfaces. *Surface Science*, 602:747–754, 2008.

[51] Sung Chul Jung and Myung Ho Kang. Dynamical nature of the high-temperature Pb/Si(111)-1 × 1 phase. *Physical Review B*, 84:155422, 2011.

[52] Won Hoon Choi, Keun Su Kim, and Han Woong Yeom. High-resolution core-level photoemission study of dense Pb overlayers on Si(111). *Physical Review B*, 78:195425, 2008.

[53] M. Hupalo, J. Schmalian, and M. C. Tringides. "Devil's Staircase" in P b / S i (111) Ordered Phases. *Physical Review Letters*, 90:216106, 2003.

[54] Chia-Hsiu Hsu, Feng-Chuan Chuang, Marvin A. Albao, and V. Yeh. Electronic structure of the Pb / Si (111) - ($\sqrt{7} \times \sqrt{3}$) surface reconstruction: A first-principles study. *Physical Review B*, 81:033407, 2010.

[55] Keun Su Kim, Sung Chul Jung, Myung Ho Kang, and Han Woong Yeom. Nearly Massless Electrons in the Silicon Interface with a Metal Film. *Physical Review Letters*, 104:246803, 2010.

[56] W. H. Choi, H. Koh, E. Rotenberg, and H. W. Yeom. Electronic structure of dense Pb overlayers on Si(111) investigated using angle-resolved photoemission. *Physical Review B*, 75:075329, 2007.

[57] Tong Zhang, Peng Cheng, Wen-Juan Li, Yu-Jie Sun, Guang Wang, Xie-Gang Zhu, Ke He, Lili Wang, Xucun Ma, Xi Chen, Yayu Wang, Ying Liu, Hai-Qing Lin, Jin-Feng Jia, and Qi-Kun Xue. Superconductivity in one-atomic-layer metal films grown on Si(111). *Nature Physics*, 6(2):104–108, February 2010.

[58] L. Seehofer, G. Falkenberg, D. Daboul, and R. L. Johnson. Structural study of the close-packed two-dimensional phases of Pb on Ge(111) and Si(111). *Physical Review B*, 51:13503, 1995.

[59] Ing-Shouh Hwang, R. E. Martinez, Chien Liu, and J. A. Golovchenko. Soft incommensurate reconstruction on Pb/Si(111): Structure, stress modulation, and phase transition. *Physical Review B*, 51:10193, 1995.

[60] A. Petkova, J. Wollschläger, H.-L. Günter, and M. Henzler. Formation and commensurate analysis of "incommensurate" superstructures of Pb on Si(111). *Surface Science*, 471:11–20, 2001.

[61] Xiao-Yan Ren, Hyun-Jung Kim, Seho Yi, Yu Jia, and Jun-Hyung Cho. Spin-orbit coupling effects on the stability of two competing structures in Pb/Si(111) and Pb/Ge(111). *Physical Review B*, 94:075436, 2016.

[62] M. Hupalo, T. L. Chan, C. Z. Wang, K. M. Ho, and M. C. Tringides. Atomic models, domain-wall arrangement, and electronic structure of the dense P b / S i (111) - $\sqrt{3} \times \sqrt{3}$ phase. *Physical Review B*, 66:161410(R), 2002.

[63] Wen-Juan Li, Yu-Jie Sun, Tong Zhang, Xie-Gang Zhu, Guang Wang, Jin-Feng Jia, Xucun Ma, Xi Chen, and Qi-Kun Xue. Enhancement of superconductivity of Pb ultra-thin films by the interface effect. *Surface Review and Letters*, 17:437–440, 2010.

[64] Ing-Souh Hwang, Shih-Hsin Chang, Chung-Kai Fang, Tien.T Tsong, and Lih-Juann Chen. Scanning Tunneling Microscope Study of Structural Transformations on One Monolayer Pb/Si(111). In *AIP Conference Proceedings*, volume 696, page 760, 2003.

[65] Ing-Shouh Hwang, Shih-Hsin Chang, Chung-Kai Fang, Lih-Juann Chen, and Tien T. Tsong. Observation of Finite-Size Effects on a Structural Phase Transition of 2D Nanoislands. *Physical Review Letters*, 93:106101, 2004.

[66] L. W. Liu, K. Yang, W. D. Xiao, Y. H. Jiang, B. Q. Song, S. X. Du, and H.-J. Gao. Selective adsorption of metal-phthalocyanine on Au(111) surface with hydrogen atoms. *Applied Physics Letters*, 103(2):023110, July 2013.

[67] Ji Shuai-Hua, Fu Ying-Shuang, Zhang Tong, Chen Xi, Jia Jin-Feng, Xue Qi-Kun, and Ma Xu-Cun. Kondo Effect in Self-Assembled Manganese Phthalocyanine Monolayer on Pb Islands. *Chinese Physics Letters*, 27(8):087202, August 2010.

[68] Dan Hao, Canli Song, Yanxiao Ning, Yilin Wang, Lili Wang, Xu-Cun Ma, Xi Chen, and Qi-Kun Xue. Self-assembly of manganese phthalocyanine on Pb(111) surface: A scanning tunneling microscopy study. *The Journal of Chemical Physics*, 134(15):154703, April 2011.

[69] K. Yang, W. D. Xiao, Y. H. Jiang, H. G. Zhang, L. W. Liu, J. H. Mao, H. T. Zhou, S. X. Du, and H.-J. Gao. Molecule–Substrate Coupling between Metal Phthalocyanines and Epitaxial Graphene Grown on Ru(0001) and Pt(111). *The Journal of Physical Chemistry C*, 116(26):14052–14056, July 2012.

[70] Y. H. Jiang, W. D. Xiao, L. W. Liu, L. Z. Zhang, J. C. Lian, K. Yang, S. X. Du, and H.-J. Gao. Self-Assembly of Metal Phthalocyanines on Pb(111) and Au(111) Surfaces at Submonolayer Coverage. *The Journal of Physical Chemistry C*, 115(44):21750–21754, November 2011.

[71] Shunsuke Yoshizawa, Emi Minamitani, Saranyan Vijayaraghavan, Puneet Mishra, Yasumasa Takagi, Toshihiko Yokoyama, Hiroaki Oba, Jun Nitta, Kazuyuki Sakamoto, Satoshi Watanabe, Tomonobu Nakayama, and Takashi Uchihashi. Controlled Modification of Superconductivity in Epitaxial Atomic Layer–Organic Molecule Heterostructures. *Nano Letters*, 17(4):2287–2293, April 2017.

[72] L. W. Liu, K. Yang, W. D. Xiao, Y. H. Jiang, B. Q. Song, S. X. Du, and H.-J. Gao. Selective adsorption of metal-phthalocyanine on Au(111) surface with hydrogen atoms. *Applied Physics Letters*, 103(2):023110, July 2013.

[73] K. J. Franke, G. Schulze, and J. I. Pascual. Competition of Superconducting Phenomena and Kondo Screening at the Nanoscale. *Science*, 332:940, 2011.

[74] Shih-Hsin Chang, Ing-Shouh Hwang, Chung-Kai Fang, and Tien T. Tsong. Adsorption and motion of C 60 molecules on the Pb-covered Si(111) surface. *Physical Review B*, 77:155421, 2008.

[75] A V Matetskiy, L V Bondarenko, D V Gruznev, A V Zotov, A A Saranin, and M C Tringides. Structural transformations in Pb/Si(111) phases induced by C $_{60}$ adsorption. *Journal of Physics: Condensed Matter*, 25:395006, 2013.

[76] Harald Ibach. The role of surface stress in reconstruction, epitaxial growth and stabilization of mesoscopic structures. *Surface Science Reports*, 29:195–263, 1997.

[77] J. T. Sun, L. Gao, X. B. He, Z. H. Cheng, Z. T. Deng, X. Lin, H. Hu, S. X. Du, Feng Liu, and H.-J. Gao. Surface reconstruction transition of metals induced by molecular adsorption. *Physical Review B*, 83:115419, 2011.

[78] Meng-Sheng Liao, John D. Watts, and Ming-Ju Huang. DFT Study of Unligated and Ligated Manganese ^{ii} Porphyrins and Phthalocyanines. *Inorganic Chemistry*, 44:1941–1949, 2005.

[79] Xiao Tong, Kotaro Horikoshi, and Shuji Hasegawa. Structure and electrical conductance of Pb-covered Si(111) surfaces. *Physical Review B*, 60:5653, 1999.

[80] L V Bondarenko, A V Matetskiy, A A Yakovlev, A Y Tupchaya, D V Gruznev, M V Ryzhkova, D A Tsukanov, E A Borisenko, E N Chukurov, N V Denisov, O Vilkov, D V Vyalikh, A V Zotov, and A A Saranin. Effect of Na adsorption on the structural and electronic properties of Si(111) $\sqrt{3} \times \sqrt{3}$ -Au surface. *Journal of Physics: Condensed Matter*, 26:055009, 2014.

[81] L. V. Bondarenko, D. V. Gruznev, A. A. Yakovlev, A. Y. Tupchaya, D. Usachov, O. Vilkov, A. Fedorov, D. V. Vyalikh, S. V. Eremeev, E. V. Chulkov, A. V. Zotov, and A. A. Saranin. Large spin splitting of metallic surface-state bands at adsorbate-modified gold/silicon surfaces. *Scientific Reports*, 3:1826, 2013.

[82] Lin-Lin Wang, Duane D. Johnson, and Michael C. Tringides. C 60 -induced Devil's Staircase transformation on a Pb/Si(111) wetting layer. *Physical Review B*, 92:245405, 2015.

[83] M Milun, P Pervan, and D P Woodruff. Quantum well structures in thin metal films: simple model physics in reality? *Reports on Progress in Physics*, 65(2):99–141, February 2002.

[84] L. Bürgi, O. Jeandupeux, A. Hirstein, H. Brune, and K. Kern. Confinement of Surface State Electrons in Fabry-Pérot Resonators. *Physical Review Letters*, 81(24):5370–5373, December 1998.

[85] Michael C. Tringides, Mieczyslaw Jałochowski, and Ernst Bauer. Quantum size effects in metallic nanostructures. *Physics Today*, 60(4):50–54, April 2007.

[86] M. Hupalo, V. Yeh, T. L. Chan, C. Z. Wang, K. M. Ho, and M. C. Tringides. Interface relaxation and electronic corrugation in the Pb/Si(111)-Pb-α-$\sqrt{3} \times \sqrt{3}$. *Physical Review B*, 71(19), May 2005.

[87] M. Hupalo and M. C. Tringides. Correlation between height selection and electronic structure of the uniform height Pb/Si(111) islands. *Physical Review B*, 65(11), February 2002.

[88] C. M. Wei and M. Y. Chou. Theory of quantum size effects in thin Pb(111) films. *Physical Review B*, 66(23), December 2002.

[89] V. Yeh, L. Berbil-Bautista, C. Z. Wang, K. M. Ho, and M. C. Tringides. Role of the Metal/Semiconductor Interface in Quantum Size Effects: Pb / Si(111). *Physical Review Letters*, 85:5158–5161, 2000.

[90] W. B. Su, S. H. Chang, W. B. Jian, C. S. Chang, L. J. Chen, and Tien T. Tsong. Correlation between Quantized Electronic States and Oscillatory Thickness Relaxations of 2d Pb Islands on Si(111)-(7 × 7) Surfaces. *Physical Review Letters*, 86(22):5116–5119, May 2001.

[91] Giuliana Materzanini, Peter Saalfrank, and Philip J. D. Lindan. Quantum size effects in metal films: Energies and charge densities of Pb(111) grown on Cu(111). *Physical Review B*, 63(23), May 2001.

[92] F.K. Schulte. A theory of thin metal films: electron density, potentials and work function. *Surface Science*, 55(2):427–444, May 1976.

[93] Yan-Feng Zhang, Jin-Feng Jia, Zhe Tang, Tie-Zhu Han, Xu-Cun Ma, and Qi-Kun Xue. Growth, stability and morphology evolution of Pb films on Si(111) prepared at low temperature. *Surface Science*, 596(1-3):L331–L338, December 2005.

[94] Yan-feng Zhang, Shao-chun Li, Xu-cun Ma, Jin-feng Jia, and Qi-kun Xue. Quantum oscillations in Pb/Si (111) heterostructure system. *Frontiers of Physics in China*, 1(3):323–333, September 2006.

[95] Hawoong Hong, C.-M. Wei, M. Y. Chou, Z. Wu, L. Basile, H. Chen, M. Holt, and T.-C. Chiang. Alternating Layer and Island Growth of Pb on Si by Spontaneous Quantum Phase Separation. *Physical Review Letters*, 90(7), February 2003.

[96] Zhenyu Zhang, Qian Niu, and Chih-Kang Shih. "Electronic Growth" of Metallic Overlayers on Semiconductor Substrates. *Physical Review Letters*, 80(24):5381–5384, June 1998.

[97] Yang Guo, Yan-Feng Zhang, Tie-Zhu Han, Zhe Tang, Li-Xin Zhang, Wen-Guang Zhu, E G Wang, Qian Niu, Z Q Qiu, Jin-Feng Jia, Zhong-Xian Zhao, and Qi-Kun Xue. Superconductivity Modulated by Quantum Size Effects. 306:3, 2004.

[98] P. Czoschke, Hawoong Hong, L. Basile, and T.-C. Chiang. Quantum Oscillations in the Layer Structure of Thin Metal Films. *Physical Review Letters*, 91(22), November 2003.

[99] A. Crottini, D. Cvetko, L. Floreano, R. Gotter, A. Morgante, and F. Tommasini. Step Height Oscillations during Layer-by-Layer Growth of Pb on Ge(001). *Physical Review Letters*, 79(8):1527–1530, August 1997.

[100] J. Kim, S. Qin, W. Yao, Q. Niu, M. Y. Chou, and C.-K. Shih. Quantum size effects on the work function of metallic thin film nanostructures. *Proceedings of the National Academy of Sciences*, 107(29):12761–12765, July 2010.

[101] Yan-Feng Zhang, Jin-Feng Jia, Tie-Zhu Han, Zhe Tang, Quan-Tong Shen, Yang Guo, Z. Q. Qiu, and Qi-Kun Xue. Band Structure and Oscillatory Electron-Phonon Coupling of Pb Thin Films Determined by Atomic-Layer-Resolved Quantum-Well States. *Physical Review Letters*, 95(9), August 2005.

[102] M Ligges, M Sandhofer, I Sklyadneva, R Heid, K-P Bohnen, S Freutel, L Rettig, P Zhou, P M Echenique, E V Chulkov, and U Bovensiepen. Electron–phonon coupling in quantum-well states of the Pb/Si(1 1 1) system. *Journal of Physics: Condensed Matter*, 26(35):352001, September 2014.

[103] Fu Ying-Shuang, Ji Shuai-Hua, Zhang Tong, Chen Xi, Jia Jin-Feng, Xue Qi-Kun, and Ma Xu-Cun. Modifying Quantum Well States of Pb Thin Films via Interface Engineering. *Chinese Physics Letters*, 27(6):066804, June 2010.

[104] I. B. Altfeder, V. Narayanamurti, and D. M. Chen. Imaging Subsurface Reflection Phase with Quantized Electrons. *Physical Review Letters*, 88(20), May 2002.

[105] K Budde, E Abram, V Yeh, and M C Tringides. Uniform, self-organized, seven-step height Pb / Si(111)-(7 × 7)... islands at low temperatures. *Physical Review B*, 61:R10602, 2000.

[106] I. B. Altfeder, D. M. Chen, and K. A. Matveev. Imaging Buried Interfacial Lattices with Quantized Electrons. *Physical Review Letters*, 80(22):4895–4898, June 1998.

[107] V. Yeh, L. Berbil-Bautista, C. Z. Wang, K. M. Ho, and M. C. Tringides. Role of the Metal/Semiconductor Interface in Quantum Size Effects: Pb / Si(111). *Physical Review Letters*, 85(24):5158–5161, December 2000.

[108] H. H. Weitering, D. R. Heslinga, and T. Hibma. Structure and growth of epitaxial Pb on Si(111). *Physical Review B*, 45(11):5991–6002, March 1992.

[109] Howon Kim and Yukio Hasegawa. Spatial variation in local work function as an origin of moiré contrast in scanning tunneling microscopy images of Pb thin films/Si(111). *Japanese Journal of Applied Physics*, 55(8S1):08NA03, August 2016.

[110] I. B. Altfeder, K. A. Matveev, and D. M. Chen. Electron Fringes on a Quantum Wedge. *Physical Review Letters*, 78(14):2815–2818, April 1997.

[111] J.H. Dil, J.W. Kim, T. Kampen, K. Horn, and A.R.H.F Ettema. Electron localization in metallic quantum wells: Pb versus in on si(111). *Physical Review B*, 73(16):161308, 2006.

[112] T.L. Chan, C.Z. Wang, M. Hupalo, M.C. Tringides, W.C. Lu, and K.M. Ho. Impact of interface relaxation on the nanoscale corrugation in Pb/Si(111) islands. *Surface Science*, 600(14):179–183, July 2006.

[113] W. B. Jian, W. B. Su, C. S. Chang, and T. T. Tsong. Vertical Friedel Oscillations in Interface-Induced Surface Charge Modulations of Ultrathin Quantum Islands. *Physical Review Letters*, 90(19), May 2003.

[114] Patrick Zeller and Sebastian Günther. What are the possible moiré patterns of graphene on hexagonally packed surfaces? Universal solution for hexagonal coincidence lattices, derived by a geometric construction. *New Journal of Physics*, 16(8):083028, August 2014.

[115] Elena Loginova, Shu Nie, Konrad Thürmer, Norman C. Bartelt, and Kevin F. McCarty. Defects of graphene on Ir(111): Rotational domains and ridges. *Physical Review B*, 80(8), August 2009.

[116] M. Yakes and M. C. Tringides. Probing the Buried Pb/Si(111) Interface with SPA LEED and STM on Si(111)-Pb$\alpha\sqrt{3} \times \sqrt{3}$. *The Journal of Physical Chemistry A*, 115(25):7096–7104, June 2011.

[117] Shengyong Qin, Jungdae Kim, Qian Niu, and Chih-Kang Shih. Superconductivity at the Two-Dimensional Limit. *Science*, 324:1314, 2009.

[118] P. B. Howes, K. A. Edwards, J. E. Macdonald, T. Hibma, T. Bootsman, M. A. James, and C. L. Nicklin. The Atomic Structure of the Si(111)-Pb Buried Interface Grown on the Pb/Si(111)-$\sqrt{3} \times \sqrt{3}$ Reconstruction. *Surface Review and Letters*, 05(01):163–166, February 1998.

[119] Katsuyoshi Kobayashi. Moiré pattern in scanning tunneling microscopy: Mechanism in observation of subsurface nanostructures. *Physical Review B*, 53(16):11091–11099, April 1996.

[120] S. M. Lu, M. C. Yang, W. B. Su, C. L. Jiang, T. Hsu, C. S. Chang, and Tien T. Tsong. Strength modulation of quantum-well states in Pb islands with periodic distortions on Si(111). *Physical Review B*, 75(11), March 2007.

[121] M. Hupalo, V. Yeh, T. L. Chan, C. Z. Wang, K. M. Ho, and M. C. Tringides. Interface relaxation and electronic corrugation in the Pb/Si(111)-Pb-α-$\sqrt{3} \times \sqrt{3}$. *Physical Review B*, 71(19), May 2005.

[122] C. Brun, T. Cren, V. Cherkez, F. Debontridder, S. Pons, D. Fokin, M. C. Tringides, S. Bozhko, L. B. Ioffe, B. L. Altshuler, and D. Roditchev. Remarkable effects of disorder on superconductivity of single atomic layers of lead on silicon. *Nature Physics*, 10(6):444–450, June 2014.

[123] Michael Ruby, Benjamin W. Heinrich, Jose I. Pascual, and Katharina J. Franke. Experimental Demonstration of a Two-Band Superconducting State for Lead Using Scanning Tunneling Spectroscopy. *Physical Review Letters*, 114(15), April 2015.

[124] K. Pöyhönen, I. Sahlberg, A. Westström, and T. Ojanen. Amorphous topological superconductivity in a Shiba glass. *Nature Communications*, 9(2103):1–5, 2018.

[125] Y. R. Song, Y. Y. Zhang, F. Yang, K. F. Zhang, Canhua Liu, Dong Qian, C. L. Gao, S. B. Zhang, and Jin-Feng Jia. Magnetic anisotropy of van der Waals absorbed iron(II) phthalocyanine layer on Bi 2 Te 3. *Physical Review B*, 90(18), November 2014.

[126] Joel Röntynen and Teemu Ojanen. Topological Superconductivity and High Chern Numbers in 2d Ferromagnetic Shiba Lattices. *Physical Review Letters*, 114(23), June 2015.

Sorbonne Université

École Doctorale 397 Physique et Chimie des Matériaux

Institut des NanoSciences de Paris

Résumé de thèse:

Ingénierie des états topologiques dans des réseaux de molécules magnétiques en interaction avec un supraconducteur 2D

par Danilo LONGO

Presentée et soutenue publiquement le 13 mai 2019

Introduction

La recherche sur la supraconductivité a trouvé un regain d'intérêt à partir de la dernière décennie, lorsque des travaux théoriques ont annoncé la possibilité de "fabriquer" de nouvelles phases topologiques dans des systèmes supraconducteurs dans l'état solide possédant des propriétés électroniques particulières telles que la présence d'états de bord de Majorana. L'observation expérimentale de ces états aurait un impact technologique énorme car ils sont de bons candidats pour l'ingénierie des qubits et leur manipulation pourrait en principe conduire au développement de véritables systèmes de calcul quantique. Des travaux récents ont prédit que la combinaison de la supraconductivité avec le couplage spin-orbite et un splitting Zeeman peut, dans certaines conditions, induire une supraconductivité topologique avec l'apparition d'états de bord de type Majorana. Ces trois ingrédients, indépendamment, ont fait l'objet de travaux intensifs en physique de l'état solide. Cependant, leur combinaison et le contrôle de leur force relative sont extrêmement difficiles du point de vue expérimental pour l'ingénierie des états topologiques dans un supraconducteur.
Dans ma thèse, pour relever ce défi, j'ai étudié un candidat prometteur consistant en des aimants moléculaires auto-assemblés sur des films très minces de plomb épitaxiés sur des surfaces de Si(111). Une étude récente de films très minces de Pb/Si(111) a révélé l'existence d'une supraconductivité 2D jusqu'à une seule couche atomique de plomb. De plus, des conditions de croissance appropriées permettent d'obtenir des films de plomb hautement cristallins dont l'épaisseur peut être ajustée au niveau atomique. Plus intéressant encore, la faible dimensionnalité des films de plomb induit un fort couplage spin-orbite de type Rashba. Il est clair que l'utilisation de films minces de Pb nous fournit deux des trois ingrédients nécessaires à une transition topologique: la supraconductivité et le couplage spin-orbite. Le magnétisme local peut être introduit au travers du dépôt d'aimants moléculaires organo-métalliques, tels que les phtalocyanines de manganèse (MnPcs), qui héberge un ion magnétique au centre de leur structure. L'idée d'utiliser des molécules organiques au lieu d'atomes simples découle de la nécessité de créer de grands domaines magnétiques qui peuvent être facilement obtenus grâce à leurs propriétés d'auto-assemblage. La manipulation atomique serait une alternative viable mais elle peut prendre beaucoup de temps si de très grands domaines sont ciblés. De plus, en cas de forte interaction entre les molécules et le substrat, celui-ci peut naturellement conduire à la formation d'une grande variété d'auto-assemblages avec de structures différentes. Un dernier avantage des aimants moléculaires par rapport aux atomes magnétiques simples est la possibilité d'ajuster leur spin et donc leurs propriétés magnétiques, par exemple en remplaçant l'ion magnétique central, tout en préservant les autres propriétés mentionnées ci-dessus.
En général le dépôt d'aimants moléculaires sur un supraconducteur 2D induit l'apparition

d'états liés localisés dans le gap supraconducteur connus sous le nom d'états de Shiba. Dans de bonnes conditions, l'interaction entre plusieurs états de Shiba induite par un réseau d'aimants moléculaires auto-assemblés peut conduire à leur hybridation et par conséquent à la réalisation de nouvelles phases supraconductrices topologiques. La signature expérimentale de telles phases serait l'apparition d'états de bord chiraux entourant le réseau magnétique, c'est-à-dire à la frontière entre la région topologique (celle recouverte de molécules) et la région non topologique (le reste de l'échantillon). Cependant, toutes ces conditions de couplage entre les molécules et le substrat ne sont pas automatiquement remplies car de nombreux autres effets peuvent intervenir lorsque des molécules organiques sont adsorbées sur un substrat. Beaucoup de ces effets dépendent de la force relative de l'interaction entre molécules et celle entre molécules et substrat. Pour cette raison, afin de mieux comprendre l'interaction entre les MnPcs et les couches minces de plomb, une étude approfondie de la structure et des propriétés d'auto-assemblage des MnPcs est nécessaire pour étudier de manière contrôlée l'émergence de la supraconductivité topologique.

Ce résumé est organisé en six sections. La première section contient tous les outils théoriques nécessaires pour lire le reste du résumé. Les deuxième et troisième sections contiennent les résultats expérimentaux obtenus à travers des expériences de microscopie et spectroscopie à effet tunnel sur deux échantillons différents: molécules de MnPcs déposées sur une monocouche de Pb epitaxiée sur du Si(111) (Section 2) et molécules de MnPc déposées sur des îlots/films tricouches de plomb deposées sur Si(111) (Section 3). La quatrième section contient les résultats expérimentaux concernant la caractérisation de la supraconductivité des îlots tricouches de Pb/Si(111). En conclusion, les cinquième et sixième sections contiennent les résultats expérimentaux liés à l'étude du couplage magnétique entre des MnPcs isolés (Section 5) ou auto-assemblés (Section 6) sur des tricouches de Pb/Si(111).

1 Supraconductivité et interaction avec des impuretés magnétiques

1.1 Notions de supraconductivité

La supraconductivité est un état de la matière intrigant découvert en 1911 par Hieke Kamerlingh Onnes. Les signatures expérimentales caractérisant l'état supraconducteur sont la chute brutale à zéro de la résistivité en dessous d'une certaine température T_C, dite température critique supraconductrice, et l'émergence d'un comportement diamagnétique parfait du matériau lui-même (effet Meissner-Ochsenfeld). Le premier paramètre macroscopique

décrivant l'état supraconducteur est la longueur de pénétration λ_L, définie comme la longueur caractéristique de décroissance d'un champ magnétique appliqué dans un supraconducteur. Le deuxième paramètre macroscopique est la longueur de cohérence ξ, définie comme la longueur caractéristique sur laquelle l'effet d'une perturbation est atténué de manière exponentielle dans un supraconducteur. La théorie la plus importante décrivant la supraconductivité d'un point de vue microscopique est la théorie BCS, développée par Bardeen, Cooper et Schrieffer. La théorie est basée sur l'idée que, au-dessous de la température critique T_C, une interaction attractive médiée par la vibration de la structure cristalline (interaction électron-phonon) déstabilise les électrons de conduction proches de la surface de Fermi et conduit à la formation des paires d'électrons connues sous le nom de paires de Cooper. De cette façon, le système peut réduire son énergie totale. A partir de cette description, on peut déduire la densité d'états BCS d'un supraconducteur par:

$$\rho(E) = \rho_0 \frac{|E|}{\sqrt{E^2 - \Delta^2}} \tag{1}$$

où ρ_0 est la densité d'états au niveau de Fermi dans l'état normal et Δ représente le gap énergétique dans la densité d'états du supraconducteur qui peut être interprété comme l'énergie d'appariement des paires de Cooper ou de la même manière comme l'énergie nécessaire pour les casser. Pour cette raison, la densité d'états 1, également montrée dans la Fig. 1, peut être vue comme une densité d'états d'excitation de quasi-particule. Les propriétés électroniques d'un supraconducteur peuvent être sondées par des mesures de spectroscopie à effet tunnel (STS). En particulier, la densité électornique de'états locale 1 est directement accessible en mesurant la conductance différentielle dI/dV. Dans le contexte du modèle à semi-conducteur décrivant le processus de tunnel électronique dans un supraconducteur, les excitations à énergie positive correspondent à l'ajout d'un électron dans le système. Inversement, les excitations à énergie négative correspondent à l'élimination d'un électron (l'ajout d'un trou) dans le système. Il est intéressant de mentionner qu'aux températures finies, toutes les signatures spectrales mesurées en STS sont élargies thermiquement de $\sim$3.5 k_BT. Afin d'éviter l'élargissement thermique, tous les expériences spectroscopiques ont été effectuées à des températures aussi basses que possible. Notamment, notre système expérimental nous a permis de travailler à 300 mK, disposant ainsi d'une résolution spectrale de l'ordre de100 μeV dans les mesures. L'utilisation de pointes supraconductrices est un autre moyen d'améliorer la résolution d'énergie dans les expériences STS.

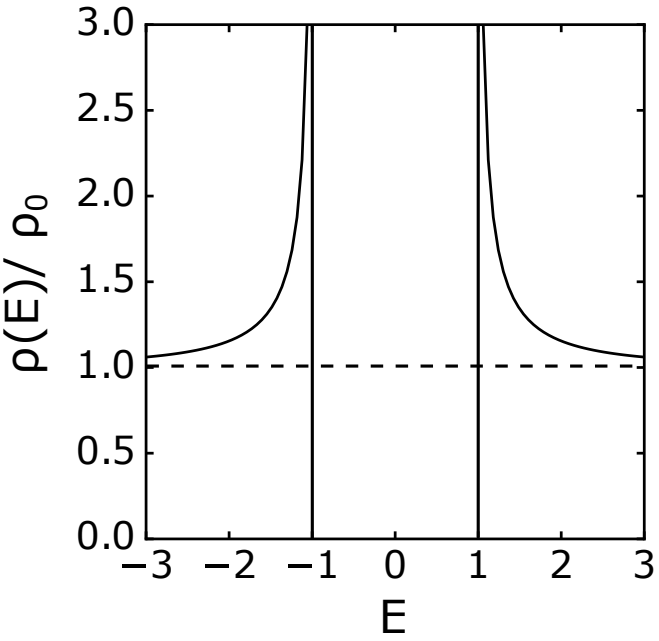

Fig. 1 Densité d'états BCS calculée en fonction de l'énergie et normalisée à la valeur de ρ_0. La ligne pointillée horizontale représente la densité d'états dans l'état normal. Notez que pour $E >> \Delta$ la densité d'états normale est récupérée par le supraconducteur.

1.2 Impuretés magnétiques et supraconductivité: Etats de Yu-Shiba-Rusinov

La théorie de Abrikosov Gor'kov est le modèle le plus utilisé pour décrire l'interaction entre une distribution aléatoire d'impuretés magnétiques et la supraconductivité. En particulier, il décrit l'effet d'impuretés magnétiques sur la densité d'états BCS et la température critique du supraconducteur. La théorie est basée sur l'idée que le spin associé à une impureté magnétique ajoute une interaction d'échange au potentiel de diffusion non-magnétique habituel entre l'impureté elle-même et les électrons de conduction du supraconducteur (paires de Cooper). Ce terme magnétique constitue en définitive une interaction de rupture de paire. Par conséquent, l'augmentation de la concentration d'impuretés affaiblit la supraconductivité conduisant à une perte de cohérence locale et création d'états d'impureté dans le gap. En pratique, cet effet conduit à la réduction des amplitudes des pics de cohérence situés en bordure de gap et au remplissage du gap supraconducteur. Pour des concentrations d'impuretés supérieures à une valeur critique, l'état supraconducteur est complètement détruit.

Dans le cas d'une impureté magnétique unique déposé sur un supraconducteur (par exemple un atome isolé ou une molécule), l'interaction entre les paires de Cooper et le spin de

l'impureté peut être écrite comme la somme d'un terme magnétique et d'un terme non-magnétique:

$$\hat{H}_{int} = -\frac{JS}{2}(\hat{c}^{\dagger}_{0\uparrow}\hat{c}_{0\uparrow} - \hat{c}^{\dagger}_{0\downarrow}\hat{c}_{0\downarrow}) + K(\hat{c}^{\dagger}_{0\uparrow}\hat{c}_{0\uparrow} + \hat{c}^{\dagger}_{0\downarrow}\hat{c}_{0\downarrow}) \tag{2}$$

où J est l'interaction d'échange entre les électrons de conduction et l'impureté (ferromagnétique si $J > 0$ et antiferromagnétique si $J < 0$), S est le spin de l'impureté et K est lié au potentiel de diffusion non-magnétique des électrons de conduction par l'impureté. Finalement, l'interaction entre les paires de Cooper et l'impureté magnétique affecte la densité d'états locale du système, conduisant à l'émergence d'états liés dans le gap. Ces états sont connus sous le nom d'états de Yu-Shiba-Rusinov ou simplement états de Shiba. Un seul état de Shiba se manifeste dans le gap par une paire de pics centrés spatialement sur l'impureté avec des énergies symétriques par rapport au niveau de Fermi (voir la partie supérieure de la Fig. 2):

$$E^{\pm}_{Sh} = \pm\Delta\frac{1-\alpha^2+\beta^2}{\sqrt{4\alpha^2+(1-\alpha^2+\beta^2)^2}} \tag{3}$$

où ρ_0 représente la densité d'états au niveau de Fermi dans l'état normal et les deux paramètres $\alpha = \pi\rho_0 JS/2$ et $\beta = \pi\rho_0 K$ sont liés à J et K respectivement. Aussi dans ce cas, la signature spectrale des impuretés magnétiques sur un supraconducteur du aux états de Shiba peut être sondée à travers des mesures STS.

La partie inférieure de la Fig. 2 montre que l'énergie des états de Shiba est strictement liée à la force du couplage magnétique J (le lien entre α et J est établi dans l'équation 3). Notez que, dans ce graphique, la contribution non-magnétique est négligée, c'est-à-dire $\beta = 0$. De plus, que le couplage magnétique soit ferromagnétique ($J > 0$) ou antiferromagnétique ($J < 0$), l'énergie des états de Shiba ne dépend pas du signe de J. Une impureté magnétique est appelée "impureté classique" si ses degrés de liberté internes ne peuvent pas être modifiés par l'interaction avec le supraconducteur. En conséquence, le spin d'une impureté classique ne peut pas être écranté (effet Kondo par exemple). La figure 2 montre que, dans le cas d'une impureté classique, pour $J \sim 0$, les états de Shiba sont proches au bord du gap ($E^{\pm}_{Sh} \sim \pm\Delta$). Dans ce cas, étant donné que l'impureté magnétique est faiblement couplée au supraconducteur, le système n'est pas affecté par l'impureté elle-même et il reste dans l'état fondamental de singulet de spin (le spin total du condensat est $S = 0$). Cette situation est illustrée dans la Fig. 3a. L'augmentation du couplage magnétique J amène les états de Shiba à se déplacer dans le gap vers le niveau de Fermi (voir la partie inférieure de la Fig. 2). Lorsque J dépasse la valeur critique correspondant à l'énergie de liaison d'une paire de Cooper ($J_{cri} \sim \Delta$), les pics associés aux états de Shiba traversent le niveau de Fermi et inversent leur position d'énergie réciproque. En particulier, pour $J \sim \Delta$, une paire de Cooper

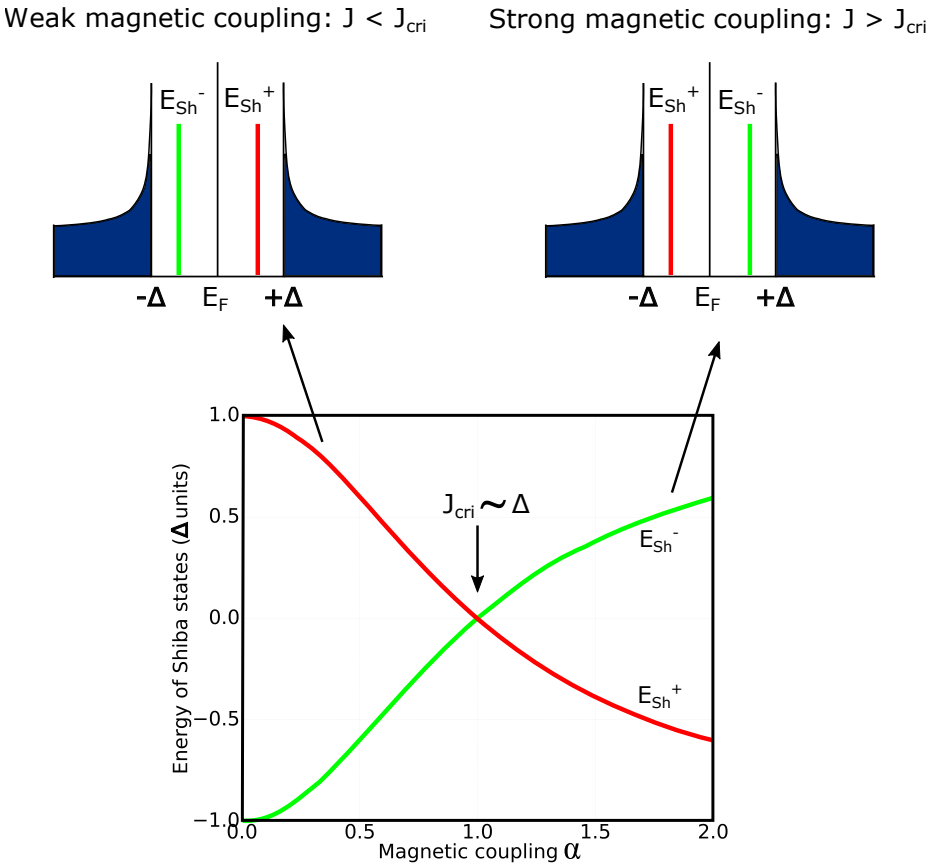

Fig. 2 Tracé des énergies des pics associé à un état de Shiba en fonction du terme magnétique α. Le lien entre α et J est établi dans l'équation 3. La figure montre également qu'au-dessus d'une valeur critique J_{cri} les énergies des pics se renversent.

peut être rompue et l'un des deux électrons de la paire peut être considéré comme localisé près du site de l'impureté et couplé magnétiquement à celui-ci. La présence de cet électron non apparié avec une direction de spin préférentielle modifie le spin total du condensat de $\pm 1/2$. Le signe "+" ou "-" de la variation de spin totale est déterminé par la nature du couplage magnétique entre l'électron non apparié et l'impureté magnétique qui peut être ferromagnétique ($J > 0$) ou antiferromagnétique ($J < 0$). Cette situation est illustrée dans la Fig. 3b. Il faut toujours garder à l'esprit que le mécanisme que nous venons de décrire et illustré sur la Fig. 3b répresente seulement une image simplifiée de la physique réelle, impliquant de plus des événements à plusieurs corps dans lesquels les paires de Cooper sont brisées et formées en continu. Le message principal de ce paragraphe est que la force du couplage magnétique J, entre une impureté à spin classique et un supraconducteur, affecte profondément l'énergie des états de Shiba et est responsable de la nature de l'état fondamental

du condensat.

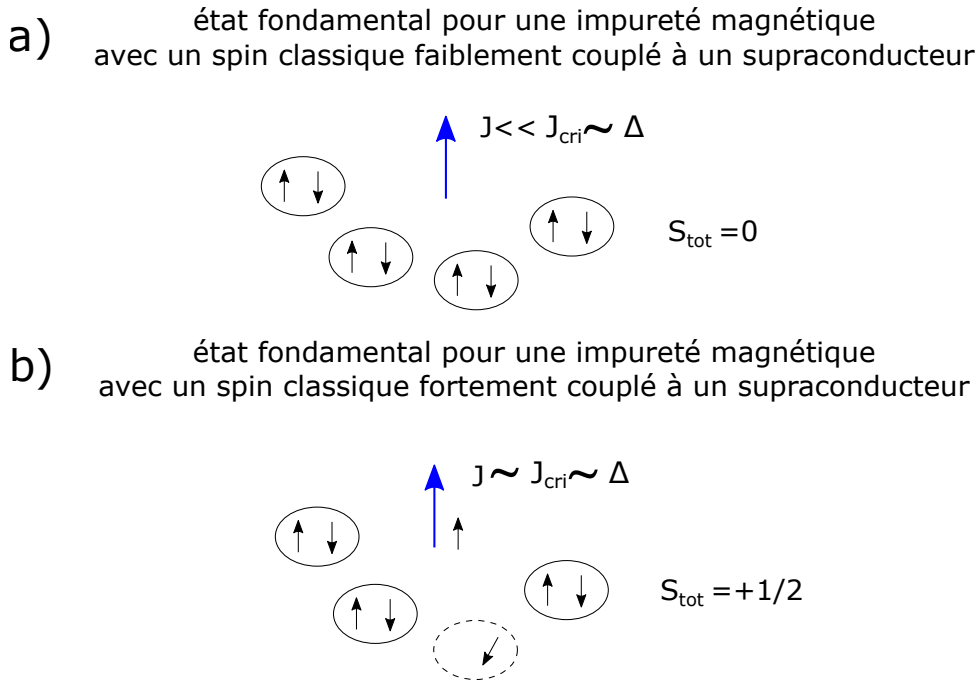

Fig. 3 (a) état fondamental du condensat dans le cas d'un spin classique faiblement couplé à un supraconducteur. Les paires de Cooper ne sont que légèrement affectées par la présence de l'impureté et le spin total du condensat reste donc $S = 0$. (b) état fondamental du condensat dans le cas d'un spin classique fortement couplé à un supraconducteur. Dans ce cas, l'interaction d'échange est capable de rompre les paires de Cooper et de localiser l'un des électrons sur le site de l'impureté. Le spin total du condensat est modifié de $\pm 1/2$ selon que le couplage magnétique entre l'électron localisé et le spin d'impureté soit ferromagnétique ($J > 0$) ou antiferromagnétique ($J < 0$).

La prise en compte de la diffusion non-magnétique des électrons de conduction par l'impureté magnétique, en considérant $\beta \neq 0$ dans l'équation 3, a principalement deux effets. Le premier effet est illustré sur la Fig. 4 qui presente un tracé des énergies des pics d'un état de Shiba $E_{Sh}^{\pm}$ en fonction du paramètre magnétique α pour differentes valeurs de β. Il ressort clairement de cette figure que l'augmentation du couplage non magnétique β pousse le point d'inversion des deux pics vers des valeurs plus élevées de α (résultat indépendant du signe de β). En d'autres termes, plus le couplage non-magnétique est fort, plus la valeur critique J_{cri} nécessaire pour passer d'un couplage magnétique faible (correspondant à un état fondamental de singulet de spin $S = 0$) à un couplage fort (correspondant à un état fondamental de doublet de spin $S = 1/2$) augmente.

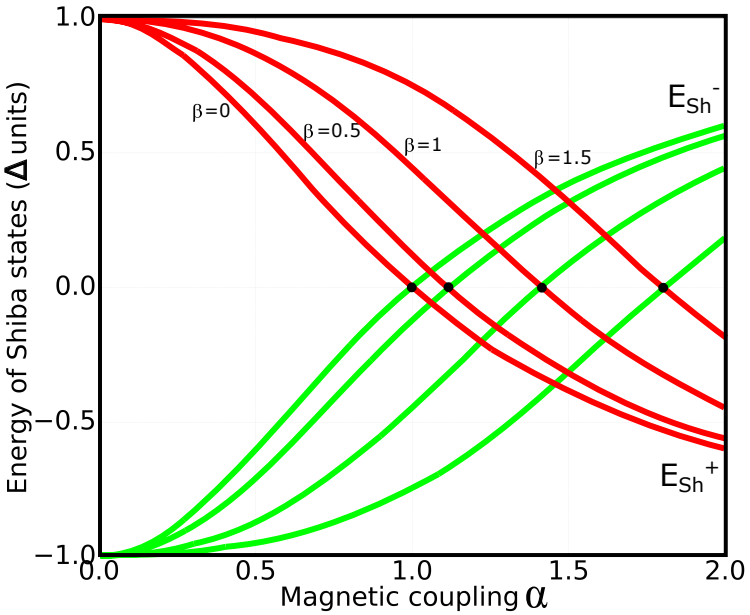

Fig. 4 Tracé des énergies des pics associé à un état de Shiba $E_{Sh}^{\pm}$ en fonction du paramètre magnétique α. Les différentes courbes correspondent à différentes valeurs du paramètre non-magnétique β. Le principal effet de l'interaction non-magnétique est le déplacement du point d'inversion des des deux pics vers des valeurs plus élevées de J.

Le deuxième effet de l'interaction non-magnétique est d'introduire une asymétrie dans l'amplitude relative des pics associés à un état de Shiba. Ceci est lié à la rupture de la symétrie particule-trou à cause du potentiel de Coulomb écranté généré par la charge distribuée sur l'impureté elle-même. L'origine de la charge d'impureté dépend à la fois du type d'impureté et de la nature du substrat impliqué. Par exemple, dans le cas de molécules magnétiques déposés sur une surface métallique, le transfert de charge pourrait être l'un des mécanismes responsables du chargement de la molécule et donc de l'interaction non magnétique avec les électrons de conduction du matériau hôte. La fig. 5 montre un aperçu des asymétries possibles pouvant être rencontrées en fonction du type de couplage magnétique et non-magnétique. Cette figure comprend également les cas dans lesquels la force du couplage magnétique J est plus petit ou plus grand que la valeur critique J_{cri} nécessaire pour passer d'un régime de couplage faible à un régime de couplage fort.

L'extension spatiale de la fonction d'onde associée aux états de Shiba dépend essentiellement de la dimensionnalité du supraconducteur. En particulier, l'interaction entre impuretés magnétiques et supraconducteur 2D induit des états de Shiba qui s'étendent jusqu'à 10 nm de l'impureté. Ceci est différent de ce qui est observé dans le cas d'un supraconducteur 3D où les états de Shiba sont localisés sur quelques distances atomiques autour de l'impureté (quelques

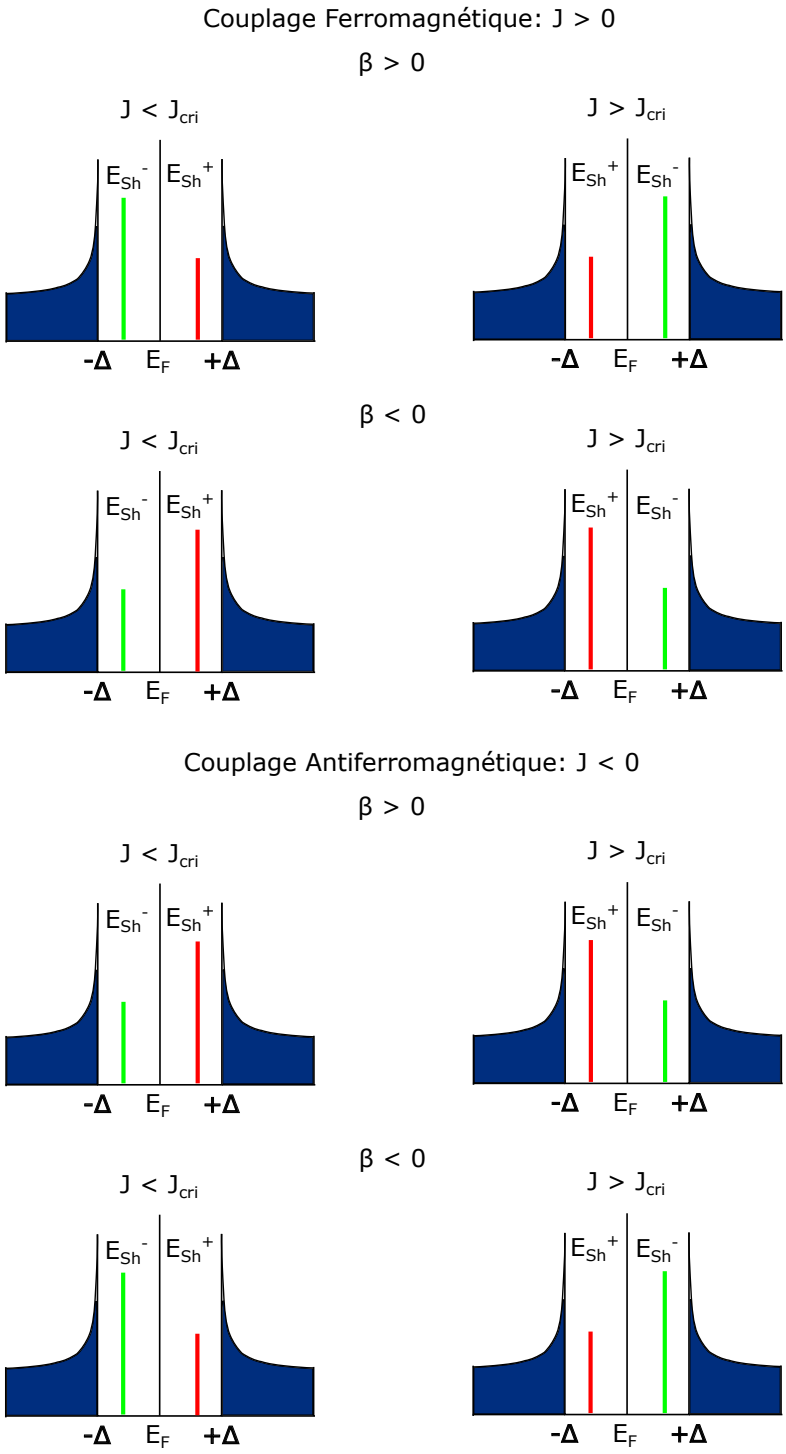

Fig. 5 Croquis des asymétries possibles pour les états de Shiba en fonction du type de couplage magnétique (J) et non-magnétique (K). Les cas $J < J_{cri}$ et $J > cri$ sont aussi pris en compte.

Å). En effet le recouvrement est alors plus important lorsque l'extension spatiale des etats de Shiba est accrue. Le recouvrement des états de Shiba dans un dimère peut conduire à leur hybridation et, par conséquent, au splitting en états de liaison et de anti-liaison. Ce processus d'hybridation est similaire à la formation d'orbitales moléculaires à partir d'atomes isolés. En conséquence, le chevauchement d'états de Shiba associé à une concentration finie d'impuretés magnétiques peut conduire à la formation de bandes dites de Shiba. Fait intéressant, le chevauchement et l'hybridation de plusieurs états de Shiba peuvent jouer un rôle dans la formation d'un ordre magnétique parmi les impuretés.

L'idée de base de la présente étude est d'utiliser un système hybride formé par des couches minces de Pb, déposés sur un substrat de Si(111), et des molécules métallo-organiques magnétiques adsorbés sur la surface (phtalocyanines de manganèse ou MnPcs). L'utilisation de couches minces de Pb nous permet d'avoir une supraconductivité 2D associée à un fort couplage spin-orbite de type Rashba. D'autre part, le magnétisme est intégré à travers les molécules organiques. Comme déjà mentionné ci-dessus, l'interaction entre le spin moléculaire et la supraconductivité conduit à l'apparition d'états de Shiba dans le gap. Dans certaines conditions, l'auto-assemblage de molécules peut conduire au chevauchement des états de Shiba correspondants et donc à leur hybridation. Dans ce cas, la formation des bandes de Shiba peut entraîner un ordre magnétique sur le domaine moléculaire auto-organisé (par exemple and couplage ferromagnétique) et finalement une transition topologique. Toutes ces conditions de couplage ne sont pas automatiquement satisfaites dans des systèmes réelles car de nombreux autres effets peuvent intervenir lors de l'adsorption des molécules. Pour cette raison, l'objectif principal de cette thèse est d'étudier, à travers des techniques de caractérisation de surface (LEED, STM et STS) toutes les étapes de la préparation du système hybride pour essayer de comprendre quelles sont les conditions qui permettent d'obtenir une transition topologique.

2 Adsorption de MnPcs sur la monocouche de Pb/Si(111)

La maîtrise de ce système est extrêmement delicate car une petite différence du taux de couverture de plomb (1%) aboutit à une phase structurale différente de la monocouche. L'idée de ces expériences est d'utiliser la structure particulière de la phase $\sqrt{7} \times \sqrt{3}$-Pb, présentant des rangée atomiques (voir Fig. 6a), comme surface modèle pour guider l'auto-organisation des chaînes linéaires d'aimants moléculaires. Cependant, l'adsorption moléculaire sur la monocouche de plomb entraîne des effets inattendus et surprenants. Nos expériences ont révélé que l'adsorption de MnPcs sur la phase $\sqrt{7} \times \sqrt{3}$, correspondant à 1,2 ML de Pb, induit

une transition de phase structurelle macroscopique de la monocouche de Pb vers la phase SIC (Striped Incommensurate phase) correspondant à 1,3 ML de Pb (voir Fig. 6).

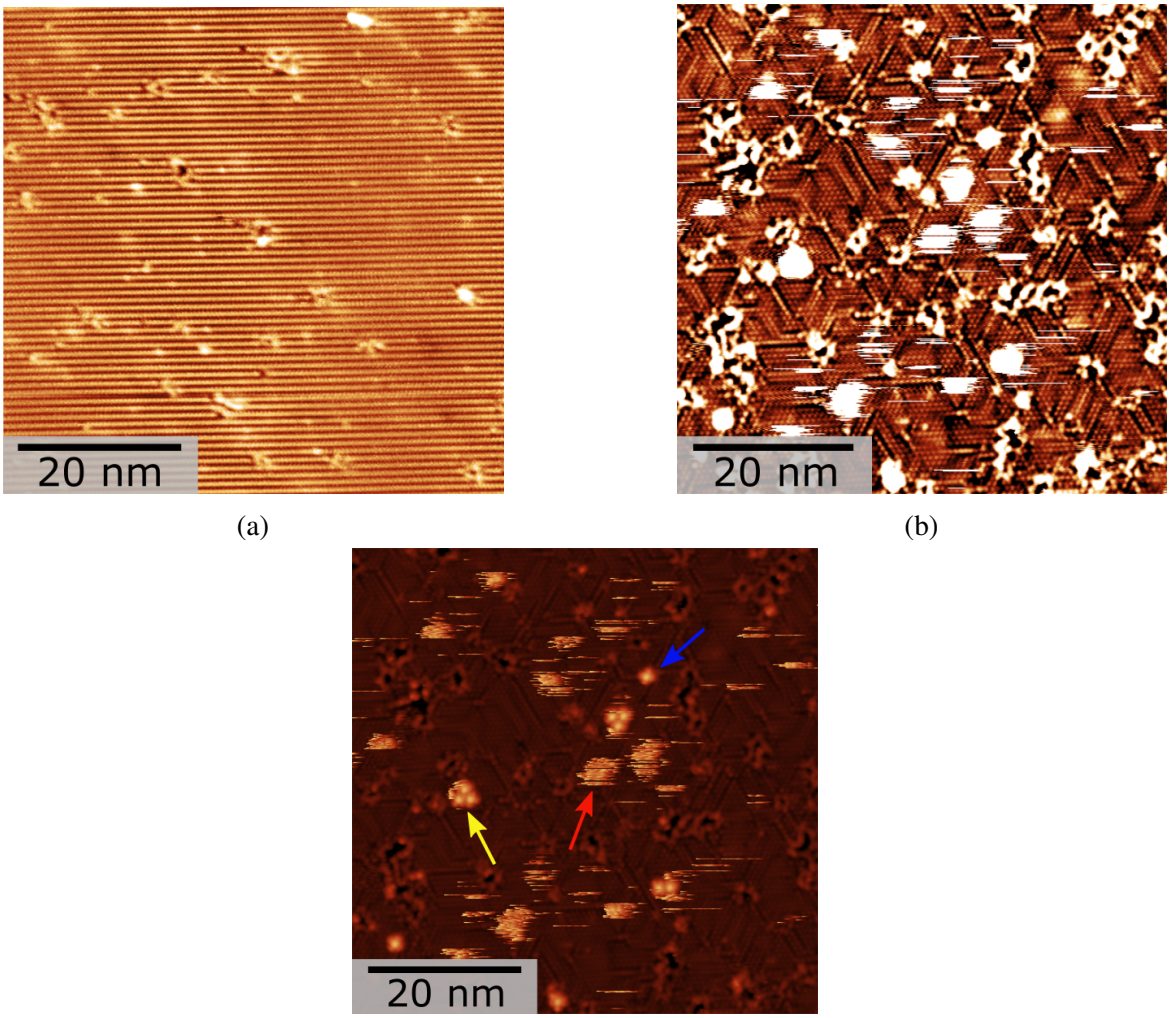

(a) (b)

(c)

Fig. 6 (a) Image STM de la phase $\sqrt{7} \times \sqrt{3}$-Pb/Si(111) avec 1,2 ML de Pb. (b) Image STM montrant la reconstruction de surface induite par l'adsorption de $\sim$0.7 molécules/100 nm^2 de MnPcs sur la phase $\sqrt{7} \times \sqrt{3}$-Pb montrée dans la figure (a). Le substrat est maintenu entre 70 K et 250 K pendant l'évaporation des MnPcs.(c) La même image STM que celle affichée en (b) avec le contraste ajusté pour rendre les MnPcs visibles. La flèche bleue indique une MnPc isolée. La flèche jaune identifie un trimère des MnPcs. La flèche rouge indique un objet moléculaire diffusant sur la surface. (a) Taille de l'image= 60×60 nm^2, V_T: +1 V et I_T : 20 pA. (b) et (c): Taille de l'image= 60×60 nm^2, V_T: +0.3 V et I_T : 20 pA. Toutes les images STM ont été mesurés à 77 K.

L'adsorption de $\sim$ 0.18 molécules/100 nm^2 de MnPcs sur un substrat maintenu entre 77 K et la température ambiante suffit déjà à reconstruire complètement la structure $\sqrt{7} \times \sqrt{3}$ dans la phase SIC. Plusieurs groupes ont déjà déposé des MnPc sur des monocristaux de Pb, mais une telle transition de phase abrupte induite par si peu de molécules n'a jamais été rapportée auparavant. Ainsi, dans le cas d'un systeme très proche de phtalocyanines déposées sur une bicouche d'Indium sur Si(111) et présentant une phase $\sqrt{7} \times \sqrt{3}$, aucune reconstruction de surface n'a pu être observée. Notre estimation quantitative de la variation de densité atomique du Pb à travers la transformation structurelle induite par les MnPcs va dans le sens d'une transition de la phase $\sqrt{7} \times \sqrt{3}$ vers la SIC. Cette hypothèse est également corroborée par la similitude de l'auto-assemblage des MnPcs sur la phase SIC de la monocouche préparée avec 1.3 ML de plomb et sur la SIC induit par les MnPcs déposés sur la $\sqrt{7} \times \sqrt{3}$ avec 1.2 ML. Nous avons proposé une explication du mécanisme à la base de la transition de phase de la monocouche de Pb induite par les MnPcs. L'idée est que l'adsorption moléculaire peut affecter certaines des liaisons chimiques responsables de la stabilité de la $\sqrt{7} \times \sqrt{3}$ (ceux entre les atomes de Pb et le substrat de silicium). Dans le même temps, il peut être envisagé que les MnPcs transfèrent une charge électronique à la surface du plomb, ce qui entraînerait une augmentation de la force de tension dans le film de plomb. La combinaison de ces deux effets peut représenter la force motrice de la contraction de la couche de plomb et donc de la reconstruction de surface observée expérimentalement.

L'analyse de l'auto-assemblage moléculaire sur la phase SIC induite par les MnPcs a révélé qu'à une couverture de MnPcs de $\sim$0.7 molécules/nm^2, la forte interaction molécule-substrat entraîne une compétition entre la symétrie 4 des MnPcs et la symétrie 3 du substrat. Cette compétition conduit à un auto-assemblage moléculaire très différent de celui observé sur des substrats ayant un caractére 3D. En particulier, l'auto-assemblage carré des MnPcs généralement observé sur des surfaces métalliques est fortement frustré sur la monocouche de plomb et seulement quelques configurations moléculaires stables sont observées expérimentalement, c'est-à-dire des molécules isolées et des trimères reflétant la symétrie 3 du substrat (voir Fig. 7 et Fig. 8). L'analyse des images STM montre que l'orientation d'adsorption de molécules de MnPcs isolées sur le substrat se répartit en trois configurations reflétant la symétrie 3 du substrat lui-même (voir la figure 7). Le croquis de la Fig. 7d (dessiné à partir des données expérimentales) montre que, pour chaque configuration, l'une des directions du substrat (flèches vertes) est presque alignée avec les deux atomes d'azote de la molécule (dans l'erreur expérimentale de $\sim$2°). Les flèches rouges indiquent la position des atomes d'azote mentionnés ci-dessus.

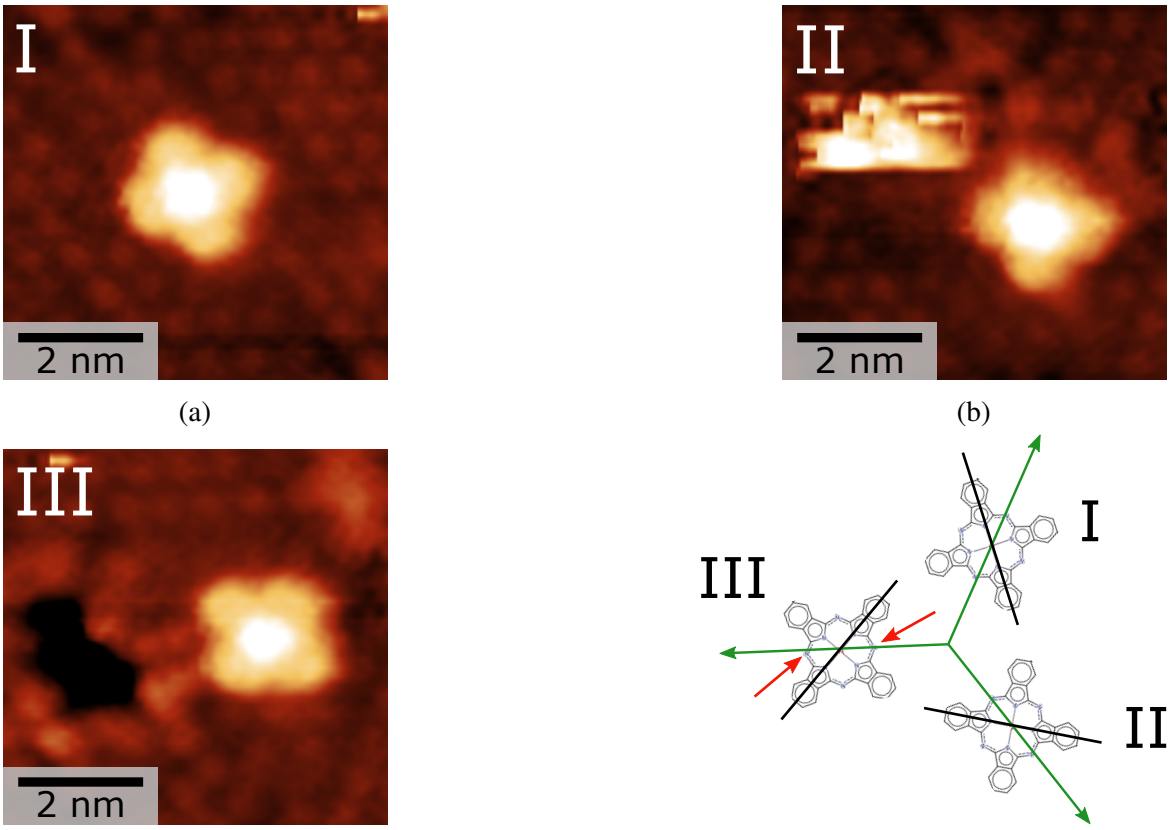

(a) (b) (c) (d)

Fig. 7 (a), (b) et (c): Images STM des trois configurations d'adsorption possibles pour les MnPcs isolés sur la monocouche de Pb/Si(111) avec 1,2 ML de Pb. Taille de l'image: $6 \times 6\ nm^2$, V_T: +0.4 V et I_T : 80 pA. Toutes les images STM ont été mesurés à 77 K. (d): Croquis dessiné à partir des données expérimentales montrant les trois orientations possibles des MnPcs isolés par rapport aux directions du substrat de Pb (représentées par des flèches vertes). Les flèches rouges indiquent les deux atomes d'azote d'un MnPc aligné avec une des directions du Pb. Les lignes noires représentent les axes principal des différentes MnPcs isolées tournés de 120° un par rapport aux autres en conséquence de la forte interaction molécule-substrat.

En ce qui concerne les trimères de MnPcs, les images STM dans le figures 8a et 8b montrent les deux seules configurations observées expérimentalement. L'analyse de ces structures révèle que chaque MnPc dans un trimère conserve exactement la même orientation par rapport au substrat que celle observé pour les MnPcs isolée (voir Fig. 7d). De plus, chaque trimère contient toujours des MnPcs présentant les trois orientations possibles observées dans le cas des MnPcs isolés, c'est-à-dire celles illustrées dans la Fig. 7d. Les croquis dans les Fig. 8c et les Fig. 8d (dessinés à partir des données expérimentales) montrent que chaque direction du substrat (flèches vertes) passe par une paire d'ions Mn appartenant à

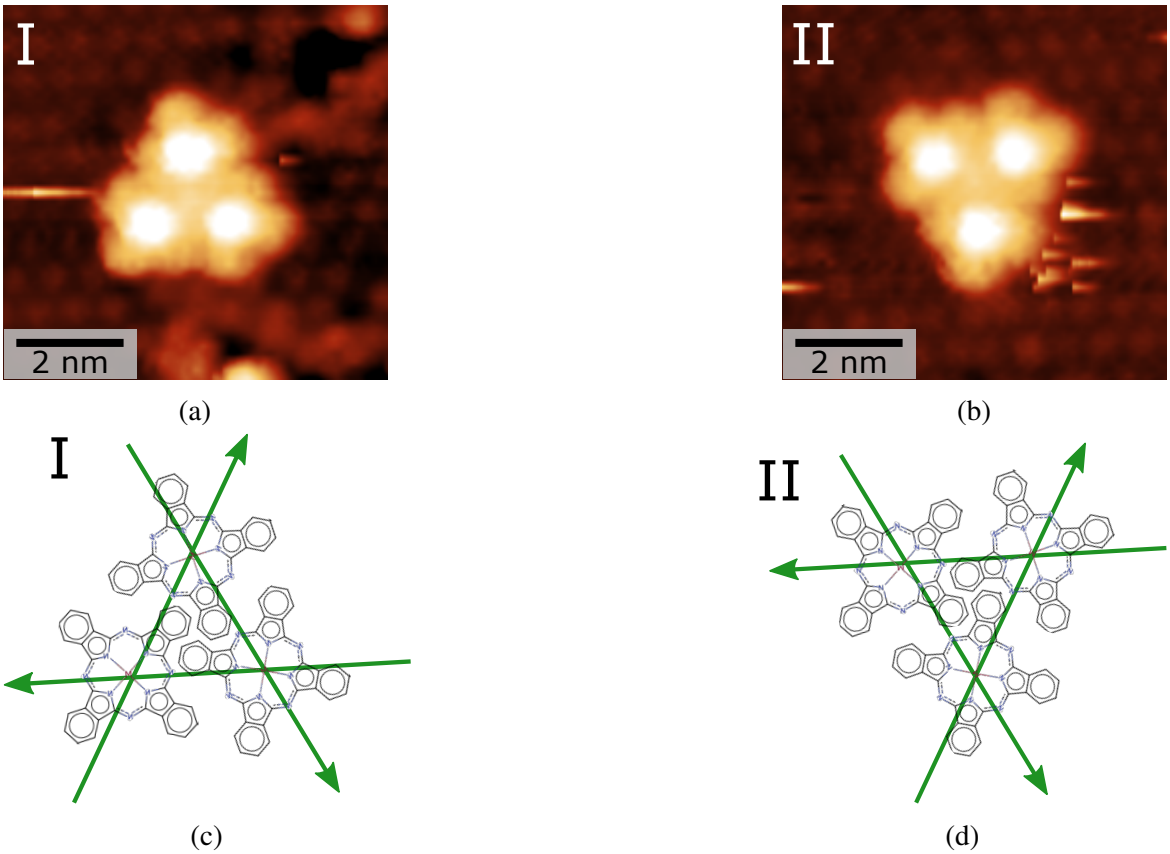

Fig. 8 (a) et (b): Images STM des deux configurations des trimères observés expérimentalement sur la monocouche de Pb/Si(111) avec 1.2 ML de Pb: trimère pointant vers le haut (a) et trimère pointant vers le bas (b). Taille de l'image: $7 \times 7\ nm^2$, V_T: +0.5 V et I_T : 50 pA. Toutes les images STM ont été mesurés à 77 K. (c) et (d): Croquis dessiné à partir des données expérimentales montrant l'orientation du trimère par rapport aux directions du substrat de Pb (représentées par des flèches vertes). Chaque direction du substrat (flèches vertes) passe par une paire d'atomes de Mn appartenant à des MnPcs différents.

des molécules différentes (dans l'erreur expérimentale de $\sim 2°$). Cet alignement suggère une orientation préférentielle du trimère par rapport au substrat induite par l'interaction d'atomes de Mn avec la surface de Pb. Toutes les distances Mn-Mn du même trimère ont des valeurs similaires, c'est-à-dire 1,46 $\pm$ 0,06 nm pour les trimères pointant vers le haut et 1,51 $\pm$ 0,06 nm pour les trimères pointant vers le bas, forment approximativement un triangle équilatéral. Ces deux valeurs pour les deux types de trimères sont cohérentes dans la limite de l'erreur expérimentale de mesure.

Pour conclure, en raison de la forte interaction molécule-substrat, les trimères de MnPcs reflètent la symétrie 3 du substrat en terme d'orientation des molécules individuelles formant un triangle équilatéral ainsi que de la structure générale et de l'orientation du trimère sur le

substrat. À notre connaissance, les trimères de MnPcs observés dans nos expériences n'ont pas été observés sur d'autres types de substrat. Lorsque la couverture moléculaire est augmentée (jusqu'à 4.9 molécules/100 nm^2), les MnPcs donnent lieu à des structures complexes incommensurables avec la symétrie du substrat (géométries linéaires sont préférés).

De plus, la transition de phase structurelle inattendue et intrigante induite par les MnPcs, ainsi que le nouvel auto-assemblage des MnPcs sur cette surface, suggèrent que l'interaction entre les MnPcs et la monocouche de Pb est probablement très forte. Des calculs DFT (Théorie de la fonctionnelle de la densité) abordant ce problème sont en cours au moment de la rédaction de cette thèse. Il serait également intéressant de mener d'autres expériences, par exemple des mesures ARPES ou STS, afin de comprendre si les propriétés électroniques de la phase SIC induite par MnPcs sont modifiées par rapport à la phase SIC propre obtenue sans dépôt de molécules.

3 Tricouches de plomb sur Si(111): films continus et îlots

Une alternative à la monocouche de plomb est donnée par les tricouches de Pb/Si(111) dans lesquels le caractère de supraconducteur 2D est conservé, ainsi qu'un fort couplage spin-orbite de type Rashba. Le confinement vertical des électrons dans les couches minces de plomb sur Si(111) conduit à l'existence d'états de puits quantiques qui induisent des oscillations quantiques des propriétés structurelles et électroniques en fonction de l'épaisseur des couches elles-mêmes. Dans la suite nous ferons référence aux états de puits quantiques à travers l'abréviation du terme anglais Quantum Well states (QWS). Le désaccord entre les paramètres de maille du film de Pb(111) et celui du substrat de Si(111) conduit à l'apparition d'un motif de moiré à la surface du Pb qui peut être observé à travers des mesures STM pour des épaisseurs allant jusqu'à $\sim$20 ML ou même plus. Fig. 9 illustre schématiquement l'origine d'un motif de moiré. En particulier, la Fig. 9a montre deux réseaux hexagonaux de points verts et rouges superposés et présentant un désaccord entre les paramètres de maille. Le motif de moiré est donné par les régions lumineuses disposées en hexagone. Il est clair que le moiré conserve la même symétrie hexagonale des deux réseaux sous-jacents et que ses axes de symétrie sont alignés en conséquence. La Fig. 9b montre que lorsqu'il y a une rotation d'un réseau par rapport à l'autre (6° pour la Fig. 9b) le motif de moiré réduit sa période par rapport au cas non-tourné et change son orientation.

Les motifs de moiré dans les tricouches de plomb proviennent de l'interface Pb/Si(111) et sont dus à une combinaison de contributions géométriques et électroniques. La contribu-

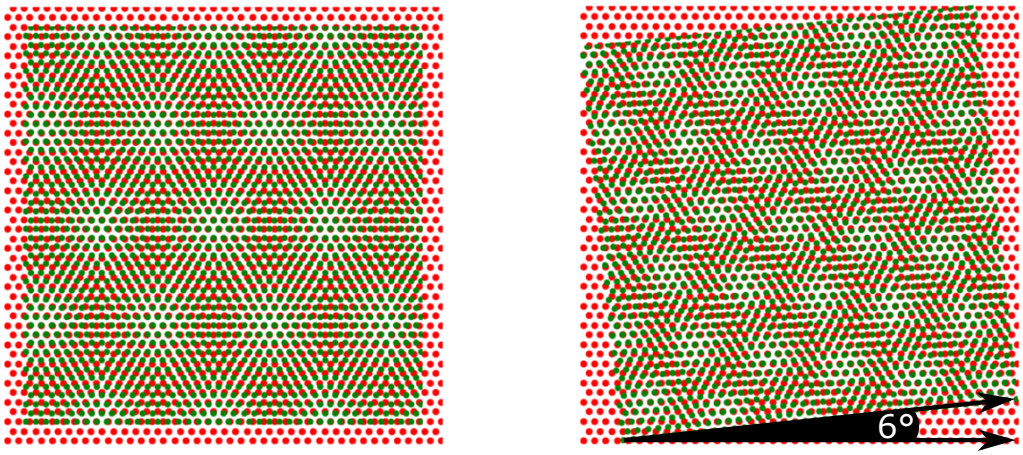

(a) (b)

Fig. 9 Illustration schématique de l'origine d'un motif de moiré. (a): Deux réseaux hexagonal de points verts et rouges superposés, présentant un désaccord entre les paramètres de maille et avec les axes de symétrie alignés. Le désaccord entre les paramètres de maille donne lieu à un motif de moiré hexagonal (régions lumineuses dans la figure). (b): Les mêmes réseaux de points sont tournés de 6° l'un par rapport à l'autre: période et orientation du moiré changent en conséquence.

tion électronique est donnée par les électrons confinés (QWS) dans le plomb même, qui transmettent l'image de l'interface Pb/Si(111) à la surface. Cette image peut être à son tour sondée avec des mesures STM. La contribution géométrique est due à la relaxation structurelle de l'interface Pb/Si(111) qui conduit à une corrugation géométrique périodique dont la longueur d'onde est liée au motif de moiré observé expérimentalement. Un autre aspect important pour comprendre l'origine structurelle du motif de moiré dans des films très minces de Pb/Si(111) est la séquence d'empilement des plans atomiques dans le film lui-même. La figure 10 montre deux îlots de Pb/Si(111) (3 monocouches d'épaisseur) présentant deux motifs de moiré différents. Dans la figure 10a, le motif de moiré apparaît comme une distribution périodique de "protubérances" alors que dans la figure 10b apparaît comme une distribution de "trous". Des études précédentes conviennent que toutes les îlots Pb ont toujours un empilement fcc et que l'aspect différent des motifs de moiré est dû à une séquence d'empilements différentes des plans atomiques Pb: ABC, ACB, etc. D'autre part, il n'est toujours pas clair si le mécanisme de formation de base est plutôt structurel ou électronique.

Il est également important de noter que d'autres motifs de moiré, comme ceux montrés dans la Fig. 11, peuvent être observés sur la surface des tricouches de plomb. Ces motifs de

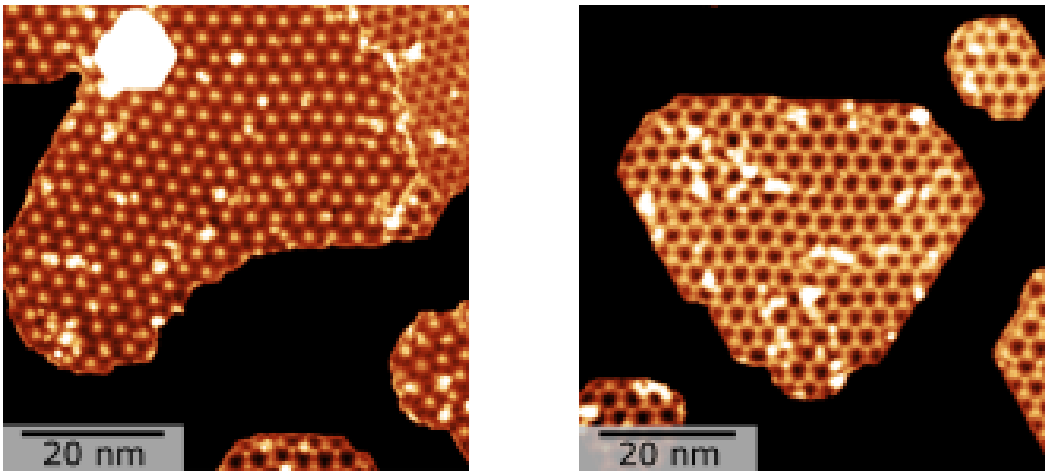

(a) (b)

Fig. 10 Images topographiques STM d'îlots tricouches de plomb sur Si(111) présentant un motif de moiré à "protubérances" (a) et à "trous" (b). (a): Taille de l'image: 65×65 nm^2, V_T: +50 mV et I_T : 50 pA. (b): Taille de l'image: 65×65 nm^2, V_T: +0.3 V et I_T : 50 pA.

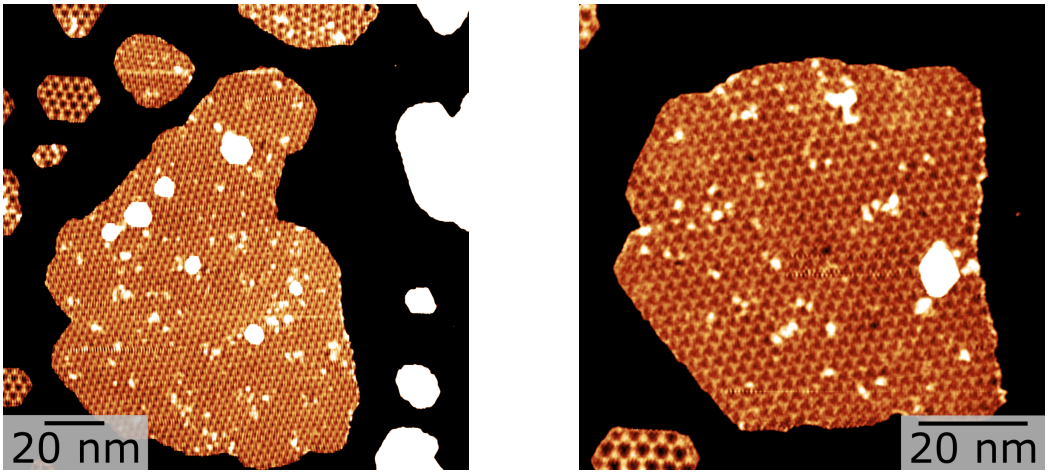

(a) (b)

Fig. 11 Images topographiques STM d'îlots tricouches de plomb sur Si(111) présentant un motif de moiré a courte période. (a): Taille de l'image: 155×155 nm^2, V_T: 1 V et I_T : 40 pA. (b): Taille de l'image: 85×85 nm^2, V_T: -1 V et I_T : 50 pA.

moiré ont une période beaucoup plus courte que celle des motifs à "trous"/"protubérances" discutées jusqu'à présent (dans la figure 11 il est possible de comparer directement des îlots présentant un motif de moiré à "trous" avec ceux qu'ils montrent un moiré a courte période). Rappelant ce qui a été dit à propos de la Fig. 9, les motifs de moiré a courte periode peuvent être compris comme une rotation des îlots de Pb par rapport au substrat de silicium. Cependant, une inspection minutieuse des "protubérances" du moiré dans la

Fig. 11b révèle une une structure interne triangulaire qui qui n'apparaît pas dans le moiré de Fig. 11a. Cette observation suggère que l'origine du motif de moiré dans un système réel ne peut pas être interprétée à travers de simples modèles géométriques mais les effets structurels et électroniques doivent être pris en compte pour décrire correctement le système lui-même. En conclusion, l'origine des motifs de moiré dans les films minces de plomb sur Si(111) n'est pas complètement comprise et cela est probablement dû au fait que les contributions électroniques et structurelles participent ensemble à leur formation. Les résultats expérimentaux présentés dans la suite du résumé ont été obtenus en mesurant des tricouches de plomb (îlots ou films) epitaxiées sur du Si(111). En particulier, les sections 3.1 et 3.2 se concentrent sur la contribution structurelle au motif de moiré observé dans les images STM et section 3.3 se concentre sur la contribution électronique due aux électrons confinés (QWS).

3.1 MnPcs sur des tricouches continus de Pb/Si(111)

La figure 12 montre une image STM représentative d'un film quasi uniforme de tricouches de plomb sur Si(111) au-dessus duquel $\sim$2,7 molécules/100 nm^2 de MnPcs ont été déposés. L'image contient deux terrasses séparées par une marche atomique de silicium représentés par deux couleurs différentes sur une échelle de fausses couleurs. Les deux terrasses contiennent de trous de forme irrégulière et deux monocouches de profondeur (zones noires sur l'image). Le film présente deux types de motifs de moiré répartis sur différentes terrasses de silicium. La terrasse supérieure dans l'image 12 révèle un moiré composée caractérisé par un motif de "trous" sombres sur un fond clair. La terrasse inférieure présente un moiré caractérisé par un motif de "protubérances" claires sur un fond sombre. Pour cette raison, les deux terrasses seront appelées terrasses à "protubérances" et à "trous".
Fig. 12 révèle également que la majorité des MnPcs s'absorbent préférentiellement sur les terrasses à "protubérances" (certains domaines moléculaires sont indiqués par des flèches jaunes). Comme observé dans d'autres systèmes, l'adsorption sélective de MnPcs suggère que la structure interne des terrasses à "protubérances" et à "trous" pourrait être différente. En se concentrant sur la terrasse à "protubérances" (voir Fig.24), il est possible de voir que les MnPcs s'auto-assemblent de différentes façons sur différentes régions de la surface, c'est-à-dire dans des réseaux carrés ou dans des structures dispersées de molécules. Pour comprendre ce comportement, il faut noter que les terrasses à "protubérances" présentent une coexistence de deux types de moiré identiques à ceux déjà présentés dans la Fig. 10 et que nous avons également appelés "trous" et "protubérances". Il est important de souligner que, même si on les appelle de la même manière, notre étude a révélé que le motif de moiré à "trous" discuté dans la figure 10 et celui discuté dans cette section ou dans la figure 15 ont une structure complètement différente. Sur la base de ce qui a déjà été dit dans la section précédente, le

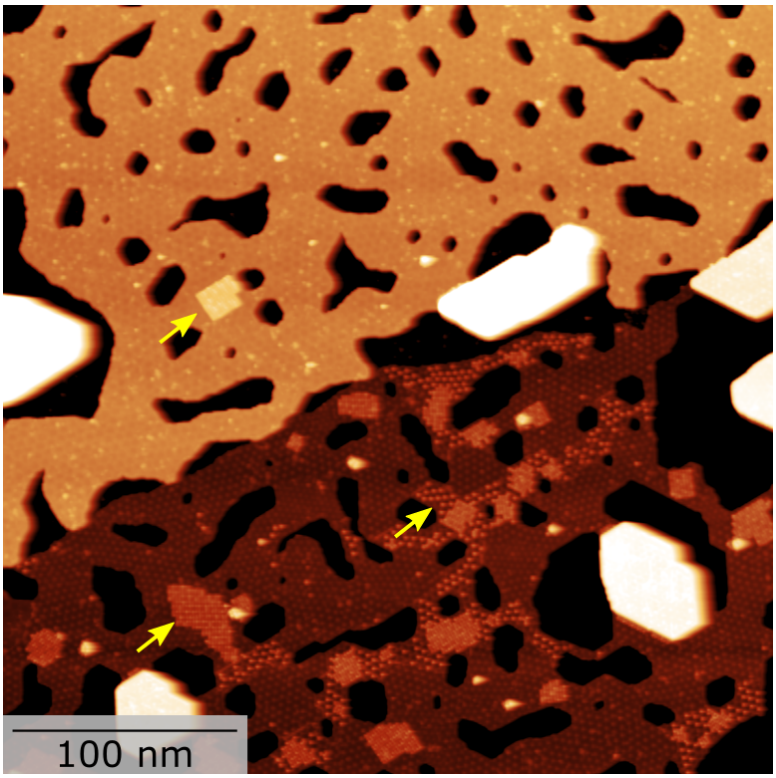

Fig. 12 Image STM montrant ∼2,7 molécules/100 nm^2 de MnPcs déposés sur des tricouches quasi-continus Pb/Si(111). Les zones noires représentent des trous de forme irrégulière dans le film (deux monocouches de profondeur). Les zones claires sont des îlots de plomb de 5 monocouches. Les deux terrasses présentent deux motifs de moiré différents: à "trous" et à "protubérances". Les flèches jaunes indiquent les MnPcs assemblés et dispersés. Taille de l'image: 340×340 nm^2, V_T: -1 V et I_T : 20 pA.

contraste différent des deux types de moiré provient d'une séquence d'empilement différente. Par conséquent, le comportement différent des MnPcs sur les deux types de moiré (voir Fig.14) peut être compris à travers l'idée d'une adsorption sélective différent qui conduit à la formation de différentes structures moléculaires. Enfin, il est intéressant de noter que l'auto-assemblage de MnPcs sur les tricouches de plomb est très différent de celui sur la monocouche. Comme déjà discuté, dans ce dernier cas, les MnPcs sont isolés ou forment tout au plus des trimères reflétant la symétrie 3 du substrat. D'autre part, dans le cas des tricouces de plomb, l'auto-assemblage réseaux carrés de MnPcs est récupéré. Cependant, l'auto-assemblage de MnPcs sur les tricouches reste très différent de celui observé sur des films plus épais ou des échantillons de plomb bulk dans lesquels des structures dispersées de MnPc ne sont pas observées.

3.2 Motif de moiré dans les tricouches de plomb sur Si(111): contribution structurelle

L'origine structurelle du motif de moiré dans les tricouches continues de plomb sur Si(111) d'un point de vue structurel a été traitée au moyen d'un modèle géométrique reliant le paramètre de maille deu moiré $L(\Theta)$ et son orientation $\Phi(\Theta)$ à l'angle de rotation Θ entre Pb(111) et Si(111) à l'interface Pb/Si(111) (voir Fig. 13 pour comprendre la notation adoptée). Ce modèle repose sur des considérations géométriques concernant la commensurabilité du film de plomb sur Si(111) c'est-à-dire la correspondence de certains atomes du film et du substrat lorsqu'ils sont orientés arbitrairement l'un par rapport à l'autre. Selon cela, un motif de moiré peut être considéré comme un battement des deux réseaux atomiques et une fréquence de battement spatiale peut être attribuée à la différence des deux vecteurs de réseau réciproque: $\mathbf{G}_{moiré} = \mathbf{k}_{Pb} - \mathbf{k}_{Si}$. En outre, différentes conditions de coïncidence, c'est-à-dire différentes fréquences de battement spatiales, peuvent se produire lorsque différents angles de rotation Θ sont pris en compte. Chacune de ces fréquences conduit alors à la formation de différents motifs de moiré. L'analyse de toutes ces fréquences spatiales de battement (par exemple de premier ordre, deuxième ordre, etc.) en termes d'angle de rotation Θ permet au modèle de prédire le paramètre de maille L du moiré et son orientation Φ en fonction de Θ. Comme ce modèle ne repose que sur des aspects géométriques, il néglige les potentiels d'interaction réels entre les réseaux atomiques et donc la vraie structure électronique et la physique réelle du système. Cependant, il a été en mesure de fournir des informations intéressantes sur la structure interne des films de tricouches de Pb sur Si(111).

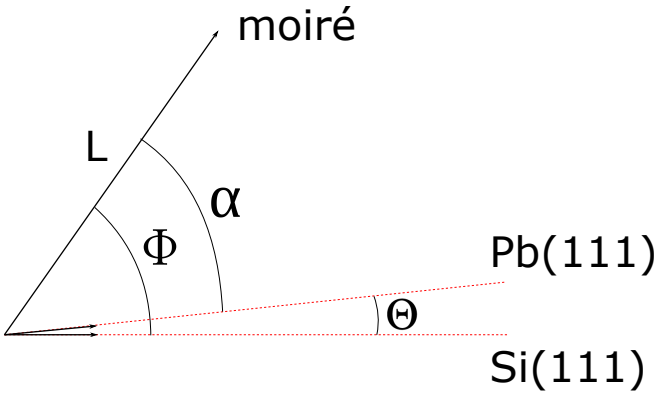

Fig. 13 Croquis des quantités impliquées dans le modèle de moiré. L représente le paramètre de maille du motif de moiré et Φ (α) son orientation par rapport au Si(111) (Pb(111)). Θ représente l'angle de rotation entre le Pb(111) et le Si(111).

En comparant le paramètre de maille du moiré L expérimentalement mesuré à partir d'images STM avec les prédictions du modèle décrit ci-dessus, j'ai pu déduire que l'aspect différent des deux motifs de moiré occupant différentes terrasses ("protubérances" ou "trous") reflètent une structure interne différente du film Pb. En particulier, le moiré à "protubérances" dans la Fig. 24 peut être décrit comme un moiré de premier ordre ne comportant que de petites rotations du film de plomb par rapport au substrat de Si(111), c'est-à-dire moins de 5°. De plus, on pense que les atomes de Pb dans le film sont proches des positions du Pb(111) bulk (a_{Pb}=3,5 Å). D'autre part, j'ai proposé que le moiré à "trous" de la Fig. 15 soit compatible

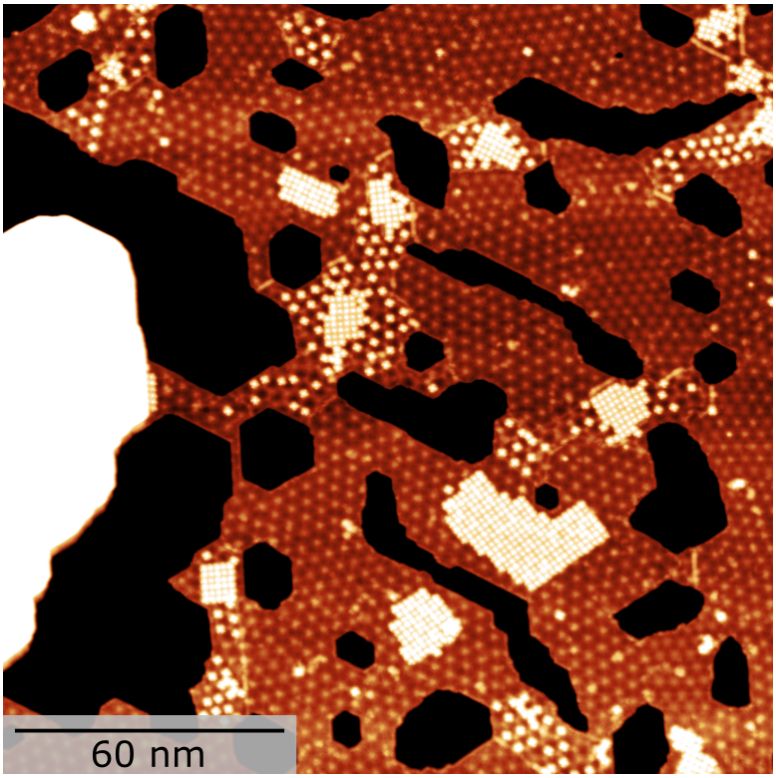

Fig. 14 Image STM d'une terrasse avec une tricouche quasi-continue de plomb sur Si(111) présentant un motif de moiré à "protubérances". Les régions claires sur le film de plomb sont des îlots auto-assemblées de MnPcs. Taille de l'image: 170×170 nm^2, V_T: 0.3 V et I_T: 40 pA.

avec un moiré du second ordre impliquant une rotation de 30° du film de Pb par rapport au substrat de Si(111). Dans ce cas, le modèle décrit mieux les résultats expérimentaux si l'on suppose que les atomes de Pb sont légèrement compressés par rapport aux positions du Pb(111) bulk (c'est-à-dire que a_{Pb}=3,46 Å).

À notre connaissance, il n'existe qu'une étude rapportant des tricouches continues de plomb sur Si(111) avec des terrasses présentant une structure interne différente et ainsi de suite un

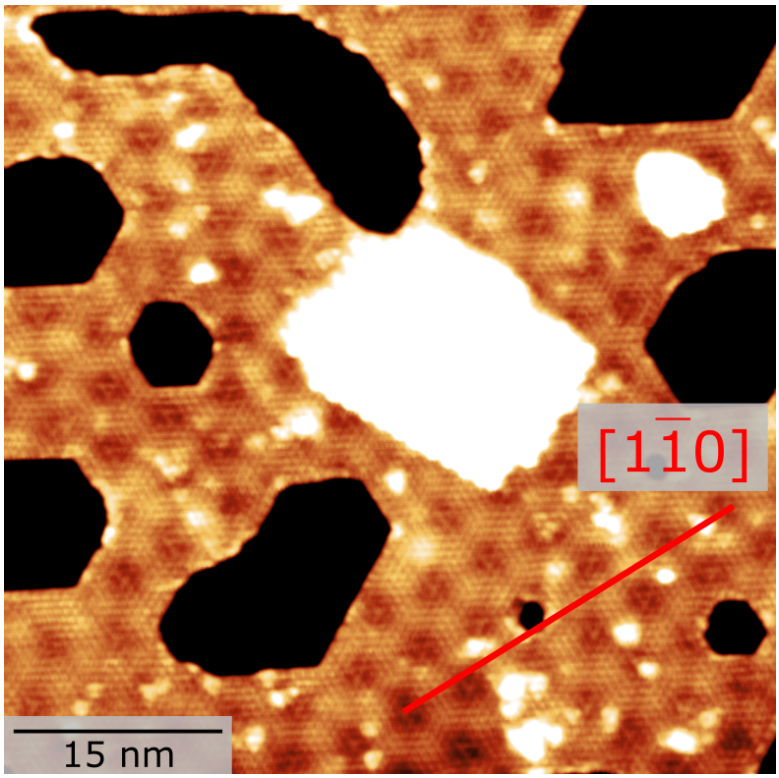

Fig. 15 Image STM d'une terrasse avec une tricouche quasi-continue de plomb sur Si(111) présentant un motif de moiré à "trous". Les régions claires sur le film de plomb correspondent à des auto-assemblages de MnPcs. La direction [1$\bar{1}$0] du Si(111) est indiquée dans la même figure. Taille de l'image: $55 \times 55\ nm^2$, V_T: -1 V et I_T : 40 pA.

motif de moiré différent. Dans toutes les autres études, des échantillons discontinus avec des îlots de plomb déconnectés sont rapportés et un seul type de moiré est observé, c'est à dire celui qui tourne légèrement par rapport au Si(111) avec les atomes de plomb proches des positions du Pb (111) bulk. Pour cette raison, j'ai proposé que, pour des couvertures faibles de plomb, les îlots déconnectées ne présentent qu'un seul type de structure. D'autre part, pour des couvertures elevées, lorsqu'un film continu de plomb est formé, le système se divise en deux phases occupant des terrasses différentes. Le premier type de terrasse a une structure similaire à celle observée pour les îlots déconnectées. Plus intéressant, le second type de terrasse révèle une nouvelle structure constituée de films de plomb tournés fortement (30°) par rapport au substrat de silicium. De plus, j'ai proposé que les atomes de Pb dans cette nouvelle structure soient légèrement compressés par rapport au Pb(111) avec un paramètre de maille de $a_{Pb} \sim 3.46$ Å.

3.3 Motifs de moiré dans les tricouches de plomb sur Si(111): contribution électronique

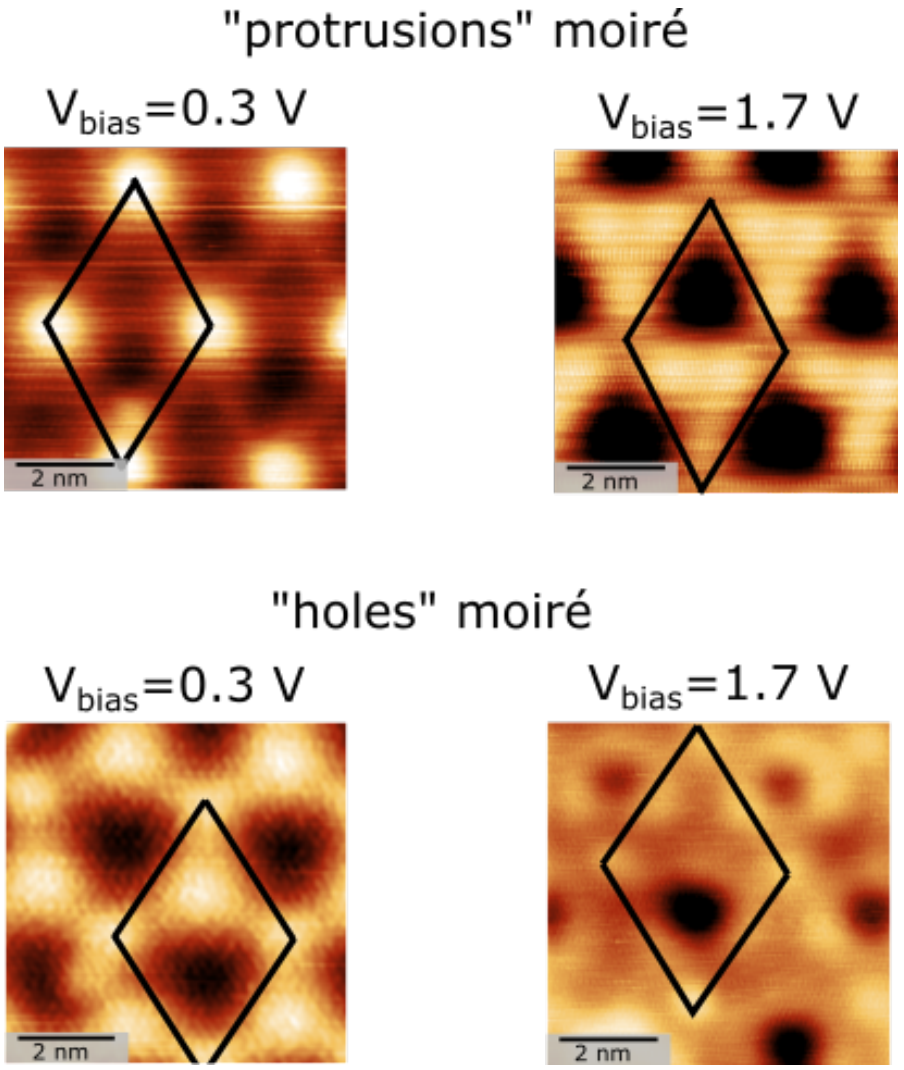

Fig. 16 Images STM d'îlots de tricouches de plomb présentant un motif de moiré à "protubérances" (En haut) et à "trous" (En bas) mesurées avec des tensions de polarisation différentes. (En haut à gauche): Taille de l'image: $6.9 \times 6.9\ nm^2$, V_T: +0.3 V et I_T : 50 pA. (En haut à droite): Taille de l'image: $6.9 \times 6.9\ nm^2$, V_T: +1.7 V et I_T : 50 pA. (En bas à gauche): Taille de l'image: $6.9 \times 6.9\ nm^2$, V_T: +0.3 V et I_T : 100 pA. (En bas à droite): Taille de l'image: $6.9 \times 6.9\ nm^2$, V_T: +1.7 V et I_T : 50 pA.

Avant d'aller plus loin, il est important de noter que l'apparition des moiré à "protubérances" et à "trous" montrés dans les figures 17b et 18b diffèrent fortement de celle montré dans les figures 10a 10b. Fig. 16 compare directement les images STM des deux types de moiré acquis à différentes tensions de polarisation V_{bias}. Pour les deux types d'îlots, V_{bias}=1.7 V est proche

de l'énergie d'un état de puits quantique QWS (voir les figures 17a et 18a). Ce fait indique que l'apparition des images STM à cette tension inclut la contribution électronique du QWS lui-même. Ceci est lié au fait que la quantité réellement mesurée dans les images STM est la densité d'états intégrée (IDOS). En d'autres termes, pour une tension de polarisation donnée V_{bias}, les états électroniques contribuant au courant tunnel sont ceux compris entre E_F et $E_F + eV_{bias}$. Si la tension de polarisation atteint la position d'un QWS, ce dernier contribuera à l'image STM proportionnellement à son intensité. En conséquence, si la contribution électronique est suffisamment forte, l'image STM résultante montrera une topographie très différente de celle de la surface réelle. En ce sens, les images STM sont toujours une convolution de la vrai topographie d'une surface et de sa structure électronique. C'est pour la même raison que les images STM prises à très basse tension sont considérées comme représentant la topographie réelle d'une surface, car dans ce cas, la contribution électronique due à l'IDOS peut généralement être négligée. En accord avec ce fait, on peut considérer que les images de Fig. 16, acquises à basse tension (V_{bias}=0.3 V), montrent quelque chose qui est très proche de la vraie structure de surface. Ceci est également corroboré par les spectres de Fig.17 et Fig.18 qui montrent qu'à proximité de 0,3 mV la densité d'états est suffisamment basse pour négliger la contribution électronique dans les images STM.

Les expériences de spectroscopie à effet tunnel (1.2 K) sur des îlots de tricouche de plomb présentant des motifs de moiré à "protubérances" et à "trous" ont révélé que les positions énergétiques des états de puits quantiques (QWS) sont modulées spatialement par le motif de moiré lui-même (voir Fig. 17 et Fig. 18). Cet effet est surprenant car en considérant des électrons confinés dans un film métallique d'une certaine épaisseur, les QWS sont supposés avoir des énergies définies tout comme dans le cas d'une particule confinée dans une boîte quantique. Dans le cas du film métallique la largeur du puits quantique est définie par l'épaisseur du film lui-même. Il est intéressant de noter que la modulation spatiale des énergies QWS dans les tricouches de plomb peut être associée à une relaxation atomique perpendiculaire à l'interface Pb/Si(111) qui modifie localement la largeur du puits quantique et donc les énergies des QWS. En comparant nos cartes conductance différentielle aux calculs disponibles dans la littérature, nous avons pu confirmer la forte corrélation entre les électrons confinés et la structure interne des îlots de plomb. Cette corrélation est corroborée par la modulation différente des états de puits quantiques observée sur des îlots présentant des motifs de moiré différents (à "protubérances" dans la figure 17 et à "trous" dans la figure 18). Cette différence peut être comprise en considérant que ces deux types d'îlots sont caractérisés par une structure différente à l'interface Pb/Si(111) induisant des modifications locales de la largeur du puits quantique différentes. Ces résultats, ainsi que ceux de la section précédente,

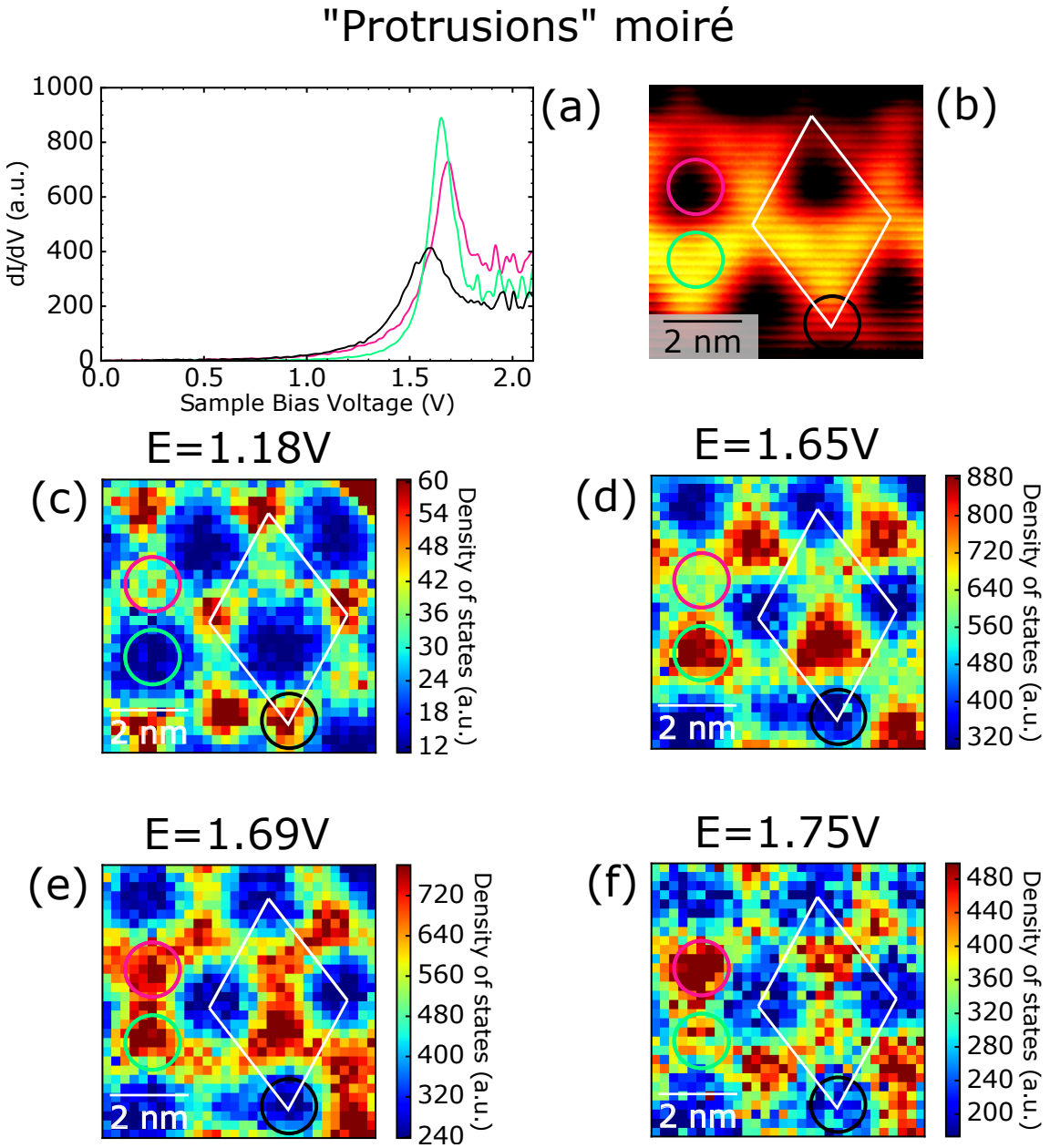

Fig. 17 (a): Spectres STS locaux acquis sur sur un îlot de plomb (tricouche) qui montre un motif de moiré à "protubérances". (b): Image STM prise pendant les expériences STS et représentant la région de l'îlot mesurée. Taille de l'image: $6.9 \times 6.9\ nm^2$, V_T: +1.7 V et I_T : 50 pA. Les couleurs des cercles correspondent à celles des spectres dans l'image (a) et chaque spectre a été tracé en effectuant une moyenne sur tous les spectres contenus dans le cercle correspondant. (c)-(f): Cartes de conductance différentielle 2D mesurées à différentes énergies sur la région représentée en (b). La cellule unitaire du motif moiré est indiquée par un parallélogramme blanc.

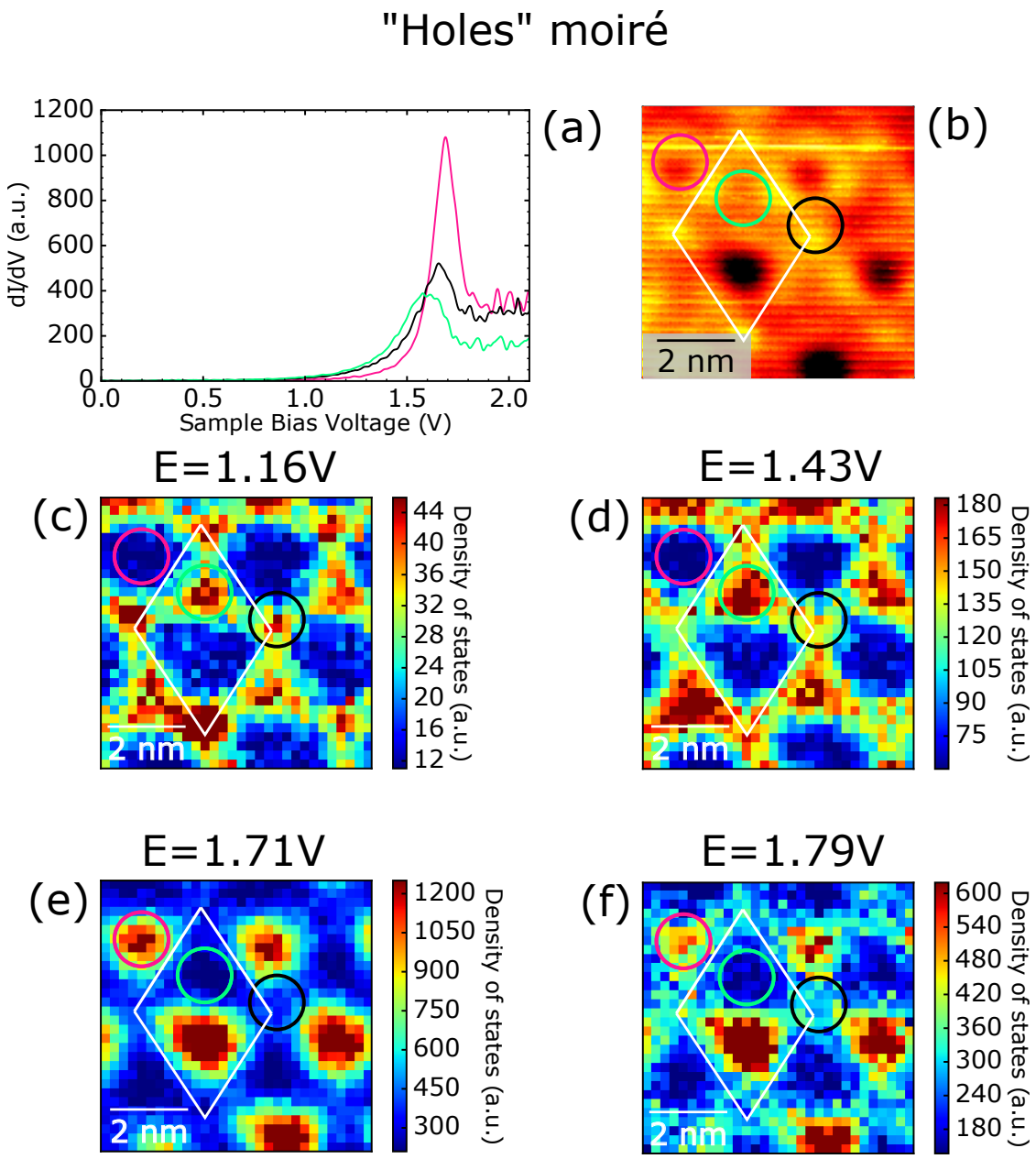

Fig. 18 (a): Spectres STS locaux acquis sur sur un îlot de plomb (tricouche) qui montre un motif de moiré à "trous". (b): Image STM prise pendant les expériences STS et représentant la région de l'îlot mesurée. Taille de l'image: $6.9 \times 6.9\ nm^2$, V_T: +1.7 V et I_T : 50 pA. Les couleurs des cercles correspondent à celles des spectres dans l'image (a) et chaque spectre a été tracé en effectuant une moyenne sur tous les spectres contenus dans le cercle correspondant (c)-(f): Cartes de conductance différentielle 2D mesurées à différentes énergies sur la région représentée en (b). La cellule unitaire du motif moiré est indiquée par un parallélogramme blanc.

confirment que les motifs de moiré dans les tricouches de plomb sur Si(111) sont le résultat d'une interaction complexe entre les effets électroniques et structurels. Pour cette raison, un modèle théorique raffiné incluant toute la physique (substrat, séquence d'empilement, effets de relaxation, couplage spin-orbite, etc.), est hautement souhaitable pour mieux comprendre la relation complexe entre l'électronique et la structure dans ce système.

4 Supraconductivité des tricouches de plomb sur Si(111)

Les expériences STS effectuées à 300 mK sur plusieurs îlots de Pb (tricouches) dans l'état supraconducteur ont montré que le gap supraconducteur n'est pas affecté par les différences de structure interne (séquence d'empilement ou rotations par rapport au substrat de silicium) existant entre îlots avec différents motifs de moiré (voir Fig. 19).

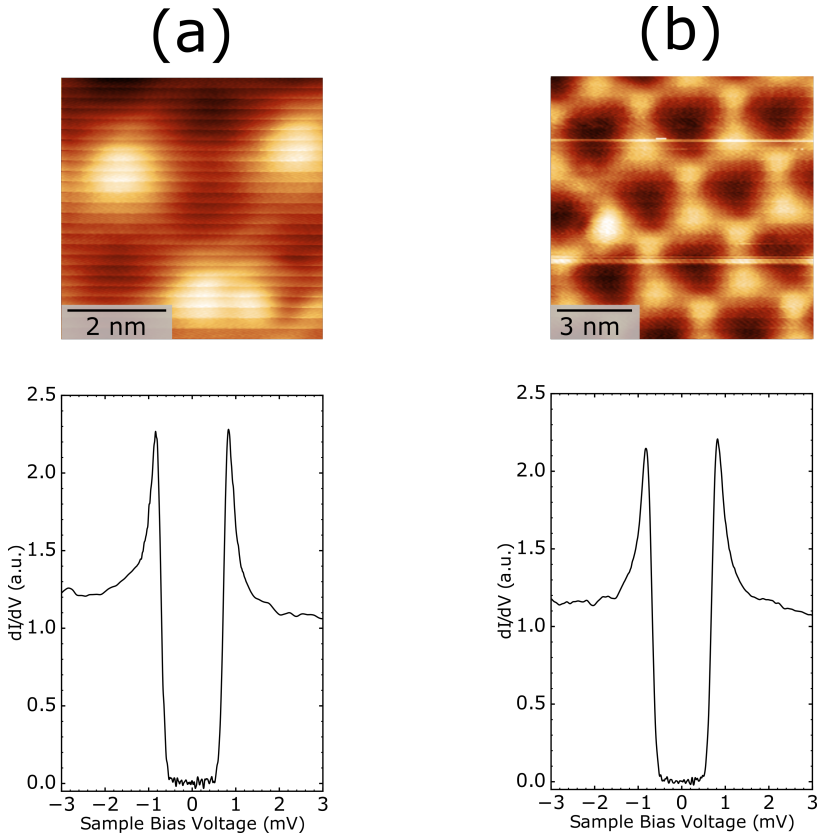

Fig. 19 En haut de (a) et (b): Images STM montrant îlots de tricouches de plomb sur Si(111) présentant un motif de moiré à "protubérances" et à "trous" respectivement. (a) Taille de l'image: $5.3 \times 5.4\ nm^2$, V_T: +50 mV et I_T: 40 pA. (b) Taille de l'image: $10.4 \times 10.4\ nm^2$, V_T: +50 mV et I_T: 40 pA. En bas de (a) et (b): Spectres STS moyennés sur toute la région topographique indiquée dans la partie supérieure de l'image correspondante ($V_{set\,point} = 8\ mV, I_{set\,point} = 200\ pA$).

D'autre part, nous avons constaté que le motif de moiré peut affecter les amplitudes de pic de cohérence sur une longueur d'échelle beaucoup plus petite que la longueur de cohérence supraconductrice du système: le paramètre de maille du moiré est de l'ordre de 2-4 nm (voir Fig. 20) alors que la longueur de cohérence des tricouches de plomb est autour de 30 nm. En particulier, le pic de cohérence à énergie négative a une amplitude de 2,49 a.u. pour le spectre noir et de 2,28 a.u. pour le rose (voir Fig. 20). Cela signifie que la modulation d'amplitude des pics est réellement très faible, c'est-à-dire inférieure à 10 %.
Ce résultat est très intéressant car les amplitudes de pic de cohérence ne devraient pas être affectées à des échelles de longueur inférieures à la longueur de cohérence supraconductrice. Un comportement similaire des pics de cohérence a été précédemment observé dans le cas d'une monocouche de Pb epitaxiée sur du Si(111). Dans ce cas également, les fluctuations se produisent sur une échelle de longueur beaucoup plus petite que la longueur de cohérence de la monocouche de plomb. L'origine de ces fluctuations n'est pas encore bien comprises, mais on pense qu'elles sont liées aux fluctuations à courte portée de la constante de couplage électron-phonon, allant au-delà de la théorie du désordre sur les systèmes diffusifs qui médie généralement les variations sur de courtes distances.
Partant de cette interprétation, nous pensons que les modulations spatiales des amplitudes des pics de cohérence montrées dans la Fig. 20 ont la même origine. L'aspect intéressant dans notre cas est que nous pouvons relier les modulations spectroscopiques à une caractéristique directement observable dans les images topographiques de la surface, c'est-à-dire le motif de moiré. Ce comportement réside probablement dans le fait que les déformations structurelles sous-jacentes au moiré agissent comme un potentiel périodique de désordre affectant le couplage électron-phonon de manière à son tour périodique et donc la cohérence de l'état supraconducteur sur une échelle de longueur beaucoup plus courte que la longueur de cohérence du système. Jusqu'ici, les fluctuations des amplitudes des pics de cohérence n'ont été observées que dans des systèmes purement 2D (par exemple dans la monocouche de Pb epitaxiée sur du Si(111)). Le fait que dans les tricouches de plomb l'effet soit beaucoup plus faible que ce que l'on observe dans les systèmes 2D suggère qu'ils ne sont pas purement 2D mais restent dans un régime quasi-2D. Ce résultat intrigant confirme la présence d'une physique de basse dimensionnalité dans les tricouches de plomb sur Si(111).

La résolution énergétique améliorée par l'utilisation de pointes supraconductrices couvertes de plomb a permis de détecter pour la première fois la présence de supraconductivité à caractère multibande dans des îlots tricouches de plomb ainsi que dans des îlots 5 couches. La signature expérimentale de la supraconductivité multibande est donnée par les petits pics indiqués par les flèches rouges dans les figures 21 et 22. En raison des effets de taille

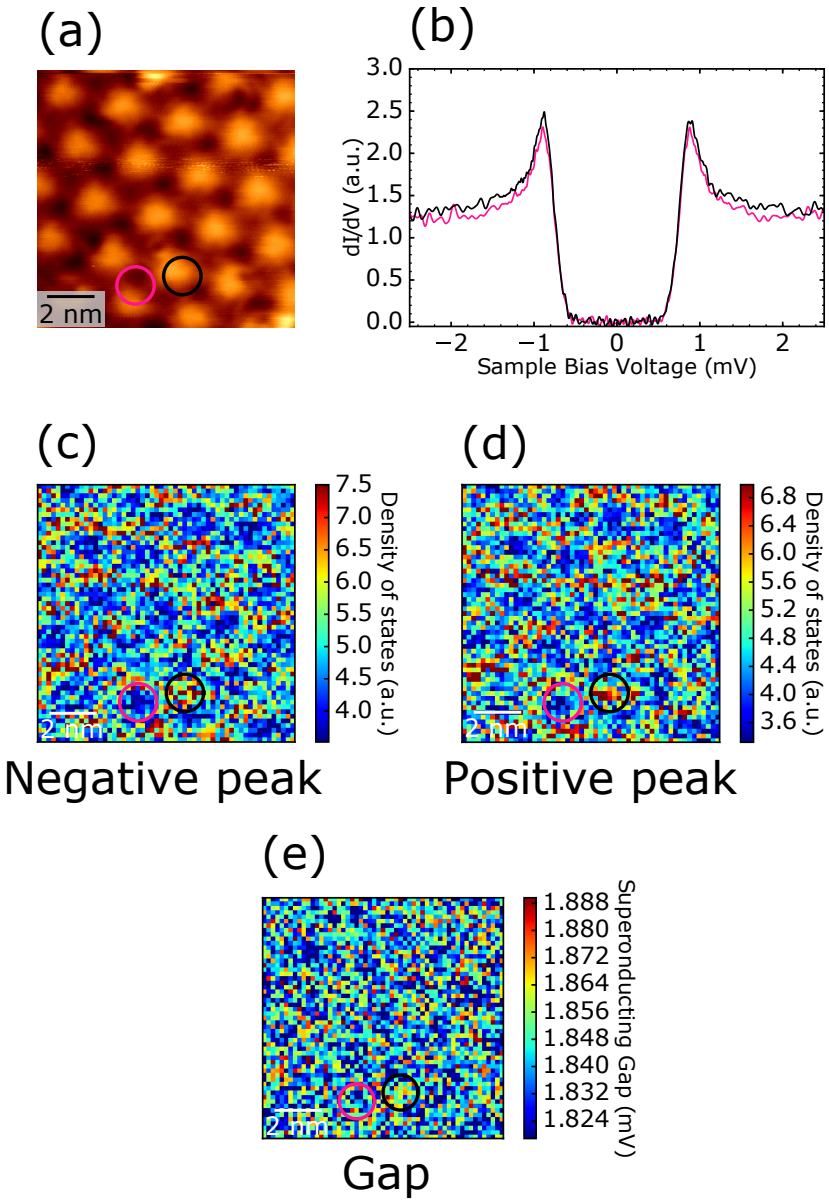

Fig. 20 (a): Image STM montrant un îlot de tricouches de plom sur Si(111) présentant un motif de moiré à courte period. (a) Taille de l'image: 10.8×10.9 nm^2, V_T: +50 mV et I_T: 30 pA. (b): Deux spectres STS locaux moyennés dans la zone à l'intérieur des cercles dessinés en (a) de la couleur correspondante ($V_{set\,point}$=8 mV, $I_{set\,point}$=200 pA). Le pic de cohérence à énergie négative a une amplitude de 2.49 a.u. pour le spectre noir et de 2.28 a.u. pour le rose. Cela signifie que la modulation de l'amplitude est très petite, c'est-à-dire inférieure à 10 %. (c) and (d): Cartes de conductance différentielle 2D mesurées aux énergies des pics de cohérence et révélant les fluctuations spatiales liées au motif de moiré. (e): Carte 2D représentant la distribution spatiale de la distance en énergie entre les deux pics de cohérence (2Δ) sur la région balayée.

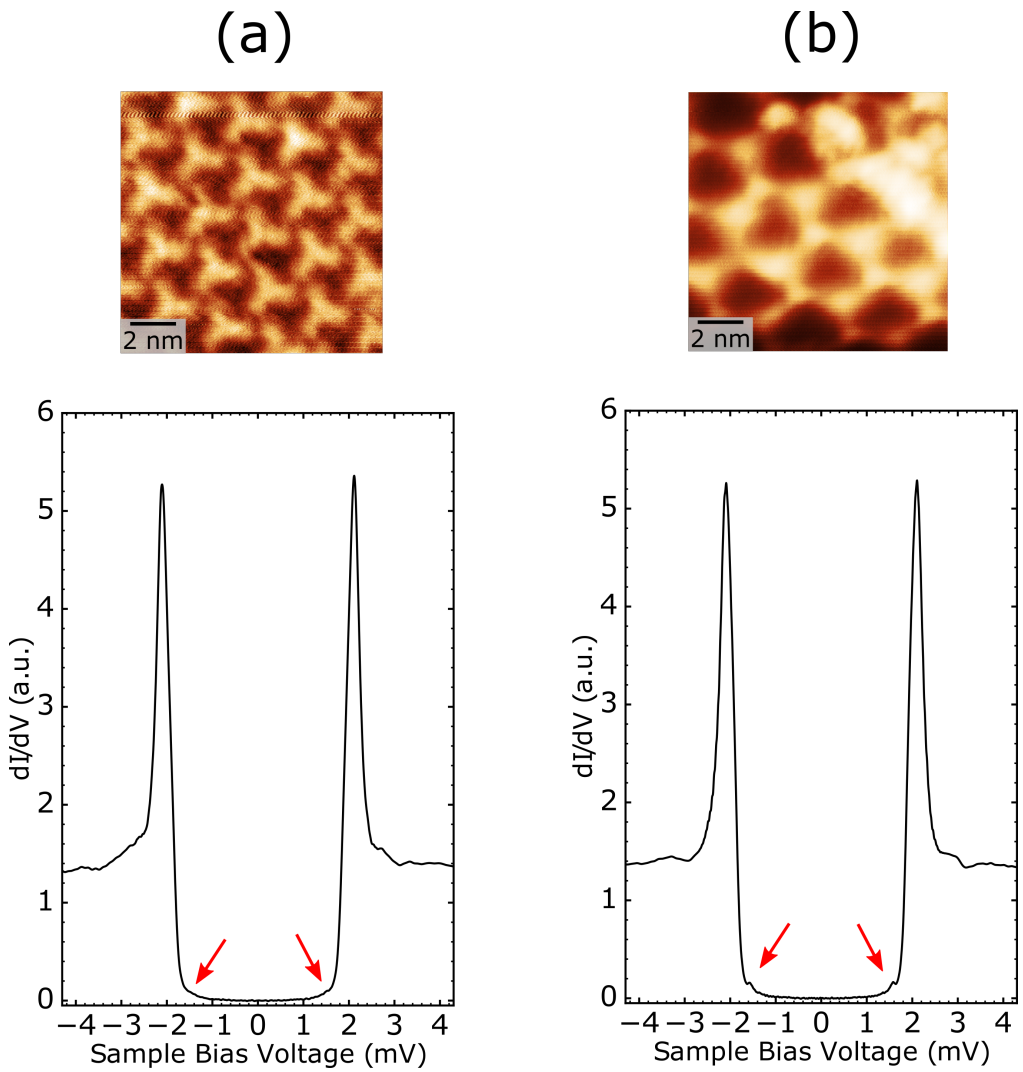

Fig. 21 En haut de (a) et (b): Images STM montrant des îlots de tricouches de plomb sur Si(111) avec un motif de moiré à courte periode ("protubérances" et "trous" respectivement). (a) Taille de l'image: $11.2 \times 11.2\ nm^2$, V_T: +10 mV et I_T: 50 pA. (b) Taille de l'image: $11.1 \times 11.1\ nm^2$, V_T: +10 mV et I_T: 50 pA. En bas de (a) et (b): Spectres STS moyennés sur toute la région topographique montrée dans la partie supérieure de l'image ($V_{set\,point}$=8 mV, $I_{set\,point}$=200 pA). Les flèches rouges indiquent deux petits pics liés au caractère multibande des îlots eux-mêmes.

quantique, on ne prévoit que 2 (3) sous-bandes traversant le niveau de Fermi dans les îlots de plomb de 3 (5) couches. La participation de ces sous-bandes à la supraconductivité conduit à l'apparition de deux (trois) gap superconducteurs. Des études précédentes sur des monocristaux de plomb ont montré que l'amplitude relative de pics liés aux différents gap dépend de l'orientation de la surface ainsi que de la structure électronique et des propriétés de tunnel sélectif à travers les différentes sous-bandes. Ces arguments pourraient être utilisés

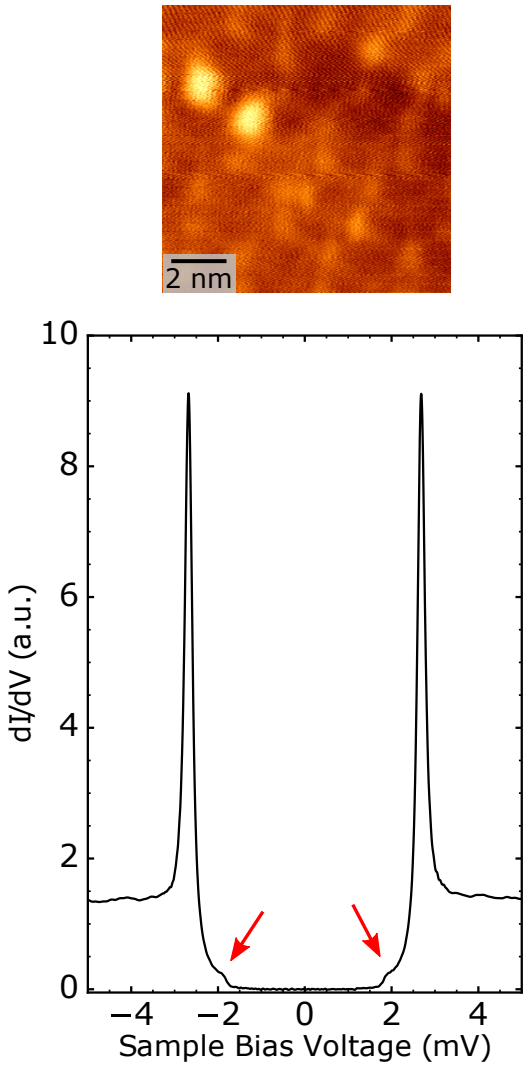

Fig. 22 En haut: Image STM montrant un îlot de plomb (5 monocouches) sur Si (111). Taille de l'image: $10.4 \times 10.4\ nm^2$, V_T: +0.20 mV et I_T: 50 pA. En bas: Spectres STS moyennés sur toute la région topographique respective montrée dans la partie supérieure de l'image ($V_{set\,point}$=8 mV, $I_{set\,point}$=200 pA). Les flèches rouges indiquent les caractéristiques spectroscopiques liées au caractère multi-bandes de l'îlot lui-même.

pour expliquer la forme des spectres montrés dans les figures 21a et 21b présentent un gap très prononcé et un deuxième gap beaucoup plus faible (indiqué par les flèches rouges). Dans la figure 22 un seul un grand gap est visible. La caractéristique spectrale (indiquée par les flèches rouges) que nous associons au caractère multi-bande n'apparaît pas comme un pic ou un ensemble de pics. Nous attribuons ce comportement à des effets de tunnel sélectif qui réduisent l'intensité des deux petits pics et qui ne peuvent donc pas être résolus sous forme de pics séparés.

5 Etats de Shiba induit par de MnPcs isolées déposées sur de tricouches de Pb/Si(111)

La caractérisation de l'interaction entre le magnétisme moléculaire de MnPcs et la supraconductivité de tricouhes de Pb/Si(111) à travers d'expériences STS (300 mK) a été rendue difficile par la mesure des spectres eux-mêmes qui provoque l'excitation de certaines modes de vibration moléculaires entraînant un déplacement des molécules au cours des expériences (voir Fig. 23a et Fig. 23b). Malgré ce problème, j'ai pu extraire des informations intéressantes dans le cas de molécules isolées. Fig. 23c et Fig. 23d montrent que l'interaction locale entre les MnPcs et la tricouche de plomb conduit à l'émergence d'états de Shiba dans le gap supraconducteur. De plus, la comparaison des spectres mesurés sur la même MnPc se trouvant dans deux sites d'adsorption différents révèle que l'énergie des états de Shiba est différente dans les deux cas. Comme l'énergie des états de Shiba dépend de la force du couplage d'échange J, les spectres de Fig. 23c nous indiquent que la force du couplage magnétique entre les MnPcs et la tricouche de plomb est modulée par le site d'adsorption. Les cartes de conductance différentielle de Fig. 23d corroborent la présence de deux états de Shiba distincts associés aux deux configurations d'adsorption de la molécule. Une dépendance similaire du couplage d'échange par le site d'adsorption a déjà été rapportée pour les mêmes molécules déposées sur des substrats de Pb plus épais ou bulk.

Fait intéressant et contrairement à ce qui a été observé sur des substrats de Plomb bulk, les états de Shiba induits par des MnPcs isolés sur les îlots tricouches de Pb/Si(111) s'étendent sur toute la molécule y compris les ligands avec une plus grande amplitude située sur l'atome magnétique de la molécule (l'atome de manganèse). Au contraire, dans le cas de substrats de plomb bulk, les états de Shiba induits par les MnPc sont localisés uniquement sur l'atome magnétique de la molécule. Un autre aspect intéressant des états de Shiba induits par des MnPcs isolés sur les tricouches de Pb/Si(111) est qu'ils se trouvent toujours près du bord du gap et avec la même asymétrie, c'est-à-dire que l'amplitude du pic à énergie négative est toujours supérieure à celle du pic à énergie positive. Ce fait suggère que la force du couplage entre les MnPcs et les îlots tricouches de plomb tombe toujours dans le même régime. Partant de nos résultats expérimentaux et de considérations simples sur le système, j'ai proposé que les MnPc sont couplées de manière antiferromagnétique au plomb, soit $J < 0$, et qu'une charge positive soit uniformément répartie sur la molécule à la suite d'un transfert de charge de MnPcs à la surface de plomb, c'est-à-dire $K < 0$. Cette condition m'a permis de déduire, en accord avec nos observations expérimentales, que les MnPcs situés sur des îlots tricouches de Pb sont toujours faiblement couplés. Ce type de résultat n'a pas été signalé auparavant

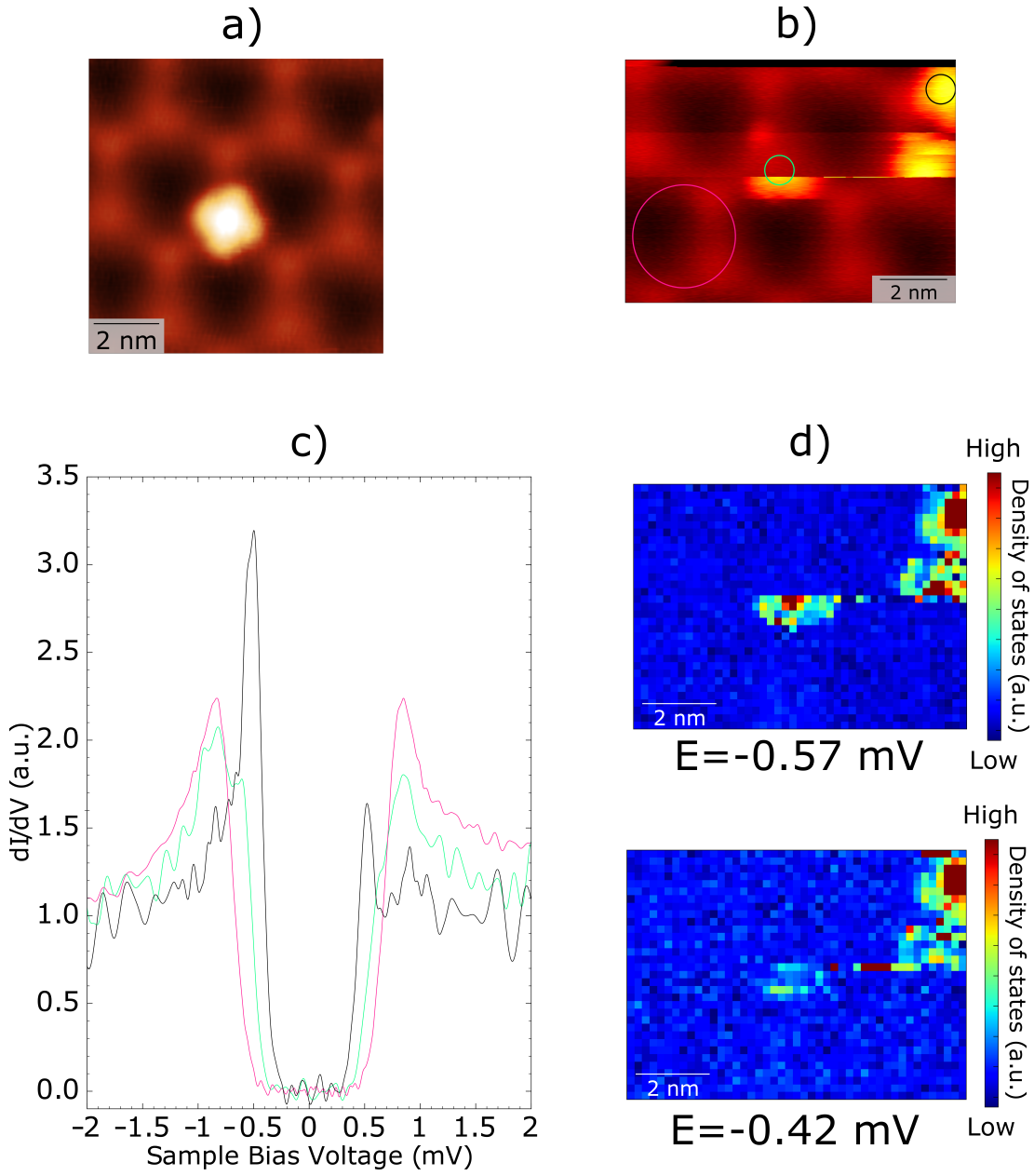

Fig. 23 Interaction magnétique entre une MnPc isolée et un îlot tricouche de plomb sur Si(111) présentant un motif de moiré à "trous". (a): Image topographique STM prise avant l'expérience STS. Taille de l'image: $9 \times 9\ nm^2$, V_T: +0.25 V et I_T : 100 pA. (b): Image topographique STM prise pendant l'expérience STS (Taille de l'image: $9 \times 6.5\ nm^2$). (c) Spectres dI/dV locaux mesurés dans les régions identifiées par les cercles de la couleur correspondante. (d): Cartes de conductance différentielle 2D mesuréees à -0,57 mV et -0,42 mV sur la région indiquée en (b).

dans des systèmes similaires et, pour cette raison, des investigations supplémentaires sont

nécessaires. En particulier, des calculs théoriques tenant compte de la physique impliquée dans notre système sont nécessaires pour confirmer le régime de couplage faible proposé.

6 Couplage entre états de Shiba induit par des îlots 2D de MnPcs auto-organisées sur des tricouches de Pb/Si(111)

Les expériences STS, réalisées à 300 mK, sur des domaines 2D de MnPcs auto-organisées sur des tricouches de Pb/(111) ont permis d'obtenir des informations sur le couplage entre les états de Shiba induit par différents MnPcs. En particulier, le domaine moléculaire étudié dans ces expériences est indiqué dans la Fig. 24 et se trouve sur une terrasse de Pb présentant un motif de moiré à "protubérances".

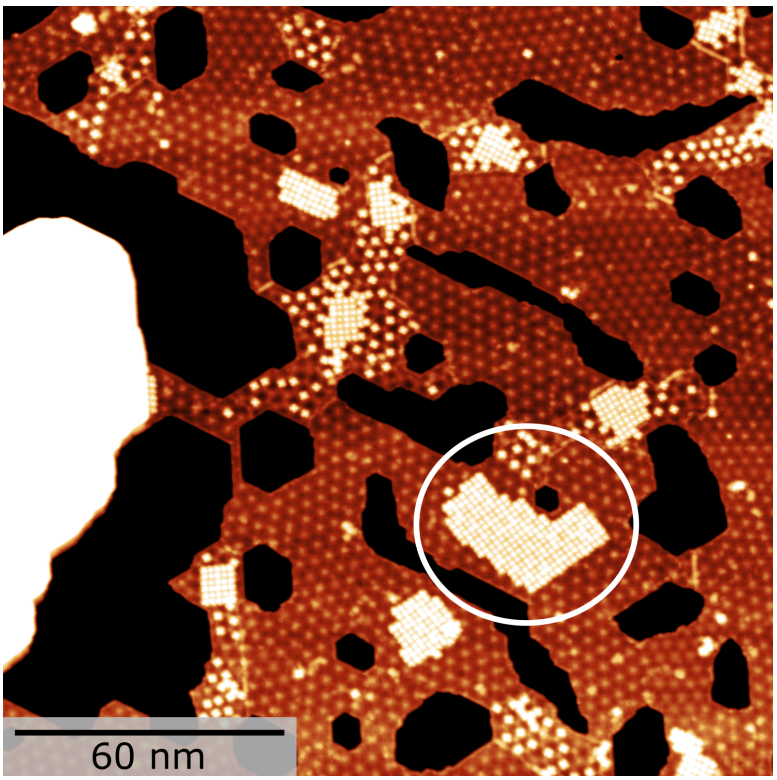

Fig. 24 Image STM d'une terrasse avec une tricouche quasi-continue de Pb/Si(111) présentant un motif de moiré à "protubérances". Les régions claires situées sur le film de plomb sont des îlots auto-assemblées de MnPcs. Taille de l'image: 170×170 nm^2, V_T: 0.3 V et I_T: 40 pA. Le cercle blanc indique l'îlot de MnPcs mesuré dans nos expériences STS.

Les résultats les plus importants de ces expériences sont illustrés dans la Fig. 25. En particulier, la Fig. 25a montre une image STM prise juste avant l'expérience STS et présent un

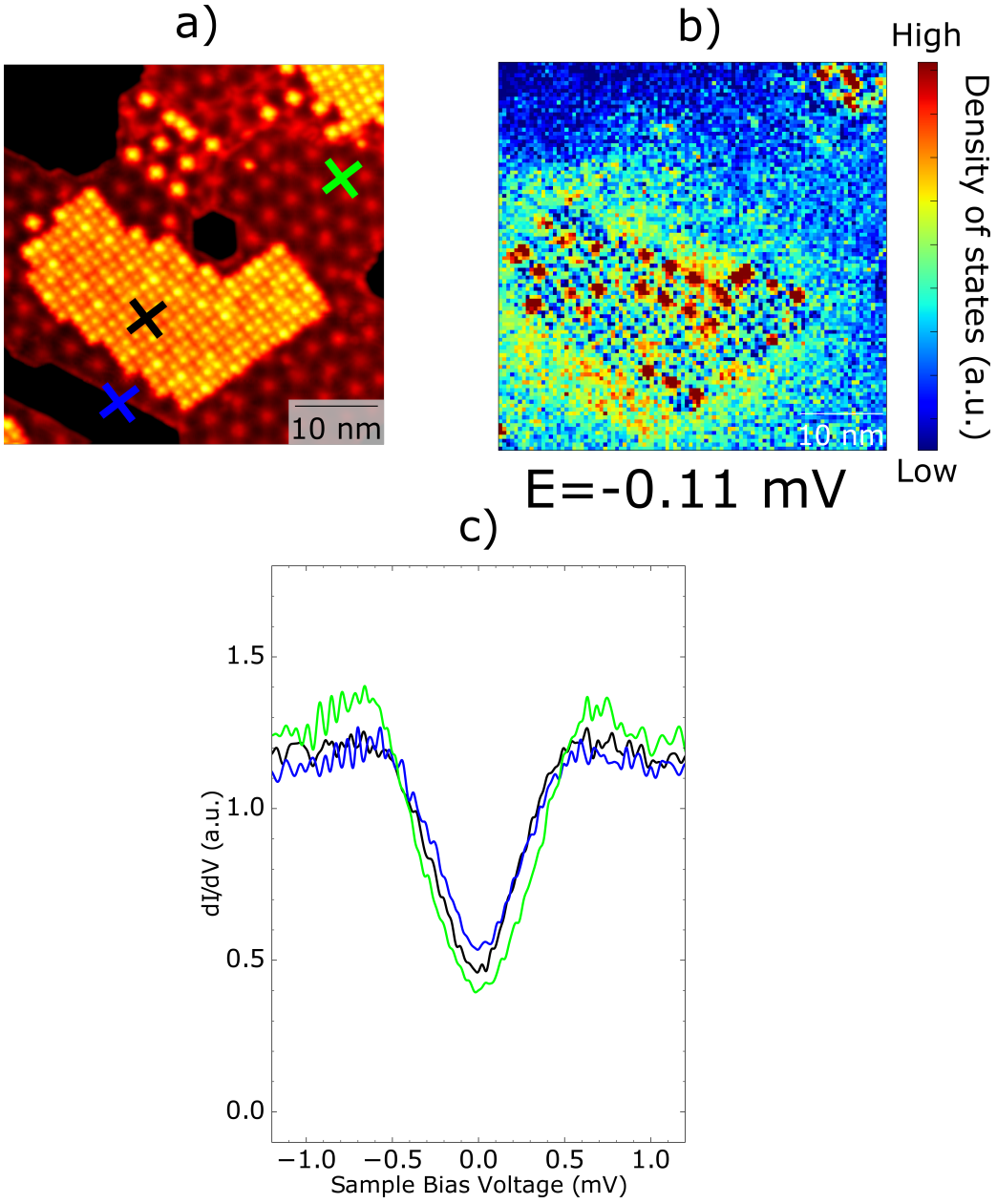

Fig. 25 Interaction magnétique entre un auto-assemblage 2D de MnPcs sur une tricouche quasi-continue de Pb/Si(111) présentant un motif de moiré à "protubérances". (a): Image STM topographique prise avant l'expérience STS. Taille de l'image: $45.7 \times 45.7\ nm^2$, V_T: -0.05 V et I_T : 20 pA. (b): Carte de conductance différentielle 2D mesurée à -0,11 mV sur la région montrée en (a). (c): Spectres locaux dI/dV mesurés en correspondance des régions identifiées par les croix de la couleur correspondante en (a). Les expériences ont été réalisées à 300 mK.

îlot 2D auto-assemblé de MnPcs. La Fig. 25b montre une carte de conductance différentielle mesurée à -0.11 mV, c'est-à-dire à l'intérieur du gap supraconducteur, sur la même région

que celle illustrée dans la Fig. 25a. Loin du domaine moléculaire, la densité d'états dans le gap supraconducteur associée au film de plomb est remplie d'états de quasi-particule. Cela est probablement dû au fait que la concentration élevée de molécules magnétiques sur l'échantillon affecte la supraconductivité du système non seulement à proximité des molécules (voir Fig. 24 pour avoir une idée de la concentration moléculaire sur l'échantillon). De la même manière, à l'intérieur du domaine moléculaire on peut trouver des régions assez uniformes avec une densité d'états finie dans le gap supraconducteur indiquant la présence d'états de quasi-particule (régions blue). L'aspect le plus intéressant de cette image est la présence d'une signature spectroscopique "de bord" liée au domaine moléculaire qui définit son contour. Il est remarquable que cette caractéristique "de bord" ne disperse pas à l'intérieur du domaine moléculaire mais reste confinée à son bord et s'étend loin des molécules elles-mêmes. La figure 25c montre des spectres dI/dV obtenus en faisant la moyenne de tous les spectres dans la région définie par la croix de la couleur correspondant. L'analyse du comportement de ces spectres confirme le scénario décrit ci-dessus. En particulier, le spectre vert a été mesuré loin du domaine moléculaire et représente donc un spectre de référence. La courbe noire mesurée à l'intérieur du domaine ressemble beaucoup au spectre de référence (même si dans ce cas le spectre présente un gap un peu plus rempli). Plus intéressant encore, le spectre bleu montre que en correspondance de la caractéristique "de bord", qui s'étend hors du domaine moléculaire (voir la position de la croix bleue sur la 25a), le gap supraconducteur est plus rempli que celui de la courbe noire (mesurée sur les molécules). Fig. 26 montre plusieurs cartes de conductance différentielle 2D mesurées à différentes énergies révélant l'effet des MnPc sur la supraconductivité du film de Pb. Il ressort clairement de cette figure que la caracteristique de "bord" dispose de sa propre dispersion d'énergie et reste toujours liée au bord du domaine moléculaire.

Partant de ces observations et de celles présentées dans la section précédente à propos des états de Shiba (près du bord du gap en raison du couplage faible) induits par des MnPcs isolés nous pensons que, contrairement à ce qui a été observé sur des substrats de Pb(111) bulk, les MnPcs se s'auto-organisent dans des domaines 2D donnent lieu à des états de Shiba à énergies similaires qui peuvent se coupler en conduisant à la formation de bandes de Shiba. Ce mécanisme serait responsable d'une transition topologique en correspondance du domaine magnétique dont la signature spectroscopique est donnée par l'émergence de la caractéristique "de bord" entourant le domaine moléculaire lui-même. Dans cette situation, la zone mesurée dans la Fig. 25 reste divisée en deux régions différentes: une région topologique située sous le domaine magnétique de MnPcs et une région non topologique correspondant au reste de l'échantillon. En conséquence, les deux régions sont finalement séparés par la caractéristique "de bord".

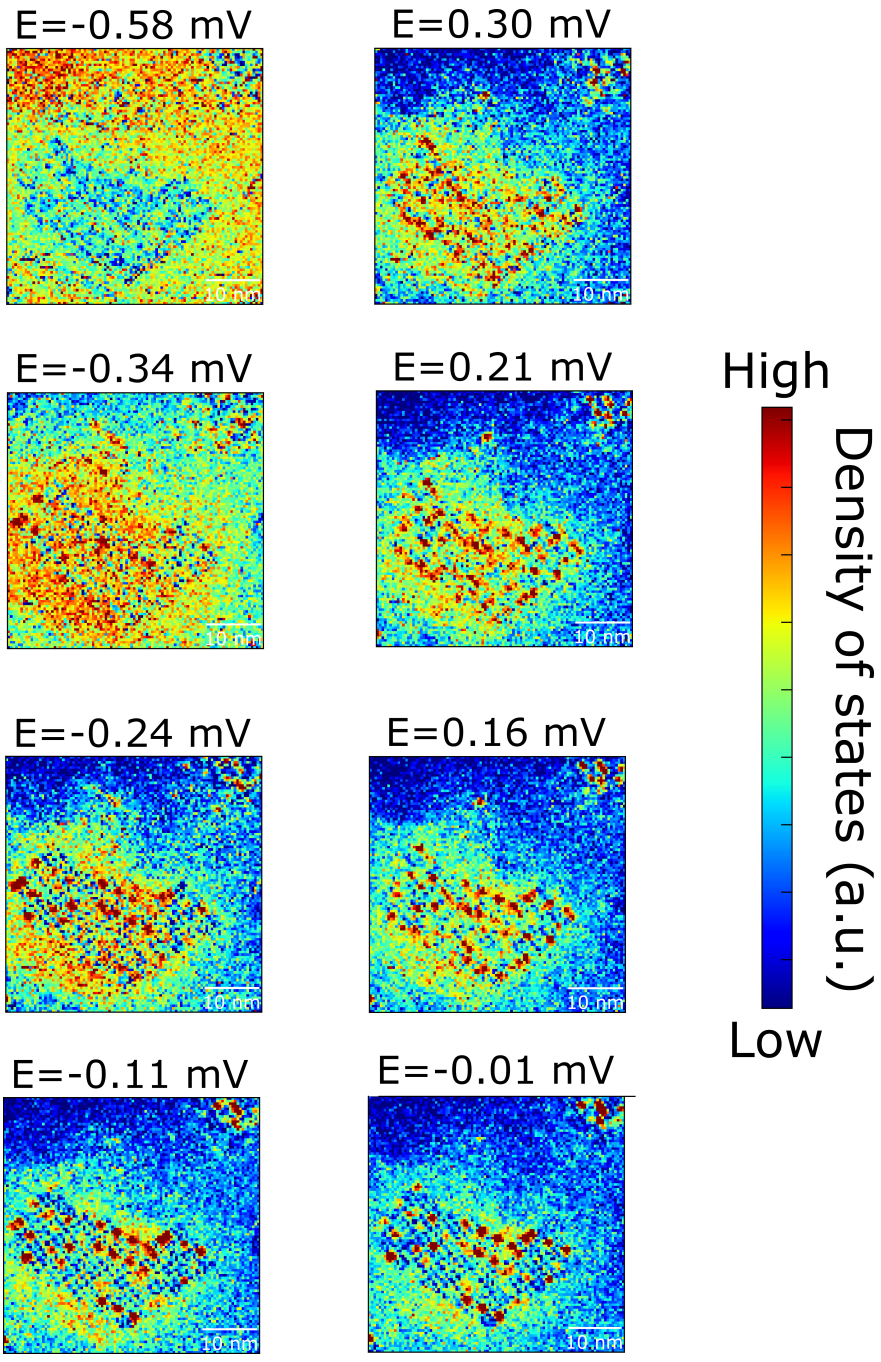

Fig. 26 Interaction magnétique entre un auto-assemblage 2D de MnPcs sur une tricouche quasi-continue de Pb/Si(111) présentant un motif moiré à "protubérances". Cartes de conductance différentielle 2D mesurées à différentes énergies et à 300 mK.

D'autre part, les états de Shiba isolés dans la Fig. 25 (points rouges dans le domaine moléculaire), apparaissant à des énergies bien définies, sont interprétés comme étant du à la présence de molécules non couplées aux autres qui ne peut pas participer à la formation d'une

bande de Shiba. Il est intéressant de noter que les molécules donnant lieu à des états de Shiba isolés peuvent être facilement identifiées à partir de l'image topographique STM car elles ont une apparence plus brillante par rapport aux autres molécules (comparer Fig. 25b et Fig. 25a). Pour conclure, la figure 26 montre plusieurs cartes de conductance différentielle 2D mesurées à différentes énergies, révélant l'effet des MnPcs sur la supraconductivité du film de Pb. Cette figure révèle clairement que la caractéristique "de bord" a sa propre dispersion d'énergie, différente de celui des autres régions, et reste toujours liée au bord du domaine moléculaire. Des expériences supplémentaires sont nécessaires pour confirmer ce nouveau résultat. En particulier, il est très important de reproduire des conditions similaires à celles présentées dans cette section, éventuellement avec des domaines moléculaires plus grands. D'autre part, des calculs théoriques sont nécessaires pour explorer les détails physiques derrière ce système et pour savoir si une transition topologique peut réellement être induite. D'après nos résultats préliminaires, il semble que nous sommes dans un régime de couplage faible avec J et K négatifs. Calculs théoriques précédents ont prédit l'existence des phases topologiques dans le cas d'états de Shiba faiblement couplés en supposant que $J > 0$ et $K = 0$ (mais l'interaction non magnétique est négligée).

Conclusions

Dans cette thèse, j'ai présenté les effets structurels et électroniques de l'interaction entre des aimants moléculaires (MnPcs), et des systèmes supraconducteurs 2D (monocouche de Pb/Si(111) et 3 ML de Pb/Si(111)) afin d'ingénierie de la supraconductivité topologique.

Dans le cas de la monocouche de plomb, l'objectif était d'utiliser la structure particulière de la phase $\sqrt{7} \times \sqrt{3}$-Pb, présentant des domaines striés, comme surface modèle pour obtenir des chaînes moléculaires linéaires auto-assemblées avec un ordre magnétique éventuellement couplé au substrat supraconducteur. Cependant, les expériences ont révélé des effets secondaires inattendus et intéressants de l'adsorption moléculaire. En particulier, le dépôt d'une quantité infime de MnPcs ($\sim$0,18 molécules/100 nm^2) sur la monocouche de Pb induit une transition de phase structurelle macroscopique. Une telle transition de phase abrupte induite par des molécules diluées n'a jamais été observée jusqu'à présent. J'ai proposé un mécanisme possible derrière cet effet dans lequel l'adsorption moléculaire pourrait affecter certaines des liaisons chimiques entre les atomes de Pb et le substrat de silicium responsables de la stabilité de la phase $\sqrt{7} \times \sqrt{3}$-Pb. Simultanément, il a été proposé que les MnPc donnent une charge électronique à la surface du plomb augmentant la contrainte de traction dans le film de plomb. La combinaison de l'affaiblissement de la liaison et de l'augmentation de la contrainte de

traction peut être la force motrice de la contraction de la couche de plomb et donc de la reconstruction de surface. De plus, j'ai observé que l'auto-assemblage moléculaire au-dessus de la monocouche de Pb est très différent de celui observée sur des films de plus épais. En particulier, l'auto-assemblage carré des aimants moléculaires généralement observé sur des surfaces métalliques est fortement frustré, et les molécules restent isolées ou forment tout au plus des structures à trimère reflétant la symétrie 3 du substrat. Ce nouveau comportement est probablement dû à la forte interaction molécule-substrat prévalant sur celle entre molécules. Des calculs DFT abordant ce problème sont en cours au moment de la rédaction de cette thèse.

Pour éviter ce comportement, nous avons également étudié un système quasi-2D consistant en une tricouche de Pb sur Si(111). Étant un système métastable, sa croissance est particulièrement difficile à contrôler. Une analyse minutieuse des motifs de moiré observées dans les images STM m'a permis de déterminer la présence de deux structures très différentes coexistant sur le même échantillon. J'ai proposé qu'à une petite couverture de Pb, c'est-à-dire en présence d'îlots de Pb déconnectés, il n'y a qu'un seul type de structure consistant en îlots de Pb alignés avec le substrat de silicium ou tout au plus légèrement tournées (moins de 5°). Dans cette structure, les atomes de Pb sont proches des positions du Pb(111) bulk avec un paramètre de maille de a_{Pb}=3.5 Å. D'autre part, à plus forte couverture, c'est-à-dire en présence d'un film continu, le système se divise en deux phases occupant différentes terrasses. Le premier type de terrasse a une structure similaire à celle observée pour les îlots déconnectés. Plus intéressant, le second type de terrasse révèle une nouvelle structure constituée de films de plomb fortement tournés par rapport au substrat de silicium (30°). De plus, j'ai proposé que les atomes de Pb dans cette nouvelle structure soient légèrement compressés par rapport aux positions du Pb(111) bulk avec un paramètre de maille de a_{Pb} $\sim$3.46 Å. Contrairement au cas de la monocouche, sur le système quasi-2D des tricouches de plomb, un auto-assemblage carré d'aimants moléculaires est récupéré.

Afin d'examiner la contribution électronique aux motifs de moiré observés dans ce système, j'ai effectué des expériences sur des îlots tricouches de Pb/Si(111). Le confinement vertical existant dans ce système conduit à l'existence d'États à puits quantiques (QWS). Les mesures de ces états ont révélé que la densité d'états d'électrons confinés et leur énergies sont modulées par la corrugation de moiré observée dans les images STM. L'observation expérimentale de QWS sur des îlots présentant différentes motifs de moiré et la comparaison avec des calculs disponibles dans la bibliographie m'ont permis de corroborer la forte corrélation entre les modulations spatiales des énergies QWS et la structure interne des îlots elles-mêmes (en particulier la structure de l'interface Pb/Si(111)). En conclusion, le motif de

moiré observé dans les images STM des tricouches de plomb pourrait être considérée comme le résultat d'une interaction complexe entre les effets de relaxation structurelle et les effets électroniques. Pour cette raison, un modèle théorique raffiné incluant toute la physique du système (le substrat, la séquence d'empilement, la relaxation, le couplage spin-orbite, etc.) sont hautement souhaitables pour mieux comprendre les propriétés intrigantes de ce système.

Les expériences menées dans l'état supraconducteur à 300 mK ont révélé que, de manière générale, le gap supraconducteur n'est pas affecté de manière dramatique par les différences structurelles existant entre îlots ayant différentes motifs de moiré (séquence d'empilement et rotations par rapport au substrat de silicium (moins de 5°)). D'autre part, j'ai pu détecter de petites fluctuations spatiales des amplitudes des pics de cohérence liées avec le motif de moiré. Sur la base d'observations précédentes d'un comportement similaire des pics de cohérence sur la monocouche de Pb, j'ai proposé que cet effet soit corrélé aux déformations structurelles périodiques sous-jacentes un motif de moiré. En d'autres termes, les motifs de moiré agissent comme un potentiel périodique de désordre affectant le couplage électron-phonon de manière périodique et ainsi aussi la cohérence de l'état supraconducteur sur des échelles de longueur beaucoup plus courtes que la longueur de cohérence supraconductrice. Ce résultat intrigant révèle la présence de physique de basse dimensionnalité dans les îlots tricouches de plomb observées auparavant uniquement dans des systèmes purement 2D. Les expériences STS avec une pointe supraconductrice ont également permis de détecter pour la première fois la présence de supraconductivité à caractère multibande dans les îlots tricouches et 5 monocouches de Pb/Si(111).

Dernier mais non le moindre, j'ai étudié l'interaction magnétique entre MnPcs et la supraconductivité des îlots tricouches Pb/Si(111). Dans tous les cas, il était très difficile de réaliser des expériences STS car la mesure elle-même induisait des modes de vibrations moléculaires qui conduisait au déplacement des molécules. Malgré cela, j'ai pu extraire des informations intéressantes dans le cas de molécules isolées. Les données expérimentales montrent que la force du couplage dépend de manière cruciale du site d'adsorption comme déjà observé précédemment pour les mêmes molécules déposées sur des substrats de Pb(111) bulk. Fait intéressant et contrairement à ce qui a été observé sur des substrats de Pb bulk, les états de Shiba induits par des MnPc isolés se trouvent toujours près du bord du gap et avec la même asymétrie des pics correspondants. Sur la base d'hypothèses simples sur le système, j'ai interprété les résultats expérimentaux en considérant que les MnPc sont toujours faiblement couplés aux îlots supraconductrices de Pb suggérant des paramètres négatifs pour J et K. Dans le cas de domaines 2D auto-organisés de MnPcs sur des tricouches de plomb, malgré

la présence massive de molécules sur l'échantillon induisant un remplissage du gap, une signature spectroscopique intra-gap située au bord d'un domaine moléculaire pourrait être lié à des effets de supraconductivité non triviale.

En conclusion, l'objectif principal de cette thèse était d'étudier la nature de l'interaction des MnPc déposés sur des films très minces de Pb/Si(111) et d'essayer de comprendre les conditions conduisant à un couplage favorable pour induire une transition topologique. Tous les résultats originaux énumérés ci-dessus montrent que les interactions entre molécules et substrat sont très complexes et impliquent des facettes non triviales. L'observation intéressante de la caractéristique spectroscopique de "bord" sur un îlot 2D d'aimants moléculaires auto-assemblés ouvre la voie à de futures études de ce système. D'autre part, maintenant que les données spectroscopiques sur des aimants moléculaires isolés (MnPcs) sur des îlots tricouches de plomb ont été obtenues, une modélisation ab-initio qui comprend l'interaction d'échange comme aussi le couplage spin-orbite serait hautement souhaitable. Cela aiderait alors à fournir des paramètres raisonnables permettant de modéliser le couplage correct des états de Shiba dans des auto-assemblages moléculaires 2D sur des tricouches de Pb/Si(111). Etant donné que des phases topologiques peuvent être formées dans ces conditions, cela clarifierait la gamme expérimentale de paramètres sous lesquels ceux-ci pourraient être observés.